UNIVERSIDAD POLITÉCNICA DE MADRID
ESCUELA TÉCNICA SUPERIOR DE INGENIEROS DE TELECOMUNICACIÓN

ANALYSIS AND DESIGN OF MULTIPLIERS AND MIXERS VIA MONTE CARLO MODELLING AT THZ BANDS

ANÁLISIS Y DISEÑO DE MULTIPLICADORES Y MEZCLADORES MEDIANTE EL MÉTODO DE MONTE CARLO EN LA BANDA DE THZ

TESIS DOCTORAL

Diego Pardo Santos
Licenciado en Física

2014

DEPARTAMENTO DE SEÑALES, SISTEMAS Y RADIOCOMUNICACIONES
ESCUELA TÉCNICA SUPERIOR DE INGENIEROS DE TELECOMUNICACIÓN

UNIVERSIDAD POLITÉCNICA DE MADRID

ANALYSIS AND DESIGN OF MULTIPLIERS AND MIXERS VIA MONTE CARLO MODELLING AT THZ BANDS

ANÁLISIS Y DISEÑO DE MULTIPLICADORES Y MEZCLADORES MEDIANTE EL MÉTODO DE MONTE CARLO EN LA BANDA DE THZ

TESIS DOCTORAL

Autor:

Diego Pardo Santos

Licenciado en Física

Directores:

Jesús Grajal de la Fuente

Profesor Titular del Dpto. de Señales Sistemas y Radiocomunicaciones
Universidad Politécnica de Madrid

Susana Pérez Santos

Profesora Titular del Dpto. de Física Aplicada
Universidad de Salamanca

2014

TESIS DOCTORAL

ANALYSIS AND DESIGN OF MULTIPLIERS AND MIXERS VIA MONTE CARLO MODELLING AT THZ BANDS

ANÁLISIS Y DISEÑO DE MULTIPLICADORES Y MEZCLADORES MEDIANTE EL MÉTODO DE MONTE CARLO EN LA BANDA DE THZ

AUTOR: Diego Pardo Santos
DIRECTORES: Jesús Grajal de la Fuente
Susana Pérez Santos

Tribunal nombrado por el Mgfco. y Excmo. Sr. Rector de la Universidad Politécnica de Madrid, el día __ de _____ de 2014.

PRESIDENTE: Viktor Krozer

SECRETARIO: Mariano Barba Gea

VOCAL: Mario Fernández Pantoja

VOCAL: Javier Mateos López

VOCAL: Peter Huggard

SUPLENTE: Javier Gismero Menoyo

SUPLENTE: José Luis Vázquez Roy

Realizado el acto de defensa y lectura de la Tesis el día __ de _____ de 2014, en la E.T.S. de Ingenieros de Telecomunicación, Madrid.

Calificación:

EL PRESIDENTE LOS VOCALES

EL SECRETARIO

Acknowledgment

Resumen

La región del espectro electromagnético comprendida entre 100 GHz y 10 THz alberga una gran variedad de aplicaciones en campos tan dispares como la radioastronomía, espectroscopía molecular, medicina, seguridad, radar, etc. Los principales inconvenientes en el desarrollo de estas aplicaciones son los altos costes de producción de los sistemas trabajando a estas frecuencias, su costoso mantenimiento, gran volumen y baja fiabilidad. Entre las diferentes tecnologías a frecuencias de THz, la tecnología de los diodos Schottky juega un importante papel debido a su madurez y a la sencillez de estos dispositivos. Además, los diodos Schottky pueden operar tanto a temperatura ambiente como a temperaturas criogénicas, con altas eficiencias cuando se usan como multiplicadores y con moderadas temperaturas de ruido en mezcladores. El principal objetivo de esta tesis doctoral es analizar los fenómenos físicos responsables de las características eléctricas y del ruido en los diodos Schottky, así como analizar y diseñar circuitos multiplicadores y mezcladores en bandas milimétricas y submilimétricas.

La primera parte de la tesis presenta un análisis de los fenómenos físicos que limitan el comportamiento de los diodos Schottky de GaAs y GaN y de las características del espectro de ruido de estos dispositivos. Para llevar a cabo este análisis, un modelo del diodo basado en la técnica de Monte Carlo se ha considerado como referencia debido a la elevada precisión y fiabilidad de este modelo. Además, el modelo de Monte Carlo permite calcular directamente el espectro de ruido de los diodos sin necesidad de utilizar ningún modelo analítico o empírico. Se han analizado fenómenos físicos como saturación de la velocidad, inercia de los portadores, dependencia de la movilidad electrónica con la longitud de la epicapa, resonancias del plasma y efectos no locales y no estacionarios. También se ha presentado un completo análisis del espectro de ruido para diodos Schottky de GaAs y GaN operando tanto en condiciones estáticas como variables con el tiempo. Los resultados obtenidos en esta parte de la tesis contribuyen a mejorar la comprensión de la respuesta eléctrica y del ruido de los diodos Schottky en condiciones de altas frecuencias y/o altos campos eléctricos. También, estos resultados han ayudado a determinar las limitaciones de modelos numéricos y analíticos usados en el análisis de la respuesta eléctrica y del ruido electrónico en los diodos Schottky.

La segunda parte de la tesis está dedicada al análisis de multiplicadores y mezcladores mediante una herramienta de simulación de circuitos basada en la técnica de balance armónico. Diferentes modelos basados en circuitos equivalentes del dispositivo, en las ecuaciones de arrastre-difusión y en la técnica de Monte Carlo se han considerado en este análisis. El modelo de Monte Carlo acoplado a la técnica de balance armónico se ha usado como referencia para evaluar las limitaciones y el rango de validez de modelos basados en circuitos equivalentes y en las ecuaciones de arrastre-difusión para el diseño de circuitos multiplicadores y mezcladores. Una notable característica de esta herramienta de simulación es que permite diseñar circuitos Schottky teniendo en cuenta tanto la respuesta eléctrica como el ruido generado en los dispositivos. Los resultados de las simulaciones presentados en esta parte de la tesis, tanto para multiplicadores como mezcladores, se han comparado con resultados experimentales publicados en la literatura. El simulador que integra el modelo de Monte Carlo con la técnica de balance armónico permite analizar y diseñar circuitos a frecuencias superiores a 1 THz.

Abstract

The terahertz region of the electromagnetic spectrum (100 GHz-10 THz) presents a wide range of applications such as radio-astronomy, molecular spectroscopy, medicine, security and radar, among others. The main obstacles for the development of these applications are the high production cost of the systems working at these frequencies, high maintenance, high volume and low reliability. Among the different THz technologies, Schottky technology plays an important rule due to its maturity and the inherent simplicity of these devices. Besides, Schottky diodes can operate at both room and cryogenic temperatures, with high efficiency in multipliers and moderate noise temperature in mixers. This PhD. thesis is mainly concerned with the analysis of the physical processes responsible for the characteristics of the electrical response and noise of Schottky diodes, as well as the analysis and design of frequency multipliers and mixers at millimeter and submillimeter wavelengths.

The first part of the thesis deals with the analysis of the physical phenomena limiting the electrical performance of GaAs and GaN Schottky diodes and their noise performance. To carry out this analysis, a Monte Carlo model of the diode has been used as a reference due to the high accuracy and reliability of this diode model at millimeter and submillimter wavelengths. Besides, the Monte Carlo model provides a direct description of the noise spectra of the devices without the necessity of any additional analytical or empirical model. Physical phenomena like velocity saturation, carrier inertia, dependence of the electron mobility on the epilayer length, plasma resonance and nonlocal effects in time and space have been analysed. Also, a complete analysis of the current noise spectra of GaAs and GaN Schottky diodes operating under static and time varying conditions is presented in this part of the thesis. The obtained results provide a better understanding of the electrical and the noise responses of Schottky diodes under high frequency and/or high electric field conditions. Also these results have helped to determine the limitations of numerical and analytical models used in the analysis of the electrical and the noise responses of these devices.

The second part of the thesis is devoted to the analysis of frequency multipliers and mixers by means of an in-house circuit simulation tool based on the harmonic balance technique. Different lumped equivalent circuits, drift-diffusion and Monte Carlo models have been considered in this analysis. The Monte Carlo model coupled to the harmonic balance technique has been used as a reference to evaluate the limitations and range of validity of lumped equivalent circuit and drift-diffusion models for the design of frequency multipliers and mixers. A remarkable feature of this reference simulation tool is that it enables the design of Schottky circuits from both electrical and noise considerations. The simulation results presented in this part of the thesis for both multipliers and mixers have been compared with measured results available in the literature. In addition, the Monte Carlo simulation tool allows the analysis and design of circuits above 1 THz.

Contents

List of Figures

List of Tables

Acronyms and Abbreviations

AlGaAs	Aluminum Gallium Arsenide
ALMA	Atacama Large Millimeter Array
ALP	Alpha Industries Inc.
APEX	Atacama Pathfinder Experiment
AM	Analytical Model
BTE	Boltzmann Transport Equation
CAD	Computer Aided Design
COBE	Cosmic Background Explorer
CUT	Chalmers University of Technology
DD	Drift Diffusion
DDHB	DD model coupled to the Harmonic Balance technique
DD_0	Drift Diffusion with constant low field mobility
DD_0HB	DD_0 coupled to the Harmonic Balance technique
DD_e	Enhanced Drift Diffusion
DD_eHB	DD_e coupled to the Harmonic Balance technique
DSB	Double Side Band
ET	Energy Transport
GaAs	Gallium Arsenide
GaN	Galium Nitride
Ge	Germanium
GHz	Gigahertz
HB	Harmonic Balance
HBT	Heterojunction Bipolar Transistor
HBV	Heterostructure Barrier Varactor
HD	Hydrodynamic
HEB	Hot Electron Bolometer
HEMT	High Electron Mobility Transistor

HFSS	High Frequency Structure Simulator
HP	Hybrid Plasma
IF	Intermediate Frequency
IMPATT	Impact Ionization Avalanche Transit-Time
InP	Indium Phosphide
InSb	Indium Antimonide
IR	Infrared
JPL	Jet Propulsion Laboratory
LEC	Lumped Equivalent Circuit
$\mathrm{LEC}_{R_{s,dc}}$	Lumped Equivalent Circuit based on the dc series resistance $R_{s,dc}$
$\mathrm{LEC}_{R_{s,dc}}$HB	$\mathrm{LEC}_{R_{s,dc}}$ model coupled to the Harmonic Balance technique
$\mathrm{LEC}_{R_{s,R_sxC_j(0)}}$	Lumped Equivalent Circuit where the series resistance is obtained from the $R_sxC_j(0)$ rule
$\mathrm{LEC}_{R_{s,R_sxC_j(0)}}$HB	$\mathrm{LEC}_{R_{s,R_sxC_j(0)}}$ model coupled to the Harmonic Balance technique
$\mathrm{LEC}_{R_s(t)}$	Lumped Equivalent Circuit based on the time varying series resistance $R_s(t)$
$\mathrm{LEC}_{R_s(t)}$HB	$\mathrm{LEC}_{R_s(t)}$ model coupled to the Harmonic Balance technique
$\mathrm{LEC}_{R_sLC(t)}$	Lumped Equivalent Circuit based on the time varying elements series resistance $R_s(t)$, inductance L(t) and capacitance C(t) for the undepleted epilayer and the substrate of the Schottky diode
$\mathrm{LEC}_{R_sLC(t)}$HB	$\mathrm{LEC}_{R_sLC(t)}$ model coupled to the Harmonic Balance technique
LERMA	Laboratoire d'Etude du Rayonnement de la Matière en Astrophysique
LNA	Low Noise Amplifier
LO	Local Oscillator
MC	Monte Carlo
MCHB	MC model coupled to the Harmonic Balance technique
MMIC	Monolithic Microwave Integrated Circuit
NDT	Non-Destructive Testing
NHO	Nonharmonic Oscillation
QCL	Quantum Cascade Laser
RAL	Rutherford Appleton Laboratory
RC	Returning Carrier
RF	Radio Frequency
SET	Single Electron Transistor
Si	Silicon
SIN	Superconductor-Insulator-Normal junction

SIS	Superconductor-Insulator-Superconductor junction
SHP	Subharmonically-Pumped
SSB	Single Side Band
THz	Terahertz
TUD	Technical University of Darmstadt
TUNNETT	Tunnel Injection Transit-Time
UMi	University of Michigan
UMS	United Monolithic Semiconductors
UVa	University of Virginia
VDI	Virginia Diodes Inc.
YBCO	Yttrium Barium Copper Oxide

List of Symbols

Re[.]	Real part of the argument
Im[.]	Imaginary part of the argument
q	Electron charge (q=1.60217646x10^{-19} C)
ε_0	Dielectric permittivity of free space (ε_0= 8.8541878176x10^{12} F/m)
ε_r	Relative dielectric permittivity of the semiconductor
k_B	Boltzmann's constant (k_B= 1.3806503x10^{-23} J/K)
T	Lattice temperature
R_s	Series resistance of the Schottky diode
$R_{s,dc}$	Series resistance of the Schottky diode measured when the epilayer is undepleted
$R_s(t)$	Series resistance of the Schottky diode assumed time varying
$< R_s >$	Series resistance of the Schottky diode obtained averaging $R_s(t)$
R_j	Junction resistance of the Schottky diode
$R_{spr,0}$	Spreading resistance of the substrate of the Schottky diode under low field and low frequency conditions
Z_{spr}	Spreading impedance
δ_s	Skin depth
Z_{skin}	Skin impedance
C_j	Junction capacitance of the Schottky diode
$C_j(0)$	Zero voltage junction capacitance of the Schottky diode
I_0	Reverse saturation current
η	Ideality factor of the Schottky junction
w_{depl}	Width of the depletion region (or space charge region)
A	Anode area of the Schottky diode
E_0	Local vacuum level
E_C	Conduction band energy
E_F	Fermi level

E_V	Valance band energy
ϕ_s	Work function of the semiconductor
ϕ_m	Work function of the metal
χ_s	Electronic affinity
ϕ_b	Schottky barrier height
V_{bi}	Schottky diode built-in potential
α_{np}	Non-parabolicity coefficient
m^*	Effective mass for electrons in the semiconductor
N_c	Effective density of states in the conduction band
N_v	Effective density of states in the valence band
N_e	Doping concentration in the epitaxial layer of the Schottky diode
N_s	Doping concentration in the substrate of the Schottky diode
L_e	Length of the epitaxial layer of the Schottky diode
L_s	Length of the substrate of the Schottky diode
$\mu_{e,0}$	Low field electron mobility in the epitaxial layer of the Schottky diode
$\mu_{s,0}$	Low field electron mobility in the substrate of the Schottky diode
μ_{ac}	AC electron mobility
$\sigma_{e,0}$	Low field conductivity in the epitaxial layer of the Schottky diode
$\sigma_{s,0}$	Low field conductivity in the substrate of the Schottky diode
$\omega_{s,e}$	Scattering frequency in the epitaxial layer of the Schottky diode
$\omega_{s,s}$	Scattering frequency in the substrate of the Schottky diode
$\omega_{s,eff}$	Effective scattering frequency in the epitaxial layer of the Schottky diode
$\omega_{d,e}$	Dielectric relaxation frequency in the epitaxial layer of the Schottky diode
$\omega_{d,s}$	Dielectric relaxation frequency in the substrate of the Schottky diode
ω_{pe}	Angular plasma frequency of the epitaxial layer of the Schottky diode
ω_{ps}	Angular plasma frequency of the substrate of the Schottky diode
ω_c	Angular cut-off frequency
f_{pe}	Plasma frequency of the epitaxial layer of the Schottky diode
f_{ps}	Plasma frequency of the substrate of the Schottky diode
f_c	Cut-off frequency
$f(\mathbf{r},\mathbf{k},t)$	Distribution function of the carriers
$n(\mathbf{r},t)$	Electron concentration
$\varepsilon_n(\mathbf{r},t)$	Density of kinetic electron energy
$\varepsilon_{n,th}$	Density of kinetic electron energy in thermal equilibrium with the lattice

$\xi(\mathbf{k})$	Kinetic energy of a particle in the energy band with moment $\mathbf{k}$
ε	Average electron energy
ε_{th}	Average electron energy in thermal equilibrium with the lattice
$\mathbf{F}_{\varepsilon_n}$	Density of energy flux
$\mathbf{J}_n$	Current density due to electrons
$\mathbf{v}_d$	Average velocity of the electrons
ϕ	Electrostatic potential
$\tau_m(\varepsilon)$	Momentum relaxation time
$\tau_\varepsilon(\varepsilon)$	Energy relaxation time
τ_R	Characteristic time to return to the neutral region of the epilayer for those electrons which have crossed the depletion region and come back to the neutral region of the epilayer.
τ_F	Characteristic time to cross the depletion region for those electrons which have the lowest kinetic energy necessary to reach the Schottky contact.
τ_g	Characteristic time of intergroup exchange
D_n	Electron diffusion constant
D_p	Hole diffusion constant
$S_I(f)$	Spectral density of the current fluctuations in the Schottky diode
$S_V(f)$	Spectral density of the voltage fluctuations at the terminals of the Schottky diode
f_{HP}	Frequency of the hybrid plasma resonance of the current noise spectra of the Schottky diode
f_{RC}	Frequency of the returning carrier resonance of the current noise spectra of the Schottky diode
α_H	The Hooge parameter
V_{bias}	Bias voltage
P_{av}	Available power
P_{del}	Delivered power
P_{in}	Input power delivered to the circuit
P_{out}	Output power delivered to the external circuit
$P_{d,in}$	Input power delivered to the diode
$P_{d,out}$	Output power delivered by the diode
P_{RF}	RF power
P_{LO}	LO power
P_{IF}	IF power
f_{RF}	RF frequency
f_{LO}	LO frequency

f_{IF}	IF frequency
Δf	Frequency bandwidth
η_d	Conversion efficiency of the diode (frequency multipliers)
η_c	Conversion efficiency of the circuit (frequency multipliers)
α	Coupling factor of the input power
β	Coupling factor of the output power
Z_d	Impedance of the Schottky diode
Z_c	Impedance of the circuit
$Z_{d,SS}$	Small signal impedance of the Schottky diode
L_d	Conversion loss of the Schottky diode
L_{qo}	Losses in the quasy-optical parts of the systems
L_{rf}	Losses in the feed-horn, filters and mixer waveguides
L_{if}	Resistive and reflected losses in the IF matching circuit
L_{mixer}	Conversion loss of the frequency mixer
L_{rec}	Conversion loss of the receiver
C_p	Parasitic capacitance of the Schottky diode
T_d	Equivalent input noise temperature of the Schottky diode
$T_{n,diode}$	Equivalent noise temperature of the Schottky diode
T_{mixer}	Equivalent input noise temperature of the mixer
T_{rec}	Equivalent input noise temperature of the receiver
dt	Time step used in the Monte Carlo simulations
dx	Size of the spatial mesh in the Monte Carlo simulations

Part I

INTRODUCTION

Chapter 1

Introduction

1.1 The THz region. Applications and technology

The Terahertz (THz) region, which lies between the microwave and the infrared regions of the electromagnetic spectrum (loosely defined from 100 GHz to 10 THz [Cro05]), is in the interface of the electronics and optics, see Fig. 1.1. The development of terahertz technology has been mainly driven by applications in astronomy and space science [Cro05, Sie07, Cha11a]. Today, there are several advanced radio telescopes at submillimeter frequencies (300 GHz-3 THz) devoted to explore the Universe: the ALMA interferometer project [Woo09], the APEX telescope [Kum05], the Herschel Space Observatory [Doy09] and COBE [Ric07].

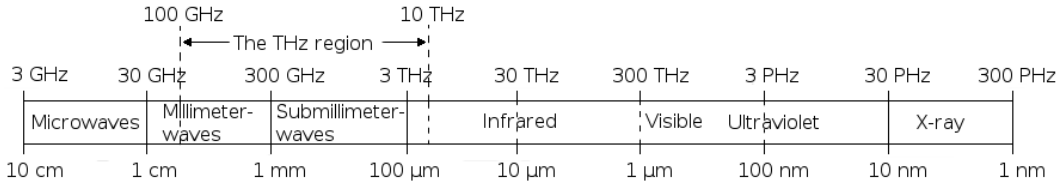

Figure 1.1: The electromagnetic spectrum.

In addition, the development of the THz technology is enabling THz research to be applied in many more sectors: atmospheric pollution monitoring [Ton07]; identification and classification of planetary atmospheric gases and interstellar dust regions [Sie07]; DNA sequencing and images acquisition of in vivo tissues for medical and biological studies [Sie04, Tay11]; food inspection [Yan06]; imaging for authentication and characterization of artworks [Sec13]; 3D imaging required for material non-destructive testing (NDT) in quality compliance industrial procedures [Red06] and for stand-off detection of weapons or explosives in security check points [App07].

A general overview will be given in following sections of the different THz technologies that have arisen in the last decades. They broadly fall into two categories: sources and detectors.

1.1.1 Sources

Fig. 1.2 shows a graph of output power versus frequency for typical terahertz sources [Cro05, Mae10b]. Below 100 GHz, the most common ways to generate power are amplifiers, oscillators, p-i-n diode comb generators and similar devices [Sie02, Cro05, Cha11a]. Recent development of Indium-Phosphide (InP) and Galium-Nitride (GaN) high electron mobility transistors (HEMT) and heterojunction bipolar transistors (HBT) has shown that these devices are a future key for the design

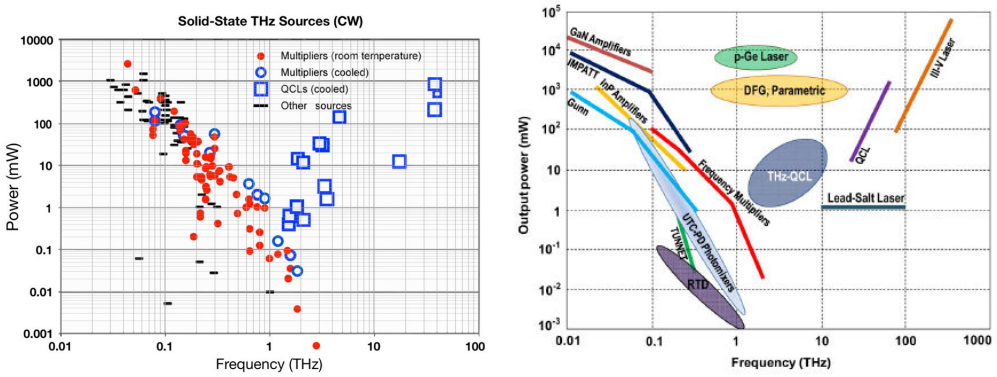

(a) (b)

Figure 1.2: Terahertz gap with respect to source technology. Quantum cascade lasers (cryogenic temperatures) are progressing downward from higher frequencies, while electronic technology is progressing upward. Frequency multipliers dominate other electronic devices above about 150 GHz. IMPACTT diode stands for impact ionizaton avalanche transist-time, MMIC stands for microwave monolithic integrated circuit, and TUNNET stands for tunnel injection transit time. (a) Adapted from [Cro05]. New data added by Maestrini *el al.*, December 2009. Reprinted from [Mae10b]. (b) Reprinted from [Cha11a].

of systems up to submillimeter-wave bands [Rad07, Sam08, Sam11, Seo11, Ree12]. Above 10 THz, gas lasers, Quantum Cascaded Lasers (QCLs) and other optical devices are available [Sie02, Cro05, Cha11a]. Summarizing, there are three major approaches to develop sources in the THz region: Optical THz generation, THz QCLs, and solid-state electronic devices.

Optical THz generation considers methods as ultrafast photocurrent in a photoconductive switch or semiconductor using electric field carrier acceleration or the photo-Dember effect, and nonlinear optical effects such as optical rectification, difference-frequency generation or optical parametric oscillation [Ton07]. Other two methods for optical THz generation are photomixing and IR-pumped gas lasers. Photomixing is a promising technique for THz generation that consists of a high-speed photoconductive device driven with two frequency offset lasers. The internal photoelectric effect generates an electrical photocurrent at the difference frequency. The resultant current generates THz power by connecting it to a suitable load [Bro03]. Photomixers offer lower powers than other solutions: 1.8 mW at 252 GHz [Pey13], and up to 24 μW at 914 GHz [Ren08]. Other important optical devices are IR-pumped gas lasers, which are usually based on grating CO_2 pump lasers (20-100 W) injected into low-pressure flowing-gas cavities that lase at THz frequencies [Sie02]. Power between 10-20 mW is commonly obtained in the region between 500 GHz and 3 THz [Sie02]. However, not all frequencies in that range can be covered with these devices because a strong emission line is necessary at the desired frequency to obtain enough power at such frequency. As an example, methanol has a strong emission line at 2522.78 GHz.

Terahertz QCLs are a class of unipolar semiconductor lasers that use intersubband transitions between electronic states of a GaAs/AlGaAs quantum well superlattice that is engineered to produce the desired wavelength of emitted radiation. The problem of QCL is the need for cryogenic cooling below 4 THz and some other issues like frequency stability, tuning bandwidth and lifetime [Cro05, Cha11a]. State-of-the-art THz-QCLs work at a lowest frequency of 0.68 THz and a temperature of 225 K with external magnetic field, and a power of 140 mW and 250 mW at continuous wave and pulsed operation, respectively [Lee07, Wad09]. QCLs at 4.4 THz have been demonstrated with peak power 138 mW at temperatures of 10 K [Wil06].

Among the different technologies available to build THz sources, solid-state electronic sources based on planar Gallium Arsenide (GaAs) Schottky technology play a crucial rule. Frequency multipliers based on Schottky diodes use the reactive and the resistive nonlinearities of the device to generate harmonics of the input signal [Cro05, Cha11a]. This technology enables build-

Table 1.1: Some representative examples of the state-of-the-art of SIS, HEB and Schottky mixer technologies. SIS and HEB mixers are working at cryogenic temperature while Schottky mixers are operating at room temperature.

Technology	Design	RF freq. (GHz)	LO power, (μW)	T_{noise}^{DSB}, (K)	Year	Ref.
SIS	Balanced	246	∼0.25-2.5	33	2014	[Koo14]
	Balanced	520	∼0.25-2.5	61	2014	[Koo14]
	Two junctions	800-960		300	2008	[Jac06]
	Two junctions	1030-1150		500	2008	[Jac06]
	Two junctions	870-1120	∼1	353	2009	[Kar07, Kar09]
HEB		1630	∼0.03	700	2007	[Gao07]
		2740	∼0.1	965	2012	[Bou12]
		2840	∼0.3	1050	2007	[Gao07]
		3100		2100	2012	[Shi12]
		3420	0.29	2100	2008	[Kho08]
Schottky	Subharmonic	300-360	$\sim 3x10^{3}$	700	2005	[Tho05]
	Balanced	520-590	$\sim 1.5x10^{5}$	2200	2010	[Sch10]
	Balanced	835-900	$\sim 1x10^{5}$	2300	2010	[Tho10b, Tho10c]
	Single-ended	2500	$\sim 5x10^{5}$	9000	1999	[Sie99]
	Single-ended	5000	$\sim 1x10^{5}$	70000	1996	[Bet96]

ing compact, robust and high efficiency frequency multipliers capable of reaching the THz region [Sie02, Cro05, Mae10b]. Schottky diodes can operate at room temperatures as well as cryogenic temperatures with enhanced performance. Besides, due to the maturity of this technology, Schottky diodes can be produced with low cost and high reliability. At room temperature, the local oscillator power provided by these sources range from 48 mW at 300 GHz [Mae08, Mae10a] to 1 mW at 900 GHz [Mae10a] and 18 μW at 2.75 THz [Mae12].

Other solid-state devices such as Heterostructures Barrier Varactors (HBVs) are also used in frequency multipliers. They are symmetric devices, composed of a series of high band-gap undoped or slightly undoped semiconductor (barriers), placed between two low band-gap highly doped modulation layers. They constitute an interesting alternative to Schottky diodes as local oscillators because they offer the possibility of stacking various barriers in a single device [Sta06]. However, today, the power and the efficiency provided by the HBVs are lower than that obtained from multiplier chains based on Schottky diodes: 184 mW of output power (efficiency 23 %) at 103 GHz [Mal12, Mal13], 60 mW (efficiency 6.3 %) for a frequency quintupler at 175 GHz [Bry12] and 31 mW (efficiency 7 %) at 282 GHz [Xia07, Vuk12].

1.1.2 Detectors

The detectors at submillimeter wavelengths can be broadly categorized into two distinct sets: coherent detectors and incoherent (direct) detectors. For coherent detection the signal received at submillimeter wavelengths is down-converted to the gigahertz band over a limited bandwidth. The frequency conversion relies on a nonlinear element and a local oscillator (LO). The output or intermediate-frequency (IF) signal can then be further processed using additional electronics. On the other hand, for incoherent detection, the submillimeter-wave photons are directly absorbed by some material, creating either electronic excitations or thermal energy [Cha07, Cha08].

In coherent detectors, to perform the down-conversion in heterodyne receivers, the use of three kind of devices is widely extended: Superconductor-Insulator-Superconductor (SIS) tunnel junction diodes, Hot Electron Bolometers (HEB), and Schottky diodes. The use of one or another technology depends on several factors: The available local oscillator power, the required sensitivity of the application, the operation frequency, and the possibility of cooling the device.

Nowadays, high sensitivity detectors used for submillimeter wave radio astronomy are based on cryogenic SIS and HEB. The current flow mechanism in SIS diodes is based on the photon-assisted

tunneling process [Sie02]. Mixers based on SIS diodes reach quantum noise levels with modest LO power requirements, of the order of μW. Table 1.1 presents some representative examples of the state-of-the-art SIS technology. SIS mixers have an upper operation frequency limit of around 1.4 THz for all niobium junction and somewhat higher for Nb/AlN/NbTiN junctions. This limit is imposed by the reverse photon assisted tunneling process [Zmu07].

HEB mixers are based on extremely small microbridges of niobium, niobium-nitride, niobium-titanium-nitride, aluminum or YBCO that respond thermally to terahertz radiation [Sie02]. Sensitivities are predicted to be only a few times higher than the quantum limit and the required LO power is even lower than for SIS mixers, falling in the 1-100 nW range, see Table 1.1. Operation above 5 THz [Sem00] have been reported for HEB technology.

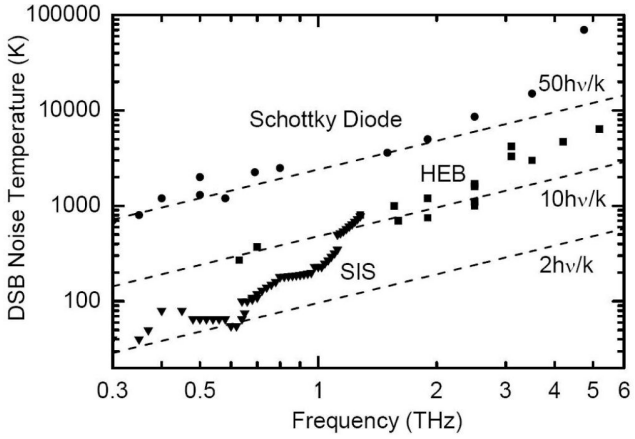

Figure 1.3: DSB noise temperature performance of SIS (▼), HEB (■) and Schottky diode (•) mixers. Also shown are the 2-, 10-, and 50-times quantum noise limit lines for comparison. Reprinted from [Cha08].

Schottky mixers are the technology most used in heterodyne receivers, although they are noisier and require higher LO power than SIS and HEB mixers. Schottky mixers have the advantage over other sensor technologies to work at room temperature as well as cryogenic temperatures for improved noise performance, which make them the technology of choice for long term atmospheric and planetary missions, as well as ground applications (medicine, security, etc.) [Sie02, Mae10b, Cha11a]. Room temperature Schottky technology follows approximately the 50 times quantum noise limit, with LO power requirements of the order of mW, see Table 1.1. Schottky mixers up to 5 THz have been demonstrated, with noise temperature 70000 K [Bet96], although this noise temperature is far from optimum. Fig. 1.3 presents a comparison of the noise temperature of different sensor technologies as a function of the frequency.

With respect to direct detectors, they are becoming popular for applications that do not need high spectral resolutions. The most important room temperature detectors are: Schottky diodes used as square law detectors, conventional bolometers, composite bolometers, microbolometers, acoustic bolometers and fast calorimeters [Sie02]. However, their use is not widely extended due to sensitivity constraints. The most commercially used cooled detectors for THz applications are Si, Ge and InSb composite bolometers and some traditional IR detectors that also respond in the submillimeter wave band. Non-commercially available cooled detectors include transition edge bolometers (based on the change of state of a superconductor), superconductor-insulator-normal (SIN) metal tunnel junction composite bolometers, and, more recently, the quantum dot single photon detector, which uses a cold (50mK) single electron transistor (SET) and a quantum dot in a high magnetic field. The incident photons are coupled into the quantum dot via small dipole antennas [Kom00, Sie02, Cha07].

1.2 Planar Schottky diode technology

Schottky diodes based on GaAs are one of the most important devices for operation at millimeter and submillimeter wavelengths. As the semiconductor technology became more mature, whisker contact Schottky diodes were substituted by planar diodes which replace the fragile whisker with mechanically robust integrated finger [Bis93, Mar01]. While the integration of multiple whisker diodes in a multiplier circuit is very difficult, planar technology allows for multiple anodes on-chip, in a wide variety of configurations. Although the parasitics in planar diodes are not so low as in whisker diodes, they have been reduced to acceptable levels [Bis93, Mar01]. Planar Schottky diodes have been successfully developed at millimeter and submillimeter frequencies by different laboratories.

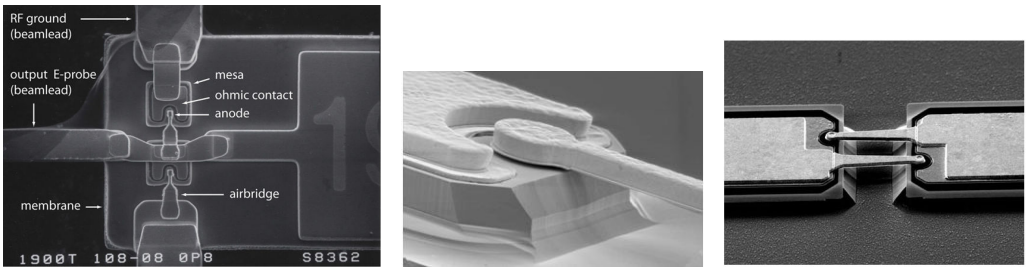

(a) (b) (c)

Figure 1.4: Images of (a) an anti-parallel Schottky diode pair fabricated by *JPL* for a 1.9 THz tripler, (b) a Schottky diode fabricated by *VDI* and (c) an anti-parallel Schottky diode pair fabricated by *RAL*, available on [Mae10b], [Virg] and [Ald08] respectively.

Planar Schottky diodes with state-of-the-art performance and reliability have been provided since 1996 at the University of Virginia [Ali14] now at Virginia Diodes Inc. (*VDI*) [Virg], and later, at the Jet Propulsion Laboratory (*JPL*) [Mar01, Pea11]. In Europe, high quality planar Schottky diodes have been developed by Rutherford Appleton Laboratory (*RAL*) [Ald08, Ald11], the Technical University of Darmstadt (*TUD*) [Sim93] and recently at the Technical University of Chalmers [Dra13] and at the *Laboratoire d'Etude du Rayonnement de la Matière en Astrophysique* (*LERMA*) [Jun08], see Fig. 1.4. The company Advanced Compound Semiconductor Technologies (ACST) GmbH also provides Schottky diodes for application in the THz band. Also the French-German company United Monolithic Semiconductors (*UMS*) [Unit] develops Schottky diodes for applications up to 100 GHz.

1.3 Importance of modelling

Due to the demand for wide-bandwidth frequency multipliers and mixers working above 1 THz, there is a continuous effort to optimize, develop and implement Schottky diode technology. Accurate simulation tools that account for both linear and nonlinear performance are essential for this task.

Generally, the methodology for the design of Schottky based multipliers and mixer is based on the following three-step process [Cha04, Tho05, Mae10b, Cha11a]:

- A harmonic-balance simulator and an analytical model (nonlinear model) of the Schottky diode are used to optimize the doping level and diode dimensions such as the anode and mesa sizes and the number of diodes to be used in the circuit for a given input pump power.
- The embedding circuits are synthesized using a 3D electromagnetic simulator, such as Ansoft-HFSS, to calculate their S-parameters in an iterative procedure. To simplify and speed up the process, the passive circuitry is divided into individual elements giving several S-parameter

matrices. They are then entered into a linear circuit simulator along with the diode impedances obtained from the nonlinear simulator. Most of the impedance matching is accomplished using waveguide and stripline sections, which can be accurately represented in the linear simulator, simplifying their optimization.

- Finally, the nonlinear diode models and the S-parameter matrices of the complete passive circuits obtained from HFSS simulations are recombined in the nonlinear harmonic balance simulator to determine the overall performance.

The design of nonlinear circuits is a complex task, since the performance of the nonlinear devices is defined not only by their inherent characteristics, but also by the embedding circuit. This coupling has to be taken into account by including the device model into a circuit simulator [Hel78a, Fab95, Gra00]. The main problem of the described methodology for THz circuit design is the simplicity of the Schtottky diode models considered in commercial simulators that are unable to reproduce the experimental results without additional empirical parameters. Accurate physics-based modelling of the nonlinear devices has to be considered in the design process to take into account the important physical effects that limit the performance of the devices at high power and/or high frequencies.

Lumped equivalent circuits (LEC) are commonly used to model the performance of the Schottky diode in the design process because of their simplicity and ease of use in commercial CAD tools [Cha78, Cro89, Eri98, Sch01b, Mae10b, Mae12]. However, at terahertz frequencies, frequency dependent effects that can often be neglected at lower frequencies become more important. These effects include velocity saturation, carrier inertia, displacement current in undepleted regions of the diode, plasma oscillations or the nonstationary dynamics of the carriers [Cha78, Ais84, Cro89, Kol92, Jon95, Eas95, Sch95, Lip97, Lip98, Gra00, Sch01b, Sch01a]. To account for these effects in the lumped equivalent circuit models, some empirical rules have been developed. One commonly used is the R_sx$C_j(0)$ rule. In this rule, the series resistance of the diode model, R_s, is calculated using empirical values of the product R_sx$C_j(0)$ that depend on the output frequency, doping concentration and the operation temperature [Eri98, New99, Mae03, Mae05b]. However, the validity of the approximations considered in lumped equivalent circuit models is questionable at millimeter and submillimeter wavelengths because of the large-signal nonstationary high frequency dynamics of carrier transport [Jon95, Eas95, Bha95, Lip97, Lip98, Gra00, Cha11a].

Higher level models based on the different approximations of the Boltzmann Transport equation (BTE) offer higher accuracy and solve some of the limitations of lumped equivalent circuit models. Physics-based drift-diffusion (DD) model [Sel84, Lun00] for Schottky diodes, based on the first two moments of the BTE and the Poisson's equation, assumes that transport parameters such as mobility and diffusion coefficients are determined by local values of the electric field. The velocity saturation, that becomes a limiting effect of the diode performance at input frequencies above 100 GHz [Kol92], is taken into account in the drift-diffusion model by means of a field dependent mobility. This model has been used to analyse physical effects limiting the performance of Schottky diodes like breakdown effect or velocity saturation [Gra00] and also to optimize the performance of Schottky multipliers [Sil10]. However, the drift-diffusion model does not take into account nonstationary characteristics such as carrier heating and velocity overshoot [San89, Lun00, Sch95]. These effects are important in the performance of GaAs nanometric diodes operating at submillimeter wavelengths [Lun00, Lee99].

Other approaches derived from the BTE are the hydrodynamic (HD) and energy transport (ET) models, which are obtained by taking the first three moments of the BTE (conservation of particles, momentum, and energy) [Blo70, San89, Lun00, Hje94, Lee99]. The effects of scattering are described by macroscopic relaxation times [Lun00, Lee99]. In addition to velocity saturation, these approximations model nonstationary effects due to energy and momentum relaxation, that are important at frequencies of the order of the inverse of the energy and momentum relaxation times, above 300 GHz and 1 THz for GaAs semiconductor, respectively [Lun00, Lee99]. Hydrodynamic models have been used to model the performance of Schottky didoes [Hje91, Hje94], analyse hot electron effects [Hje90, Gru93c, Gru93a, Gru93b] and also in the simulation of multipliers [Lee99].

A different approach is the Monte Carlo (MC) method, that is based on the microscopic mod-

elling of the interactions of the charge carriers with the crystal lattice (scattering mechanisms) and the external fields [Fis88, Jac89a, Lun00]. Due to its microscopic nature, this technique provides an accurate description of physical phenomena in the device up to THz frequencies. This technique has been widely used for the simulation of electron transport in semiconductor devices [Maz87, Fis88, Gon91, Gru94b, Bha95, Gon96, Bha97, Mat00, Shi04, Pas07]. Although the Monte Carlo model has been applied to analyse Schottky multipliers -a 200 GHz doubler in [Lip97]-, it was not commonly used for the analysis of nonlinear circuits, because its computational cost is higher compared to simpler models.

1.3.1 Modelling of noise

The most important limitation of Schottky technology for mixers is its high noise, compared with other sensor technology like SIS and HEB, see Fig. 1.3. Hence, the characterization of the noise sources and the accurate modelling of noise in Schottky diodes is a fundamental aspect for the development of this technology.

The noise temperature is the parameter most widely used for the experimental characterization of noise in devices [Zie70, Hel78a]. D. N. Held and A. Kerr developed a theoretical model based on small-signal-large-signal analysis known as conversion matrix formalism to evaluate the conversion loss and the noise temperature in Schottky mixers operating at microwave and millimeter wave bands [Hel78a, Hel78b]. Shot and thermal noise contributions and their correlation properties are modeled with this technique, using simple equivalent circuit models of the diode. Despite of the success of these models, already in 1975, Kerr pointed out that the conventional noise models predict considerably lower noise temperature than those measured [Ker75]. Additional noise mechanisms were proposed to explain the observed discrepancies. They were associated to additional fluctuations in the velocity and the number of carriers due to hot electron, increment of the Schottky junction temperature, intervalley scattering mechanisms and generation-recombination process in the neighborhood of the metal-semiconductor contact [Mat77, Kee83, Jel84, Heg85, Cro87]. Currently, the original conversion matrix in [Ker79a] is commonly used to simulate the noise temperature in the design of Schottky mixers [Sie99, Tho05, Sch07a, Sch10, Tho10b, Tho11]. Although noise analysis with the conversion matrix formalism has being enhanced with the inclusion of hot electron and shallow traps near the Schottky junction [Heg85, Zir86, Cro87, Fab95], it presents important limitations as the operation frequency increases: The accuracy of the noise temperature evaluated with the conversion matrix formalism is limited by the accuracy of the lumped equivalent circuit. Besides, the model for thermal noise is only valid under equilibrium conditions. Although the model of hot electron noise can be integrated in the conversion matrix for out of equilibrium conditions, it depends on parameters that can only be obtained with higher level models like Monte Carlo, or measurements. Additional physical effects become important as the operation frequency and/or the LO power increases, like intervalley transfer effect, that increase the noise level.

Noise can also be analysed with physics-based drift-diffusion or hydrodynamic models using the framework of Langevin's approach and the Green's function technique (impedance field method) [Vli71, Sta98, Shi00, Bon01a]. Some research groups have implemented this method in a drift-diffusion model and it has been used to simulate the noise performance of nonlinear circuits under large-signal conditions [Bon01a, Bon01b, Bon03]. However, the results obtained with this method are affected by the limitations of the drift-diffusion model. For higher order models, the derivation of the Langevin sources for noise analysis and their implementation in numerical simulators is complicated and is under development [Gru93c, Gru94c, Shi99, Bon01a]. A fundamental limitation of these techniques is that they require the knowledge of the spectral performance of the noise sources in the devices.

The Monte Carlo (MC) model presents an interesting alternative to these methods, since it simulates the noise spectral density of the diode in an intrinsic way, due to its microscopic nature. The MC method is recognized as the most rigorous technique for noise investigations since it al-

lows the appropriate correlation functions to be calculated directly from a time averaging over a multi-particle history simulated during a sufficiently long-time interval [Fis88, Lun00, Var94]. It has been widely used to describe the noise features of GaAs Schottky diodes under static conditions [Gon93c, Gon93b, Var94, Gon97, Shi05]. Shot noise, thermal noise and additional noise due to hot electrons and intervalley transitions are inherently simulated with the MC model even under large-signal time varying conditions [Shi03b, Shi04, Per04a, Per04b]. Generation-recombination noise associated to defects introduced during the growth process can also be included in the MC model [Reg90, Per00, Per05]. The 1/f or Flicker noise is very difficult to model with the Monte Carlo method because it appears at very low frequencies and there does not exist a clear model to explain its physical origin [Han75, Hoo76, Zie88, Vli91].

1.4 Objectives and organization of the work

This thesis is mainly concerned with the analysis of the physical processes responsible for the characteristics of the electrical response and noise in Schottky diodes, as well as the analysis and design of frequency multipliers and mixers at millimeter and submillimeter wavelengths. For this task, a Schottky diode model based on the Monte Carlo method[1] has been considered as a reference, due to the accuracy and reliability of this technique even under high frequency and high electric field conditions. It has been used to analyse the physical mechanisms that limit the performance of these devices and determine the simplest model that accounts for such effects. Lumped equivalent circuit and drift-diffusion models[2] which are commonly used in the design of Schottky based nonlinear circuits have been evaluated. These models as well as the Monte Carlo model of the Schottky diode have been coupled to a Harmonic Balance (HB) technique[2] to analyse the range of validity of LEC and DD models in the design of frequency multipliers and mixers up to THz frequencies. Besides, the CAD tool based on the Monte Carlo model coupled to HB (MCHB) has been used to explore the capabilities of Schottky circuits above 3 THz.

This Ph.D. thesis has been divided into two main parts. The first part is devoted to the analysis of the physical effects limiting the performance of the Schottky diodes and the behavior of the noise spectra of these devices at millimeter and submillimeter wavelengths. This part contains the following chapters:

- Chapter 2 presents a brief review of the physical principles of the Schottky diode, as well as an overview of different models for Schottky diodes available in the literature.
- Chapter 3 presents an analysis of physical phenomena that are important in the performance of Schottky diodes up to THz frequencies using as a reference the Monte Carlo model. Physical processes like nonlocal effects, velocity saturation, carrier inertia, dependence of the electron mobility on the epilayer length, plasma effects or nonstationary phenomena are considered.
- Chapter 4 presents a complete analysis of the noise spectra of GaAs and GaN based Schottky diodes operating under static and time varying conditions. A systematic study of the dependence of the intrinsic noise with the applied voltage and the device structure is carried out employing the Monte Carlo method and published analytical models. The analysis of the noise spectra based on MC simulations is also used to determine the accuracy and the range of validity of analytical models published in the literature.

In the second part of the thesis, an analysis of the limitations of Schottky based multipliers and mixers is carried out. The MC model coupled to a harmonic balance technique is used for the design

[1] The Monte Carlo models used in this thesis have been developed by the *Grupo de Investigación en Dispositivos Semiconductores* of the *University of Salamanca*.

[2] The drift-diffusion models and the harmonic balanced technique used in this thesis have been developed by *Grupo de Microondas y Radar* of the *Technical University of Madrid*

and optimization of these circuits at THz bands. The accuracy and range of validity of lumped equivalent circuit and drift-diffusion models for the design of Schottky circuits is also analysed, selecting as a reference the results from MCHB. The following chapters are included in this part:

- Chapter 5 is devoted to the analysis of frequency multipliers. Doublers and triplers have been analysed and a comparison with measured results published in the literature is carried out. Also, the MCHB is used to analyse the capabilities of Schottky multipliers above 3 THz.
- Chapter 6 is devoted to the analysis of both fundamental and subharmonically-pumped Schottky mixers. The two main figure-of-merits for mixers are analysed: (i) Conversion losses, and (ii) equivalent input noise temperature. Analytical models commonly used in the design of mixers, DD and MC models have been used to evaluate these parameters. A comparison with measured results is also considered. Besides, the MCHB is used for the design of mixers up to 10 THz.

Chapter 7 sums up the conclusions and the planned future tasks. Appendices A through G deal with several issues such as characterization and description of models and simulation techniques used in the development of this work, analysis of interesting effects in Schottky diodes like non-harmonic oscillations, and additional results for the multipliers and mixers considered.

1.5 Publications

The main results of the research activities compiled in this thesis have been published in the following journals and conferences:

- D. Pardo, J .Grajal, C. G. Pérez-Moreno, and S. Pérez, "An Assessment of Available Models for the Design of Schottky-Based Multipliers Up to THz Frequencies", *IEEE Trans. Terahertz Sci. Technol.*, vol. 4, no. 2, Mar. 2014.
- D. Pardo, J. Grajal and C. G. Pérez-Moreno, "Critical Assessment of Schottky Diode Models Up to THz Frequencies", *24st International Symposium on Space Terahertz Technology*, Groningen, The Netherlands, Apr. 2013.
- D. Pardo, J .Grajal, S. Pérez, T. González and J. Mateos, "Analysis of nonharmonic oscillations in Schottky diodes", *J. Appl. Phys.*, vol. 112, Sep. 2012.
- D. Pardo, J. Grajal, S. Pérez, J. Mateos and T. González, "Comparison of Noise Characteristics of GaAs and GaN Schottky Diodes for High Frequency Applications", *21st International Conference on Noise and Fluctuations*, Toronto, Canada, Jun. 2011.
- D. Pardo, J .Grajal, B. Mencía, S. Pérez, J. Mateos and T. González, "Analysis of noise spectra in GaAs and GaN Schottky barrier diodes", *Semicond. Sci. Technol.*, vol. 26, n. 5, Mar. 2011.
- D. Pardo, J. Grajal, S. Pérez, J. Mateos and T. González, "Static and Large Signal Noise Analysis in GaAs and GaN Schottky Diodes for High Frequency Applications", *8th Spanish Conference on Electron Devices*, Palma de Mallorca, Spain, Feb. 2011.
- D. Pardo, J. Grajal, B. Mencía, S. Pérez, J. Mateos and T. González, "Harmonic Generation and Noise in GaAs and GaN Schottky Diodes", *21st International Symposium on Space Terahertz Technology*, Oxfordshire, UK, Mar. 2010.

Part II

PHYSICAL ANALYSIS OF SCHOTTKY DIODES

Chapter 2

Modelling of Schottky diodes

Design and optimization of circuits based on Schottky diodes require reliable and accurate predictions of the device performance. The diode model has to carefully describe the processes limiting the performance of the diode at high powers and/or high frequencies, like velocity saturation or carrier inertia among others. The literature provides models with increasing accuracy and complexity to account for such phenomena, like lumped element equivalent circuit [Pen62, Cha78, Cro89, Eri98, Sch01b], drift-diffusion [Sel84, Lun00, Gra00], hydrodynamic or energy transport [Blo70, Lun00, Hje94, Lee99] and Monte Carlo [Jac89a, Lun00, Gon91, Bha95, Eas95, Lip97]. This chapter presents an overview of different models for Schottky diodes available in the literature in order to understand their potentialities and limitations.

2.1 Physical description of Schottky diodes

The principle of operation of Schottky diodes is based on the nonlinear properties of a metal-semiconductor contact. The rectifying properties arise from the presence of an electrostatic barrier between the metal and the semiconductor, created by the alignment of the Fermi level of each material. Conduction is mainly controlled by thermodynamic emission of majority carriers over the created barrier. Therefore, the Schottky diode is a majority carrier device whose switching speed is not limited by minority carrier effects [Fab95].

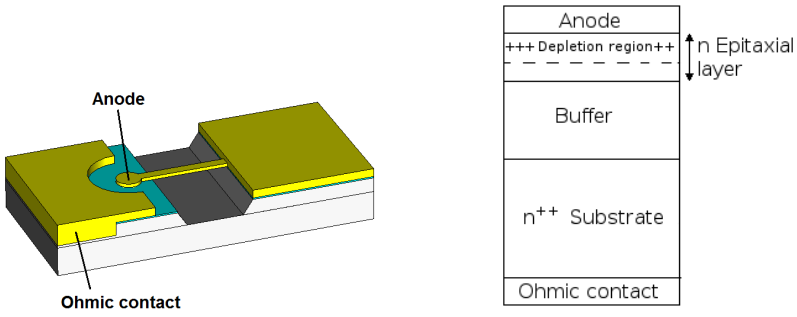

(a) (b)

Figure 2.1: (a) Structure of a planar surface channel etched diode and (b) one-dimensional model of a Schottky diode.

Fig. 2.1 shows the general structure of a Schottky barrier diode and the one-dimensional model commonly used in simulations. It includes the epitaxial layer or epilayer (with doping level between

$1x10^{17}$ and $5x10^{17}$ cm^{-3} for GaAs Schottky diodes), a high conductivity buffer (very high doping level) to prevent the diffusion of impurities from the substrate to the epilayer and the substrate (with doping between $1x10^{18}$ and $5x10^{18}$ cm^{-3}) to assure a low series resistance and a good quality metallic contact at the cathode [Maa88].

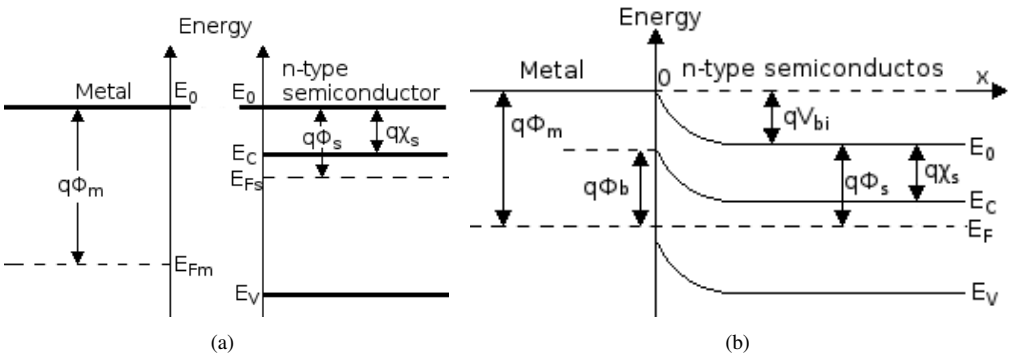

Figure 2.2: (a) Band structure of the metal and the semiconductor before contact and (b) after contact (ideal Schottky junction).

Fig. 2.2(a) shows the energy-band diagrams of a metal and an n-type semiconductor such that electrons in the metal have less energy, on average, than those in the semiconductor (energy-band diagram of a metal-semiconductor rectifying junction before contact). In this figure, the difference between the Fermi level E_F and the free-space energy level E_0 is the work function, $q\phi_m$ and $q\phi_s$, for the metal and the semiconductor, respectively, E_C and E_V represent the conduction band energy and the valence band energy, respectively. $q\chi_s$ is the electron affinity, i.e., the energy required to remove an electron from the conduction band to free space. When the metal and the semiconductor are joined, higher energy electrons in the semiconductor move into the metal, leaving behind ionized donor locations (positively charged). An electric field is created between these two groups of charges, which opposes further movement of electrons until a dynamic equilibrium is reached. The joining of the materials results in the band structure shown in Fig. 2.2(b), where the built-in potential V_{bi} is the potential difference between the neutral semiconductor and the anode, and ϕ_b is the ideal barrier height (the difference between the Fermi level and the peak of the conduction band) [Fab95].

Assuming that the region of the semiconductor where the bands are bent is completely depleted of electrons (depletion approximation, i.e. the edge of the depletion region is abrupt), the space charge is completely due to uncompensated donor. Under this approximation and if the donors are uniformly distributed, a linear electric field exists in the depletion region with value $E|_{SC} = E_{max} = -qN_e/\varepsilon_0\varepsilon_r$ at the Schottky contact (SC) and $E|_{edge\,DR}$= 0 at the edge of the depletion region (DR). The width of the depletion region is given by [Fab95]:

$$w_{dept} = \sqrt{\frac{2\varepsilon_0\varepsilon_r(V_{bi} - V_j)}{qN_e}} \tag{2.1}$$

where V_{bi} is the built-in potential, $\varepsilon_0\varepsilon_r$ is the permittivity of the semiconductor, N_e is the doping concentration of the epilayer, q is the absolute value of the electron charge and V_j is an external voltage applied to the Schottky junction. The capacitance of the junction is defined as the derivative of the charge in the depletion region with respect to the junction voltage, and, using the depletion approximation, is given by [Maa93]:

$$C_j(V_j) = \frac{C_j(0)}{\sqrt{1 - \frac{V_j}{V_{bi}}}} \tag{2.2}$$

where $C_j(0) = \sqrt{q\varepsilon_0\varepsilon_r N_e/(2V_{bi})}$. This expression is commonly used in LEC diode models. It can be used below flat-band condition ($V_j < V_{bi}$). Above flat-band, when the depletion region disappears,

this model is not longer applicable. Analytical models are also available in the literature to avoid the singularity of eq. (2.2) at $V_j = V_{bi}$. In [Poo69], Poon and Gummel presented a model for the capacitance which is free of singularities and allows modelling the capacitance for voltages up to the built-in voltage:

$$C_j(x) = \frac{C_j(0)}{(x^2+b)^{n/2}} \left(1 + \frac{n}{n-1}\frac{b}{x^2+b}\right) \tag{2.3}$$

where $x = (V_j - V_{bi})/V_{bi}$, b is an adjustable parameter ($0 \leq b \leq 1$) and n= 0.5 for the abrupt-junction approach. Fig. 2.3 compares the capacitance-voltage characteristic of a GaAs Schottky diode calculated according to eq. (2.2), eq. (2.3) and physics-based models like drift-diffusion and Monte Carlo (described in the following sections). Replacing $C_j(V)$ of eq. (2.2) with eq. (2.3) or with the numerically modeled capacitance-voltage characteristic has almost no effect on the performance of a reverse-biased diode, since it does not change the shape of the C-V during the main part of the voltage swing (see chapter 5). In this thesis, $C_j(V_j)$ in lumped equivalent circuit models is described by eq. (2.2), using a linear interpolation at voltages close to V_{bi} to avoid the singularity of eq. (2.2) at $V_j = V_{bi}$, as described in [Ant90].

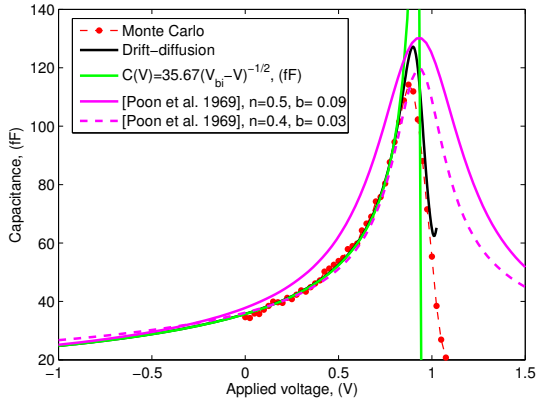

Figure 2.3: Capacitance-voltage characteristic of a GaAs Schottky diode characterized by L_e= 350 nm, N_e= 1x10^{17} cm^{-3}, L_s= 500 nm, N_s= 2x10^{18} cm^{-3}, A= 36 μm^2, ϕ_b= 0.99 V, at 300 K evaluated with eqs. (2.2), (2.3), drift-diffusion and Monte Carlo models.

2.1.1 Transport mechanisms

The most important mechanisms in determining the current-voltage characteristic of a Schottky diode are thermionic emission of carriers over the barrier, and quantum-mechanical tunneling through the barrier. In addition, barrier lowering due to image force, while not being a carrier transport mechanism, affects the carrier transport by altering the height and shape of the Schottky barrier.

Thermionic emission

In the diffusion theory [Sch38, Sze07] it is assumed that the conduction current in the Schottky diode is limited by the drift and diffusion mechanisms in the semiconductor, whereas the thermionic-emission theory [Bet42, Sze07] proposes that the current is limited by the transfer of electrons across the interface between the metal and the semiconductor. The thermionic-emission/diffusion theory considers the two current limiting effects to be in series and assumes that the thermionic-emission current must equal the current determined by the drift and diffusion [Cro66, Fab95, Sze07]. This

combined theory predicts the following expression for the current flowing through the junction:

$$I_j = [\frac{Am^*(k_BT)^2}{2\pi^2\hbar^3}\exp\left(-\frac{q\phi_b}{k_BT}\right)][\exp\left(\frac{qV_j}{k_BT}\right)-1] \tag{2.4}$$

$$I_j = I_0[\exp\left(\frac{qV_j}{k_BT}\right)-1] \tag{2.5}$$

where q and m^* are the charge and the effective mass of the electron, k_B is the Boltzmann's constant, $\hbar = h/2\pi$ is the reduced Planck's constant, A is the anode area, T is the operation temperature, I_0 is the reverse saturation current and V_j is an external voltage applied to the Schottky junction. This expression is valid between breakdown and flat-band voltages. At applied voltages higher than V_{bi}, the Schottky barrier disappears and the performance of the diode is like a linear resistance. Fig. 2.4(a) compares the current-voltage characteristic of a GaAs Schottky diode calculated according to eq. (2.5) and different physics-based models[1]. The resistance of the diode is presented in Fig.2.4(b). At voltages higher than V_{bi}, Monte Carlo shows that the series resistance increases due to the intervalley transfer of carriers from the Γ to L valley, where the electron mobility is lower, see the inset of Fig. 2.4(b). In this thesis, eq. (2.5) is used in the equivalent circuit models of the Schottky junction even for voltages higher than V_{bi}. The good agreement among eq. (2.5), the enhanced drift-diffusion and Monte Carlo under dc conditions in Fig. 2.4 at flat band justifies the approach considered.

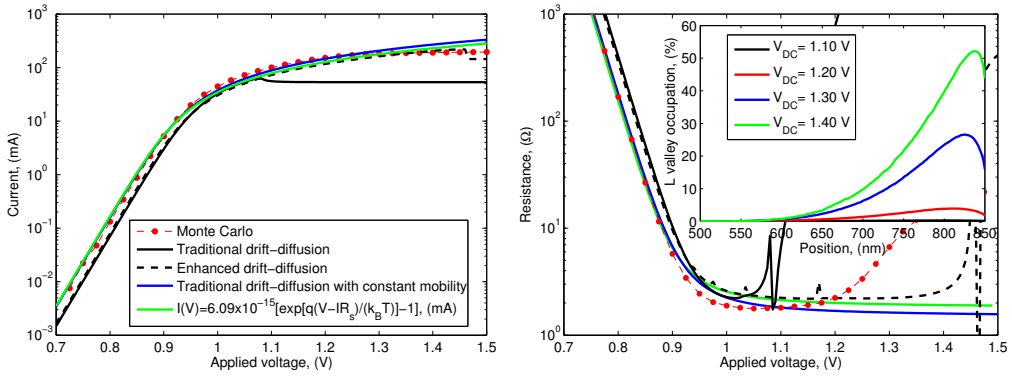

(a) (b)

Figure 2.4: (a) Current-voltage and (b) differential resistance-voltage characteristics of a GaAs Schottky diode characterized by L_e= 350 nm, N_e= 1x10^{17} cm^{-3}, L_s= 500 nm, N_s= 2x10^{18} cm^{-3}, A= 36 μm^2, ϕ_b= 0.99 V, evaluated with eq. (2.5), drift-diffusion and the Monte Carlo model. The inset of subfigure (b) shows the occupation of the L valley as a function of the position (ohmic contact at position 0 nm) obtained with the MC model.

Tunneling through the barrier

Electrons with energies below the top of the barrier can traverse the barrier by quantum-mechanical tunneling through the barrier. At low temperatures and high doping, electrons with energies close to the Fermi level in the semiconductor can tunnel through the barrier into the metal. This is called field emission. Increasing the temperature, the electrons are excited at higher energies and they see a thinner and lower barrier. The probability of tunneling increases with energy but the number of

[1]The I-V curve obtained with the traditional drift-diffusion model shows a small peak at voltages close to flat band followed by a slight decrease in the current until it becomes constant with the applied voltage. This occurs because the drift-diffusion model is a quasi-static model while, according to Monte Carlo simulations, important overshoot of the electron velocity close to the Schottky contact is expected above flat band conditions. Enhanced DD models have been developed for flat band conditions [Sel84, Lun00].

electrons with a particular energy decreases. As a result, the current is stabilized at a certain value which depends on the temperature. This contribution is called thermionic-field emission. Further increase in temperature lead to a point where virtually all carriers have sufficient energy to go over the top of the barrier and pure thermionic emission is achieved. Experimentally it has been found that in *n*-type GaAs with doping up to $2x10^{17}$ cm^{-3} the tunneling of electrons may be neglected at temperatures above 100 K [Fab95]. Tunneling has not been considered in any of the simulations presented in this thesis.

The concept of ideality factor η of the junction is introduced to describe the deviation of the current from the ideal pure thermionic emission ($\eta = 1$):

$$I_j = I_0[\exp\left(\frac{qV_j}{\eta k_B T}\right) - 1] \tag{2.6}$$

Deviations from the ideal behavior arise from imperfections in the fabrication or factors that are not included in the simple pure thermionic emission theory [Maa93]: barrier lowering due to image force, tunneling or edge effects.

2.2 Description of Schottky diode models

This section presents a description of the models available in the literature for Schottky diodes based on Lumped Equivalent Circuits (LEC) and physics-based equations. Among the last ones, Drift-Diffusion (DD), Hydrodynamic (HD) and Monte Carlo (MC) models are presented and they are analysed in more detail in the following sections. An overview of the limitations and range of validity of the different models is presented.

2.2.1 Lumped equivalent circuit models

The simplest lumped equivalent circuit (LEC) models represent the Schottky diode by means of an equivalent circuit shown in Fig. 2.5, where the Schottky junction is represented by a nonlinear capacitance described by eq. (2.2) in parallel with the conduction current through the Schottky contact, usually described by the combined thermionic-emission/diffusion theory eq. (2.5). Since Schottky diodes are majority carrier devices, the junction capacitance and current change almost instantaneously (*quasistatic* assumption) with the junction voltage, and the dc expressions for these quantities are valid up to several hundred gigahertz [Maa93].

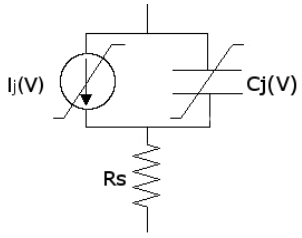

Figure 2.5: Simplified equivalent circuit model of the Schottky diode.

The series resistance R_s accounts for the power losses in the device. At low frequencies, the dc series resistance of the diode $R_{s,dc}$ (the series resistance measured when the epilayer is undepleted) can be a good estimate for R_s in the LEC model of Fig. 2.5 [Cha11a]. Some authors consider a constant effective series resistance different from $R_{s,dc}$ to account for the time variation of the width of the depletion region under time dependent conditions [Pen62]. However, for a rigorous analysis, the series resistance has to be considered time varying (R_s(t)) [Pen62, Bur65, Lip98].

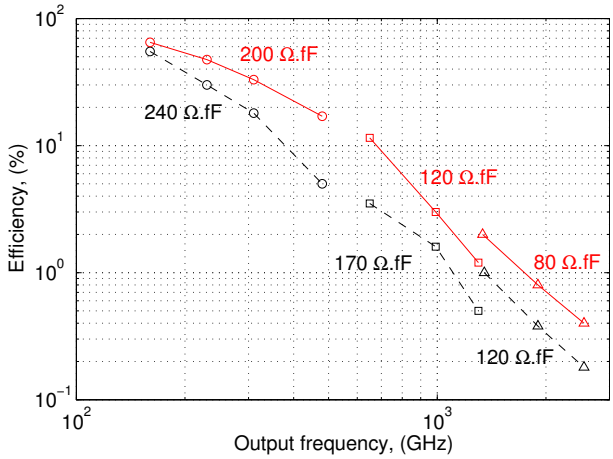

Figure 2.6: Theoretical efficiency of diode doublers and values of R_sx$C_j(0)$ presented by Erickson in [Eri98]. Black lines are for room temperature and red lines are for 100-150 K.

For the particular case of frequency multipliers, as the frequency of operation and/or the input power increase, the value of R_s used in the simulations is increased in order to reproduce measured results. Usually, the value of the product R_sx$C_j(0)$ in simulations is fixed to values that depend on the output frequency, the operation temperature, the epilayer doping and the epilayer length [Eri98]. With this procedure, the impact of limiting effects like velocity saturation -see section 3.1.2- are indirectly included in the diode model. Following [Eri98], an R_sx$C_j(0)$ product of 120 Ω.fF at 300 K is used for output frequencies between 1.3 and 2.7 THz (different values must be considered at different frequency ranges, see Fig. 2.6). The R_sx$C_j(0)$ rule in [Eri98] was determined regardless of diode doping (according to [Mae10b], doping 1x10^{17} cm^{-3} was considered in the development of this rule). It has been successfully applied in the design of a tripler at 540-640 GHz [Mae05b, Mae10b], but only some publications have clearly declared the use of this rule [New99, Mae03, Mae05b].

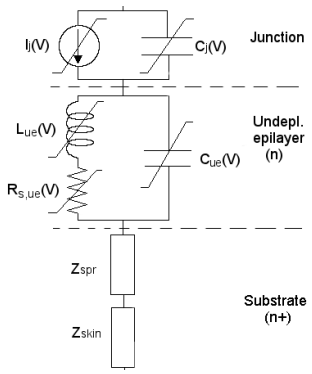

Figure 2.7: Extended equivalent circuit model of the Schottky diode.

LEC models can be updated to account for charge carrier inertia, which becomes important at frequencies of the order of 1 THz, see section 3.1.3, and the displacement current in the undepleted regions of these devices. Fig. 2.7 presents a more sophisticated model for the Schottky diode that includes those effects in the undepleted region of the epilayer through an inductance (L_{ue}) and a

capacitance (C_{ue}), respectively [Cha78, Cro89]. According to [Cha64]:

$$R_{s,ue} = \frac{1}{q\mu_{e,0}N_e}\frac{L(V_j)}{A} \tag{2.7}$$

$$L_{ue} = \frac{m^*}{N_e q^2}\frac{L(V_j)}{A} = \frac{1}{\sigma_{e,0}\omega_{s,e}}\frac{L(V_j)}{A} \tag{2.8}$$

$$C_{ue} = \varepsilon_0\varepsilon_r\frac{A}{L(V_j)} = \frac{\sigma_{e,0}}{\omega_{d,e}}\frac{A}{L(V_j)} \tag{2.9}$$

where A is the anode area, N_e is the epilayer doping, $L(V_j)$ is the length of the undepleted epilayer which depends on the voltage applied to the Schottky junction V_j, $\mu_{e,0}$ is the low field electron mobility in the epilayer, $\sigma_{e,0} = q\mu_{e,0}N_e$ is the low field conductivity of the epilayer, $\omega_{s,e} = q/(m^*\mu_{e,0})$ and $\omega_{d,e} = \sigma_{e,0}/(\varepsilon_0\varepsilon_r)$ are the scattering frequency and the dielectric relaxation frequency in the epilayer, respectively. $R_{s,ue}$ represents the series resistance of the undepleted epilayer in the model of Fig. 2.7. The impedance of the undepleted epilayer is (see Fig. 2.7):

$$Z_{ue} = R_{s,ue}\left[\frac{1}{1+j\omega\frac{L_{ue}}{R_{s,ue}}} + j\omega C_{ue}\right]^{-1} = R_{s,ue}\left[\frac{1}{1+j(\omega/\omega_{s,e})} + j\frac{\omega}{\omega_{d,e}}\right]^{-1} \tag{2.10}$$

where ω is the angular frequency. Under time varying voltages, the length of the undepleted epilayer is time dependent and $R_{s,ue}$, C_{ue} and L_{ue} can be considered also time dependent to model the diode rigorously.

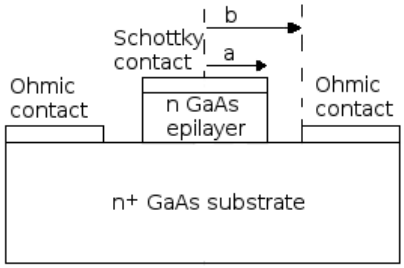

Figure 2.8: Geometry of a cylindrical planar diode.

In the simple LEC model of Fig. 2.5, the power losses in the substrate are included in the series resistance R_s. According to [Dic67, Bha92], the dc series resistance of the substrate for a cylindrical diode is given by (see Fig. 2.8):

$$R_{spr,0} = \frac{1}{2\pi a\sigma_{s,0}}\arctan\left(\frac{b}{a}\right) \tag{2.11}$$

where a is the anode radius, b is the radius of the chip, $\sigma_{s,0} = q\mu_{s,0}N_s$ is the low field conductivity of the substrate and $\mu_{s,0}$ is the low field electron mobility in the substrate doped N_s. This term is called the spreading resistance, because most of the resistance occurs in the substrate near the epilayer-substrate transition. According to [Dic67] this expression is only valid when b is much greater than a. With increasing frequency, the substrate impedance increases due to different phenomena. The skin effect is one of the most important. This phenomenon constrains the high frequency current to a thin surface layer of the of the order of the skin depth δ_s=$(2/(\omega\mu_{s,0}\sigma_{s,0}))^{0.5}$. The additional series impedance due to skin effect is [Cha78]:

$$Z_{skin} = \frac{(1+j)}{2\pi\sigma_{s,0}\delta_s}\ln(\frac{b}{a}) \tag{2.12}$$

where j is the imaginary unit. When the carrier inertia and the displacement current are considered in the substrate, the spreading and skin impedances are approximated by [Cha78, Kel79] (see Fig. 2.7):

$$Z_{spr} = \frac{1}{2\pi\sigma_{s,0}a}\arctan\left(\frac{b}{a}\right)\left[\frac{1}{1+j(\omega/\omega_{s,s})}+j\frac{\omega}{\omega_{d,s}}\right]^{-1} \tag{2.13}$$

$$Z_{skin} = \frac{\ln(b/a)}{2\pi}\left(\frac{j\omega\mu_{s,0}}{\sigma_{s,0}}\right)^{1/2}\left[\frac{1}{1+j(\omega/\omega_{s,s})}+j\frac{\omega}{\omega_{d,s}}\right]^{-1/2} \tag{2.14}$$

where $\omega_{s,s}$ and $\omega_{d,s}$ are the scattering frequency and the dielectric relaxation frequency in the substrate, respectively. The total impedance of the substrate is:

$$Z_{subs} = Z_{spr} + Z_{skin}. \tag{2.15}$$

Comparing eq. (2.13) and eq. (2.10), it is observed that the spreading resistance can be described in terms of three frequency independent elements like that for the undepleted epilayer defined by eqs. (2.7), (2.8) and (2.9), see Fig. 2.7. However, the skin effect term cannot be represented simply[2]. To account for $R_{spr,0}$ eqs. (2.11) and (2.13) in the LEC models, an effective substrate length L_s has been defined in eq. (2.7) particularized for the substrate[3], instead of using eq. (2.11) directly. The effective substrate length has been used to characterize the substrate series resistance because one dimensional diode models are used in this work.

In the design of millimeter and submillimeter circuits, Schottky diodes are often modeled with simple LEC models, because of their simplicity and ease of use in commercial harmonic balance simulators [Sch01a, Mae10b, Cha11a, Mae12]. Although LEC models present important limitations at high frequencies and power levels when the nonstationary carrier dynamics begins to dominate device operation [Jon95, Eas95, Bha95, Lip97, Lip98, Gra00], they have been proven to be useful in the design of Schottky based THz circuits [Sch02, Cro05, Mae10b, Tho10b, Cha11a, Mae12]. An evaluation of the accuracy and limitations of these models for the design of multipliers and mixers is carried out in chapters 5 and 6, respectively.

Figure-of-merit cut-off frequency

The use of Schottky diodes at THz frequencies requires an optimized diode design in order to achieve the optimum performance of nonlinear circuits. A commonly accepted criterion for the optimization of the diode parameters is the cut-off frequency f_c which makes use of constant values of the diode series resistance R_s and the zero bias junction capacitance $C_j(0)$ for the optimization:

$$f_c = \frac{1}{2\pi}\frac{1}{R_s C_j(0)}. \tag{2.16}$$

R_s and $C_j(0)$ are both dependent on the anode diameter, the epilayer doping concentration and the epilayer thickness. The diode design parameters are then chosen such that the cut-off frequency becomes as large as possible.

Other definitions of the cut-off frequency can be found in the literature. In [Pen62], the following definition is proposed to characterize the varactor quality:

$$f_c = \frac{1}{2\pi}\frac{\frac{1}{C_{min}}-\frac{1}{C_{max}}}{R_s} \tag{2.17}$$

[2]Unless otherwise is stated, skin effect has been neglected in the simulations and designs of this thesis, see the discussion in section 3.1.6.

[3]With this definition, the effective substrate length depends on the anode area of the diode (compare eq. (2.11) and eq. (2.7) particularized for the substrate parameters).

where C_{min} and C_{max} are a minimum and a maximum values between which the capacitance is restricted. In [Pen62] it is shown that the cut-off frequency defined by eq. (2.17) gives a better characterization of the varactor quality of diodes than eq. (2.16), since it indicates how high the diode capacitance can be pumped.

More realistic cut-off frequency based on bias dependent parameters and taking into account all elements of the diode equivalent circuit have been developed [Gru94a].

2.2.2 Physics-based models

Carrier transport is commonly described by the semiclassical Boltzmann Transport Equation (BTE) [Sel84, Lun00]. The solution to the BTE is the distribution function of the carriers $f(\mathbf{r},\mathbf{k},t)$ which describes the average distribution of carriers in both position $\mathbf{r}$ and momentum $\mathbf{k}$ spaces at time t and can be used to obtain quantities such as carrier concentration, current or energy densities.

The derivative of the distribution function along a particle trajectory ($\mathbf{r}$(t), $\mathbf{k}$(t)) with respect to time is zero in the entire phase space in compliance with the Liouville's theorem about the invariance of the phase volume for a system moving along the phase paths [Sel84]:

$$\frac{d}{dt}f(\mathbf{r}(t),\mathbf{k}(t),t) = 0. \tag{2.18}$$

This is known as the implicit form of the BTE. Eq. (2.18) can be expanded:

$$\frac{\partial f}{\partial t} + \nabla_{\mathbf{k}} f.\frac{d\mathbf{k}}{dt} + \nabla f.\frac{d\mathbf{r}}{dt} = 0 \tag{2.19}$$

where $\nabla_{\mathbf{k}}$ and ∇ denote the gradient operator with respect to the momentum and spatial coordinates, respectively.

The sum of all the forces acting on a particle can be expressed as:

$$\mathbf{F} = \hbar\frac{d\mathbf{k}}{dt} \tag{2.20}$$

The force $\mathbf{F}$ is constituted by forces due to external electromagnetic fields $\mathbf{F}_e$ and internal forces due to the interaction with the crystal $\mathbf{F} = \mathbf{F}_e + \mathbf{F}_i$. The effect of the internal forces on the distribution function can be evaluated introducing the quantity $P(\mathbf{k},\mathbf{k'})$, that represents the probability per unit time that a carrier in the state $\mathbf{k}$ will be scattered to $\mathbf{k'}$:

$$\begin{aligned}\nabla_{\mathbf{k}} f.\frac{\mathbf{F}_i}{\hbar} = \int_{V_{\mathbf{k}'}} &(f(\mathbf{r},\mathbf{k},t).(1-f(\mathbf{r},\mathbf{k'},t)).P(\mathbf{k},\mathbf{k'}) - \\ &-f(\mathbf{r},\mathbf{k'},t).(1-f(\mathbf{r},\mathbf{k},t)).P(\mathbf{k'},\mathbf{k}))\,.d\mathbf{k'}\end{aligned} \tag{2.21}$$

Substituting eqs. (2.20) and (2.21) into eq. (2.19) and taking into account that the group velocity of the carriers can be expressed by $\mathbf{v} = d\mathbf{r}/dt$, we obtain the integro-differential Boltzmann equation:

$$\begin{aligned}\frac{\partial f}{\partial t} + \frac{\mathbf{F}_e}{\hbar}.\nabla_{\mathbf{k}} f + \mathbf{v}.\nabla f = \\ -\int_{V_{\mathbf{k}'}} (f(\mathbf{r},\mathbf{k},t).(1-f(\mathbf{r},\mathbf{k'},t)).P(\mathbf{k},\mathbf{k'}) - f(\mathbf{r},\mathbf{k'},t).(1-f(\mathbf{r},\mathbf{k},t)).P(\mathbf{k'},\mathbf{k}))\,.d\mathbf{k'}.\end{aligned} \tag{2.22}$$

Finding the exact solution to this equation is a very difficult task, so different approximations are introduced to simplify the problem [Sel84]. Firstly, it is assumed that the scattering probability is independent of the external force and consider elastic scattering mechanisms; besides, the scattering mechanisms are considered instantaneous, (it is assumed that the duration of a scattering mechanism is much lower than the mean time between two consecutive collisions of a carrier). It is also assumed that the interaction between carriers is negligible. With these simplifications and neglecting the

Lorentz force due to the magnetic field, so $\mathbf{F}_e = q.\mathbf{E}$ where $\mathbf{E}$ is the electric field, the Boltzmann transport equation can be written as:

$$\frac{\partial f}{\partial t} + \frac{\mathbf{F}_e}{\hbar}.\nabla_{\mathbf{k}} f + \mathbf{v}.\nabla f = \left(\frac{\partial f}{\partial t}\right)_{col} \tag{2.23}$$

where $\left(\frac{\partial f}{\partial t}\right)_{col}$ represents the internal collisions with the lattice.

The method of moments is the most common method to obtain approximated models from the BTE, eq. 2.23, [Lun00]. It consists of multiplying the BTE by different weight functions and carry out the integration over the momentum space. The first fourth moments of the BTE are:

$$n(\mathbf{r},t) = \frac{1}{4\pi^3}\int_{-\infty}^{\infty} f(\mathbf{r},\mathbf{k},t)d\mathbf{k} \tag{2.24}$$

$$\mathbf{J}_n(\mathbf{r},t) = \frac{-q}{4\pi^3}\int_{-\infty}^{\infty} \mathbf{v}(\mathbf{k}) f(\mathbf{r},\mathbf{k},t)d\mathbf{k} \tag{2.25}$$

$$\varepsilon_n(\mathbf{r},t) = \frac{1}{4\pi^3}\int_{-\infty}^{\infty} \xi(\mathbf{k}) f(\mathbf{r},\mathbf{k},t)d\mathbf{k} \tag{2.26}$$

$$\mathbf{F}_{\varepsilon_n}(\mathbf{r},t) = \frac{1}{4\pi^3}\int_{-\infty}^{\infty} \mathbf{v}(\mathbf{k})\xi(\mathbf{k}) f(\mathbf{r},\mathbf{k},t)d\mathbf{k} \tag{2.27}$$

where $n(\mathbf{r},t)$ represents the density of electrons, $\mathbf{v}(\mathbf{k}) = \frac{1}{\hbar}\nabla_{\mathbf{k}}\xi(\mathbf{k})$, $\xi(\mathbf{k})$ is the kinetic energy of a particle in the energy band with moment $\mathbf{k}$, $\mathbf{J}_n$ is the conduction current density due to electrons ($\mathbf{J}_n = -qn\mathbf{v}_{d_n}$, where $\mathbf{v}_{d_n}$ is the average velocity of the electrons), $\varepsilon_n(\mathbf{r},t)$ is the density of kinetic energy and $\mathbf{F}_{\varepsilon_n}$ the density of energy flux.

The result of this method is a set of equations in partial derivatives, which represent the conservation of certain macroscopic variables. The first three moments of the BTE represent the conservation of carriers, momentum and energy [Lun00]:

$$\frac{\partial n}{\partial t} = \nabla\cdot\mathbf{J}_n + \left(\frac{\partial n}{\partial t}\right)_{col} \tag{2.28}$$

$$\frac{\partial \mathbf{J}_n}{\partial t} = \frac{-2(-q)}{m^*}\nabla\cdot\widehat{\varepsilon_n} + \frac{q^2 n}{m^*}\mathbf{E} + \left(\frac{\partial \mathbf{J}_n}{\partial t}\right)_{col} \tag{2.29}$$

$$\frac{\partial \varepsilon_n}{\partial t} = -\nabla\cdot\mathbf{F}_{\varepsilon_n} + \mathbf{J}_n\cdot\mathbf{E} + S_{\varepsilon_n} + \left(\frac{\partial \varepsilon_n}{\partial t}\right)_{col} \tag{2.30}$$

where $-q$ is the electron charge and $\widehat{\varepsilon_n}$ is the tensor of kinetic energy, whose components are given by:

$$\varepsilon_{n_{ij}}(\mathbf{r},t) = \frac{1}{2}\left\{\frac{1}{4\pi^3}\int_{-\infty}^{\infty} v_{n_i} p_{n_j} f(\mathbf{r},\mathbf{k},t)d\mathbf{k}\right\} \tag{2.31}$$

where $\mathbf{v}_n$ is the velocity of the electrons and $\mathbf{p} = m^*\mathbf{v}$. The trace of $\widehat{\varepsilon_n}$ is the average kinetic energy of the electrons $\varepsilon_n(\mathbf{r},t)$. The total kinetic energy can be expressed as the sum of a drift term related to the average velocity of the electrons, $\mathbf{v}_{d_n}$, and a term related to the random motion of the electrons, thermal energy:

$$\varepsilon_{n_{ij}} = K_{n_{ij}} + \frac{1}{2}nk_B T_{n_{ij}} = \frac{1}{2}nm^* v_{d_i} v_{d_j} + \frac{1}{2}nk_B T_{n_{ij}}. \tag{2.32}$$

and in tensorial notation:

$$\widehat{\varepsilon_n} = \widehat{K_n} + \frac{1}{2}nk_B\widehat{T_n} \tag{2.33}$$

The term S_{ε_n} in eq. (2.30) represents the variation of the density of kinetic energy due to the generation of carries. Following [Lun00], it is possible to express the fourth moment of the BTE, $\mathbf{F}_{\varepsilon_n}$, by:

$$\mathbf{F}_{\varepsilon_n} = \varepsilon_n\mathbf{v}_{d_n} + nk_B\mathbf{v}_{d_n}\cdot\widehat{T_n} + \mathbf{Q}_n. \tag{2.34}$$

The term $\mathbf{Q}_n$ represents an energy flux in a coordinate system moving at the average carrier velocity. Since it is associated with the random component of the carrier velocity, $\mathbf{Q}_n$ is associated with the flow of thermal energy, or heat. Indeed, the quantity $\mathbf{Q}_n$ is commonly termed the heat flux.

To truncate the infinite series of equations in the method of moments, it is usually assumed that the moments of the BTE of high order are negligible. Therefore, some approximations have to be carried out in order to close the system of equations of the model. In eq. (2.30), an equation for $\mathbf{F}_{\varepsilon_n}$ is necessary. There are different possibilities: Ignore the higher moments of the BTE, use the knowledge about the physics of the problem to approximate those terms, or assume a momentum dependence for the distribution function to evaluate the required terms. The first possibility leads to incorrect results. The second method requires an equation to model the heat flux. Usually the Fourier law $\mathbf{Q}_n = -\kappa_n \nabla T_n$ has been used, where κ_n is the thermal conductivity. This equation is approximate. It ignores the Peltier effect, and the linear form of the equation applies only when the temperature gradient is gentle [Ste94, Lun00]. The assumption of a distribution function is the simplest solution, but it supposes a loss of generality and requires the Monte Carlo method to validate the model [Lun00].

Characteristic times

The collision terms in eqs. (2.28), (2.29) and (2.30) represent the effect of the interaction of the electrons with the crystal lattice in the different moments. To evaluate these terms, the relaxation approximation is commonly used:

$$\left(\frac{\partial n}{\partial t}\right)_{col} = -G(\tau_c) \tag{2.35}$$

$$\left(\frac{\partial \mathbf{J}_n}{\partial t}\right)_{col} = -\frac{\mathbf{J}_n}{\tau_m(\varepsilon)} \tag{2.36}$$

$$\left(\frac{\partial \varepsilon_n}{\partial t}\right)_{col} = -\frac{\varepsilon_n - \varepsilon_{n,th}}{\tau_\varepsilon(\varepsilon)} \tag{2.37}$$

where G is the velocity of generation-recombination processes (it is set to zero for unipolar conditions) that depends on the mean life of the carriers, τ_c; $\tau_m(\varepsilon)$ is the characteristic time of the momentum relaxation and $\tau_\varepsilon(\varepsilon)$ is the characteristic time of the energy relaxation. $\tau_m(\varepsilon)$ and $\tau_\varepsilon(\varepsilon)$ are usually assumed dependent on the average energy of the carriers ε. $\varepsilon_{n,th}$ represents the energy density of the electrons in thermal equilibrium with the lattice. Monte Carlo simulations are commonly used to calculate the relaxation times. They are evaluated in bulk material and under steady-state conditions and then are used to simulate semiconductors devices with a defined geometry and under time varying conditions. The validity of this approximation is questionable at high frequencies and/or high electric fields. Another possibility is to assume a distribution function to evaluate the relaxation times [Lun00].

In the following sections, different approaches of the BTE are described: The drift-diffusion model, based on the first two moments of the BTE, hydrodynamic models, based on the first three moments of the BTE, and the Monte Carlo model. The Monte Carlo model provides a solution of the BTE by simulating the trajectories of individual carriers as they move through a device under the influence of electric fields and random scattering forces.

2.3 Drift-diffusion model

The drift-diffusion (DD) model [Sel84, Lun00] is based on the Poisson's equation and the first two moments of the BTE (conservation of particles eq. (2.28) and momentum eq. (2.29)). The equation of momentum conservation eq. (2.29) is simplified assuming that $\nabla \cdot \widehat{T}_n$ is negligible, that is, the electrons are always in equilibrium with the lattice, i.e. T_n= T, where T is the lattice temperature,

and the term $\nabla\widehat{K_n}$ is small compared with other terms. It is also assumed that the current does not vary appreciably over a momentum relaxation time, τ_m, eq. (2.36). With these simplifications, eq. (2.29) for electrons can be written as:

$$\mathbf{J}_n = qn\mu_n\mathbf{E} + qD_n\nabla n \tag{2.38}$$

where the mobility of the electrons μ_n is defined as:

$$\mu_n = \frac{q\tau_{m,n}}{m^*} \tag{2.39}$$

and D_n is the diffusion coefficient of the electrons:

$$D_n = \frac{k_B T\mu_n}{q} \tag{2.40}$$

Eq. (2.40) is known as the Einstein's relation. Both μ_n and D_n are considered dependent on the electric field. The DD equations to be solved self-consistently with adequate boundary conditions for electrons and holes are:

$$\frac{\partial n}{\partial t} = \frac{1}{q}\nabla\cdot\mathbf{J}_n + G \tag{2.41}$$

$$\frac{\partial p}{\partial t} = \frac{1}{q}\nabla\cdot\mathbf{J}_p - G \tag{2.42}$$

$$\mathbf{J}_n = qn\mu_n\mathbf{E} + qD_n\nabla n \tag{2.43}$$

$$\mathbf{J}_p = qp\mu_p\mathbf{E} - qD_p\nabla p \tag{2.44}$$

$$-\nabla^2\phi = \frac{q}{\varepsilon_0\varepsilon_r}(N_D^+ - n + p - N_A^-) \tag{2.45}$$

where n is the electron concentration, p the hole concentration (subindexes $_n$ and $_p$ refer to electrons and holes respectively), $\mathbf{J}_n$ and $\mathbf{J}_p$ are the electron and hole current densities, ϕ is the electrostatic potential, N_D^+ is ionized impurity donor concentration, and N_A^- is the ionized impurity acceptor concentration. G is the velocity of generation-recombination of electrons and holes, see eq. (2.35). Models for the different physical mechanisms responsible for generation-recombination in semiconductor devices can be found in [Sel84]. In the DD simulator employed in this thesis [Fue98], the generation and recombination rates are modeled by the Shockley-Read-Hall and impact ionization mechanisms.

Drift-diffusion model presents important limitations:

- It assumes that the charge carriers are in thermal equilibrium with the lattice. However, drift-diffusion equations can be updated to take into account heating effects and non-homogeneous temperature distribution of the charge carriers [Sel84].
- DD model considers a static relation between the velocity of the charge carriers and the electric field. Hence, the velocity of the carriers is updated instantaneously to the variations of the local electric field. DD model does not treat nonlocal effects such as velocity overshoot. While steady-state is being approached, carriers travel a distance that in GaAs is around 150 nm [Lun00]. Since DD does not model these effects, it cannot be appropriate for sub-micron dimension for GaAs devices.

The details about the practical implementation of the DD equations as well as the boundary and interface conditions for the DD model used in this thesis can be found in [Sel84, Fue98].

Table 2.1 summarizes the values employed in the DD model for the most important physical parameters of GaAs [Sel84, Kro97, Mad04] and GaN [Anw01, Lev01, Sch05] semiconductors. The field-dependent mobility models for GaAs and GaN implemented in the DD model are those presented in [Sel84] and [Sch05], respectively.

Table 2.1: Physical parameters of GaAs and GaN semiconductors used in the DD model.

	GaAs		*GaN*	
Dielectric constant	ε_r	12.9	ε_r	8.9
Bottom valley energy	ε_Γ, (eV)	1.5435-3.95x10^{-4}T-2x10$^{-11}\sqrt{n}$	ε_Γ, (eV)	3.47-7.710x10$^{-4}\frac{T}{T+600}$-2x10$^{-11}\sqrt{n}$
Electron effective mass	$m^*_\Gamma(m_0)$	0.067	$m^*_\Gamma(m_0)$	0.21
Holes effective mass	$m^*_{hh}(m_0)$	0.5	$m^*_{hh}(m_0)$	1.4
	$m^*_{lh}(m_0)$	0.068	$m^*_{lh}(m_0)$	0.3
Effective density of states in the conduction band	N_c, (cm^{-3})	4.8923x10$^{15}T^{3/2}m^{*3/2}_\Gamma$	N_c, (cm^{-3})	4.8923x10$^{15}T^{3/2}m^{*3/2}_\Gamma$
Effective density of states in the valence band	N_v, (cm^{-3})	4.8923x10$^{15}T^{3/2}(m^{*3/2}_{lh}+m^{*3/2}_{hh})$	N_v, (cm^{-3})	4.8923x10$^{15}T^{3/2}(m^{*3/2}_{lh}+m^{*3/2}_{hh})$

2.4 Hydrodynamic and energy transport models

These models are based on the the first three moments of the BTE (conservation of particles eq. (2.28), momentum eq. (2.29), and energy eq. (2.30)) and the Poisson's equation. They are commonly simplified assuming that the tensor of temperature can be represented by a scalar magnitude: $T_{n_{ij}} = T_n\delta_{ij}$ with δ_{ij}= 0 for $i \neq j$.

In the hydrodynamic models, the system of equations is closed using an equation for the heat flux. Since the Fourier law $\mathbf{Q}_n = -\kappa_n\nabla T_n$ is not appropriated for semiconductor devices [Ste94], equations for the heat flux $\mathbf{Q}_n$ based on the sum of a diffusion term and a convection term have been proposed [Lun00]:

$$\mathbf{Q}_n = \mathbf{Q}_{diff,n} + \mathbf{Q}_{conv,n} = -\kappa_n(T_n)\nabla T_n + \Pi_n(T_n)\mathbf{J}_n \tag{2.46}$$

where κ_n and Π_n are the thermal conductivity and the Peltier's coefficient for electrons.

In the energy transport models, the conservation equations are calculated using a solution of the BTE [Str62, Lun00]. First, the distribution function is split into the even and odd parts:

$$f(\mathbf{r},\mathbf{k},t) = f_0(\mathbf{r},\mathbf{k},t) + f_1(\mathbf{r},\mathbf{k},t) \tag{2.47}$$

Assuming that the collision operator is linear and invoking a microscopic relaxation time approximation for the collision term in eq. (2.23):

$$\left(\frac{\partial f}{\partial t}\right)_c = -\frac{f - f_{eq}}{\tau} \tag{2.48}$$

the BTE can be split into two coupled equations. In particular, f_1 is related to f_0 via:

$$f_1 = -\tau\left(\mathbf{v}\nabla f_0 - \frac{q}{\hbar}\mathbf{E}\cdot\nabla_{\mathbf{k}} f_0\right) \tag{2.49}$$

Different approximation have been suggested for f_0: a maxwellian distribution function [Str62], a Fermi-Dirac distribution function [McA87] and modified maxwellian in order to take into account the non-parabolic energy and and non-maxwellian effects [Che92]. Including the expressions for the distribution function eqs. (2.47) and (2.49) in the BTE, the different moments can be calculated as was previously described. Contrary to hydrodynamic models, energy transport models do not need an equation for the heat flux to close the system.

Unlike DD model, these models take into account nonstationary effects in the device. They also take into account heating of the carriers, since they assume that the carrier temperature depends on the energy. The limitations of these models are:

- Hydrodynamic and energy transport models need a method to obtain the energy dependence of the parameters in the equations, usually the Monte Carlo method.

- They do not provide the instantaneous velocity distribution function. Hence, they are not adequate for noise analysis. Hydrodynamic and energy transport models can be used in conjunction with impedance field methods [Gru93c, Gru94c, Shi99], as the DD models [Bon01a, Bon01b, Bon03].
- The accuracy of these models is limited because they only use energy and momentum relaxation parameters to describe the complexity of the scattering mechanisms involved in carrier transport.

2.5 Monte Carlo model

The Monte Carlo method applied to the physics of semiconductors is able to provide an exact solution of the BTE. It consists of the microscopic description of the motion of the charge carriers in the semiconductor under the interaction with the crystal lattice and the electric field [Jac89a, Lun00, San94, Bha95, Eas95, Lip97]. The interaction with the crystal lattice is the origin of the effective mass of the carriers and the modification of their motion due to different scattering mechanisms. Every scattering mechanism is characterized by a probability of transition between different states, that is used to determine the frequency with which the carriers deviate from the path imposed by the applied electric field, which scattering mechanism is acting on each carrier and which state of the carrier after the scattering is.

The motion of the carriers is described as a succession of free flights under the action of the electric field and scattering mechanisms. The electric field is self-consistently solved (Poisson's equation) every certain time step using the instantaneous charge carriers and impurity distributions. The results obtained from this iterative process can be directly used to evaluate the electrical response and the noise spectral density of the device under study.

The Monte Carlo method solves most of the limitations of the models previously described. But it also presents important limitations [Fis88]:

- MC does not describe quantum phenomena occurring in devices (or regions of devices) of a scale length comparable to the de Broglie wavelength of the carriers. Quantum wells, inversion and accumulation layers, heterostructures and tunneling are some examples. However, these quantum effects are well understood and have been coupled to the semiclassical MC simulations [Fis88, Lun00, Sch98].
- The intrinsic limitation of the BTE at high electric fields, high carrier energies, and very short lifetimes [Fis88]. When very intense electric fields are applied, collisions become so active that the hypothesis of single point-like events fails. The finite collision duration cannot be neglected and the effect of the electric field during the scattering process must be accounted for. Furthermore, the collision rate can be so high that the time between two successive collisions becomes shorter than the time necessary to achieve the strict energy conservation required by the Fermi golden rule and the scattering energy balance must account for quantum collision broadening [Sch98].
- The physical models used in the Monte Carlo model should be improved [Fis88]. For example, the simple band structure commonly used, which is appropriate only in low-field ($\lesssim 10^5$ V/cm for GaAs) and low energy situations ($\lesssim$ 0.2-0.5 eV for GaAs), but which is often extended outside this range [Fis88]. In the MC simulations presented in this work, the maximum electric fields reached in the undepleted regions of the GaAs diodes are lower than 120 KV/cm, and, according to [Gon91], a band structure model with three valleys -see the following section- is expected to provide accurate results under such conditions.

For an accurate MC simulation of the carrier transport in semiconductor devices, it is fundamental to describe correctly the scattering mechanisms and the band structure of the semiconductor.

The following section presents a description of these features for GaAs and GaN, which are the semiconductors considered in this work.

2.5.1 Energy band structure

Gallium Arsenide is a direct gap semiconductor with Zinc-Blend crystal lattice. Fig. 2.9(a) presents the energy bands of this semiconductor [Mad04]. Only the conduction band is considered in our unipolar Monte Carlo model because we analyse n-type Schottky diodes. The zero of energy in our Monte Carlo model is assumed at the bottom of the conduction band. The first minimum of the first conduction sub-band is located in the center of the first Brillouin zone (point Γ) at 1.42 eV above the maximum of the valence band. The second minimum is in the direction $< 111 >$ corresponding to the point L with 8 equivalent valleys, and the third minimum is in the direction $< 100 >$ with 6 equivalent valleys.

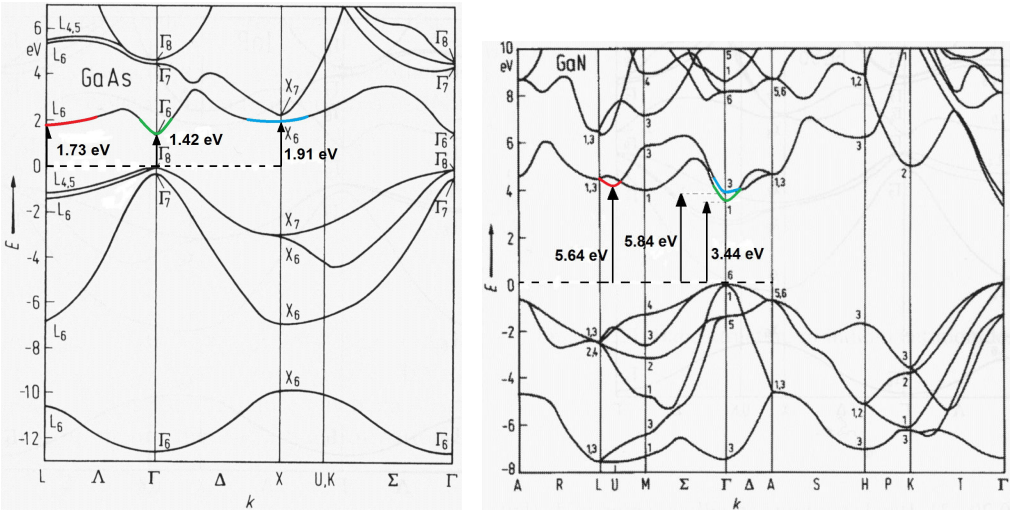

(a) (b)

Figure 2.9: Band structure of (a) GaAs and (b) GaN semiconductor. Reprinted from [Mad04].

For electric fields lower than 75-100 KV/cm, it is enough to model the valley Γ, four L equivalent valleys and three X equivalent valleys [Gon91]. Higher valleys are totally empty. The energy of the electrons in the valleys considered can be approximated by non-parabolic spherical valleys:

$$\varepsilon(\mathbf{k})(1+\alpha_{np}\varepsilon(\mathbf{k})) = \gamma(\mathbf{k}) = \frac{\hbar^2\mathbf{k}^2}{2m^*} \tag{2.50}$$

where $\mathbf{k}$ is the wavevector, m^* is the effective mass and α_{np} is the non-parabolicity coefficient depending on the valley where the electron is situated.

The Gallium Nitrate crystallizes in three different lattices: (i) Wurtzite (packed hexagonal); (ii) Zinc-Blend (cubic) and (iii) Rocksalt (sodium chloride structure). Wurtzite GaN is considered in this work since it is the most stable at room temperature and it is typically used in semiconductor devices [Mad04].

The conduction band of the GaN is modeled by three nonparabolic spherical valleys, see Fig. 2.9(b). The valleys considered are: (i) one valley in the point Γ (valley Γ_1) at 3.44 eV from the maximum of the valence band; (ii) 6 equivalent valleys located between M and L points, denoted valley U and (iii) the valley located in the point Γ_3.

Table 2.2 summarizes the parameters employed to model GaAs [Gon91, Gon93a, Mad04] and GaN [Fou99, Goa00b, Goa00a, Mat07] semiconductors in the MC simulations. The literature of MC simulations of bulk material and devices based on GaN semiconductor is not extensive [Bha97, Alb98, Far01, Anw01], and they do not provide enough information about the models and parameters used. Also, there exits a high dispersion in the values of some parameters [Fou99, Goa00b, Goa00a, Mad04]. In the calibration of our GaN MC model, the reliable values in the literature for some common parameters were used. On the other hand, the parameters with a high dispersion were selected to reproduce measured velocity-field curves [Bar02, Bar05], see Table 2.2 and the tables for the scattering mechanisms in the following section.

Table 2.2: Physical parameters of GaAs and GaN semiconductors used in the MC simulations.

	GaAs			*GaN*		
Density, (kg/m^3)	5370			6150		
Sound velocity, (m/s)	5220			6560		
Low frequency permittivity	12.9			8.9		
High frequency permittivity	10.92			5.35		
Lattice constant, $\overset{\circ}{A}$	5.65			5.185		
GAP, (eV)	1.42			3.44		
Valley	Γ	L	X	Γ_1	U	Γ_3
Effective mass	0.067	0.3	0.85	0.21	0.39	0.28
Non paraboloid coefficient, (eV^{-1})	0.61	0.222	0.061	0.37	0.50	0.22
Energy level from Γ/Γ_1, (eV)	—	0.309	0.486	—	2.20	2.4
Number of equivalent valleys	1	4	3	1	6	1

2.5.2 Scattering mechanisms

The scattering mechanisms can be classified as scattering with defects, carrier-carrier and with the lattice, see Fig. 2.10 from [San94]. They can be also classified as elastic and inelastic, if the energy of the carrier is modified or not after the mechanism, respectively. Also, they can be classified as isotropic or anisotropic, if the direction of the final state of the wave-vector of the carrier is completely random or it depends on the direction of the initial state. A description of the scattering mechanisms is presented, for the particular case of GaAs and GaN materials. The scattering probabilities shown in this subsection are those in the MC simulator used in this thesis, which was developed by the *University of Salamanca*. Carrier-carrier scattering mechanisms have not been taken into account in our simulations.

Among the interactions with defects, the most important is the scattering with ionized impurities which is elastic and anisotropic of Coulombic type with screening. It is important at doping concentrations higher than 10^{15} cm^{-3}. Two models are usually used: the screened potentials of Brooks-Herring [Bro50], and of Conwell-Weisskopf [Con50]. The original model of Brooks has been modified to include the effect of non-parabolicity [Ruc70]. This model, including the effect of the non-parabolicity, has been considered in the MC simulator. Fig. 2.11 compares the scattering probability associated to interactions with ionized impurities in the valleys Γ and L for GaAs and Γ_1 and U for GaN semiconductor.

The interaction of the charge carriers with the thermal vibrations of the atoms in the lattice is modeled by the collision with phonons. These mechanisms can be of two types, optical and acoustic, depending on the dispersion relation. The interaction with the lattice can occur via a deformation potential (also known as non polar scattering) or be caused by electrostatic forces due to the displacement of the atoms in the lattice (known as polar scattering or piezoelectric in the case of acoustic phonons). Scattering mechanisms where the final state of the carrier after the interaction

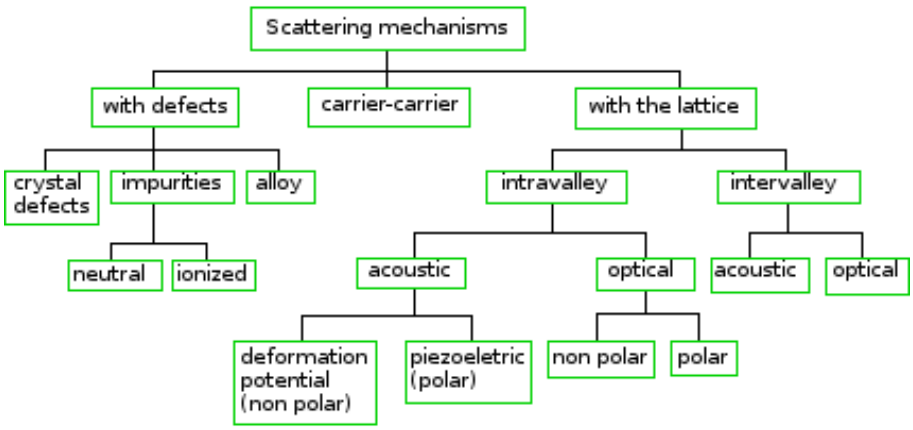

Figure 2.10: Classification of the scattering mechanisms, reproduced from [San94].

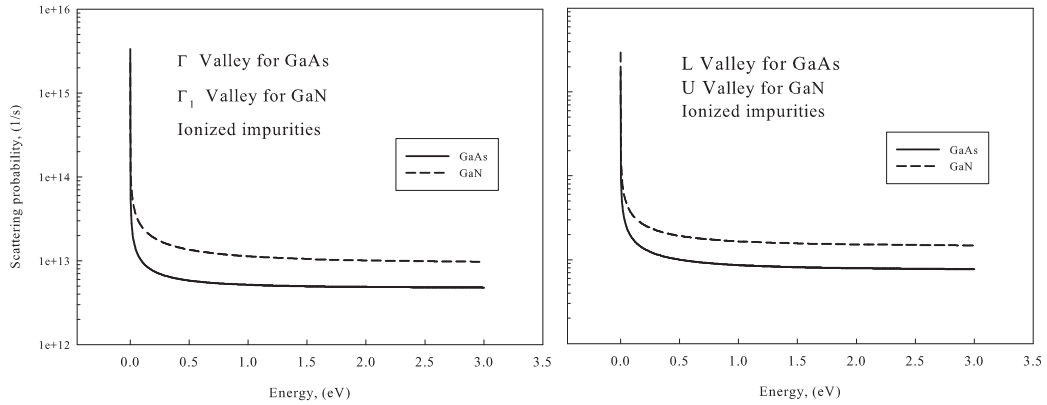

Figure 2.11: Scattering probability with ionized impurities in the valleys Γ and L for GaAs and Γ_1 and U for GaN semiconductors as a function of the energy of the carriers. Results obtained with the model of Brooks-Herring with non-parabolicity [Bro50, Ruc70] implemented in our MC simulator.

with the phonon is in the same valley as the initial state are intravalley mechanisms, while if the initial and final states are in different valleys they are intervalley mechanisms.

The interactions of the charge carriers with the thermal vibrations of the lattice through acoustic phonons can be approximated by an elastic interaction when the thermal energy, (k_BT), is much larger than the energy of the phonons involved in the interaction [Jac89b]. Table 2.3 summarizes the parameters employed to characterize this interaction in GaAs and GaN semiconductors. Fig. 2.12 compares the scattering probability with acoustic phonons in the valleys Γ and L for GaAs and Γ_1 and U for GaN semiconductor.

The inelastic scattering mechanisms included in our MC simulator are the interaction with op-

Table 2.3: Deformation potential for interactions with acoustic phonons employed in the MC simulator for GaAs [San94, Mad04] and GaN [Fou99, Mat07].

	GaAs			*GaN*		
Valley	Γ	L	X	Γ_1	U	Γ_3
Acoustic deformation potential, (eV)	5	5	5	8.3	8.3	8.3

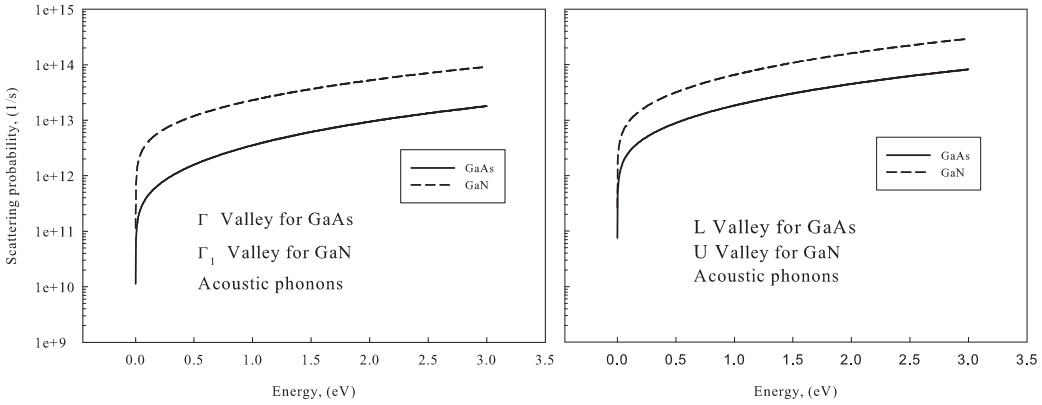

Figure 2.12: Scattering probability with acoustic phonons in the valleys Γ and L for GaAs and Γ_1 and U for GaN semiconductors as a function of the energy of the carriers.

Table 2.4: Energy of the phonons associated to the inelastic scattering mechanisms included in the MC simulator for GaAs [San94, Mad04] and GaN [Fou99, Mat07].

		GaAs			*GaN*		
Valley		Γ	L	X	Γ_1	U	Γ_3
Optical polar phonon energy, (meV)		36.13	36.13	36.13	91.2	91.2	91.2
Intervalley phonon energy, (meV)	$\Gamma or \Gamma_1$	0.0	27.80	29.30	0.01	91.2	91.2
	L or U	27.80	27.80	29.30	91.2	91.2	91.2
	$X or \Gamma_3$	29.30	29.30	29.30	91.2	91.2	0.01

Table 2.5: Non polar optical and intervalley deformation potentials employed in the MC simulator for GaAs [San94, Mad04] and GaN [Fou99, Mat07].

		GaAs			*GaN*		
Valley		Γ	L	X	Γ_1	U	Γ_3
Non polar optical deformation potential, $(10^{10}\, eV/m)$		0	3	0	0	0	0
Intervalley deformation potential, $(10^{10}\, eV/m)$	$\Gamma or \Gamma_1$	0	10	10	10^{-5}	10	10
	L or U	10	10	5	10	10	10
	$X or \Gamma_3$	10	5	7	10	10	10^{-5}

tical phonons and intervalley phonons. Table 2.4 summarizes the energy of these phonons. The interactions comprise the emission and the absorption of the corresponding phonons. Table 2.5 presents the values of the deformation potentials associated to the intervalley transitions employed in the MC model.

Fig. 2.13 and 2.14 show the scattering probability of interaction with optical polar phonons and intervalley phonons respectively, in the valleys Γ and L for GaAs and Γ_1 and U for GaN semiconductors.

The scattering with non polar optical phonons appears only for carriers in the L valley for GaAs, so, it is not included for GaN, see Fig. 2.15. The parameters used to model this scattering mechanism in our MC simulator are summarize in Table 2.5.

Fig. 2.16 compares the total scattering probability for electrons in the valleys Γ and L for GaAs and Γ_1 and U for GaN. The higher scattering probability in GaN semiconductor is the responsible of its lower electron mobility, [Sch05].

When the scattering probabilities are calculated, it is usually assumed that all the final states

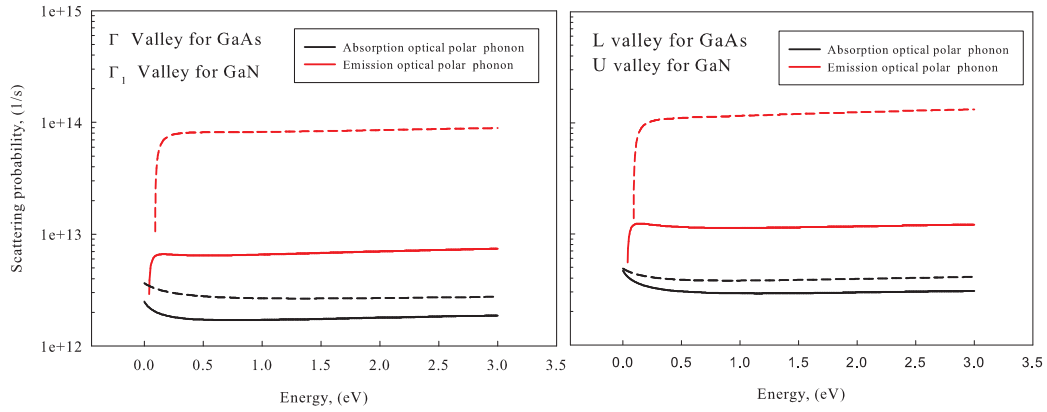

Figure 2.13: Scattering probability with optical polar phonons in the valleys Γ and L for GaAs, (continuous lines), and Γ_1 and U for GaN, (dashed lines).

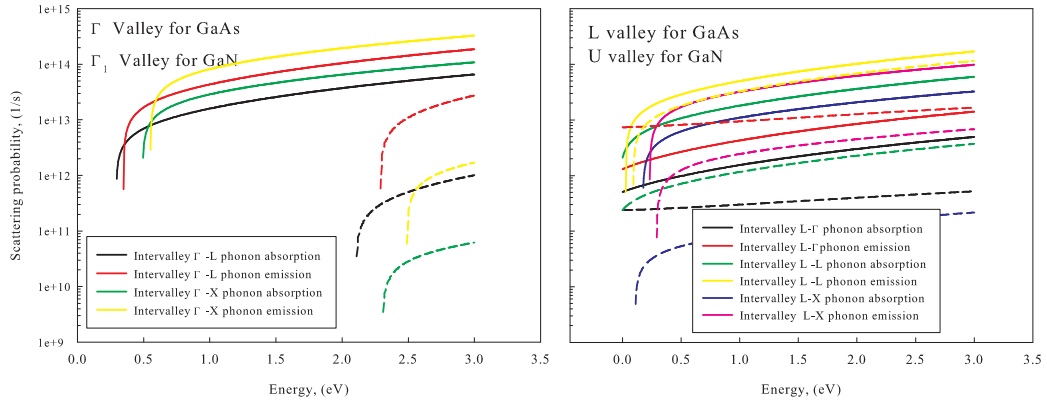

Figure 2.14: Scattering probability with intervalley phonons in the valleys Γ and L for GaAs, (continuous lines), and Γ_1 and U for GaN, (dashed lines).

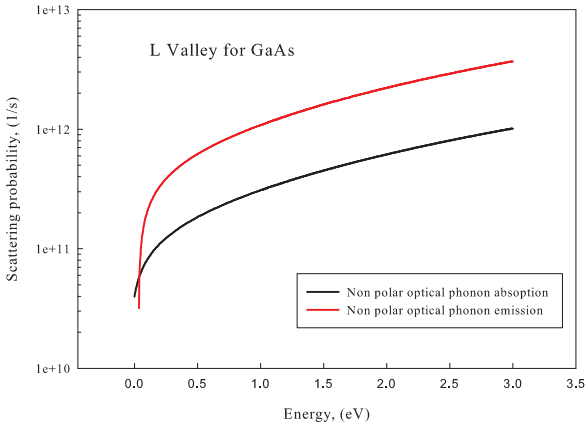

Figure 2.15: Scattering probability with non polar optical phonons for GaAs semiconductor in the Γ valley.

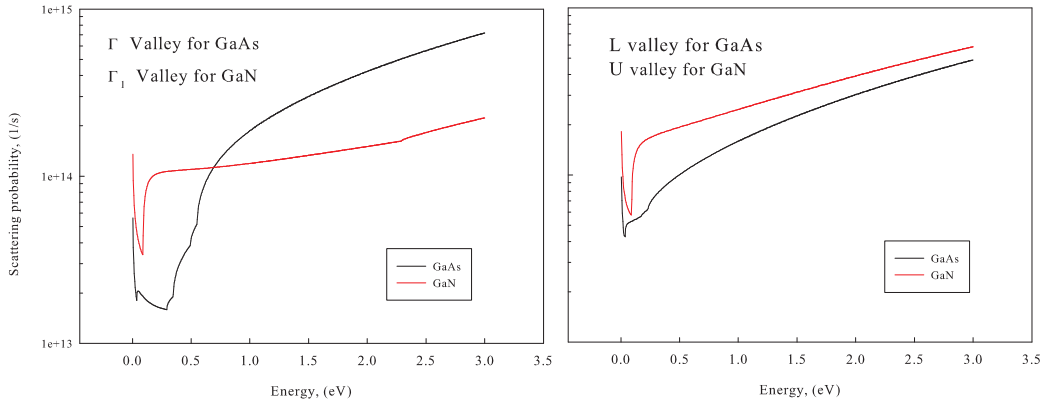

Figure 2.16: Total scattering probability for electrons in GaAs and GaN semiconductors in the valleys Γ and L for GaAs and Γ_1 and U for GaN.

are available. However, for high doping (higher than $5x10^{17}$ cm^{-3} in GaAs) Pauli's exclusion principle becomes important and it should be taken into account. The simple technique described in [Fis88, Man91] has been considered to account for the degeneracy in semiconductors: a scattering mechanism is rejected or accepted if the final state is occupied or not according to the Fermi-Dirac distribution function. Most of the Schottky diodes analysed in this thesis have epilayer doping concentrations $5x10^{17}$ cm^{-3} or lower. Hence, Pauli's exclusion principle has not been taken into account. Only for some examples of interest or when higher epilayer doping are simulated, the impact of the Pauli's exclusion principle has been analysed, see appendices D and F.

2.5.3 Single-particle Monte Carlo

For the simulation of transport under stationary and homogeneous conditions, it is enough to simulate the motion of a single carrier to obtain information about the whole gas of carriers (ergodic principle). This is the situation for the analysis of carrier transport in *infinite* homogeneous semiconductors under stationary conditions when a constant electric field is applied.

In the simulation of a time step dt (see appendix A to see the criteria to determine dt), every carrier is moved according to a succession of free flights under the existing electric field and scattering mechanisms. The duration of the free flight t_f is determined randomly according to the total scattering probability, that depends on the energy of the carrier:

$$t_f = -\frac{1}{\Gamma}\ln(r) \tag{2.51}$$

where r is a random number uniformly distributed between 0 and 1 and Γ is the total scattering probability including the self-scattering mechanisms [Ree68, Jac83]. This technique to determine t_f has been improved by different authors to reduce the time employed in the simulation of virtual mechanisms [Che88].

The evolution of the wavevector and the position of the carriers under the applied electric field is determined by the semi-classical equations:

$$\begin{cases} \hbar\frac{d\mathbf{k}}{dt} = -q\mathbf{E} \Rightarrow \mathbf{k} = \mathbf{k_0} - \frac{q\mathbf{E}t}{\hbar} \\ m^*\frac{d^2\mathbf{r}}{dt^2} = -q\mathbf{E} \Rightarrow \mathbf{r} = \mathbf{r_0} - \frac{q\mathbf{E}t^2}{2m^*} + \frac{\hbar\mathbf{k_0}t}{m^*} \end{cases} \tag{2.52}$$

where $\mathbf{k_0}$ and $\mathbf{r_0}$ are the wavevector and the position of the carrier at the initial of the free flight and $\mathbf{E}$ is the electric field applied to the carrier.

At the end of a free flight, the energy of the carrier, ε, and the probability of the carrier to suffer a particular scattering mechanism i, $\lambda_i(\varepsilon)$, are known. A particular scattering mechanism, l, is selected if it verifies that:

$$\sum_{i=1}^{l-1} \frac{\lambda_i(\varepsilon)}{\Gamma} < r < \sum_{i=1}^{l} \frac{\lambda_i(\varepsilon)}{\Gamma}. \tag{2.53}$$

It could happen that:

$$r > \sum_{i=1}^{S} \frac{\lambda_i(\varepsilon)}{\Gamma} \tag{2.54}$$

where S is the number of scattering mechanisms included in the simulation. In such a case, a self-scattering mechanism is considered, that does not modify the state of the carrier. Once the time step dt has been simulated, the instantaneous quantities of interest are stored and another time step is simulated just to the end of the total simulation time, $N\,dt$.

The single-particle Monte Carlo has been used in this thesis to evaluate the energy and momentum relaxation times in bulk GaAs and GaN semiconductors.

2.5.4 Device simulator

When the problem under study depends on time and space (non-stationary and non-homogeneous problem), it is necessary to simulate a set of particles under the action of a self-consistent electric field that is updated every time step according to Poisson's equation. To solve Poisson's equation is necessary to impose the proper boundary conditions what requires the definition of a spatial mesh in the device. A one dimensional model in coordinates space and three dimensional in momentum space Monte Carlo method has been considered in this thesis for the simulation of Schottky diodes. Boundary conditions for the 1D model are relatively simple. The ohmic contact is modeled as a surface that injects carriers in thermal equilibrium with the lattice. In addition, any carrier reaching the contact leaves the device. On the other hand, the Schottky contact is simulated as a perfect absorbent surface [San94].

The simulation begins with the definition of the physical system and the parameters of the simulations, i.e. the length and doping concentrations of every layer of the diode, the position of the ohmic and Schottky contacts, the voltage excitations applied at the terminals of the diode and the values of the time step and the spatial mesh according to the criteria of appendix A. The number of initial carries must be high enough to get reliable results, appendix A.

The initial position of the carriers is assigned following a homogeneous distribution according to the doping of each layer. The initial energy of the carriers is assigned following a Maxwell-Boltzmann/Fermi-Dirac distribution in thermal equilibrium with the crystal lattice and the modulus of the wave vector is assigned employing the initial energy of the particle and the model of the energy band considered in the simulator. The initial orientation of the wave vector is selected isotropically. An initial transient period is considered in the simulations, see appendix A.

In the simulation of a time step, every carrier is moved according to a succession of free flights under the existing electric field and the scattering mechanisms. Once the time step has been simulated for all the carriers inside the device, Poisson's equation is solved for the charge carrier concentration in the device. Then, the instantaneous quantities of interest are stored and another time step is simulated just to the end of the total simulation time, $N\,dt$.

2.6 Summary of the different models

As a summary of the models described in this and previous sections, Fig. 2.17 shows a rough estimation of the valid operation ranges for different available approaches of the BTE [Lun00].

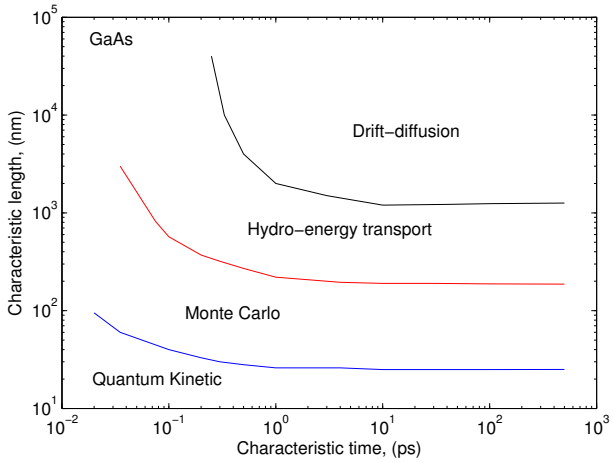

Figure 2.17: Illustration of the regions of validity of the physics-phased semiconductor models, from [Lun00].

Drift-diffusion equations do not treat nonlocal effects such as velocity overshoot. Hence this model is adequate for time scales higher than the energy and momentum relaxation times. On spatial scale, drift-diffusion equations are not adequate below about 1 μm for GaAs devices [Lun00]. An analysis of the accuracy of the DD model for the simulation of multipliers and mixers of sub-micron dimensions is presented in chapters 5 and 6, respectively.

Some of the nonlocal effects missed by drift-diffusion models can be taken into account by hydrodynamic/energy transport models. This approach, however, requires a large number of simplifying assumptions about the shape of the distribution function and about the ensemble relaxation times. For very small devices, in which these assumptions become unrealistic, direct solutions of the BTE, using techniques such as Monte Carlo simulation, may be necessary. The BTE loses validity under very short time scales, where collisions can no longer be treated as instantaneous, and when the critical regions of the device approaches the carrier's wavelength. Quantum transport approaches may be necessary to treat devices on this scale [Lun00].

In this work, the performance of circuits based on Schottky diodes is analysed in the frequency range from 100 GHz to 10 THz. On the other hand, most of the devices analysed have epilayer dimensions higher than 100 nm. Only some particular mixers at 5 THz and 10 THz with epilayer length as short as 30 nm have been considered. Hence, a diode model based on the Monte Carlo technique is adequate for the purpose of this work.

2.7 Properties of bulk GaAs and GaN

The description of the scattering mechanisms in GaAs and GaN semiconductors was carried out in subsection 2.5.2. In this section, the single-particle Monte Carlo has been used to analyse the microscopic characteristics of the electron transport (velocity, energy and valleys occupation) in bulk GaAs and GaN under steady-state conditions, see Fig. 2.18, where a doping concentration of $1x10^{17}$ cm^{-3} has been assumed. Also the velocity-field curves evaluated with the analytical models used in the DD model [Sel84, Sch05] are included in Fig. 2.18.

The velocity-field curve of GaAs shows two different regions: a linear region region up to 4 KV/cm (low field region) and a region at higher electric fields where the electron velocity decreases (high field region). At low electric field, the electrons are in the Γ valley, with low electron effective mass. In these conditions, the dominant scattering mechanisms are anisotropic (impurities and optical polar phonons, Fig. 2.18(g)). As the electric field increases, the average velocity and kinetic energy of the electrons increase. At electric fields higher than 2.5 KV/cm, the transfer of electrons

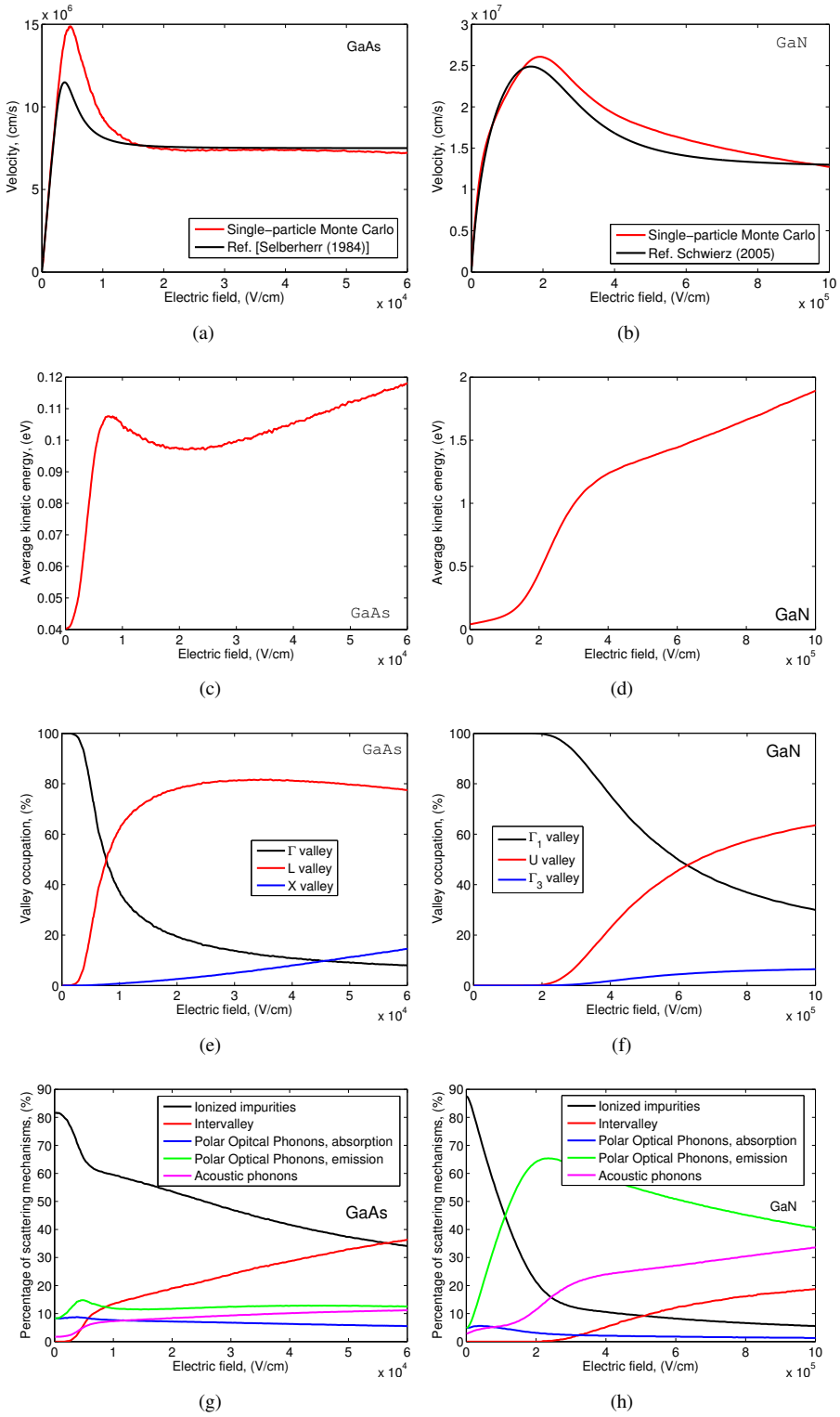

Figure 2.18: Microscopic characteristics of bulk GaAs (left column) and GaN (right column) obtained with single-particle Monte Carlo.

to the L valley begins, Fig. 2.18(e), where the effective mass is higher. The maximum velocity $\sim$ 1.5x10^7 cm/s is reached around 4 KV/cm. At higher electric fields the velocity decreases, due to the increase of the occupation of the L valley and the initiation of the electron transfer to the X valleys. At these high fields, the dominant scattering mechanisms are intervalley Fig. 2.18(g), that are isotropic, what prevents the velocity from increasing noticeably despite the increase of the electric field. Although the transfer of electron to the L valley begins at electric fields higher than 2.5 KV/cm, the kinetic energy of the electron increases up to fields $\sim$ 8 KV/cm, see Fig. 2.18(c), since the increase of the velocity for the electrons in the Γ valley is very high at these high electric fields. The increase of the average kinetic energy remains until the population of the L valley increases considerably and the kinetic energy of the electrons is transformed into potential energy in the L valley (also into the X valley at higher fields), leading even to the decrease of the kinetic energy. At electric fields higher than 25 KV/cm, the occupation of the valleys changes slower and the high electric field compensates the energy lost in the intervalley scattering, and the average kinetic energy begins to increase, [Tom93, San94].

The velocity-field curve of GaN presents four different regions, Fig. 2.18(b): two linear regions, the first up to 40 KV/cm and the second between 40 and 200 KV/cm, where the velocity increases as the electric field increases. The third region appears at fields higher than 200 KV/cm, where the electron velocity decreases as the electric field increases, and the fourth region is located at electric fields higher than $\sim$600 KV/cm, where the velocity is nearly constant despite of the increase of the electric field. In the first and second regions, the electrons are in the Γ_1 valleys with low effective mass. In these two regions, the average electron velocity and the kinetic energy increase as the electric field increase, since the electrons are in the valley of lower effective mass and the dominant scattering mechanisms are anisotropic, see Fig. 2.18(h). In the first region, the dominant scattering mechanisms is ionized impurities that is elastic, Fig. 2.18(h). At electric fields higher than 40 KV/cm (second region), the dominant scattering mechanism is the emission of polar optical phonons (inelastic mechanism) what reduces the rate of increase of the velocity as the electric field increases (lower electron mobility). At fields higher than 200 KV/cm, the velocity decreases (negative differential mobility) due to the transfer of electrons to the U valley, where the effective mass is higher. As the occupation of the U valley increases (electric fields higher than 350 KV/cm), Fig. 2.18(f), the average kinetic energy increases at lower rate.

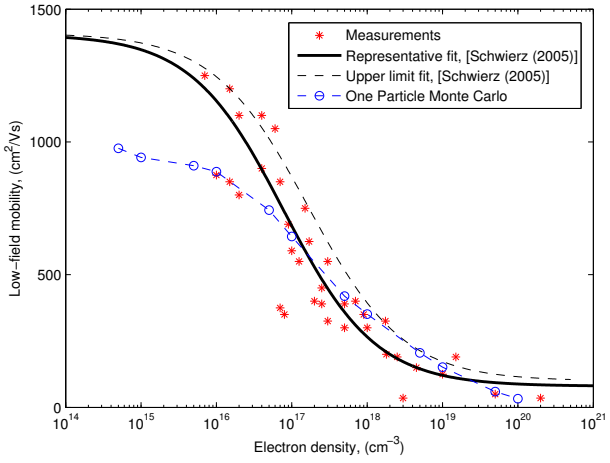

Figure 2.19: Low field mobility of bulk wurtzite n-GaN as a function of doping density obtained from measurements [Sch05], one-particle MC simulations and fitting in [Sch05].

Fig. 2.19 compares measured low field electron mobility of bulk GaN (reported in [Sch05]) as a function of doping density with the analytical model in [Sch05] and one-particle MC simulations. A good agreement is observed between measured and MC simulated results for doping concentration higher than 5x10^{16} cm^{-3}. For doping concentration lower than 5x10^{16} cm^{-3}, MC predicts electron

mobility lower than measurements.

As the electric field increases, some discrepancies appear among measured results, the analytical model [Sch05] and the one-particle MC, as is observed in Fig. 2.20 for bulk GaN with doping 1.35x10^{17} cm^{-3}. Besides the scattering mechanisms described in section 2.5.2 for the GaN MC model, scattering with threading dislocations and piezoelectric scattering are important to reproduce accurately the measured GaN velocity-field curve [Wei98, Ng98, Mat07], as is shown in Fig. 2.20. The density of threading dislocations necessary in the MC simulations to reproduce measured results depends on the doping concentration and also on the GaN growing technique used (the density of threading dislocations used in Fig. 2.20 is N$_{dis}$= 0.15x10^{10} cm^{-2}). Due to the development of the GaN technology in recent years, the scattering with threading dislocations does not represent a critical point in the performance of GaN devices. Hence, the MC model for GaN devices used in this thesis does not take into account scattering with threading dislocations. Piezoelectric scattering has also been neglected due to its low impact in the carrier transport in GaN, see Fig. 2.20.

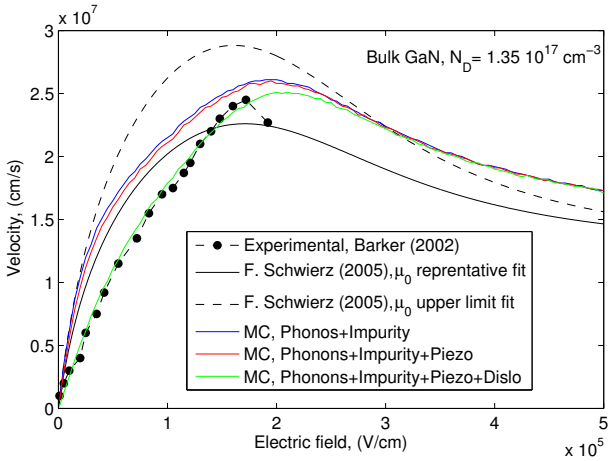

Figure 2.20: Comparison of measurement results [Bar02], MC simulations and fitting model [Sch05] for the velocity-field curves of bulk GaN doped 1.35 10^{17} cm^{-3}.

Chapter 3

Carrier transport in Schottky diodes

Understanding the limiting processes of carrier transport in semiconductor devices is fundamental to predict their performance in circuits. When a model is able to incorporate the limiting mechanisms of a device for a given working regime, the predicted performance of this model will be close to the measured results. Under certain conditions, very simple analytical models allow to describe sufficiently well such limiting effects and there is not need to use more sophisticated models.

Under high frequencies and/or high powers, the performance of the devices becomes dominated by a combination of different physical processes like velocity saturation, nonlocal effects in time and space or plasma resonance among others. An accurate and complete description of these phenomena requires high level physics-based models, like Monte Carlo method, based on the direct modelling of the carrier transport.

This chapter presents an analysis of physical phenomena that are important in the performance of Schottky diodes up to THz frequencies. To obtain reliable and accurate results, the Monte Carlo model described in chapter 2 has been used as a reference.

3.1 Limiting mechanisms of carrier transport

Table 3.1 shows a summary of different models and the physical effects that they take into account. Although the physical phenomena in the table are presented as independent processes, under the operation conditions of Schottky diodes they are usually interrelated. For GaAs Schottky diodes it is convenient to distinguish among the phenomena which appear under electric fields lower than the critical field[1], i.e. at fields lower than $\sim$ 4 KV/cm (low field transport), and the phenomena which appear at higher electric fields (high field transport). In the second group are included effects like nonlocal effects and velocity saturation. Carrier inertia, dependence of the electron mobility on the epilayer length, plasma effects and nonstationary phenomena can be enclosed in both groups. Fig. 3.1 presents a scheme of the Schottky diode to show the region where these phenomena are located.

As a reference for this section, a GaAs Schottky diode with an epilayer doping of 3x10^{17} cm^{-3}, epilayer length 250 nm, substrate doping of 2x10^{18} cm^{-3} and substrate length 500 nm is considered. The selected anode area is 1 μm^2. The ideal barrier height is 0.99 V and the temperature 300 K. The following mechanisms have been analysed: Nonlocal effects, saturation of the electron velocity, carrier inertia, dependence of the electron mobility on the epilayer length, plasma effects and nonstationary phenomena.

[1] In the steady-state velocity-field curves of bulk GaAs, the critical field is the electric field at which the electron peak velocity is achieved.

Table 3.1: Summary of Schottky diode models and physical phenomena that they take into account.

Physical phenomena	Model			
	LEC	DD	HD	MC
Carrier inertia	No[a]	No	Yes	Yes
μ_0 dependent on epilayer length	No	No	No	Yes
Displacement current in undepleted regions	No[a]	Yes	Yes	Yes
Velocity saturation	No	Yes	Yes	Yes
Nonstationary effects	No	No[b]	Yes	Yes
Nonlocal effects	No	No	Yes	Yes

[a] It can be modeled by an inductance (inertia) or a capacitance (displacement current).

[b] Nonstationary effects can be modeled by employing weighted average ac mobility models [Sch95, Lip97].

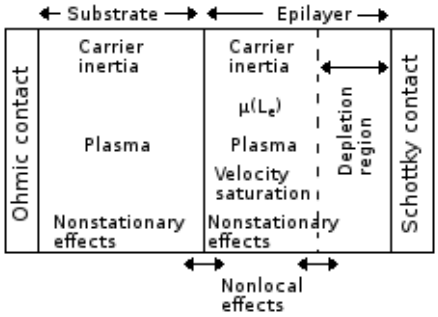

Figure 3.1: Scheme of a Schottky diode, showing the main regions where the different physical phenomena are located.

3.1.1 Nonlocal effects in the transition between the undepleted epilayer and the space-charge region

The electric field in the neighborhood of the Schottky contact is high and undergoes rapid variations over distances comparable to the carrier's mean free path. Therefore, velocity over-

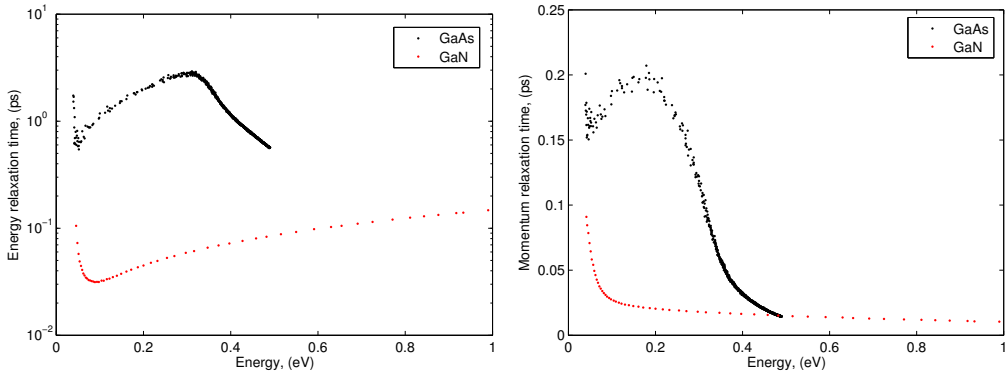

(a) (b)

Figure 3.2: Energy and momentum relaxation times as a function of the electron energy in bulk GaAs and GaN semiconductors with doping concentration 1x10^{17} cm^{-3}, obtained under steady-state conditions with the one-particle MC.

shoot/undershoot is expected to affect the motion of the electrons in that region [San89, Lun00].

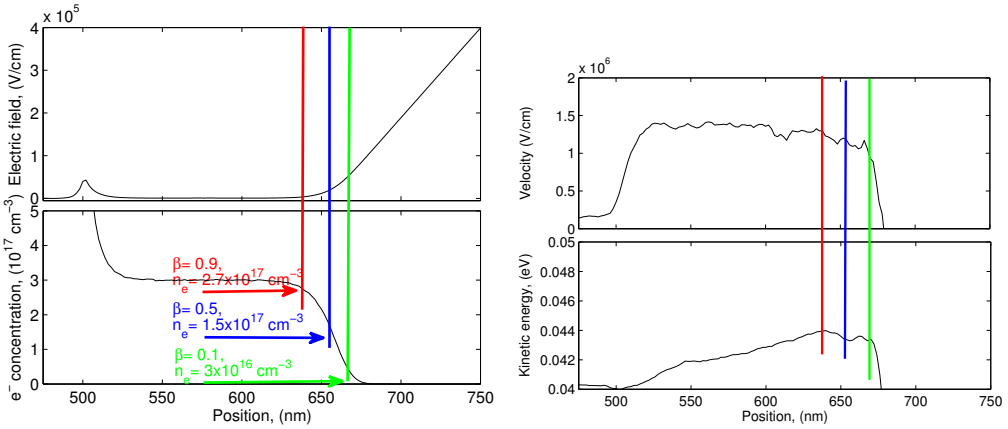

(a) (b)

Figure 3.3: Profiles of (a) the electron concentration, the electric field, (b) the kinetic energy and the velocity of the electrons in the reference diode under a sinusoidal voltage of amplitude 1 V, frequency 600 GHz and bias voltage -2 V. Results evaluated with the MC model at the maximum of the applied voltage. Position 0 nm represents the ohmic contact. Vertical lines indicate the position for different values of β.

In the transition between the neutral (low field region) and the depleted (high field region) regions of the epilayer, the electrons move in the high field region with a mobility higher than expected from the static velocity-field curves due to the delayed response of the electron velocity to the local electric field. The momentum relaxation time $\tau_m(\varepsilon)$ depends on the electron energy ε. Since the adaptation of the electron energy to the variations of the electric field is determined by τ_ε, but $\tau_\varepsilon > \tau_m$ ($\tau_\varepsilon \approx$ 3 ps, $\tau_m \approx 0.25$ ps for GaAs [Lee99], see Fig. 3.2 obtained with our one-particle Monte Carlo for bulk GaAs), the adaptation of τ_m and the electron velocity to the variations of the electric field is slow. This leads to the delayed response of the electron velocity to the variations of the electric field [Gro84, Lun00, Jos95]. This delayed response is observed in Fig. 3.3, where the velocity and the energy of the electrons remain nearly constant in the transition region despite of the variation of the electric field[2]. Since DD evaluates locally the electron mobility from the static velocity-field curves, it does not take into account this effect and overestimates the series resistance of the diode, eq. (2.7). Although the same effect is expected in the $n^+ - n$ transitions, it is not as important as is in the transition between the neutral and the depleted regions in the epilayer, since the $n^+ - n$ transition is shorter and the values of the electric field are lower than in the neutral-depleted transition of the epilayer, see Fig. 3.3.

To show the effect of this phenomenon on the impedance of the diode, an impedance $Z_\beta[f]$ of the portion of the diode located between the ohmic contact and the position with electron concentration n_e equal to a determined fraction of the epilayer doping concentration βN_e with $0 < \beta < 1$ is defined, see Fig. 3.3. $Z_\beta[f]$ has been calculated according to the following equation:

$$Z_\beta[f] = \frac{V_\beta[f]}{I[f]} \tag{3.1}$$

where $I[f]$ and $V_\beta[f]$ are the fundamental components of the Fourier series of the total current in the diode and the voltage that drops in the selected portion of the diode (calculated as $V_\beta(t) = -\int E(x,t)dx$, where E(x,t) is the electric field as a function of the position and time), respectively.

Fig. 3.4 presents the real part of $Z_\beta[f]$ normalized by the values at $\beta = 0.9$ for the reference diode, simulated with DD, DD with constant low field mobility (DD_0, see chapter 2) and MC models under

[2]The profiles in Fig. 3.3 are evaluated at a fixed time, but the change of these profiles during the time spent by an electron to cross the transition region is negligible.

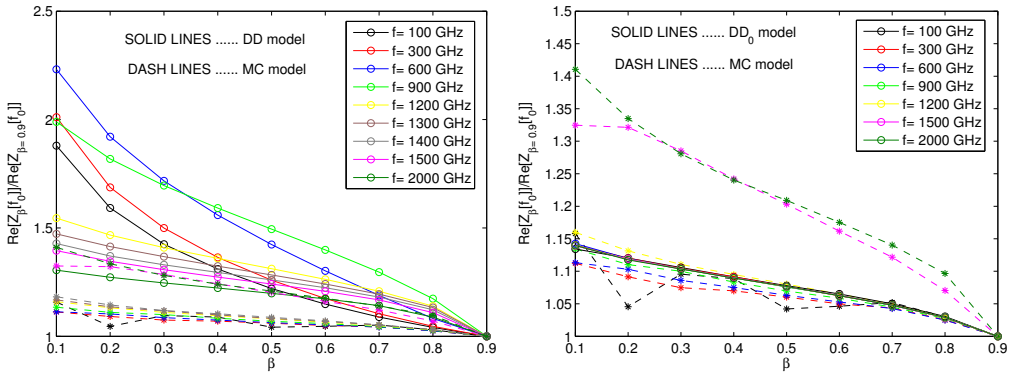

(a) (b)

Figure 3.4: Comparison of the real part of the impedance $Z_\beta[f]$ for the reference diode simulated with (a) the DD and MC and (b) DD_0 and MC models under sinusoidal applied signals of amplitude 1 V, bias point -2.0 V and different frequencies, as a function of β. The values presented have been normalized by the real part of $Z_\beta[f]$ with β= 0.9 at each simulated frequency.

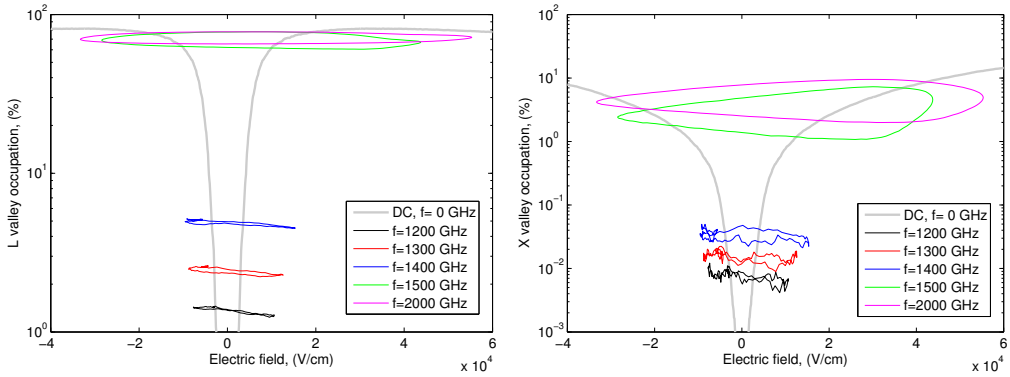

(a) (b)

Figure 3.5: (a) L valley and (b) X valley occupation of the reference Schottky diode under an applied voltage of amplitude 1 V, different frequencies and bias -2 V, obtained from MC simulations. These profiles have been evaluated in the undepleted region of the epilayer.

sinusoidal applied signals of amplitude 1 V, bias point -2 V and different frequencies f. It is observed that the real part of $Z_\beta[f]$ predicted by the DD model at β= 0.1 is nearly two times the value at β= 0.9 at input frequencies lower than 1200 GHz whereas the change in the MC simulations is only a factor 1.1. At higher frequencies, when the velocity saturation is reached (see subsection 3.1.2), high fields exist also in the undepleted epilayer, so, nonlocal effects are masked, and the increase of the real part of $Z_\beta[f]$ with β is nearly the same for both DD and MC. Fig. 3.5 presents the L and X valleys occupation in the undepleted epilayer of the reference diode at different input frequencies[3]. Note that only when the effects of velocity saturation in MC model are important (input frequencies higher than 1400 GHz), with L-valley occupations higher than 50 %, MC and DD agree in Fig. 3.4(a).

These results indicate that the DD model overestimates the series resistance of the diode because of the local evaluation of the electron mobility, and when velocity saturation appears, such an error

[3]In Fig. 3.5, the population of the Γ and L valleys in the undepleted epilayer of the reference Schottky diode under sinusoidal voltages deviates from the steady-state because the repopulation of the valleys is slower than the variation of the applied voltage.

is masked. Therefore, important discrepancies are expected between DD and MC models in the simulation of GaAs circuits while velocity saturation is not limiting the performance of the diodes.

Simulations with the DD_0 model show the same dependence on β than MC for input frequencies lower than 1500 GHz, Fig. 3.4(b). Since DD_0 assumes constant low field mobility independently of the electric field, it does not overestimates the real part of the diode impedance as DD model does. At higher frequencies, the agreement between DD_0 and MC disappears because of velocity saturation. Therefore, a good agreement is expected between DD_0 and MC simulations while there is not velocity saturation.

The same analysis has been carried out assuming an epilayer doping of $5x10^{17}$ cm^{-3} for the reference Schottky diode, Fig. 3.6. The same conclusions are obtained, but the agreement between MC and DD appears at higher frequencies $\sim$ 1800 GHz, see Fig. 3.6(a), since velocity saturation is mitigated as the doping increases, see subsection 3.1.2.

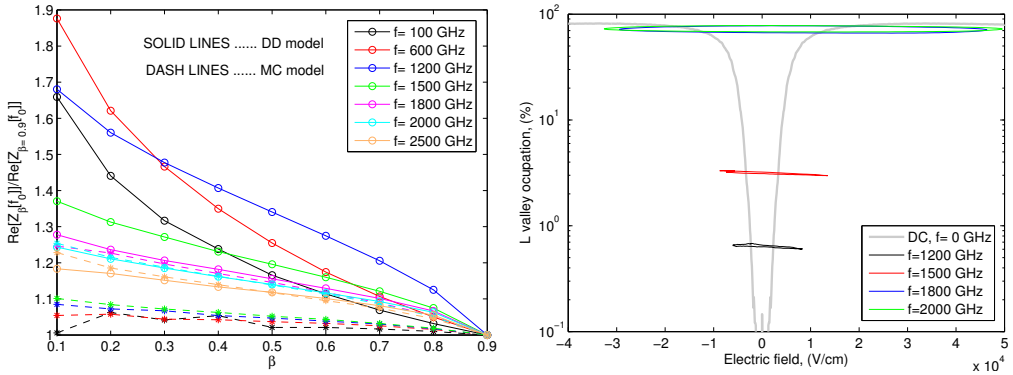

(a) (b)

Figure 3.6: (a) Real part of the impedance $Z_\beta[f]$ for the reference diode with epilayer doping $5x10^{17}$ cm^{-3} simulated with the DD and MC under sinusoidal applied signals of amplitude 1 V, bias point -2.0 V and different frequencies, as a function of β. The values presented have been normalized by the real part of $Z_\beta[\omega]$ with β= 0.9 at each simulated frequency. (b) Occupation of the L valley in the undepleted region of the epilayer.

3.1.2 Velocity saturation

In Schottky diodes, the displacement current in the depletion region has to be matched to the conduction current in the undepleted epilayer [Kol92, Cro93]. Therefore, the rate of change of the width of the depletion region w_{depl} is limited by the maximum electron velocity in the neutral semiconductor v_{max}:

$$J_{max} = qN_e v_{max} > J_{disp} = \frac{dQ}{dt} = qN_e \frac{dw_{depl}}{dt} \Rightarrow v_{max} > \frac{dw_{depl}}{dt} \tag{3.2}$$

where Q is the charge in the depletion region. At high frequencies and/or high powers, the saturation of the electron velocity limits the modulation of the nonlinear capacitance of the diode, and, therefore, the conversion efficiency of multipliers. DD, HD and MC take into account velocity saturation while models which assume constant electron mobility fail when this effect appears.

Fig. 3.7 presents the electron concentration profiles of the reference diode under sinusoidal applied signals of amplitude 1 V, bias voltage -2 V and different frequencies, obtained with DD and MC models. In this figure, the Schottky contact is located on left-hand side of the diagram (position 750 nm). With the DD model, it is shown that the edge of the depletion region can follow the voltage waveform at 100 GHz, but cannot follow the voltage waveform at 1 THz due to the limitation imposed by eq. (3.2). With the MC simulations it occurs at input frequencies higher than

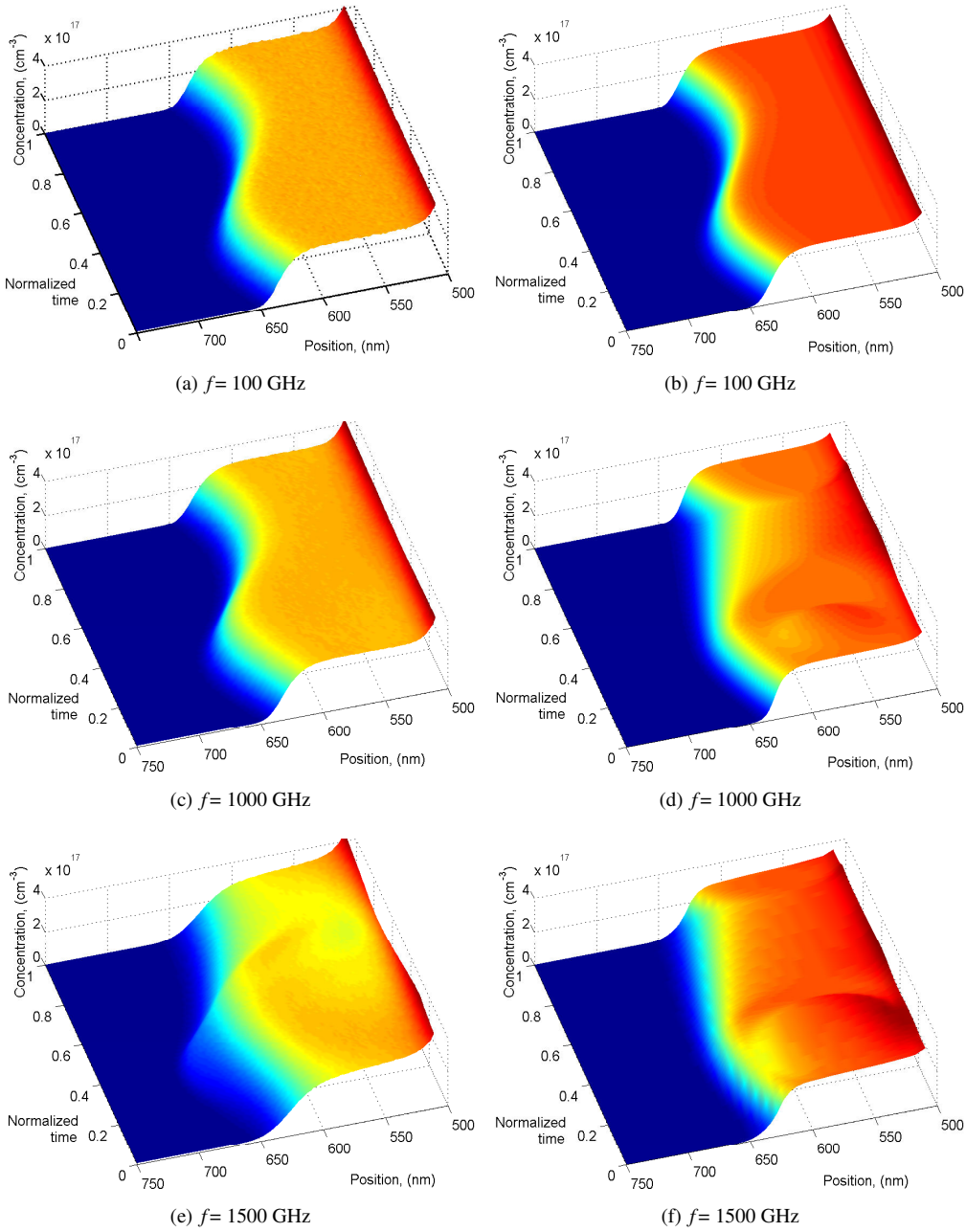

(a) f= 100 GHz (b) f= 100 GHz

(c) f= 1000 GHz (d) f= 1000 GHz

(e) f= 1500 GHz (f) f= 1500 GHz

Figure 3.7: Electron concentration profiles of the reference diode under sinusoidal voltage of amplitude 1 V, bias voltage -2 V and different frequencies f. Results obtained with MC (left column) and DD (right column) simulators.

1.2 THz, see Fig. 3.7. This performance of the depletion region is the result of the energy and momentum relaxation effects and the complexity of intervalley dynamics of the electrons under high frequency applied signals. DD accounts for velocity saturation but cannot describe correctly this phenomenon.

Velocity saturation effects are also shown in Fig. 3.8 when high electric fields are generated in the undepleted region of the epilayer. An interesting feature of this figure is that the time dependent velocity-field response of the electrons in the undepleted epilayer obtained with MC does not follow

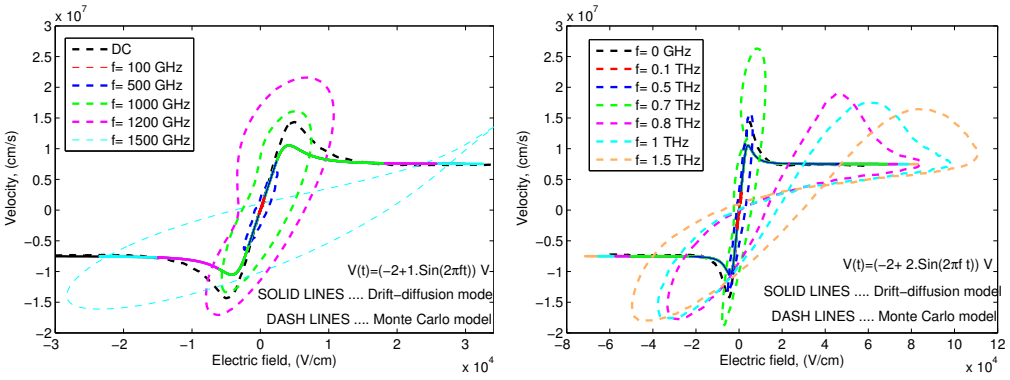

Figure 3.8: Velocity-field curves in the undepleted epilayer (evaluated at 550 nm from the Ohmic contact) of the reference diode (N_e= 3x10^{17} cm^{-3}) under a bias voltage of -2 V and a sinusoidal voltage of amplitude (a) 1 V and (b) 2 V, for different frequencies. Results obtained with MC and DD models.

the static velocity-field curve. These velocity-field loops obtained with the MC model are due to energy and momentum relaxation effects, i.e. the delayed response of the electron energy and velocity to the variation of the electric field (complex electron mobility, see 3.1.3), see section 3.1.5. In Fig. 3.8(a), at input frequency 1500 GHz the swing of the electric field increases and the slope of the main diagonal of the velocity-field loop decreases. This is due to the increase of the L valley population in the undepleted epilayer up to 70 % at this frequency, as is shown in Fig. 3.5. When the amplitude of the applied sinusoidal voltage is 2 V, Fig. 3.8(b), velocity saturation effects appear at 800 GHz and higher frequencies.

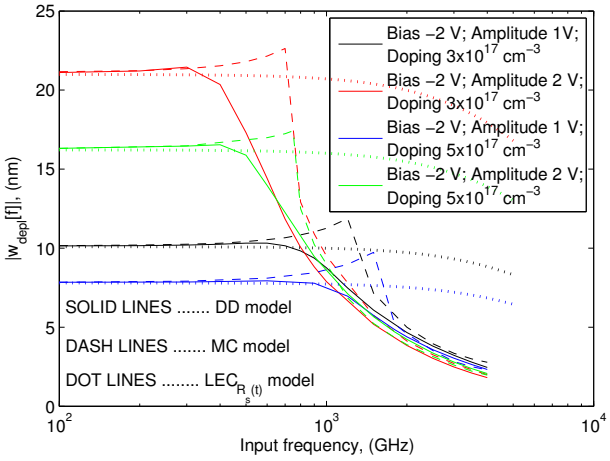

Figure 3.9: Module of the fundamental component of the Fourier series of the evolution of the width of the depletion region w$_{depl}$(t) for the reference Schottky diode with different epilayer doping under sinusoidal applied signal, obtained with LEC$_{R_s(t)}$, DD and MC simulations. w$_{depl}$=0 corresponds to the Schottky contact.

Velocity saturation effects can also be observed in the module of the fundamental component of the Fourier series of the time evolution of the width of the depletion region. In DD and MC models, the width of the depletion region w$_{depl}$ has been defined as the point where the electron concentration falls to 60 % of the epilayer doping. Fig. 3.9 shows this characteristic for the reference Schottky diode with different epilayer doping N_e. Sinusoidal voltages of constant amplitude V_1 are applied at the terminals of the diode for different input frequencies. The swing of the depletion region

evaluated with the DD and MC models decrease abruptly[4] when the frequency is high enough to produce velocity saturation, as can be observed by comparing the results of this figure for V_1= 1 V with the charge profiles of Fig. 3.7. It is evident from this figure that this performance cannot be understood with the simple LEC model of Fig. 2.5, where the width of the depletion region is evaluated according to:

$$w_{depl}(t) = \sqrt{\frac{2\varepsilon_0\varepsilon_r[V_{bi} - (V(t) - I(t)R_s(t))]}{qN_e}} \tag{3.3}$$

where $V(t)$ is the time dependent voltage applied at the terminals of the diode, *I(t)* is the current, and $R_s(t)$ is the time varying series resistance of the diode. Fig. 3.9 shows that velocity saturation depends on the amplitude of the excitation (see also Fig. 3.8) and the doping, eq. (3.2). When the amplitude of the voltage increases, velocity saturation appears at lower input frequencies, while increasing the doping concentration mitigates this effect [Kol92, Cro93].

3.1.3 Carrier inertia

Carrier inertia causes a delay in the response of the electron velocity to the variations of the electric field. This inductive effect becomes important when the frequency of the applied signal approaches the inverse of the momentum relaxation time τ_m [Cha78, Kel79, Lee99]. When the operating frequency is much less than the inverse of τ_m, the inertia of the electrons is compensated quickly by random scattering of the electrons. However, as the operating frequency increases towards the inverse of the mean scattering frequency, the scattering rate will be too low to compensate the inertia and inductive effects will appear in the device's characteristics [Cro89].

A simple approach to describe this phenomenon under low field conditions is to assume a constant momentum relaxation time in the momentum balance equation of a hydrodynamic model (neglecting thermal effects and carrier density gradients, see eqs. (3.10) and (3.18) in subsection 3.1.5), that leads to a complex, frequency dependent ac-mobility μ_{ac} [Gro84, Jos95]:

$$\mu_{ac}(f) = \frac{v_1(f)}{E_1(f)} = \frac{\mu_0}{1 + j2\pi f\tau_m} = \mu_r - j\mu_i = \frac{\mu_0}{1 + (2\pi f\tau_m)^2} - j\frac{\mu_0 2\pi f\tau_m}{1 + (2\pi f\tau_m)^2} \tag{3.4}$$

where f is the frequency of the sinusoidal applied field, $v_1(f)$ and $E_1(f)$ are the fundamental components of the Fourier series of the electron velocity and the electric field in neutral regions of the diode, respectively; μ_0 is the low field electron mobility and j represents the imaginary unit. In the DD approach, the mobility is real and independent of the input frequency [Sel84].

Fig. 3.10 shows the ac-mobility μ_{ac} obtained from MC simulations of the reference Schottky diodes with different epilayer length L_e and doping N_e under sinusoidal applied signals.It is evaluated in low field neutral regions of the epilayer. MC simulations indicate that μ_{ac} follows the dependence on the input frequency given by eq. (3.4).

Using μ_{ac} from eq. (3.4) to evaluate the impedance associated to the undepleted region of the device of length L_{und}, doping N_e and area A:

$$Z = \frac{1}{q\mu_{ac}N_e}\frac{L_{und}}{A} = \frac{1}{q\mu_0 N_e}\frac{L_{und}}{A} + j\frac{2\pi f\tau_m}{q\mu_0 N_e}\frac{L_{und}}{A} = R_s + j2\pi fL. \tag{3.5}$$

with $L = \tau_m R_s$. Therefore, the equivalent circuit associated to eq. (3.4) consists of a constant resistance (independent of the input frequency) in series with an inductance, see Fig. 2.7 and the inset of Fig. 3.10.

[4]This decrease is more abrupt for MC than DD simulations, since in the MC model for GaAs, velocity saturation is due to transfer of electrons to the upper low mobility valleys. When the energy of the electrons approaches the energy separation between the Γ and L valleys, the probability of intervalley transfer is very high, and the occupation of the L valley increases abruptly, see Fig. 3.5(a) at input frequencies 1.4 THz and 1.5 THz.

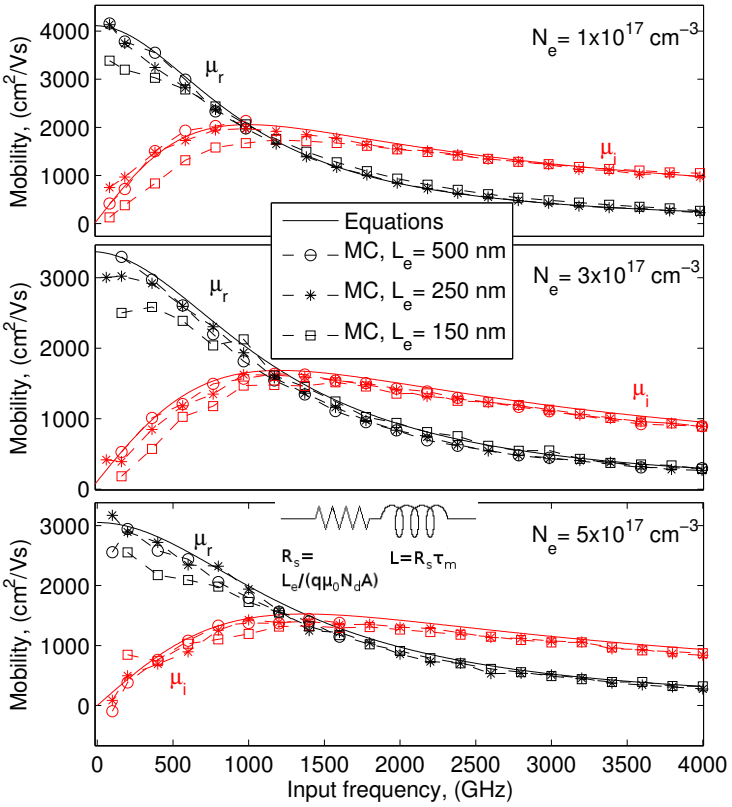

Figure 3.10: Dependence of the low field GaAs ac-mobility on the frequency of the sinusoidal applied signals of amplitude 0.1 V and bias 0.7 V, obtained from eq. (3.4) and MC simulations. Schottky diodes with different epilayer length and doping have been considered. μ_{ac} from MC simulations was evaluated in neutral regions of the epilayer.

Besides, Fig. 3.10 shows that $\mu_{ac}(f)$ from MC simulations depends on the length of the epilayer. If the length of the epilayer decreases below a certain value that depends on the epilayer doping, the real and imaginary parts of $\mu_{ac}(f)$ decrease with respect to the expected value eq. (3.4). This dependence on the epilayer length is in accordance with the discussion presented in [Cro89, Jos95, Fab95]: The electrons enter into the epilayer of the diode from the substrate with randomized net momentum. They are accelerated by the electric field towards the anode where they are emitted through the Schottky barrier or reflected back towards the substrate. On average, each electron emitted is replaced by a thermalize electron from the substrate. This phenomenon is equivalent to a *scattering* event that tends to randomize the net momentum of the electron distribution with a mean time between *scattering* events approximated by the transit time of the electrons through the epilayer, that can be approached by [Cro89, Rai92]:

$$\tau \sim \frac{L_e}{v_d} \tag{3.6}$$

where L_e is the epilayer length and v_d the average drift velocity of the electrons. The resulting effective scattering frequency can be approximated by [Cro89, Rai92, Fab95]:

$$\omega_{s,eff} = \omega_s + \frac{1}{\tau} = \frac{1}{\tau_m} + \frac{1}{\tau} = \frac{q}{m^* \mu_0} + \frac{1}{\tau} \tag{3.7}$$

where $\omega_s = 1/\tau_m$ is the scattering frequency, eq. (2.8). This effect is equivalent to an increase of the scattering frequency, and, therefore, leads to a reduction of the electron mobility, in accordance with the results in Fig. 3.10. By reducing L_e, this phenomena is more important, see eq. (3.6). The

effective momentum relaxation time $\tau_{m,eff} = 1/\omega_{s,eff}$ can be used in eq. (3.4) instead of τ_m to take into account the dependence of $\mu_{ac}(f)$ on the length of the epilayer ($\mu_0 = q\tau_m/m^*$ is also a function of τ_m).

3.1.4 Plasma resonance

The carrier inertia together with the displacement current in the undepleted regions of the device, whose equivalent circuit is a capacitance C in parallel with the R_sL circuit shown in the inset of Fig. 3.10, lead to carrier plasma resonances at the plasma frequency ω_p (resonance of the equivalent circuit of the undepleted regions, see Fig. 2.7) [Cha64, Kel79]:

$$\omega_{p\,i} = \sqrt{\omega_{s,i}\omega_{d,i}} = \sqrt{\frac{N_i q^2}{m^* \varepsilon_0 \varepsilon_r}} = \frac{1}{\sqrt{LC}}, \;\; i = e,s \tag{3.8}$$

where $\omega_{s,i}$ is the scattering frequency of the i-region ($i = s$ for the substrate and $i = e$ for the undepleted epilayer), eq. (2.8), $\omega_{d,i}$ is the dielectric relaxation frequency for the i-region, eq. (2.9), and N_i is the doping concentration of the i-region. Two plasma resonances are expected, due to the motion of the electrons in the substrate ($i = s$) and the epilayer ($i = e$), with characteristic frequencies given by eq. (3.8). Monte Carlo simulations account for the impact of the structure of the diode on the plasma frequency, providing more accurate values for $\omega_{p\,i}$ than eq. (3.8).

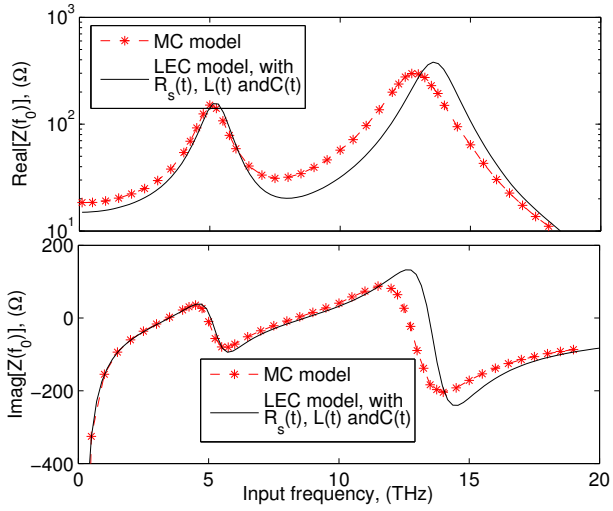

Figure 3.11: Real and imaginary parts of the impedance of the reference diode (epilayer doping 3x10^{17} cm^{-3}) as a function of the input frequency. The bias point considered is -2 V. Sinusoidal voltage of amplitude 0.1 V have been simulated. The MC and LEC based on R$_s$LC(t) models have been applied.

Fig. 3.11 shows the impedance at the fundamental frequency of the reference diode as a function of the input frequency. The diode has been excited with a sinusoidal voltage of low amplitude 0.1 V to avoid high field effects. MC and a lumped equivalent circuit like that presented in Fig. 2.7 (a R$_s$LC circuit for the substrate and a R$_s$LC(t) circuit for the undepleted epilayer) [Cha78] have been considered. Since DD model does not take into account carrier inertia, it does not model plasma effects.

When increasing the input frequency, the real part of the diode impedance increases due to the plasma resonance of the epilayer $f_{pe} = \omega_{pe}/(2\pi)$ and the substrate $f_{ps} = \omega_{ps}/(2\pi)$ [Cha78, Kel79], with peaks at 5 and 13 THz (from eq. (3.8), f_{pe}= 5.29 THz for N_e= 3x10^{17} cm^{-3}, and f_{ps}= 13.66 THz for N_s= 2x10^{18} cm^{-3}). This phenomenon also affects the imaginary part of the diode impedance, that becomes positive at frequencies close to the epilayer plasma frequency due to the dominant contribution of the charge carrier inertia over the capacitance of the Schottky junction.

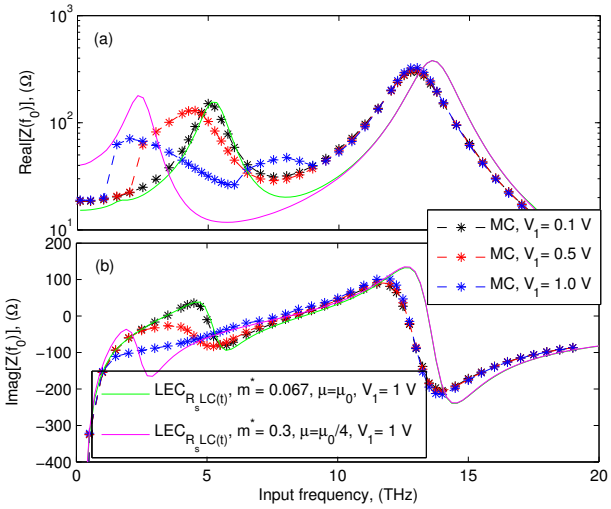

Figure 3.12: Real and imaginary parts of the impedance of the reference diode as a function of the input frequency under sinusoidal voltages of different amplitudes and bias point -2 V. Results obtained from MC simulations.

Fig. 3.12 shows the impedance of the reference diode as a function of the input frequency for different amplitudes V_1 of the sinusoidal voltage excitations obtained with the MC model. When increasing V_1 above 0.1 V, the epilayer plasma peak is shifted to lower frequencies. This performance is due to the increase of the L valley occupation where the effective mass is higher (around 0.3, Table 2.2), see eq. (3.8). According to the analysis in section 3.1.2, when the sinusoidal voltage of amplitude 1 V is applied to the reference diode, velocity saturation appears at input frequencies higher than 1.2 THz, with L valley occupation higher than 70 % at 1.5 THz, see Fig. 3.5. Similar performance is obtained for V_1= 0.5 V at input frequencies higher than 2 THz. Therefore, the plasma frequency as a function of the effective mass of the L valley in eq. (3.8) decreases the plasma frequency. In Fig. 3.12, the impedance of the diode is evaluated with $\mathrm{LEC}_{R_sLC(t)}$ using the effective mass of the L valley and an electron mobility in the epilayer that is 1/4 of the low field mobility of the GaAs[5]. Hence, when velocity saturation is important (high L valley occupation), plasma effects are shifted to lower frequencies.

According to [Cro89], increasing the operation frequency above the epilayer plasma frequency causes that the impedance of the undepleted epilayer is shunted by the displacement capacitance and the junction impedance will be shunted by the nonlinear capacitance. In this situation, the equivalent circuit of the epilayer and the Schottky junction -see Fig. 2.7- reduces to a series combination of C_j and $C_{u,e}$, which is the net capacitance:

$$C = \frac{\varepsilon_0 \varepsilon_r A}{L_e}. \tag{3.9}$$

Since the net capacitance becomes constant, the device is useless at frequencies above the epilayer plasma frequency. Fig. 3.13 presents the module of the ratio of the second and the first coefficients of the Fourier series of the current $|I[2f_0]|/|I[f_0]|$ for the reference diode under the sinusoidal voltage considered in Fig. 3.12. For the voltage of amplitude 0.1 V, $|I[2f_0]|/|I[f_0]|$ decreases when the input frequency overpass the epilayer plasma frequency, due to the effect summarized by eq. (3.9). An important consequence of this analysis is that the harmonic generation capabilities of the Schottky diodes are highly degraded at frequencies higher than the plasma resonance. Fortunately, plasma resonance in the epilayer occurs at THz frequencies ($\sim$ 5 THz for doping concentration 3x10^{17} cm^{-3}, Fig. 3.11) and can be increased by increasing the doping density of the epilayer, eq. (3.8).

[5]At the maximum swing of the electric field in Fig. 3.8(a), $\sim$ 40 KV/cm, the steady-state velocity-field curve of GaAs shows an electron mobility around 18 times lower than at low field conditions. The value of mobility used here is an average among the values of the mobility at zero field and the maximum field.

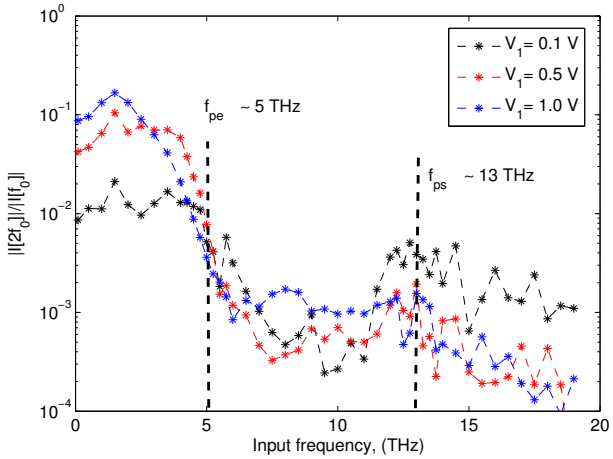

Figure 3.13: Dependence of the ratio of the module of the coefficients of the Fourier series of the current at $2f_0$ and f_0 under voltage excitations of different amplitude and input frequency, bias voltage -2 V. Results obtained from MC simulations

3.1.5 Nonstationary effects

In previous subsections, different physical phenomena have been presented separately. However, under the operation conditions of Schottky based multipliers and mixers, these phenomena are interrelated. This section presents a deeper analysis of the electron transport under large signal operation using the MC model and a HD model based on the energy and momentum balance equations. This analysis will show the relations existing among the different physical phenomena described in previous sections.

When increasing the frequency of the signals applied to the diode, the dynamics of the electron energy and momentum departs from the steady-state performance. A single electron gas relaxation time approximation, based on momentum and energy relaxation times provides a simple approach to analyse the physics of the carrier transport in the neutral regions of the device under non-equilibrium conditions [Lun00]:

$$\frac{dv}{dt} = \frac{qE}{m^*} - \frac{v}{\tau_m(\varepsilon)} \tag{3.10}$$

$$\frac{d\varepsilon}{dt} = qvE - \frac{\varepsilon - \varepsilon_{th}}{\tau_\varepsilon(\varepsilon)} \tag{3.11}$$

where $\tau_\varepsilon(\varepsilon)$ and $\tau_m(\varepsilon)$ are the energy and momentum relaxation times, ε and v are the average carrier energy and velocity (averaged over the carriers, i.e., ensemble average), respectively, ε_{th} is the electron energy in thermal equilibrium, and E is the electric field. Because the scattering rate generally increases with energy, both $\tau_m(\varepsilon)$ and $\tau_\varepsilon(\varepsilon)$ decreases as the energy increases. The momentum and energy relaxation times are typically quite different because several phonon collision's are required to reduce the energy of an electron, but a single large angle scattering event can remove all of its directed momentum. As a consequence, τ_ε is larger than τ_m, so the electron energy changes slower than the average velocity [Lun00].

For a small signal perturbation of the electric field of angular frequency ω, the following equa-

tions can be written [Jos95]:

$$E = E_0 + E_1 \exp(j\omega t) \tag{3.12}$$

$$\varepsilon = \varepsilon_0 + \varepsilon_1 \exp(j\omega t) + \varepsilon_2 \exp(2j\omega t) + ... \tag{3.13}$$

$$v = v_0 + v_1 \exp(j\omega t) + v_2 \exp(2j\omega t) + ... \tag{3.14}$$

$$\tau_m(\varepsilon) \simeq \tau_m(\varepsilon_0) + \frac{\partial \tau_m}{\partial \varepsilon}\Delta\varepsilon \tag{3.15}$$

$$\tau_\varepsilon(\varepsilon) \simeq \tau_\varepsilon(\varepsilon_0) + \frac{\partial \tau_\varepsilon}{\partial \varepsilon}\Delta\varepsilon. \tag{3.16}$$

Introducing these equations into eqs. (3.10) and (3.11), and carrying out the analysis at the fundamental frequency, the following equations are obtained:

$$v_0 = \frac{q\tau_m(\varepsilon_0)}{m^*}E_0 \tag{3.17}$$

$$v_1 = \frac{q}{m^*}\frac{\tau_m(\varepsilon_0)E_1}{1+j\omega\tau_m(\varepsilon_0)} + \frac{q}{m^*}\frac{\partial\tau_m}{\partial\varepsilon}\frac{E_0\varepsilon_1}{1+j\omega\tau_m(\varepsilon_0)} \tag{3.18}$$

$$\varepsilon_0 = \varepsilon_{th} + q\tau_\varepsilon(\varepsilon_0)E_0v_0 \tag{3.19}$$

$$\varepsilon_1 = \frac{q\tau_\varepsilon(\varepsilon_0)(v_0E_1 + v_1E_0)}{1+j\omega\tau_\varepsilon(\varepsilon_0) - q\frac{\partial\tau_\varepsilon}{\partial\varepsilon}v_0E_0}. \tag{3.20}$$

It is important to note that eqs. (3.10) and (3.11) have to be coupled with the equations which describe the carrier transport through the Schottky barrier for a complete description of the diode. However, the analysis of eqs. (3.10) and (3.11) provides valuable information about the carrier transport in the neutral region of the epilayer. Eq. (3.18) is equivalent to eq. (3.4) used in the analysis of carrier inertia when $\frac{\partial\tau_m}{\partial\varepsilon}$ is neglected.

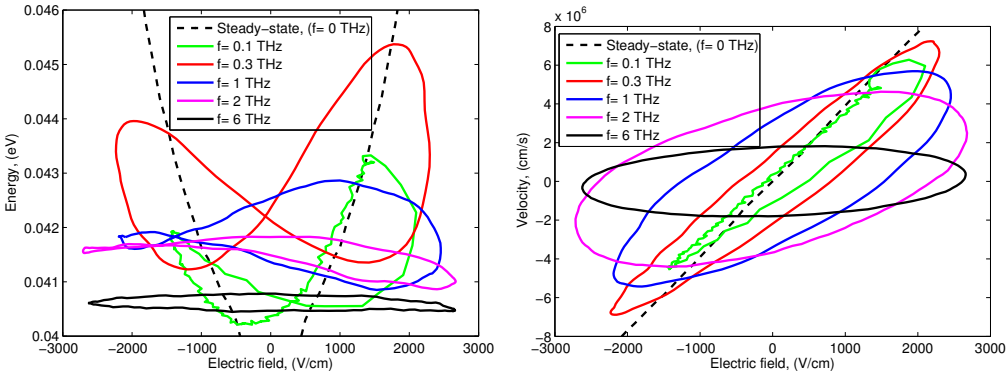

(a) (b)

Figure 3.14: (a) Energy-field and (b) velocity-field curves evaluated in the undepleted region of the epilayer of the reference diode under sinusoidal applied voltage of different amplitudes and input frequencies and bias voltage -2.0 V, obtained with the MC simulator.

To get a better insight into the nonstationary performance of the electrons in the diode, an analysis under low field conditions is initially considered. The results obtained from this analysis will be useful in the analysis under higher electric fields presented later in this section. Fig. 3.14 presents the energy-field and velocity-field curves in the undepleted epilayer of the reference diode under sinusoidal applied voltage of different input frequencies and bias voltage -2.0 V, obtained from MC simulations. The amplitudes of the applied signal have been selected at each frequency to obtain

similar swing of the electric field in the undepleted epilayer. For the electric fields considered in Fig. 3.14, the variation of ε is around 0.005 eV. Hence, in eq. (3.15), $\tau_m(\varepsilon)$ could be approached by its value at equilibrium, see Fig. 3.2(b), and the term in eq. (3.18) that is proportional to $\frac{\partial \tau_m}{\partial \varepsilon}$ is of secondary importance. For $\tau_\varepsilon(\varepsilon)$, the $\frac{\partial \tau_\varepsilon}{\partial \varepsilon}$ evaluated at $\varepsilon = \varepsilon_{th}$ is around an order of magnitude higher than $\tau_\varepsilon(\varepsilon_{th})$ and the term $\frac{\partial \tau_\varepsilon}{\partial \varepsilon}\dot{\Delta}\varepsilon$ is only four times lower than $\tau_\varepsilon(\varepsilon_{th})$ ($\varepsilon_{th} = 3K_BT/2$= 0.039 eV), see Fig. 3.2(a). Hence, the contribution of $\frac{\partial \tau_\varepsilon}{\partial \varepsilon}\dot{\Delta}\varepsilon$ can be important in eq. (3.20).

An interesting feature of Fig. 3.14 is the emergence of hysteresis loops that replace the steady-state velocity-field and energy-field curves. The reason is the delayed response of the electron's velocity and energy to the variations of the electric field (energy and momentum relaxation times). Below 300 GHz, these hysteresis loops are closer to the steady-state curves. At higher frequencies, for the characteristic time of the applied signal $\mathbf{t} \sim 1/(2\pi f)$ lower than the energy relaxation time [6], the energy of the electrons lags the electric field and the module of ε_1 decreases with increasing frequency [Ais84, Sch95]. This performance is in accordance with the performance expected from eq. (3.20). At these frequencies, the dynamics of the electrons can be described by a constant and complex mobility approximation since $\tau_m(\varepsilon)$ depends on the energy, and the energy remains nearly constant. Note that the same effect occurs for high amplitudes of the electric field as is observed in Fig. 3.8 [Sch95].

At higher frequencies, when the characteristic time of the applied signal is lower than τ_m ($\tau_m >> \mathbf{t}$, i.e. at frequencies much higher than $1/(2\pi\tau_m) \sim 1/(2\pi 0.25\,\text{ps}) \sim 630$ GHz), the electron velocity lags the electric field by $\pi/2$ radians and its amplitude v_1 decreases eq. (3.18). This is observed in Fig. 3.14(b) at frequencies higher than 2 THz. An important degradation of the performance of the device is expected at these frequencies, since the velocity of the electrons is not able to respond to the variations of the electric field.

The $\text{LEC}_{R_sLC(t)}$ model of the diode -Fig. 2.7- can be used to evaluate the velocity-field curves in Fig. 3.14(b)[7]. Fig. 3.15(a) compares the velocity-field curves in the undepleted epilayer of the reference diode obtained with the MC and LEC_{R_sLC} models. A good agreement is observed between both models. The formulation of the LEC_{R_sLC} model is equivalent to assume that the electron energy and the momentum relaxation time are constant and they take the values at equilibrium. Since the variation of the electron energy in Fig. 3.14(a) is low for the excitations considered, the approximation based on constant energy and τ_m is acceptable. Besides the conduction current characterized by the velocity-field response in Fig. 3.15, the total current in the undepleted epilayer includes also the displacement current associated to the capacitance of the equivalent circuit of the undepleted epilayer. Fig. 3.15(b) shows the quotient of the module of the first harmonic of the Fourier series of the displacement and the conduction currents in the undepleted epilayer. According to this figure, the displacement current contribution becomes dominant at frequencies higher than the plasma frequency of the epilayer ($f_{pe} \sim 5$ THz). At lower frequencies, the conduction current characterized by the velocity-field loops described in this section is the most important contribution to the total current in the undepleted epilayer.

Figs. 3.16 and 3.17 show the energy-field and velocity-field loops in the undepleted epilayer of the reference diode under sinusoidal applied voltage of different input frequencies and bias voltage

[6] $\tau_\varepsilon > \mathbf{t} > \tau_m$, $\tau_\varepsilon \approx 3$ ps, $\tau_m \approx 0.25$ ps for GaAs [Lee99], see Fig. 3.2 obtained with the one-particle Monte Carlo for bulk GaAs and GaN

[7] The electric field and the electron velocity are related to the the current and voltages used in the $\text{LEC}_{R_sLC(t)}$ as indicated in the figure:

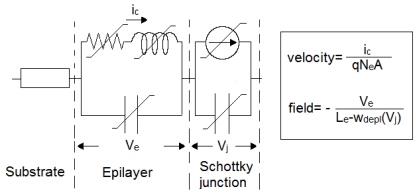

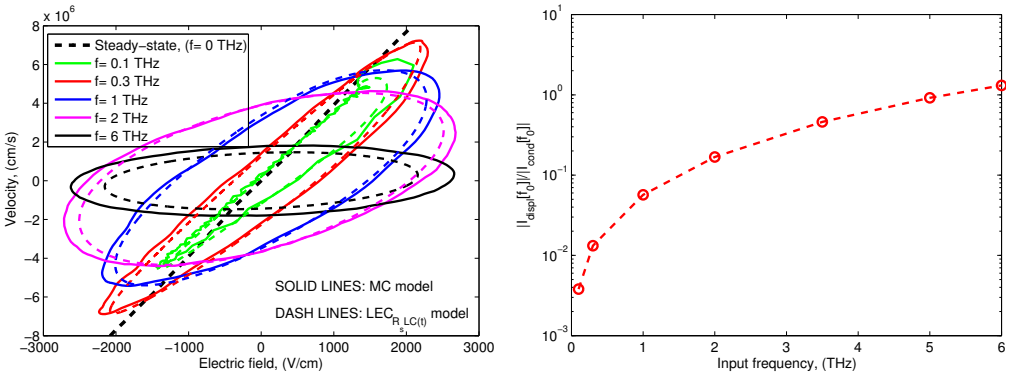

(a) (b)

Figure 3.15: (a) Velocity-field curves evaluated in the undepleted region of the epilayer of the reference diode under sinusoidal applied voltage of different amplitudes and input frequencies and bias voltage -2.0 V, obtained with the MC and $\text{LEC}_{R_sLC(t)}$ models. (b) Quotient of the module of the first harmonic of the Fourier series of the displacement and the conduction currents in the undepleted epilayer

-2.0 V [8]. The amplitudes of the applied signals have been selected at each frequency to obtain similar swing of the electric field in the undepleted epilayer, lower than 10 KV/cm and 60 KV/cm in Figs. 3.16 and 3.17, respectively. The results have been obtained with MC. In Fig. 3.16, the velocity-field curves obtained with the $\text{LEC}_{R_sLC(t)}$ model are also included, showing a good agreement with MC, even with electric fields in the undepleted epilayer as high as 10 KV/cm (higher than the critical field). According to the analysis of Fig. 3.14, this performance occurs because the energy of the electrons cannot follow the variations of the electric field at high frequencies and because of the low change of $\tau_m(\varepsilon)$ for the electron's energy under the electric fields considered in Fig. 3.16. When higher electric field are generated, Fig. 3.17, the electrons in the undepleted epilayer gain enough energy from the electric field to be transferred to the upper valleys (velocity saturation) and the simple $\text{LEC}_{R_sLC(t)}$ fails. In Fig. 3.17, the velocity and energy curves obtained with eqs. (3.10) and (3.11) coupled to the equivalent circuit model of the Schottky junction (energy transport model) have been

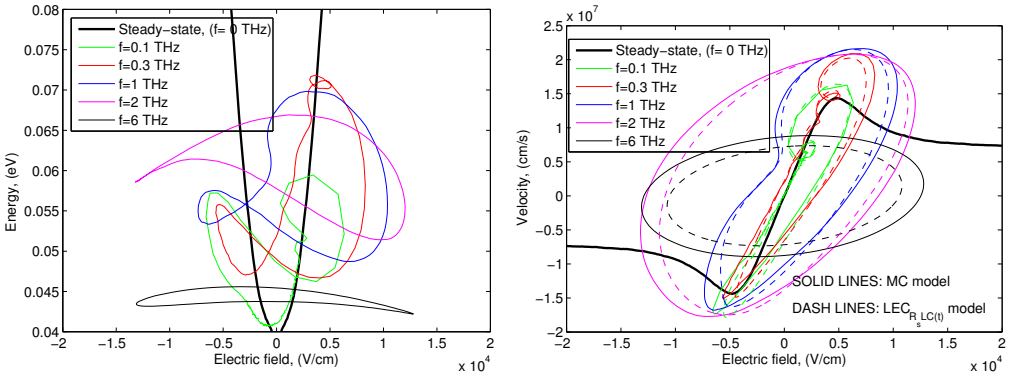

(a) (b)

Figure 3.16: (a) Energy-field and (b) velocity-field curves evaluated in the undepleted region of the epilayer of the reference diode under sinusoidal applied voltage of different amplitudes and input frequencies and bias voltage -2.0 V, obtained with the MC simulator. Maximum swing of the electric field around 10 KV/cm.

[8] To obtain the electric field swing shown in these figures at frequencies 100 GHz and 300 GHz, the bias voltage has to be set to -4 V and the epilayer length to 350 nm.

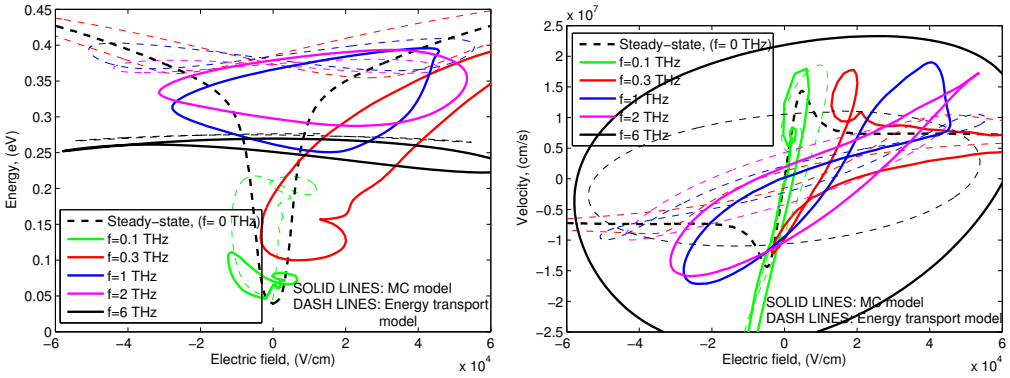

(a) (b)

Figure 3.17: (a) Energy-field and (b) velocity-field curves evaluated in the undepleted region of the epilayer of the reference diode under sinusoidal applied voltage of different amplitudes and input frequencies and bias voltage -2.0 V. Results obtained with the MC simulator and the energy transport model based on eqs. (3.10) and (3.11). Maximum swing of the electric field around 60 KV/cm.

included. $\tau_m(\varepsilon)$, $\tau_\varepsilon(\varepsilon)$ and $m^*(\varepsilon)$ used in this model have been obtained with the one-particle MC under steady-state conditions, see Fig. 3.2. These parameters reflect an average over contributions from different scattering mechanisms, each weighted according to the steady-state electron distribution in the Γ, L and X valleys. In time dependent and spatially inhomogeneous transport like that considered in Fig. 3.17, the occupation of the different valleys and the electron distribution functions in each valley may be far from steady-state [Lun00, Sch95]. Hence, the accuracy of this analytical model compared with MC under the high field conditions considered in Fig. 3.17 is poor.

The Monte Carlo results presented in this section indicate that the energy and momentum relaxation effects in GaAs are significant at millimeter and submillimeter wavelengths, and should be taken into account in the diode models used in circuit simulations. The analytical energy transport model is in good agreement with the Monte Carlo results under low field conditions (a $\mathrm{LEC}_{R_sLC(t)}$ model which constant equilibrium energy also works correctly under these conditions), but it shows important discrepancies with the MC results under high field conditions. On the other hand, the drift-diffusion model does not take into account these effects, since it is a local model based on the steady-state velocity-field curve.

3.1.6 Skin effect

Skin effect is generated by the current's own magnetic field pressing the lines of flow toward the exterior of the conductor, thus diminishing the effective conducting cross section and increasing the resistance [Dic67]. Dickens developed an integral expression for the spreading and skin effect impedances within a cylindrical diode structure by performing a field analysis for potential and current using an oblate spheroidal coordinate system. The integral could not be evaluated analytically, and Dickens introduced two approximations to obtain the results in eqs. (2.11) and (2.12) for the spreading and skin impedances, respectively.

To analyse the importance of the skin effect in the performance of the Schottky diodes, Fig. 3.18 presents a comparison of the skin impedance given by eq. (2.14) and the impedance of the reference diode simulated with MC under sinusoidal voltage of amplitude 1 V, bias -2 V as a function of the input frequency. As a reference, the radius b of the chip in eq. (2.14) has been set to 8 μm [Bha92]. The contribution of the skin effect to the real part of the impedance increases with frequency up to 15 THz. At 1 THz frequency, the real part of the impedance of the epilayer also increases due to velocity saturation and to plasma resonance of the epilayer at higher frequencies, see Fig. 3.12. Fig.

3.18(a) shows that the most important contribution to the real part of the diode impedance at THz frequencies becomes from the limiting phenomena in the epilayer, i.e. velocity saturation and plasma effects, and the substrate. Only at frequencies higher than 15 THz, skin effect dominates the real part of the diode impedance. The imaginary part of the diode is dominated by the nonlinear capacitance of the Schottky junction. Fig. 3.18(b) shows that for frequencies lower than the substrate plasma frequency the skin effect represents a low contribution to the imaginary part of the diode impedance.

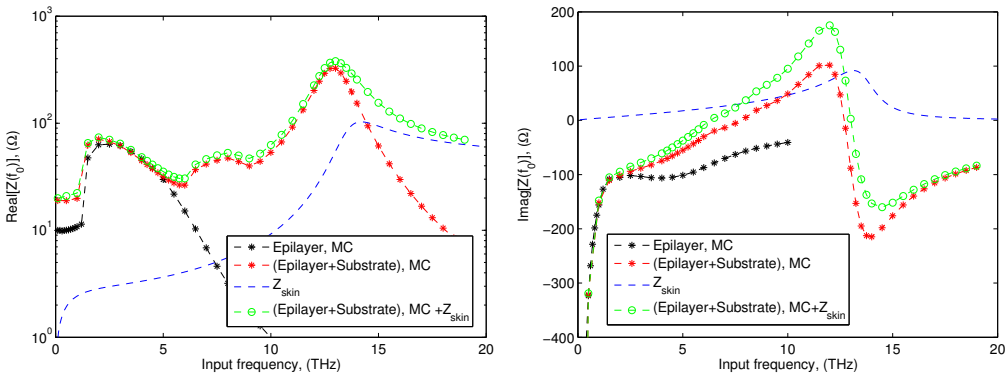

(a) (b)

Figure 3.18: (a) Real and (b) imaginary parts of the skin impedance eq. (2.14) and the impedance of the reference diode simulated with MC under sinusoidal voltages of amplitude 1 V and bias point -2 V.

Although skin effect cannot be modeled in the one-dimensional physics-based models used in this thesis, its associated impedance can be included in the linear part of a circuit when analysing nonlinear circuits (see chapter 5). It is difficult to estimate theoretically the impedance due to skin effect because it depends on the diode structure and in some cases computer simulations are necessary. The reduction of the skin effect impedance can be achieved through optimization of the diode chip geometry and by increasing the substrate doping density. One possibility to reduce highly skin effect are planar Schottky diodes using quasi-vertical approach. With mesa heights smaller than the skin depth the effective contact area is not affected by the skin effect [Sim93, Lin98, Coj04a, Ali14].

3.2 Capabilities of GaN Schottky diodes

The rapid development of the RF power electronics has motivated the introduction of wide bandgap materials due to its potential for high power applications. GaN based devices have made substantial progress in recent years due to the good properties of this semiconductor: High direct bandgap (∼3.4 eV) which results in high breakdown field, high peak and saturated electron velocity and good thermal properties. The major inconvenient of GaN in comparison with GaAs is that it has a lower electron mobility, increasing the series resistance of the devices. However, as the GaN technology becomes more mature, the high power capabilities of GaN semiconductor can be considered as an alternative to the current GaAs technology for the development of sources at millimeter wavelengths.

This section presents an analysis of the electrical properties and the physical phenomena that occur in GaN Schottky diodes. The reference diode described in section 3.1 is also used in this section. The ideal barrier of the reference GaN Schottky diode has been set to 1.20 V, according to values reported in the literature for GaN Schottky diodes [Wan96, Coj04b].

3.2.1 Modelling GaN semiconductor. Electrical properties of GaN versus GaAs

To compare the harmonic generation capabilities of GaAs and GaN Schottky diodes, two important parameters have to be evaluated, in accordance with the definition of figure-of-merit cut-off frequency, eq. (2.16): (i) The series resistance of the diode that depends on the properties of the semiconductor through the electron mobility, and (ii) the nonlinear capacitance. When an external sinusoidal voltage V(t) of amplitude V is applied to the diode of Fig. 2.5, the effective voltage that modulates the nonlinear capacitance is:

$$V_C = \frac{V}{1+\frac{R_s}{R_j}+j\omega C_j R_s} \sim \frac{V}{1+j\omega C_j R_s} = \frac{V}{1+j\frac{\omega}{\omega_c}} \tag{3.21}$$

where C_j is the junction capacitance, $\omega = 2\pi f$ is the angular frequency of the applied voltage and ω_c is the angular cut-off frequency eq. (2.16). For a given V, V_C increases as ω_c increases, and higher modulation of the nonlinear capacitance is reached, what results in better conversion efficiency.

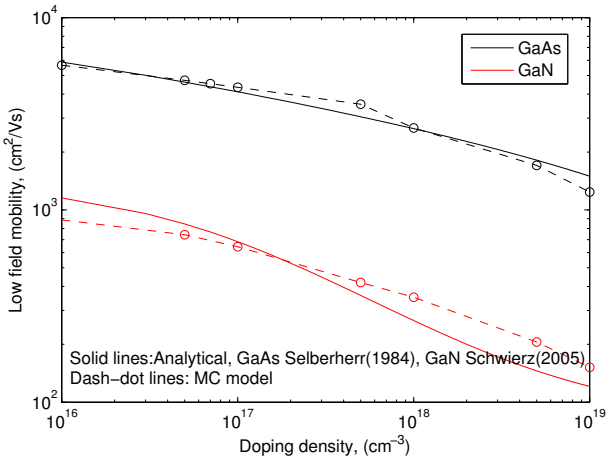

Figure 3.19: Comparison of the low field electron mobility of GaAs and GaN semiconductors as a function of the doping concentrations, obtained with the one-particle MC and the analytical models in [Sel84] and [Sch05].

The low field electron mobility of bulk GaAs and GaN is compared in Fig. 3.19. The electron mobility of the GaN is around 6-8 times lower than the mobility of GaAs. Since the series resistance is inversely proportional to the electron mobility eq. (2.7), the series resistance of GaN based devices is higher than the one for GaAs based devices.

Fig. 3.20 compares the dc capacitance of the reference diode based on GaAs and GaN semiconductors for different doping concentrations. The junction capacitance corresponding to the GaN diode is lower than the one for the GaAs diode. Higher harmonic generation capabilities are obtained when V_C is maximized as a result of the higher modulation of the nonlinear capacitance (the quotient C_{max}/C_{min} increases). GaN Schottky diodes present the inconvenience of their high series resistance, what negatively affect the modulation of the nonlinear capacitance, see eq. (3.21). However, the lower capacitance of GaN diodes can compensate partially the contribution of their higher series resistance in eq. (3.21), leading to acceptable multiplication efficiencies.

In Fig. 3.21, the joint effect of the series resistance and the nonlinear capacitance in the performance of GaAs and GaN Schottky diodes is analysed by means of a comparison of the cut-off frequency, eqs. (2.16) and (2.17), for the reference diode as a function of the epilayer doping concentrations and the epilayer length. C_{min} has been evaluated at -10 V for GaAs and -30 V for GaN, see Fig. 3.22, and C_{max} at 90 % of V_{bi} using eq. (2.2). The cut-off frequency for GaAs is higher than for GaN based Schottky diodes due to the lower series resistance of the former. f_c evaluated with

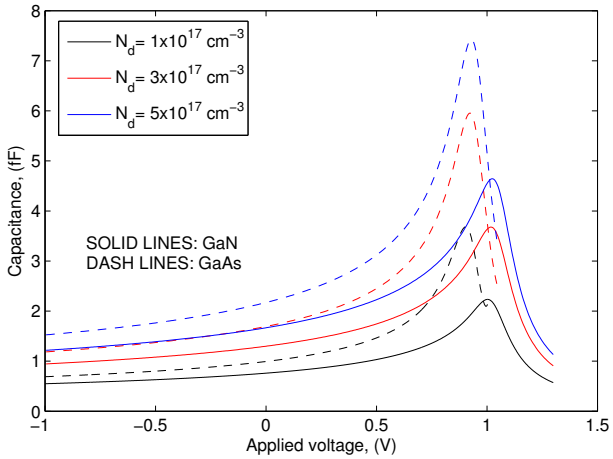

Figure 3.20: Comparison of the capacitance of the reference diode based on GaAs and Gan semiconductors for different epilayer doping concentrations. Results obtained with the DD model.

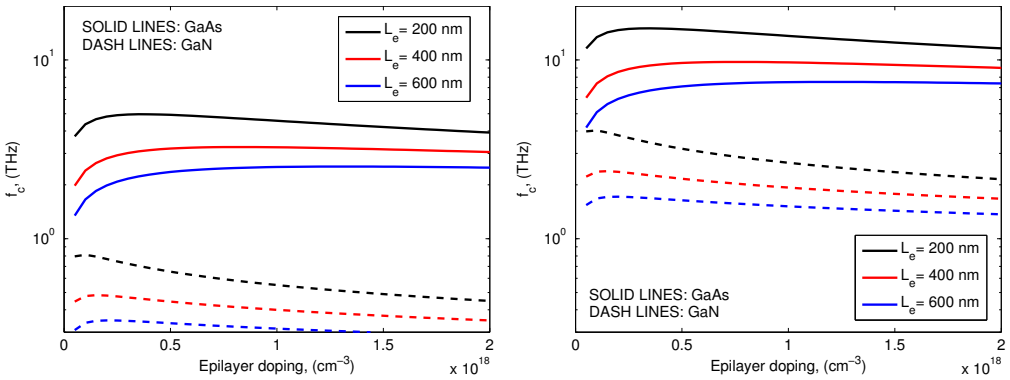

Figure 3.21: Cut-off frequency of the reference Schottky diode based on GaAs and GaN as a function of the epilayer doping concentration and the epilayer length, using (a) eq. (2.16) and (b) eq. (2.17).

eq. (2.17) shows lower differences between both GaAs and GaN based devices, since eq. (2.17) depends on the maximum swing of the nonlinear capacitance. Due to the higher breakdown voltage of GaN than GaAs (in absolute value), the maximum swing of the nonlinear capacitance is higher for GaN diodes. A comparison of the breakdown voltage is presented in Fig. 3.22 as a function of the epilayer doping concentration and the epilayer length. Since the breakdown voltage is higher in GaN than GaAs diodes, the power handling capabilities of GaN diodes are much better. Although lower efficiencies are expected with GaN based multipliers than with GaAs ones -Fig. 3.21-, the high breakdown of GaN represents the real advantage of this semiconductor over GaAs, since less number of GaN diodes are necessary for holding certain input power.

It is well-known that Schottky multipliers consist of a set of Schottky diodes on a microstrip line suspended inside a transmission wave-guide [Mar01]. In the first multiplier stages, with 400-500 mW at W-band [Mae10a, Mae12], up to 6 diodes are integrated in the same microstrip line. Also, power-combining schemes and high-thermal conductivity substrates are employed in order not to require high anode areas and to avoid thermal and breakdown limitations of GaAs technology [Mae10a, Mae12]. With further increase of the input power at frequencies around 100 GHz, more GaAs Schottky diodes will be needed in the first multiplication stages or an increase of the anode areas in order to raise the power handling capabilities of the GaAs diodes. This will result in an

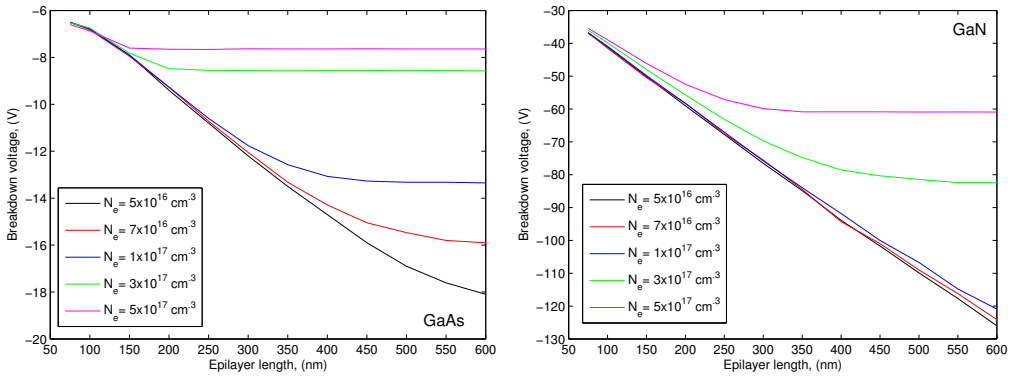

(a) (b)

Figure 3.22: DC breakdown voltage as a function of the epilayer doping and length for (a) GaAs and (b) GaN Schottky diodes calculated with the DD model.

increase of the dimensions of the microstrip branches containing the Schottky diodes. However, the maximum length is limited by the dimensions of the transmission wave-guide, fixing an upper limit to the maximum diode dimensions or number of supported diodes. In addition, the higher the number of diodes, the more difficult it is to achieve a good and symmetrical power coupling among all the diodes, as there is a major risk for the presence of asymmetries in the circuit due to the fabrication process. On the other hand, increasing the anode areas leads to the inconvenience of an increase in the parasitic capacitances since they are proportional to the anode area. GaN based multipliers might solve these problems since one-single diode or two-diode configurations can be used, reducing the complexity of the technology. Nevertheless, the application of GaN technology requires that enough power at W-band must be available to compensate its lower efficiency. In section 5.5, a detailed comparison of GaAs and GaN multipliers, based on accurate physics-based models and the harmonic balance technique is carried out.

3.2.2 Physical processes in GaN Schottky diodes

A brief review of the physical effects described in section 3.1 is presented in this subsection for GaN Schottky diodes. Because of the high breakdown of GaN, a Schottky diode with epilayer length 600 nm and doping concentration $1x10^{17}$ cm^{-3} is considered as a reference [Jin10, Jin13]. To reduce the computational cost of the MC simulations and since we are interested in the analysis of the physical phenomena in the epilayer of the diode, a substrate of doping $2x10^{18}$ cm^{-3} and length 50 nm has been simulated. An ideal barrier height of 1.20 V [Wan96,Coj04b] and 300 K of operation temperature have been assumed.

The energy τ_ε and momentum τ_m relaxation times of bulk GaAs and GaN with doping concentration $1x10^{17}$ cm^{-3} obtained with the one-particle MC were shown in Fig. 3.2. Due to the higher scattering rate for the electrons in GaN, see Fig 2.16, the energy and velocity of these electrons adapt rapidly to the variations of the electric field. Hence, the energy and momentum relaxation times, which describe the response of the electrons energy and velocity to the variation of the electric field, are lower in GaN than GaAs. Because of the lower τ_ε and τ_m in GaN, non-local effects in the transition between the undepleted and the depleted regions of the epilayer in GaN diodes are not so important as they are in GaAs, see subsection 3.1.1. This can be observed in Fig. 3.23, that shows the variation of $Z_\beta[f]$ -eq. (3.1)- for the reference GaN diode under sinusoidal voltages of amplitude 1 V, bias -2 V and amplitude 10 V, bias -10 V simulated with DD and MC models. A good agreement is observed between both models because of the high scattering rates in GaN. The DD model does not overestimate the series resistance of GaN diodes due to the nonlocal effects in

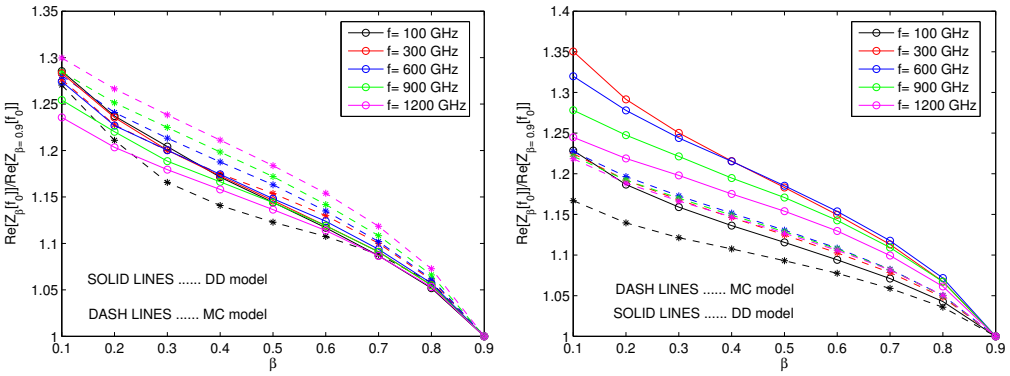

(a) (b)

Figure 3.23: Comparison of the real part of the diode impedance of the reference GaN Schottky diode simulated with the DD and MC models under sinusoidal applied signals of amplitude (a) 1 V, bias point -2.0 V and amplitude (b) 10 V, bias point -10 V for different frequencies, as a function of β. The values presented have been normalized by the real part of $Z_\beta[\omega]$ with β= 0.9 at each simulated frequency.

the transition between the neutral and the depleted region of the epilayer as it does for GaAs diodes, see section 3.1.1.

To provide a better understanding of the dynamics of the electrons in GaN under high fields, Fig. 3.24 shows the average velocity and energy of the electrons in the undepleted epilayer of the reference GaN Schottky diode with doping 1x10^{17} cm^{-3} under the excitation considered in Fig. 3.23(b) (a bias voltage of -10 V and a sinusoidal voltage of amplitude V_1= 10 V). Fig. 3.24(a) shows that the average energy of the electrons is not enough to be scattered into the upper valleys (Γ_1-U energy gap $\sim$ 2.2 eV, Table 2.2). Besides, MC simulations show that the higher valleys of the GaN diode are empty under these conditions.

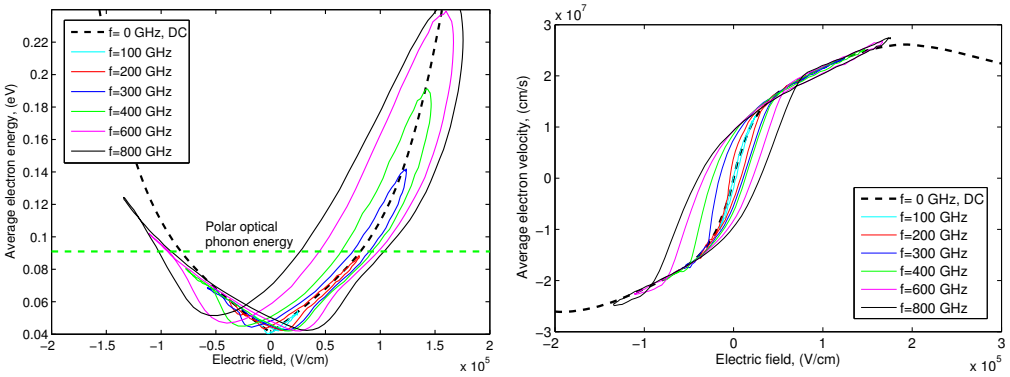

(a) (b)

Figure 3.24: (a) Energy-field and (b) velocity-field curves evaluated in the undepleted region of the epilayer of the reference GaN diode under sinusoidal applied voltage of amplitude 10 V, different frequencies and bias -10.0 V. Results from MC simulations.

When the energy of the electrons is higher than the energy of the polar optical phonons $\hbar\omega_{opt}$, the emission of polar optical phonons is the dominant scattering mechanisms in GaN. This is shown in Fig. 3.25, that presents the percentage of the different scattering mechanisms in bulk GaN doped 1x10^{17} cm^{-3} as a function of the electric field, obtained with the one-particle MC. These high energy interactions ($\hbar\omega_{opt} \sim$ 91.2 meV for GaN while it is 36.13 meV for GaAs) limit the electron

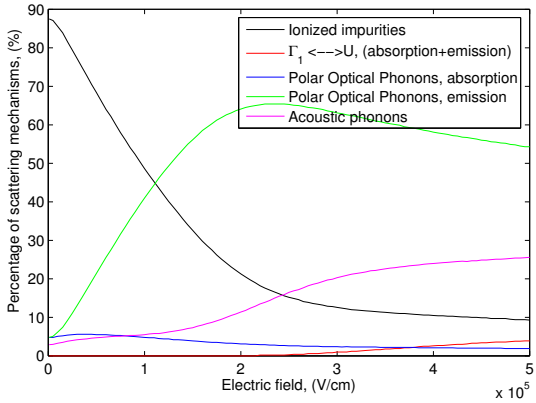

Figure 3.25: Percentage of the different scattering mechanisms in bulk GaN doped 1x10^{17} cm^{-3} as function of the electric field, obtained under dc conditions with the one-particle MC. $U \leftrightarrow \Gamma_3$ intervalley scattering have not been included since they are negligible. $\Gamma_1 \leftrightarrow U$ intervalley scattering due to absorption/emission between these valley are shown together.

velocity in GaN (this performance appears when the GaN diode begins to operate in the second region described in section 2.7 for bulk GaN). Unlike GaAs Schottky diodes in Fig. 3.8, Fig. 3.24(b) shows that the velocity-field loops obtained in the undepleted epilayer of the GaN Schottky diode under time varying conditions are close to the steady-state velocity, because of the lower values of τ_ε and τ_m in GaN, see Fig. 3.2. Therefore, static velocity-field curves are a good approximation of the velocity-field response of GaN under time varying conditions up to frequencies close to 1 THz.

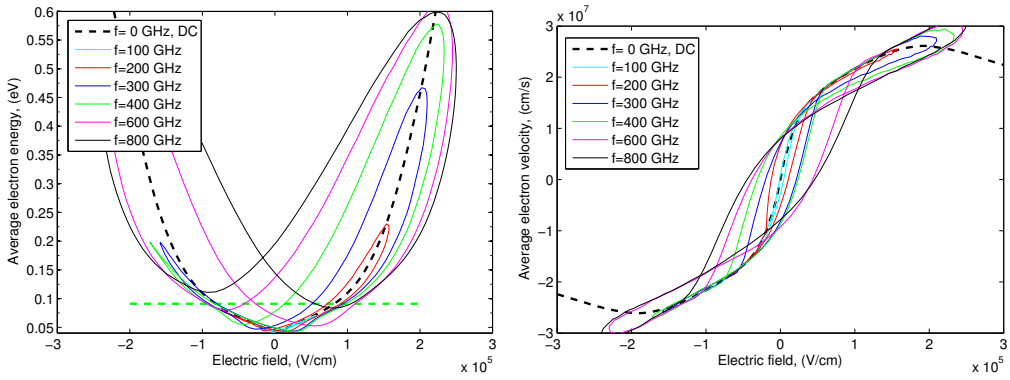

(a) (b)

Figure 3.26: (a) Energy-field and (b) velocity-field curves evaluated in the undepleted region of the epilayer of the reference GaN diode under sinusoidal applied voltage of amplitude 20 V, different frequencies and bias -20.0 V. Results from MC simulations.

Due to the high breakdown voltage (in absolute value) of the GaN diodes, see Fig. 3.22, bias voltages lower than -10 V used in 3.24 can be applied to these devices. Fig. 3.26 shows the velocity-field and the energy-field curves of the electrons in the undepleted epilayer of the reference diode[9] doped 1x10^{17} cm^{-3} under sinusoidal voltages of amplitude 20 V and bias voltage -20 V. These results have been obtained with the MC model. Fig. 3.26(a) shows that the energy of the electrons is able to follow the changes of the electric field. As was described in Fig. 3.24, the velocity-field

[9]To assure that the epilayer of the reference GaN diode is not completely depleted under the operation conditions considered in Fig. 3.26 and evaluate correctly the velocity-field and the energy-field curves, the epilayer length has been set to 800 nm in these simulations.

loops in Fig. 3.26(b) are close to the steady-state curve. On the other hand, the upper valleys of the GaN diode are empty under the operation conditions considered in Fig. 3.26.

The degradation of the electron velocity due to the emission of polar optical phonons can be also observed in Fig. 3.27, that shows the module of the fundamental component of the Fourier series of the time evolution of the width of the depletion region. In this figure, the reference diode has been excited with a bias voltage of -10 V and a sinusoidal voltage of constant amplitude V_1= 10 V. Different epilayer doping have been analysed. Results from DD and MC simulations are included. A $\mathrm{LEC}_{R_s(t)}$[10] model which assumes a constant low field mobility is also included, see subsection 3.1.2. When the emission of polar optical phonons becomes important, the predictions of the physics based models depart from $\mathrm{LEC}_{R_s(t)}$ results. By increasing the doping, the degradation of $|w_{depl}[f]|$ in Fig. 3.27 is mitigated. A good agreement is observed between both DD and MC because the scattering rate is high in GaN, and the energy and the velocity of the electrons adapt quickly to the variations of the electric field.

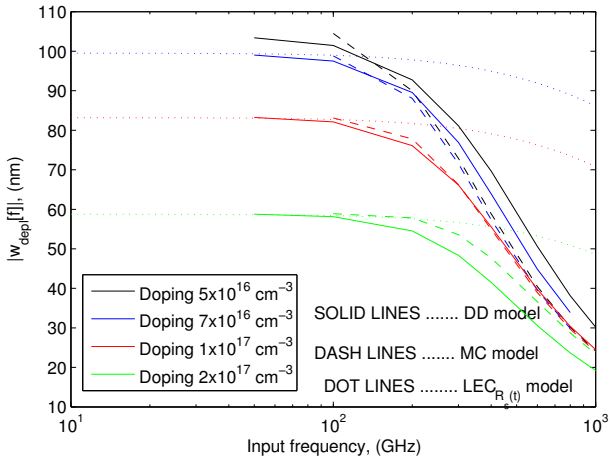

Figure 3.27: Module of the fundamental component of the Fourier series of the evolution of the width of the depletion region w_{depl}(t) for the reference GaN Schottky diode with different epilayer doping under sinusoidal applied signal of amplitude 10 V and bias -10 V, obtained from $\mathrm{LEC}_{R_s(t)}$, DD and MC simulations. The width of the depletion region has been defined as the point where the electron concentration falls to 60 % of the epilayer doping.

Due to the low impact of nonlocal effects in the performance of GaN Schottky diodes and the good agreement between velocity saturation effects obtained with DD (based on the steady-state velocity-field curves) and MC models, a good agreement is expected between DD and MC for the simulation of GaN based multipliers, as will be shown in section 5.5.

[10] $\mathrm{LEC}_{R_s(t)}$ for doping 5x10^{16} cm^{-3} is not included in Fig. 3.27 because the depletion regions enters into the substrate, what is not correctly simulated by this model

Chapter 4

Analysis of noise spectra in GaAs and GaN Schottky diodes

The use of Schottky diodes as sources and sensors is limited by the intrinsic noise generated by the devices, characterized by random fluctuations of the electrical variables such as terminal voltages and currents. Therefore, the characterization of these fluctuations and the study of the noise sources are fundamental aspects in the design of high performance electrical devices and circuits. Special attention has to be paid to high frequency physical effects, because they can degrade the noise characteristics of the devices for THz applications. The joint analysis of both the electrical response and the intrinsic noise is required to obtain accurate designs of devices and circuits.

Noise in Schottky diodes is usually described by Nyquist's theorem for thermal noise, Schottky's theorem for shot noise [Zie70] and empirical models for hot electron noise [Heg85, Cro87]. Due to THz applications of Schottky diodes, an analysis of the intrinsic high frequency noise is demanded. Trippe, Bosman and Van der Ziel [Tri86] presented an analytical approach to describe the resonances that appear in the high frequency region of the noise spectra of Schottky diodes. This model presents important limitations: (i) it does not provide the dependence of the resonances of the noise spectra on the characteristics of the diode or the applied voltage, (ii) it does not predict the hybrid plasma peak, and (iii) it does not take into account the self consistent solution of the Poisson's equation. Due to these drawbacks, Shiktorov *et al.* [Shi05] presented an analytical and more sophisticated model for the high frequency noise of Schottky diodes under dc conditions. These analytical models present the inconvenient that they are limited to applications under a reduced set of conditions and they require additional results from MC simulations or experimental data for validation.

Higher level models for noise analysis in semiconductor devices are based on the framework of Langevin's approach and the Green's function technique (impedance field method, transfer impedance field method) with physics-based models like DD or HD [Vli71, Sta98, Shi00, Bon01a]. An important limitation of these techniques is that they require the knowledge of the spectral performance of the noise sources in the device, that must be provided externally by analytical expressions or Monte Carlo simulations. Besides, these noise evaluation techniques are strongly affected by the limitations of the physics-based models considered. For example, in DD model, carriers inertia is not taken into account; hence, noise models from tools based on DD are not expected to describe the high frequency resonances in the noise spectra of Schottky diodes. HD models are necessary to solve this problem, but the derivation of the Langevin's sources needed to carry out noise analysis and their implementation in HD numerical simulators is complicated and is still under development [Gru93c, Gru94c, Shi99, Bon01a].

The Monte Carlo method applied to the description of the charge transport in semiconductor devices has demonstrated to be a very rigorous technique for the analysis of the electrical response and the intrinsic noise of the devices, since it naturally incorporates the microscopic noise sources

present in the devices. A lot of efforts have been dedicated to understand and analyse the noise features of Schottky diodes employing this technique, especially for GaAs based devices [Gru94b, Shi03a, Per04a, Shi04]. However only a partial analysis of the noise spectra of GaAs Schottky diodes has been performed. In addition, the study of the noise spectra of GaN based Schottky diodes is an unexplored topic to the knowledge of the authors.

Therefore a complete analysis of the noise spectra of GaAs and GaN based Schottky diodes operating under static and time varying conditions is carried out in this chapter. A systematic study of the dependence of the intrinsic noise with the excitation and the device structure is presented by employing the classic MC method and published analytical models. The analysis of the noise spectra based on MC simulations performed along the chapter are also used to determine the accuracy and the range of validity of the analytical model published in [Shi05] for the high-frequency noise in Schottky diodes.

4.1 Modelling of noise sources in Schottky diodes

This section presents a brief review of the most important noise sources in Schottky diodes and some available models and techniques used for noise analysis.

4.1.1 Some statistical concepts

Random fluctuations in the electrical variables such as voltages and currents at the terminals can be interpreted as the macroscopic effect of random fluctuations in the velocity and in the number of carriers in the devices by different mechanisms occurring at microscopic level [Zie70]. Despite its random nature, noise has certain predictable characteristics that allow to characterize it in a useful way (random process). In this section, a few concepts related to probability and random processes that are essential to understand noise in circuits are introduced, see [Pap91].

Consider a fluctuating quantity X that describes the electronic noise behavior, such as the voltage at the terminals, the current through the device, the average velocity of the carriers, the number of carriers, etc. The most important way to characterize a random variable is through its moments of order 1 and 2, i.e. $< X >$ and $< X^2 >$. The brackets $< ... >$ mean ensemble average. The moment of order m is calculated according to:

$$< X^m >= \int_{-\infty}^{\infty} x^m f_X(x) dx \tag{4.1}$$

where $f_X(x)$ is the probability density associated to the random variable X. If $< X >\neq 0$, it is usual to work with the random variable defined by $\delta X = X - < X >$, such that $< \delta X >= 0$.

A random process is a random variable depending on an independently varying parameter, usually time. Most of the noise processes that occur in Schottky diodes are stationary and it is possible to consider them as ergodic processes, so the ensemble averages are replaced by temporal averages in one realization of the process over a sufficiently long time:

$$< X^m >= \overline{X^m} = \lim_{T\to\infty} \frac{1}{T} \int_0^T X^m(t) dt \tag{4.2}$$

The autocorrelation function of a random process $X(t)$ is the correlation of the two random variables $X(t)$ and $X(t')$:

$$R_X(t,t') =< X(t)X(t') >= \int_{-\infty}^{\infty}\int_{-\infty}^{\infty} xx' f_{X(t)X(t')}(x,x') dx dx' \tag{4.3}$$

where $f_{X(t)X(t')}(x,x')$ is the joint probability density. The autocorrelation function measures how a given perturbation persists at later times. The most important properties of autocorrelation function can be found in [Zie70]. In stationary random processes the statistics are not function of time and the correlation can be written $R_X(\tau)$ where $\tau = t' - t$. If it is assumed that the process is ergodic, the statistical correlation given by eq. (4.3) is equal to the temporal correlation:

$$R_X(\tau) = \overline{X(t)X(t+\tau)} = \lim_{T\to\infty} \frac{1}{T} \int_{-T/2}^{T/2} x(t)x(t+\tau)dt. \tag{4.4}$$

It is possible to show that the power spectral density function (usually named power spectrum) of a process $S_X(f)$ is the Fourier transform of the autocorrelation function:

$$S_X(f) = 2\int_{-\infty}^{\infty} R_X(\tau)\exp(-j2\pi f\tau)d\tau = 4\int_0^{\infty} R_X(\tau)\cos(2\pi f\tau)d\tau. \tag{4.5}$$

The factor 2 after the first equal appears because the spectral density $S_X(f)$ is only considered for positive frequencies. The second equality is obtained taking into account that $R_X(\tau)$ is a symmetric function [Zie70]. $S_X(f)$, that is a real quantity, represents the power per unit bandwidth of the random process.

Since a random process is not periodic or limited in time, it cannot be treated directly by a Fourier series or transform. However it can be analysed in the following manner. It is considered a single sample of the random process over a period of time T. The Fourier transform of this sample is:

$$x(f,T) = \int_{-T/2}^{T/2} x(t)\exp(-j2\pi ft)dt. \tag{4.6}$$

The power spectrum can be obtained as the limit as $T \to \infty$ of the average of a large number of such spectral components:

$$S_X(f) = \lim_{T\to\infty} \frac{<|x(f,T)|^2>}{T} \tag{4.7}$$

The Wiener-Khintchine theorem establishes the equivalence of eqs. (4.5) and (4.7) [Zie70]. Due to eq. (4.7) (with *X(t)* representing current or voltage fluctuations in a device), noise power spectral density is traditionally expressed as a moment of order two.

Analysis of noise from Monte Carlo simulations

As was described in chapter 2, the Monte Carlo method is a particle simulation tool, and the carriers distribution function can be evaluated directly from simulation results. The correlation function of current (voltage, average electron velocity, etc.) fluctuations under stationary conditions can be evaluated directly by time-averaging over a multi-particle history simulated during a sufficiently long-time interval. For a total simulation time $T = n\,dt$, divided into n intervals of duration dt, it is possible to obtain the instantaneous values of the magnitude X at the discrete time moments 0, dt, $2dt$, $3dt$.... The autocorrelation function of the fluctuations of X, δX, eq. (4.4), written for discrete time moments is [Bru84]:

$$R_{\delta X}(j\,dt) = \frac{1}{n-j+1}\sum_{i=j}^{n} \delta X(i\,dt)\delta X((i-j)\,dt) \tag{4.8}$$

The evaluation of the spectral density as the Fourier transform of the discrete autocorrelation function, for a correlation time kdt (it is assumed that the autocorrelation function is zero for times higher than kdt), results:

$$S_X(f) = 4dt\sum_{m=0}^{k} R_{\delta X}(m\,dt)\cos(2\pi fm\,dt) \tag{4.9}$$

Under periodic voltage excitations, the magnitude X is also periodic, i.e. $< X(t+mT_{f_0}) >=< X(t) >$, where $m = 0,1,2,3...$ and $T_{f_0} = 1/f_0$ is the period of the applied signal of frequency f_0. The brackets mean average over an ensemble of different realizations of $X(t)$. Since this process is nonstationary, the two-time correlation function given by eq. (4.3) must be used. Nevertheless, due to the periodicity of the applied voltage and thus of the deterministic current response, the ensemble average in eq. (4.3) can be replaced by the average over the sequence of equivalent time moments $t = \theta + mT_{f_0}$, where $\theta \varepsilon [0, T_{f_0}]$. As a consequence, the correlation function is conveniently represented as a function of the two relevant times, namely, θ and the correlation time $\tau = t' - t$ (eq. (4.3)) [Shi03a, Per04a]:

$$R_{\delta X}(\theta, \tau) =< \delta X(\theta)\delta X(\theta+\tau) > \tag{4.10}$$

Noise under these conditions is modelled as cyclostationary, i.e. noise that is stationary in a periodic sense. The Fourier transform of $R_{\delta X}(\theta, \tau)$ with respect to τ gives the instantaneous spectral density at time moment θ:

$$S_X(\theta, f) = \int_{-\infty}^{\infty} R_{\delta X}(\theta, \tau)\exp(-j2\pi f\tau)d\tau. \tag{4.11}$$

$S_X(\theta, f)$ is a periodic function in θ and it can be expressed as a Fourier series, see appendix G. The zero-coefficient of this Fourier series is the power spectral density and it can be calculated by averaging $S_X(\theta, f)$ over θ during the period T_{f_0} (mean spectral density):

$$\overline{S}_X(f) = \frac{1}{T_{f_0}} \int_0^{T_f} S_X(\theta, f)d\theta \tag{4.12}$$

that it is a real quantity, [Shi02, Per04a].

The mean spectral density of the fluctuations of the magnitude X can be also calculated using eq. (4.7). A sufficiently long history of X is simulated with the MC model. This history is subdivided into a set of intervals of duration $T = NT_{f_0}$, usually a large integer number N of periods T_{f_0} of the applied signal. The spectral density of the fluctuations of X is defined as:

$$\overline{S}_X(f) = \lim_{T\to\infty} 2T < g(f)g^*(f) > \tag{4.13}$$

where $< ... >$ represents the average over a large number of such spectral components -see eq. (4.7)- and the Fourier coefficients are given by:

$$g(f) = \frac{1}{T} \int_0^T \delta X(t)\exp(-j2\pi ft)dt \tag{4.14}$$

$\overline{S}_X(f)$ is usually evaluated at frequencies $f_n = n/T$, with n= 0, 1, 2, ..., and the fast Fourier transform (FFT) can be used to compute the average spectral density. $\overline{S}_X(f)$ given by eq. (4.13) coincides with the mean spectral density calculated with the correlation function formalism given by eq. 4.12 [Shi02, Shi03a]. This statement can be considered as a generalization of the Wiener-Khintchine theorem for the case of a cyclostationary process [Shi02, Shi03a].

Eq. 4.13 can be used for the magnitude X instead of the fluctuations of X. In this case, the spectral density given by eq. (4.13) contains both the periodic average of X and the noise contribution, i.e. $X(t) =< X(t) > +\delta X(t)$. Using the FFT to calculate eq. 4.13 for X, the Fourier coefficients $g(f_n)$ for which the ratio n/N is an integer number m ($f_n = mf_0$) will contain the contribution of the deterministic part $< X(t) >$ at the frequency of the m-th harmonic. All the other coefficients $g(f_n)$ corresponding to fractional values of n/N will contain the noise part. Hence, the spectral density of the magnitude X eq. (4.13) can be represented as:

$$S_X(f_n) = \overline{S}_X(f_n) + 2T|X_m|^2\delta_{f_n f_m} \tag{4.15}$$

where $f_m = mf_0$, X_m is the Fourier coefficient of the of the deterministic part of X at frequency $f_m = mf_0$ (m-th harmonic, m=1,2,3,...), $< X(t) >$, and $\delta_{f_n f_m}$ is the Kronecker symbol.

Noise spectra from MC simulations of Schottky diodes under time varying conditions presented in this thesis have been calculated according to eq. (4.13) for the current fluctuations, i.e. $\delta i(t) = i(t) - < i(t) >$, using the FFT.

4.1.2 Noise sources in Schottky diodes

This section presents a brief description of the most important noise sources in Schottky diodes [Reg92, Nou94, San94]:

Thermal noise

This noise is also known as Johnson-Nyquist noise. It is originated by the fluctuations of the carriers' velocity in their random or brownian motion in the semiconductor. The Nyquist's theorem describing the equilibrium current fluctuation (current noise) properties of a linear semiconductor resistor can be derived from a microscopic analysis of the system based on the Fockker-Planck equation or the Langevin's equation [Bon01a]:

$$S_I(f) = \frac{4k_BTG}{1+(2\pi f)^2\tau_m^2} \tag{4.16}$$

where τ_m is the average momentum relaxation time, G is the low-frequency conductance of the resistor, T is the temperature of the lattice in Kelvin and k_B is Boltzmann's constant. At low frequencies, i.e. for $2\pi f\tau_m << 1$, the customary Nyquist relation is obtained:

$$S_I(f) = 4k_BTG. \tag{4.17}$$

Equivalently, the voltage fluctuations at the terminals of the linear resistance at open-circuit conditions are characterized by:

$$S_V(f) = 4k_BTR \tag{4.18}$$

where *R=1/G* is the resistance. From eq. (4.18), the available noise spectral power is:

$$S(f) = \frac{S_V(f)}{4R} = k_BT \tag{4.19}$$

Because the available spectral power of thermal noise depends only on the temperature eq. (4.19), the idea of noise temperature is introduced to characterize a noise source although it is not thermal. The noise temperature is the temperature that would create the same available noise spectral power as the source if it were a thermal resistive noise source [Maa05].

The discussion about thermal noise can be extended to the nonequilibrium case, i.e. when an external electric field is applied to the device. A generalized Nyquist's relationship has been formally introduced [Nou94]:

$$S_I(f) = 4k_BT_n(f)\mathrm{Re}[Y(f)] \tag{4.20}$$

$$S_V(f) = 4k_BT_n(f)\mathrm{Re}[Z(f)] \tag{4.21}$$

$$\tag{4.22}$$

and

$$\frac{S_V(f)}{S_I(f)} = |Z(f)|^2 \tag{4.23}$$

where $Z(f)$ and $Y(f) = 1/Z(f)$ are the are the small-signal impedance and admittance around the dc bias point, and Re means the real part. From eq. (4.20) or eq. (4.21), a generalized frequency dependent noise temperature is defined [Nou94, Bon01a].

This noise source under equilibrium and out of equilibrium conditions is naturally simulated with the Monte Carlo method.

Shot noise

Shot noise in the Schottky diodes is due to carriers crossing the potential barrier in the Schottky contact in a random way [Zie70, Tri86]. The noise spectral density associated to shot noise is:

$$S_I(f) = 2qI \tag{4.24}$$

where I is the average current crossing the Schottky barrier. This spectral density is white up to frequencies on the order of the reciprocal time τ_F -see following subsection- employed by the carriers to surmounting the barrier. It is naturally included in the Monte Carlo simulator, [Gon93c].

1/f or Flicker noise

There does not exist a unique and satisfactory theory for the $1/f$ noise. The most extended one is a phenomenological description representing the $1/f$ noise as a sum of generation-recombination noises produced by sub-bands of impurities or defects, or by mobility fluctuations, with a continuous distribution of relaxation times according to a hyperbolic law over a wide range. It also could be related to quantum fluctuations of the material, [Han75, Zie88, Vli91]. The phenomenological expression for the 1/f spectral density is given by:

$$S_I(f) = \frac{I^2}{N}\frac{\alpha_H}{f} \tag{4.25}$$

where α_H is the Hooge parameter [Hoo76].

It is very difficult to include the 1/f noise source in the Monte Carlo simulator, because it appears at very low frequencies. Therefore it exhibits a very high characteristic time in comparison with those of the typical scattering mechanisms. In addition, there does not exist a clear model to explain its origin.

Generation-recombination noise

Generation-recombination noise is due to the local fluctuations of the number of carriers inside the Schottky diode. For generation-recombination noise involving only two levels, the spectral density associated is given by:

$$S_I(f) = \frac{4\alpha_{gr}I^2}{N}\frac{\tau_{gr}}{1+\omega^2\tau_{gr}^2} \tag{4.26}$$

where I is the average current , N the total number of carriers, α_{gr} and τ_{gr} are two constant that characterize the generation- recombination process. Generation-recombination times τ_{gr} from 66 ps to 450 ps have been reported [Fab95]. This noise is important at low frequencies. Therefore, its inclusion in the Monte Carlo simulator is also problematic due to the large difference existing between the scattering rates of the generation-recombination process and the scattering mechanisms included in the simulator which leads to very long computation times, [Vli75, Reg87, Per00, San01, Per05]. The MC simulator employed in this work does not consider this noise source.

Partition noise

This noise appears when the system is divided into a number of subsystems characterized by different dynamical properties, but interconnected among them. In semiconductor materials and devices, the partition noise results from random transitions of carriers between two or more physically distinct groups of electron states located in momentum space. For such a subdivision into groups to take place, the characteristic time of carriers exchange between groups must be much longer than for the intragroup transitions [Nou94, Shi03b]. An example is the noise related to the stochastic

transitions between the lowest (Γ) and the upper (L, X) valleys that occur in semiconductors (GaAs) when the electric field is high enough for intervalley transitions to take place. Characteristic time of intergroup exchange in GaAs is around 2 ps, [Shi03b]. This noise mechanism is included in the Monte Carlo simulator if an adequate model of the band structure is considered. Also carrier transport involving trapping levels leads to partition noise (trapping-detrapping processes). In this case, the partition noise is merely generation-recombination noise.

In addition, cross correlations between the fluctuations in the number and the velocity of the electrons or between the velocity and the energy can be important under certain conditions. These correlations are inherently considered in the MC simulations.

4.1.3 Description of analytical models for noise spectra in Schottky diodes

Because of the complexity to carry out a complete description of the microscopic processes of random nature that give rise to the noise spectrum of Schottky diodes, the number of analytical models published, based on this approach, is reduced. In this section the models presented in [Tri86] by M. Trippe *et al.* and [Shi05] by P. Shiktorov *et al.* are briefly described. These two models are chosen because they are considered as good examples of complete models for noise analysis of Schottky diodes.

Model of Trippe *et al.*, [Tri86]

In 1986, Trippe, Bosman and Van der Ziel published an analytical model for the noise spectra of Schottky diodes, [Tri86]. In this model, the electrons in the semiconductor participating in charge transport are subdivided into four groups.

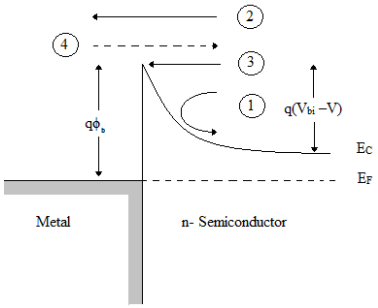

Figure 4.1: Band diagram of the metal-semiconductor contact and classification of the electrons attending to their kinetic energy, presented in [Tri86].

The first group is constituted by electrons with insufficient kinetic energy, K, to surmount the Schottky barrier, $K < q(V_{bi} - V)$, Fig. 4.1. These electrons always return to the neutral region of the epilayer. From the equation of motion for a single electron of this group moving in the depletion region, the electron velocity in the direction of the electric field is $v(t) = v_0 \cos(2\pi f_{pe} t)$, where v_0 is the velocity of the electron at the beginning of the depletion region and f_{pe} is the plasma frequency of the epilayer [Tri86]. According to the equation of $v(t)$ for the electrons of this group, regardless of their initial velocity upon entering the space charge region, all require the same characteristic time to return to the neutral semiconductor region. Since $v(t) = v_0 \cos(2\pi f_{pe} t)$, that time, and the frequency associated to the process, f_R, are given by:

$$\begin{cases} \tau_R = \frac{1}{2 f_{pe}} \\ f_R = \frac{1}{2\pi\tau_R} = \frac{f_{pe}}{\pi} \end{cases} \tag{4.27}$$

The contribution of this group of electrons to the noise spectrum of the Schottky diodes is zero at zero frequency, rises initially as f^2 with the frequency, reaching a maximum at frequencies close to f_R and then decreases. The noise associated to this group of electrons does not change significantly with the bias, since they occupy states near the bottom of the conduction band and a modification of the barrier height does not produce an appreciable change in the number of electrons in group 1. These electrons give rise to a peak in the noise spectrum usually named *returning carrier* resonance, since, according to this model, it is generated by electrons which return to the neutral region of the semiconductor.

The electrons which have enough kinetic energy to always pass the energy barrier belong to group 2. The electrons with sufficient kinetic energy to just reach the Schottky contact, $K \sim q(V_{bi} - V)$, constitute the group 3. Electrons of groups 2 and 3 contribute in the same way to the spectral density of the noise. According to [Tri86], the noise due to these groups of electrons is shot noise. The contribution of these passing electrons to noise spectrum of the diode is white up to frequencies of the order of the the reciprocal time τ_F employed by the electrons to cross the depletion region. For electrons which have the lowest kinetic energy to just reach the Schottky contact (group 3), $K = \frac{1}{2}m^* v_0^2 = q(V_{bi} - V)$, τ_F takes the value $\tau_F = \frac{1}{2\pi f_{pe}} \arcsin(\frac{2\pi f_{pe} w_{depl}}{v_0}) = \frac{1}{4 f_{pe}}$ and its characteristic frequency is defined by $f_F = \frac{1}{2\pi\tau_F} = \frac{2 f_{pe}}{\pi}$, see [Tri86]. This τ_F for the electrons of group 3 is half of τ_R, eq. (4.27), since the electrons of group 1 enter into the space charge region and then come back to the neutral epilayer, while the electrons of group 3 cross the Schottky contact.

The group 4 is constituted by electrons in the metal with sufficient kinetic energy to pass the energy barrier and reach the semiconductor. Once in the semiconductor, the electric field swept these electrons to the neutral region of the semiconductor. The noise spectrum due to this group of electrons has the same performance that shot noise [Tri86]. Since the energy barrier $q\phi_b$ (see Fig. 4.1) is not a function of the applied voltage in this simple model, the magnitude of the current due to this group of electrons (reverse saturation current) and theirs associated noise contribution are considered constant[1]. For applied voltages higher than 0 V, the contribution of the group 4 to the electrical and noise response of the diode can be neglected when compared to the contributions of groups 2 and 3. This group of electrons is not included in our MC simulator.

The main drawback of this classical model is that the provided analytical expressions to describe the returning carrier resonance of the current noise spectra are not able to describe the dependence of the spectra with the diode parameters and the applied voltage. Besides, this model does not predict the peak in the noise spectra that appears at frequencies between the plasma frequency of the substrate and the epilayer. In the following subsection, this peak (hybrid plasma peak) is predicted using the model of [Shi05].

In order to calculate the spectral density of the current fluctuations of the diode, the contribution of each group of electrons must be calculated. The total noise spectral density is found by summing the contribution of each electron. Only two groups of electrons have to be considered in this calculation: electrons which can cross the depletion region and those which cannot. Since the spectral density is calculated for the case of an ac short-circuit, groups 2 and 3 may be combined [Tri86].

The procedure used in [Tri86] to evaluate the noise spectral density is as follows: (i) calculate the current which flows as a function of time for a given initial velocity of an electron; (ii) take the Fourier transform of the current pulse due to electrons with this initial velocity; (iii) calculate the number of electrons with this velocity; (iv) apply Carson's theorem [Zie70] in order to find the spectral density for an initial velocity; and (v) sum over all possible initial velocities in order to find the total spectral density.

Following this procedure, the current noise spectral density due to electrons which reach the

[1] According to [Rho88], there are different phenomena that cause the reverse current to departure from this ideal behavior, like field dependence of the barrier height, the effect of tunneling or generation of electron-hole pairs.

Schottky contact is given by [Tri86]:

$$S_{I_2}(f) = \sum_K \frac{2\lambda(K)C_1^2}{\omega_{pe}^2} \frac{2}{(1+\frac{f}{f_{pe}})(1-\frac{f}{f_{pe}})} \left\{ (1-\cos\left[(1-\frac{f}{f_{pe}})2\pi f_{pe}\tau_F(K)\right]) \frac{2\frac{f}{f_{pe}}}{1-\frac{f}{f_{pe}}} \right.$$
$$\left. -(1-\cos\left[(1+\frac{f}{f_{pe}})2\pi f_{pe}\tau_F(K)\right]) \frac{2\frac{f}{f_{pe}}}{1+\frac{f}{f_{pe}}} + (1-\cos[(4\pi f_{pe}\tau_F(K))] \right\} \quad (4.28)$$

where $C_1 = qv(0)/2w_{depl}$, w_{depl} is the width of the depletion region, the index K refers to a particular velocity interval, selected small enough to assure the accuracy of the results and $\lambda(K)$ is the average number of electrons being emitted per unite time with a velocity in the interval K. This spectral density due to passing electrons is equal to the shot noise of the dc current at low frequencies. At frequencies on the order of the reciprocal transit time, τ_F, the spectral intensity falls off steeply, see [Tri86].

The total noise spectral density of those electrons which do not reach the metal contact and them return to the neutral semiconductor becomes [Tri86]:

$$S_{I_1}(f) = \sum_K \frac{2\lambda(K)C_1^2}{(2\pi f_{pe})^2} \frac{8\left(\frac{f}{f_{pe}}\right)^2}{\left(1-\left(\frac{f}{f_{pe}}\right)^2\right)^2} \left(1+\cos\left[\frac{f}{f_{pe}}\pi\right]\right). \quad (4.29)$$

This noise contribution originates the returning carrier peak.

In addition to these noise contributions, $S_{I_1}(f)$ and $S_{I_2}(f)$, thermal noise due to the series resistance of the diode has to be taken into account. According to [Tri86], the low frequency region of the current noise spectrum due to the combined contribution of shot and thermal noise is given by:

$$S_I(0) = \frac{2qIR_j^2}{(R_s+R_j)^2} + \frac{4K_BTR_s}{(R_s+R_j)^2} \quad (4.30)$$

where R_s is the series resistance of the substrate and the non-depleted region of the epitaxial layer, R_j represents the junction resistance and I is the current through the device. A justification of eq. (4.30) is presented in appendix E[2]. From eq. (4.30), when V<V_{bi}, corresponding to $R_j >> R_s$, $S_I(0)$ behaves as 2qI, the well-known shot-noise law eq. (4.24). For V> V_{bi}, the Schottky barrier disappears, $R_s >> R_j$, and the spectral density is due to thermal noise related to the series resistance R_s, $S_I(0) \sim \frac{4K_BT}{R_s}$ eq. (4.17).

Model of Shiktorov *et al.*, [Shi05]

In contrast to the model of [Tri86], which considered the individual motion of the carriers in the depletion region only in the presence of a static electric field, the model presented in [Shi05]

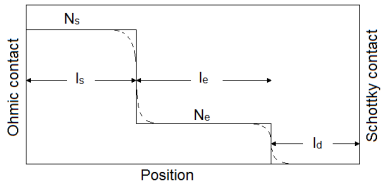

Figure 4.2: Schematic representation of the $n^+ - n$ Schottky diode with the depletion region near the Schottky contact.

[2]Shot and thermal noise sources in the LEC model of a noisy diode are replaced by an equivalent noise source whose noise spectral density is shown to be given by eq. (4.30)

considers carriers moving in the whole Schottky diode in the presence of the self-consistent electric field. To evaluate the current noise spectra in [Shi05] under a constant voltage applied between the terminals of the diode (the electric field is calculated self-consistently inside the device), it is assumed that the change of the free carrier concentration in the $n^+ - n$ interface and near the edge of the depletion region is abrupt, see Fig. 4.2. It also assumes that the depletion region is empty (see Fig. 4.2), so shot noise is not considered and, therefore, the model fails in the low frequency region of noise spectrum. Another simplification considered is that the potential drop in the $n^+ - n$ interface is negligible. Although these assumptions simplify the model, they also limit its accuracy.

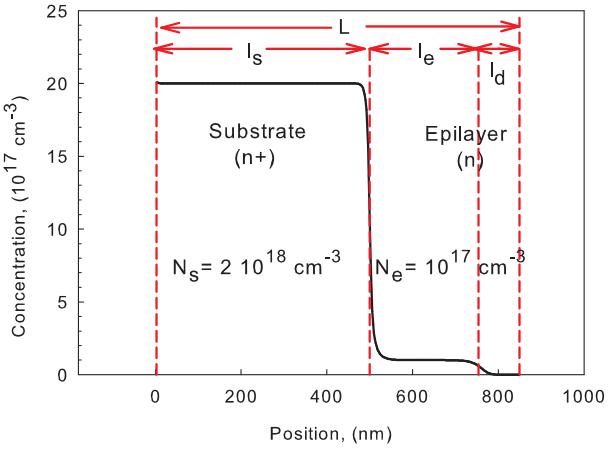

Figure 4.3: Schematic representation of the $n^+ - n$ reference Schottky diode, showing the notation employed for the different regions of the diode.

Under constant voltage conditions, the instantaneous response to any local perturbation originated by a scattering event of a free carrier results in the appearance inside the whole Schottky diode of a homogeneous component of the electric field fluctuation, $\delta E(x) = \Delta E$, which at the initial stage of its spatiotemporal evolution leads to a synchronous motion (negligible shift with respect to the characteristic lengths of the diode) of all the free carries in the device. As a consequence of such homogeneous shift, an uncompensated charge will be formed in regions internal to the borders between n^+, n and depletion regions characterized by the abrupt change of the free carrier concentration. This extra charge will initiate corrections of the initial perturbation δE that are different in the n^+ and n regions. As a consequence, the further evolution of the collective shifts of the two groups of free carriers becomes different. By assuming that at a certain stage of the initial perturbation evolution the collective shifts of free carriers with respect to the donor levels in the n^+ and n regions are equal to δx_s and δx_e, respectively, the $\delta E(x)$ fluctuation self-consistent with these shifts can be written as:

$$\delta E(x) = \begin{cases} \Delta E - (q/\varepsilon_0\varepsilon_r)N_s\delta x_s & 0 < x < l_s \\ \Delta E - (q/\varepsilon_0\varepsilon_r)N_e\delta x_e & l_s < x < l_s + l_e \\ \Delta E & l_s + l_e < x < L \end{cases} \tag{4.31}$$

where the notation of the regions of the diode is shown in Fig. 4.3. By assuming that the voltage fluctuation between the terminals of the diode is zero $\delta U = 0$, the homogeneous part of the fluctuation of the electric field can be determined $\Delta E = (q/\varepsilon_0\varepsilon_r L)(N_s l_s \delta x_s + N_e l_e \delta x_e)$. The fluctuation of the current in the external circuit δI is determined by the rate of change of the surface charge density in the Schottky contact $\delta\sigma_M = \varepsilon_0\varepsilon_r\Delta E$, and $\delta I = A\frac{d\sigma_M}{dt}$, where A is the anode area. The fluctuations of the free carriers in the different regions of the diode can be described with Langevin's approach. The system of equation that results is easily solved in the frequency domain and the solution is used to evaluate $\delta I(f)$ and the spectral density of the current fluctuations $S_I(f)$ [Shi05]. The general

expression obtained for $S_I(f)$ under short-circuit conditions is:

$$S_I(f) = 4k_BT\frac{q^2}{m^*}\frac{A}{L^2}\left[2\pi f_{sc,s}N_s l_s\left[\frac{f\cdot(a_{22}-a_{12})}{2\pi\Delta(f)}\right]^2 + 2\pi f_{sc,e}N_e l_e\left[\frac{f\cdot(a_{11}-a_{21})}{2\pi\Delta(f)}\right]^2\right] \tag{4.32}$$

where A is the cross section area of the diode, $f_{sc,i} = q/(2\pi m^*\mu_i)$ $(i = s,e)$ is the carrier momentum relaxation rate for the substrate $(i = s)$ and the undepleted epilayer $(i = e)$, m^* the effective mass of the electrons and μ_i the low field electron mobility of the i-region; $r_i = l_i/L$ $(i = s,e,d)$ is the relative length of the i-region; the coefficients a_{mn} are given by: $a_{12} = -r_e(2\pi f_{pe})^2$, $a_{21} = -r_s(2\pi f_{ps})^2$, $a_{11} = (2\pi f_{ps})^2 - (2\pi f)^2 + j4\pi^2 f\, f_{sc,s} + a_{21}$, $a_{22} = (2\pi f_{pe})^2 - (2\pi f)^2 + j4\pi^2 f\, f_{sc,e} + a_{12}$, and $\Delta(f) = a_{11}a_{22} - a_{12}a_{21}$; f_{ps} and f_{pe} are the plasma frequency of the substrate and epilayer respectively. Eq. (4.32) can be simplified assuming a constant mobility μ in the substrate and the epilayer:

$$S_I(f) = 4k_BT2\pi f_{sc}Cf^2\frac{r_s f_{ps}^2\phi(f_{pe}) + r_e f_{pe}^2\phi(f_{ps})}{\phi(f_{HP})\phi(f_{RC})} \tag{4.33}$$

where $C = \varepsilon_0\varepsilon_r A/L$ is the geometrical capacitance of the diode, $\phi(f_i) = (f^2 - f_i^2)^2 + f_{sc}^2 f^2$, $f_{sc} = q/(2\pi m^*\mu)$ is the carrier momentum relaxation rate assuming an electron mobility μ. When $l_d < L - l_s$, f_{HP} and f_{RC} can be approximated by:

$$f_{HP}^2 = f_h^2 - \beta f_{pe}^2 r_d \tag{4.34}$$

$$f_{RC}^2 = (1+\beta)f_{pe}^2 r_d \tag{4.35}$$

where $f_h^2 = f_{ps}^2(r_e + r_d) + f_{pe}^2 r_s$ and $\beta = r_s(f_{ps}^2 - f_{pe}^2)/f_h^2 = r_s(N_s - N_e)/[N_s(1-r_s) + N_e r_s]$. According to this model, the abrupt change of the free carrier concentration in the $n^+ - n$ homojunction is responsible of the generation of a high frequency peak, usually known as hybrid plasma peak, (notation: HP resonance) with frequency f_{HP}, centered at the intermediate frequency of the plasma frequency of the substrate and the epilayer. The abrupt change of the free carrier concentration in the depletion region gives rise to a resonance in the intermediate-high frequency region of the noise spectrum, known as the returning carrier resonance, (notation: RC resonance) with central frequency

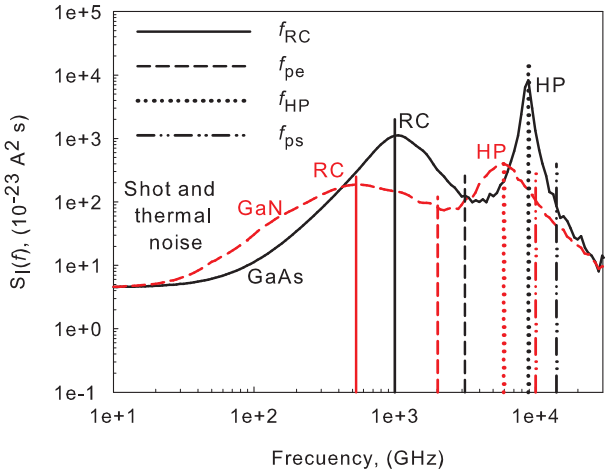

Figure 4.4: Identification of the main features of the noise spectra of GaAs and GaN Schottky diodes, under applied voltages V_{dc}= 0.80 V and V_{dc}= 0.97 V respectively. Curves obtained with the MC model. The vertical lines in the spectra identify the central frequency of the RC resonance (f_{RC}), the plasma frequency of the epilayer (f_{pe}), the central frequency of the HP resonance (f_{HP}) and the plasma frequency of the substrate (f_{ps}).

f_{RC}. Although the interpretation of this peak in the model presented in [Shi05] is different from the classical interpretation of Trippe *et al.* [Tri86], the name of *returning carrier* peak is commonly used in the literature. Besides, the frequency f_{RC}, eq. (4.35), is different from the frequency f_R, eq. (4.27). Fig. 4.4 shows the noise spectra for the reference Schottky diodes described in section 4.2, based on GaAs and GaN semiconductor operating under static conditions, ($V_{dc} = 0.80$ V for the GaAs diode and $V_{dc} = 0.97$ V for the GaN diode to obtain similar values of current flowing in these diodes). The RC and the HP resonances are identified in this figure. The plasma frequency of the substrate and the epilayer of the GaAs and GaN reference diode are also shown, (the doping concentrations and lengths for the substrate and the epilayer of the reference Schottky diode can be observed in Fig. 4.3).

Together with MC simulations, the general expression developed in [Shi05] for $S_I(f)$ eq. (4.32) as well as eqs. (4.33) to (4.35) are used to describe the high-frequency region of the noise spectra of Schottky diodes, (RC and HP resonances). Since the model developed in [Shi05] is not able to predict shot noise, the model published in [Tri86] for shot and thermal noise is employed to interpret the low frequency region of the noise spectra obtained from MC simulation of the diodes.

4.2 Analysis of noise in Schottky diodes under dc conditions

As a reference, the selected Schottky diode has an epilayer length of 350 nm with a doping concentration of 1x10^{17} cm^{-3}. The length of the substrate is 500 nm, which has been shortened as compared to the typical values of fabricated devices in order to reduce the computational cost of the Monte Carlo method. The doping concentration of the substrate is 2x10^{18} cm^{-3}. The anode area is 36 μm^2. The ideal barrier height has been set at 0.99 V for GaAs and 1.20 V for GaN diodes, respectively. The technological parameters of the reference diode has been selected according to Schottky-based multipliers fabricated by *JPL* operating in the near THz region [Mai03, Cha04, Mae05b, Mae08] where the application of GaN Schottky diodes is justified [Coj04b, Sil08, Jin13], see chapters 3 and 5.

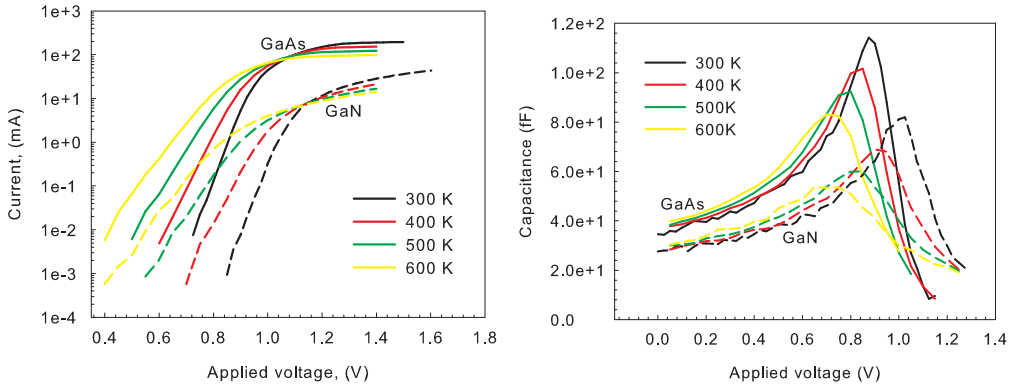

Figure 4.5: (a) I-V curves and (b) C-V curves for the GaAs and GaN reference diodes at different room temperatures obtained from MC simulations

Fig. 4.5 shows the I-V and C-V curves obtained from Monte Carlo simulations of GaAs and GaN reference Schottky diodes at room temperatures between 300 K and 600 K. For voltages lower than the built-in potential ($V_{bi}(T)$, 0.95 V for GaAs and 1.11 V for GaN at 300 K) the I-V curves show the typical non linear conductance region associated to thermionic emission through Schottky barriers. For $V > V_{bi}$, the current curves show a linear dependence with the applied voltage, which is associated to an ohmic behavior. Due to the lower electron mobility of GaN than GaAs, see section

3.2, the dc series resistance of the GaN diode is higher (about 1.8 Ω and 12.1 Ω for GaAs and GaN reference diodes, respectively), resulting in a lower slope for the variation of the current with the applied voltage in Fig. 4.5(a). As the temperature increases, the electron mobility decreases and the series resistance of the didoes increases. Besides, $V_{bi}(T)$ decreases with increasing temperature and the I-V and C-V curves shift to lower voltages. A detailed comparison of the electrical characteristics of GaAs and GaN diodes was presented in section 3.2.

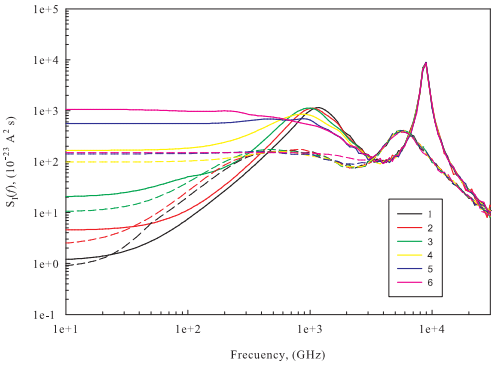

(a)

Label	I_{dc}, (mA)	V_{dc}, (V)	
		GaAs	GaN
1	0.022	0.75	0.93
2	0.13	0.80	0.97
3	0.88	0.85	1.03
4	5.21	0.90	1.11
5	19.77	0.95	1.30
6	44.38	1.00	1.60

(b)

Figure 4.6: (a) Current noise spectra for GaAs (continuous lines) and GaN (dashed lines) $n^+ - n$ reference Schottky diodes at 300 K under forward bias conditions obtained from MC simulations. Labels 1 to 6 correspond to voltage values indicated in the table on the right.

Fig. 4.6 shows the typical spectral density of current fluctuations for GaAs (continuous lines) and GaN (dashed lines) reference Schottky diodes under forward bias conditions at 300 K. Noise spectral densities of both materials are compared under similar values of current crossing the Schottky contact of the diodes. Labels 1 to 6 of the legend correspond to the voltage values indicated in the table of Fig. 4.6(b).

The following subsections present an analysis of the main features of the current noise spectra of GaAs and GaN diodes under static conditions at room temperature 300 K, employing the MC method and the analytical models of [Shi05] and [Tri86]. For this analysis, the noise spectrum has been divided into three regions: The low frequency region of the noise spectra, limited by the beginning of the RC peak, and the regions associated to the RC and the HP resonances, see Fig. 4.6. To analyze the influence of the HP resonance in the performance of the RC resonance, homogeneous Schottky diodes have been simulated, that is, Schottky diodes without substrate. Since for homogeneous diodes the $n^+ - n$ homojunction does not exist, the HP resonance, which is related to the $n^+ - n$ homojunction, is not present in their noise spectra.

4.2.1 Low frequency noise

Fig. 4.7(a) shows the current noise spectral density of the reference diodes based on GaAs (black symbols) and GaN (red symbols) as a function of the current flowing in the diodes at f= 0, $S_I(0)$. The Monte Carlo simulator employed to obtain these data neither implement generation-recombination phenomena nor 1/f noise. Therefore, $S_I(0)$ provided by the simulator is in accordance with eq. (4.30), where R_s is evaluated from the slope of the linear region of the I-V characteristic of Fig. 4.5 for applied voltages $V > V_{bi}$ (about 1.8 Ω and 12.1 Ω for GaAs and GaN reference diodes respectively).

From this expression, for $V < V_{bi}$ corresponding to $R_j >> R_s$, the low frequency spectral density, $S_I(0)$, behaves as 2qI, the shot-noise law eq. (4.24). For $V > V_{bi}$, the Schottky barrier disappears, $R_s >> R_j$, and the spectral density is due to thermal noise related to the series resistance R_s, $S_I(0) \sim$

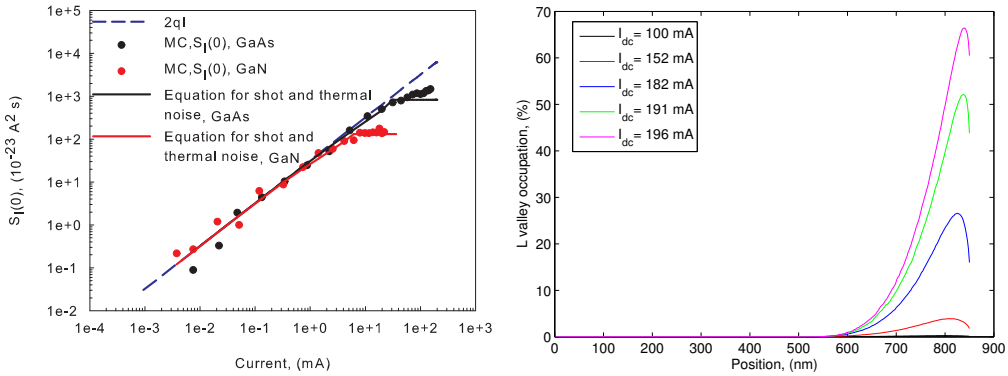

(a) (b)

Figure 4.7: (a) Low frequency current noise for GaAs and GaN $n^+ - n$ reference diodes as a function of the current flow through the diodes. Symbols represent the results from Monte Carlo simulations and continuous lines correspond to eq. (4.30). (b) Occupation of the L valley as a function of the position (Ohmic contact at position 0 nm and Schottky contact at position 850 nm) for the reference GaAs diode at different dc currents, obtained with the MC model.

$4K_BT/R_s$ eq. (4.17). Due to the higher electron mobility of GaAs than GaN semiconductor [Sch05], thermal noise contribution to $S_I(0)$ is higher for GaAs than GaN reference diode. Under applied voltage $V >> V_{bi}$, $S_I(0)$ for GaAs Schottky diode is higher than predicted in eq. (4.30), due to the contribution of hot carrier and intervalley transfer noise to the low frequency region of the noise spectrum [San94, Shi03b]. Such performance is confirmed in Fig. 4.7(b), where it is shown that the increase of $S_I(0)$ for the GaAs diode is related to the increase of the occupation of the upper valleys of the semiconductor. For the GaN diode, the intervalley transfer is not observed because of the higher energy gap between the valleys of the conduction band.

4.2.2 Returning carriers resonance

In this subsection we evaluate the dependence of the central frequency and amplitude of the RC resonance of the noise spectra with the applied voltage, (Figs. 4.8(a) and 4.8(b)), the doping of the epilayer, (Figs. 4.8(c) and 4.8(d)) and the length of the epilayer, (Figs. 4.8(e) and 4.8(f)). Lines in Fig. 4.8 correspond to the predictions of the analytical model of [Shi05] (denoted AM model) and the symbols correspond to the results obtained from MC simulations. In addition, each subfigure shows analytical expressions for f_{RC} or $S_I(f_{RC})$ derived with the analytical model of [Shi05] particularized for homogeneous diodes (diodes without substrate). In Figs. 4.8(c)-4.8(f), the applied voltages have been selected as 0.80 V for the GaAs diode and 0.97 V for GaN diode, in such a way that the current flowing through both diodes is the same.

From the particularization of eq. (4.33) made in appendix C.1 for homogeneous Schottky diodes, the amplitude of the RC resonance is proportional to average mobility of the electrons in the diode. The lower electron mobility of GaN [Sch05] is the fundamental reason of the lower amplitude of the RC resonance, $S_I(f_{RC})$, for GaN Schottky diodes. Besides, the central frequency of the RC resonance, f_{RC}, is proportional to $(\varepsilon_r m^{*2})^{-1/4}$. For voltages applied to the GaAs and GaN diodes such that the Schottky barrier height seen by the electrons in the neutral region of the epilayer, $V_{bi} - V$, is the same in both devices, the ratio between f_{RC} of GaN and GaAs diodes is ~ 0.58, as appendix C.1 shows.

Fig. 4.8 shows that the most effective way to shift the RC resonances to higher frequencies is achieved by higher doping concentrations of the epilayer and by the reduction of its length. Besides, for diodes with short epilayer length and high epilayer doping concentration (L_e lower than 100 nm

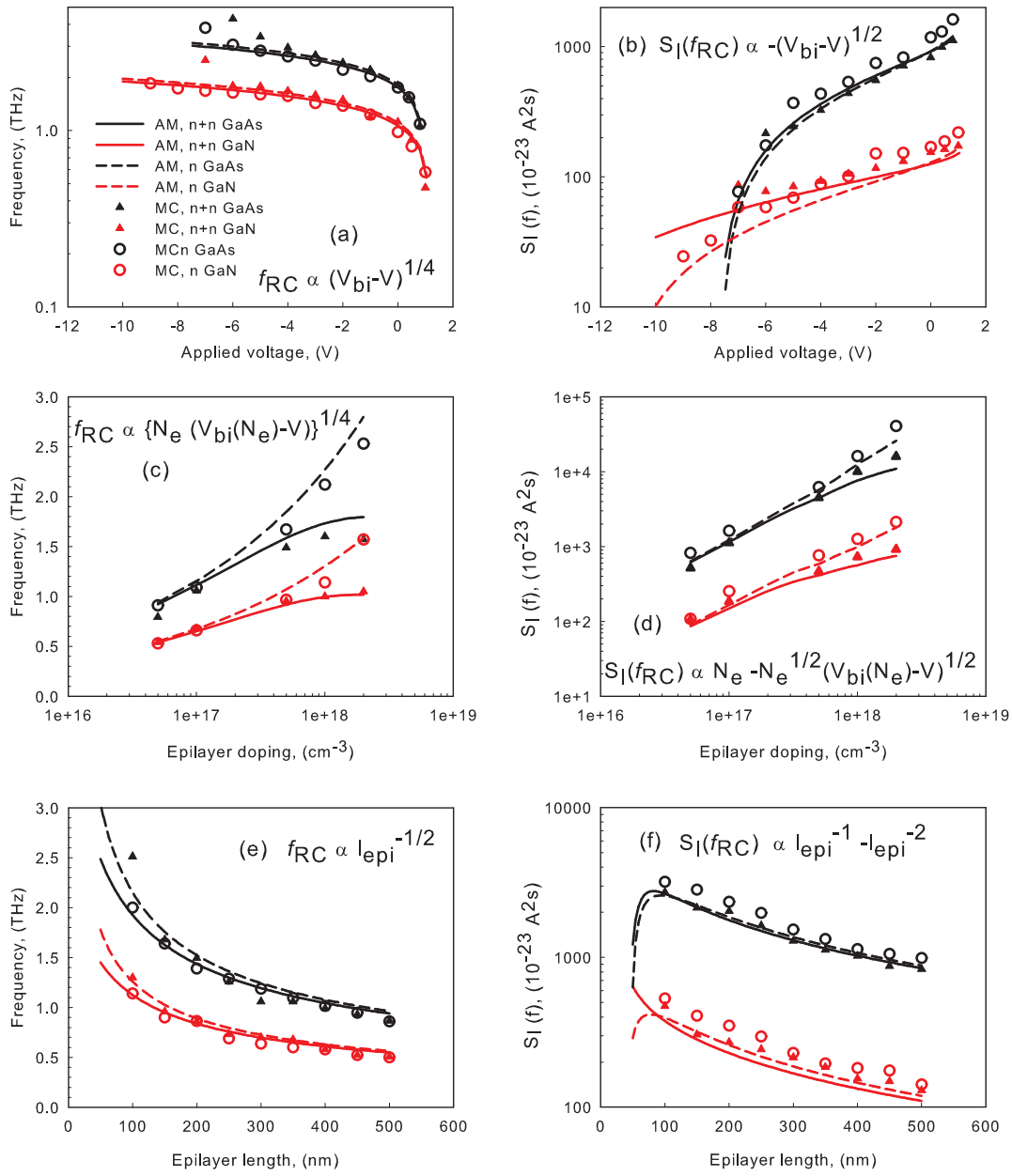

Figure 4.8: Evolution of the frequency and the amplitude of the RC resonance with the applied voltage ((a), (b)), the doping of the epilayer ((c), (d)) and the length of the epilayer ((e), (f)), for GaAs and GaN. Both $n^+ - n$ and homogeneous (n) structures are analyzed. Results from MC simulations and the analytical model of [Shi05] *AM* are shown. In Figs. 4.8(c)-4.8(f), the applied voltages are 0.80 V for GaAs and 0.97 V for GaN Schottky diodes in order to obtain the same current.

and N_e higher than 5x10^{17} cm^{-3}, Figs. 4.8(c) and 4.8(e)), we observe that the central frequency of the RC resonance is lower for $n^+ - n$ diodes than for diodes without substrate.

4.2.3 Hybrid plasma resonance

This subsection evaluates the dependence of the HP resonance with the applied voltage, doping and length of the epilayer, employing the analytical model of [Shi05] (continuous and dashed lines in Figs. 4.9, 4.10 and 4.11) together with MC simulations (symbols).

According to eq. (4.34), the central frequency of the HP resonance is located between the plasma frequencies of the substrate and the epilayer. Since the effective mass of the electrons in GaN is higher than in GaAs, the plasma frequency of the substrate and the epilayer is lower for GaN and the central frequency of the HP resonance in GaN is lower than in GaAs based Schottky diodes. The description of the self-consistent coupling of the fluctuations of the carrier velocity and the electric field originated by the $n^+ - n$ inhomogeneity through Langevin's equation, let the analytical model [Shi05] to predict correctly the performance of the HP resonance. When the doping of the substrate is equal to the epilayer doping, $N_s = N_e$=1x10^{17} cm^{-3}, the epilayer-substrate homojunction does not exist and the HP resonance disappears. Fig. 4.9 shows a low sensitivity of the HP

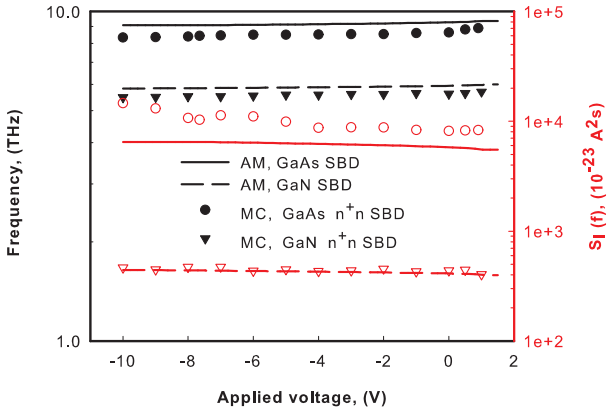

Figure 4.9: Evolution of the frequency (black data) and the amplitude (red data) of the HP resonance with the applied voltage for GaAs and GaN reference Schottky diodes, from MC simulations (symbols) and the analytical model of [Shi05] AM (lines).

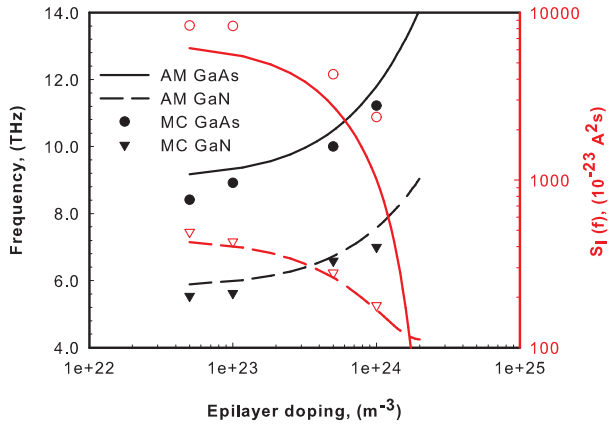

Figure 4.10: Evolution of the frequency (black data) and the amplitude (red data) of the HP resonance with the doping concentration of the epilayer for GaAs and GaN reference Schottky diodes from MC simulations (symbols) and the analytical model of [Shi05] AM (lines). The applied voltages have been selected as 0.80 V for GaAs and 0.97 V for GaN diodes.

resonance with the applied voltage. Figs. 4.10 and 4.11 present the dependence of the HP peak

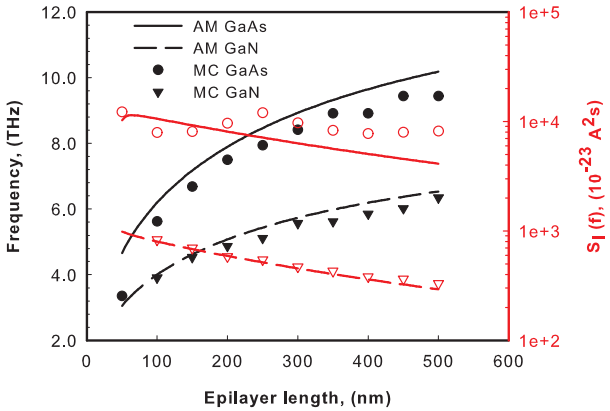

Figure 4.11: Evolution of the frequency (black data) and the amplitude (red data) of the HP resonance with the length of the epilayer for GaAs and GaN reference Schottky diodes, from MC simulations (symbols) and the analytical model of [Shi05] AM (lines). The applied voltages have been selected as 0.80 V for GaAs and 0.97 V for GaN diodes.

with the doping and the length of the epilayer, respectively. The results presented in these figures have been obtained under the same applied voltage of figures 4.8(c)-4.8(f), corresponding to similar values of current flowing through the GaAs and GaN reference diodes.

This section has presented an analysis of the noise spectra of Schottky diodes under dc conditions. It has been shown that the low frequency region of the noise spectra is characterized by shot and thermal noise contributions (1/f noise and generation-recombination noise have not been considered in this analysis). At voltages higher than the built-in potential, hot electron noise and intervalley transfer noise have to be taken into account. A systematic study of the returning carrier and hybrid plasma peaks with the applied voltage and the device structure has been carried out. An important noise reduction in the THz region can be reached by shifting the RC peak at higher frequencies using short and highly doped epitaxial layers. Also high epilayer doping are used at THz frequencies to avoid velocity saturation effects. Besides, the study presented in this section has helped to validate the analytical noise model presented in [Shi05] under very different conditions for GaAs and GaN Schottky diodes.

4.3 Analysis of noise in Schottky diodes under time varying conditions

This section analyses the main features of the current noise spectra of Schottky diodes operating under periodic excitations at 300 K.

The response of GaAs and GaN based Schottky diodes employing MC simulations for two different sinusoidal excitations at different frequencies f_{ex}, ($V(t) = V_0 + V_1 \sin(2\pi f_{ex} t)$) is evaluated: varistor mode defined by a bias $V_0 = 0.8$ V and amplitude $V_1 = 0.1\,V$, and varactor mode defined by $V_0 = 0.0V, V_1 = 0.9V$. The former excitation, which is denoted by $V_{mix}(t, f_{ex})$, is typical of Schottky mixers while the latter one, which is denoted by $V_{mul}(t, f_{ex})$, is typical of Schottky multipliers at high frequencies.

4.3.1 Low frequency noise

Fig. 4.12(a) shows the low frequency noise spectral density, $S_I(0)$, obtained from MC simulations for the GaAs reference SBD under applied signals $V_{mix}(t, f_{ex})$ and $V_{mul}(t, f_{ex})$ for different f_{ex}. Lines in Fig. 4.12(a), which represent the $2q\overline{I}$ law for shot noise ($\overline{I}$ represents the average current flowing in the diode), show a good agreement with $S_I(0)$ calculated with MC. The average current $\overline{I}$, and consequently the $2q\overline{I}$ noise, increase as the frequency of the applied signal rises, reaching a maximum at frequencies f_{max}= 650 GHz and f_{max}= 900 GHz under V_{mul} and V_{mix}, respectively, and they drop slowly at higher frequencies. While the frequency of the applied signal is lower than f_{max}, the average current flowing through the diode increases with f_{ex} due to the modulation of the non-linear resistance of the junction, see Fig. 4.12(b). Also the displacement current increases. When $f_{ex} > f_{max}$, velocity saturation takes place, see section 3.1.2, and, therefore, the current through the diode is limited because the edge of the depletion region cannot move faster than allowed by the maximum electron velocity. f_{max} varies depending on the working conditions, $V_{mix}(t, f_{ex})$ or $V_{mul}(t, f_{ex})$, because of the non-linear dependence of the width of the depletion region with the applied voltage.

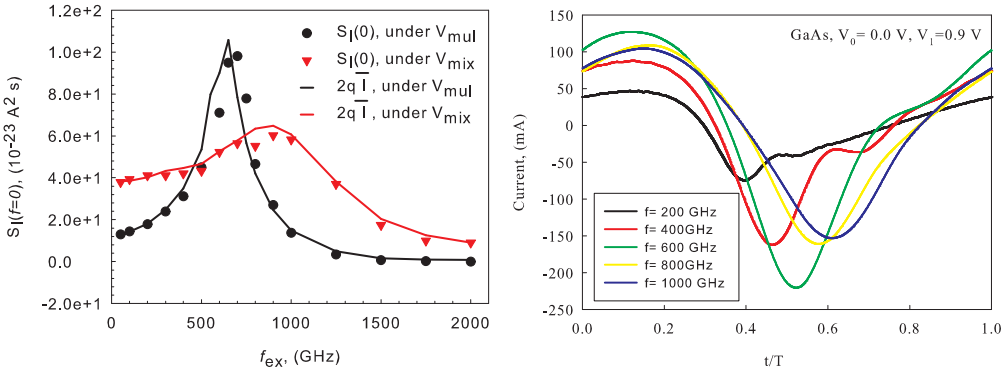

Figure 4.12: (a) Noise spectral density at f= 0 Hz and the $2q\overline{I}$ law for GaAs reference diodes under V_{mix} and V_{mul} for different f_{ex} (b) Current response of the GaAs diode under V_{mul} for different f_{ex}. Results obtained with the MC model.

Table 4.1 shows the average current, $\overline{I}$, and phasor at the fundamental frequency of the current

Table 4.1: Average current and fundamental phasor of the current response for the GaAs reference Schottky diode under V_{mul} and V_{mix} for different f_{ex}.

	V_{mul}		V_{mix}	
f_{ex}, (GHz)	$\overline{I}$, (mA)	I_1, (mA)	$\overline{I}$, (mA)	I_1, (mA)
50	0.41	$11.6e^{-\imath 0.027\pi}$	1.19	$3.6e^{-\imath 0.120\pi}$
100	0.45	$23.3e^{-\imath 0.023\pi}$	1.2.0	$6.3e^{-\imath 0.129\pi}$
300	0.77	$71.3e^{-\imath 0.045\pi}$	1.35	$18.6e^{-\imath 0.124\pi}$
600	2.81	$143.0e^{-\imath 0.115\pi}$	1.64	$38.9e^{-\imath 0.217\pi}$
900	0.77	$118.0e^{-\imath 0.224\pi}$	2.03	$57.1e^{-\imath 0.376\pi}$
1250	0.15	$123.0e^{-\imath 0.230\pi}$	1.19	$54.5e^{-\imath 0.571\pi}$
1500	0.05	$127.1e^{-\imath 0.226\pi}$	0.64	$43.3e^{-\imath 0.656\pi}$
1750	0.03	$130.2e^{-\imath 0.220\pi}$	0.39	$32.9e^{-\imath 0.702\pi}$
2000	0.02	$133.2e^{-\imath 0.208\pi}$	0.28	$24.6e^{-\imath 0.721\pi}$

response of the GaAs reference diode under V_{mul} and V_{mix} for different f_{ex}. The electron velocity saturation results in the reduction of the current as frequency increases.

The velocity saturation effect is more severe for GaN diodes because of its lower mobility. When $f_{ex} \gtrsim 200$ GHz, the diode performance is limited by the velocity saturation, see section 3.2.

4.3.2 Medium-high frequency noise

Figs. 4.13 and 4.14 show the noise spectra obtained from MC simulations of GaAs and GaN reference diodes respectively, under excitation $V_{mul}(t, f_{ex})$ and $V_{mix}(t, f_{ex})$ for different f_{ex}. Black dashed lines have been obtained with the analytical model of [Shi05] as a superposition of noise spectra of the Schottky diodes under static conditions with a sinusoidal distribution between $V_{min} = V_0 - V_1$ and $V_{max} = V_0 + V_1$ (denoted as superposition of AM in the figure); i.e., the AM noise spectra in Figs. 4.13 and 4.14 are the average of the set of noise spectra obtained with the AM model of the diode under N samples of the applied voltage given by $V_{mul}(t = n/(Nf_{ex}))$ (or V_{mix}) with n= 0, 1, 2, ..., N-1. Also, the noise spectra with the AM model under the bias point is included (red dashed lines).

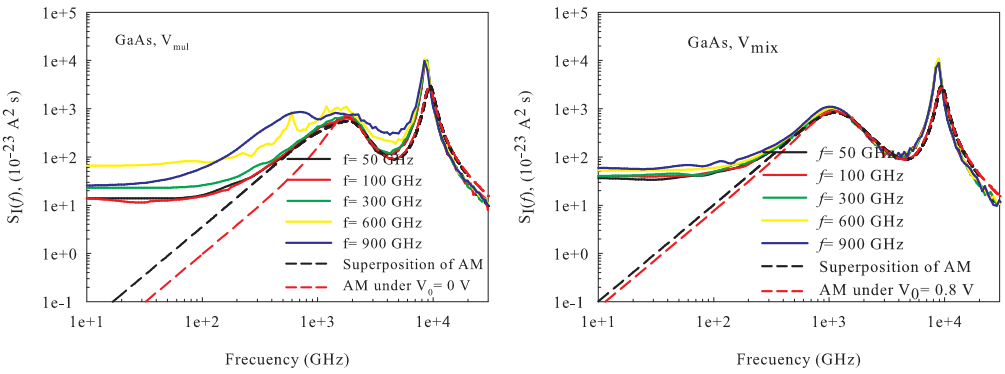

Figure 4.13: Noise spectral density of GaAs reference Schottky diode under (a) V_{mul} and (b) V_{mix} for different frequencies.

Fig. 4.13(a) shows that the medium-high frequency range of the noise spectra obtained from MC simulations of GaAs diodes under applied signals V_{mul} with $f_{ex} \lesssim 300$ GHz can be correctly described with the AM model (the low frequency range of the current noise spectra, which has been analysed in the previous subsection, is not described by the AM model). The HP resonance observed in the figure is understood as a superposition of noise spectra under static conditions, i.e. it does not vary with the frequency of the simulated excitations.

The noise spectra for f_{ex}= 600 GHz and 900 GHz show a peak at the frequency of the applied signal and an increase of the noise level in the frequency region near f_{ex}. Under these conditions, the electric field is high enough for intervalley transfer to take place, the stochastic transitions between the lowest (Γ) and upper valleys (L, X) of the semiconductor generate a new contribution to the noise spectrum with Lorentzian shape. Under cyclostationary conditions, part of the low frequency noise generated by intervalley transfer is upconverted, generating a peak at the frequency of the excitation [Shi03b], as is observed in Fig. 4.13(a) at f_{ex}= 600 GHz. With the further increase of the input frequency, f_{ex}= 900 GHz, i.e. with the increase of the electric field in the undepleted regions of the diode, the peak starts to decrease and shifts to higher frequencies and the low frequency region of the noise spectrum decrease, since most of the electrons are in the upper valleys. The described performance will take place only when the frequency of the applied signal is higher than the inverse of the characteristic time of the intergroup exchange τ_g. τ_g= 2 ps has been obtained in [Shi03a] with

the MC model for bulk GaAs under a sinusoidal electric field of amplitude 10 KV/cm and frequency 600 GHz. Under excitations $V_{mix}(t, f_{ex})$ for different f_{ex}, Fig. 4.13(b), the small amplitude of the applied signal is insufficient to give rise to intervalley transitions in the semiconductor and the noise spectra obtained from the MC simulations can be described as a superposition of noise spectra obtained under static conditions.

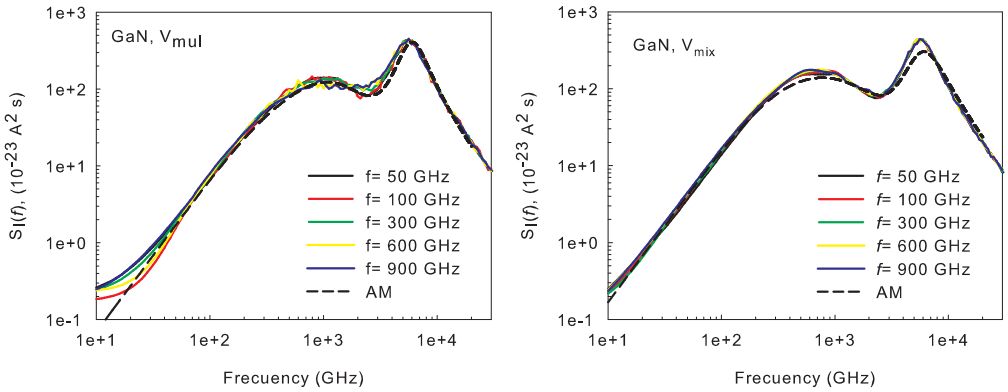

(a) (b)

Figure 4.14: Noise spectral density of GaN reference Schottky diode under (a) V_{mul} and (b) V_{mix} for different frequencies.

The high energy gap of GaN [Sch05] prevents GaN diode from intervalley transitions under conditions V_{mul}, as Fig. 4.14 shows. Consequently, the related noise spectra obtained from the MC simulations are correctly described as a superposition of noise spectra under static conditions.

This analysis shows that the noise spectra in GaAs and GaN diodes operating under time varying conditions can be described as a superposition of noise spectra under static conditions while hot carrier effects are not present. Consequently, the rules presented in the previous section to reduce the noise level of Schottky diodes under static conditions in the near THz region, are valid under time varying operation of the devices.

4.4 Temperature dependence of the noise spectra

To analyze the impact of the external temperature on noise, this section evaluates the temperature dependence of the noise spectra of GaAs and GaN diodes from dc to THz range conditions.

4.4.1 Noise spectra under static conditions

Fig. 4.15 shows the temperature dependence of the noise spectra obtained from MC simulations of the GaAs and GaN reference didoes under static conditions. The applied voltages have been selected to obtain similar values of current in GaAs and GaN diodes at all the simulated temperatures T ($\sim$ 0.13 mA, Fig. 4.5). These applied voltages are lower than $V_{bi}(T)$ and, therefore, the low frequency noise is described by the $2qI$ law for shot noise.

Under these conditions, the width of the depletion region for GaAs and GaN diodes increases with T, see eq. (2.1). According to eqs. (4.34) and (4.35), the central frequency of the RC resonance increases and the central frequency of the HP resonance decreases with increasing temperature ($f_{RC} \sim r_d$ and $f_{HP} \sim \gamma - r_d$, where γ does not depend on$T$, Fig. 4.3 and eq. (2.7)). The variations of the noise spectra with the temperature are more pronounced for GaN than for GaAs diodes because of the different performance of the electron mobility with the temperature [Sch05].

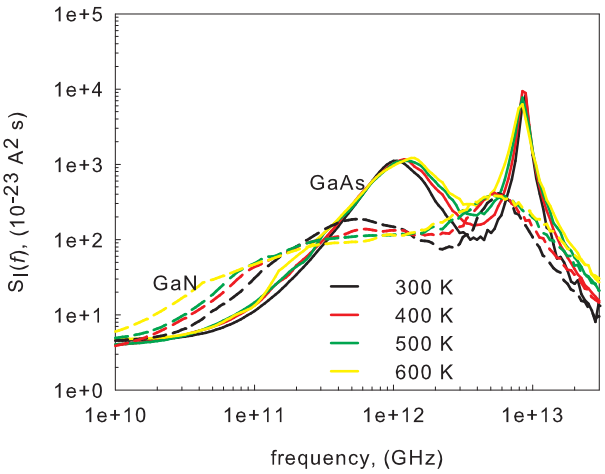

Figure 4.15: Noise spectra obtained from MC simulations of the GaAs and GaN reference diodes under constant voltage conditions and temperatures from 300 K to 600 K. The applied voltages have been selected to obtain similar values of current ($\sim$ 0.13 mA) in GaAs and GaN diodes at all the simulated temperatures.

4.4.2 Noise under time varying conditions

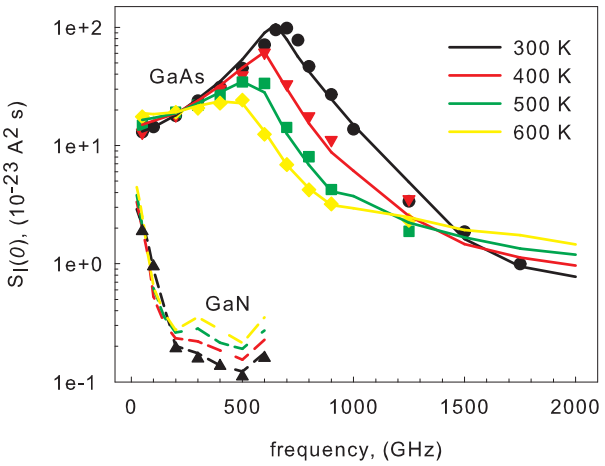

Figure 4.16: Noise spectral density at f= 0 Hz (marks, obtained from MC simulations) and the $2q\overline{I}$ law for GaAs and GaN diodes under applied signals of amplitude corresponding to the maximum dc voltage without entering the ohmic regime at each simulated temperature, bias point 0 V and different frequencies.

The results of the study for the temperature dependence of the low frequency noise of the diodes under time varying conditions are shown in Fig. 4.16. This figure shows the noise spectral density at $f = 0$ Hz, $S_I(0)$, for the GaAs and GaN reference diodes as a function of the frequency of the applied signal and temperatures from 300 K to 600 K. The bias point is 0 V and the amplitude of the RF signal, V_1, corresponds to the maximum dc voltage for the GaAs and GaN reference diodes at each temperature without entering the ohmic regime ($V_1 \sim V_{bi}(T)$), Fig. 4.5. The results of $S_I(0)$ from MC simulations show a good agreement with the $2q\overline{I}$ law for shot noise (continuous and dashed lines of Fig. 4.16).

For the GaAs Schottky diode, the peak of $S_I(0)$, which is related to current velocity saturation as was shown in section 4.3.1, shifts to lower frequencies as the temperature increases because of the reduction of the electron mobility with temperature [Sch05]. The reduction of the amplitude of this

peak with temperature is due to the increase of the series resistance of the diode and the reduction of the modulation of the nonlinear resistance with the increase of T, Fig. 4.5. The performance of the GaN diode is dominated by a higher series resistance even at low frequencies.

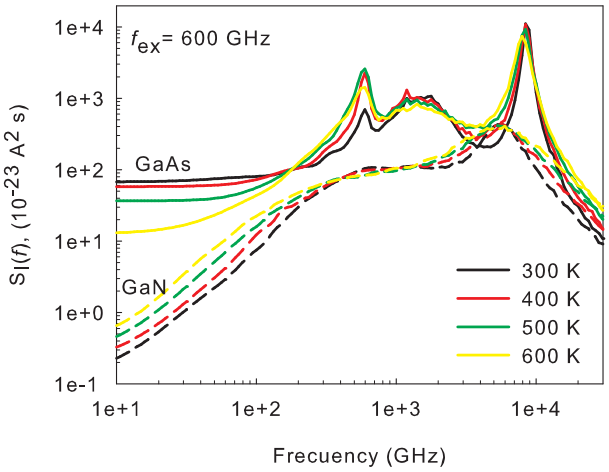

Figure 4.17: Noise spectral density of the GaAs and GaN reference diodes under applied signals simulated to obtain the results of Fig. 4.16 at 600 GHz. Results obtained with the MC model.

Regarding the medium-high frequency range, i.e, the frequency region where RC and HP peaks appear, the noise performance can be reproduced by the analytical model of [Shi05] as a superposition of noise spectra under static conditions up to THz regime for GaN diode, and up to 300 GHz for GaAs diode, section 4.3.2. Fig. 4.17 shows the temperature dependence of the medium-high frequency noise of the GaAs and GaN diodes under applied signals of frequency 600 GHz. At this frequency and higher, the intervalley transitions between Γ and L valleys in the GaAs diode described in section 4.3.2 appear, giving rise to a peak at the frequency of the applied signal. As T increases, the average energy of the carriers increases, and the average occupation of the L-valley increases. Therefore, the amplitude of the peak associated to these transitions rises according to [Shi03a].

In conclusion, this chapter has presented a systematic study of the noise features of GaAs and GaN Schottky diodes operating under static and time varying conditions based on the Monte Carlo method. Low-frequency mechanisms such as shot and thermal noise and high frequency mechanisms such as returning carriers and plasma phenomena have been characterized as a function of the device structure, temperature, and working regimes. Contributions of hot electrons and intervalley transfer to noise have also been discussed. Besides, this chapter has validated analytical models available in the literature to describe the noise spectra of Schottky diodes under very different working regimes, with emphasis on the limits of application of these models.

The analysis of the noise spectra of Schottky diodes presented in this chapter plays an important role in the noise analysis of multipliers and mixers that is carried out in chapters 5 and 6 respectively. High noise levels can limit the extraction of the signals of interest generated in these circuits. In THz multipliers, limited levels of power are generated at the output frequency, and high frequency noise mechanisms such as returning carriers and intervalley transfer noise can highly degrade the extraction of the output signal in the THz region. In the same way, the operation of Schottky mixers is limited by the noise generated by the diodes. Since the output frequency of these circuits is usually in the low frequency region (at the difference of the radio frequency and the local oscillator frequency, see chapter 6), the most important noise contributions in mixers are shot noise, thermal noise, hot electron noise and intervalley transfer noise. A simulation tool able to account simultaneously for both the electrical response and the noise of the device is essential in the design and optimization

of frequency multipliers and mixers. The analysis presented in the chapter 3 and the current chapter has shown the excellent capabilities of the MC model to be used in such a task. In the following part of the thesis, an analysis of frequency multipliers and mixers is carried out, using simulation tools where the diode models are integrated into a circuital simulator based on the harmonic balance technique.

Part III

SCHOTTKY DIODE BASED CIRCUITS

Chapter 5

Design of Schottky diode frequency multipliers at millimeter and submillimeter-wave bands: Modelling and limitations

GaAs Schottky barrier diodes are presently one of the most used solid-state devices for terahertz applications [Sie02, Cro05, Sie07, Mae10b, Cha11a]. Because of their high efficiency in frequency multipliers capable of reaching into the THz region, Schottky diodes are the technology most often used for building compact and robust local oscillators for heterodyne receivers [War03, Mae05b, Mae05c, Gra10, Mae10a, Cro11, Mae12]. Planar GaAs Schottky diode frequency multipliers operating at frequencies up to 3 THz have been designed and fabricated in [Mae12].

Design and optimization of circuits based on Schottky diodes for high frequency applications require reliable predictions of the device performance. The literature provides device models with increasing accuracy and complexity, like lumped element equivalent circuit (LEC) [Pen62, Cha78, Cro89, Eri98, Sch01b], drift-diffusion (DD) [Sel84, Lun00, Gra00], hydrodynamic (HD) [Blo70, Lun00, Hje94, Lee99] and Monte Carlo (MC) [Jac89a, Lun00, Gon91, Bha95, Eas95, Lip97], see chapter 2.

Successful results have been obtained by different research groups in the design and fabrication of Schottky based millimeter and submillimeter circuits by employing LEC models [Sch02, Cro05, Mae10b, Tho10b, Cha11a, Mae12]. LEC models are used for simplicity and ease implementation in CAD tools [Cha78, Cro89, Eri98, Sch01b, Mae10b, Mae12]. However, these models are expected to fail at millimeter and submillimeter wavelength and/or high power levels, where physical processes in the device like velocity saturation [Kol92, Jon95, Eas95, Lip98, Gra00, Sch01b, Sch01a], carrier inertia, displacement current in undepleted regions of the diode, plasma oscillations [Cha78, Cro89, Jon95, Sch01b, Sch01a] or the nonstationary dynamics [Ais84, Sch95, Jon95, Lip97] of the carriers begin to dominate the device operation, see chapter 3. Therefore, the validity of LEC models for the design of millimeter and submillimeter circuits has to be evaluated.

This chapter analyses the range of validity of LEC and DD models in the design of frequency multipliers up to THz bands. The MC model has been selected as a reference. Doublers and triplers have been analysed through the coupling of the different diode models to a harmonic-balance-based circuit simulator [Ker75, Lip97, Gra00]. The performance of frequency multipliers above 3 THz has been also explored taking into account the most significant limiting transport phenomena.

5.1 Methodology for the simulation of frequency multipliers

5.1.1 Operating principles of Schottky based multipliers

Frequency multiplication in Schottky diodes occurs due to the nonlinearities generated by the Schottky contact. Usually, the nonlinear capacitance-voltage characteristic of the diode is used to convert a periodic input signal into a harmonic output signal containing components at the multiples of the input frequency (varactor mode of operation). A typical frequency multiplier is composed of a power source at the input frequency f_0, $V_g(f_0)$, one or several nonlinear devices, source (Z_g) and load (Z_l) impedances, filters to separate the source from the generated signals and select the desired components of the output, and input and output matching circuits. Fig. 5.1 shows a scheme of a single diode multiplier. A detailed analysis of the principle of operation of frequency multipliers can be found in the literature [Pen62, Maa88, Fab95].

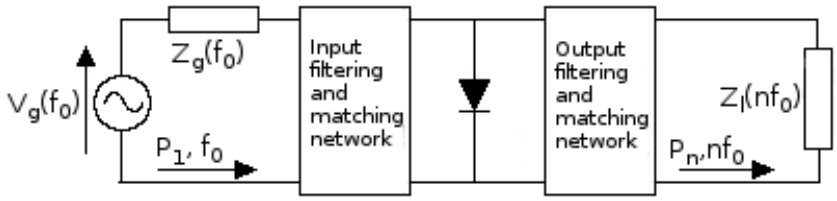

Figure 5.1: Frequency multiplier with a single diode.

Manley and Rowe [Man56] developed a set of general relations among the real powers at all mixing frequencies in a lossless nonlinear reactance pumped by a two-tone excitation. They can be used to establish limits to the gain or loss of nonlinear devices. The particularization of these formulas for a nonlinear capacitor with only one driving frequency f_0 is:

$$\sum_{n=1}^{\infty} P_n = 0 \;\Leftrightarrow\; P_1 = -\sum_{n=2}^{\infty} P_n, \tag{5.1}$$

where P_n represents the real power at frequency nf_0 and n is a natural number. According to eq. (5.1), the highest possible real power generated at the desired output frequency $f_m = mf_0$ occurs when only real powers exist at the input and output frequencies. In this situation, eq.(5.1) leads to a theoretical efficiency of power conversion of 100 %. However, this efficiency is not achievable in real diodes because of the series resistance of the diode.

Alternatively, the diode can operate in varistor mode, where, according to [Pag58], it has a quite limited conversion efficiency:

$$\frac{P_1}{P_m} \geq m^2 \tag{5.2}$$

Varactor operation mode is preferable because of its higher conversion efficiency. The Schottky contact can be modeled as a nonlinear capacitance in parallel with a nonlinear resistance, subsection 2.2.1. Fig. 5.2 presents the results of the simulation of a doubler based on the lumped equivalent circuit model of an ideal Schottky diode (the model of the Schottky contact without series resistance, see Fig. 2.5). The efficiency of the doubler is 100 % while it operates in varactor mode (eq. (5.1)) and decreases at input power higher than 15 dBm because it reaches the varistor mode (eq. (5.2)), as is observed by the increase of the dc current.

The analysis of the simple LEC model of Fig. 5.3 for a Schottky diode operating in varactor mode provides a set of equations for the performance of frequency multipliers [Pen62, Lip98]. The total current in the diode is given by:

$$i(t) = C_j(t)\frac{dv_j(t)}{dt}, \tag{5.3}$$

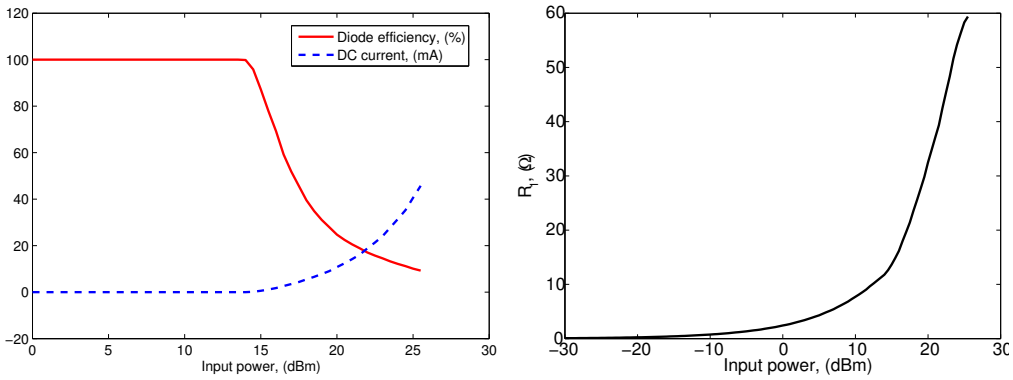

(a) (b)

Figure 5.2: (a)Diode efficiency (solid line), dc current (dash line) and (b) the real part of the diode impedance at the input frequency R_1 of a 200 GHz doubler based on an ideal Schottky contact (LEC model of Fig. 2.5 without series resistance). The parameters of the ideal Schottky contact are those of the first 200 GHz doubler in Table 5.1 ($C_j(0) = 35.8fF$, ϕ_b= 0.99, A= 36 μm^2, V_{bias}= -6 V). The circuit impedance at the input frequency is matched at each input power, $Z[2f_0] = (22.77 + 55.12j)\Omega$ and $Z[nf_0] = (0 + 0j)\Omega$ for $n > 2$, see Table 5.1.

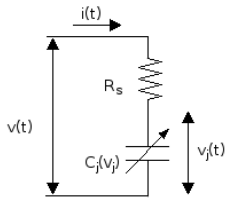

Figure 5.3: Simplified equivalent circuit model of the Schottky diode in varactor operation mode.

where $v_j(t)$ represents the voltage that drops in the nonlinear capacitance. From eq.(5.3):

$$v_j(t) = \int_0^t \frac{1}{C_j(\tau)} i(\tau) d\tau = \int_0^t S(\tau) i(\tau) d\tau, \tag{5.4}$$

where $S(t) = 1/C_j(t)$ is the elastance. Therefore, the voltage at the terminals of the diode is:

$$v(t) = R_s i(t) + \int_0^t S(\tau) i(\tau) d\tau. \tag{5.5}$$

If the diode is excited by periodic signals of frequency f_0, the voltage, current and elastance can be represented by their Fourier series:

$$v(t) = \sum_{k=-\infty}^{\infty} V_k e^{jk\omega_0 t} \tag{5.6}$$

$$i(t) = \sum_{k=-\infty}^{\infty} I_k e^{jk\omega_0 t} \tag{5.7}$$

$$S(t) = \sum_{k=-\infty}^{\infty} S_k e^{jk\omega_0 t} \tag{5.8}$$

where $\omega_0 = 2\pi f_0$. Since $i(t)$, $v(t)$ and $S(t)$ are real, the following relations are verified:

$$V_{-k} = V_k^* \tag{5.9}$$

$$I_{-k} = I_k^* \tag{5.10}$$

$$S_{-k} = S_k^* \tag{5.11}$$

Replacing the Fourier expansion of $i(t)$, $v(t)$ and $S(t)$ in eq. (5.5):

$$V_k = R_s I_k + \frac{1}{jk\omega_0}\sum_l I_l S_{k-l}. \tag{5.12}$$

Assuming the fully depleted approximation for the Schottky junction, the current and the charge are related according to:

$$i(t) = \frac{dQ(t)}{dt} = A^2 q N_e \varepsilon_0 \varepsilon_r \frac{dS(t)}{dt}, \tag{5.13}$$

that in the frequency domain is expressed as:

$$\sum_k I_k e^{jk\omega_0 t} = A^2 q N_e \varepsilon_0 \varepsilon_r (jk\omega_0) \sum_k S_k e^{jk\omega_0 t}. \tag{5.14}$$

From eq. (5.14), the following relation exists between the Fourier coefficients of $i(t)$ and $S(t)$:

$$I_k = jk\omega_0 A^2 q N_e \varepsilon_0 \varepsilon_r S_k. \tag{5.15}$$

The complex modulation ratio M_k is defined as the normalized elastance coefficient:

$$M_k = \frac{S_k}{S_{avg}}, \tag{5.16}$$

where $S_{avg} = (S_{max} + S_{min})/2$, S_{max} is the reciprocal of the minimum of capacitance (usually the capacitance at breakdown), and S_{min} is the reciprocal of the maximum of capacitance. Substituting eqs. (5.15) and (5.16) into eq. (5.12) gives the expression for the k-harmonic of the voltage:

$$V_k = R_s I_k + A^2 q N_e S_{avg}^2 \sum_r M_r M_{k-r}. \tag{5.17}$$

Including the definition of M_k in eq. (5.15) and dividing eq. (5.17) by eq. (5.15), the input impedance at the nth-harmonic is given by

$$Z_n = \frac{V_n}{I_n} = R_s + S_{avg}\frac{\sum_r M_r M_{n-r}}{jn\omega_0 M_n}. \tag{5.18}$$

The real part of Z_n, denoted by R_n, is:

$$R_n = \mathrm{Re}[Z_n] = R_s + S_{avg}\frac{A_n}{n\omega}, \tag{5.19}$$

where A_n represents the imaginary component of the summation in r in eq. (5.18). Note that R_n eq. (5.19) is the sum of the series resistance of the diode and a contribution from the nonlinear capacitance. Eqs. (5.18) and (5.19) indicate that the input and output circuit impedances for optimum coupling [1] of a pure nonlinear reactance (forgetting for a moment the series resistance of the diode) have resistive components due to the contribution of the second term in eq. (5.19), see Fig. 5.2(b). These resistive components of the input and output impedances depend on the available input power, as well as the coupling efficiency of the circuit at the output frequency [Eri98].

For a doubler, it is desirable to design embedding circuit to open-circuited the diode at the unwanted harmonics to avoid power dissipation at those harmonics[2]. High efficiency of the multipliers is only reached if the input power from the source is effectively coupled to the diode, i.e. a conjugate matching of the input source for each drive level. Since the diode is working as a generator at the

[1] Conjugately matched impedance of the diode impedance at the input frequency Z_1, eq. (5.18).

[2] Since these conditions are difficult to achieve, loads at the unwanted harmonics should be reactive to avoid power losses in the external circuit.

output frequency, R_2 is negative[3] and the optimal load is minus the diode impedance at the output frequency [Lip98]. The input and the output powers are:

$$P_1 = 2|I_1|^2 R_1 = 2|I_1|^2 R_s + 2|I_1|^2 S_{avg} \frac{A_1}{\omega_0} = P_{1,R_s} + P_{1,pnc}, \tag{5.20}$$

$$P_2 = 2|I_2|^2 R_2 = 2|I_2|^2 R_s + 2|I_2|^2 S_{avg} \frac{A_2}{2\omega_0} = P_{2,R_s} + P_{2,pnc} \tag{5.21}$$

where P_{i,R_s} represents the power loss in the series resistance and $P_{i,pnc}$ represents the power to the nonlinear capacitance. According to these expressions, the input power can be written as the sum of the power delivered to the series resistance P_{1,R_s} and the power delivered to the "pure" nonlinear capacitance part of the diode $P_{1,pnc}$. Following Manley-Rowe eq. (5.1), $P_{1,pnc}$ accounts for the power transferred to the higher harmonics of the input signal by the nonlinear capacitance. Since power is generated by the diode at the second harmonic, both R_2 and P_2 are negative [Lip98] (from the particularization of eq. (5.1) for a doubler open-circuited at the unwanted harmonics, $P_{1,pnc} = -P_2$). The efficiency of a doubler can be written:

$$\eta = -\frac{P_2}{P_1} = -\frac{|I_2|^2 R_2}{|I_1|^2 R_1} = -\frac{4|S_2|^2}{|S_1|^2} \frac{R_s + S_{avg}\frac{A_2}{2\omega_0}}{R_s + S_{avg}\frac{A_1}{\omega_0}}. \tag{5.22}$$

Assuming $P_2 = -P_{1,pnc}$ (doubler open-circuited at the unwanted harmonics), the efficiency can be written:

$$\eta = (1 + \frac{P_{1,R_s}}{P_{1,pnc}})^{-1} = \frac{1}{1 + \frac{R_s \omega_0}{A_1 S_{avg}}}. \tag{5.23}$$

According to eq. (5.23), the efficiency decreases as the frequency increases. Besides, R_s increases with frequency because of phenomena like velocity saturation or skin effect contributing to degrade the efficiency. Whereas the efficiency decreases with frequency, the output power of a varactor increases with frequency, see eqs. (5.15) and (5.21) for the dependence of the output power on the input frequency f_0. However, as the frequency increases the available input power of the sources decreases leading to a lower modulation of the nonlinear capacitance. Hence the net effect is the reduction of the output power eq. (5.21) as the frequency increases.

For triplers and higher order multipliers, it is important to analyse the effect of currents at the intermediate harmonics. These intermediate harmonics are known as idlers. With the abrupt junction model, it is impossible to generate harmonics higher than the second if currents are allowed only at the input and output frequencies. The reason is that the voltage at the junction is a square function of the charge and, therefore, cannot generate voltage components above the second harmonic unless harmonic current components also exist [Maa88, Fab95]. The ideal charge-voltage of the diode junction is, eq. (2.2):

$$Q(V_j) = -2C_{j0}V_{bi}\left(1 - \frac{V_j}{V_{bi}}\right)^{1/2} \tag{5.24}$$

and the voltage can be expressed as:

$$V_j = V_{bi}\left(\frac{(2C_{j0}V_{bi})^2 - Q^2}{(2C_{j0}V_{bi})^2}\right). \tag{5.25}$$

If the diode is open-circuited at all unwanted harmonics, there will not be voltage component across the junction at any harmonic above the second one. In order to get an output at the third harmonic, it is necessary to have current at the second harmonic. This can be done by imposing reactive terminations (to avoid power loss in the external circuit at unwanted harmonics) at the second harmonic, and, then, the third harmonic arises as a result of mixing the fundamental and second harmonic components, see [Maa88]. Real diodes deviate from the ideal model and allow higher order harmonics without idlers. However, theory and experiments have shown that the use of idlers improves the output power and the efficiency of the frequency multipliers [Maa88, Fab95].

[3] From eq. (5.1), $P_1 + P_2 = 0$. $P_1 > 0 \rightarrow P_2 < 0$. According to eq. (5.21), $P_2 = 2|I_2|^2 R_2 < 0 \rightarrow R_2 < 0$.

5.1.2 Simulation of Schottky based frequency multipliers

The Harmonic Balance (HB) technique is a widely used method to analyse nonlinear circuits like power amplifiers, frequency multipliers or mixers. In this technique, the circuit is divided into a linear part that is analysed in the frequency domain and a nonlinear part corresponding to the device, that is analysed in the time domain [Ker75, Maa93]. A description of the piecewise HB technique used in this thesis can be found in [Gis89, Fue98].

MC, DD, and LEC diode models have been coupled to the harmonic-balance circuit analysis technique (denoted by MCHB, DDHB, and LECHB, respectively) to analyse the performance of multiplier circuits. Since the Monte Carlo technique provides the most accurate description of the electron dynamics at high frequencies and high electric fields, the predictions of the MCHB are considered as a reference. A drift-diffusion model that imposes a constant low field mobility independently of the electric field but dependent on the doping concentration (denoted by DD_0 model) will be also considered. DD_0HB will provide the upper limit of the circuit efficiency since it neglects velocity saturation. LEC models based on a constant series resistance (denoted by $LEC_{R_s}HB$) and a time varying resistance ($LEC_{R_s(t)}HB$) due to time varying space charge region are considered. Among the first ones, LEC models based on the dc series resistance ($LEC_{R_{s,dc}}HB$) and R_s from the R_sx$C_j(0)$ rule ($LEC_{R_{s,R_s\text{x}C_j(0)}}HB$) are used in the following sections, see section 2.2.1.

The data of the *JPL* multipliers analysed in this chapter are compiled in Table 5.1. These circuits are representative examples of the state of the art of Schottky based THz multipliers. The values of the epilayer doping, zero-voltage junction capacitance and available input power provided in the literature for *JPL* circuits are employed in the simulations, see Table 5.1. However, because of the lack of information, unknown characteristics like the epilayer length and bias voltage have been optimized to obtain the maximum efficiency [Sil10]. In some cases, the anode areas employed in the numerical simulations have been slightly modified with respect to the nominal values provided in the literature so that the measured and simulated capacitances coincide. To determine the characteristics of the substrate of the diodes used in the simulations, measurements of the series resistance $R_{s,dc}$ (see chapter 2) are required. However, due to the lack of this information, the substrates of the diodes were selected to obtain efficiencies with MCHB similar to measurements at the available input power[4], leading to the $R_{s,dc}$ shown in Table 5.1 (substrate doping of $2\text{x}10^{18}$ cm^{-3} has been assumed in simulations). These values of $R_{s,dc}$ are close to those presented by *JPL* in [Mai02].

In the design of the multipliers presented in Table 5.1, *JPL* uses a lumped equivalent circuit to model the nonlinear Schottky diode and a 3-D electromagnetic field solver to take into account the three dimensional topology of the full diode structure [Eri98, Sch01a, Mae05b, Mae10b]. This modelling technique has led to simulation results in good agreement with measured results up to THz frequencies [Mai03, Cha02, Cha04, Mae05b, Mae10a, Mae12]. The R_sx$C_j(0)$ rule [Eri98] has been used in some of these designs [Mae05b], so, this magnitude is presented in Table 5.1 for the diodes considered, calculated with $R_{s,dc}$ and $C_j(0)$ from dc simulations.

In the circuit simulations, diodes are always matched at the fundamental frequency. On the other hand, the load impedance at the output frequency is optimized for maximum conversion efficiency at the available input power. However, in real circuits, coupling the input power to the diodes and the output power to the circuit presents limitations [Hes98, Mae05b, Mae10a]. Thus, to account for these losses in our simulations, the efficiencies predicted for the diodes η_d must be modified by the coupling efficiencies of the input and output circuits to obtain the flange-to-flange efficiency of the circuit η_c [Fab85, Tan12]:

$$\eta_c = \frac{P_{out}}{P_{in}} = \frac{\beta P_{d,out}}{P_{d,in}/\alpha} = \alpha\beta\frac{P_{d,out}}{P_{d,in}} = \alpha\beta\eta_d \tag{5.26}$$

where P_{in} is the input power delivered to the circuit, P_{out} is the output power delivered to the external load, $P_{d,in}$ is the input power delivered to the diodes, $P_{d,out}$ is the output power delivered by the

[4]The substrate doping concentrations were fixed to $2\text{x}10^{18}$ cm^{-3} in simulations and the substrate lengths were selected to verify the indicated condition.

Table 5.1: Schottky diode structures used in *JPL* multipliers and data considered in our simulations.

Stage	Data from literature, (*JPL*)							Numerical simulations (data per anode)										
	f_{out}, (GHz)	$P_{in,tot}$, (mW)	N_e, (cm^{-3})	L_e, (nm)	Area, (μm^2)	$C_j(0)$, (fF)	η_c, (%)	V_{bias},[a] (V)	N_e, (cm^{-3})	L_e, (nm)	L_s, (μm)	V_{BD}, (V)	Area, (μm^2)	$C_j(0)$, (fF)	$R_{s,dc}$[b] (Ω)	$R_{s,dc}$x$C_j(0)$,[c] (Ω.fF)	Z[$2f_0$][g] (Ω)	Z[$3f_0$][g] (Ω)
0.2 THz doubler, 6 anodes [Mai03]	194	150	1x10^{17}	–	36	–	26.0	-6	1x10^{17}	350	13.5	-12.8	36	35.8	7.2	257.8	23+55j	0+0j
0.2 THz doubler, 6 anodes [Cha04]	190	100	2x10^{17}	–	37.8	58	34.0	-4	2x10^{17}	350	5.5	-10.1	37.8	52.5	3.05[e]	160.12	12+30j	0+0j
0.4 THz doubler, 4 anodes [Mai03]	375	40	2x10^{17}	–	6.5	10.4	18.3	-4	2x10^{17}	200	6	-9.3	6.75	10.4	16.2	168.5	34+89j	0+0j
0.8 THz doubler, 2 anodes [Cha02]	775	8	4x10^{17}	–	1.1	2.7	13.5	-2.5	4x10^{17}	200	2.6	-8.4	1.38	2.7	36.0	97.2	91+152j	0+0j
1.5 THz doubler, 2 anodes [Cha04]	1510	0.4	5x10^{17}	200	0.16	0.5	4.5	-3	5x10^{17}	200	0.67	-7.1	0.23	0.5	89.3	44.6	158+475j	0+0j
0.3 THz tripler, 12 anodes[f] [Mae05a, Mae06, Mae08]	286.2	50-250	2x10^{17}	–	–	16	14.1	-2.33	2x10^{17}	200	5.8	-9.3	11.6	16.13	9.17[e]	147.91	0+25j	25.0+50j
0.6 THz tripler, 4 anodes [Mae05b]	600	24	1x10^{17}	500	6	6	4.5-9	-2.25	1x10^{17}	500	7	-13.5	6	6.4	32.3	206.7	0+105j	49+69j
0.9 THz tripler, 8 anodes[h] [Mae10a]	900	45	5x10^{17}	–	1.2	4	2.4	-0.5[e]	5x10^{17}	200	4	-7.1	1.85	4.02	35.9	144.3	0+85j	51+47j
1.2 THz tripler, 2 anodes [Mae01, Bru01, Mai02, Mai03]	1200	7	5x10^{17}	–	0.76[i]	–	1.9	-0.5[i]	5x10^{17}	200	3.4	-7.1	0.76	1.65	76.6	125.9	0+150j	95+85j
1.8 THz tripler, 2 anodes [Mae05c]	1640	2	5x10^{17}	–	0.4	–	1	-0.5	5x10^{17}	100	2.5	-7.1	0.4	0.87	104.2	90.6	0+185j	120+122j
2.7 THz tripler, 2 anodes [Mae12]	2580	1	–	–	0.15	–	1.5	0	5x10^{17}	100	0.5	-7.1	0.15	0.32	94	30.1	0+450j	181+257j

[a] Bias point is not provided in the literature. It has been optimized to obtain maximum efficiency.
[b] Calculated with the DD model under dc conditions (MC predicts similar $R_{s,dc}$).
[c] Obtained with $R_{s,dc}$ and $C_j(0)$ from DD simulations under dc conditions.
[d] An ideal barrier height of ϕ_b= 0.99 V is assumed except for the 0.6 THz tripler where ϕ_b= 0.85 V [Mae05b].
[e] Data given in the papers [Mae05a] for the 0.3 THz tripler and in [Mae10a] for the 0.9 THz tripler.
[f] 6 anodes per chip, 2 chips in a power combined scheme.
[g] Optimized with DDHB for doublers and with DD_0HB for triplers.
[h] 4 anodes per chip, 2 chips in a power combined scheme.
[i] The anode area presented in [Mai02] has been considered. Different anode areas are provided in [Mae01, Bru01]. Bias close to zero are indicated in references. The best efficiency in [Mai03] is shown in the table.

diodes to the output. α represents the coupling factor of the input power and β the coupling factor of the output power. α= 0.8 and β= 0.875 ($\alpha\beta$= 0.7) have been assumed to relate η_c and η_d for the multipliers in this section. These values are in accordance with published data [Fab85, Mae05b, Mae10a].

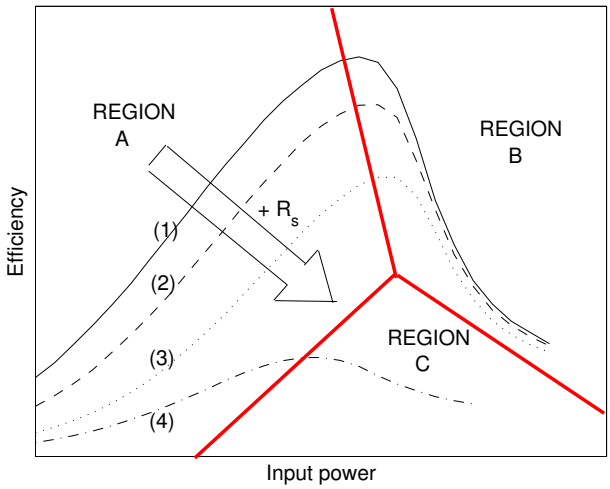

Figure 5.4: Efficiency of frequency multipliers. Regions of operation. The series resistance of curves (1) to (4) evaluated in region A are 3 Ω, 4 Ω, 6 Ω and 8 Ω, respectively.

Fig. 5.4 presents a schematic efficiency-versus-power diagram for frequency multipliers. Three different regimes of operation can be identified. Region A represents a low power regime, where circuit performance is dominated by the series resistance. In Region B the efficiency is limited by forward or reverse conduction if this regime is reached. In region C, velocity saturation limits the efficiency of the multipliers before entering region B. The arrow in the figure means that if the device geometry and doping change and these changes produce an increase in the series resistance of the diode, there is a decrease in the efficiency.

5.1.3 Optimization of the load impedances

An essential requirement to maximize the efficiency of multipliers is the correct selection of the impedances of the external circuit at each harmonic of the fundamental frequency f_0. The circuit impedance Z_c at the fundamental frequency has to match the diode input impedance to deliver maximum power to the diode. This is done automatically in our harmonic-balance simulator for each diode model selected. Regarding the impedance at the harmonics of f_0 (nf_0 with $n > 1$), they must be selected to maximize the output power or the conversion efficiency at the desired harmonic of f_0.

This section presents an analysis of the optimal circuit impedance at the output frequency obtained with different physics-based diode models. Fig. 5.5 shows the normalized diode efficiency (normalized by the maximum efficiency in the impedance range) obtained with DDHB, DD_0HB and MCHB as a function of the load impedance for the 400 GHz doubler, the 1500 GHz doubler, the 600 GHz tripler and the 2.7 THz tripler described in Table 5.1. For each multiplier, the analysis is carried out at the available input power indicated in the table. The impedance presented are given per anode. The impedance at the input frequency is conjugately matched in each simulation.

For the 400 GHz doubler, the optimum circuit impedance at the output frequency obtained with the different models (MC, DD and DD_0) is very similar, although the agreement between MC and DD_0 is better than between MC and DD, due to the overestimation of the series resistance of the DD model, see section 3.1.1. Because of this limitation of the DD model, the voltage drop in the series resistance of the diode is higher than with MC or DD_0 models, resulting in a lower modulation of

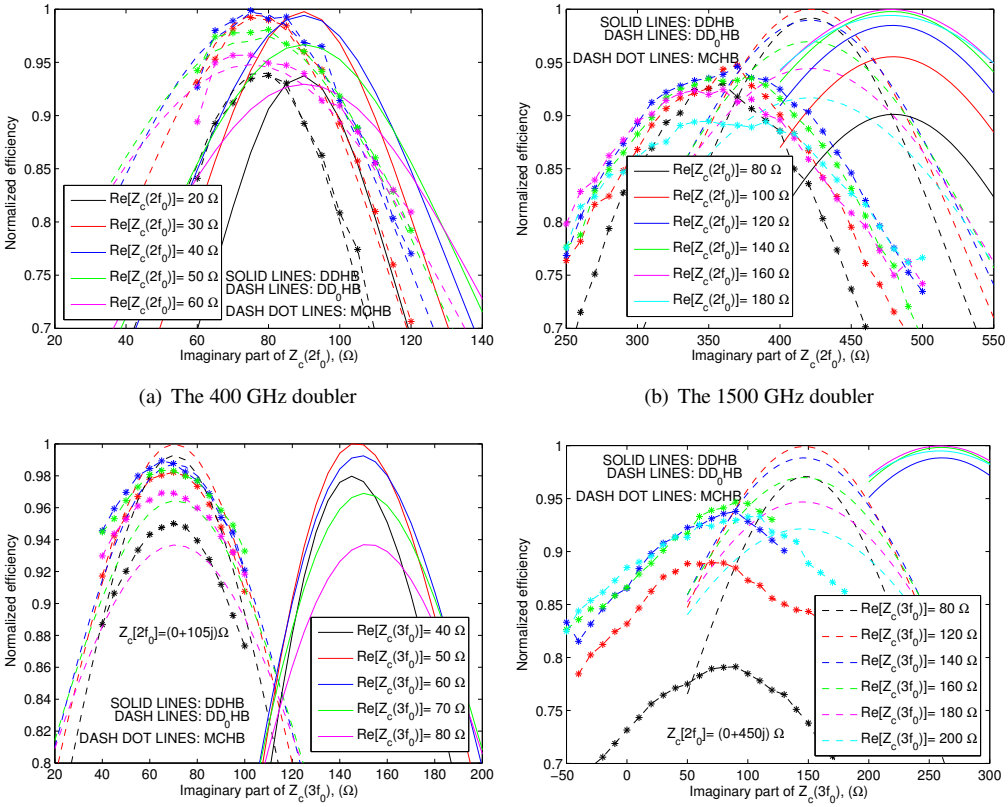

(a) The 400 GHz doubler

(b) The 1500 GHz doubler

(c) The 600 GHz tripler

(d) The 2.7 THz tripler

Figure 5.5: Normalized diode efficiency of (a) the 400 GHz and (b) the 1500 GHz doublers and (c) the 600 GHz and (d) the 2.7 THz triplers described in Table 5.1 [Mai03, Cha04, Mae05b, Mae12] as a function of circuit impedance per anode at the output frequency, evaluated with different models. For each multiplier, the available input power indicated in the table has been considered. The impedance at the second harmonic for the triplers has been optimized with DDHB.

the nonlinear capacitance at a given input power. Since the imaginary part of the diode impedance $\mathrm{Im}[Z_d(nf_0)]$ is inversely proportional to the capacitance, the optimum $\mathrm{Im}[Z_c(2f_0)]$ obtained with DD is higher than the values obtained with MC and DD_0, as is observed in Fig. 5.5(a). For the 1.5 THz doubler Fig. 5.5(b), the agreement between MC and DD_0 disappears: the optimum $\mathrm{Re}[Z_c(2f_0)]$ is higher with MC due to velocity saturation effects, that increase the series resistance of the diode. On the other hand, the optimum $\mathrm{Im}[Z_c(2f_0)]$ is lower with MC due to carrier inertia effects, that are important at this frequency. To evaluate the impact of carrier inertia in the results for the 1.5 THz doubler, it has been analysed in Fig. 5.6 using $\mathrm{LEC}_{R_s(t)}$HB and $\mathrm{LEC}_{R_sLC(t)}$HB. The results with $\mathrm{LEC}_{R_s(t)}$HB are similar to those ones with DD_0HB. The imaginary part of the optimum $Z_c(2f_0)$ with $\mathrm{LEC}_{R_sLC(t)}$HB is in good agreement with MCHB. This indicates that carrier inertia is the origin of the discrepancy between the imaginary part of the optimum $Z_c(2f_0)$ obtained with MCHB and DD_0HB.

For the 600 GHz tripler, Fig. 5.5(c), a good agreement is observed between the optimum $Z_c(3f_0)$ obtained with MC and DD_0. For the 2.7 THz tripler, velocity saturation and carrier inertia effects (see next section and appendix D) lead to important differences between $Z_c(3f_0)$ evaluated with MC and DD_0, as was explained for the 1.5 THz doubler. The most important differences between DD_0 and DD are in the $\mathrm{Im}[Z_c(3f_0)]$, originated by the overestimation of the series resistance as was explained for the doublers.

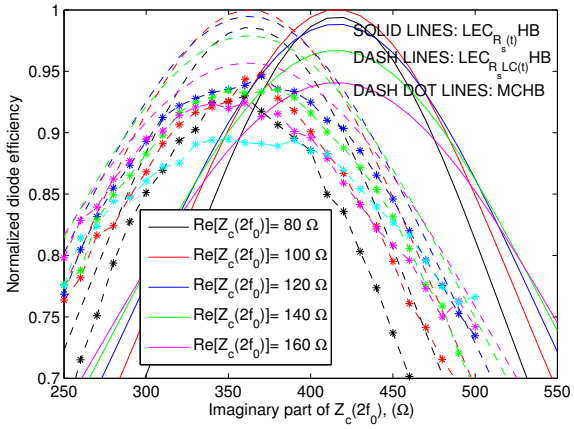

Figure 5.6: Normalized diode efficiency of the 1500 GHz doubler described in Table 5.1 [Cha04] as a function of the circuit impedance per anode at the output frequency, evaluated with MC and LECs models.

As a conclusion of this analysis, DD_0HB could be used to optimize the circuit impedance of the multipliers while velocity saturation and carrier inertia are not important in the performance of the diodes (usually at frequencies lower than 800 GHz, for diodes with high epilayer doping to avoid velocity saturation effects, see chapter 3 and section 5.2). DDHB predicts optimum $\mathrm{Im}[Z_c]$ higher than expected because DD overestimates the series resistance of the diode. In the multipliers simulated in the next section, the load impedances have been optimized with DDHB for the doublers and with DD_0HB for the triplers, to avoid the high computational cost of MCHB in this task. Although the circuit impedances obtained with these models are not optimum, they are acceptable, due to the moderate sensitivity of the efficiency to the variation of the load impedance.

5.2 Frequency multipliers performance evaluated with different models

This section presents a comparison between measurements of multipliers designed and fabricated by *JPL* in the frequency range 200-2700 GHz and simulation results obtained with different diode models.

5.2.1 Doublers up to 1.5 THz

Among the frequency doublers described in Table 5.1, the 200 GHz doubler in [Cha04] (second row of Table 5.1), the 400 GHz [Mai03], the 800 GHz [Cha02] and the 1500 GHz [Cha04] doublers have been selected as representative circuits to compare the predictions of the different models and measurements. Fig. 5.7 shows the diode efficiency obtained from simulations of the selected *JPL* doublers, as a function of the input power delivered to the diode $P_{d,in}$ eq. (5.26). The most relevant results from the analysis of Fig. 5.7 are summarized in the following items:

1. For the 200 and 400 GHz doublers, a good agreement is observed between MCHB and DD_0HB since there is no velocity saturation and DD_0HB does not overestimate the series resistance of the diodes, see section 3.1.1. For the 200 GHz doubler, a good agreement is observed between DD_0HB and LEC$_{R_s(t)}$HB. LEC model based on the constant $R_{s,dc}$ overestimates the series resistance of the diode and predicts lower efficiencies than MCHB for this doubler. For the 400 GHz doubler, physics-based models show that the depletion region reaches the substrate degrading the nonlinear capacitance of the junction, so, the predictions of LECHB are not

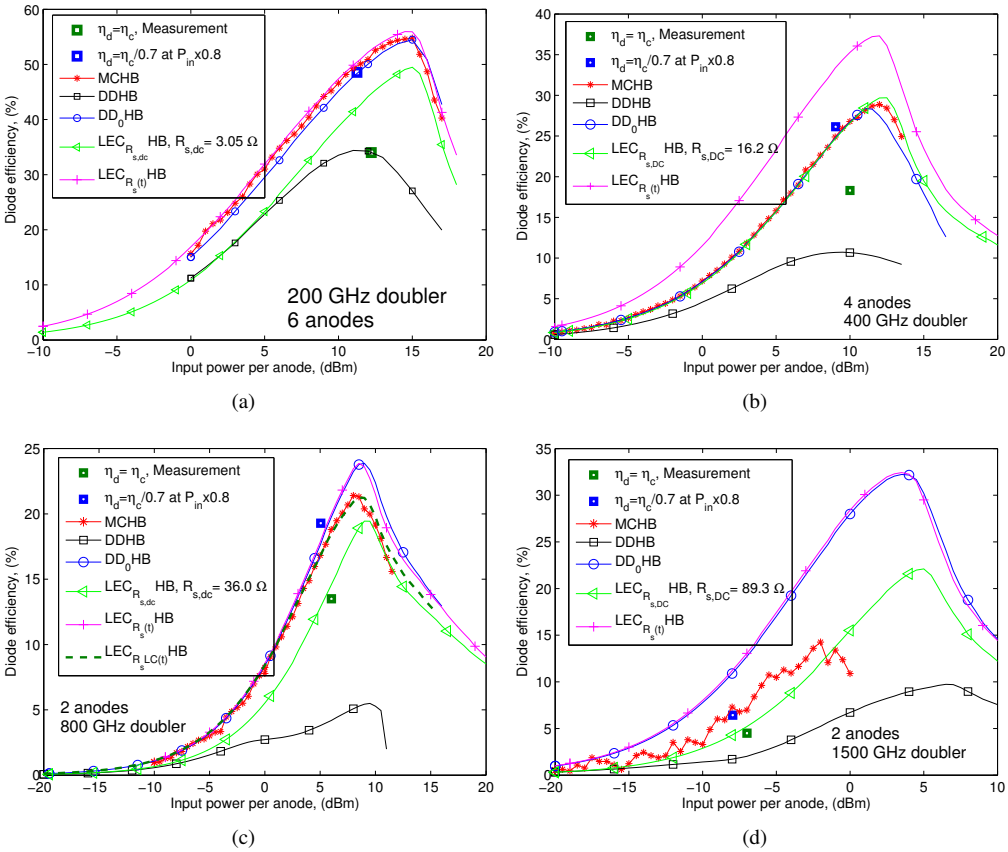

Figure 5.7: Diode efficiency of doublers described in Table 5.1 [Cha04, Mai03, Cha02] as a function of the input power delivered to the diode $P_{d,in}$ eq. (5.26), simulated with LECHB, DD_0HB, DDHB and MCHB tools.

reliable, since they are based on the simple Schottky junction model[5]. A more sophisticated LEC model that takes into account the time variation of the series resistance $R_s(t)$ and the degradation of the nonlinear capacitance when the depletion region reaches de substrate will work correctly until velocity saturation becomes important. The efficiency of these doublers decreases at input powers higher than 15 and 12 dBm, respectively, due to the onset of the varistor operation mode.

2. For the 800 GHz doubler, the agreement between MCHB and DD_0HB disappears at input powers higher than 5 dBm. This discrepancy is due to carrier inertia effects, that are important at this frequency (the epilayer plasma frequency is f_{pe}= 6.1 THz, eq. (3.8)). Carrier inertia effects can be described by a nonlinear inductance (it is nonlinear due to the time variation of the width of the depletion region) in series with the series resistance of the undepleted epilayer, see section 3.1.3. These effects are analysed in more detail in Fig. 5.8 for the 1500 GHz doubler.

3. For the 1500 GHz doubler, velocity saturation limits the efficiency of the device (region C in Fig. 5.4), so, the efficiency from MCHB becomes lower than that from DD_0HB simulations as the input power increases. This device has higher epilayer doping to mitigate velocity saturation effects. A good agreement is observed between DD_0HB and $LEC_{R_s(t)}HB$.

[5] $LEC_{R_{s,dc}}HB$ is in good agreement with MCHB for the 400 GHz doubler, because the overestimation of the series resistance described for the 200 GHz doubler is compensated by the degradation of the nonlinear capacitance when the depletion region reaches the substrate, that is not taken into account in this model.

4. DD model overestimates the series resistance of the diodes due to the local evaluation of the electron mobility in the transition between the neutral and the depleted regions of the epilayer, see section 3.1.1. Therefore, according to the performance of region A in Fig. 5.4, DDHB presents a conservative approach for the efficiency compared with measurements and MCHB.

5. As the input frequency increases, the available input power decreases, see Table 5.1, limiting the voltage swing at the nonlinear capacitance of the diode. The anode area must be made smaller in order to avoid this limitation[6]. Fig. 5.7(d) shows that the anode area of the diodes in the 1.5 THz doubler is not optimum (too large), since it is working far from the maximum of efficiency.

A physical analysis of the limitations in the performance of these doublers is presented in appendix D.

In Fig. 5.8 the 1500 GHz doubler is analysed with different LEC models. The performance of this doubler is limited by velocity saturation. Besides the models used in Fig. 5.7(d), a LEC model based on the constant average series resistance of the diode (denoted by LEC$_{<R_s>}$HB, where the average resistance has been evaluated from the simulations with LEC$_{R_s(t)}$HB) and the predictions of the R_sx$C_j(0)$ rule are also included. Also, a LEC model that takes into account the displacement current and carrier inertia in the undepleted epilayer and the substrate by means of a capacitance and an inductance (see section 2.2.1) has been considered in Fig. 5.8 (denoted by LEC$_{R_sLC(t)}$HB). The efficiency obtained with LEC$_{<R_s>}$HB is similar to that obtained assuming $R_s(t)$ in the LEC model. The results obtained with LEC$_{R_sLC(t)}$HB show that carrier inertia is important in the performance of this doubler at input powers higher than -5 dBm. On the other hand, the R_sx$C_j(0)$= 120 Ω·fF rule (LEC$_{R_{s,120}}$HB), see section 2.2.1, leads to simulated efficiencies lower than measurements and lower than the predictions of MCHB. Fig. 5.8 shows that R_sx$C_j(0)$= 40 Ω·fF (LEC$_{R_{s,40}}$HB) is necessary to reproduce measured efficiencies. The R_sx$C_j(0)$ rule was developed for doping 1x10^{17} cm^{-3} and output frequencies lower than 3 THz [Eri98, Mae10b] while the doping of this doubler is 5x10^{17} cm^{-3}. The extension of the rule for higher doping and frequencies requires the knowledge of the performance of the diode at such conditions, that can be provided by simulation tools like MC.

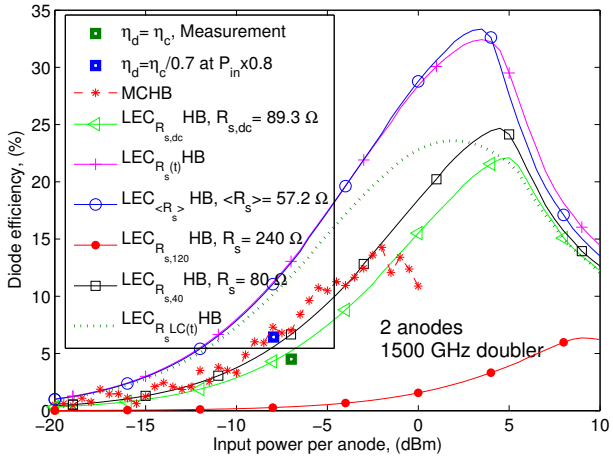

Figure 5.8: Diode efficiency of the 1500 GHz doubler described in Table 5.1 as a function of the input power delivered to the diode $P_{d,in}$ eq. (5.26), simulated with MCHB and different LECHB.

[6]The maximum efficiency can be located at the desired input power by scaling the anode area [Gra00].

5.2.2 Triplers up to 2.7 THz

Fig. 5.9 shows the diode efficiency obtained for the 300 GHz, the 600 GHz, the 900 GHz and the 2.7 THz triplers presented in [Mae08, Mae05b, Mae10a, Mae12], see Table 5.1. Unlike the doublers analyzed in the previous section, a complete set of parameters is provided for the 600 GHz tripler in [Mae05b]. The 300 GHz, the 900 GHz and the 2.7 THz triplers are the three stages of the Schottky based multiplier source in the 2.48 to 2.75 THz band presented in [Mae12], that delivers a record output power of 18 μW at 2.58 THz at room temperature when driven by 350-450 mW in W-band.

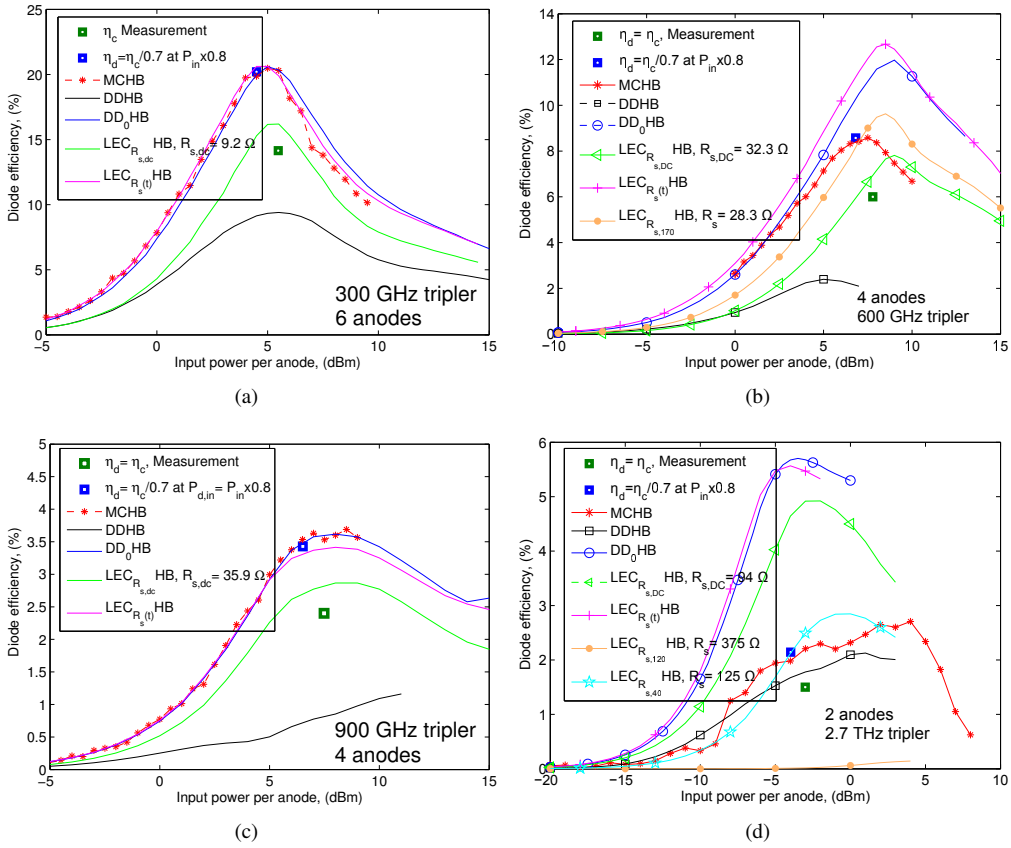

Figure 5.9: Diode efficiency of the (a) 300 GHz, (b) 600 GHz, (c) 900 GHz and (d) 2.7 THz triplers presented in [Mae08, Mae05b, Mae10a, Mae12], Table 5.1, as a function of the input power delivered to one diode $P_{d,in}$ (5.26), simulated with LECHB, DD$_0$HB, DDHB and MCHB tools.

The following conclusions are extracted from the analysis of Fig. 5.9:

1. For the 300 GHz and the 900 GHz triplers, with epilayer doping N$_e$= 2x10^{17} cm^{-3} and 5x10^{17} cm^{-3}, respectively, a good agreement is observed between MCHB and DD$_0$HB since velocity saturation is not affecting the performance of these triplers. Theirs efficiencies decrease at input powers higher than 5 and 8 dBm, respectively, due the initiation of the varistor operation mode.

2. Velocity saturation limits the efficiency of the 600 GHz and 2.7 THz triplers. MCHB shows that there are high electric fields in the undepleted epilayer of the diodes at $P_{d,in}$ higher than 5 dBm and -15 dBm for the 600 GHz and the 2.7 THz triplers respectively, see appendix D, leading to discrepancies between DD$_0$HB and MCHB. Unlike the 900 GHz tripler or the 400

GHz doubler described in section 5.2, velocity saturation is important for the 600 GHz tripler since its epilayer doping is only 1x10^{17} cm^{-3}, see Table 5.1.

3. Neither LEC$_{R_{s,dc}}$HB nor LEC$_{R_s(t)}$HB lead to correct efficiency estimates for the 600 GHz and the 2.7 THz triplers, since they do not model velocity saturation effects. For the 600 GHz tripler, Erickson's rule [Eri98] establishes R_sx$C_j(0)$= 170 Ω·fF (see Fig. 2.6), that leads to a good agreement with measurements (LEC$_{R_{s,170}}$HB in Fig. 5.9). For the 2.7 THz tripler, R_sx$C_j(0)$= 120 Ω·fF developed for doping concentration of 1x10^{17} cm^{-3} is suggested by Erickson [Eri98], but R_sx$C_j(0)$= 40 Ω·fF is necessary to obtain efficiencies close to measurements (epilayer doping of the 2.7 THz tripler is 5x10^{17} cm^{-3}).

4. A good agreement is observed between LEC$_{R_s(t)}$HB and DD$_0$HB for all these triplers since theirs depletion regions are not reaching the substrate.

5. As was indicated for the doublers, DDHB underestimates the efficiency of the 300 GHz, 600 GHz and 900 GHz triplers. However, a good agreement is observed between DDHB and MCHB simulators for the 2.7 THz tripler, since the effect of velocity saturation is more important for this tripler than the overestimation of the series resistance in DD simulations, see section 3.1.1.

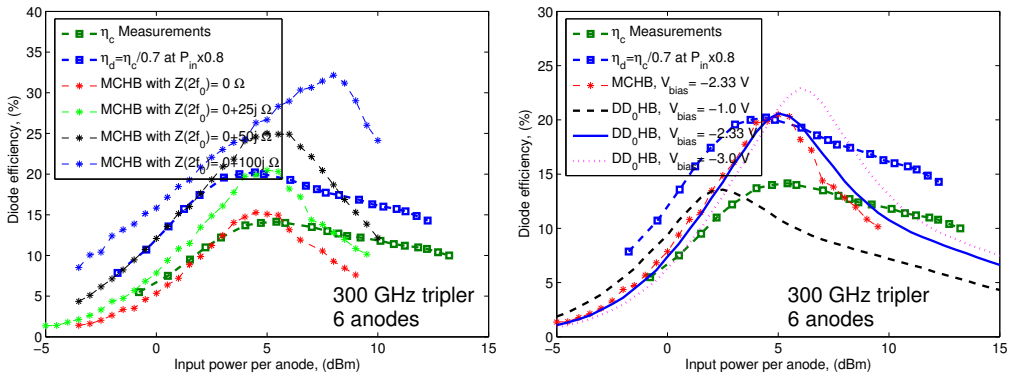

(a) (b)

Figure 5.10: Diode efficiency of the 300 GHz tripler in [Mae08] (see Table 5.1) as a function of the input power per anode $P_{d,in}$ eq. (5.26), (a) simulated with MCHB and different $Z_c[2f_0]$ and (b) simulated with DD$_0$HB and MCHB tools, $Z_c[2f_0]$= (0+25j) Ω and different bias voltages.

For the 300 GHz tripler, there are published measurements of the efficiency as a function of the input power at 292.2 GHz [Mae08]. Because of the lack of information about the load impedances, an analysis of the impact of the load impedances at the second harmonic of the fundamental frequency $Z_c[2f_0]$ has been carried out in Fig. 5.10(a) using MCHB, while $Z_c[3f_0]$ was fixed to (25+50j) Ω to optimize the efficiency (optimized with DD$_0$HB) at the input power of maximum measured efficiency. The analysis shows an important enhancement of the efficiency by optimizing $Z_c[2f_0]$. Measurements in [Mae08] were carried out optimizing the bias point for each applied input power, while in simulations in Fig. 5.10 with MCHB approach it was fixed to -2.33 V, see Table 5.1. Hence, in Fig. 5.10(b), $Z[2f_0]$= (0+25j) Ω was selected and simulations with different bias point are presented (these simulations at different bias were performed with DD$_0$HB due to its good agreement with MCHB, Fig. 5.9(a)). Results in Fig. 5.10(b) show that measurements can be reproduced by fitting the bias point at each input power, according to [Mae08].

5.2.3 Results of the simulation of the state-of-the-art *JPL* multipliers

To conclude the analysis of the limitations of the different diode models, Fig. 5.11 shows a comparison of the state-of-the-art efficiency from measured GaAs Schottky multipliers [Mai03, Cha02, Cha04, Mae05b, Mae05c, Mae08, Mae10a, Mae12], Table 5.1, with simulation results obtained using different diode models. The efficiencies have been evaluated at the input power delivered to the circuit indicated in the third column of Table 5.1. According to the discussion about coupling efficiency, a factor $\alpha\beta \sim 0.7$ (see eq. (5.26)) has been assumed to calculate the circuit efficiency from the simulated diode efficiency. An empirical relation published in [War04] for the efficiency of doublers as a function of the output frequency has been included in Fig. 5.11. This relation, obtained by fitting measured flange-to-flange (or circuit) efficiencies of planar *JPL* doublers, is of the form $\eta(f) = \eta_0 \exp(-f/f_0)$ (at 295 K, η_0= 0.45 and f_0= 600 GHz). A similar relation is not observed for measured efficiencies of triplers, see 5.11(b). However, optimizing the parameters of the triplers with MCHB to maximize the efficiency, see Table 5.2, the same $\eta(f)$ dependence can be proposed for triplers, using η_0= 0.18 and f_0= 950 GHz, see Fig. 5.11(b). Table 5.2 shows the results of the optimization of the 900 GHz, the 1200 GHz and the 1800 GHz triplers described in Table 5.1. The bias points have been decreased (higher in absolute value) in order to increase the swept of the nonlinear capacitance of the diodes without entering into breakdown regime. The anode areas of the optimized diodes have been decreased to shift the maximum of efficiency at the available input power [Gra00] (the available input powers in the table are those provided in the literature, see Table 5.1). Also the epilayer length of the 1800 GHz tripler has been increased up to 200 nm for the optimized bias of -3 V. The optimum anode area of the 1800 GHz tripler is similar to that of the 2.7 THz tripler [Mae12] (anode area of 0.15 μm^2), but the available input power per anode of the 2.7 THz tripler is 0.5 mW and V_{bias} is 0 V. The dependence of the output power on the output frequency is shown in Fig. 5.12.

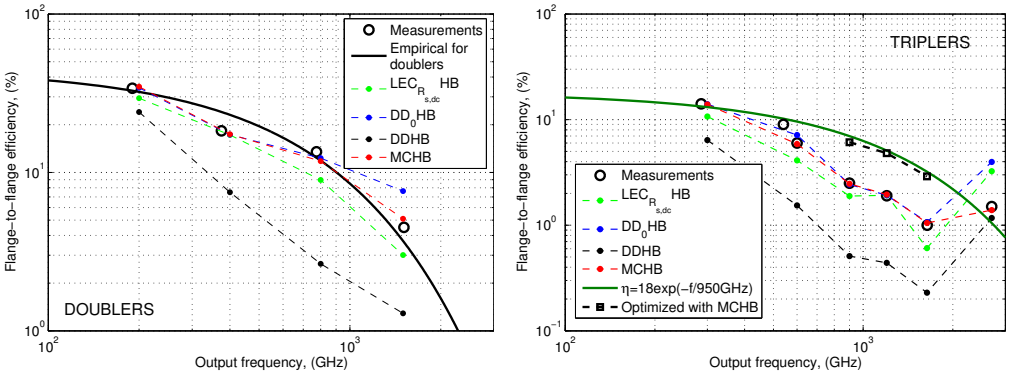

(a) (b)

Figure 5.11: Efficiency of the doublers and triplers [Mai03, Cha02, Cha04, Mae05b, Mae05c, Mae08, Mae10a, Mae12] in Table 5.1 as a function of the output frequency, evaluated at the input power delivered to the circuit, the third column of Table 5.1. A factor $\alpha\beta \sim 0.7$ has been assumed to account for coupling losses and transform the simulated diode efficiencies to circuit efficiencies or flange-to-flange efficiencies.

The most important conclusions from the analysis of doubler and triplers in the previous sections are summarized in Figs. 5.11 and 5.12: DD$_0$HB shows a good agreement with MCHB until velocity saturation is relevant in the performance of the diode, as happens in the 1500 GHz doubler, the 600 GHz tripler and the 2.7 THz tripler, see Fig. 5.11. The LEC model based on the dc series resistance $R_{s,dc}$ underestimates the efficiency of the multipliers which are not limited by velocity saturation. Section 5.2.1 shown the limitations of the LEC models and the modifications that improve its performance: a time varying resistance R_s(t) and the degradation of the nonlinear capacitance when the depletion region reaches the substrate. These simple improvements make LEC performance very

Table 5.2: Results from the optimization with MCHB of some triplers presented in Table 5.1.

Stage	f_{out}, (GHz)	$P_{in,tot}$, (mW)	V_{bias} (V)	Effi.;[a] (%)	N_e;[c] (cm^{-3})	L_e, (nm)	Area, (μm^2)	$C_j(0)$, (fF)	$R_{s,dc}$, (Ω)	Z[$2f_0$], (Ω)	Z[$3f_0$], (Ω)
0.9 THz tripler, 8 anodes[b][Mae10a]	900	45	-3	6.1	5x10^{17}	200	0.83	1.8	80	240j	120+157j
1.2 THz tripler, 2 anodes [Mae01, Mai03]	1200	7	-3	4.8	5x10^{17}	200	0.27	0.59	215	640j	314+366j
1.8 THz tripler, 2 anodes [Mae05c]	1640	2	-3	2.9	5x10^{17}	200	0.13	0.28	351	800j	413+565j

[a] Flange-to-flange efficiency evaluated with MCHB, assuming $\alpha\beta = 0.7$.
[b] 4 anodes per chip, 2 chips in a power combined scheme.
[c] Breakdown voltage of -7 V.

similar to DD_0 performance. However, none of them takes into account velocity saturation and they fail when this phenomenon is limiting the performance of the diode. Velocity saturation effects can be included in the LEC model by setting an adequate series resistance in the model (e.g., the R_s provided by the R_sx$C_j(0)$ rule).

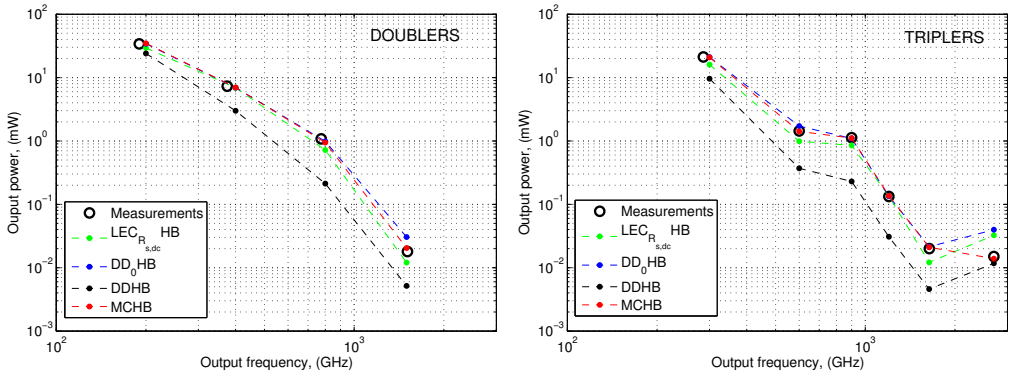

(a) (b)

Figure 5.12: Output power of the doublers and triplers [Mai03, Cha02, Cha04, Mae05b, Mae05c, Mae08, Mae10a, Mae12] in Table 5.1 as a function of the output frequency, evaluated at the input power delivered to the circuit, the third column of Table 5.1. A factor $\alpha\beta \sim 0.7$ has been assumed to account for coupling losses and transform the simulated diode efficiencies to circuit efficiencies or flange-to-flange efficiencies.

On the other hand, although in DD models velocity saturation is taken into account, it overestimates the contribution to the series resistance of the diode from the region close to the depletion region since this model evaluates locally the electron mobility, see section 3.1.1. Therefore, DDHB underestimates the efficiency of the multipliers. Only when velocity saturation is the limiting effect as occurs in the 2.7 THz tripler, DDHB predicts the measured efficiency results.

Hydrodynamic models are foreseen as the appropriate models since they solve the limitations of the DD model and they have a computational cost lower than the MC model.

5.3 Frequency multipliers with Schottky diodes above 3 THz

Nowadays, Schottky based multipliers have reached the 2.48 - 2.75 THz band, with a record output power of 18 μW at 2.58 THz at room temperature with an input power around 1 mW for the last tripler stage [Mae12]. Table 5.3 shows a summary of published data on Schottky based multipliers operating at frequencies above 1 THz. This section presents an analysis of the performance of

multiplier circuits at output frequencies above 3 THz.

Three fundamental phenomena must be considered for the accurate simulation of Schottky diodes at these frequencies:

1. Velocity saturation, see section 3.1.2.
2. Plasma resonance of the epilayer and the substrate of the Schottky diode. This phenomenon leads to the fast increase of the real part of the diode impedance at input frequencies near to the plasma frequency. This phenomenon also affects to the imaginary part of the diode impedance, that becomes positive at frequencies close to the epilayer plasma frequency [Cha64, Kel79, Cro89], see section 3.1.4.
3. Nonstationary effects become important when the time-scale of the applied signal is lower than the energy and/or the momentum relaxation times τ_ε and τ_m respectively ($\tau_\varepsilon \simeq 3$ ps and $\tau_m \simeq 0.25$ ps for GaAs [Lee99]), see section 3.1.5.

For the doublers and triplers presented in this section, only MCHB gives reliable results because MC is the only model that takes into account correctly these phenomena.

Table 5.3: Main published data on Schottky based multipliers at room temperature operating at output frequencies higher than 0.9 THz.

Stage	N. of anodes	f_{out}, (GHz)	P_{in}, (mW)	P_{out}, (μW)	Effi., (%)	N_e, (cm^{-3})	L_e, (nm)	Area, (μm^2)	Year	Ref.
0.9 THz tripler	4	857	48	1200	2.5	5x10^{17}		1.2	2010	[Mae10a]
1.2 THz tripler	2	21130	8	70	0.9	5x10^{17}		0.4	2001	[Bru01, Mae01, Mai03]
1.5 THz doubler	2	1522	5.2[a]	55	~ 1	5x10^{17}	150		2001	[Eri01, Eri02]
1.5 THz doubler	2	1500	~ 0.4	~ 15	~ 4	5x10^{17}	200	0.16	2004	[Cha04]
1.8 THz tripler	2	1810	5	1.5	~ 0.03	5x10^{17}		0.32	2003	[Mae03, War03]
1.8 THz tripler	2	1740		3	0.2	5x10^{17}		0.32	2004	[Mae04]
1.8 THz tripler	2	1640		21		5x10^{17}		0.4	2005	[Mae05c]
1.8 THz tripler		1900		11				0.5	2010	[Cro10, Cro11]
2.7 THz tripler	2	2550	6-7.5[a]	0.1	0.002	5x10^{17}	100	0.76	2001	[Mai01b, Mai01a]
2.7 THz tripler	2	2580	~ 1	14-18	~ 1.5			0.15	2011	[Pea11, Mae11, Mae12]
2.7 THz tripler		2500		3					2011	[Cro11]

[a] Laser pump source.

As a reference in this section, one anode multipliers based on a Schottky diode like that described in Table 5.1 for the 2.7 THz tripler are considered: Epilayer doping 5x10^{17} cm^{-3}, epilayer length 100 nm and bias point 0 V. The anode area of the diodes has been fixed to 0.15 μm^2 and a nominal input power per anode has been considered like the diodes in the 2.7 THz tripler [Mae12] (0.5 mW per anode, see Table 5.1). The input power required to achieve maximum efficiency for a certain Schottky multiplier is proportional to the anode area of the diodes [Gra00]. Hence, the anode area can be modified to place the peak of efficiency at the available input power. A modification of the anode area also changes the impedances.

Fig. 5.13 presents a comparison of the optimum load impedance obtained with DD_0HB, DDHB and MCHB for a 3 THz and a 6 THz doublers based on the reference diode. As was described in section 5.1.3, the optimum imaginary part of the load impedance $\mathrm{Im}[Z_c(2f_0)]$ obtained with DDHB is larger than MCHB and DD_0HB. The optimum $\mathrm{Im}[Z_c(2f_0)]$ obtained with DD_0HB is higher than with MCHB, and this discrepancy is more important as the input frequency increases, due to the charge carrier inertia, that represents an inductive contribution. As the input frequency increases, the optimum $\mathrm{Re}[Z_c(2f_0)]$ obtained with MCHB becomes larger than with DD_0HB due plasma effects that increase the real part of the diode impedance. Results of Fig. 5.13 indicate that simulations based on MCHB are necessary to accurately determine the optimum load impedance. However,

due to the high computational cost of the load optimization process with MCHB, and the moderate sensitivity of the efficiency to the variation of the load impedance, DD_0HB has been used for the starting point of the optimization of the load impedance.

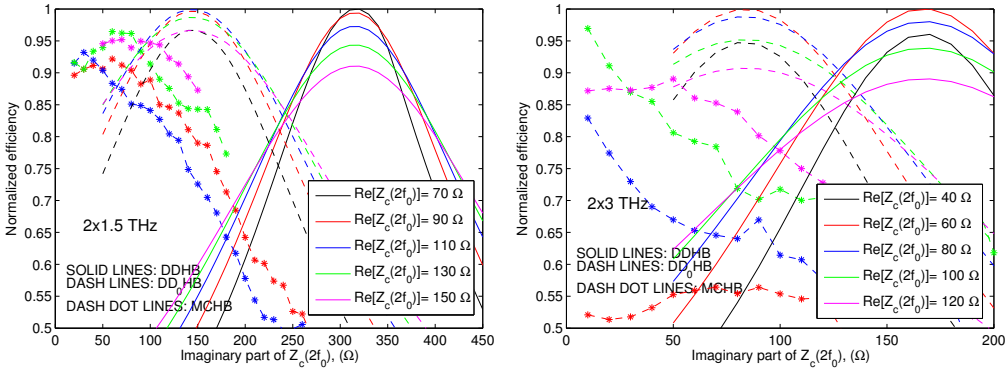

(a) (b)

Figure 5.13: Diode efficiency of (a) a 3 THz and (b) a 6 THz doublers based on the reference diode as a function of circuit impedance per anode, evaluated with different models, for an available input power of 0.5 mW.

5.3.1 Doublers above 3 THz

Fig. 5.14 presents the efficiencies and the circuit impedances obtained with MCHB. The load impedances at the output frequency used in the simulation of these doublers are shown in Table 5.4. At low input powers in Fig. 5.14(c), the real part of the impedance increases as the input frequency increases, due to plasma effects (plasma frequency for doping 5x10^{17} cm^{-3} is around 6.8 THz, eq. (3.8)). The imaginary part of the circuit impedance Im$[Z_c(f_0)]$ decreases -see Fig. 5.14(d)- because of the capacitive performance of the Schottky junction. Up to an input frequency of 3.3 THz, it follows the $1/\omega C$ performance with a constant capacitance. At higher frequencies, Im$[Z_c(f_0)]$ becomes negative due to the dominant contribution of the carrier inertia[7].

Table 5.4: Load impedances at $2f_0$ for the reference doublers above 3 THz obtained by maximizing the efficiency at the available input power 0.5 mW. Optimization carried out with DD_0HB tool.

Stage	$Z_c[2f_0]$, (Ω)
2x1.5 THz	101+144j
2x1.8 THz	85+125j
2x2.1 THz	75+112j
2x2.4 THz	69+100j
2x2.7 THz	66+91j
2x3.0 THz	63+83j
2x3.3 THz	62+77j
2x3.6 THz	61+72j
2x3.9 THz	60+67j
2x4.2 THz	59+63j

When increasing the input power, the electrons gain enough energy from the field to scatter into the upper valleys and this produces velocity saturation, leading to the abrupt increase of the real part

[7]Since Im$[Z_c(f_0)]$= -Im$[Z_d(f_0)]$, the imaginary part of the diode impedance $Z_d(f_0)$ is negative for lower frequencies and it increases according to -$1/\omega C$ when the frequency increases. But Im$[Z_d(f_0)]$ becomes positive when the carrier inertia becomes the dominant contribution to the imaginary part of the diode impedance, that occurs for the higher frequencies.

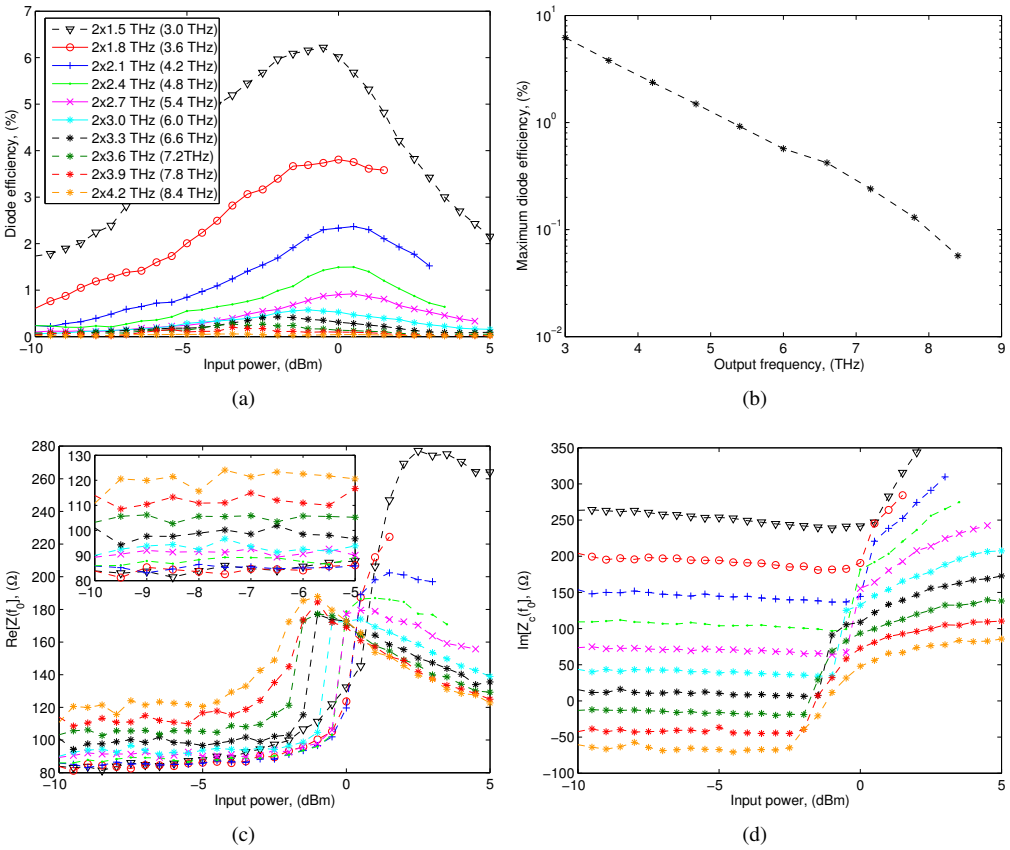

Figure 5.14: (a) Diode efficiency, (b) maximum efficiency in figure (a), (c) real part and (d) imaginary part of the circuit impedance at f_0 (conjugate of the diode impedance) as a function of the input power delivered to the diode for doublers based on the reference diode at different input frequencies, obtained with MCHB. The anode area is fixed to 0.15 μm^2.

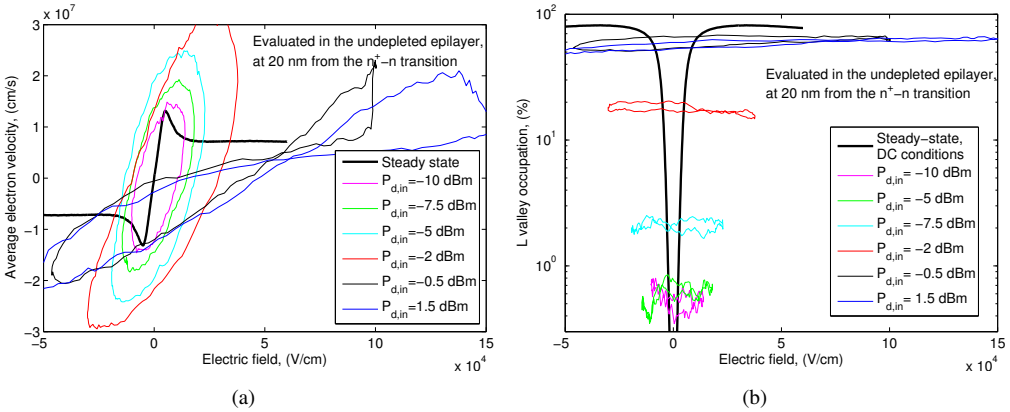

Figure 5.15: (a) Velocity versus field loops and (b) occupation of the L valley in the undepleted epilayer (evaluated at 20 nm from the n^+-n transition) of the 6 THz doubler at different input powers, obtained from MCHB.

of the diode impedance observed in Fig. 5.14(c) at $P_{d,in}$ around 0 dBm. This phenomenon also affects the imaginary part of the diode impedance: By increasing the input power, the swing of the nonlinear

capacitance increases and Im$[Z_c(f_0)]$ decreases, according to the performance $1/\omega C$. When the L valley is highly populated, the modulation of the nonlinear capacitance decreases and Im$[Z_c(f_0)]$ increases, see Fig. 5.14(d). Fig. 5.15 analyses velocity saturation in the 2x3 THz doubler: At input powers lower than -2 dBm, electric fields in the undepleted epilayer are higher than 10 KV/cm but the L valley occupation remains lower than 3 %, see Fig. 5.15. When the input power is increased to -0.5 dBm, the occupation of the L valley increases up to 60 %, what corresponds to the abrupt increase of Re$[Z_d(f_0)]$ observed in Fig. 5.14(c). This abrupt increase of Re$[Z_d(f_0)]$ causes the decrease of the efficiency observed in Fig. 5.14(a). Note that as the input frequency increases in Fig. 5.14, the abrupt increase of the Re$[Z_d(f_0)]$ occurs at lower input powers, see eq. (3.2) and section 3.1.2.

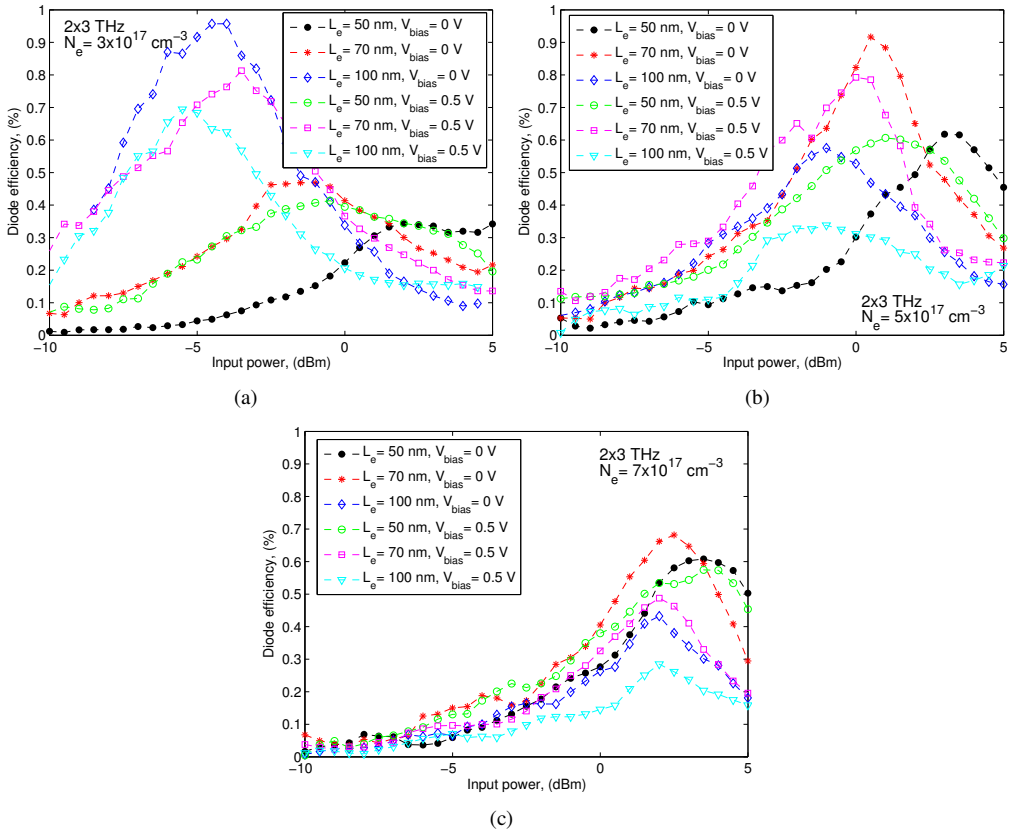

Figure 5.16: Diode efficiency of 6 THz doublers based on the reference diode with epilayer doping (a) 3x10^{17} cm^{-3}, (b) 5x10^{17} cm^{-3} and (c) 7x10^{17} cm^{-3}, different epilayer length and bias point, obtained with MCHB. The anode area is fixed to 0.15 μm^2.

To mitigate both plasma resonance and saturation velocity effects, the epilayer doping can be increased. However, to maximize the diode efficiency a joint optimization of the epilayer doping N_e, epilayer length L_e and bias point V_{bias} is necessary. Fig. 5.16 presents results from MCHB simulations for the optimization of the 6 THz doubler. For each curve in these figures, the load impedances have been optimized with DD$_0$HB at the input power corresponding to maximum efficiency. The following conclusions are obtained from the analysis of these figures:

- For each bias point, V_{bias}, and doping concentration, N_e, considered, there is a value of the epilayer length L_e that maximizes the efficiency ($L_{e,opt}(N_e, V_{bias})$). If $L_e < L_{e,opt}$, the efficiency is degraded because the depletion region reaches the substrate, limiting the nonlinear capacitance. If $L_e > L_{e,opt}$, the efficiency is also degraded because the series resistance increases due

to the undepleted epilayer.

- When the bias is changed from 0 V to 0.5 V, the maximum of efficiency is shifted to lower input powers, e.g. see Fig. 5.16(a) with L_e= 50 nm for the two values of bias. Also the maximum efficiency decreases when V_{bias} increases, since the modulation of the nonlinear capacitance is lower.

- Increasing the doping mitigates velocity saturation effects (the decrease of the efficiency due to high L valley occupations occurs at higher input power as N_e increases, e.g. see Fig. 5.16 for L_e= 100 nm, V_{bias}= 0 V and the different N_e), but also causes the reduction of the maximum efficiency due to the reduction of the modulation of the nonlinear capacitance (e.g. see Fig. 5.16 for L_e= 100 nm, V_{bias}= 0 V and the different N_e).

From the simulation results in Fig. 5.16, the optimum parameters that maximize the efficiency of the 6 THz doubler are: N_e= 5x10^{17} cm^{-3}, L_e= 70 nm and V_{bias}= 0 V. Similar efficiency is obtained with N_e= 3x10^{17} cm^{-3}, L_e= 100 nm and V_{bias}= 0 V.

5.3.2 Triplers above 3 THz

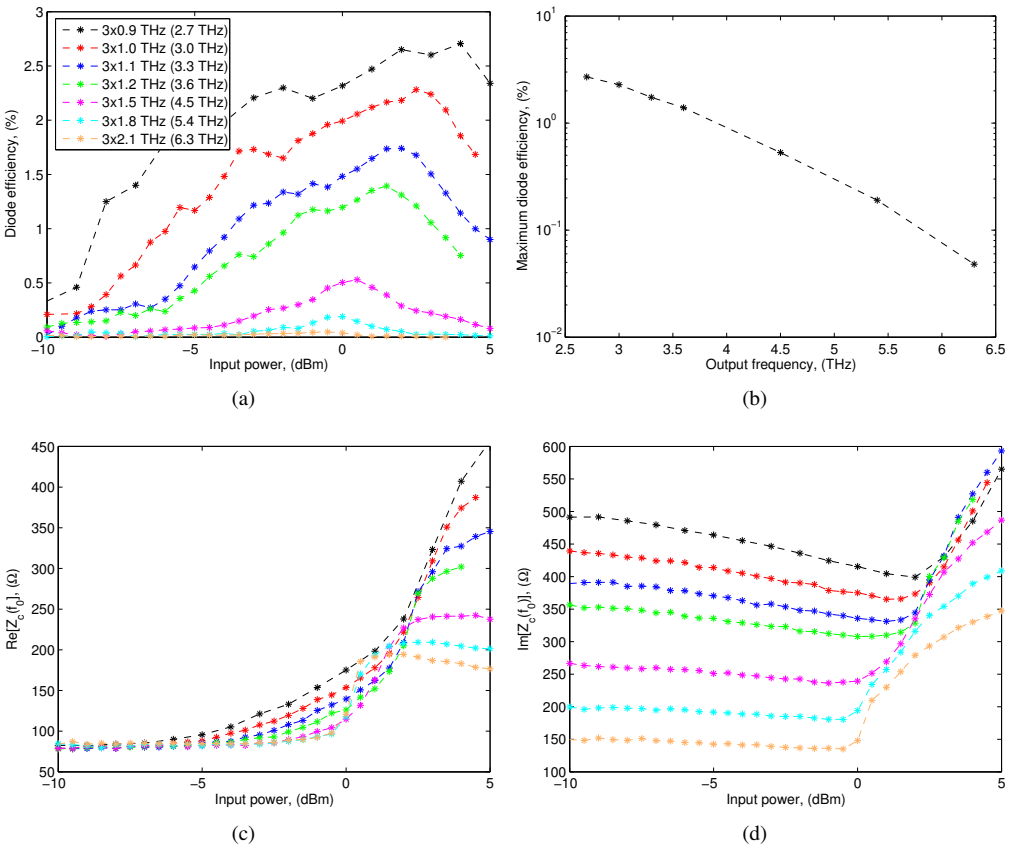

Figure 5.17: (a) Diode efficiency, (b) maximum efficiency in subfigure (a), (c) real part and (d) imaginary part of the circuit impedance (conjugate of the diode impedance) as a function of the input power delivered to the diode for triplers based on the reference diode at different input frequencies, obtained with MCHB.

Fig. 5.17(a) presents the diode efficiency for triplers based on the reference diode. The load impedances at the output frequency used in the simulation of these triplers are shown in Table 5.5.

The performance of the triplers is similar to that described for the doublers. Plasma effects are not so important as they are for doublers analysed in the previous section, since these triplers are operating at lower input frequencies. Hence, at low input powers, the real part of the diode impedance (Fig. 5.17(c)) remains nearly constant as the input frequency increases within the frequency band presented in the figure, and the the imaginary part of the circuit impedance follows the $1/\omega C$ performance, see Fig. 5.17(d). Velocity saturation also limits the performance of the triplers, as was shown for the doublers. For each simulated frequency, velocity saturation cause the increase of the real part of the diode impedance in Fig. 5.17(c) as the input power increases. Comparing Fig. 5.14(c) for doublers and Fig. 5.17(c) for triplers, $\mathrm{Re}[Z_d(f_0)]$ has the same performance and similar values for doublers and triplers with the same input frequency, e.g. the 2x1.5 THz and the 3x1.5 THz.

Table 5.5: Load impedances at $2f_0$ and $3f_0$ for the reference triplers above 3 THz obtained by maximizing the efficiency at the available input power 0.5 mW. Optimization carried out with DD_0HB tool.

Stage	$Z_c[2f_0]$, (Ω)	$Z_c[3f_0]$, (Ω)
3x0.9 THz	0+450j	181+257j
3x1.0 THz	0+425j	150+238j
3x1.1 THz	0+410j	148+228j
3x1.2 THz	0+370j	132+211j
3x1.5 THz	0+310j	109+180j
3x1.8 THz	0+270j	95+158j
3x2.1 THz	0+270j	63+151j

To conclude the analysis of multipliers above 3 THz, Fig. 5.18 presents the measured output power per anode for *JPL* doublers and triplers [Mai03, Cha02, Cha04, Mae05b, Mae08, Mae10a, Mae12] (Table 5.1) and simulation results for multipliers above 3 THz, Figs. 5.14 and 5.17. Regarding the experimental results, the output power has been evaluated at the available input power, which is close to the power for maximum efficiency -Figs. 5.7 and 5.9- except for the 1.5 THz doubler and the 1.64 THz tripler. These two multipliers are not optimum designs because their output powers are similar to the power of the 2.7 THz tripler. Besides, MCHB simulations show that they are working far from maximum efficiency of the designs, see Fig. 5.7(d). The 600 GHz tripler in [Mae05b] is limited by velocity saturation and its performance can be optimized. Also the performance of the 900 GHz tripler and the 1.2 THz tripler -Table 5.1- can be enhanced by optimizing the bias point, the epilayer length and anode area. Table 5.2 presents the optimum characteristics of these multipliers obtained with the MCHB. These optimum designs have been also considered in this analysis. For the simulated multipliers above 3 THz, the predicted output power has been calculated with the maximum efficiency in Figs. 5.14 and 5.17 for a fixed input power per anode of -7 dBm, which is the available input power for the 1.5 THz doubler [8]. The coupling factor $\alpha\beta$= 0.7 has been taken into account to calculate the output powers from the simulations.

The experimental output power per anode is approximately proportional to f^{-2} and $f^{-2.5}$ for doublers and triplers, respectively. The output power for the 900 GHz and 1.2 THz triplers optimized with MCHB is proportional to f^{-2}, showing that it is possible to improve the performance of these multipliers. When the performance is limited by velocity saturation (doublers above 1500 GHz and triplers above 1600 GHz according to the discussion in section 5.2), the output power is proportional to f^{-3}. The output power drops at higher rates when the electron transport is dominated by nonstationary phenomena in the momentum and energy and plasma effects [Cha64, Kel79, Ais84, Sch95], see sections 3.1.4 and 3.1.5.

According to Monte Carlo simulations, doublers and triplers based on GaAs Schottky diodes are expected to operate up to 6 THz and 4 THz respectively with efficiency higher than 0.5 %.

[8] The maximum efficiency can be located at the desired input power by scaling the anode area [Gra00].

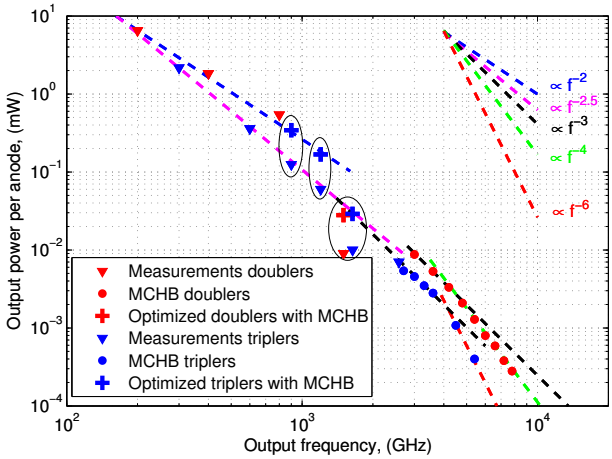

Figure 5.18: Measured output power per anode for *JPL* doublers and triplers [Mai03, Cha02, Cha04, Mae05b, Mae08, Mae10a, Mae12] (Table 5.1) and simulation results for the multipliers above 3 THz, Figs. 5.14 and 5.17, at room temperature.

5.4 Noise response of Schottky multipliers

Schottky based frequency multipliers are commonly used as local oscillators (LO) in heterodyne receivers (coherent detectors) at millimeter and submillimeter wavelengths. Although the noise temperature of the mixer very often determines the overall noise temperature of the of the receiver, noise contributions from the local oscillator cannot be ignored. Due to the low available LO power at submillimeter wavelengths, a significant amount of LO noise can be injected into the receiver along with the LO signal, significantly increasing the noise temperature of the receiver. As a result, low noise LO systems are required for low noise heterodyne receivers [Fab95, Cha03].

This section presents an analysis of the noise response of the 1.5 THz doubler and the 2.7 THz tripler described in sections 5.2.1 and 5.2.2, respectively, -see Table 5.1- by means of Monte Carlo simulations. The procedure described in chapter 4 to calculate the current noise spectral density $\overline{S_I}(f)$ of the diode under periodic time varying conditions has been used.

5.4.1 A 1.5 THz doubler

Fig. 5.19 shows the current noise spectral density $S_I(f)$ of the diode in the 1.5 THz doubler under the voltage waveforms obtained with MCHB for different input powers, see section 5.2.1. According to the results in chapter 4, the noise spectra in Fig. 5.19(a) show a low frequency region due to shot and thermal noise contributions, which is limited by the beginning of the returning carrier peak ($f_{RC} \sim 3.7$ THz). The second peak of the noise spectra in Fig. 5.19(a), at frequencies around 8 THz, is the hybrid plasma peak. Since the diode is working under reverse bias voltage, shot noise is the most important contribution to the low frequency region of $S_I(f)$ ($R_j >> R_s$ in eq. (4.30)), as is shown by the good agreement between $S_I(f)$ from MC and the $2qI_0$ law in Fig. 5.19(b). As the input power increases, the occupation of the upper valleys begins what generates partition noise. Under periodic time varying conditions, the low frequency partition noise is upconverted to the input frequency [Shi03b], see section 4.3 and appendix C.2. At $P_{d,in}$= 0 dBm, the average occupation of the L valley in the undepleted epilayer is around 15 % -appendix D-, and a peak is observed in Fig. 5.19(a) at 750 GHz due to partition noise.

The most important noise contribution at the output frequency (f_{out}= 1.5 THz) is due to the rise of the returning carrier peak. As the input power increases, $S_I(f_{out})$ increases since the swing of the voltage waveform at the terminals of the diode increases and the modulation of the different

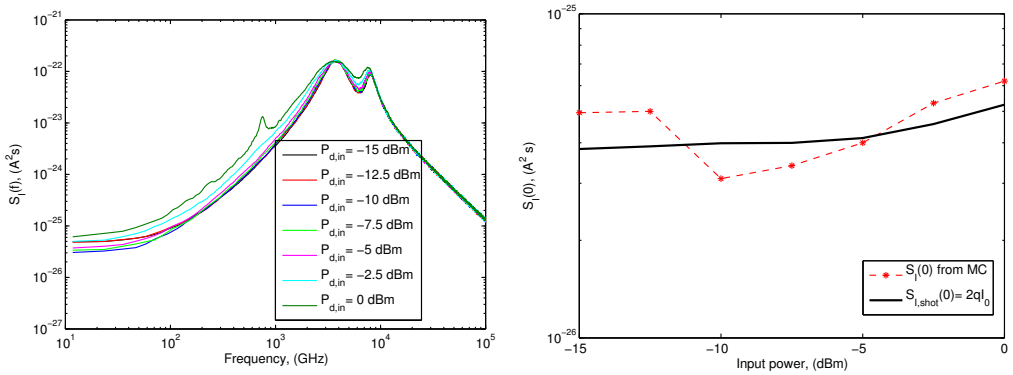

(a) (b)

Figure 5.19: (a) Current noise spectral density of the diode in the 1.5 THz doubler described in Table 5.1, obtained with the MC model under the voltage waveforms from MCHB for different input powers $P_{d,in}$. (b) $S_I(0)$ from MC and the expected $2qI_0$ law with I_0 from MC simulations.

noise sources is higher, see section 4.3. In order to decrease the current noise spectral density at the output frequency f_{out}= 1.5 THz, the returning carrier peak can be shifted to higher frequencies by increasing the epilayer doping and/or decreasing the epilayer length, see section 4.2.

5.4.2 A 2.7 THz tripler

Fig. 5.20 shows the current noise spectral density $S_I(f)$ of the diode in the 2.7 THz tripler under the voltage waveforms obtained with MCHB for different input powers, see section 5.2.2. The bias voltage of this diode is 0 V, and, hence, the combined shot and thermal noise contribution, eq. (4.30), has to be considered to explain the performance of the low frequency region of the noise spectra. Eq. (4.30), which is used under dc conditions, has been converted to a time varying function $S_I(t,f)$ by assuming that the conduction current, the junction resistance and the series resistance of the diode are time varying under the voltage waveforms obtained with MCHB, see appendix G. The average value of $S_I(t,f)$ from eq. (4.30) evaluated with a $\text{LEC}_{R_s(t)}$ and a $\text{LEC}_{R_sLC(t)}$ models are calculated and compared with $S_I(f\sim 0)$ from MC in Fig. 5.20(b). At input powers lower than 0 dBm, a good agreement between MC and the results from eq. (4.30) evaluated with $\text{LEC}_{R_sLC(t)}$ is observed. Note that the inclusion of the carrier inertia effects in the LEC model is fundamental to reproduce the results from MC. At higher input powers, $S_I(f\sim 0)$ from MC increases with respect to eq. (4.30) evaluated with the $\text{LEC}_{R_sLC(t)}$ model due to the partition noise associated to intervalley transfer (at 0 dBm, the occupation of the L valley in the undepleted epilayer is around 15 %, and around 40 % at $P_{d,in}$= 3 dBm, see appendix D). Upconversion of the partition noise by the periodic excitation generates a peak in the noise spectra at the input frequency for input powers higher than -3 dBm. This peak disappears at $P_{d,in}$= 5 dBm and higher input powers, since most of the electrons are in the upper valleys, see section 4.3 and appendix C.2.

The output frequency, f_{out}= 2.7 THz, is located close to the maximum of the returning carrier peak, see Fig. 5.20(a). As a result, a significant amount of noise is generated together with the output signal. As was indicated for the 1.5 THz doubler, $S_I(f_{out})$ can be reduced by shifting the returning carrier peak to higher frequencies. According to chapter 4, this can be carried out by increasing the epilayer doping and/or decreasing the epilayer length.

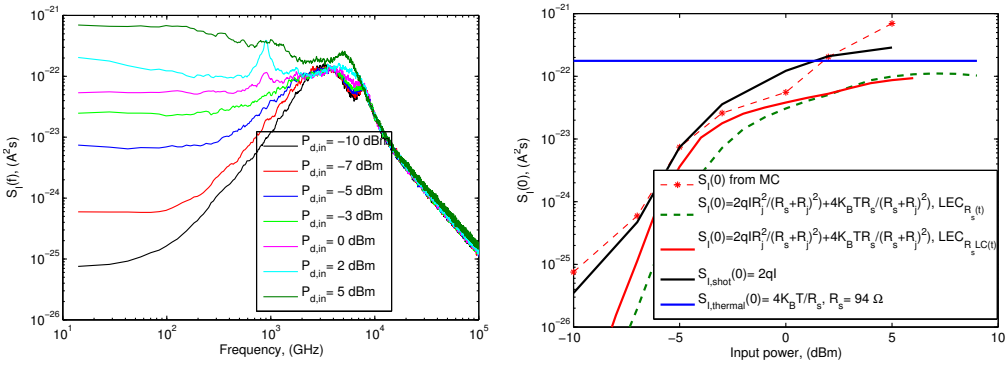

(a) (b)

Figure 5.20: (a) Current noise spectral density of the diode in the 2.7 THz tripler described in Table 5.1, obtained with the MC model under the voltage waveforms from MCHB for different input powers $P_{d,in}$. (b) $S_I(0)$ from MC and the expected $2qI_0$ law with I_0 from MC simulations.

5.5 Analysis of GaN Schottky multipliers at millimeter-wave bands

With the advantages in the output power at W-band (400-500 mW W-band HEMT power module has been reported [Mae10a, Mae12]), power-combining schemes and high-thermal conductivity substrates have been developed to avoid thermal or breakdown limitation of GaAs technology [Mae08, Mae10a, Mae12]. Besides, the design of frequency multipliers at these short wavelengths with more than six anodes and still achieve efficient conversion and broad bandwidth is difficult [Por07, Mae08]. In a near future, higher values of input power at W-band are expected, and the high complexity necessary for the first stages of multiplier chains based on GaAs technology can degrade the efficiency of these stages. As the GaN technology becomes more mature, the high power capabilities of GaN semiconductor can be considered as an interesting alternative for the development of sources at millimeter wavelengths. Due to the wide bandgap of GaN which results in a high breakdown field, GaN Schottky multipliers allow for high temperature and high power operation. However, GaN has the inconvenient of a lower electron mobility compared to GaAs, which results in an increase in the series resistance, and thereby, in lower efficiencies, see the discussion in section 3.2.

This section presents an analysis of the accuracy and the range of validity of LEC and DD models for the simulation of GaN based frequency multipliers, considering as a reference the results from MC model. Although there are not any measurements of GaN Schottky based multipliers at millimeter wavelengths, the results from MC simulations are reliable due to its microscopic nature, and the success obtained in the description of electron transport in bulk GaN with this model [Bha97, Fou99, Far01, Bar02, Sta05, Mat07]. Additionally, the analysis of the capabilities of GaN Schottky diodes presented in section 3.2 is completed in this section with the simulation of different multipliers. An available input power around 400-500 mW at 100 GHz has been assumed, according to [Mae12]. A 400 GHz multiplier chain (2 stage chain) and a 300 GHz tripler based on GaN Schottky diodes have been analysed and optimized.

Table 5.6 presents the characteristics of the simulated GaN multipliers. The epilayer length, doping, anode area, bias point and load impedance of each stage have been optimized to maximize the efficiency at the available input power, see appendix D. A substrate length of 5 μm and doping $2x10^{18}$ cm^{-3} have been assumed in all the diodes simulated since there is not data available about the series resistance of GaN Schottky diodes. Reducing the series resistance associated to the substrate will enhance the efficiency of the multipliers presented in this section. As was indicated in the simulation of GaAs multipliers, diodes are always conjugately matched at the fundamental frequency

Table 5.6: Characteristics of the GaN frequency multipliers considered in the simulations.

Stage	f_{out}, (GHz)	$P_{in,tot}$, (mW)	V_{bias}, (V)	N_e, (cm^{-3})	L_e, (nm)	Area, (μm^2)	$C_{j,0}$,[1] (fF)	$R_{s,dc}$[1] (Ω)	V_{BD},[1] (V)	$Z[2f_0]$, (Ω)	$Z[3f_0]$, (Ω)
0.2 THz doubler, 2 anodes	200	400	-15	5x10^{16}	650	40	21.7	49.9	-133	84+127j	0+0j
0.4 THz doubler, 1 anode	400	70	-5	5x10^{16}	400	10	5.4	156.8	-94	153+176j	0+0j
0.3 THz tripler, 2 anodes	300	400	-10	5x10^{16}	550	57	30.9	32.2	-118	0+70j	36+53j

[1] Calculated with the DD model. For $R_{s,dc}$, similar values are obtained with MC.

and the circuit impedances at the output frequency are optimized to maximize the efficiency at the available input power.

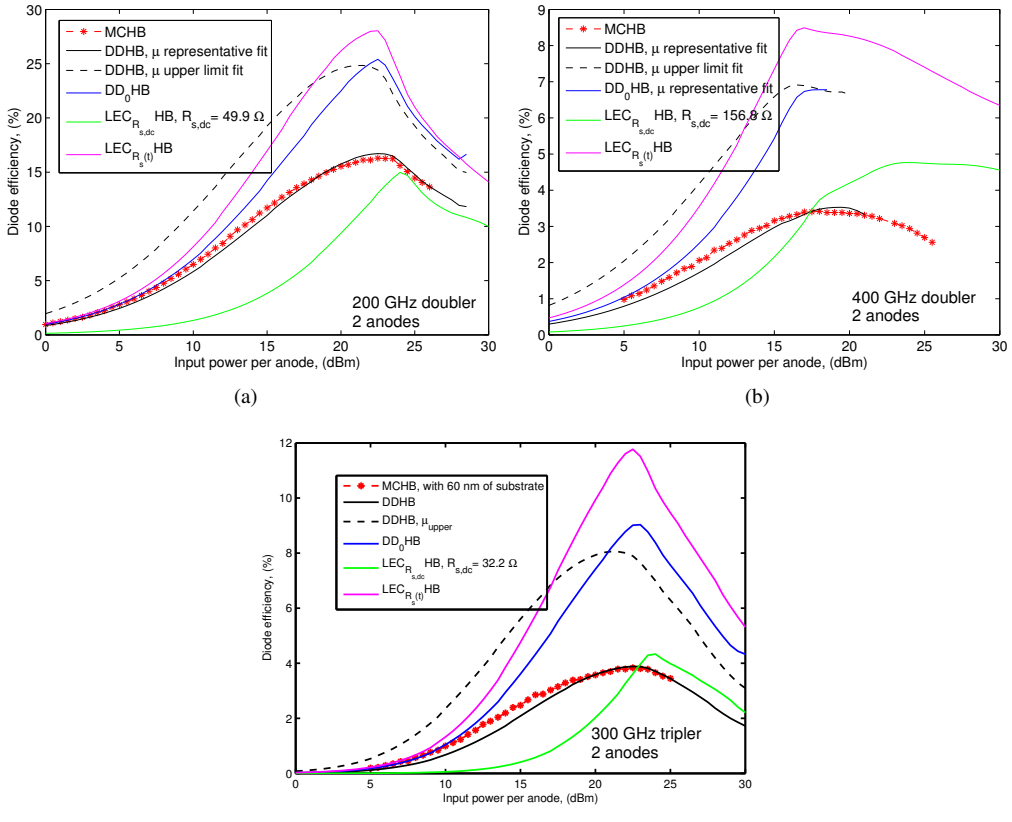

Figure 5.21: Diode efficiency of the doublers and the tripler described in Table 5.1 as a function of the input power per anode, simulated with LECHB, DD$_0$HB, DDHB and MCHB tools.

Fig. 5.21 presents the efficiency as a function of the input power per anode for the multipliers described in Table 5.6, obtained with different diode models. The following conclusions are derived from the analysis of this figure:

1. A good agreement is observed between MCHB and DDHB for these multipliers. Because the energy and momentum relaxation times τ_ε and τ_m respectively are lower in GaN than GaAs, non-local effects are not as important in GaN as they are in GaAs based devices, see section 3.2, leading to a good agreement between both models. Therefore, DDHB tool can be used in

the design and optimization of GaN based multipliers at millimeter wavelengths with the same accuracy as MCHB. As was shown in section 5.2, this is not true for GaAs based multipliers, where DDHB leads to an important underestimation of the efficiency due to non-local effects.

2. The performance of these multipliers is limited by the degradation of the electron mobility when the emission of polar optical phonons appears, see section 3.2. Although higher doping can be selected to avoid this phenomenon, the efficiencies reached would be lower because of the reduction in the modulation of the nonlinear capacitance. Appendix D presents results of the optimization and a physical analysis of the limitations of these GaN multipliers.

3. DD_0HB overestimates the efficiency since it assumes a low field constant mobility.

4. The predictions of LEC models are not reliable: They do not model the degradation of the efficiency due to the degradation of the electron mobility. Besides, our implementation of the LEC models does not take into account the degradation of the nonlinear capacitance of the diodes when the depletion region reaches the substrate (see appendix D), as was discussed in section 5.2 for the for the GaAs based 400 GHz doubler.

5. Because of the high gap of GaN, breakdown effect does not limit the performance of these multipliers as can occur in the design of GaAs based multipliers. According to the results in Fig. 5.21(c), two GaN Schottky diodes in the 300 GHz tripler are enough for the available input power considered. One diode configuration is possible, but a balance configuration has been selected to maintain low anode sizes and the symmetry of the circuit. In comparison, the first stage 300 GHz tripler of the 2.7 THz source [Mae12] requires four power-combined chips, each one with six GaAs Schottky diodes (24 GaAs Schottky diodes) to avoid breakdown effects for an input power around 400 mW at 100 GHz.

6. If the upper limit fit in Fig. 2.19 for the electron mobility of GaN is used in the DDHB tool, which is based in the most recent results regarding measured low-field GaN mobilities, an important enhancement in the efficiency is obtained (black dash curves in Fig. 5.21).

In the simulation of GaAs multipliers, input and output coupling factors α= 0.8 and β= 0.875 ($\alpha\beta$= 0.7) were assumed in order to relate the efficiency of the diode and the efficiency of the circuit, see section 5.1.2. For GaN based multipliers better coupling factors are expected since it is possible to employ configurations with one or two diodes, decreasing the complexity of the circuit. Hence, $\alpha\beta$= 0.9 has been assumed for the GaN multipliers. In a near future, higher values of input power at W-band are expected, and the high complexity necessary for the first stages of multiplier chains based on GaAs technology can degrade the efficiency of these stages, i.e. $\alpha\beta$ can decrease for GaAs circuits. In Table 5.7, a comparison of the maximum circuit efficiency of the GaN multipliers in Fig. 5.21 and the state of the art circuit efficiency of GaAs multipliers is presented. Different values of $\alpha\beta$ have been considered ($\alpha\beta$= 0.7 has been assumed for measured efficiency, see section 5.1.2) in order to take into account the expected degradation of the efficiency of the GaAs multipliers when

Table 5.7: Maximum circuit efficiency, (%), of the GaN based multipliers in Fig. 5.21 and measured efficiency of GaAs multipliers ($\alpha\beta$= 0.7), see Table 5.1. Efficiencies with different values of $\alpha\beta$ are shown for the GaAs multipliers.

Stage	GaN[1]	GaAs				
	$\alpha\beta$=0.9	$\alpha\beta$=0.7	$\alpha\beta$=0.6	$\alpha\beta$=0.5	$\alpha\beta$=0.4	$\alpha\beta$=0.3
0.2 THz doubler	15.0-22.3	34	29.1	24.3	19.4	14.6
0.4 THz doubler	3.1-6.2	18.3	15.7	13.1	10.4	7.8
0.3 THz tripler,	3.5-7.2	14.1	12.1	10.1	8.1	6.0

[1] The two values of the circuit efficiency for the GaN multipliers have been obtained with the representative fit and the upper limit fit of the GaN mobility, respectively, see Fig. 2.19.

higher values of input power at W-band will be available. The 200 GHz doubler and the 300 GHz tripler based on GaN have similar circuit efficiency than those based on GaAs only when $\alpha\beta$ is lower than 0.4 in GaAs circuits.

The simulation results presented in this section have shown that the major inconvenience of GaN multipliers with respect to GaAs ones is their lower efficiencies ($\sim$ 15 % for the 200 GHz GaN doubler compared to $\sim$ 34 % for the 200 GHz GaAs doubler in [Cha04]; $\sim$ 25 % can be reached with the upper limit fit of the GaN mobility in Fig. 2.19). However, due to the excellent power handling capabilities of GaN diodes, they offer the possibility of simplified structures by including just 1 or 2 diodes for multipliers in the upper part of the millimeter-wave region (100-300 GHz). On the other hand, the good agreement between simulation results obtained with MCHB and DDHB indicates that the DDHB tool can be used in the design and optimization of GaN based multipliers at millimeter wavelengths with the same accuracy as MCHB.

Chapter 6

Modelling and analysis of frequency mixers at millimeter and submillimeter-wave bands

Ultimate low noise heterodyne receivers used in radio-astronomy at submillimeter-wave frequencies are based on SIS tunnel junctions and HEBs, see chapter 1. SIS mixers based on niobium junctions have an upper operation frequency limit of around 1.4 THz, reaching quantum noise level with power requirements of about 1 μW (below 1 μW at 1 THz in [Shi07, Kar09]). Noise performance of HEBs (1050 K at 2.84 THz [Gao07]) is not as good as for SIS, with LO power requirements from 1 to 100 nW (30 nW at 2 THz [Gao07]), see Fig. 1.3. Despite of the low noise level and LO power requirement of these technologies, Schottky mixers are still the technology most used in heterodyne receivers. Schottky mixers have the advantage over other sensor technologies to work at room temperature as well as cryogenic temperatures for improving noise performance, which make them the technology of choice for long term atmospheric and planetary missions. Besides, GaAs Schottky diodes are based on a mature technology and can be produced with high reliability [Mae10b, Cha11a].

In the design and optimization of Schottky mixers, two main figures of merit have to be considered: (i) Conversion loss and (ii) equivalent input noise temperature. Device models based on LEC and the conversion matrix approach [Hel78a, Maa93] are commonly used in the design of Schottky mixers at millimeter-wave and submillimeter-wave frequencies [Tho05, Sch07a, Tho10a, Sch10, Tho12]. The limitations of LEC models at these frequencies have been analysed in chapter 5 for multipliers. Besides, the conversion matrix approach allows to calculate the mixer performance as a function of the LO power exclusively, assuming that the RF power is much lower than the LO. Noise analysis based on this technique is able to account for thermal noise, shot noise and the correlations effects in shot noise when a LO excitation is applied. However, this approach is based on expressions for thermal noise obtained under equilibrium conditions. At high frequencies and/or high LO powers, the accuracy of this noise model is questionable. In fact, this approach has been updated to take into account excess noise due to hot electron effects [Heg85, Cro87].

The development of physics-based numerical modelling of semiconductor devices is becoming increasingly important for the design and optimization of non-linear circuits. In models like DD and HD, noise in semiconductor devices can be analysed in the framework of Langevin's approach and the Green's function technique (impedance field method) [Vli71, Sta98, Shi00, Bon01a]. Some research groups have implemented this method in a DD model and it has been used to simulate the noise performance of non-linear circuits under large-signal conditions [Bon01a, Bon01b, Bon03]. However, the results obtained with this method are affected by the limitations of the DD model, see chapter 2. Although higher order models (i.e. HD) are important when non-local and non-

stationary transport effects appear (see Fig. 2.17), the derivation of the Langevin's sources for noise analysis and their implementation in numerical simulators are complicated and are under development [Gru93c, Gru94c, Shi99, Bon01a]. A fundamental limitation of these techniques is that they required the knowledge of the spectral performance of the noise source in the devices.

The MC model presents an interesting alternative to these methods, since it simulates the noise spectral density of the diode in a natural way, due to its microscopic nature, see chapters 2 and 4. The MC model is one of the most reliable methods for noise analysis even at nonequilibrium conditions. Shot noise, thermal noise and noise due to hot electrons and intervalley transitions are modeled with this tool. The difficulties in the inclusion of cross-correlation terms in Langevin's equation for noise analysis with high order physics-based models are inherently solved in the MC model, see chapter 4.

This chapter presents a simulation tool based on the MC model coupled to a multi-tone HB (MCHB) which enables the joint design of Schottky mixers from both electrical and noise considerations. This simulation tool is validated by means of a comparison with measured conversion losses and noise temperature of Schottky mixers available in the literature. The limitations of the Schottky diodes as mixers are analysed with the MCHB tool. An analysis of the range of validity and the accuracy of LECHB and DDHB tools for the simulation of mixers at millimeter and submillimeter frequencies is also carried out, considering as a reference the results obtained with the MCHB tool. Both fundamental and sub-harmonic mixers are considered in this chapter. While the conversion losses of the mixers have been evaluated with LECHB, DDHB and MCHB tools, the equivalent input noise temperature has been only evaluated with LEC models in the framework of the conversion matrix formalism (see appendix E), and with the MCHB tool.

6.1 Operating principles of Schottky mixers

6.1.1 Description of Schottky mixers

Mixers convert the signal power from one frequency band to another through an intermodulation process with a local oscillator (LO) signal. In Schottky diode frequency mixers, this conversion is generally carried out by the nonlinear junction resistance. The nonlinear reactance of the junction is not desirable for mixers, since it is potentially unstable in down-conversion [Sal70]. Two types of Schottky mixers are commonly used: fundamental mixers, where a radio frequency (RF) signal is down-converted to an intermediate frequency (IF) according to $f_{IF} = |f_{RF} - f_{LO}|$, and subharmonically pumped (SHP) mixers where the IF frequency results from the difference between the RF and the second harmonic of the LO frequency ($f_{IF} = |f_{RF} - 2f_{LO}|$).

Fundamental mixers are presented in two different configurations: single-ended fundamental mixers and fundamental balanced mixers, that employ an even number of diodes. The capabilities of these two configurations are summarized below.

The most common topology of sub-harmonic mixers employs a pair of planar Schottky diodes in anti-parallel configuration. The anti-parallel diode pair has an antisymmetric current-voltage relationship that cause the suppression of even harmonics ($mf_{LO} + nf_{RF}$, m+n even) when pumped by the LO signal. Since the anti-parallel diode pair conducts current for the positive and the negative periods of an applied sinusoidal LO voltage, the small RF signal will see a conductance time domain waveform with half the period of the LO signal, which is the fundamental principle behind subharmonic mixing. Depending on circuit design any even order harmonic of the LO can be used for down-conversion, and for an ideal perfectly balanced diode pair only odd order harmonics will be generated outside the diode loop. Currents containing the even harmonics are confined within the diode loop and canceled outside the diode circuit [Coh75, Sob11].

The main advantages and inconveniences of these two types of mixers are compiled in the following items [Maa93, Sch03, Mae10b]:

Fundamental planar Schottky mixers

- Single-ended fundamental mixers present a simple design and the bias circuit can be easily implemented.
- Single-ended fundamental mixers show good broadband performance.
- They require LO power at double frequency than its counterpart sub-harmonic. Fundamental mixers pumped by solid-state sources have been demonstrated up to 900 GHz [Tho10c, Tho10b].
- They have a single port for coupling the RF and the LO signal, requiring external LO/RF diplexing outside the mixer block. This attenuates both the RF signal and the LO signal.
- Since the LO is near the RF in frequency, LO phase and amplitude (AM) noise can be mixed down as well.

Fundamental balanced mixers overcome some of the problems of single-ended fundamental mixers:

- They provide independent ports for the RF and the LO signal removing the external LO/RF diplexing stage.
- The diodes are in parallel configuration at the IF, decreasing the impedance and facilitating the matching of the IF signal with the LNA.
- They cancel the AM noise injected by the local oscillator but their intrinsic noise is higher than for single diode mixer, since they use an even number of diodes.
- The polarization of fundamental balanced mixer is more difficult than in single-ended fundamental mixer.
- They need greater LO power than single-ended fundamental mixer to drive the increased number of diodes.

Sub-harmonic Schottky mixers

- They require LO power at half the RF frequency.
- The RF and the LO ports are independent.
- The impedance at the IF is lower than in single-ended fundamental mixer.
- Cancelation of the AM noise.
- They have conversion losses in the order of 1 and 2 dB higher than fundamental mixers.
- They archive lower bandwidth than single-ended fundamental mixers.

Tables 6.1 and 6.2 and Fig. 6.1 show a compilation of the state-of-the-art of fundamental and sub-harmonic mixers. Similar noise performance are obtained with both types of mixers.

6.1.2 Evaluation of the figures of merit

This section presents a brief description of the techniques used to evaluate the figures of merit of Schottky mixers: (i) the conversion loss and (ii) the equivalent input noise temperature.

The harmonic balance method properly adapted for multi-tone excitations enables the possibility of performing a general mixer simulation without any assumption regarding the LO and RF frequencies and power levels. Therefore, it is possible to take into account the influence of all the desired

Table 6.1: Compilation of data published in the literature on fundamental mixers based on planar Schottky diodes (except the 4.75 THz mixer, based on whisker diodes) at room temperature. The bandwidth of operation of the mixers and the frequencies at which the measurements in the table were done have been included.

Year	Ref.	Type[a]	RF band, (GHz)	IF band, (GHz)	f_{RF} (GHz)	f_{LO}, (GHz)	f_{IF}, (GHz)	V_{bias} (V)	P_{LO}, (mW)	L_{DSB}, (dB)	T_{DSB}, (K)	L_{epi}, (nm)	N_{epi}, (cm^{-3})	Area, (μm^2)	V_{bi} (V)	R_s, (Ω)	$C_j(0)$, (fF)	Z_{RF} (Ω)	Z_{LO} (Ω)	Z_{IF} (Ω)
2010	[Tho10b, Tho10c]	2B,JPL	835-900		865.8				1	7.38	2330		$5x10^{17}$	0.4	0.73	30	1	90+j200	17+j50	200
2010	[Sch07a, Sch10]	2B,JPL	520-590	10		540	4		1.5	8.5	2500		$2x10^{17}$	1.5				35+j35	35+j35	50
2010	[Eri10, Eri08]	2B,JPL	1250-1650	5-40		1561	10		1.5	10	3000		$5x10^{17}$	0.2			1			
2000	[Mar00]	SE,UVa			585				1.74	6.6	1135	100	$4x10^{17}$	0.9		10-12	1.5			
2000	[Hui00]	SE,UVa				585			1	8	1200		$4x10^{17}$	0.9		11	1.5			
1999	[Sie99]	SE,JPL	2500	7-21		2522	8.4	0.3-0.6	5[b]	16.9	9000	100	$1x10^{18}$	0.35		15-20				
1998	[Sie98]	SE,JPL		1.5-11		640	8	0.35	0.7	8.1	1640			0.8		7				
1997	[Hes97][c]	SE,UVa			585		1.8		1.16	7.6	2380		$2x10^{17}$	1.13		14	2	45+j30	45+j30	150
1996	[Bet96][b,c,e]	SE,UVa			4750		6.6				70000									
1995	[Gau95]	SE,ALP			91.4	90	1.4	0.73	3-4	6.3	1000				0.78	8	18			70
1994	[Gea94]	SE,UMi			258		1.4	0.73	1.1	7.8	1600	70	$2x10^{17}$	2.01	0.7	13	4	72+j28	57+j53	110
1994	[Ali94]	SE,UVa				335				8.5	1750			1.33		10-12	2-3			
1993	[Ali93c]	SE,UVa	230-280		258		1.4		2	7.2	1310			1.13		9-11	2-3			
1993	[Ali93a]	SE,UVa	86-106		91.4	90	1.4	0.65	1.5-2	5.5	770	80	$2x10^{17}$	4.91		2.5-3	5-6	80+j1	64+j51	110+j8
1993	[Gea93]	SE,UVa				761	1.4	0.4	5	14.9	8900	90	$2x10^{17}$	0.5		25	1-1.5			
1991	[Gar91]	SE,UVa	90-110			94	1.4			2.3[d]	259[d]	1000	$2-5x10^{17}$	4.91		5-6	5-6			
1991	[New91]	SE,UVa	300-365			345	1.4			4.2[d]	1640			1.77		14	2.3			
1984	[Sie84]	SE,UVa	140-220			150		0.8		2.7[d]	250[d]	80	$2x10^{17}$	3.14		6.3	6.2			

[a] 2B: Two diodes in a balance configuration. SE: single-ended mixer (1 diode). It is also indicated the laboratory which built the diodes. ALP: Alpha Industries Inc. JPL: Jet Propulsion Laboratory. UVa: University of Virginia. UMi: University of Michigan

[b] Laser pumped.

[c] System conversion loss and system noise temperature.

[d] Data given in single side band (SSD), transformed to double side band (DSB): L_{DSB}(dB)= L_{SSB}(dB)-3 dB, T_{DSB}=T_{SSB}/2.

[e] Whisker diode.

Table 6.2: Compilation of data published in the literature of SHP mixers based on planar Schottky diodes at room temperature. The bandwidth of operation of the mixers and the frequencies at which the measurements in the table were done have been included.

Year	Ref.	Type[f]	RF band, (GHz)	IF band, (GHz)	f_{RF} (GHz)	f_{LO}, (GHz)	f_{IF}, (GHz)	V_{bias} (V)	P_{LO}, (mW)	L_{DSB}, (dB)	T_{DSB}, (K)	L_{epi}, (nm)	N_{epi}, (cm^{-3})	Area, (μm^2)	V_{bi} (V)	R_s, (Ω)	$C_j(0)$, (fF)	Z_{RF} (Ω)	Z_{LO} (Ω)	Z_{IF} (Ω)
2012	[Zha12]	CUT	530-590	0-20		260.6			1.5	9	1100	50	3-5x10^{17}	0.4-0.8		18.4-9.5[a]				
2012	[Tho12][c]	JPL	1100-1300			600		0.85[b]	1-1.5	15	6000									
2011	[Tho11]	JPL		2-11	590		4-6	0		7.5	1400									
2011	[Tho11]	JPL		2-11	670		–		5	10	2500					17-21	1.5			
2011	[Cha11b]	JPL			670		70			16-18										
2011	[Hen10]	RAL		0.5-11	325				3	6.5	1200									
2010	[Tho10a]	JPL	520-600	2-11	590		4-6			5.3	1710									
2009	[Tre09]	UMS	360-400		390		1.5		2.5	10.9	3667				0.8	19.88-40.4[c]				
2009	[Tho09][d]	RAL	320-360	2-8/6-14					7-11	7.2-24.1	3400									
2008	[Wan08]	UMS	150-205	2-4	175				2.5	9.5	2500					21 and 12.5				
2008	[Tho08b]	JPL	820-920		800-856					10.5-12	3000-4300				0.8	20	1.15	43+j53	55+j135	
2008	[Tho08a]	VDI	368-392		372		1.5		1.5	8	1625			1.33	0.8	10	2.5	47+j46	63+j121	100
2007	[Sch07b]	JPL	520-590			280			5	12	4000									
2005	[Tho05]	UVa	300-360	1-4/4-8	330		1.5			5.7	700	100	2x10^{17}	0.8	0.73	11-15	1.3	83+j53	147+j207	100
1999	[Hes99]	UVa	380-425		420				5	8	1120	100	2x10^{17}	0.9		18	1.3	65+j140	70+j130	100
1998	[Meh98]	JPL		1.5-15		320	2		3.5-3.8	9	2500	100	2x10^{17}			8.5	2			
1994	[Lee94]					92	1.4		4.5	9.7	1850		3x10^{17}	1.13	0.72	14	2.3			
1993	[Sie93]		195-230		205		1.4		5.7	5.7[e]	795[e]			1.54	1.10	12	3	65+j80	70-j12	

[a] Series resistance of the low doped layer, i.e. the epilayer.
[b] Bias for the two diodes in series.
[c] Series resistance of each diode of the subharmonic pair.
[d] Subharmonically pumped image rejection mixer.
[e] Data given in SSD, transformed to DSB: L_{DSB}(dB)= L_{SSB}(dB)-3 dB, T_{DSB}=T_{SSB}/2
[f] Laboratory which built the diodes.
CUT: Chalmers University of Technology. JPL: Jet Propulsion Laboratory. RAL: Rutherford Appelton Laboratory.
UMS: United Monolithic Semiconductor. UVa: University of Virginia. VDI: Virginia Diodes, Inc.

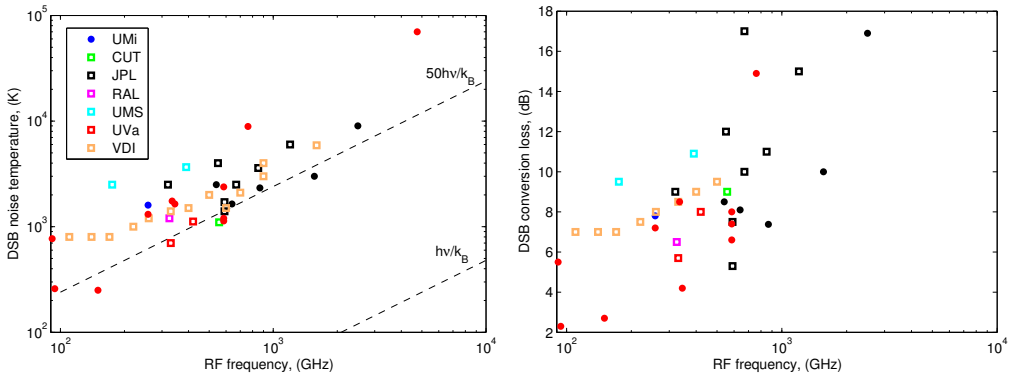

(a) (b)

Figure 6.1: Measured (a) DSB equivalent input noise temperature and (b) DSB conversion loss for fundamental (solid circles) and SHP (squares) Schottky mixers described in Tables 6.1 and 6.2.

harmonics and intermodulation products of the LO and RF frequencies in the analysis, even in the case that they are not commensurable, i.e. the quotient f_{LO}/f_{RF} is not rational [Per08]. In the multi-tone harmonic balance technique, the conversion loss of the diode L_d from the RF to the IF signal is evaluated directly according to its definition:

$$L_d = \frac{Power\,available\,at\,the\,RF\,signal\,port}{Power\,delivered\,to\,output\,load\,(IF)}. \tag{6.1}$$

Different diode models (LEC, DD and MC) have been coupled to a multi-tone harmonic balance circuit simulator to evaluate L_d eq. (6.1).

The analysis of mixers developed by Held and Kerr [Hel78a] is based on the LEC model and the conversion matrix formalism, see appendix E. This technique takes into account the impact of the embedding impedances seen by the diode at any finite number of sidebands in the performance of the mixer. Noise sources usually considered in this technique are thermal noise in the constant series resistance, shot noise and its correlation contributions due to the modulation of the noise sources when a LO excitation is applied [Hel78a, Maa93]. The original analysis in [Hel78a] does not include the correlation of the frequency components of the thermal noise of the diode, since it assumes that the series resistance of the diode is constant under the LO excitation. Besides, the noise analysis in the conversion matrix formalism is based on expressions for shot and thermal noise obtained under equilibrium conditions while the operation conditions of the mixer are far from equilibrium. To account for the limitations of these models, additional noise contributions due to hot electrons have been included in the conversion matrix formalism [Heg85, Cro87], see appendix E. On the other hand, the limitations of LEC models to describe high frequency and/or high power conditions limit the accuracy of the noise models used in the conversion matrix formalism. For example, hot electron noise appears when high electric fields are generated in the undepleted epilayer of the diode [Zir86, Cro87, Fab95]. The analytical model for this noise contribution depends on the square of the current through the epilayer [Heg85, Cro87], see appendix E. However the LEC model is unable to model correctly the current in the diode under high field conditions, what affects the accuracy of the model for hot electron noise when it is evaluated with the LEC model.

The MC model can be used to evaluate directly the mean current noise spectral density of the diode $\overline{S_I}(f)$ under the voltage waveforms at the terminals of the diode obtained from HB simulations of the mixer. Noise models or techniques like the conversion matrix are not necessary for noise calculation with the MC model, see appendix G. The total time needed to simulate the noise in mixers with the MC model is higher than the time necessary to calculate their electrical response. In the calculation of the electrical response, it is only necessary to simulate one IF period in addition to the transitory periods, see appendix A. However, to calculate the noise response of the diode, a high

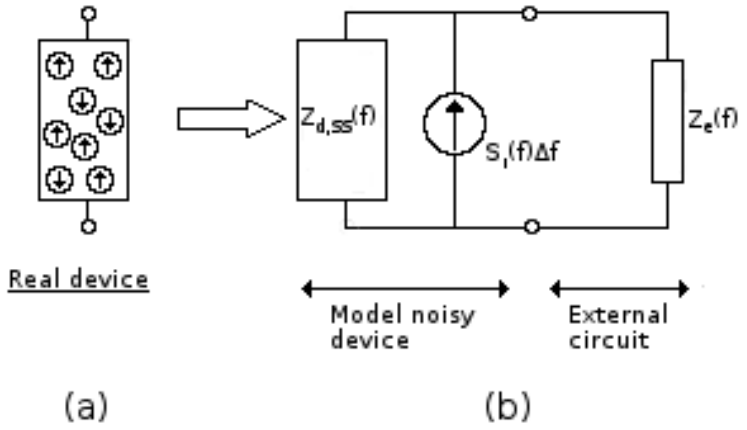

Figure 6.2: (a) Noisy device and (b) equivalent circuit of the mixer at frequency f.

number of realizations has to be simulated to evaluate the average noise spectral density, eq. (4.13), see appendix A.

Applying Thévenin's theorem, a noisy diode can be represented by a noise current generator in parallel with the driving point impedance of the diode $Z_{d,SS}$ or by a voltage in series with $Z_{d,SS}$ [Zie70]. The driven point impedance $Z_{d,SS}$ is the net small-signal impedance of the whole system which relates the fluctuations of the current and the voltage at the terminals the diode. $Z_{d,SS}$ depends on the LO signal, bias point and also on the embedding impedance of the circuits, and, hence, $Z_{d,SS}$ is referred to the whole circuit [Per04a, Shi06]. Therefore, to calculate the noise power dissipated in the load impedance of the mixer circuit at the IF frequency, the noisy diode can be replaced by a noise current generator characterized by $\overline{S}_I(f)$ obtained from MC simulations and the impedance $Z_{d,SS}$ at the driving point, see Fig. 6.2. The small-signal impedance $Z_{d,SS}(f)$ at the frequency of interest f (usually $f = f_{IF}$) used in Thévenin's theorem is calculated as:

$$Z_{d,SS}(f) = \left.\frac{V_{SS}(f)}{I_{SS}(f)}\right|_{V_{LO}} \tag{6.2}$$

where V_{LO} indicates that the diode is driven by a LO excitation of frequency f_{LO}, $V_{SS}(f)$ and $I_{SS}(f)$ are small-signal voltage and current of frequency f at the terminals of the diode. $Z_{d,SS}(f)$ is determined by exciting the device with a voltage perturbation of frequency f superimpose to the large-signal LO excitation of frequency f_{LO} that exists at the terminals of the diode for each LO power considered. Note that the particularization of eq. (6.2) at the IF frequency is the small-signal output impedance of the pumped diode defined in the conversion matrix formalism [Hel78a, Maa93], eq. (E.14). According to the conversion matrix formalism, the output impedance of the diode can be found by setting the signal source to that frequency (IF frequency), see Fig. E.1, and calculating [Maa93]:

$$Z_{out}(f_{IF}) = \frac{V_s(f_{IF})}{I_0} - Z_e(f_{IF}) = Z_{0,-N}\frac{I_{-N}}{I_0} + \ldots + Z_{0,0}\frac{I_0}{I_0} + \ldots + Z_{0,N}\frac{I_N}{I_0} \tag{6.3}$$

$$= Z_{c,0,-N}\frac{I_{-N}}{I_0} + \ldots + Z_{c,0,0} + \ldots + Z_{0,N}\frac{I_N}{I_0}, \tag{6.4}$$

where $V_s(f_{IF})$ is the voltage source at frequency f_{IF}, I_n are the current phasors at frequency $f_n = f_{IF} + nf_{LO}$ (n=0 corresponds to the IF frequency), Z_{pq} and $Z_{c,pq}$ are the elements of the extended matrix, eq. (E.12), and the diode matrix, eq. (E.8), see appendix A. Eq. (6.3) -see [Maa93]- is equivalent to eqs. (E.14) and (E.21) presented in [Maa88] and [Hel78a], respectively. This definition, eq. (6.3), coincides with the process described to evaluate $Z_{d,SS}(f_{IF})$.

From the analysis of the circuit in Fig. 6.2(b), the noise power delivered to the output impedance at IF frequency is:

$$P_{del}(f_{IF}) = \frac{\overline{S}_I(f_{IF})\Delta f \cdot Re[Z_e(f_{IF})] \cdot |Z_{d,SS}(f_{IF})|^2}{|Z_{d,SS}(f_{IF}) + Z_e(f_{IF})|^2} \tag{6.5}$$

where Δf is the bandwidth of interest. The single-sideband input noise temperature of the mixer is defined as [Hel78a, Maa93]:

$$T_{d,SSB} = \frac{P_{del} L_{d,SSB}}{k_B \Delta f} \tag{6.6}$$

where $L_{d,SSB}$ is the single-sideband conversion loss from the RF source to the IF load, eq. (6.1).

In this chapter, it has been assumed that the single sideband conversion loss of the diode is two times the double sideband conversion loss [Maa93]:

$$L_{d,SSB}(dB) = L_{d,DSB}(dB) + 3\,dB \tag{6.7}$$

It is also assumed that the SSB and DSB mixer noise temperatures are related by [Maa93]:

$$T_{d,SSB}(K) = 2 \cdot T_{d,DSB}(K). \tag{6.8}$$

6.1.3 Figures of merit for the receiver

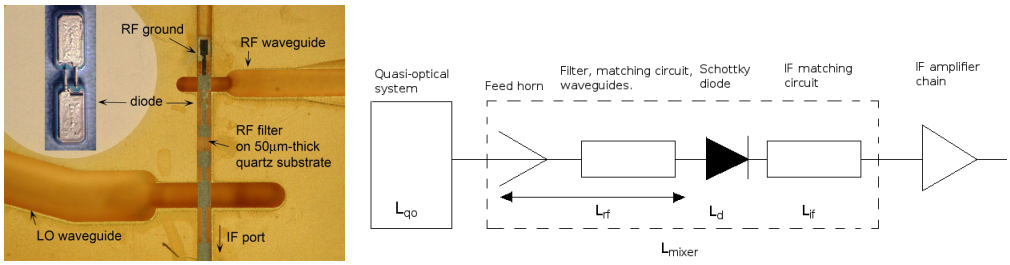

(a) (b)

Figure 6.3: (a) Photograph of the 330 GHz SHP mixer described in [Tho04] (available online [Alai]) and (b) block diagram of a receiver.

With the simulation tools considered in this thesis, diode conversion loss and equivalent input noise temperature eqs. (6.1) and (6.6) (SSB or DSB) can be evaluated. In order to compare measured and simulated results, losses in different elements of real receivers have to be evaluated. Fig. 6.3 shows a photograph of a 330 GHz SHP mixer [Tho04, Alai] and a general block diagram of a receiver. Optical systems are required in single-ended mixers to combine the RF and the LO beams while providing adequate RF-to-LO isolation (Martin-Puplett diplexer, Fabry-Perot diplexer, etc.). Also, quasi-optical polarization grills are used to separate the two polarizations of the RF signal. In the mixer block, the feed-horn, filters at the different frequencies of interest and the required matching circuits are usually integrated. A low noise amplifier chain is used to amplify the IF signal. To evaluate the conversion loss of the whole receiver, the losses in these elements have to be considered:

$$L_{rec} = L_{qo} L_{rf} L_d L_{if} \tag{6.9}$$

where

- L_{qo}: Losses in the quasy-optical parts of the systems (lens, diplexers, ...).
- L_{rf}: Losses in the feed-horn, filters and mixer waveguides.

- L_d: The diode conversion losses.
- L_{if}: Resistive and reflected losses in the IF matching circuit.

The noise temperature of the receiver is evaluated using Friis' formula in the block diagram of Fig. 6.3:

$$T_{rec,DSB} = (L_{qo} - 1)T_{phys} + L_{qo}T_{mixer,DSB} + L_{qo}L_{mixer,DSB}T_{if} \tag{6.10}$$

where T_{phys} is the physical temperature, T_{if} is the noise temperature of the IF amplifier chain, and the mixer conversion loss $L_{mixer,DSB}$ and noise temperature $T_{mixer,DSB}$ are defined as:

$$L_{mixer,DSB} = L_{rf}L_{d,DSB}L_{if} \tag{6.11}$$

$$T_{mixer,DSB} = (L_{rf} - 1)T_{phys} + L_{rf}T_{d,DSB} + L_{rf}L_{d,DSB}(L_{if} - 1)T_{phys} \tag{6.12}$$

Eqs. (6.9) and (6.10) assume that the different stages considered in the receiver are matched.

To carry out a comparison with measured results, simulation results of the conversion losses and noise temperature of the diode have been transformed to receiver or mixer results as defined by these equations, using the data provided in the literature for L_{qo}, L_{rf}, L_{if}, T_{phys} and T_{if} when available.

6.1.4 Simulation of Schottky mixers

The simulation tool we use for the design and optimization of the Schottky mixers is based on the multi-tone HB technique presented in [Fue98, Per08]. Both fundamental Schottky mixers and subharmonically-pumped antiparallel-pair Schottky mixers can be analysed. The presence of multi-tone excitations makes it necessary to take into account not only the different harmonics of the LO and the RF signals but also their intermodulation products $mf_{LO} + nf_{RF}$, with m and n integers[1]. When f_{LO} and f_{RF} are commensurate, i.e. the quotient f_{LO}/f_{RF} is rational, the multi-tone excitation can be defined as a periodic waveform by using the great common divider of the LO and the RF frequencies, so the fast Fourier transform (FFT) can be employed. In the case f_{LO} and f_{RF} are noncommensurate, the almost periodic Fourier transform (APTF) is employed to perform the time-frequency transforms [Kun88, Maa88, Per08].

MC, DD, and LEC diode models have been coupled to the multi-tone HB technique to analyse the performance of mixer circuits. As was done in the analysis on multipliers, the results of the MCHB are considered as a reference. The drift-diffusion model that imposes a constant low field mobility and the traditional drift-diffusion model are considered, see chapter 2. The enhanced version of the DD model (denoted by DD_e) described in [Per08, Sil09] to model the important overshoot of the electron velocity close to the Schottky contact when the flat band regime is reached has been also considered. The DD_e uses the recombination velocity calculated from Monte Carlo as the boundary condition for the continuity equation at the Schottky contact[2]. The results from LEC models based on the dc series resistance ($LEC_{R_{s,dc}}HB$) and a time varying resistance ($LEC_{R_s(t)}HB$) are also included in the analysis. These models have been used to evaluate the conversion losses of the mixers. For noise analysis of the mixers, only MC (see section 6.1.2) and the conversion matrix formalism based on $LEC_{R_{s,dc}}$ and $LEC_{R_s(t)}$ (see appendix E) have been used. In appendix E, the evaluation of the conversion matrix formalism with the DD model, that can be applied to calculate the noise temperature, is explained.

From the different mixers shown in Tables 6.1 and 6.2, some of then have been chosen as the most representative and are compiled in Table 6.3. In this table are included measured data available in the literature as well as data used in our simulations for the mixers analysed in this chapter. These mixers use diodes fabricated by the University of Virginia, except the 835-900 GHz [Tho10b, Tho10c] and the 2.5 THz [Sie99] mixers which are fabricated with *JPL* diodes. The values of the epilayer doping,

[1] A 5x3 box truncation scheme has been considered in simulations, where 5 and 3 are the highest intermodulation products of the LO and the RF frequencies considered, respectively.

[2] Fig. 2.4 shows the importance of the enhanced version close to flat band voltages.

Table 6.3: Schottky diode mixers published in the literature and data used in our simulations.

Data published in the literature for Schottky mixers																					
Mixer[a]	f_{RF} (GHz)	f_{LO}, (GHz)	P_{LO} (mW)	V_{bias} (V)	N_e, (cm^{-3})	L_e, (nm)	L_s, (nm)	Area, (μm^2)	ϕ_b, (V)	R_s, (Ω)	$C_j(0)$, (fF)	C_P, (fF)	Z_{RF} (Ω)	Z_{LO} (Ω)	Z_{IF} (Ω)	L_{qo} (dB)	L_{rf} (dB)	L_{if} (dB)	$L_{mixer,DSB}$, (dB)	$T_{mixer,DSB}$, (K)	T_{if} (K)
Fundamental single-ended [Ali93a]	93.4	92	1.5-2	0.65	$2x10^{17}$	100		4.91	0.85	7	6	8.5	80-j1	64+j51	110+j8[b]		1.2		4.5	770	129
SHP pair [Tho04, Tho05]	330	164.25	1.5-5.5	0	$2x10^{17}$	100		0.8	0.85	11-15	1.3	5	83+j53	147+j207	100		0.7	1	6	700	
Fundamental single-ended [Hes96, Hes97][a]	585	583.2	1.16		$2x10^{17}$			1.13		14	2		45+j30	45+j30	150	0.7	1.6	0.7	7.6	2380	~65
Fundamental balanced [Tho10b, Tho10c]	865.8		1		$5x10^{17}$			0.4	0.73	30	1		90+j200	17+j50	200		0.7	1.2	9.25	2660	
Fundamental single-ended [Sie99][a]	2514	2522	6	0.3-0.6	$1x10^{18}$	100		0.35		15-20						2		0.4	16.9	16500	150
Fundamental single-ended [Bet96][a]	4744	4750	1		$1x10^{18}$	30		0.05		20-40	0.25									70000	30
Data for Schottky mixers in our simulations																					
Mixer[a]	f_{RF}[d], (GHz)	f_{LO}[d], (GHz)	P_{LO} (mW)	V_{bias} (V)	N_e, (cm^{-3})	L_e, (nm)	L_s, (μm)	Area, (μm^2)	ϕ_b, (V)	R_s, (Ω)	$C_j(0)$, (fF)	C_P, (fF)	Z_{RF} (Ω)	Z_{LO} (Ω)	Z_{IF} (Ω)	L_{qo} (dB)	L_{rf} (dB)	L_{if} (dB)	$L_{mixer,DSB}$[g], (dB)	$T_{mixer,DSB}$[g], (K)	T_{if} (K)
Fundamental single-ended [Ali93a]	100	90	1.5	0.65	$2x10^{17}$	100	1.2	4.91	0.85	7.01	7.3	8.5	80-j1	64+j51	110+j8		1.2		3.7	~360	129
SHP pair [Tho04, Tho05]	360	168	1.5-5.5	0	$2x10^{17}$	100	0.1	0.8	0.95[e]	24.4[c]	1.15	5	83+j53	147+j207	100		0.7	1	5.7	~700	
Fundamental single-ended [Hes96, Hes97][a]	600	570	1.16	0.6	$2x10^{17}$	80[h]	0.05	1.13	0.85	15	1.8	5	45+j30	45+j30	150	0.7	1.6	0.7	7.5	~2400	~65
Fundamental balanced [Tho10b, Tho10c]	900	870	1	0.65	$5x10^{17}$	100	0.35	0.4	0.75	30.3	1		90+j200	17+j50	200		0.7	1.2	9.9	~2000	
Fundamental single-ended [Sie99][a]	2500	2475	6	0.6	$1x10^{18}$	100	0.45	0.35	0.99	20.27	1.07		70+j113	86+j36	250	2		0.4	15	~15000	150
Fundamental single-ended [Bet96][a]	4750	4725	1	0.6	$1x10^{18}$	30	0.03	0.07[f]	0.99	35.9	0.25		130+j220	130+j220	250				6.4	~19500	30

[a] Conversion losses and noise temperature for these receivers refer to mixer as defined by eqs. (6.11) and (6.12), respectively, except for 585 GHz mixer in [Hes97], the 2.5 THz mixer in [Sie99] and the 4.75 THz mixer in [Bet96] that refer to the receiver.

[b] Circuit impedances at different intermodulation products are provided for this mixer [Ali93b] and they have been considered in simulations: $Z[3f_{LO} - f_{RF}] = Z[f_{LO} + f_{RF}] = Z[2f_{LO}] = (6+28j)\ \Omega$; $Z[2f_{LO} - f_{RF}] = Z[f_{RF}] = (80-1j)\ \Omega$.

[c] Physics-based models with the parameters for the diodes in the 300-360 GHz SHP mixer (doping, length, anode area, barrier height) lead to dc series resistance around 25 Ω which are larger than the values provided in the literature for the LEC model of the diode *sim* 11-15 Ω, [Tho04, Tho05].

[d] The values of f_{RF} and f_{LO} used in simulations have been modified with respect to those used in measurements to reduce the computational cost of the MCHB simulations. However, it has been shown that this does not affect too much simulated results of conversion losses and noise temperature, see the discussion in the following sections.

[e] ϕ_b has been slightly increased with respect to the value provided in [Tho05] to get a better agreement between measured and simulated conversion losses. Increasing ϕ_b, conversion loss versus LO power curves are shifted to higher LO powers.

[f] The anode area has been selected to reproduce in simulations values of $C_j(0)$ given in literature for this diode.

[g] Results from MC simulations at the indicated P_{LO}, see following sections.

[h] Value not provided in the literature. Selected to minimize the conversion loss.

zero-voltage junction capacitance and available LO power provided in the literature for these circuits are employed in the simulations. Unknown characteristics in some devices like the bias voltage have been optimized to obtain the minimum conversion loss. In some cases the anode areas employed in the numerical simulations have been slightly modified with respect to the nominal values provided in the literature so that the measured and simulated capacitance coincide. The characteristics of the substrate used in the simulation are selected to reproduce the series resistance provided in the literature. The substrate doping was set to $2\text{x}10^{18}$ cm^{-3} for the simulated mixers except for the 2.5 THz and the 4.75 THz mixers where it was fixed to $5\text{x}10^{18}$ cm^{-3} as indicated in [Sie99] and [Bet96]. For some of the mixers simulated, literature provides information about the parasitic capacitance C_p of the diode. In those cases, it has been included in the simulations as a linear capacitance in parallel with the diode. [3]

To optimize the performance of the mixers, it is fundamental to provide the adequate matching to the Schottky diodes at the different frequencies involved in the design. The impedances at the LO, RF and IF frequencies have a major impact in the performance of the mixer. Although our simulator provides the possibility to conjugately match automatically the input impedances at the LO and RF frequencies at each operating point, the values presented in Table 6.3 have been used in the simulations since they are the values provided in the literature, except for the 2.5 THz and the 4.75 THz mixer (there are not any published data about the circuit impedances for these two mixers). For these two mixers, the circuit impedances used in the simulations have been selected to minimize the conversion losses at the available LO power, see Table 6.3. Due to the practical impossibility of achieving optimum terminations at a large number of mixing frequencies, the impedances at mixing frequencies other than LO, RF and IF frequencies have been set to zero in the simulations.

In order to compare simulated and measured results, diode conversion loss and noise temperature from simulations are transformed to the corresponding mixer ones through eqs. 6.11 and 6.12 taking into account losses in different elements of the receiver (L_{qo}, L_{rf} and L_{if}) when indicated in the literature, see Table 6.3 in section 6.1.3. The available LO power used in the simulations has been corrected to take into account losses in elements before the diodes in the receiver (L_{qo} and L_{rf} in section 6.1.3). The RF power has been assumed 0.01 mW in all simulations. This has been done to analyse the practical situation where the RF power is much lower than the LO power. If lower RF power is considered, greater number of particles is necessary in the MC simulations, see appendix A.

Three different types of mixers have been simulated: single-ended fundamental mixer with a single Schottky diode, balanced fundamental mixer based on two diodes in a balanced configuration and SHP mixers based on an antiparallel diode pair, see Fig. 6.4. The advantages and limitations of these types of mixers were discussed in section 6.1. The analysis of single-ended fundamental mixers is straightforward. Any balanced fundamental mixer (two diodes in a balanced configurations) can be reduced to an equivalent single diode mixer having the same conversion loss and noise temperature [Maa93]. The topology of the 835-900 GHz fundamental balanced mixer [Tho10b,Tho10c] analysed in this section is based on a cross-bar balanced architecture [Maa93]. Both diodes are located inside the RF waveguide in a series configuration across a central suspended stripline. The architecture of this balanced mixer implies that the pair of Schottky diodes are seen in series by the RF signal and in anti-parallel configuration by the LO and IF signals, see Fig. 6.4. As indicated previously, for the simulation of this fundamental balanced mixer a single-diode equivalent circuit of the balanced mixer has been used. The single-diode equivalent circuit resembles that of the single-ended fundamental mixer. The only difference is in the LO, RF and IF impedances. The IF and LO impedances in the single-diode equivalent circuit are twice the actual IF and LO impedances and the RF impedance is half the actual RF circuit impedance. The balanced mixer requires twice the LO power of the single-diode equivalent mixer. The results (conversion losses, noise temperature, etc) presented for the

[3] The parasitic capacitance degrades the performance of Schottky mixers by increasing the required LO power to achieve minimum conversion losses. Although it is possible to tuned it out, it is difficult to known in advance the exact value of C_p since it depends on the fabrication process and electromagnetic environment. However, approximate values are normally available and the influence of C_p can be accounted for during the design process.

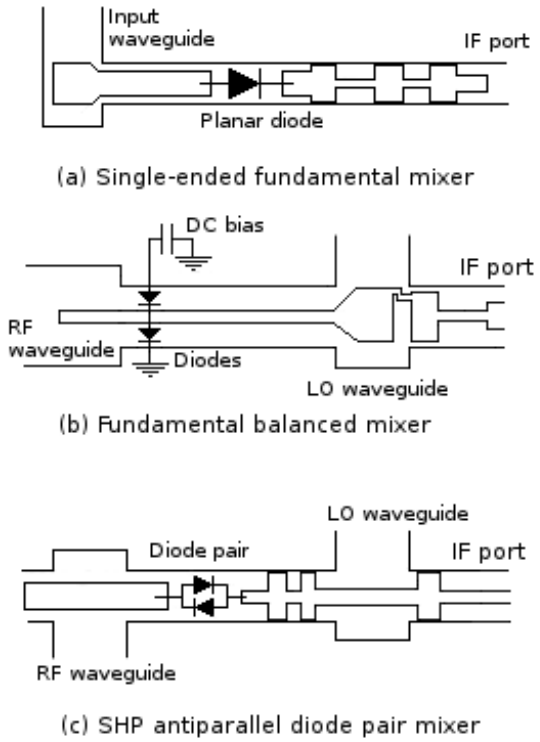

Figure 6.4: Schematic of the types of mixers analised: (a) single-ended fundamental mixer (1 diode), (b) fundamental balanced mixer (2 diodes) and (c) subharmonically pumped antiparallel diode pair mixer (2 diodes).

835-900 GHz fundamental balanced mixer will refer to the complete balanced mixer as a function of the total LO power. For the 300-360 GHz SHP antiparallel diode pair mixer [Tho05], the simulator analyses the real structure with two diodes in antiparallel connection. Thereby, the results presented for this mixer will refer to the complete antiparallel-pair.

6.2 Conversion losses of frequency mixers evaluated with different models

This section presents a comparison between measured and simulated conversion losses for the mixers compiled in Table 6.3. The comparison of the equivalent input noise temperature is carried out in the next section.

Fig. 6.5 presents the DSB mixer conversion losses as defined by eq. (6.11) for the mixers described in Table 6.3 as a function of the available LO power. They have been analysed with LECHB, DDHB and MCHB tools. For the 585 GHz and the 2.5 THz mixers, published measured results are receiver conversion losses, eq. (6.9), and they have been transformed to mixer conversion losses using eqs. (6.11) and (6.9). For the 4.75 THz mixer there are not published data of its conversion losses. The most relevant results from the analysis of these figures are:

- The agreement between simulated and measured results slightly enhances when the simulated IF frequency coincides with the IF frequency in measurements. This is shown in appendix F for the mixers described in Table 6.5, where simulations with DD$_e$HB and different IF frequencies are compared.

- The discrepancies observed in Fig. 6.5(a) between measured and simulated results for the 86-

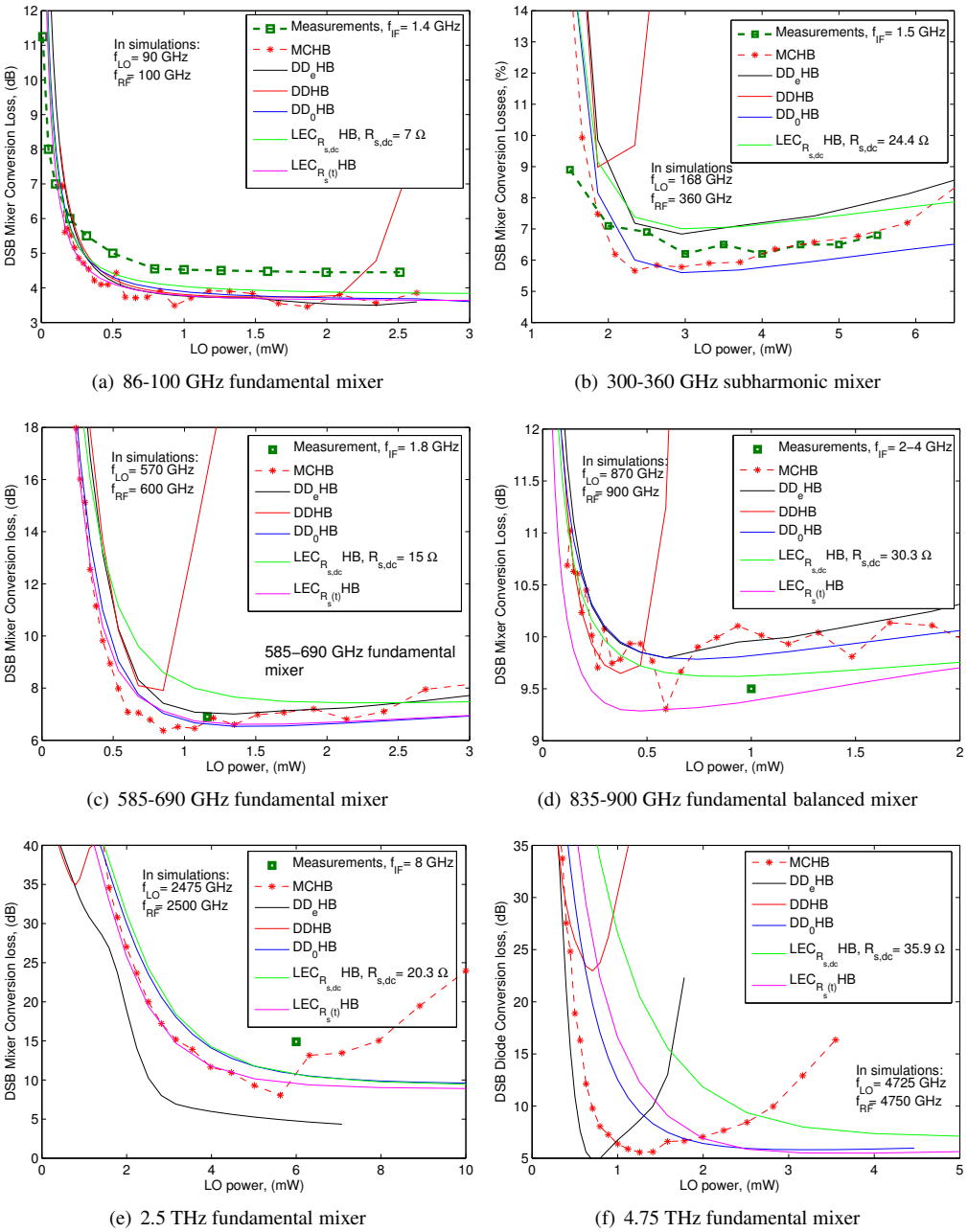

(a) 86-100 GHz fundamental mixer

(b) 300-360 GHz subharmonic mixer

(c) 585-690 GHz fundamental mixer

(d) 835-900 GHz fundamental balanced mixer

(e) 2.5 THz fundamental mixer

(f) 4.75 THz fundamental mixer

Figure 6.5: DSB conversion losses of the mixers described in Table 6.3 [Ali93a, Tho05, Hes97, Tho10c, Sie99, Bet96] as a function of the LO input power, simulated with LECHB, DDHB and MCHB tools.

106 GHz fundamental mixer were also described in [Ali93a, Ali93b]. According to [Ali93b], they could be due to power losses by conversion to other frequencies where the terminating embedding impedances have real parts and discrepancies in the measured embedding impedances at the first and second harmonics between the microwave model of the receiver structure and the actual receiver at 90 GHz.

- For the mixers up to 1 THz, a good agreement is observed between the predictions of MCHB and DD$_e$HB. As was described in section 3.1.1, the DD model overestimates the series resis-

tance of the diode due to the local evaluation of the electron mobility in the transition between the neutral and the depleted epilayer. This effect, which is the origin of the underestimation of the efficiency of multipliers with the DDHB tool, see section 5.2.1, also affects the conversion losses of the mixers evaluated with DD and DD_e. When the diodes are working below flat band conditions, DD_eHB and DDHB overestimate the conversion losses due to the overestimation of the series resistance, see Figs. 6.5(a)-(d). Under such conditions, a very good agreement is observed between MCHB and DD_0HB since DD_0 assumes a constant low field electron mobility. When the LO power increases and the diodes reach flat band conditions (around the minimum of conversion loss, see appendix F), the DD_0 and DD models fail, and DD_eHB and MCHB give the same conversion loss, since DD_e model has been updated to work under flat band conditions, see section 2.3.

- The traditional DD model (DDHB) fails when the diodes are working close to flat band conditions, since DD is a local model, unable to model the important overshoot of the electron velocity close to the Schottky contact when the flat band regime is reached, see section 2.3. Neither DD_0 is able to model correctly these conditions, since it assumes a constant low field mobility. This limitation of the DD model above flat band conditions is not present in the simulation of frequency multipliers with DDHB, since, in those circuits, harmonic generation is carried out by the nonlinear capacitance of the Schottky junction and the conversion efficiency decreases when varistor regime is reached or velocity saturation effects appear.

- The predictions of the $LEC_{R_s(t)}$HB are in good agreement with the results from DD_0HB. On the other hand, since $LEC_{R_{s,dc}}$HB uses constant $R_{s,dc}$, it overestimates the series resistance of the diode and, hence, overestimates the conversion losses.

- Velocity saturation does not affect the performance of the mixers up to 1 THz, as is shown in appendix F, due to the high doping and bias voltages used in mixers, see section 3.1.2.

- For the 2.5 THz and the 4.75 THz fundamental mixers, there is not a good agreement between MCHB and DD_eHB. The electron mobility model used in the DD_e model has to be updated in order to extend the validity of DD_e at these conditions. Besides, velocity saturation is very important in the performance of these mixers due to the high LO frequency, see appendix F, hence DD_0HB and LECHB underestimate the conversion loss for high LO power.

- The conversion losses from MCHB for the 835-900 GHz fundamental mixer present fluctuations of $\pm$ 0.5 dB from numerical origin, which are related to dependence of the accuracy of the MC simulations with the number of particles and realizations simulated, see appendix A. These fluctuations can be avoided by increasing the number of simulated particles and/or the number of realizations, but with an increased computational cost.

- The minimum diode conversion loss for the 4.75 THz mixer is lower and occurs at lower LO powers than for the 2.5 THz mixer (L_{mix} in Fig. 6.5(e) minus 0.4 dB due to L_{if}, see Table 6.3). This is due to the higher L-valley occupation in the undepleted region of the epilayer for the diode in the 2.5 THz mixer ($\sim$ 20 % for the 2.5 THz mixer and 10 % for the 4.75 THz mixer at the LO power for minimum conversion loss, see appendix F). Also, shunting effects [Cro92] are more important for the 2.5 THz fundamental mixer than for the 4.75 THz fundamental mixer (anode area 0.35 μm^2 for the 2.5 THz mixer and 0.07 μm^2 for the 4.75 THz mixer), what results in higher LO power to reach minimum conversion loss and higher values of the minimum conversion loss for the 2.5 THz mixer. A detailed analysis of the performance of these two mixers is presented in section 6.4.3.

These results show that Monte Carlo is a good model to predict accurately the conversion losses of Schottky mixers up to 5 THz, since it takes into account the important physical effects in the diodes. The traditional DD model fails when the diodes are working close to flat band conditions and the enhanced DD_e model becomes necessary. The DD_e shows a good agreement with the conversion

losses evaluated with MCHB up to signal frequency 1 THz (the mobility model used in our DD$_e$ will be updated to extend its validity at higher frequencies). Simple lumped equivalent circuit model usually overestimates the conversion losses. A LEC model assuming time varying series resistance shows a better agreement with MCHB. But they are limited when velocity saturation effects appear.

6.3 Equivalent input noise temperature of frequency mixers evaluated with different models

The equivalent input noise temperature for the mixers described in Table 6.3 is analysed in this section using the MC model, which includes the diode noise sources intrinsically, see appendix G, and LEC models, where noise is evaluated according to the conversion matrix formalism, see appendix E. Table 6.4 presents a summary of the procedure to calculate the noise temperature of the mixers with the MC model. The noise spectra of current fluctuations (the cyclostationary current response is subtracted from the total current response, i.e. $\delta i(t) = i(t) - < i(t) >$) from MC presented in this section have been calculated as described in section 4.1.1 under cyclostationary conditions.

Table 6.4: Steps to evaluate the equivalent input noise temperature of Schottky mixers using the MCHB tool.

Noise temperature $T_{d,SSB}$ at the IF frequency in Schottky mixers with MCHB
1. Calculate the voltage waveform at the terminals of the diodes and the conversion loss of the mixer for a given LO power with the MCHB tool. 2. Simulate the current noise spectral density $S_I(f)$ of the diode with the MC model under the voltage waveform obtained in step 1). 3. Calculate the small-signal impedance of the diode $Z_{d,SS}(f)$, eq. (6.2), at the IF frequency using the MC model of the diode under the LO voltage waveform obtained in step 1). 4. Evaluate the equivalent input noise temperature of the diode $T_{d,SSB}$ at f_{IF} with eq. (6.6), using the conversion loss obtained in 1), $S_I(f_{IF})$ from 2) and $Z_{d,SS}(f_{IF})$ from 3).

6.3.1 The 86-106 GHz fundamental mixer

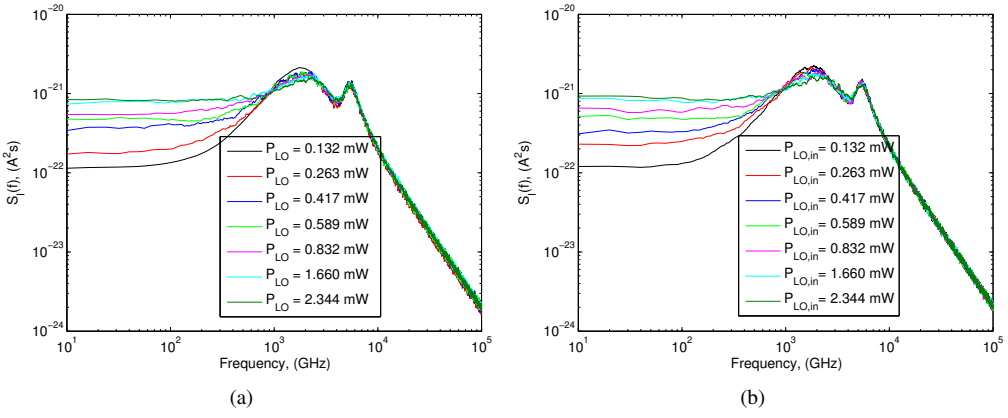

(a) (b)

Figure 6.6: Noise spectra of the current fluctuations at the terminals of the diode in the 86-106 GHz fundamental mixer [Ali93a], see Table 6.3, under voltage waveforms from (a) DD$_e$HB with f_{IF}= 2 GHz and from (b) MCHB with f_{IF}= 10 GHz, for different LO powers.

Fig. 6.6 presents the current noise spectral density $S_I(f)$ [4] of the diode in the 86-106 GHz fundamental mixer obtained from MC simulations under the voltage waveforms from DD$_e$HB at f_{IF}= 2 GHz and with voltage waveforms from MCHB at f_{IF}= 10 GHz, for different LO powers. The good agreement between MCHB and DD$_e$HB in Fig. 6.5 for f_{IF}= 10 GHz is also expected when f_{IF}= 2 GHz. Hence, to calculate the current noise spectra when the IF frequency is 2 GHz, the voltage waveforms at the terminals of the diode obtained with DD$_e$HB can be used instead of those obtained with MCHB, to avoid the high computational cost of MCHB at such a low IF frequency.

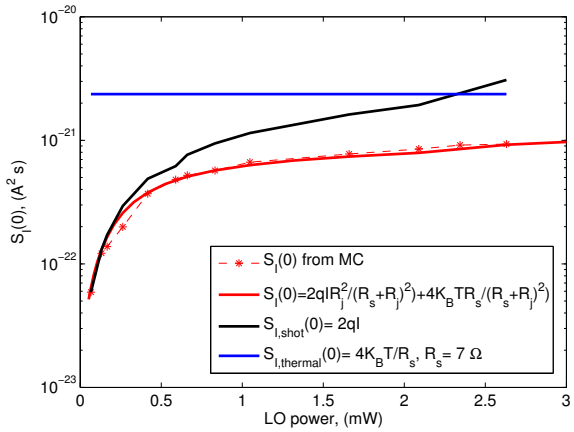

Figure 6.7: Comparison of the low frequency current noise spectra for the diode in the 86-106 GHz fundamental mixer [Ali93a] obtained with the MC model (evaluated at the lowest frequency in the noise spectra of Fig. 6.6(a)) and the shot and thermal noise contribution given by eq. (4.30). To evaluate eq. (4.30) under the voltage waveforms of DD$_e$HB at f_{IF}= 2 GHz, LEC$_{R_s(t)}$ has been used. The values presented in the figure are the average of eq. (4.30) in a period of the IF. The 2qI_0 with I_0 evaluated with the MC model and the $4k_B$T/R$_s$ terms are also included.

The low frequency region of the noise spectra presented in Fig. 6.6(a) is compared in Fig. 6.7[5] with the shot and thermal noise contribution given by eq. (4.30). This equation was given for dc conditions. When a time varying signal is applied $S_I(0)$ in eq. (4.30) becomes time dependent. According to the extension of the Wiener-Khintchine theorem for cyclostationary conditions in section 4.1.1, the current noise spectral density can be evaluated as the time dependent spectral density obtained with the correlation function formalism averaged in an IF period. In Fig. 6.7, the values presented for $S_I(0)$ from eq. (4.30) have been obtained evaluating eq. (4.30) for each sample of the voltage waveform and averaging in an IF period ($R_j(t)$, $I_j(t)$, and R$_s(t)$ are time dependent in eq. (4.30), what results in $S_I(0,t)$; the average value of $S_I(0,t)$ is used in Fig. 6.7). A good agreement is observed between MC simulations and the shot and thermal noise contribution approximated by eq. (4.30). The medium-high frequency region of the noise spectra Fig. 6.6 present the peaks due to the RC and HP resonances described in chapter 4. According to chapter 4, the amplitude of the RC peak decreases when the LO power increases (LO voltage swing closer to flat band). Fig. 6.6 shows that $S_I(f)$ is not affected if f_{IF} 10 GHz is considered instead of 2 GHz, that is closer to the IF frequency in the experimental characterization.

The small-signal impedance of the diode at f_{IF}= 2 GHz under the LO signal of frequency 92 GHz has been evaluated with MC and DD models in Fig. 6.8, see section 6.1.2. The real part of Z$_{d,SS}$ decreases as the input power increases because the nonlinear resistance of the Schottky junction decreases as it approaches flat band conditions. The imaginary part of Z$_{d,SS}$ is determined by the nonlinear capacitance of the diode ($-1/j\omega C$). Increasing the input power, the swing of the nonlinear capacitance increases until the voltage waveform at the terminals of the diode is close to

[4]The noise spectra of current fluctuations calculated with MC have been smoothed to reduce numerical fluctuations. This process does not affect following results.

[5]Since the 1/f noise is not taken into account in our simulations, the noise spectrum at frequencies lower than those presented in the x-axis of Fig. 6.6 is assumed flat and $S_I(0)$ can be approximated by $S_I(f \sim 15\,GHz)$.

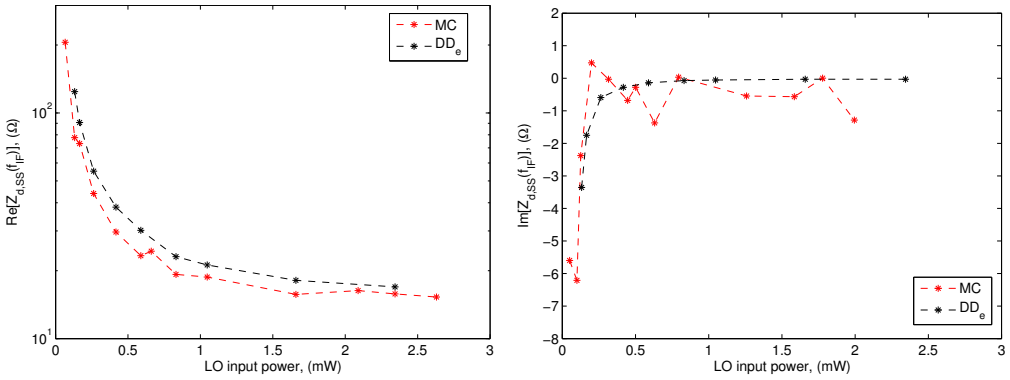

(a) (b)

Figure 6.8: (a) Real and (b) imaginary part of the small-signal impedance $Z_{d,SS}(f_{IF})$ for the 86-106 fundamental mixer at IF frequency 2 GHz under the large signal LO excitations at different powers.

flat-band conditions. Due to the stochastic nature of the MC model, it is necessary to simulate a large number of particles and periods of IF frequency to average over and obtain $Z_{d,SS}$ with the required accuracy. Due to the good agreement between MC and DD_e in Fig. 6.8, DD_e can be used instead of MC to calculate $Z_{d,SS}$.

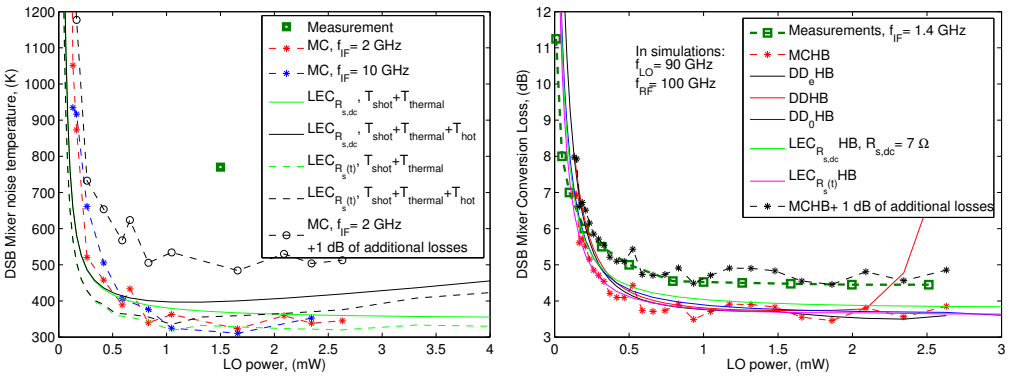

(a) (b)

Figure 6.9: Comparison of (a) the double side band equivalent input noise temperature of the mixer and (b) mixer conversion losses obtained with different diode models and measured results for the 86-106 GHz fundamental mixer [Ali93a].

Using $S_I(f_{IF})$ and $Z_{d,SS}(f_{IF})$ from Figs. 6.6 and 6.8 respectively, the IF load impedance of the circuit from Table 6.3 and the conversion loss of the mixer from DD_eHB with f_{IF}= 2 GHz, the equivalent input noise temperature of the mixer is evaluated using eqs. (6.5), (6.6) and (6.10), see Fig. 6.9. The equivalent input noise temperature obtained with the conversion matrix formalism is also included in Fig. 6.9. The values provided in [Ali93a] for L_{rf} and L_{if} (compiled in Table 6.3) have been used to evaluate the equivalent input noise temperature of the mixer, eq. (6.12).

A good agreement is observed for $T_{mix,DSB}$ obtained with MC and LEC (conversion matrix) because of the good agreement between the conversion losses predicted by these models 6.9(b) and because noise contribution due to hot electrons and intervalley transfer are of low importance for this mixer (low electric fields in the undepleted epilayer, see appendix F). Fig. 6.9(a) indicates that $T_{mix,DSB}$ is not affected by assuming f_{IF}= 10 GHz instead of 2 GHz, what supposes an important reduction in the MCHB simulation cost. When the series resistance is assumed time varying in

the conversion matrix formalism, the equivalent input noise temperature decreases showing a better agreement with MC than the model based on the constant $R_{s,dc}$. The decrease of the equivalent input noise temperature when $R_s(t)$ is used in the conversion matrix is due to the decrease of the conversion loss Fig. 6.9(b) and the decrease of the thermal noise contribution.

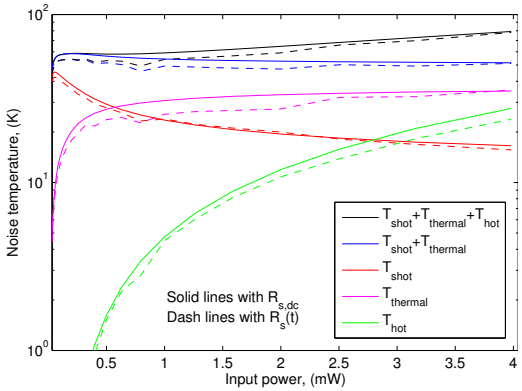

Figure 6.10: Contributions to the equivalent noise temperature (not referred to the input) of the diode in the 86-106 GHz mixer calculated with the conversion matrix formalism assuming a constant and a time varying series resistance.

Fig. 6.10 compares the different contributions to the equivalent noise temperature of the diode (not referred to the input, i.e., $T_{n,diode} = P_{del}/(k_B \Delta f)$, see eq. (E.50)) obtained assuming a constant R_s and a time varying $R_s(t)$ series resistance in the conversion matrix formalism, see appendix E. Shot and hot electron noise contributions are essentially the same with both models of series resistance, while the thermal noise contribution decreases slightly when $R_s(t)$ is assumed.

In the analysis of the conversion loss of this mixer, see Fig. 6.9(b) and appendix F, it was indicated that the discrepancies between measurements and simulations can be due to additional losses [Ali93a, Ali93b]. If additional losses between 1-2 dB are considered, see Fig. 6.9(b), their contribution to the noise of the mixer leads to a simulated $T_{mix,DSB}$ closer to measurements.

6.3.2 The 300-360 GHz sub-harmonically pumped mixer

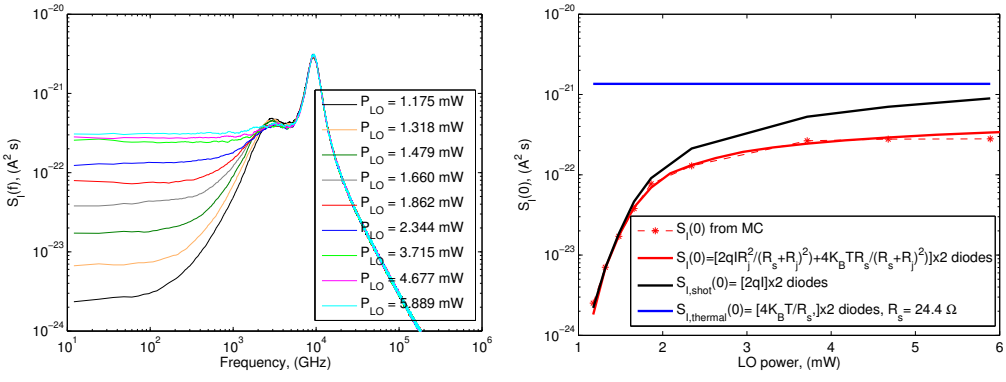

(a) (b)

Figure 6.11: (a) Current noise spectra at the terminals of the antiparallel diode pair in the 300-360 SHP mixer [Tho05], see Table 6.3, at different input powers with f_{IF}= 24 GHz (voltage waveforms from MCHB). (b) Comparison of $S_I(0)$ from MC with shot and thermal noise contribution from eq. (4.30) evaluated with $\text{LEC}_{R_{s,dc}}$ under the waveforms obtained with MCHB at f_{IF}= 24 GHz.

The current noise spectra of the sub-harmonically pumped (SHP) antiparallel diode pair in the 300-360 GHz mixer has been calculated using the MC model with the voltage waveforms from MCHB at f_{IF}= 24 GHz, see Fig. 6.11. Both diodes in antiparallel configuration have been simulated with the MC model to evaluate $S_I(f)$ of the total current.

In Fig. 6.11(b), $S_I(0)$ is approximated by shot and thermal noise contributions, eq. (4.30), evaluated with LEC$_{R_{s,dc}}$ under the waveforms obtained with MCHB at f_{IF}= 24 GHz, as was described for the 86-106 GHz mixer. The good agreement between MC and this analytical approximation for $S_I(0)$ indicates that the low frequency region of the noise spectra is determined by shot and thermal noise contribution and that hot electron noise is not very important in the performance of this SHP mixer.

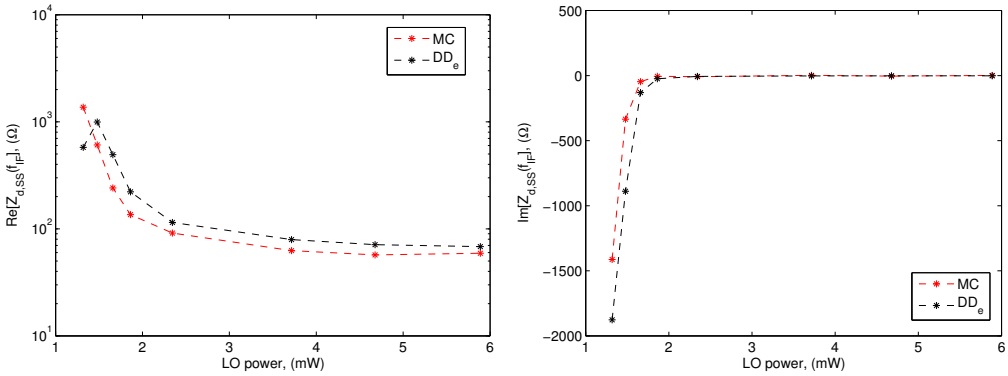

(a) (b)

Figure 6.12: (a) Real and (b) imaginary part of the small-signal impedance $Z_{d,SS}(f_{IF})$ of the antiparallel diode pair in the 300-360 GHz SHP mixer at IF frequency 24 GHz under the large signal LO excitations at different LO powers.

The small-signal impedance of the diode pair at f_{IF} = 24 GHz has been evaluated in Fig. 6.12 with MC and DD models. $Z_{d,SS}$ changes rapidly with LO power until flat band conditions are reached, at input powers higher than 2.5 mW.

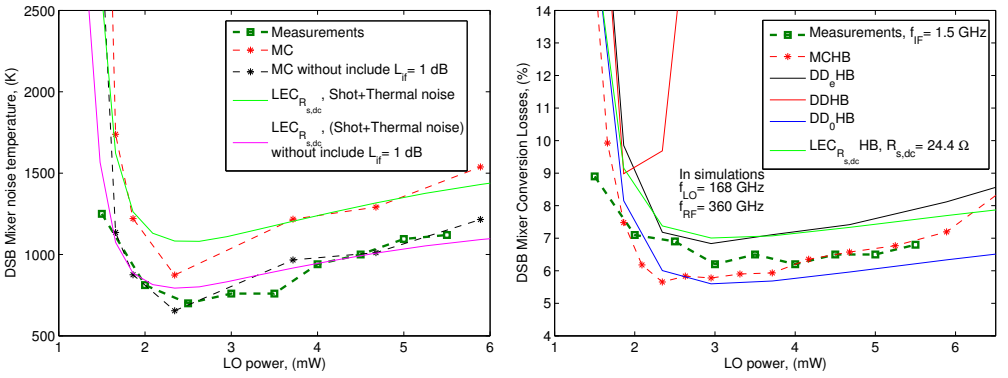

(a) (b)

Figure 6.13: Comparison of (a) the double side band equivalent input noise temperature of the mixer and (b) mixer conversion losses obtained with different diode models and measured results for the 300-360 GHz SHP antiparallel diode pair mixer [Tho05].

In Fig. 6.13, the equivalent input noise temperature of the SHP mixer has been evaluated using the data of Figs. 6.11 and 6.12. A good agreement is observed between measurements and simulated

results with MC when the losses L_{if}= 1 dB indicated in [Tho05] are not included in $T_{mix,DSB}$. $T_{mix,DSB}$ predicted by the conversion matrix formalism in Fig. 6.13 is in good agreement with the results from MCHB.

6.3.3 The 585-690 GHz fundamental mixer

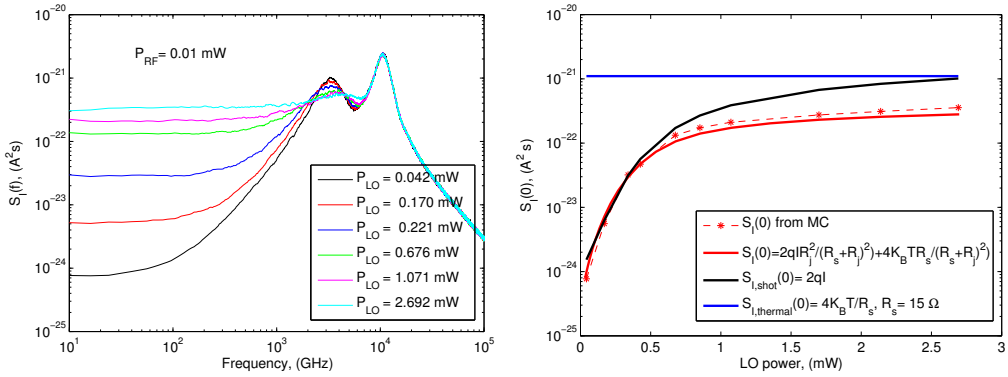

(a) (b)

Figure 6.14: (a) Noise spectra of the current fluctuations at the terminals of the diode in the 585-690 GHz fundamental mixer [Hes96, Hes97], see Table 6.3 (voltages waveforms from DD$_e$HB at f_{IF}= 2 GHz were used in the MC simulation of the noise spectra). (b) Comparison of the low frequency current noise spectra obtained with MC model in (a) and the shot and thermal noise contribution given by eq. (4.30) evaluated with LEC$_{R_s(t)}$.

Fig. 6.14(a) shows $S_I(f)$ for the diode in the 585 GHz fundamental mixer calculated with the MC model under the voltage waveforms obtained with DD$_e$HB at f_{IF}= 2 GHz. Fig. 6.14(b) shows a good agreement between $S_I(0)$ from MC with the shot and thermal noise contributions described by eq. (4.30), what indicates that hot electron noise is not important in the performance of this mixer, see appendix F.

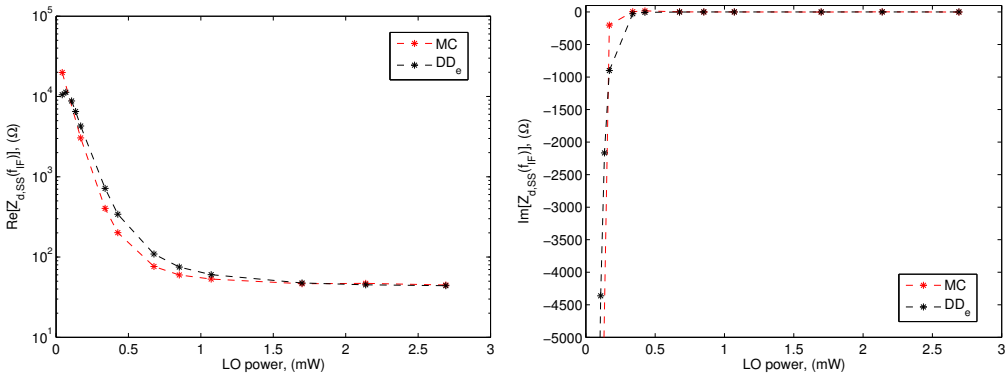

(a) (b)

Figure 6.15: (a) Real and (b) imaginary part of the small-signal impedance $Z_{d,SS}(f_{IF})$ for the diode in the 585-690 GHz fundamental mixer at IF frequency 2 GHz as a function of the LO power obtained with MC and DD$_e$ models.

The small-signal impedance of the diode calculated with MC and DD$_e$ in Fig. 6.15 and the noise spectra of Fig. 6.14 have been used to evaluate the equivalent input noise temperature of the receiver. Fig. 6.16(a) presents simulated and measured results for $T_{rec,DSB}$. Values of L_{qo},

L_{rf} and L_{if} provided by [Hes97], Table 6.3, have been used in the Friis' formula to evaluate the equivalent input noise temperature of the whole receiver, eq. (6.10). Due to the higher conversion losses obtained with LEC$_{R_{s,dc}}$HB than MCHB, Fig. 6.16(b), the noise temperature evaluated with the conversion matrix formalism (green curves) is higher than that obtained with MC. According to the model [Cro87] for hot electron noise integrated in the conversion matrix formalism, black lines in Fig. 6.16(a), this contribution becomes important at LO powers higher than 1 mW. However, the noise spectra obtained from MC simulations in Fig. 6.14(b) show a very good agreement with shot and thermal noise contributions indicating that hot electron noise contribution can be neglected. Besides, measured noise temperature remains nearly constant at LO power higher than 0.5 mW, what indicates that there is not hot electron noise. The discrepancies between measurements and MC can be explained because the bias point simulated is not the one considered in measurements ([Hes96] indicates that the bias point was optimized at each LO power to minimize the noise temperature). When higher bias point is considered (V_{bias}= 0.75 V for the dash-dot blue and the solid pink lines of Fig. 6.16(a)), the discrepancies between simulations and measurements are mitigated.

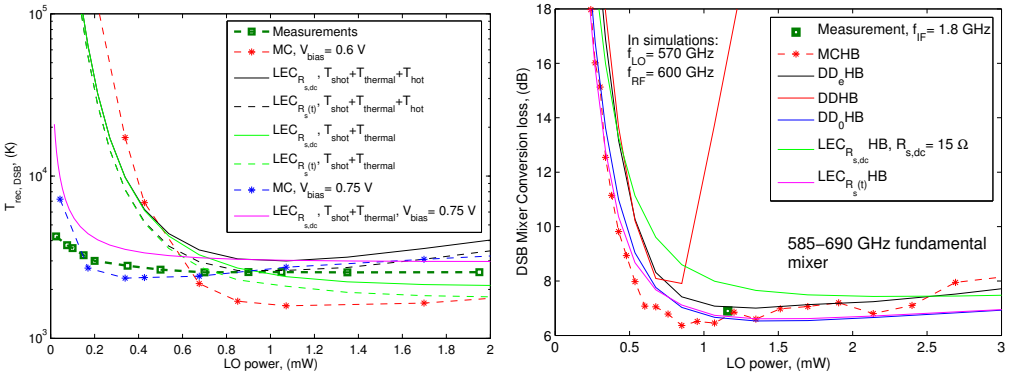

(a) (b)

Figure 6.16: Comparison of (a) the double side band equivalent input noise temperature of the receiver and (b) mixer conversion losses obtained with different diode models and measured results for the 585-690 GHz fundamental mixer [Hes97].

6.3.4 The 835-900 GHz fundamental balanced mixer

Fig. 6.17 presents the current noise spectra of the diode in the equivalent single diode circuit of the 835-900 GHz fundamental balanced mixer, obtained with the MC model of the diode excited by the voltage waveforms obtained from DD$_e$HB at f_{IF}= 5 GHz. The comparison of the low frequency region of the noise spectra from MC with the shot and thermal noise contribution from eq. (4.30) shows a good agreement, see Fig. 6.17(b).

The small-signal impedance of the diode in the equivalent single-diode circuit of the balanced mixer at f_{IF}= 5 GHz under the large-signal LO excitations at different LO powers has been calculated with MC and DD$_e$, see Fig. 6.18. The data from Figs. 6.17 and 6.18 are used to evaluate the equivalent input noise temperature of the mixers, eqs. (6.5), (6.6) and (6.12). Fig. 6.19 compiles the equivalent input noise temperature of the 835-900 GHz fundamental balanced mixer, obtained with MC and the conversion matrix formalism as a function of the total LO power (two diodes). To evaluate the noise temperature of the balanced pair of diodes, the equivalent single-diode circuit described in Fig. 6.4 has been simulated with the different models.

A good agreement is observed among the noise temperature evaluated with MCHB, LEC$_{R_{s,dc}}$HB and LEC$_{R_s(t)}$HB when only shot and thermal noise contributions are considered, since similar conversion losses are obtained with these models. The agreement is better when the series resistance is

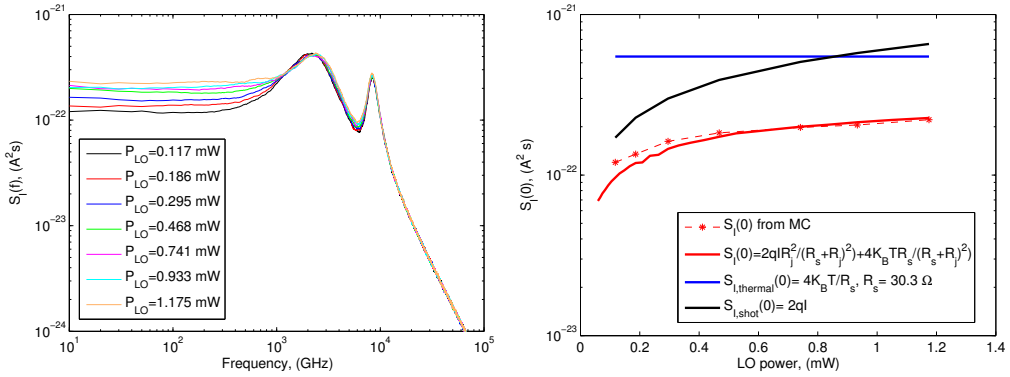

(a) (b)

Figure 6.17: (a) Current noise spectra at the terminals of the diode in the equivalent single-diode circuit of the 835-900 GHz fundamental balanced mixer [Tho10c], see Table 6.3, at different LO powers per anode (the voltages waveforms from DD$_e$HB at f_{IF}= 5 GHz were used in the MC simulation of the noise spectra). (b) Comparison of $S_I(0)$ from MC with shot and thermal noise contribution given by eq. (4.30), evaluated with LEC$_{R_s(t)}$, averaged in a IF period of the waveforms from DD$_e$HB.

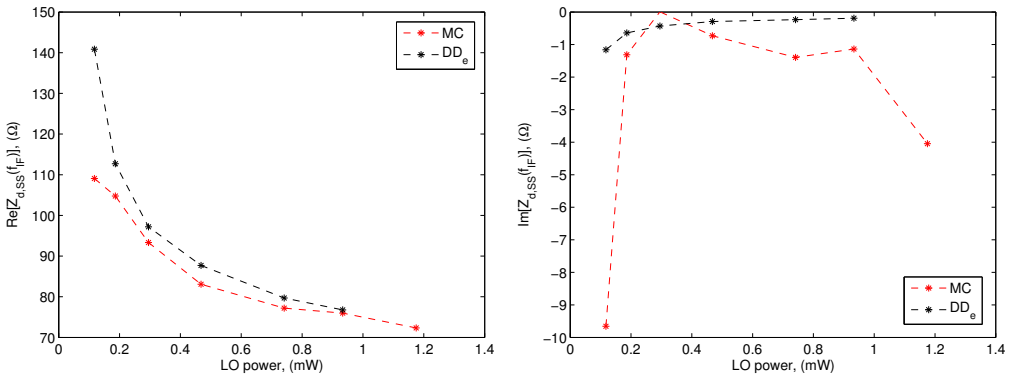

(a) (b)

Figure 6.18: (a) Real and (b) imaginary part of the small-signal impedance $Z_{d,SS}(f_{IF})$ of the diode in the equivalent single-diode circuit of the 835-900 GHz fundamental balanced mixer at IF frequency 5 GHz under the large signal LO excitation at different LO powers per anode.

assumed time varying in the LEC model. According to the results obtained with MC, hot electron noise contribution has a low impact on the performance of this mixer, see Fig. 6.17(b)[6]. The analytical model for hot electron noise (τ_ε= 1 ps, as is indicated in [Tho10c]) in the conversion matrix formalism overestimates this noise contribution as compared with MC results, see Fig. 6.19(a). The doping of these diodes is 5x10^{17} cm^{-3}, higher than considered in [Heg85, Cro87]. Hence, the energy relaxation time provided in [Heg85] for the hot electron noise model has to be updated using measured results or high level simulators like MC. Important discrepancies are observed between measured and MC simulated results in Fig. 6.19(a). Additional loss in the mixer around 1 dB could explain the underestimation of the noise temperature in simulations (blue curve in Fig. 6.19). In

[6]Despite of electric fields as high as 10 KV/cm in the undepleted region of the epilayer of this diode, see appendix F, the velocity-field loops of the electrons in this region can be approached by a constant low field electron mobility performance, due to nonstationary effects (overshoot of the electrons velocity), see chapter 3.1.5. Besides, the average kinetic energy of the electrons in the undepleted epilayer is nearly $3k_B$T/q (equilibrium conditions) for LO powers lower than 1 mW, see appendix F. At higher LO powers, the average kinetic energy increases with respect to the equilibrium value; however, such departure from equilibrium conditions is not very significant.

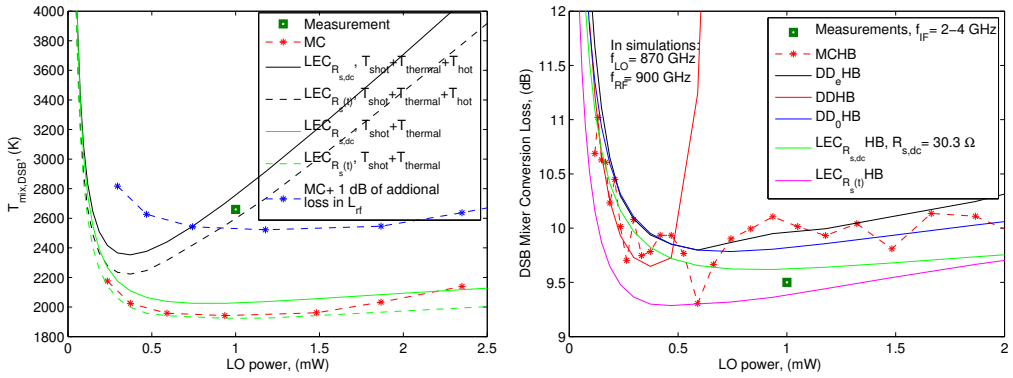

(a) (b)

Figure 6.19: Comparison of (a) the double side band mixer equivalent input noise temperature and (b) mixer conversion losses obtained with different diode models and measured results for the 835-900 GHz fundamental balanced mixer [Tho10c].

fact, in [Tho10c] it is indicated that if the mixer performances are corrected for IF external cables loss (0.64 dB), DSB mixer noise temperature drops to 2330 K. The good agreement observed between measured results and $\mathrm{LEC}_{R_s(t)}$ simulations when hot electron noise is considered is due to the overestimation of this noise contribution with the model in [Heg85, Cro87].

6.3.5 The 2.5 THz fundamental mixer

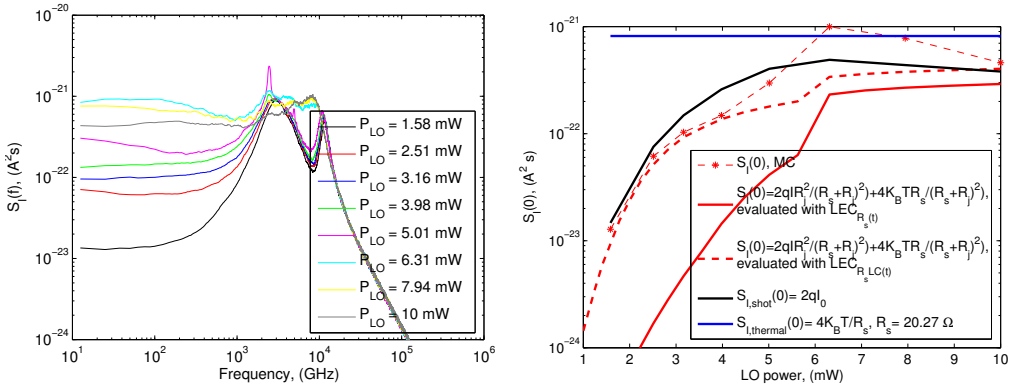

(a) (b)

Figure 6.20: (a) Current noise spectra at the terminals the diode in the 2.5 THz fundamental mixer [Sie99], see Table 6.3, at different LO powers (voltages waveforms from MCHB at f_{IF}= 25 GHz were used in the MC simulation of the noise spectra). (b) Comparison of $S_I(0)$ from MC with shot and thermal noise contribution given by eq. (4.30), evaluated with $\mathrm{LEC}_{R_s(t)}$ and $\mathrm{LEC}_{R_sLC(t)}$ averaged in an IF period of the waveforms.

The noise spectra of the 2.5 THz fundamental mixer are shown in Fig. 6.20. The waveforms obtained with MCHB at f_{IF}= 25 GHz have been considered in the noise evaluation of this mixer (the waveforms from DD$_e$HB at the IF frequency used in measurements f_{IF}= 8 GHz [Sie99] cannot be used to evaluate the noise temperature as was done in the analysis of other mixers, since DD$_e$HB is not reliable for this mixer, see section 6.2). At LO powers lower than 4 mW, shot noise is the most important contribution to the low frequency region of $S_I(f)$, as is shown in Fig. 6.20(b). At these frequencies, carrier inertia effects are very important in the performance of the mixer, and a

$LEC_{R_sLC(t)}$ model that takes into account this effect, is necessary to evaluate shot and thermal noise contribution given by eq. (4.30) and reproduce $S_I(0)$ from MC, see Fig. 6.20(b).

When the electric field is high enough for intervalley transfer to take place (P_{LO} higher than 3 mW, see appendix F), the stochastic transitions between the lowest (Γ) and upper valleys (L, X) of the semiconductor generate a new contribution to the noise spectrum with Lorentzian shape. The contribution of this noise component to the low frequency region of the noise spectrum is observed in Fig. 6.20(b) at P_{LO} higher than 4 mW as an increase of $S_I(0)$ from MC with respect to the analytical model for shot and thermal noise contribution. Under cyclostationary conditions, part of the low frequency noise generated by intervalley transfer is upconverted, generating a peak at the frequency of the excitation [Shi03b], as is observed in Fig. 6.20(a) at P_{LO} higher than 3.5 mW. As the LO power increases, more pronounced is this peak (P_{LO}= 5 mW). With the further increase of the LO power, i.e. with the increase of the electric field in the undepleted regions of the diode, the peak starts to decrease and shifts to higher frequencies and the low frequency region of the noise spectrum decrease, since most of the electrons are in the upper valleys (at P_{LO}= 6.3 mW, the occupation of the L and X valleys in the undepleted epilayer is around 70 % and 15 % respectively, and at higher LO power, the onset of the L-X intervalley transitions decrease the L valley occupation and increase the occupation of the X valley, see appendix F).

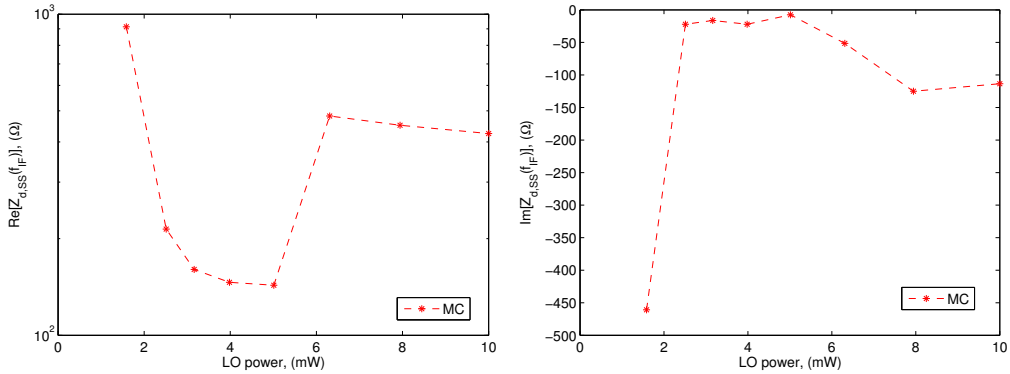

(a) (b)

Figure 6.21: (a) Real and (b) imaginary part of the small-signal impedance $Z_{d,SS}(f_{IF})$ at IF frequency 25 GHz under the large signal LO excitation at different powers.

The small-signal impedance of the diode calculated with MC is presented in Fig. 6.21. The real part of $Z_{d,SS}$ obtained from MC presents an abrupt increase due to the increase of the series resistance of the diode when the L-valley occupation is high (20 % at P_{LO}= 5 mW and 70 % at P_{LO}= 6.3 mW, appendix F).

Fig. 6.22 presents the equivalent input noise temperature of the receiver evaluated with the MC model and the conversion matrix approach (based on $LEC_{R_{s,dc}}$ and $LEC_{R_s(t)}$). $T_{rec,DSB}$ obtained with MC shows an abrupt increase at P_{LO} higher than 5 mW due to intervalley transfer, which affects the conversion loss, $Z_{d,SS}$, and the noise spectrum of the mixers as has been described. The noise temperature evaluated with the conversion matrix including shot and thermal noise shows a good agreement with MC at P_{LO} lower than 5 mW, when the intervalley transfer is of low importance in the performance of the mixer. At high LO powers, although the inclusion of the hot electron noise in the conversion matrix leads to noise temperature in good agreement with measured results, this model for hot electron noise is questionable: The transfer of electrons to the higher valleys eliminates the hottest electrons of the Γ valley, and, consequently, the rate of increase of the electron temperature due to hot electron is reduced near and above the input power when the intervalley transfer begins [Zir86, Fab95]. Hence, the results obtained with the LEC models in the conversion matrix formalism including hot electron noise model [Heg85, Cro87] are not valid. The noise contribution due to

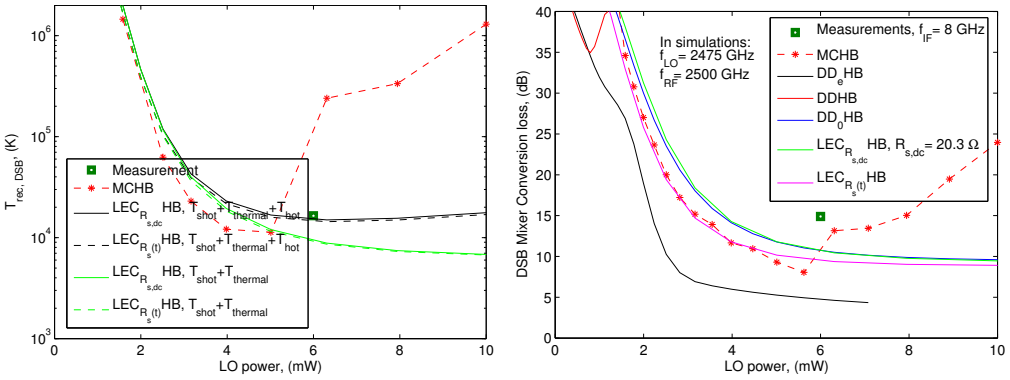

(a) (b)

Figure 6.22: Comparison of (a) the double side band receiver equivalent input noise temperature and (b) mixer conversion losses obtained with different diode models and measured results for the 2.5 THz mixer [Sie99].

intervalley transfer and its influence in hot electron noise have to be considered for accurate noise modelling at THz frequencies.

6.3.6 The 4.75 THz fundamental mixer

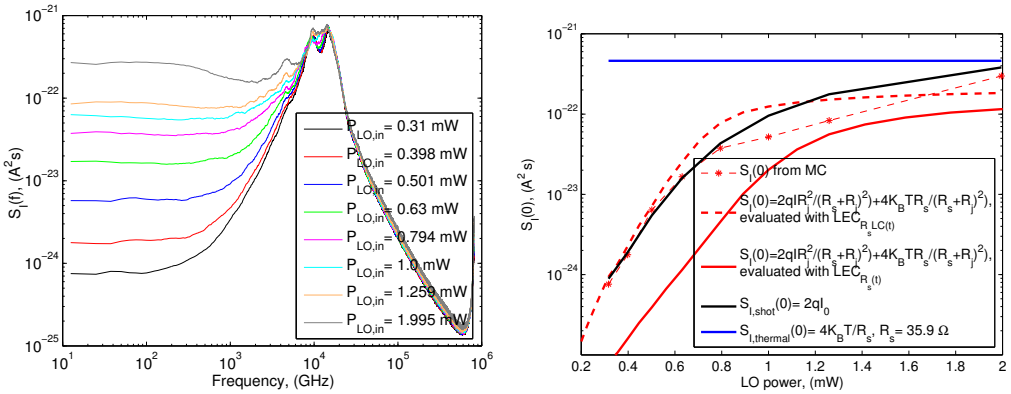

(a) (b)

Figure 6.23: (a) Current noise spectra at the terminals the diode in the 4.75 THz fundamental mixer [Bet96], see Table 6.3, at different LO powers (voltages waveforms from MCHB at f_{IF}= 25 GHz were used in the MC simulation of the noise spectra). (b) Comparison of $S_I(0)$ from MC with shot and thermal noise contribution given by eq. (4.30), evaluated with $\mathrm{LEC}_{R_s(t)}$ and $\mathrm{LEC}_{R_sLC(t)}$ averaged in an IF period of the waveforms.

Fig. 6.23 shows the noise spectra of the diode in the 4.75 THz fundamental mixer [Bet96] calculated with MC under voltage waveforms from MCHB at f_{IF}= 25 GHz. At LO powers lower than 0.5 mW, the low frequency region of the noise spectra is in agreement with the shot and thermal noise contribution given by eq. (4.30) evaluated with a $\mathrm{LEC}_{R_sLC(t)}$. However, for P_{LO} higher than 0.5 mW, the depletion region reaches the substrate of the diode, and the results from our implementation of the $\mathrm{LEC}_{R_sLC(t)}$ are not reliable, see appendix F. At 0.63 mW, the occupation of the L-valley is nearly 5 % and a peak at the excitation frequency appears in the noise spectra and rise at higher LO powers, as described for the 2.5 THz mixer (noise contribution due to intervalley transfer). Due to the nonlocal dynamics of the electron transport in the short epilayer of the diode (this is discussed

in detail in section 6.4.3), intervalley transfer in the undepleted epilayer is highly mitigated (the occupation of the L valley is lower than 25 % at P_{LO}= 2 mW) and its influence in the noise spectra is not as important as was observed for the 2.5 THz mixer (L_e= 100 nm and L valley occupation is close to 70 % at P_{LO}= 6.3 mW for the 2.5 THz fundamental mixer).

Although the doping of the substrate and the epilayer of this mixer are the same of the diode in the 2.5 THz mixer, the RC and the HP peaks are shifted to higher frequencies due to the shorter epilayer and substrate lengths of the diode in the 4.75 THz mixer, see chapter 4.

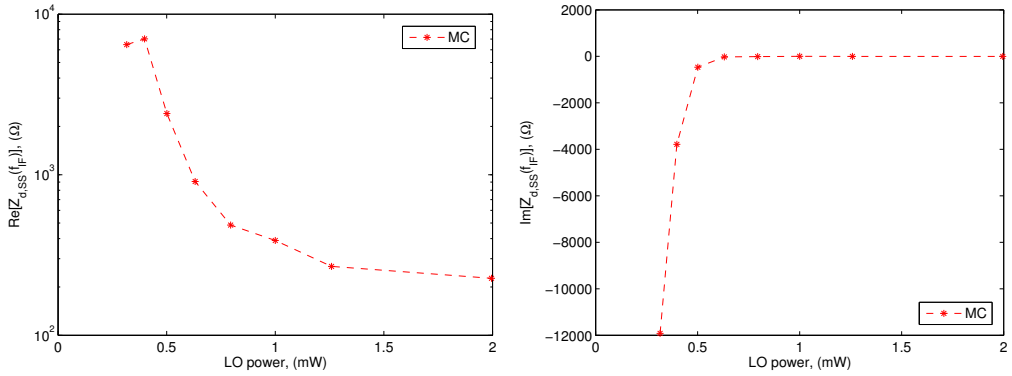

(a) (b)

Figure 6.24: (a) Real and (b) imaginary part of the small-signal impedance $Z_{d,SS}(f_{IF})$ at IF frequency 25 GHz under the large signal LO signal at different input powers.

The small-signal impedance of the diode calculated with MC is shown in Fig. 6.24. Since the occupation of the upper valleys is highly mitigated in the 5 THz mixer, the real part of $Z_{s,DD}$ does not show the abrupt increase observed in Fig. 6.21(a) for the 2.5 THz mixer.

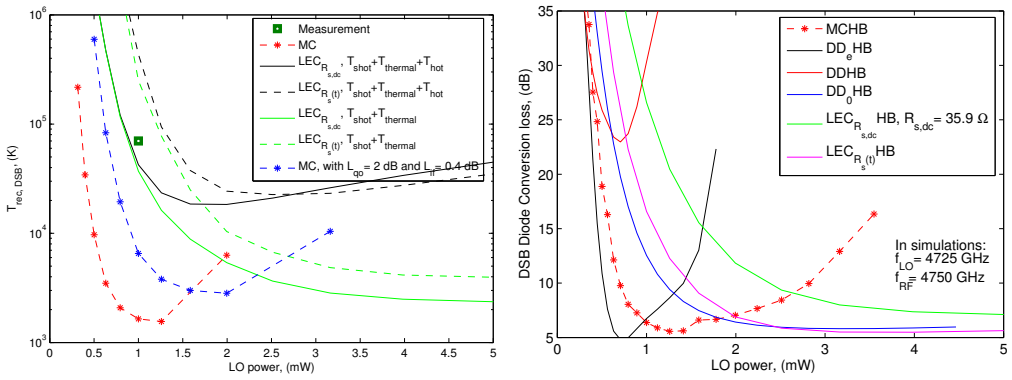

(a) (b)

Figure 6.25: Comparison of (a) the double side band receiver equivalent input noise temperature and (b) diode conversion losses (there are not published data of the conversion losses, L_{op}, L_{rf} and L_{if} for this mixer [Bet96]) obtained with different diode models and measured results for the 4.75 THz mixer [Bet96].

In Fig. 6.25, the equivalent input noise temperature has been evaluated using the MC and the conversion matrix formalism. The equivalent input noise temperature obtained with the conversion matrix formalism is affected by the inability of $\text{LEC}_{R_{s,dc}}$HB and $\text{LEC}_{R_s(t)}$HB to model this high frequency mixer. These models do not account for intervalley transfer effects that are important in the performance of this mixer and interfere with hot electron noise contribution. Since there is not published data for L_{op}, L_{rf} and L_{if} [Bet96], $T_{rec,DSB}$ from MC is lower than measurements. Using the

values provided for these parameters in the 2.5 THz fundamental mixer [Sie99], a better agreement is observed (dash-dot blue line in Fig. 6.25(a)). According to the dependence on the frequency of the measured noise temperature of mixers in Fig. 6.1(a) ($\sim 50h\nu/k_B$), the expected noise temperature of this mixer should be around 20000 K, value which is in good agreement with the results from MC in Fig. 6.25(a). The measured noise temperature of this receiver is 70000 K, more than three times the expected value. However, the expected noise temperature $50h\nu/k_B$ K is for the mixer noise temperature while the measured result in [Bet96] is for the receiver noise temperature. Accurate information about the parameters L_{op}, L_{rf} and L_{if}, mismatch of the elements of the mixer, coupling of the LO plus RF beam with the Schottky mixer, absorption from the air, etc. are necessary to interpret the origin of the discrepancies between measurements and the expected noise temperature.

6.3.7 Conclusions about noise in mixers

The most relevant results from the analysis of the noise temperature carried out are summarized in the following items:

- At RF frequencies lower than 1 THz, the low frequency region of the noise spectra (where IF frequencies usually are) of current fluctuations at the terminals of the diodes is determined by shot and thermal noise contributions.
- The evaluation of these contributions with the conversion matrix approach is highly affected by the accuracy of the LEC model considered: using a $\text{LEC}_{R_{s,dc}}$, the noise temperature is overestimated since this model overestimates the series resistance of the diode, i.e. the conversion loss. Noise temperature evaluated with a time varying series resistance shows a better agreement with the results obtained with MC up to RF frequencies around 1 THz.
- The evaluation of the noise contribution due to hot electron using the equations in [Heg85, Cro87], that are easily integrated in the conversion matrix formalism, is overestimated, since the model in [Heg85, Cro87] depends on the energy relaxation time τ_ε, that is used as an empirical parameter. τ_ε depends on the energy of the electrons in the device, i.e. τ_ε has to be modeled as a function of the operation conditions, epilayer doping concentration and epilayer length. Also the hot electron noise model depends on the square of the current in the diode, eq. (E.42). Hence, for a consistent evaluation of this noise model, the diode model has to describe high field transport effects like velocity saturation and nonstationary effects.
- Results from Monte Carlo simulations indicate that intervalley transfer generates an important noise contribution at frequencies higher than 1 THz. When this phenomenon appears, the model for hot electron noise evaluated with the simple LEC models cannot be applied, since the hottest electrons are transferred to the upper valleys, decreasing hot electron noise contribution.
- Adequate values for the epilayer length as a function of the signal frequency and the LO power is mandatory to get optimum results. This will be shown in the following section.

6.4 Optimization of the noise temperature in mixers

This section presents an investigation about the impact of the parameters of the diode and the circuit impedances on the noise of the mixers. It is expected that the conditions that minimize the noise temperature do not correspond to the minimum conversion loss of the mixer [Cro87, Hes97, Maa05].

In this analysis, the equivalent noise temperature of the diode $T_{n,diode}$ is evaluated instead of the equivalent input noise temperature T_d, eq. (6.6), since the performance of T_d is affected by

the performance of the conversion loss, while $T_{n,diode}$ informs exclusively about the noise power delivered to the IF load:

$$T_{n,diode} = \frac{P_{del}}{k_B \Delta f}. \tag{6.13}$$

For RF frequencies lower than 1 THz, the conversion matrix formalism based on the simple lumped equivalent circuit model has been considered. Although the accuracy of this model is limited according to the results in previous section, it is not expected to significantly affect the general trends analysed in this section. At higher RF frequencies, the impact of the intervalley transfer into the noise temperature can be important, and the results obtained with the conversion matrix formalism are not reliable. Therefore, the MC model has been used.

Firstly, an analysis of the equivalent noise temperature, eq. 6.13, as a function of the RF circuit impedance is carried out for the mixers described in Table 6.3 at RF frequencies lower than 1 THz. In this analysis, the LO and the IF impedances are those presented in Table 6.3. An analysis of the noise temperature with the thickness and doping concentration of the epitaxial layer and the anode area is also carried out. The section ends with an analysis of the performance of Schottky mixer above 2 THz, using the MCHB tool.

6.4.1 Impact of the circuit impedance

Fig. 6.26 presents the diode conversion loss $L_{d,DSB}$ eq. (6.1) and the diode noise temperature $T_{n,diode}$ eq. (6.13) as a function of the RF circuit impedance for the mixers described in Table 6.3 at RF frequencies lower than 1 THz. The conversion matrix formalism based on the $\text{LEC}_{R_{s,dc}}$ model has been used to obtain these results. Hot electron noise contribution has not been included in this figure, since according to the analysis in previous section, it is not important in the performance of these mixers. The figure shows that the impedances that minimize the conversion losses are close to the conjugate impedance of the diode at the RF frequency[7]. It is also observed in Fig. 6.26 that the impedances that minimize the conversion losses are different from those which minimize the noise temperature of the diodes. However, the low sensitivity observed in the Fig. 6.26 for both the noise temperature and the conversion loss, let us to determine an optimum RF circuit impedance that is close to the minimum of $T_{n,diode}$ and L_d.

6.4.2 Impact of the parameters of the diode

Fig. 6.27 shows an analysis of the conversion loss L_d and noise temperature $T_{n,diode}$ of the diodes for the mixers described in Table 6.3 as a function of the epilayer length L_e, doping concentration N_e and anode area A. The equivalent input noise temperature T_d is also presented in this figure. The simulation tool used for this task is the same used in Fig. 6.26. For each individual curve, one diode parameter is varied independently while the others are held at the nominal values indicated in Table 6.3. L_d, $T_{n,diode}$ and T_d in Fig. 6.27 have been evaluated at the LO power for minimum L_d in a LO power swept. Note that $T_{n,diode}$ increases when the LO power increases[8]. Since the minimum of L_d occurs in the vicinity of flat-band conditions, the combined shot and thermal noise contribution determines the performance of $T_{n,diode}$. According to the comparison with MC simulation results, hot electron noise contribution can be neglected at these RF frequencies. The most important conclusions obtained from the analysis of Fig. 6.27 are:

- When L_e increases, the series resistance of the diode increases, what degrades the conversion loss of the diode. Also $T_{n,diode}$ increases, due to the increase of the thermal noise contribution (for a linear resistance $\overline{v_t^2} = 4k_BTR_s\Delta f$, see eqs. (4.18) and (E.24)), as can be observed in

[7] The RF port should not in general be conjugate matched for minimum conversion loss [Hel78a]

[8] The minimum of equivalent input noise temperature T_d eq. (6.6) is reached at LO powers in the vicinity of the minimum of the conversion losses since $T_d = T_{n,diode}\dot{L}_d$

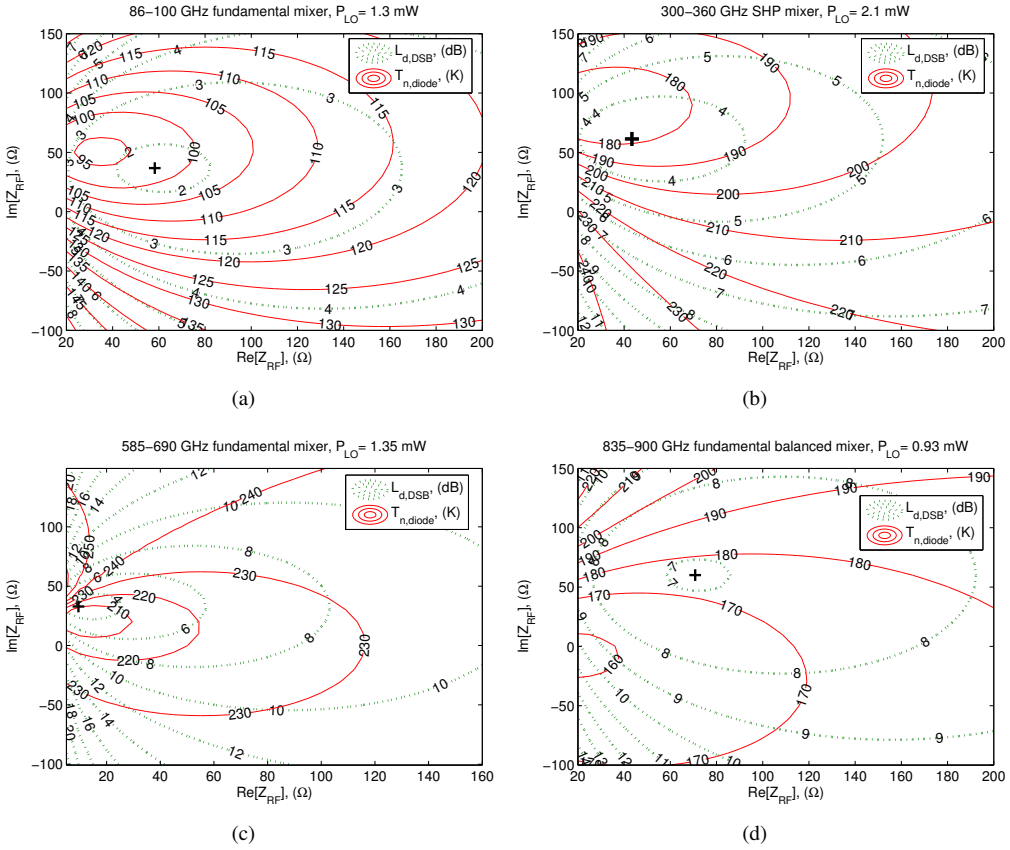

Figure 6.26: Contours of constant conversion loss and equivalent noise temperature eq. (6.13) for the mixers described in Table 6.3 as a function of the RF circuit impedance. The cross (+) represents the conjugate impedance of the diode at the RF frequency (parasitic capacitances indicated in Table 6.3 are considered as part of the diode impedance). The impedances at LO and IF frequencies and the bias point are those indicated in Table 6.3. The LO power considered for each mixer has been selected close to the minimum conversion loss in Fig. 6.5. Results obtained with the LEC$_{R_{s,dc}}$ model in the conversion matrix formalism.

Fig. 6.28 that shows the different contributions to the noise temperature for the 835-900 GHz fundamental balanced mixer. Shot noise contribution slightly varies when L_e changes and hot electron noise is nearly constant.

- The dependence of L_d on N_e presents a minimum, that results from the competition of the decrease of the series resistance and the increase of the nonlinear capacitance when N_e increases. The increase of the junction capacitance degrades L_d due to the shunting effect by the junction capacitance. $T_{n,diode}$ decreases when N_e increases, due to the decrease of the thermal noise contribution when the series resistance decreases, see the performance of this noise contribution in Fig. 6.28. On the other hand, shot noise contribution increases when N_e increases. The simulations in Fig. 6.27 have shown that the dc current slightly decreases when N_e increases. But according to eq. (4.30), shot noise contribution is affected by the inverse of the series resistance of the diode. Since for the LO powers considered in Fig. 6.27 the diodes are working in the vicinity of flat band conditions, the series resistance of the diodes is important in the performance of shot noise contribution. Due to the decrease of the series resistance when N_e increases, shot noise contribution increases.

- For low doping concentrations hot electron noise is expected to increase the noise level, see Fig. 6.28, due to the generation of high electric fields in the undepleted region of the epilayer.

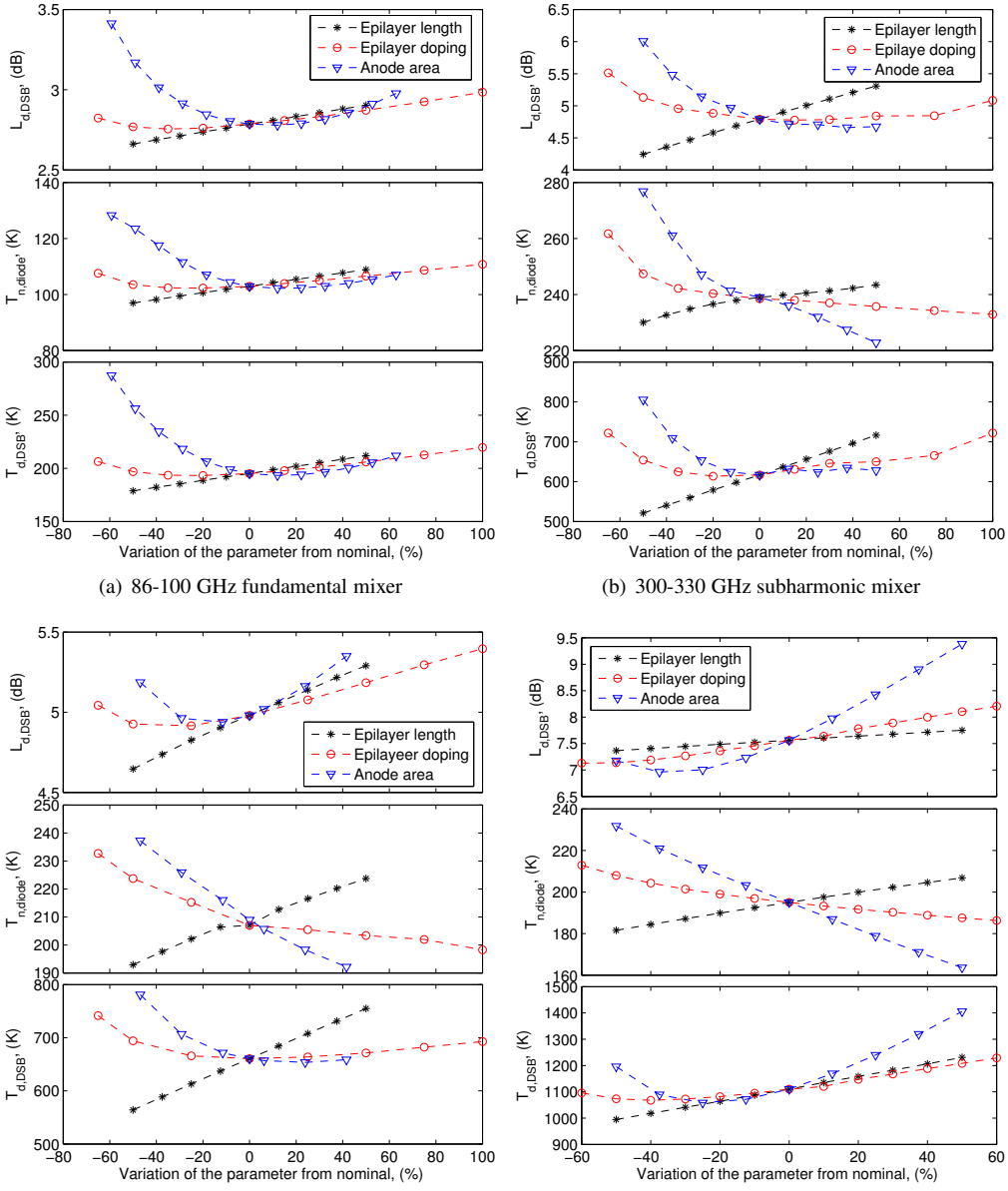

(a) 86-100 GHz fundamental mixer

(b) 300-330 GHz subharmonic mixer

(c) 585-690 GHz fundamental mixer

(d) 835-900 GHz fundamental balanced mixer

Figure 6.27: Noise temperature and conversion loss for the mixers described in Table 6.3 evaluated at the P_{LO} for minimum L_d as a function of the epilayer length, doping concentration and anode area. These results have been obtained with the conversion matrix formalism based on $\text{LEC}_{R_{s,dc}}$. Hot electron noise contribution has not been considered.

- Decreasing the anode area, decreases the junction capacitance, but increases the series resistance. Hence, the dependence of L_d on A is similar to its dependence on N_e [9].

- Fig. 6.27 shows that $T_{n,diode}$ increases when the anode area A decreases: Thermal noise contribution increases due to the increase of the series resistance. Shot noise decreases due to the

[9] As the operation frequency increases, the available LO power decreases, and it is necessary to reduce the anode area to properly pump the mixer diode. Also, the anode area plays an important role in the matching of the diode and its RF circuit. A collateral effect of reducing the anode area is an increase in the optimum input and output impedances of the design, leading to easier-to-synthesize impedance matching networks in practice [Cro92].

decrease of the conduction current. For a given LO power, when the anode area decreases, the voltage swing at the terminals of the diode increases what is expected to increase the electric field inside the device, and, hence, the hot electron noise contribution (according to hot electron noise model eq. (E.43), the constant K is inversely proportional to the square of the anode area, hence, this noise contribution is expected to increase when A decreases).

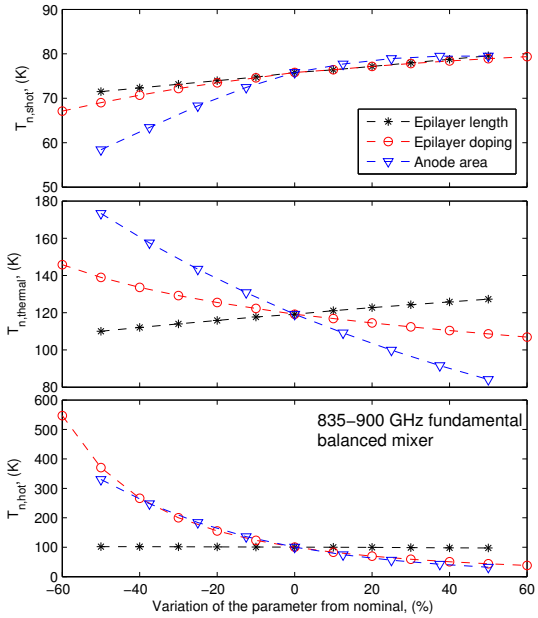

Figure 6.28: Shot, thermal and hot electron nosie contributions to the total noise of the 835-900 GHz fundamental balanced mixer described in Table 6.3, evaluated with the conversion matrix formalism based on $\mathrm{LEC}_{R_{s,dc}}$ at the LO power for minimum L_d in a LO power swept.

Mixer diodes typically have shorter epilayer length and greater doping concentration than varactor diodes, and velocity saturation effects are expected to be less important in mixers. However, for frequencies high enough, velocity saturation effects become important in the performance of mixers [Cro92]. Simple LEC models are not able to account for velocity saturation, and tools like DD_eHB and MCHB become essential for the accurate design of mixers. In the previous section, MC shown that velocity saturation leads to the increase of the conversion loss and the noise temperature. The following section shows that high doping concentration and low epilayer thickness mitigate these effects.

6.4.3 Optimization of the 2.5 THz fundamental mixers

In section 6.3.5, it was shown that the high occupation of the upper valleys in this diode leads to an important increase of the conversion losses and the noise temperature of the mixer. To avoid these effects, a shorter epilayer length has been considered. It will be shown that nonlocal transport in a short epilayer mitigates intervalley transfer. The epilayer length has been set to 30 nm, like that in the 4.75 THz mixer [Bet96], while the other parameters of this mixer have been kept unaltered, Table 6.3. The conversion losses of the 2.5 THz fundamental mixer with the two values of epilayer length (100 nm given in [Sie99] and 30 nm) are shown in Fig. 6.29, calculated with MCHB.

As was explained in section 6.2, the abrupt increase of the conversion losses of the 2.5 THz mixer with L_e= 100 nm at $\mathrm{P}_{LO} \sim 6$ mW is originated by the increase of the upper valleys population

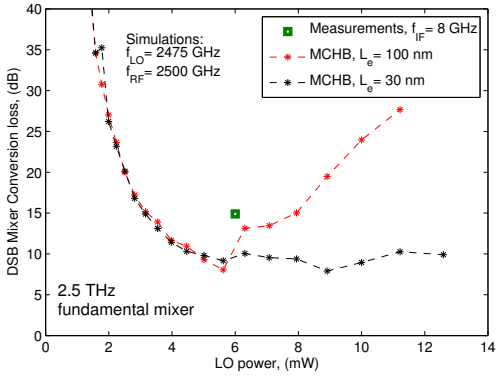

Figure 6.29: Conversion loss of the 2.5 THz fundamental mixer described in Table 6.3 with L_e= 100 nm and 30 nm, obtained with MCHB at f_{IF}= 25 GHz.

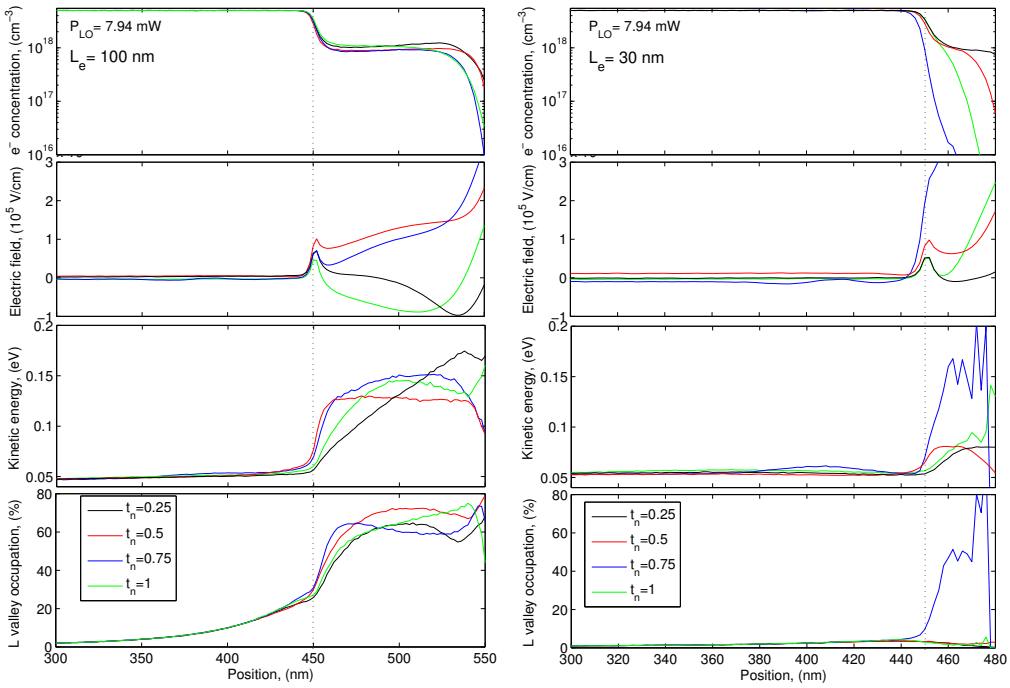

(a) (b)

Figure 6.30: Profiles of the electron concentration, the electric field, the electron energy and the occupation of the L valley for the 2.5 THz mixer with (a) L_e= 100 nm and (b) L_e= 30 nm, obtained with MC.

of the semiconductor in the undepleted region of the diode[10]. When L_e is set to 30 nm, this abrupt increase of the conversion loss disappears. Fig. 6.30 shows different profiles of the 2.5 THz mixer for the two values of L_e at an LO power of 8 mW. The electrons in the substrate (low field region) enter in the epilayer (high field region), where they move with a velocity higher than expected from the equilibrium velocity field curve (nonlocal effects, see section 3.1.1). Due to the short epilayer length of the diode with L_e= 30 nm, the electrons are able to cross the epilayer without suffering

[10]For the mixer with L_e= 100 nm, the occupation of the L valley is around 5 % in the undepleted epilayer at P_{LO}= 2.5 mW and increases as P_{LO} increases, reaching $\sim$ 20 % at 5 mW; at higher LO power, the population of the L valley increases quickly, reaching 60 % at $P_{LO} \sim$ 6.3 mW. Also, the transfer to the X valley increases abruptly when the LO power increases from 5 mW to 6.3 mW, rising from occupations lower than 5 % to 20 %, see appendix F

scattering mechanisms (ballistic transport), hence, most of the electrons remain in the lower valley, see Fig. 6.30. However, when L_e= 100 nm, the motion of the electrons in the epilayer is not ballistic and they gain energy enough from the electric field to be transfered to the upper valleys, see Fig. 6.30 where the L valley occupation for L_e= 100 nm and 30 nm are around 60 % and 5 % respectively.

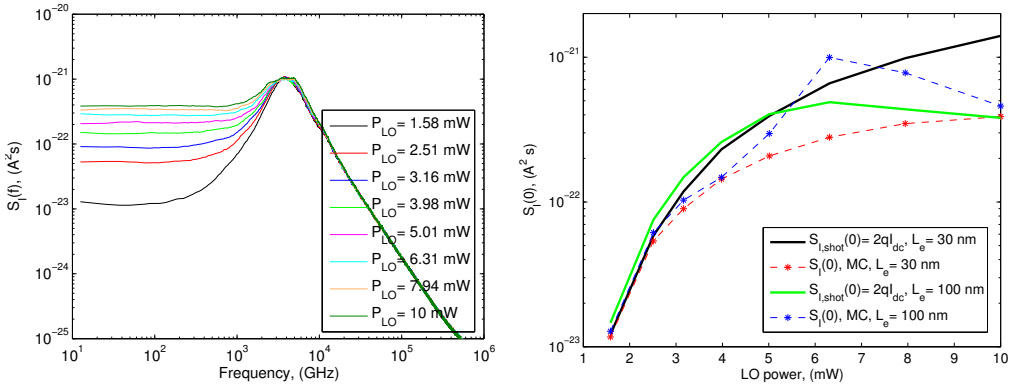

(a) (b)

Figure 6.31: (a) Current noise spectra at the terminals the diode in the 2.5 THz fundamental mixer based on the diode with L_e= 30 nm, at different LO powers (voltages waveforms from MCHB at f_{IF}= 25 GHz were used in the MC simulation of the noise spectra). (b) Comparison of $S_I(0)$ from MC with shot noise contribution (I_{dc} obtained with the MC model) for the 2.5 THz mixer based on the diodes with L_e= 30 nm and 100 nm.

The current noise spectra of the diode with L_e= 30 nm in the 2.5 THz mixer is presented in Fig. 6.31, calculated with MC for the waveforms obtained with MCHB at f_{IF}= 25 GHz. The typical peaks associated to the intervalley transfer observed in Fig. 6.20 when L_e= 100 nm are not observed in Fig. 6.31(a) due to the low occupation of the upper valleys. The comparison of $S_I(0)$ for the 2.5 THz mixer with the two values of L_e in Fig. 6.31(b) shows clearly the important contribution of intervalley transfer noise to the low frequency region of the noise spectrum.

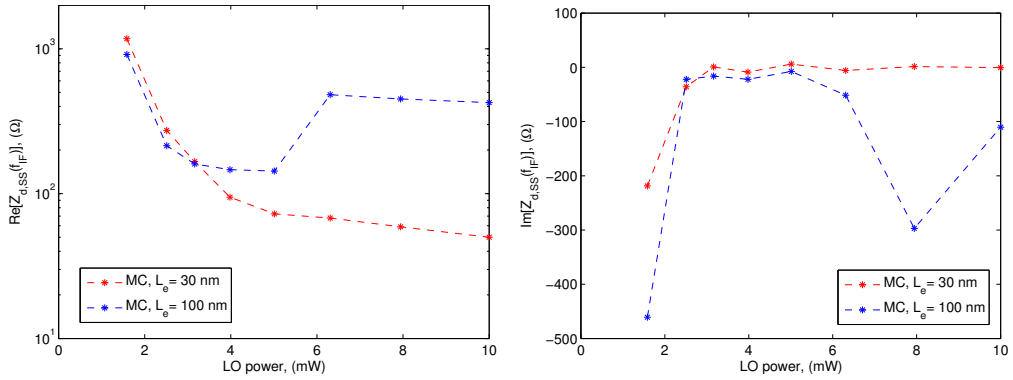

(a) (b)

Figure 6.32: (a) Real and (b) imaginary part of the small-signal impedance $Z_{d,SS}(f_{IF})$ for the 2.5 THz mixer with L_e= 30 nm and 100 nm at IF frequency 25 GHz, under the large signal LO excitation at different input powers.

Noise spectra in Fig. 6.31(a) present the RC peak with a central frequency similar to those for the case with L_e= 100 nm in Fig. 6.20(a). However, the HP peak is not observed when L_e= 30 nm Fig. 6.31(a), due to the decrease of the amplitude of HP peak when L_e decreases and the substrate length is much larger than L_e (this performance has been observed with the analytical model presented in

chapter 4).

Fig. 6.32 compares the small-signal impedance of the diodes $Z_{d,SS}$ in the 2.5 THz mixer with the two values of epilayer length considered. The abrupt increase of the real part of the $Z_{d,SS}$ at $P_{LO} \sim$ 6.3 mW for the mixer with L_e= 100 nm is avoided by using L_e= 30 nm.

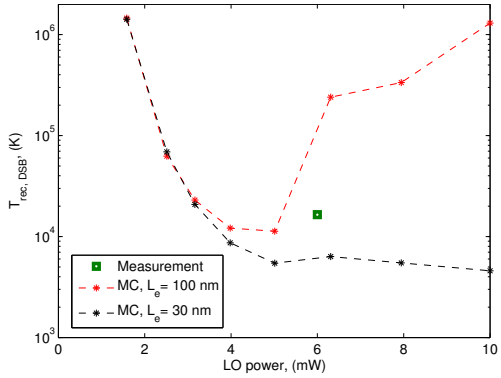

Figure 6.33: Double side band equivalent input noise temperature the 2.5 THz receiver for diodes with L_e= 30 nm and 100 nm, obtained with the MC model.

Fig. 6.33 shows that an important decrease of the equivalent input noise temperature of the mixer is obtained when intervalley transfer effects are mitigated using L_e= 30 nm.

6.5 Schottky mixers above 2 THz

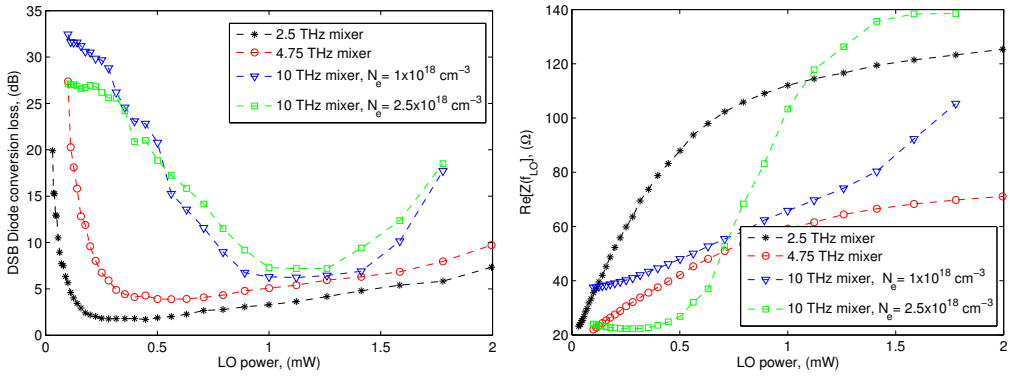

(a) (b)

Figure 6.34: Comparison of (a) the diode conversion losses and (b) the real part of the diode impedance at the LO frequency for the 2.5 THz, 4.75 THz and the 10 THz fundamental mixers, all of them based on the diode for the 4.75 THz mixer described in Table 6.3. The 10 THz mixer has been also simulated with epilayer doping 2.5x10^{18} cm^{-3}. Results obtained with MCHB.

To conclude this chapter, a comparison of the performance of single-ended fundamental mixers at RF above 2 THz is presented based on MC simulation results. The diode described in Table 6.3 for the 4.75 THz mixer [Bet96] has been used for all the mixers in this section. The circuit impedances at the RF and LO frequencies have been conjugately matched for each LO power considered, while the IF impedance has been set to 250 Ω in all the designs (to optimize the conversion loss at an available LO power of 1 mW, see Table 6.3). Since there are not published data about the losses

L_{op}, L_{rf}, and L_{if} at RF frequencies higher than 2.5 THz, diode conversion loss and diode equivalent input noise temperature have been evaluated.

Fig. 6.34(a) shows the diode conversion loss of the 2.5 THz, 4.75 THz and 10 THz fundamental mixers simulated with MCHB as indicated. When the signal frequency is increased, both the minimum conversion loss and the LO power to achieve this minimum conversion loss increase. This degradation of the conversion loss is due to shunting effect of the junction capacitance (C_j) over the junction resistance (R_j) of the diode [Cro92]. Since the IF is generated by the nonlinear resistance of the junction, it is necessary to maximize the modulation of this resistance in order to minimize the conversion loss. The voltage swing over the nonlinear resistance is controlled by the Schottky junction internal impedance Z_j:

$$Z_j = \frac{R_j - j\omega C_j R_j^2}{1+(\omega C_j R_j)^2} \tag{6.14}$$

In the ideal case without shunting effect of the capacitance, the junction capacitance should be 0, and $Z_j = R_j$. Hence, the closer $\mathrm{Re}[Z_j]$ to R_j, the lower the shunting effect of the capacitance:

$$Re[Z_j] = \frac{R_j}{1+(\omega C_j R_j)^2}. \tag{6.15}$$

Fig. 6.34(b) shows the real part of the diode impedance Z_d of the mixers. When the signal frequency is increased from 2.5 THz to 4.75 THz, the real part of the diode impedance decreases according to the contribution of the junction impedance given by eq. (6.15). But when the signal frequency is increased to 10 THz, $\mathrm{Re}[Z_d]$ increases due to plasma effects in the undepleted epilayer (according to eq. (3.8), f_{pe}= 9.6 THz). Increasing the epilayer doping to 2.5x10^{18} cm^{-3} for the 10 THz mixer, plasma effects are shifted to higher frequencies and the $\mathrm{Re}[Z_d]$ decreases in Fig. 6.34(b). However, the nonlinear capacitance of the Schottky junction increases when N_e increases, what increase shunting effects. Hence, the conversion losses of the 10 THz mixer with N_e= 2.5x10^{18} cm^{-3} are higher than with the doping concentration 1x10^{18} cm^{-3}, as it is shown in Fig. 6.34(a) from MCHB.

Under conjugate matching conditions, the effective voltage V_{eff} that modulates the nonlinear resistance of the Schottky junction is given by:

$$V_{eff} = \sqrt{\frac{2P_{av}Z_j^2}{\mathrm{Re}[Z_s]+\mathrm{Re}[Z_j]}} \tag{6.16}$$

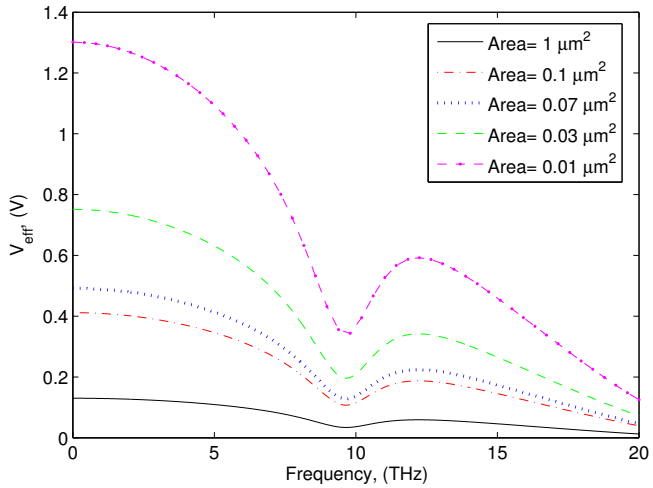

Figure 6.35: Effective voltage applied to the junction resistance eq. (6.16) as a function of the frequency and the anode area. The parameters of the reference diode in this section has been considered: P_{av}= 1 mW, $C_{j,0}$= 0.25 fF, R_j= 150 Ω evaluated in the vicinity of flat band, (parameters evaluated are referred to the anode area 0.07 μm^2), characteristics of the epilayer and substrate described in Table 6.3 for the 4.75 THz mixer.

where Z_s represents the impedance associated to the substrate and the undepleted epilayer (R_sLC circuit of Fig. 2.7) and P_{av} represents the available power at the input. From eqs. (6.14) and (6.16), it can be deduced that an increase of the signal frequency results in the decrease of V_{eff} due to shunting effect. Fig. 6.35 shows the evolution of the effective voltage as a function of the frequency. It can be observed that the effective voltage decreases when the signal frequency increases, and a larger percentage of input power will be dissipated in the series resistance [Cro92]. Hence, a large input power is necessary to maintain a proper modulation of the junction resistance. At frequencies close to the plasma frequency, the series resistance of the diode increases, increasing the voltage drop in the undepleted epilayer and leading to a further decrease of V_{eff}.

The shunting effect cannot be avoided by changing the anode area since the product R_jC_j is constant. However, it has been demonstrated experimentally that reducing the anode area at high frequencies mitigates the shunting effect [Cro92]. When the anode area is decreased, R_j increases and Z_j is maximized. Thereby, the modulation of R_j increases as is observed in Fig. 6.35, and the minimum conversion loss is achieved at lower LO powers.

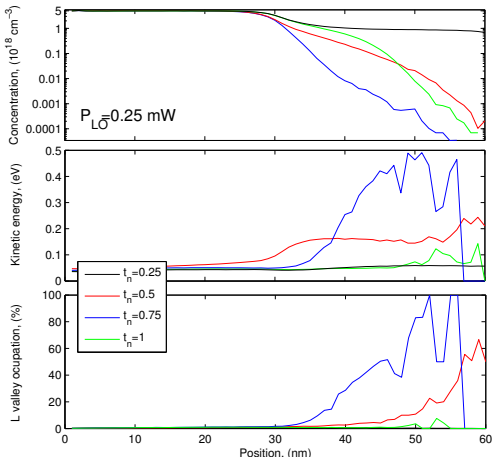

(a) 2.5 THz fundamental mixer

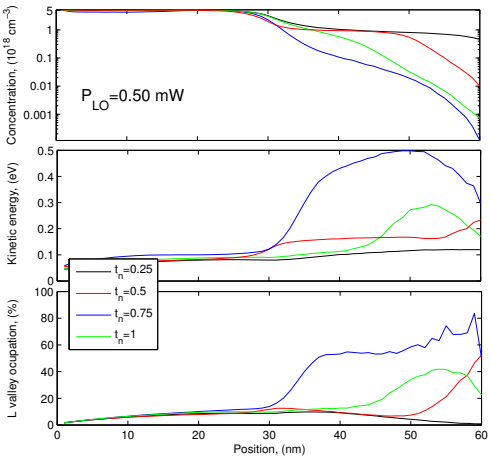

(b) 4.75 THz fundamental mixer

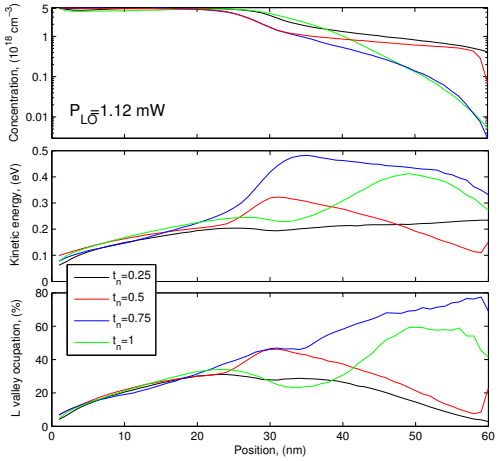

(c) 10 THz fundamental mixer with N_e= 1x10^{18} cm^{-3}

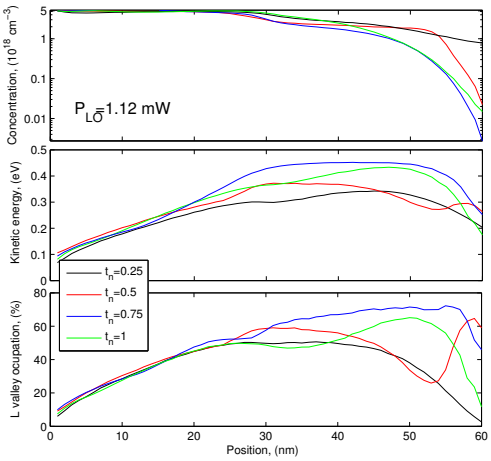

(d) 10 THz fundamental mixer with N_e= 2.5x10^{18} cm^{-3}

Figure 6.36: Profiles of the electron concentration, the kinetic energy and the L valley occupation as a function of the position (ohmic contact at 0 nm) for the diodes in the (a) 2.5 THz mixer, (b) the 4.75 THz mixer, (c) the 10 THz mixer with N_e= 1x10^{18} cm^{-3} and (d) the 10 THz mixer with N_e= 1x10^{18} cm^{-3}. Results obtained with the MCHB tool at the LO powers for minimum conversion loss in Fig. 6.34(a).

As the LO power increases in Fig.6.34(a), the conversion losses increase. This increase is more abrupt for the 10 THz mixers, due to the increase of the occupation of the upper valleys at this high frequency. In addition to shunting effect, the increase of the series resistance of the diodes due to intervalley transfer degrades the conversion losses of the mixers. Fig. 6.36 shows the electron concentration, the electron energy and the L valley occupation for the mixers above 2 THz described in this section at the LO power that minimizes the conversion losses for each mixer. While the occupation of the L valley in the undepleted region of the epilayer is negligible for the 2.5 THz mixer and lower than 10 % for the 4.75 THz mixer, it reaches 30 % and 50 % for the 10 THz mixers with N_e= 1x10^{18} cm^{-3} and N_e= 2.5x10^{18} cm^{-3}, respectively, due to the higher frequency of these mixers.

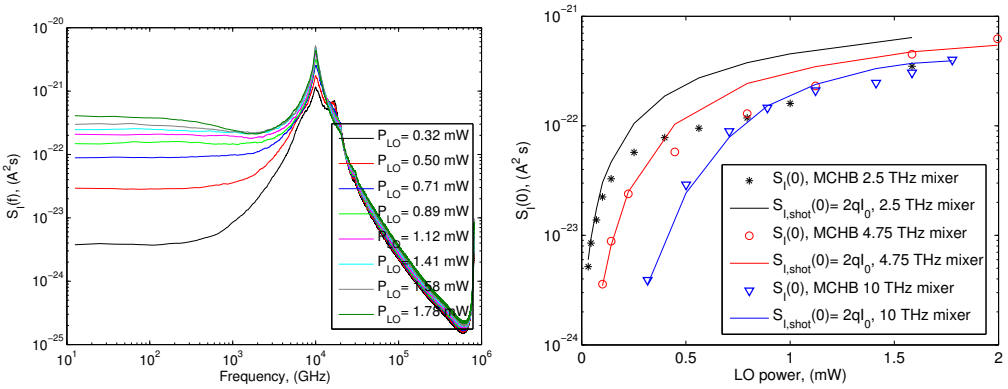

(a) (b)

Figure 6.37: (a) Current noise spectra at the terminals the diode in the 10 THz fundamental mixer, at different LO powers (voltages waveforms from MCHB at f_{IF}= 25 GHz were used in the MC simulation of the noise spectra). (b) Comparison of $S_I(0)$ from MC with the 2qI$_0$ low for the 2.5 THz, 4.75 THz and the 10 THz mixers, all of them based on the diode for the 4.75 THz mixer described in Table 6.3.

Fig. 6.37 shows the current noise spectra of the diode in the 10 THz fundamental mixer calculated with MC under voltage waveforms from MCHB at f_{IF}= 25 GHz. For LO power lower than 1 mW, the diode is below flat band conditions, and the low frequency region of the noise spectra is in good agreement with the shot noise contribution for the dc diode current, see Fig. 6.37(b). At higher LO powers, the electron energy increases and intervalley transfer becomes important, see Fig. 6.36(c). Hence, the low frequency noise is the result of the combined shot and thermal noise, hot electron and intervalley transfer noise. Intervalley transfer in the 10 THz mixer, which begin at LO powers as low as 0.2 mW, generates peaks in the noise spectra of the diode at the LO frequency and its harmonics, see Fig. 6.37(a). Similar peaks were observed in Fig. 6.23, but of lower amplitude since intervalley transfer is lower in the 4.75 THz mixer than in the 10 THz mixer. Since f_{LO} for the 10 THz mixer coincides with the central frequency of the RC peak for this diode (see Fig. 6.23 for the 4.75 THz fundamental mixer, that uses the same diode, where the RC peak is observed around 10 THz), the RC peak is masked by intervalley transfer noise. Also the hybrid plasma peak of the noise spectra, located around 20 THz according to Fig. 6.23, is affected by the intervalley transfer noise peak generated at the second harmonic of the LO frequency.

Fig. 6.38 presents the small-signal impedance $Z_{d,SS}(f_{IF})$ for the fundamental mixers considered in this section. It observed that the real part of the impedances evaluated at the LO power corresponding to minimum conversion losses in Fig. 6.34(a) (voltage waveforms in the vicinity of flat band) increase as the RF frequency increases due to increase of the series resistance of the diode associated to the epilayer plasma resonance. Also, the increase of the occupation of the upper valleys when the frequency increases leads to the increase of Re$[Z_{d,SS}]$. When N_e= 2.5x10^{18} is considered in the 10 THz mixer, the Re$[Z_{d,SS}]$ decreases because the plasma resonance is shifted to higher frequencies, see Fig. 6.34(b)

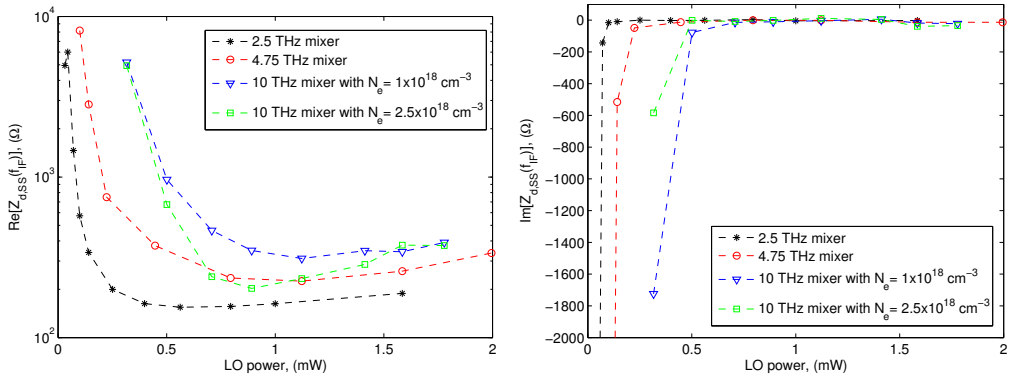

Figure 6.38: (a) Real and (b) imaginary part of the small-signal impedance $Z_{d,SS}(f_{IF})$ of the reference fundamental mixers considered in this section at IF frequency 25 GHz at different LO powers, evaluated with MC.

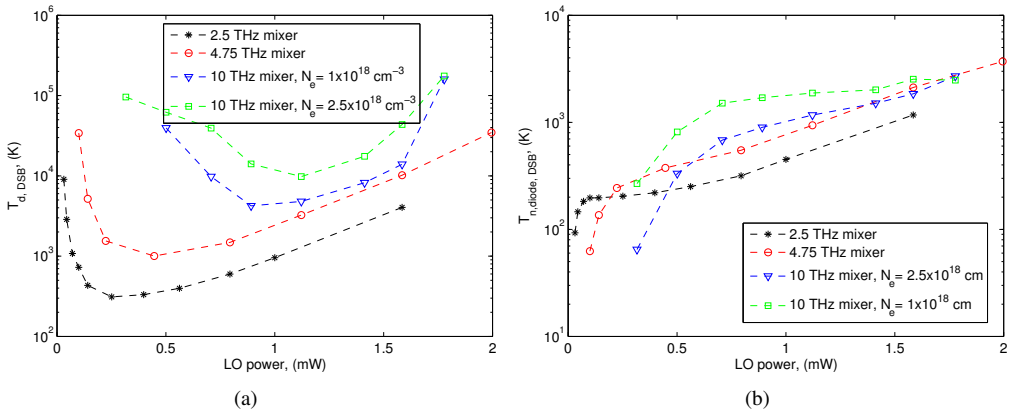

Figure 6.39: (a) Double side band equivalent input noise temperature and (b) equivalent noise temperature as defined by eq. (6.13) of the diode in the 2.5 THz, 4.75 THz and the 10 THz fundamental mixers, all of them based on the diode for the 5 THz mixer described in Table 6.3. Results obtained with the MC model.

The equivalent input noise temperature T_d and the equivalent noise temperature as defined by eq. (6.13) of the diode in the 2.5 THz, 4.75 THz and the 10 THz fundamental mixers are presented in Fig. 6.39.

It is observed an important increase of T_d as the operation frequency increases Fig. 6.39(a) due to the increase of the conversion losses, see Fig. 6.34(a), and $T_{n,diode}$. The performance of the conversion losses for these mixers has already been discussed. $T_{n,diode}$ increases as the LO power increases. Once the voltage waveforms at the terminals of the diode are above flat band, the increase of $T_{n,diode}$ is due to hot electron and intervalley transfer noise. As the frequency increase, these noise contributions become more important, due to the increase of the electric fields, the electron energy and the occupation of the upper valleys in the undepleted regions of the diode, see Fig. 6.36. Note that $T_{n,diode}$ increases at higher LO powers as the RF frequency increases because shunting effect is more important.

To carry out a comparison of the noise temperature of the mixers analysed in this section with the expected $50h\nu/k_B$ performance observed for measured Schottky mixers, see Fig. 6.1(a), additional losses L_{op}= 1 dB, L_{rf}= 2 dB and L_{if}= 1 dB have been assumed. The values assumed for these losses are similar to those given for mixers at lower frequencies, see Table 6.3. Fig. 6.40 shows the

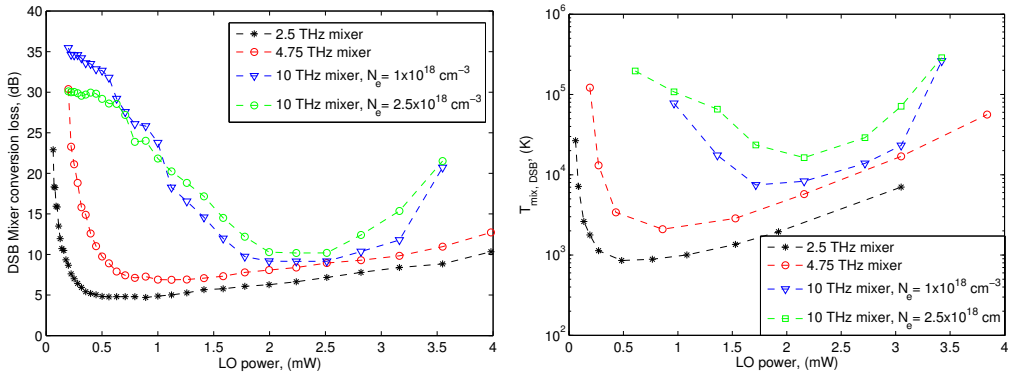

(a) (b)

Figure 6.40: (a) Double side band equivalent input noise temperature and (b) equivalent noise temperature as defined by eq. (6.13) of the diode in the 2.5 THz, 4.75 THz and the 10 THz fundamental mixers, all of them based on the diode for the 5 THz mixer described in Table 6.3. Results obtained with the MC model.

conversion losses and the equivalent input noise temperature of the reference mixers in this section assuming the additional losses indicated, eqs. (6.11) and (6.12).

The expected $50h\nu/k_B$ mixer noise temperature at 2.5 THz is around 6000 K. Measured mixer noise temperature in [Sie99] at this frequency is 9000 K, in good agreement with the MCHB simulation results for that mixer, see subsection 6.3.5. The simulations of the 2.5 THz mixer presented in this section -optimization of the mixer in [Sie99], see subsection 6.4.3- predict an important reduction of the noise temperature, see Fig. 6.40(b). Also, an important improvement of the conversion losses is expected with our design of the 2.5 THz mixer, when comparing with the state-of-art presented in Fig. 6.1(b) (mixer conversion loss $\sim$ 10 dB).

The noise temperatures in Fig. 6.40(b) for the 4.75 THz mixer and the 10 THz mixer are of the order of the values expected according to the $50h\nu/k_B$ performance (12000 K at RF 5 THz and 24000 K at RF 10 THz), see Fig. 6.1(a). The minimum noise temperature predicted by our designs of these mixers indicate that it is possible an important enhancement of the temperature with respect to the expected value. However, at these high frequencies, losses L_{op}, L_{rf} and L_{if} higher than those considered in our simulations can degrade the results presented in Fig. 6.40.

Part IV

CONCLUSIONS

Chapter 7

Conclusions and future work

7.1 Conclusions

In this thesis, a Monte Carlo simulator has been selected as a reference model to analyse the performance of Schottky diodes, since this simulator provides a reliable description of the electrical and the noise responses of the semiconductor devices at millimeter and submillimeter wavelengths. The Monte Carlo model has been coupled with a harmonic balance technique to analyse the performance of frequency multipliers and mixers. It is, therefore, possible to perform the joint optimization of both the external circuit and the internal structure of the semiconductor device for the applications of interest. The most important conclusions of this work are the following:

- The MC simulator has been used to provide a better understanding of the physical phenomena responsible for the electrical and the noise performances of the Schottky diodes operating in the THz band.
- MCHB has been used as a tool for analysis and design of multipliers and mixers in the millimeter and submillimeter-wave bands.
- The accuracy and the range of validity of different lumped equivalent circuit and drift-diffusion models commonly used in the design of Schottky based multipliers have been evaluated, using as a reference MCHB. The enhanced LECHB is limited to frequencies lower than 1 THz, where velocity saturation can be avoided using high epilayer doping. The DDHB underestimates the efficiency of multipliers and it only works correctly when velocity saturation is the dominant effect. The development of Schottky multipliers above 3 THz requires models that account for different phenomena: Saturation velocity, plasma resonance and the nonstationary performance of the electron energy and velocity. The use of MCHB at these frequencies is essential.
- For the first time, MCHB has been used to analyse the conversion losses and equivalent input noise temperature of mixer circuits. The analysis of Schottky mixers using different models has shown that improved LEC models that take into account the time variation of the series resistance describe correctly the conversion losses if velocity saturation is not important. Due to the high doping and bias point commonly used in mixers, velocity saturation is not important in these circuits up to frequencies around 1 THz. The traditional DD model fails when the diodes are working close to flat band and an enhanced version of the DD model has to be used for the design of mixers. Taking as a reference MC, the enhanced DD offers better accuracy and a larger frequency range of validity than the improved LEC. At higher frequencies, intervalley transfer and nonlocal effects affect the performance of the Schottky mixers and only MCHB is able to reproduce measured conversion losses.

- The equivalent input noise temperature of the mixers has been evaluated with the conversion matrix formalism based on the different LEC models and also with MC. Up to frequencies around 1 THz, the noise performance is usually well predicted by the ordinary shot and thermal noise theory. However, the accuracy of the conversion matrix formalism is limited by the accuracy of the LEC model. Besides, MC simulations have shown that common analytical models for hot electron noise integrated in the conversion matrix formalism overestimate this noise contribution. At frequencies higher than 1 THz, Monte Carlo simulations have shown an important increase of the noise temperature due to intervalley transfer. A significant reduction of this noise contribution has been predicted by MC simulations when the epilayer length is decreased.

7.2 Future work

As regards future work, there are a lot of interesting directions to be followed.

- *New materials*. Semiconductor materials like GaN, InGaAs or InP among others, with promising capabilities for THz applications will play an important role in the development of Schottky diode technology. At this point, graphene offers potentially performance benefits in RF systems including low noise amplifiers, frequency multipliers and mixers. Recently, fabrication of a Schottky junction with graphene and conventional semiconductors, such as Si, GaN, GaAs and SiC has been explored [Kal13, Lin14]. A basic graphene Schottky device with an ideal current-voltage characteristic is still uncommon. The analysis and modelling of transport mechanism in this semiconductor as well as the transport through the graphene-Schottky junction is a fundamental step for the development of this technology. In particular, MC models are expected to play an important role in this task, due to its recognize accuracy in modelling carrier transport.

- *Improvement of the physics-based models*. Different improvements of the Monte Carlo model used in this work have to be carried out in order to enhance its accuracy and range of validity. To get a better description of the charge transport through the Schottky barrier, tunneling through the barrier and barrier lowering due to image force phenomena have to be considered. In heavily doped semiconductors and/or at low temperature operation conditions, tunnel effect can contribute significantly to the overall current across the barrier [Fab95]. These phenomena also affect the current noise spectra of the diode. Another important mechanism which has to be included in the MC model is generation-recombination due to electron traps in the epilayer. This phenomenon reduce the flat band voltage and can lead to significant modifications in the current noise spectra [Heg85, Reg87, Per05]. It is also important to include impact ionization as a scattering mechanism in the MC model, which leads to avalanche breakdown. Although breakdown has been considered in this work using DD models, an analysis based on MC is expected to provide a more accurate description. Self-heating is a significant performance limiting factor for frequency multipliers and mixers [Tan12, Per13]. Modelling of self-heating effects with the MC model will provide a better description of the electrical and the noise response of Schottky diodes.

  An analysis of the instability phenomena that limit the operation conditions of the nonlinear circuits must be carried out to get a better understanding of the performance of nonlinear circuits and facilitate practical applications [Sua06]. Adequate algorithms to account for the stability of the circuits will be included in our simulator.

- *Integration of a 3-D electromagnetic simulator*. Due to the high operation frequencies and small dimensions of THz circuits, strong electromagnetic interactions among the different components of the circuit become important and have to be taken into account in the design process. For the accurate modelling of such circuits, electromagnetic propagation and device

behavior have to be accounted for at the same time [Ali98]. The development of a global CAD tool able to analyse in the same framework the whole circuit, using accurate physics-based models for the nonlinear devices, opens promising alternatives for the design of nonlinear circuits [Cia96, Ali98, Leu07].

Part V

APPENDIX

Appendix A

Characteristics of the Monte Carlo simulations

This appendix presents an analysis of the precision of the Monte Carlo simulations as a function of the parameters of the model used in such simulations, i.e, the time step, the mesh size, the number of simulated particles or the total simulated time. Initially, the simulation results for a reference diode under dc and time varying conditions are analysed. The reference GaAs Schottky diode has an epilayer length of 250 nm, epilayer doping concentration of 3x10^{17} cm^{-3}, substrate length of 50 nm and substrate doping concentration of 2x10^{18} cm^{-3}. An anode area of 1 μm^2, ideal barrier height of 0.99 V and room temperature 300 K have been assumed for the reference diode. Afterwards, an analysis of the simulation results of multipliers and mixers obtained with MCHB is carried out as a function of the parameters of the MC model.

A.1 Selection of dt and dx. Stability conditions

The values of the time step dt and the spatial mesh dx employed in MC simulations must be selected according to criteria related with the plasma frequency, the dielectric relaxation time and the Debye length to guarantee the stability of the simulation.

1. According to [Hoc88], the time step, dt, must verify that $\omega_p dt < 2$, where ω_p is the plasma frequency, defined by:

$$\omega_p = \sqrt{\frac{q^2 N_D}{\varepsilon_0 \varepsilon_r m^*}} \tag{A.1}$$

   where N_D is the doping concentration in each region of the device, q is the charge of the electron, m^* is the effective mass of the electrons in the semiconductor and ε_r is the relative permittivity of the semiconductor. The highest carrier density specified in the device model must be used to estimate dt. For the multi-valley semiconductors considered in the work, the smallest effective mass of the electron in the semiconductor has to be used in eq. (A.1).

2. On the other hand, the time step must be shorter than the dielectric relaxation time of the material, $dt < \tau_d$, given by:

$$\tau_d = \frac{\varepsilon_0 \varepsilon_r}{q N_D \mu_0} \tag{A.2}$$

   where μ_0 is the low electric field mobility. Since μ_0 depends on N_D, the carrier density specified in the model with highest product of $N_D \mu_0$ must be used to estimate τ_d.

3. The mesh size dx for the spatial resolution of the potential is dictated by the charge variations. Hence, the mesh size has to be chosen smaller than the smallest wavelength of the charge variations. The smallest wavelength is approximately equal to the Debye length, given by:

$$\lambda_D = \sqrt{\frac{\varepsilon_0 \varepsilon_r K_B T}{q^2 N_D}} \tag{A.3}$$

   where k_B is the Boltzmann constant and T is the temperature of the crystal lattice. The highest carrier density specified in the model must be used to estimate λ_D.

4. In addition to condition 3 for dx, the size of the spatial mesh must be evaluated to verify that the maximum length, l_{max}, covered by the carriers in a time step be lower than dx. This maximum length is given by $l_{max} = v_{max} dt$ where v_{max} is the maximum group velocity of the electron in the semiconductor.

In addition to these restrictions, to get an efficient evaluation of the fast Fourier transform, the number of time steps in a period of the applied excitation, n, must be a power of 2.

A.2 Calculation of average magnitudes

The MC simulator can be used to evaluate different magnitudes of a device as a function of the position $\mathbf{r}$ ($\mathbf{r}$ is within the lattice p of the spatial mesh of the device), and time t as an average over the particles in the lattice p at time instant t:

$$A_p(\mathbf{r},t) = \frac{1}{N_p(t)} \sum_{i=1}^{N_p} A_i(t) \tag{A.4}$$

where $N_p(t)$ is the number of particles in the lattice p at time t and $A_i(t)$ is the value of the magnitude A for the carrier i at time t. The accuracy of the result obtained with eq. (A.4) depends on the number of simulated particles. The accuracy can be enhanced averaging over an ensemble of different realizations of $A_p(\mathbf{r},t)$. This is usually done to obtain the regular response of a device under periodic excitations.

A.2.1 DC conditions

Under dc conditions, the current in the MC model is evaluated by counting the number of particles crossing the Schottky barrier. The average current is obtained averaging over a sufficiently large number of iterations (simulated time steps) or realizations. Fig. A.1(a) shows the variation of the average current in the reference Schottky diode under dc conditions as a function of the number of iterations. In this figure, the number of particles considered is 17500 [1]. In Fig. A.1(b), the current is obtained by averaging over $2.5\text{x}10^5$ iterations and it is carried out an analysis with the number of particles initially considered in the MC model. In all the simulations of Fig. A.1, a large enough transitory ($1\text{x}10^5$ iterations) has been considered. As expected, increasing the number of iterations (realizations), Fig. A.1(a), or the number of simulated particles, Fig. A.1(b), the average value of the current is closer to the expected value of the current and the variance of the estimator of the current decreases. The lower the simulated dc point, the higher the number of iterations and/or the number of particles is necessary to obtain accurate simulation results, since for high Schottky barrier

[1] It is the number of particles considered in the initial conditions of the MC simulations. These particles are distributed in the device according to an equilibrium distribution function. The evolution of the charges when an excitation is applied to the device can result in the formation of depletion or accumulation regions, particles leaving or entering into the device through the contacts, etc. As a result, the average number of particles inside the device is different from the number of particles initially considered.

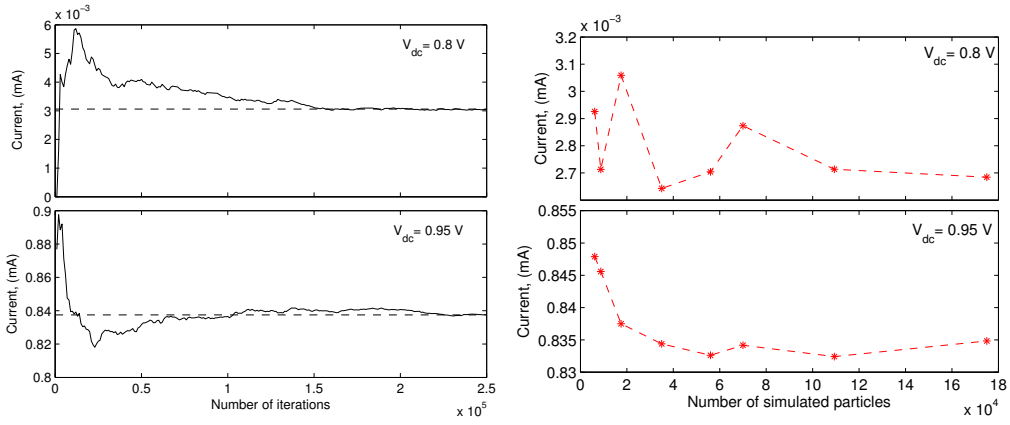

(a) (b)

Figure A.1: Current response of the reference Schottky diode under dc conditions evaluated with the MC model as a function of (a) the number of iterations used to average over and (b) the number of simulated particles. Dash lines in (a) represent the average current obtained with the larger number of simulated iterations in this subfigure (the number of particles simulated in (a) is 17500, and the number of iterations considered in (b) is 2.5x10^5).

height only the most energetic carriers are able to surmount the barrier, which are in the tail of the distribution function. For an accurate modelling of the tail of the distribution function it is necessary to consider a high enough number of particles and/or realizations.

A.2.2 AC conditions

In this section, the accuracy of the current response under sinusoidal voltages is analysed as a function of the number of particles used in the simulations and as a function of the number of realizations used to obtain the deterministic[2] current response of the diode. Under time varying conditions, the total current flowing through the diode $\mathbf{j}(\mathbf{r},t)$ includes the contribution of the conduction current and the displacement current, and, in accordance to [Reg92], it can be evaluated as:

$$I(t) = -\frac{q}{L}\sum_{i=1}^{N_T(t)} v_{ix}(t) - \varepsilon_0\varepsilon_r\frac{A}{L}\frac{d}{dt}\Delta V(L,t) = I_c(t) - \varepsilon_0\varepsilon_r\frac{A}{L}\frac{d}{dt}\Delta V(L,t) \tag{A.5}$$

where $N_T(t)$ is the total number of particles inside the device at time t, L is the length of the whole diode, A is the anode area, $v_{ix}(t)$ is the velocity of the *i-th* electron in the direction of flow of the current x at time t and $\Delta V(L,t) = V(L,t) - V(0,t)$ is the voltage drop between the diode terminals at instant t. Eq. A.5 is used in the MC simulator to evaluate the total current under time varying conditions.

To obtain correct results, it is necessary to neglect the initial periods of the simulation's results. These initial results correspond to a transient situation where the state of the carriers changes from the equilibrium distribution considered as the initial conditions in the simulations to the out of equilibrium cyclostationary conditions determined by the applied voltage, and they are not reliable. Fig. A.2 shows the current response as a function of time and the absolute value of the first three harmonics of the current response of the reference diode under sinusoidal voltages typical of (a) multipliers and (b) mixers. These figures show that three periods of the applied signal are enough to avoid the

[2]The instantaneous value of some physical quantity of interest, q(t), (e.g. the total current flowing in the diode) is decomposed into two parts: $q(t) =< q(t) > +\delta q(t)$ where $< ... >$ represents the ensemble average, $< q(t) >$ is the deterministic part describing the average response under the applied static or periodic excitation and $\delta q(t)$ describes the instantaneous fluctuations of $q(t)$ with respect to its average value $< q(t) >$.

transitory response in the first three harmonics of the simulated current. However, in all the multiplier and mixer simulations carried out in this thesis, the number of transitory periods considered has been set to six, since a dependence of the number of transient periods on the operation conditions (bias point, input power, excitation frequency,...) is expected.

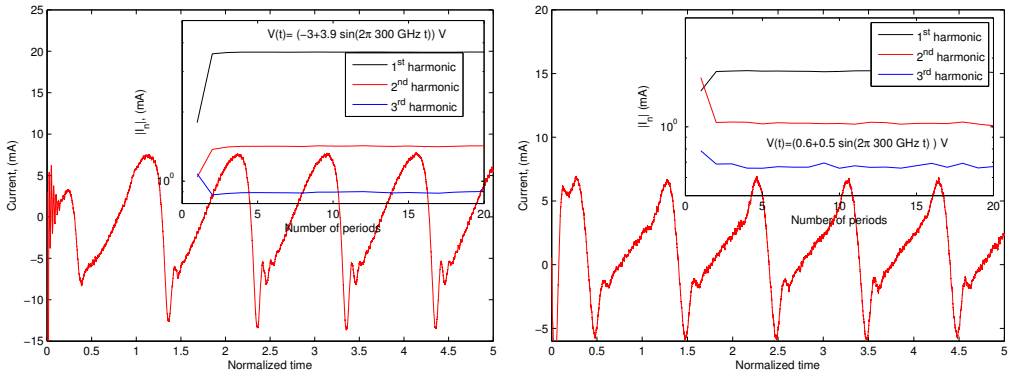

(a) (b)

Figure A.2: Current response of the reference diode under sinusoidal voltages of (a) amplitude 3.9 V, bias -3 V and (b) amplitude 0.5 V and bias 0.6 V. The frequency simulated is 300 GHz. MC model with 35000 particles has been used.

The current response obtained with MC simulations is a noisy signal, see Fig. A.2, due to the statistical character of the MC technique, see chapters 2 and 4. The time dependence of the average current (i.e., the deterministic response) during a period of the applied voltage is determined by averaging over a large number of such periods in accordance with[3]:

$$< i(\theta) >= \frac{1}{M} \sum_{i=0}^{M-1} i(t = \theta + iT_f) \tag{A.6}$$

where θ belongs to the time interval $0 \leq \theta \leq T_f$, T_f is the period of the applied signal and $i(t)$ is the instantaneous current. Since the level of the regular current response is much higher than the level of noise, the variation of the firsts harmonics of the current does not change considerably among the different periods simulated, as is shown in Fig. A.2 for the reference diode. The fundamental, second and third harmonics of the current response calculated according to eq. (A.6) for the reference diode are evaluated in Figs. A.3 and A.4 as a function of the number of periods M used to average over (number of realizations) and the number of particles considered in the MC model, under different time varying voltages (the fundamental frequency considered is 300 GHz). As expected, the variance of the harmonics of the current decreases as the number of realizations increases and lower number of realizations are required as the number of particles increases. The amplitude of the first harmonic shows higher variance than the phase, while the variance of the amplitude and the phase are similar for the second and third harmonics. The value of the variance in Figs. A.3 and A.4 is very low, and even with one period the value of the first three harmonics is acceptable.

The deterministic part of the current response obtained with the MC model is used in the harmonic balance (HB) technique to simulate multipliers and mixers, chapters 5 and 6 respectively. Since the time-domain waveforms used in the HB algorithm have to be sampled at a sampling rate lower than $1/dt_{MC}$, where dt_{MC} is the duration of a MC iteration as described in section A.1, enough MC samples are available between two consecutive samples of the discrete time-domain waveforms in the HB. The currents obtained for these MC samples are averaged to obtain an accurate estimation of the current at the corresponding sample in the HB algorithm. A phase window of 0.025 rad

[3]Periodic signal are considered.

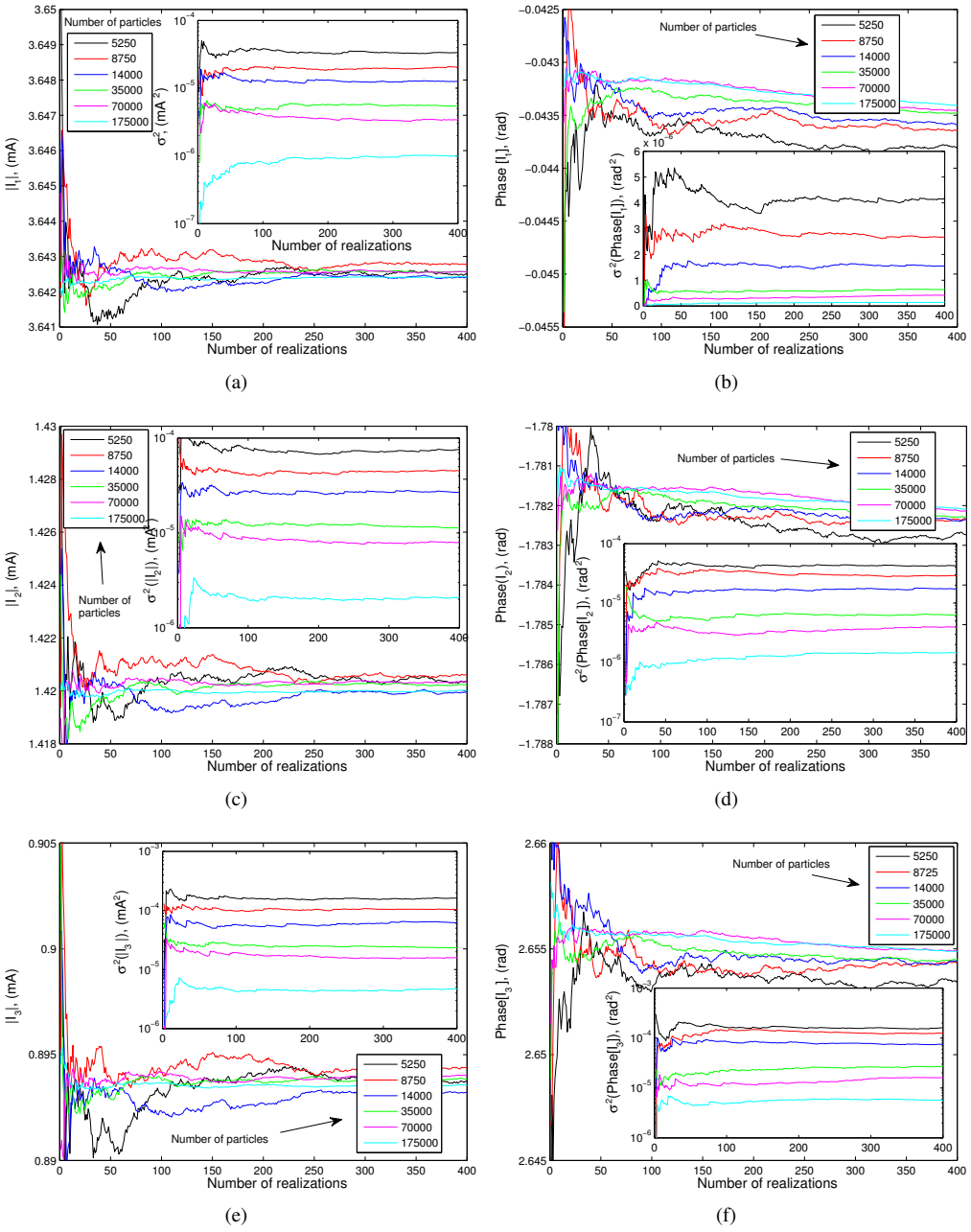

Figure A.3: Evaluation of the first three harmonics of the current response of the reference Schottky diode under sinusoidal voltages of bias -3 V, amplitude 3.9 V and frequency 300 GHz, simulated with MC, as a function of the number of simulated particles and the number of periods used to average (number of realizations). The inset of the figures shows the variance of harmonics of the current.

has been used to average the samples from MC. In the HB simulations of multipliers and mixers presented in this thesis, one period (plus the six transitory periods) has been considered with the described average among MC samples.

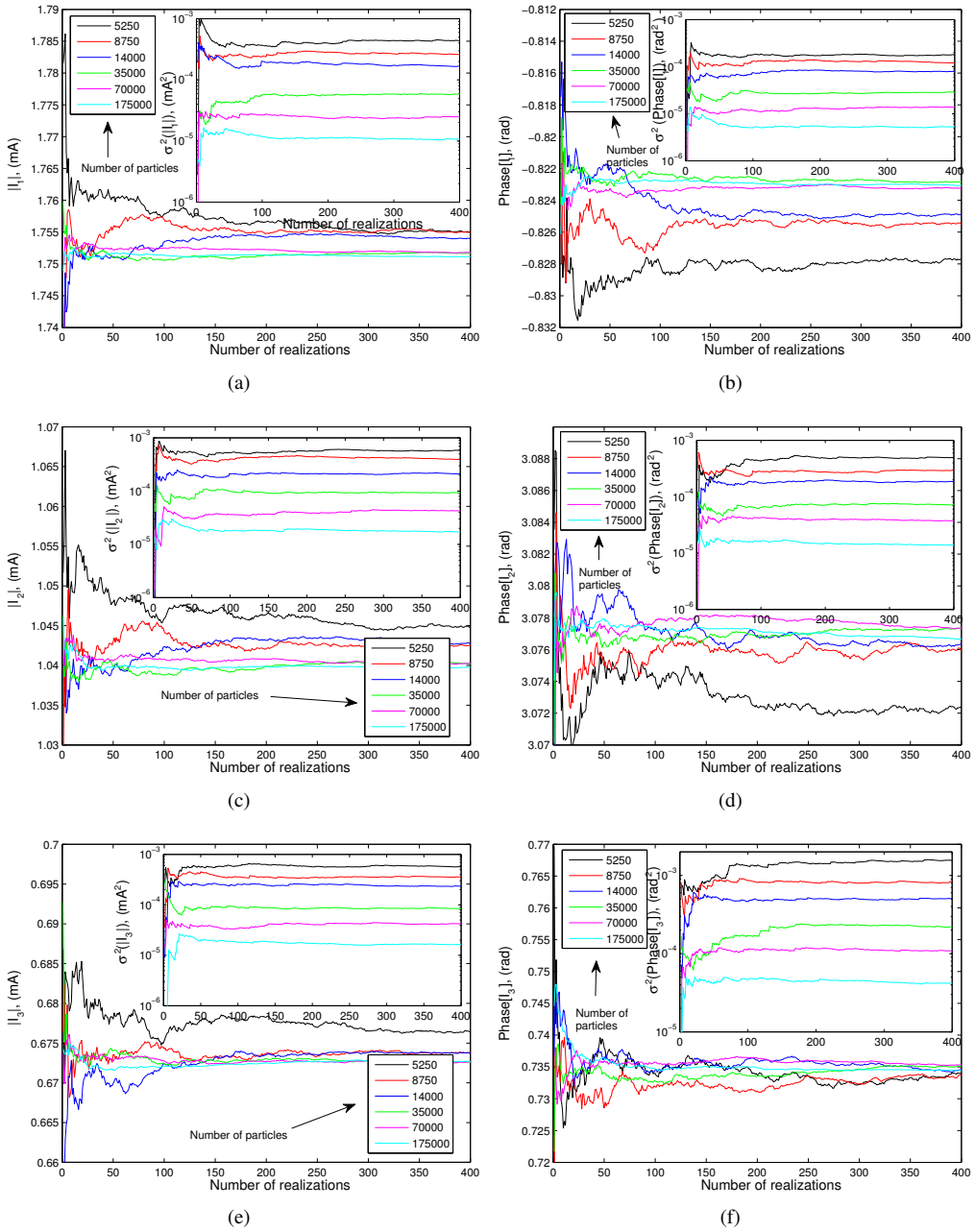

Figure A.4: Evaluation of the first three harmonics of the current response of the reference Schottky diode under sinusoidal voltages of bias 0.6 V, amplitude 0.5 V and frequency 300 GHz, simulated with MC, as a function of the number of simulated particles and the number of periods used to average (number of realizations). The inset of the figures shows the variance of harmonics of the current.

A.3 Simulation of multipliers

Table A.1 presents the parameters of the Monte Carlo model used in the HB technique for the simulation of the diodes in the multipliers described in Table 5.1. For the diodes which have a substrate length higher than 1 μm (all in Table A.1 except the 1.5 THz doubler and the 2.7 THz tripler, see Table 5.1), the number of particles that should be simulated in the MC model is very

Table A.1: Parameters of the MC model used in the simulation of the multipliers described in Table 5.1.

Stage	Input frequency simulated, (GHz)	Number of dt per f_{in} period[a,b]	dx, (nm)	Number of particles
0.2 THz doubler, 6 anodes [Mai03]	100	10240[c]	2	21875
0.2 THz doubler, 6 anodes [Cha04]	100	10240[c]	2	16875
0.4 THz doubler, 4 anodes [Mai03]	200	5632[c]	2	35200
0.8 THz doubler, 2 anodes [Cha02]	400	3072[c]	2	19200
1.5 THz doubler, 2 anodes [Cha04]	750	2048	2	46080
0.3 THz tripler, 12 anodes [Mae05a, Mae06, Mae08]	100	8192	2	19200
0.6 THz tripler, 4 anodes [Mae05b]	200	5632[c]	2	25000
0.9 THz tripler, 4 anodes [Mae10a]	300	4096	2	7500
1.2 THz tripler, 2 anodes [Mae01, Bru01, Mai03]	400	2048	2	10000
1.8 THz tripler, 2 anodes [Mae05c]	546	2048	2	12500
2.7 THz tripler, 2 anodes [Mae12]	900	2048	2	52500

[a] According to section A.1, the time steps have to be lower than 1.57 fs and the spatial mesh step dx has to be lower than 3 nm for the simulation of all the multipliers of the table.

[b] The time step in the MC model dt is given by $1/(ndt \cdot f_{in})$ where ndt is the number of dt per period of the fundamental frequency f_{in} presented in the table.

[c] Although these numbers of MC time steps in a period of f_{in} are not a power of 2, the samples in HB extracted from these MC samples are powers of 2.

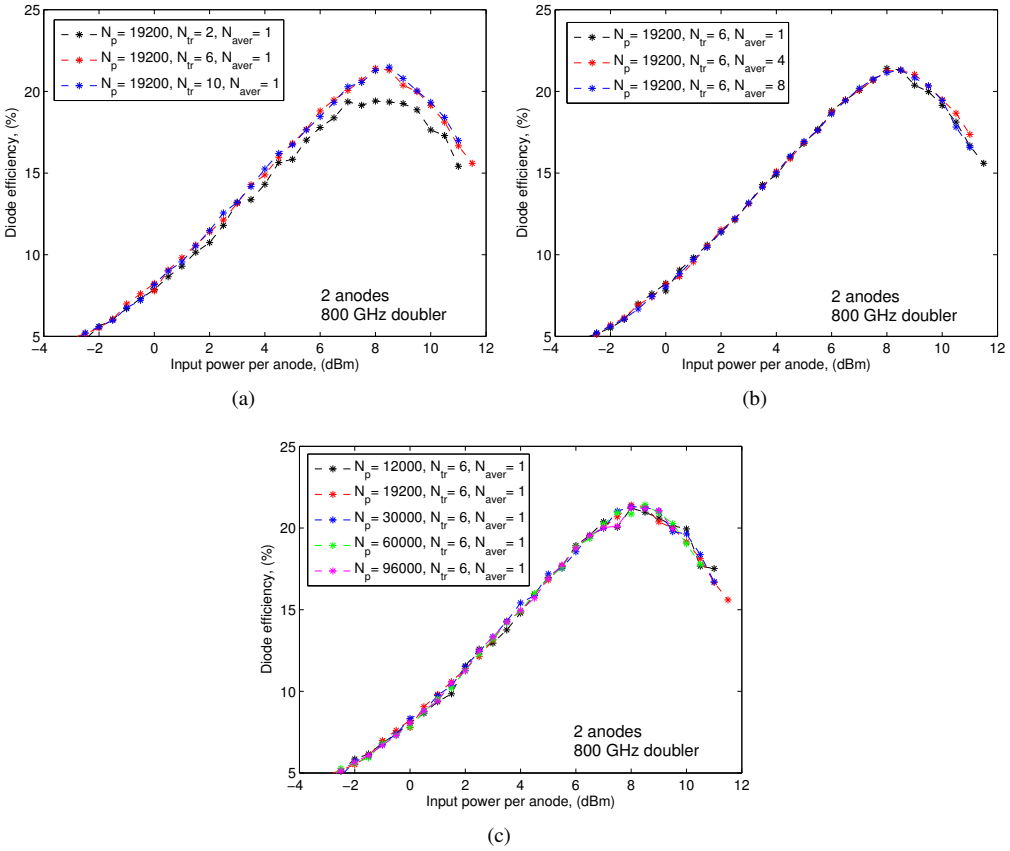

Figure A.5: Efficiency of the 800 GHz doubler described in Table 5.1 obtained with MCHB as a function of (a) the number of transient periods, (b) the number of realization considered to average and (c) the number of particles simulated.

high, what will make the simulation with MCHB computationally intensive and time consuming. Hence, for these diodes, only a substrate length of 100 nm have been simulated in the MC model (the epilayer is always completely simulated) and the remaining substrate is simulated in the linear part of the circuit. This does not affect the obtained results, since due to its high doping, the performance of the substrate is that of a linear resistance. This procedure has been only used in the simulation of multipliers, it is not necessary for mixers since their substrate lengths are lower than 1 μm, except for the 86-106 GHz fundamental mixer, see Table 6.3.

Figs. A.5 and A.6 present an analysis of the variation of the efficiency and the diode impedance at the input frequency of multipliers with the parameters used in the MC model: (a) the number of transient periods N_{tr}, (b) the number of realizations to average N_{aver} (number of periods of the input frequency considered to average) and (c) the number of simulated particles N_p. The 800 GHz doubler described in Table 5.1 has been considered as a reference for this analysis. Figs. A.5(a) and A.6(a) show that an insufficient transitory is going to affect the simulations results. Figs. A.5(b), A.6(b), A.5(c) and A.6(c) show that increasing the number of realizations or the number of particles initially considered do not change the results. In all the simulations of multipliers presented in this thesis, N_{tr}= 6 and N_{aver}= 1 have been considered (N_p used in the simulations are shown in Table A.1).

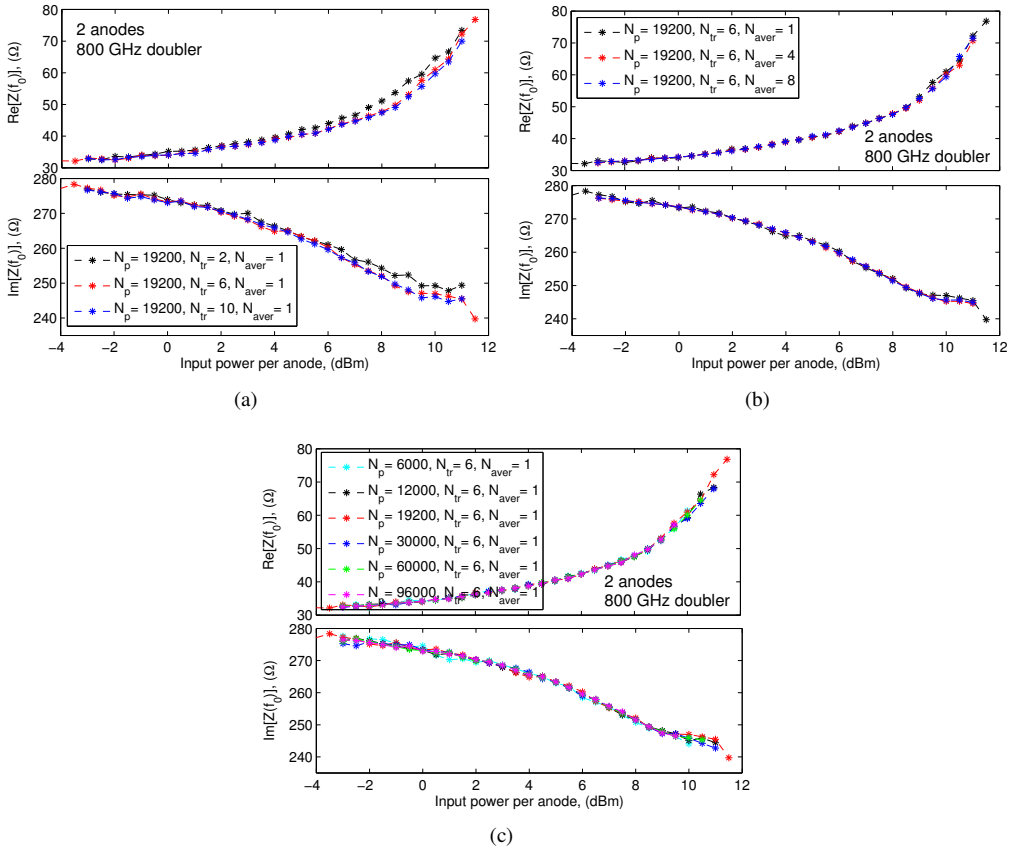

Figure A.6: Diode impedance at the input frequency for the 800 GHz doubler described in Table 5.1 obtained with MCHB as a function of (a) the number of transient periods, (b) the number of realization considered to average and (c) the number of particles simulated.

A.4 Simulation of mixers

Table A.2 presents the parameters of the Monte Carlo model used in the HB technique for the simulation of the mixers described in Table 6.3.

Table A.2: Parameters of the MC model used in the simulation of the mixers described in Table 6.3.

Stage	f_{IF} with MC (GHz)	N. of dt per IF period[a]	dx, (nm)	N. of particles
86-106 GHz fundamental single-ended mixer [Ali93a]	10	65536	2	12500
300-360 GHz subharmonic mixer [Tho04, Tho05]	24	32768	2	13750
585-690 GHz fundamental single ended mixer [Hes96, Hes97]	30	32768	2	9280
835-900 GHz fundamental balanced mixer [Tho10b, Tho10c]	30	32768	2	50000
2.5 THz fundamental single-ended mixer [Sie99]	25	40960[b]	2	56000
4.75 THz fundamental single-ended mixer [Bet96]	25	40960[b]	1	7200

[a] According to section A.1, the time step and the spatial mesh step have to be lower than 0.78 fs and 1.9 nm respectively for the 2.5 and the 4.75 THz mixers and lower than 1.57 fs and 3 nm for the simulation of the remaining mixers in the table. Lower dt_{MC} and dx are obtained for these two mixers because their substrate doping is $5\text{x}10^{18}$ cm^{-3}, while it is $2\text{x}10^{18}$ cm^{-3} for the other mixers.

[b] Although these numbers of MC time steps in a period of f_{in} are not a power of 2, the samples in HB extracted from these MC samples are powers of 2.

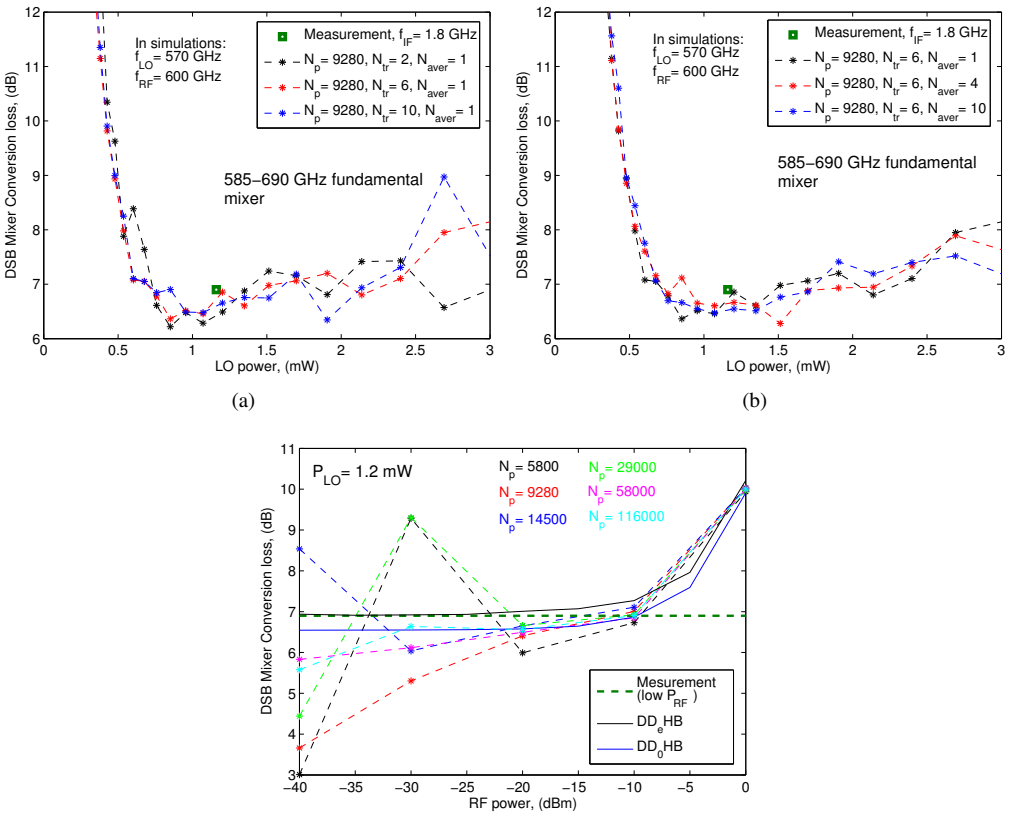

Figure A.7: Conversion loss of the 585 GHz-690 GHz fundamental mixer described in Table 6.3 obtained with MCHB as a function of (a) the number of transient periods, (b) the number of realization considered to average and (c) the number of particles simulated for different values of RF power and a fixed LO power of 1.2 mW.

Fig. A.7 presents an analysis of the conversion losses of the 570-600 GHz fundamental mixer as a function of different parameters of the MC model: (a) the number of transient IF periods N_{tr}, (b) the number of realizations considered to average N_{aver} and (c) the number of particles N_p for different values of RF power with a fixed LO power of 1.2 mW. Fig. A.7(a) shows that two IF periods are enough to avoid the transient response of the MC simulations. N_{tr}= 6 has been used for the mixers simulated in this thesis. When N_{aver} is increased Fig. A.7(b), the conversion losses do not change significantly, although the fluctuations of the results decrease. N_{aver}=1 has been used in the simulations of mixers in this thesis. The analysis with the number of particles and the RF power in Fig. A.7(c) shows that the number of particles to obtain acceptable results increases as the level of RF power decreases, since the level of the RF signal becomes closer to the noise level. Hence, the number of particles or realizations have to be increased in order to reduce the noise contribution from the regular current response. Note that more than 10^5 particles are necessary for a P_{RF}= -30 dBm. In all the simulations for mixers in this thesis, P_{RF}= -20 dBm has been assumed, and according to Fig. A.7(c), more than 6000 particles are required to obtain reliable results. The number of particles used in the simulation of mixers are presented in Table A.2.

As a guide for the simulation of multipliers and mixers with the MCHB, N_{tr}= 6 and N_{aver}= 1 have been used in this thesis. N_{tr} higher than 2 for multipliers and higher than 1 for mixers can be used to obtain good results.

A.5 Simulation of noise

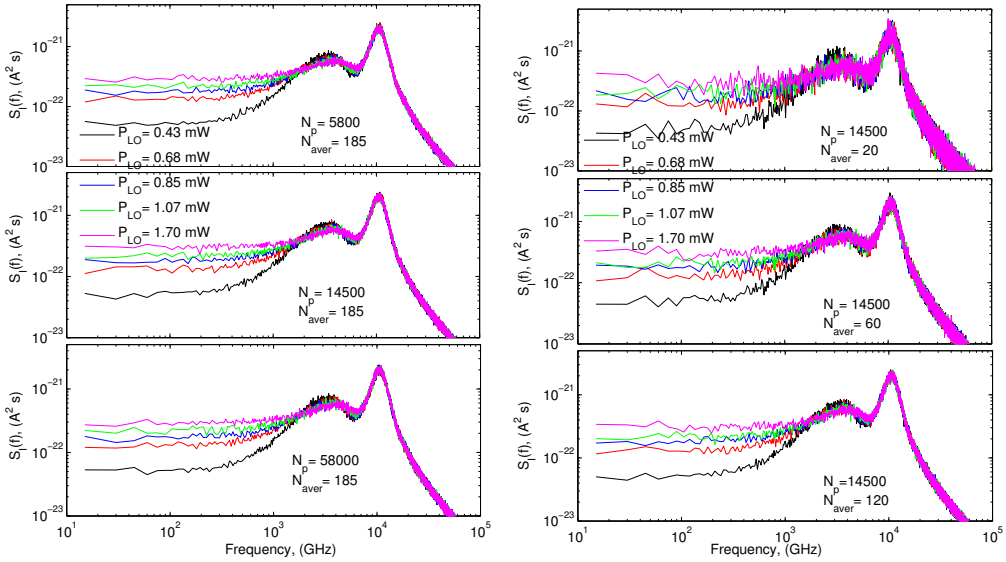

Figure A.8: Current noise spectral density of the diode in the 585 GHz-690 GHz fundamental mixer, Table 6.3, under the voltage waveforms calculated with MCHB at f_{IF}= 30 GHz, as a function of (a) the number of particles simulated N_p and (b) the number of realization considered to average N_{aver}.

This section presents an analysis of the impact of the number of particles N_p and the number of realizations N_{aver} in the results of the spectral density of the current fluctuations $S_I(f)$ -eq. (4.13)- calculated as was described in section 4.1.1. The MC model has been used to calculate $S_I(f)$ in chapters 4, 5 and 6. Besides, in chapter 6, the equivalent input noise temperature of Schottky mixers -eqs. (6.5) and (6.6)- has been calculated using $S_I(f)$, the small-signal impedance $Z_{d,SS}$, eq. (6.2), and the conversion losses. Hence, an analysis of $Z_{d,SS}$ as a function of N_p and N_{aver} is also carried

out in this section. As a reference for this analysis, the 585-690 GHz fundamental mixer described in Table 6.3 is considered. An LO frequency of 570 GHz and RF frequency of 600 GHz have been assumed.

Fig. A.8 presents $S_I(f)$ obtained with the MC model under the voltage waveforms calculated with MCHB and different LO powers. As expected, increasing N_p and/or N_{aver} used in the MC simulations, the precision of $S_I(f)$ increases. Note that the increase of N_{aver} is better to increase the precision of the results.

To calculate $Z_{d,SS}$ at f_{IF}, a small amplitude sinusoidal voltage of frequency f_{IF} (the amplitude of this signal is denoted by V_{ss}) is applied to the diode superimposed to the LO voltage waveform obtained from the MCHB simulation of the mixer. Then, the current response at f_{IF} obtained from the simulation is used to calculate $Z_{d,SS}$ as given by eq. (6.2), see section 6.1.2. Fig. A.9 shows $Z_{d,SS}$ at f_{IF}= 30 GHz as a function of the amplitude of the sinusoidal voltage V_{ss}. To calculate $Z_{d,SS}$, V_{ss} has to be chosen small enough in order to obtain the small signal, linear response of the diode at the IF frequency. A good agreement is observed in Fig. A.9 among the $Z_{d,SS}$ calculated with the different V_{ss}. $Z_{d,SS}$ can be obtained simulating only the transient periods and an IF period (N_{aver}=1). As V_{ss} decreases, N_{aver} or the number of simulated particles have to be increased in order to obtain accurate results, see the discussion about P_{RF} in section A.4. In fact, for the lowest value of V_{ss} in

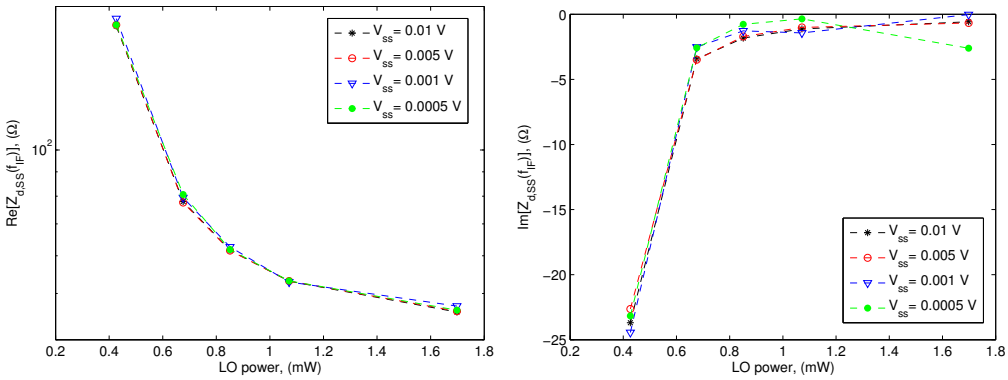

(a) (b)

Figure A.9: Small signal diode impedance $Z_{d,SS}$ of the diode in the reference mixer at f_{IF}= 30 GHz obtained with the MC model as function of the voltage amplitude V_{ss}.

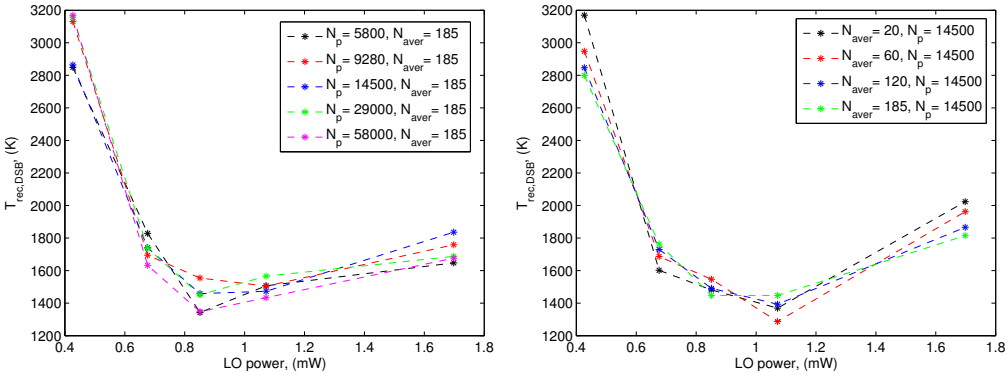

(a) (b)

Figure A.10: Equivalent input noise temperature of the 585-690 GHz receiver obtained with MC as a function of (a) N_p and (b) N_{aver} used to calculate $S_I(f)$.

Fig. A.9, some discrepancies are observed because the number of simulated particles and/or N_{aver} are low for that value of V_{ss}. As a conclusion of these results, V_{ss}= 0.01 V can be used to calculate $Z_{d,SS}$. For the results in chapter 6, V_{ss}= 0.001 V has been used.

Fig. A.10 shows the impact of N_p and N_{aver} used to calculate $S_I(f)$ in the equivalent input noise temperature of the 585-690 GHz receiver. N_p and N_{aver} have a significant impact in the precision of the equivalence input noise temperature. For this mixer, N_p= 14500 and N_{aver}=120 give good results compared to the highest values simulated. In order to obtain precise results in the evaluation of the noise temperature with the MC model, N_p has to be increased with respect to the values of N_p used in the calculation of the conversion losses with MCHB, see Table A.2. In the calculation of the noise temperature in chapter 6, N_p higher than 15000 and N_{aver}= 120 have been used for all the simulated mixers.

‡The simulations presented in this work have been carried out in two Linux Cluster. One of them has 8 nodes with 2 CPUs Intel Xeon 5140 with 2 cores at 2.33 GHz (2 GB RAM per node), 8 nodes with 2 CPUs Intel Xeon 5520 with 4 cores at 2.26 GHz (6 GB RAM per node) and 2 nodes with 2 CPUs Intel Xeon 5650 with 6 cores at 2.66 GHz (24 GB RAM per node). The other cluster has 6 nodes with 2 CPUs Intel Xeon ES-2680 with 8 cores at 2.7 GHz (32 Gb RAM per node). The compiler used is Intel® Fortran Compiler 10.1.011 for Linux.

Appendix B

Non-harmonic oscillations in GaAs Schottky diodes

From Monte Carlo simulations of Schottky diodes under time varying excitations of a few hundred GHz, it has been observed the generation of damped nonharmonic oscillations (*NHOs*) of terahertz frequencies in the current response of this device. Some publications based on MC simulations of Schottky diodes [Shi04, Bha95] show *NHOs*. However, none of these publications have paid attention to these oscillations.

The MC simulations of homogeneous diodes (Schottky diodes with substrate doping equal to the epilayer doping, denoted by HSBD) and Schottky diodes with $n^+ - n$ junction (Schottky diodes with substrate doping different from the epilayer doping, denoted by SBDs) have shown the existence of two kinds of *NHOs*. While the first kind is common to both devices, the second kind only appears in SBDs when very high electric fields are generated in the non-depleted region of the epilayer.

Nonharmonic oscillations with similar characteristics to the *NHOs* have been theoretically predicted in the solution of nonlinear systems. In most cases, it is impossible to solve analytically such systems in terms of elementary functions. Ref. [Gat91] analyses a simple damped nonharmonic oscillator, showing that the nonlinearity modifies the restoring force of the physical system and, hence, the period of the oscillator changes with the amplitude of the oscillation.

On the other hand, the theoretical examination of series RLC circuits with nonlinear elements has shown the existence of stable nonharmonic oscillatory solutions similar to the *NHOs* that we have found in Schottky diodes [Spa68, Hel07].

The terahertz sources with adequate power, frequency agility, and spectral purity are the most difficult challenge facing terahertz frequency engineers [Cha11a]. *NHOs* can be promising for harmonic generation at terahertz bands. The waveforms of *NHOs* in Schottky diodes are similar to the step-like waveforms generated by step recovery diodes [Bof60, Mol62, Lin10, Zhu10, Oh11] or nonlinear transmission lines [Lab06, Kin07]. All of them present a rich harmonic content at THz frequencies which can be used in comb generators.

The aim of this appendix is to analyse and interpret the *NHOs* obtained from Monte Carlo simulations of GaAs Schottky diodes under certain time varying excitations. It has been used an analytical model for the carrier transport based on the momentum balance equation to gain physical insight on the origin of these oscillations [Sel84]. Simpler current relations based on the drift-diffusion model are not able to predict the *NHOs* because it does not take into account carrier inertia. On the other hand, a lumped-element equivalent circuit model can be used to describe the *NHOs*, what eases the analysis of these oscillations in complex circuits.

B.1 Description of the *NHOs*

This section describes the main features of the *NHOs* observed in the current response of GaAs SBDs simulated with the MC method under sinusoidal applied signals $V_{app}(t) = V_0 + V_1 \sin(2\pi f t)$ (denoted by (V_0, V_1, f)).

The characteristics of the Schottky diodes taken as a reference for this study are presented in Table B.1. The ideal barrier height selected is 0.99 V, the anode area 0.9 μm^2 and the temperature 300 K[1]. The substrate length of the reference diode has been fixed to 50 nm to reduce the computational cost of the MC simulations.

Table B.1: Schottky diodes analysed.

	Doping, (cm^{-3})		Length, (nm)	
	Epilayer	Substrate	Epilayer	Substrate
HSBD[a]	5x10^{17}	5x10^{17}	200	50
SBD[b]	5x10^{17}	2x10^{18}	200	50

[a] Homogeneous Schottky barrier diode
[b] Schottky barrier diode

B.1.1 *NHOs* in homogeneous Schottky diodes

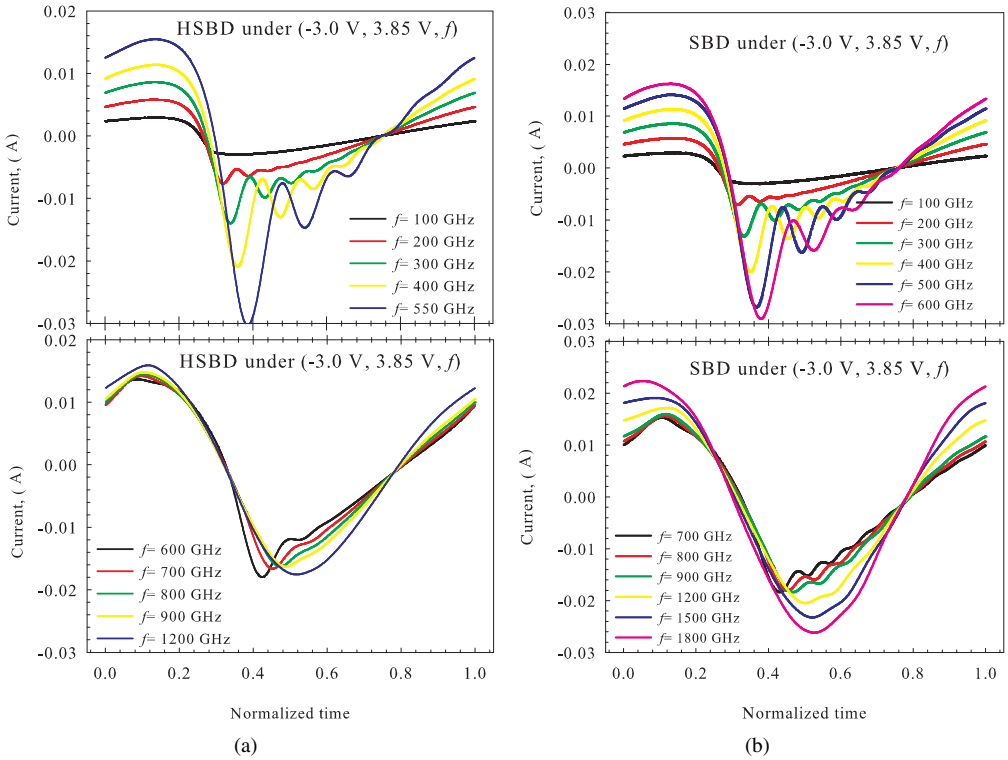

Figure B.1: Current response obtained from the MC simulation of (a) the reference HSBD and (b) the reference SBD under (-3.0 V, 3.85 V, f).

[1]The results provided by the MC simulations have been obtained by averaging 250 simulated periods of the applied signal.

Fig. B.1(a) shows the current response obtained from the MC simulation of the reference HSBD under (-3.0 V, 3.85 V, f) for different frequencies of the applied signal f. *NHOs* appear in the time domain range when the depletion region width is close to its minimum for frequencies higher than 100 GHz and they tend to disappear when f is higher than 550 GHz.

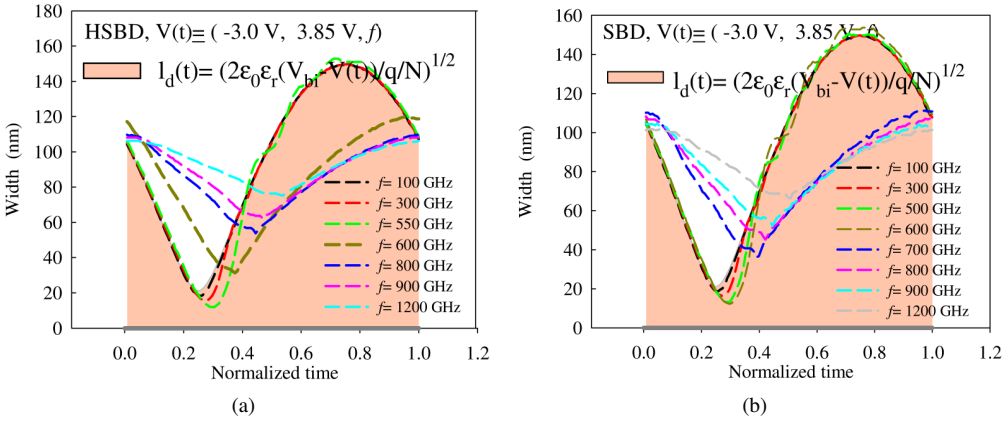

Figure B.2: Time evolution of the width of the depletion region of (a) the reference HSBD and (b) the reference SBD under (-3.0 V, 3.85 V, f) obtained from MC simulations. The width has been evaluated at the position where the charge carriers concentration falls to $0.6N_e$.

To understand why the oscillations observed in Figs. B.1(a) vanish under (-3.0 V, 3.85 V, f) with $f > 550$ GHz, Fig. B.2(a) shows the evolution of width of the depletion region for the HSBD in a period of the applied signals. The frequency f for which the *NHOs* disappear corresponds to the reduction of the swing of the edge of the depletion region with respect to the swing at lower frequencies due to the saturation of the electron velocity [Kol92, Gra00].

An estimate of the oscillation frequencies in the time domain is shown in Table B.2 (the analysis of the *NHOs* in the frequency domain is carried out in Subsection B.1.3). The frequency of the first $f_{NHO(1)}$, second $f_{NHO(2)}$ and third $f_{NHO(3)}$ periods shown in this table are obtained as the inverse of the time separation between two consecutive minima of the *NHOs*. Table B.2 shows that the frequency $f_{NHO(i)}$ of the successive periods of the *NHOs* varies with time, a characteristic performance of the damped nonharmonic oscillations [Gat91]. On the other hand, $f_{NHO(i)}$ increases with the frequency of the applied signal.

Table B.2: Frequency of the first, second and third periods of the *NHOs* directly measured from the time domain current response of the reference HSBD under applied signals (-3.0 V, 3.85 V, f) simulated with MC.

f, (GHz)	$f_{NHO(1)}$, (THz)	$f_{NHO(2)}$, (THz)	$f_{NHO(3)}$, (THz)
200	2.95	3.76	5.12
300	3.22	4.16	5.12
400	3.47	4.49	5.30
500	3.60	4.67	–
550	3.58	4.73	–
600	–	–	–

B.1.2 *NHOs* in $n^+ - n$ Schottky diodes

Fig. B.1(b) presents the current response of the reference SBD under (-3.0 V, 3.85 V, f). *NHOs* appear for $f > 100$ GHz with features similar to the *NHOs* of the reference HSBD ($f_{NHO(i)}, i = 1,2,3$ in Tables B.2 for HSBDs and B.3 for SBDs). When the frequency of the applied signal is higher than 600 GHz, Fig. B.2(b) shows that the velocity of the electrons in the epilayer saturates and the *NHOs* disappear. However, for $f > 600$ GHz, Fig. B.1(b) shows *NHOs* of lower amplitude and higher frequency than the *NHOs* observed for lower frequencies of the applied signal. Therefore, we can distinguish between two kind of *NHOs*, the first kind due to physical processes in the epilayer since they are observed both in HSBD and SBD, and the second kind due to physical processes in the substrate or to some coupling between the epilayer and the substrate: The second kind of *NHOs* do not exist for HSBDs, so they involve necessarily the substrate.

Table B.3: Frequency of the first, second and third periods of the *NHOs* directly measured from the time domain current response of the reference SBD under applied signals (-3.0 V, 3.85 V, f) simulated with MC.

f, (GHz)	$f_{NHO(1)}$, (THz)	$f_{NHO(2)}$, (THz)	$f_{NHO(3)}$, (THz)
200	3.29	3.98	5.25
300	3.53	4.44	5.34
400	3.81	4.90	5.69
500	3.99	5.22	6.01
600	4.12	5.66	–
700	9.13	11.29	11.39
800	10.71	11.54	11.62
900	11.80	11.97	–
1200	–	–	–

Table B.3 for the reference SBD shows that the frequency of the two kinds of *NHOs* increases with the frequency of the applied signal. The same dependence was observed in Table B.2 for the first kind of *NHOs* in the reference HSBD. However, the frequency of these oscillations is a few hundred GHz larger for the SBD (epilayer length 200 nm) than that for the HSBD (epilayer length 250 nm). The simulation of the HSBD with epilayer length equal to 200 nm leads to frequencies for the first kind of *NHOs* closer to the frequency of these oscillations in the reference SBD, see Table B.4. The results obtained for the HSBD with the two values of epilayer length indicate that the frequency of the NHOs increases by decreasing the epilayer length. The comparison of Tables B.3 and B.4 indicates that the presence of the substrate on the SBD also affects the frequency of the first kind of *NHOs*.

Table B.4: Frequency of the first, second and third periods of the *NHOs* directly measured from the time domain current response of the reference HSBD defined in Table B.1 but with epilayer length of 200 nm under applied signals (-3.0 V, 3.85 V, f) simulated with MC.

f, (GHz)	$f_{NHO(1)}$, (THz)	$f_{NHO(2)}$, (THz)	$f_{NHO(3)}$, (THz)
200	3.12	4.31	–
300	3.49	4.50	5.74
400	3.72	5.00	6.53
500	3.95	5.15	–

B.1.3 Spectra of *NHOs*

Figs. B.3 and B.4 show the spectra of the current response presented in Figs. B.1(a) and B.1(b) for the reference HSBD and SBD, respectively. The *NHOs* are localised in a short time span of the current response of the diodes, and, therefore, their spectral content is very broadband.

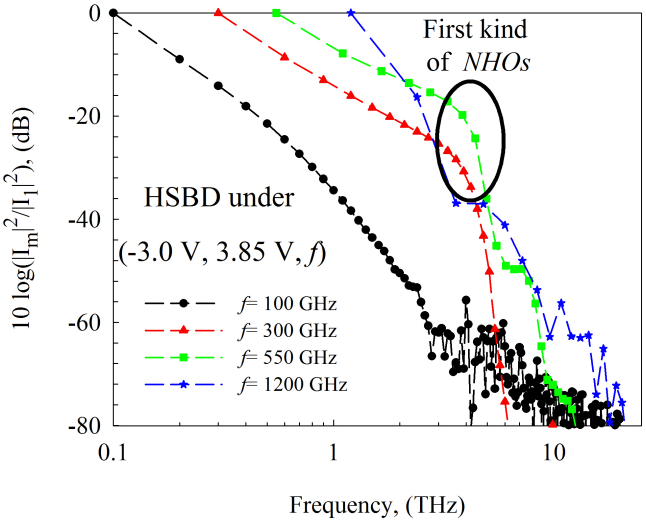

Figure B.3: Spectra of the current response presented in Fig. B.1(a) for the reference HSBD (fast Fourier transform of the current), normalized to the module of the fundamental harmonic of the currents I_1. The sampling frequency for each spectrum is the frequency of the applied signal.

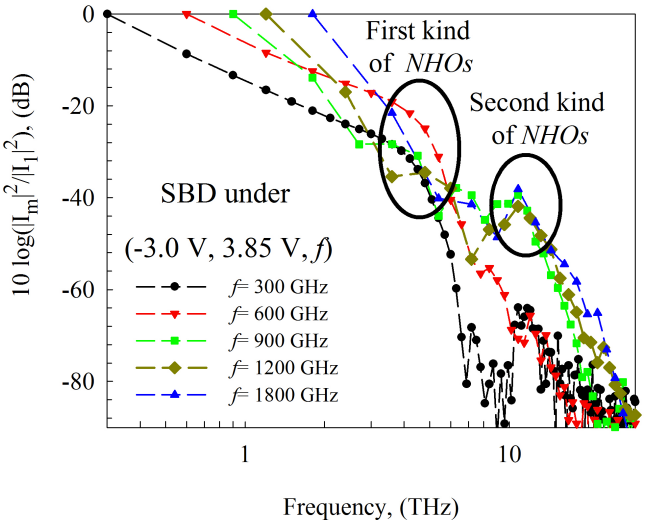

Figure B.4: Spectra of the current response presented in Figs. B.1(b) for the reference SBD (fast Fourier transform of the current), normalized to the module of the fundamental harmonic of the currents I_1. The sampling frequency for each spectrum is the frequency of the applied signal.

For frequencies of the applied signals $f \lesssim 600$ GHz, the first kind of *NHOs* (the only kind of *NHOs* excited at these frequencies) is detected in the spectra by the abrupt decay of the amplitude of the fast Fourier transform at frequencies between $f_{NHO(1)}$ and $f_{NHO(2)}$ for both HSBDs and SBDs. This is observed from the comparison of the spectra of Figs. B.3 and B.4 with the corresponding time domain data of Tables B.2 and B.3.

At higher frequencies of the applied signal the first kind of *NHOs* disappears. Only for the reference SBD appears a peak in the spectra at frequencies around 11 THz, see Fig. B.4, due to the second kind of oscillations observed in Fig. B.1(b), in accordance with the frequencies calculated from the time domain response, Table B.3.

B.1.4 Internal distributions

The signature of the *NHOs* can be observed in the time evolution of the electron concentration, the electron velocity and the electric field. Fig. B.5 shows oscillations of these quantities in the neutral region of the reference SBD under (-3.0 V, 3.85 V, 500 GHz), associated to the first kind of *NHOs*.

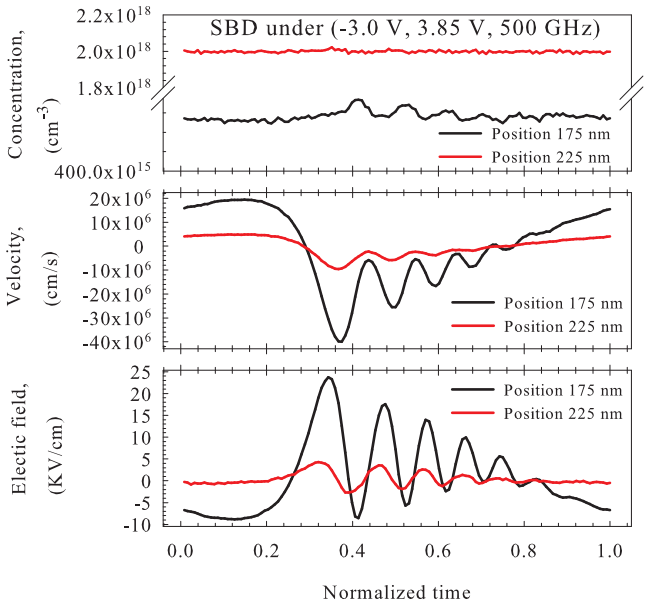

Figure B.5: Time evolution of the electron concentration, the electron velocity and the electric field in the neutral regions of the reference SBD (position 175 nm corresponds to the neutral epilayer and 225 nm to the neutral substrate, with the Schottky contact at position 0 nm) under (-3.0 V, 3.85 V, 500 GHz) from MC simulations.

Under (-3.0 V, 3.85 V, 900 GHz), oscillations of the electron velocity and the electric field appear in the substrate of the reference SBD due to the second kind of *NHOs*, as Fig. B.6 shows. However, in the neutral region of the epilayer, oscillations are only observed in the electron concentration.

B.2 Analytical device modelling

To describe the electron dynamics and interpret the features of the *NHOs* obtained from MC simulation of Schottky diodes in Section B.1, this section presents a simple analytical model for the diode. This model is based on the standard depletion approximation to define the width of the depletion region due to the Schottky contact and the momentum balance equation to describe the transport in the non-depleted regions of the diode [Sel84]. Drift-diffusion model is not able to predict the generation of the *NHOs*. A description of the *NHOs* based on a lumped element equivalent circuit of the diode is also presented. This model might be useful for circuit design.

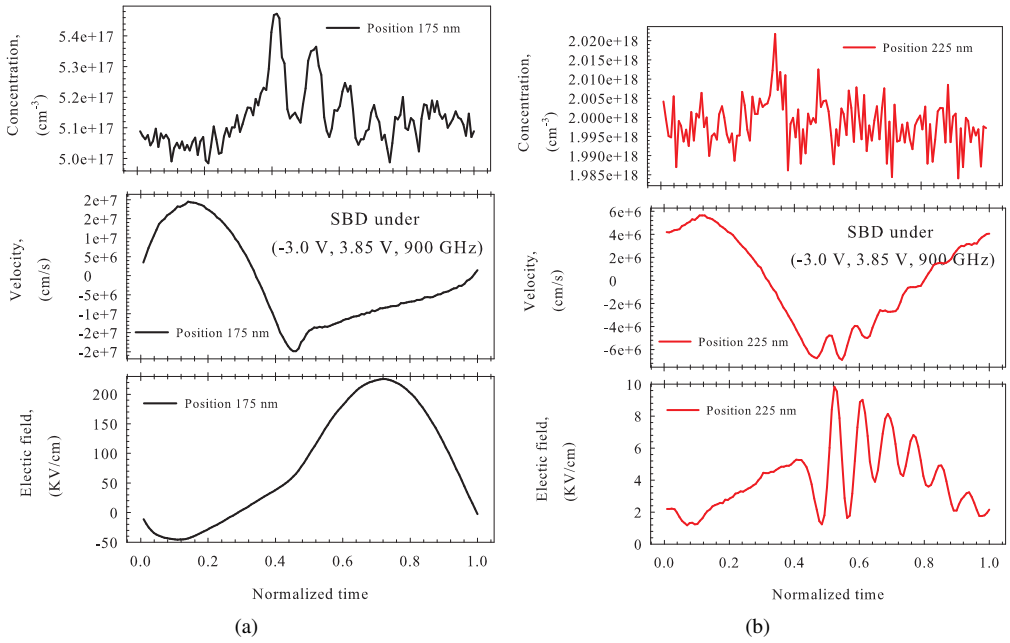

Figure B.6: Time evolution of the electron concentration, the electron velocity and the electric field in (a) the neutral region of the epilayer (position 175 nm) and (b) the substrate (position 225 nm) of the reference SBD under (-3.0 V, 3.85 V, 900 GHz) from MC simulations. The Schottky contact is at position 0 nm.

B.2.1 General approach

The Schottky diode is considered an unipolar device and, therefore, hole contributions are neglected. To analyse the current flow through the diode, the structure of the device is divided into three regions, see Fig. B.7: (i) The depleted region of the epilayer; (ii) the non-depleted epilayer and (iii) the neutral substrate region. It is assumed that the space charge region is completely depleted and that the height of the potential barrier originated by the $n^+ - n$ homojunction is independent of the applied signal: $\Delta V_{n^+-n} = (E_{f,s} - E_{f,e})/q$, where $E_{f,i}$ is the Fermi level of the i-region calculated for the bulk semiconductor in equilibrium.

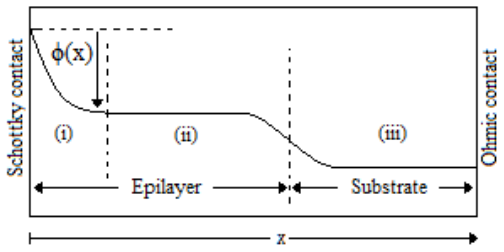

Figure B.7: Sketch of the conduction band of the SBD.

The potential across the region (i) considering the full depletion approximation is (see Fig. B.7):

$$\phi(x) = V_{bi} - V - \frac{qN_e}{2\varepsilon_0\varepsilon_r}(w_{depl} - x)^2 \,, \tag{B.1}$$

where V_{bi} is the built-in voltage of the epilayer, N_e is the epilayer doping concentration, $\varepsilon_0\varepsilon_r$ is the permittivity of the semiconductor, q the absolute value of the electron charge, V the applied voltage that drops in the depletion region and w_{depl} the width of the depletion region.

Under time varying conditions, the total current density in the depletion region (and consequently through the SBD) is the sum of the thermionic current density over the Schottky barrier and the displacement current density, that is independent of the position under full depletion approximation:

$$J = J_0(e^{qV/\eta K_b T} - 1) - qN_e \frac{dw_{depl}}{dt} , \tag{B.2}$$

where η is the ideality factor and J_0 is the reverse saturation current of the diode. Tunneling current is neglected.

The conduction current density J_i in the non-depleted epilayer (i= e, J_e) and the substrate (i= s, J_s) assuming constant temperature and neglecting carrier density gradients is described by eq. (B.3), derived from the Boltzmann transport equation [Sel84].

$$J_i + \tau_{m,i} \frac{dJ_i}{dt} = \tau_{m,i} \frac{q^2 N_i}{m^*} E_i,\ i = e, s , \tag{B.3}$$

where m^* is the effective mass of the electrons in the semiconductor, $\tau_{m,i}$ is the momentum relaxation time in the neutral i-regions, eq. (2.36). This equation means that the acceleration of the carriers (variation of the conduction current J_i) is finite and introduces a time delay between the action of the electric field and the response of the current [Cha64, Gel98] (inertia of the carriers). The momentum relaxation times, $\tau_{m,i}$, are very small, typically on the order of picoseconds ($\tau_{m,e}$= 0.11 ps and $\tau_{m,s}$= 0.09 ps have been used in this appendix for the doping concentration of the reference GaAs SBD; these values have been obtained with our one-particle MC under low field conditions). The term $\tau_{m,i} dJ_i/dt$ can be considered as a small perturbation in eq. (B.3). Drift-diffusion assumes that $\tau_{m,i} dJ_i/dt$ is negligible with respect to J_i, and, therefore, the current relation implicates the instantaneous response of the conduction current to the electric field

$$J_i = \frac{q^2 N_i \tau_{m,i}}{m^*} E_i,\ i = e, s . \tag{B.4}$$

Eq. (B.4) corresponds to the current relation used in drift-diffusion models (without considering diffusion contributions).

The electric field in the neutral epilayer and substrate E_i, i= e, s is considered independent of the position since we assume that the charge density disappears outside of the depletion region [Gel98]. Under time varying conditions, the total current in the neutral regions of the SBD is:

$$J_{t,i} = J_i + \varepsilon_0 \varepsilon_r \frac{dE_i}{dt} . \tag{B.5}$$

From eq. (B.1), the relation between the applied voltage V_{app} and w_{depl} is:

$$V_{app} = V_{bi} - \frac{qN_e}{2\varepsilon_0 \varepsilon_r} w_{depl}^2 + E_e(L_e - w_{depl}) + E_s L_s . \tag{B.6}$$

For HSBDs, by imposing the continuity of the current in the epilayer (eqs. (B.2) and (B.5)) and eq. (B.3) for the conduction current in the neutral epilayer, the system of equations for J_e and ω to solve is:

$$\frac{dJ_e}{dt} = \frac{q^2 N_e}{m^*} E_e - \frac{J_e}{\tau_{m,e}} , \tag{B.7a}$$

$$J_0(e^{qV/\eta K_b T} - 1) - qN_e \frac{dw_{depl}}{dt} = J_e + \varepsilon_0 \varepsilon_r \frac{dE_e}{dt} , \tag{B.7b}$$

where E_e is expressed in terms of J_e and ω from eq. (B.6). We denote these equations by momentum balance (MB) model since they include the momentum balance equation for J_e, eq. (B.3). If we apply eq. (B.4) to describe the conduction current in the neutral epilayer, the system of eqs. (B.7) is

reduced to the following equation for the width of the depletion region (denoted by drift diffusion (DD) model):

$$J_0(e^{qV/\eta K_b T}-1)-qN_e\frac{dw_{depl}}{dt}=\frac{q^2N_e\tau_{m,e}}{m^*}E_e+\varepsilon_0\varepsilon_r\frac{dE_e}{dt}\ , \tag{B.8}$$

where E_e and J_e are expressed in terms of w_{depl} from eqs. (B.6) and (B.4), respectively.

The generalization of the equations presented in this Section for SBDs with substrate is straightforward, leading to a system of four independent differential equations for J_e, J_s, w_{depl} and E_e. However, the model described in this section and its generalization to include the substrate only predict the first kind of the *NHOs*, as will be explained in section B.3.

B.2.2 Equivalent circuit model

The performance of the first kind of the *NHOs* can be described by means of a lumped element equivalent circuit (LEC model) Fig. B.8, see chapter 2. The Schottky junction space-charge capacitance is usually approximated by eq. (B.9) while the nonlinear resistance of the junction is neglected for the varactor operation regimes considered in this appendix.

$$C_j=\frac{C_{j0}}{\sqrt{1-V/V_{bi}}}\ , \tag{B.9}$$

where $C_{j0}=A(q\varepsilon_0\varepsilon_rN_e/(2V_{bi}))^{0.5}$ is the junction capacitance at V=0. The relation between the current and the voltage in the neutral region of the epilayer is defined by a simple RLC subcircuit shown in Fig. B.8 [Cha64]. The values of R_e, H_e and C_e are:

$$R_e(t) = \frac{m^*}{N_eq^2\tau_{m,e}}\frac{L_{ue}(t)}{A}\ , \tag{B.10a}$$

$$H_e(t) = \frac{m^*}{N_eq^2}\frac{L_{ue}(t)}{A}\ , \tag{B.10b}$$

$$C_e(t) = \varepsilon_0\varepsilon_r\frac{A}{L_{ue}(t)}\ , \tag{B.10c}$$

where $L_{ue}(t)$ is the length of the undepleted epilayer which is assumed time dependent under time varying conditions, see eqs. (2.7), (2.8) and (2.9), and the other parameters have the usual meaning. In this model we assume time independent length of the neutral region of the epilayer.

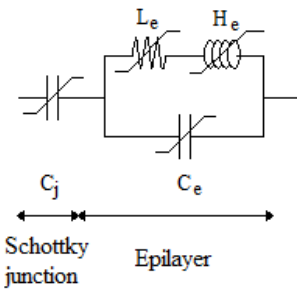

Figure B.8: Equivalent circuit of a HSBD.

There exists a direct relation between the LEC and the MB models. The capacitor C_e in the LEC model Fig. B.8 accounts for the displacement current in the neutral epilayer of the MB model $\varepsilon_0\varepsilon_r dE_e/dt$ eq. (B.5). On the other hand, the performance of the conduction current J_e described by eq. (B.3) is represented by the inductance H_e, that accounts for the delayed response of J_e to the electric field (term $\tau_e dJ_e/dt$), and R_e the series resistance of the epilayer.

B.3 Physical interpretation

The main features of the *NHOs* obtained from MC simulations of Schottky diodes in section B.1 are analysed in this section by means of the analytical MB model. We find that this model predicts correctly the first kind of the *NHOs*, but it is required an accurate model of the $n^+ - n$ junction to describe the second kind. Therefore, the analysis of the second kind of *NHOs* presented here is completely based on the results of MC simulations.

B.3.1 First kind of the *NHOs*

Section B.1 showed that the first kind of the *NHOs* are common to HSBDs and SBDs and they present similar frequencies in both devices. To simplify the analysis of these *NHOs*, this subsection takes as a reference the HSBDs. The results presented in this subsection are applicable to the first kind of oscillations in SBDs.

Qualitative analysis

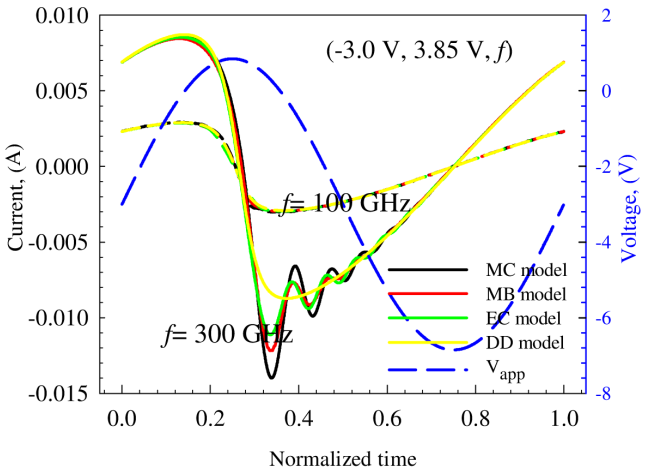

Figure B.9: Current response of the reference HSBD under (-3.0 V, 3.85 V, f) with f= 100 GHz and 300 GHz from the numerical solution of eqs. (B.7), the EC model, eq. (B.8) and MC simulations.

Fig. B.9 compares the current response of the reference HSBD under (-3.0 V, 3.85 V, f), f= 100 and 300 GHz obtained from the MB, the DD, the LEC and the MC models. At 100 GHz, the four models predict the same current response, but at 300 GHz only the MC, the MB and the LEC models predict the *NHOs* (the first kind of *NHOs* described in Section B.1). The comparison of the DD and the MB models shows that it is necessary to include the term $\tau_e dJ_e/dt$ in the conduction current equation (equivalent to H_e in the LEC model) to predict the *NHOs*. Therefore, the *NHOs* are the result of coupling the inertial performance of the charge carriers (term $\tau_e dJ_e/dt$) to the nonlinear variation of the depletion region width.

To interpret the nonharmonic oscillations, we compare the performance of the carrier dynamics described by the DD model, where the conduction current responds instantaneously to the electric field, and the MB model that includes the term $\tau_e dJ_e/dt$ in the equation for the conduction current, eq. (B.7). Figs. B.10 and B.11 show the time evolution of the electrical variables (J_e, $\tau_e dJ_e/dt$, σE_e and w_{depl}) of the reference HSBD under (-3.0 V, 3.85 V, 300 GHz) obtained with the MB and DD models. From the comparison between the response of the two diode models presented in Figs. B.10 and B.11 and according to the description of the models presented in subsection B.2.1, we can write the variables of the MB model (denoted by a tilde) as the sum of the variables of the DD

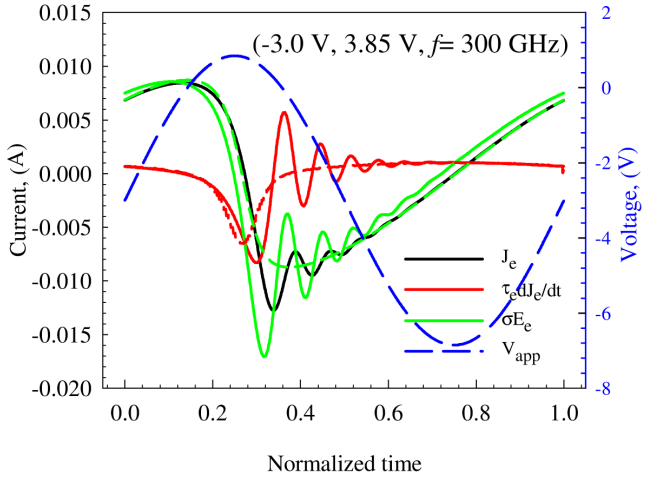

Figure B.10: Time evolution of J_e, $\tau_e dJ_e/dt$ and σE_e for the reference HSBD under applied signal (-3.0 V, 3.85 V, 300 GHz) from the MB model eqs. (B.7) (continuous lines) and the DD model eq. (B.8) (dashed lines). In the DD model eq. (B.8) $J_e = \sigma E_e$, with $\sigma = q^2 N_e \tau_e / m^*$.

model (without tilde) and a small perturbation: $\widetilde{J_e} = J_e + \delta J_e$, $\widetilde{w}_{depl} = w_{depl} + \delta w_{depl}$, $\widetilde{E_e} = E_e + \delta E_e$. According to eq. (B.7b), the time variation of w_{dept} is determined by:

$$\frac{dw_{depl}}{dt} = -\frac{1}{qN_e}\left[J_e + \varepsilon_0 \varepsilon_r \frac{dE_e}{dt} - J_0(e^{qV/\eta K_b T} - 1)\right] \tag{B.11}$$

While in the DD model the term J_e on the right hand side of eq. (B.11) depends only on the electric field, eq. (B.4), in the MB model it also depends on the term $\tau_{m,e} dJ_e/dt$, eq. (B.7a). Hence, in the MB model, the variation of the width of the depletion region, eq. (B.11), takes into account the finite acceleration of the electrons in the semiconductor -term $\tau_{m,e} dJ_e/dt$, carrier inertia- which originates the term δw_{depl} (the DD model assumes that the electron velocity adapts instantaneously to the electric field). The deviations of $\widetilde{w}_{depl}$ from the reference w_{depl} of the DD model, Fig. B.11, lead to the electric fields δE_e acting to return $\widetilde{w}_{depl}$ back to the reference w_{depl}, eqs. (B.7). These forces and electron inertia are responsible for current oscillations.

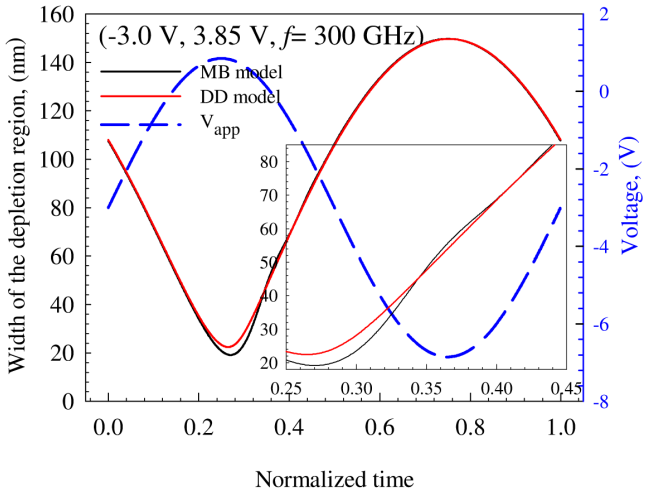

Figure B.11: Time evolution of the width of the depletion region of the reference HSBD under (-3.0 V, 3.85 V, 300 GHz) from the numerical solution of eqs. (B.7) (black line) and eq. (B.8) (red line).

Condition to generate the *NHOs*

The results presented in Section B.1 show that some conditions have to be satisfied in order to excite the first kind of the *NHOs*. Subsection B.3.1 showed that the term $\tau_{m,e}dJ_e/dt$ in the MB model is necessary to generate the oscillations. On the other hand, the current relation, eq. (B.3), indicates that this term will begin to dominate the response of the SBD when it takes values of the order of J_e. Therefore, we define the ratio between the maximum amplitude of $\tau_{m,e}dJ_{m,e}/dt$ and the maximum amplitude of J_e in a period of the applied signal ($r = \frac{\tau_{m,e}dJ_{m,e}/dt}{J_e}$) to determine when the *NHOs* appear in the current response of the diode. In the frequency domain, this ratio is expressed by $r = j\omega\tau_{m,e}$.

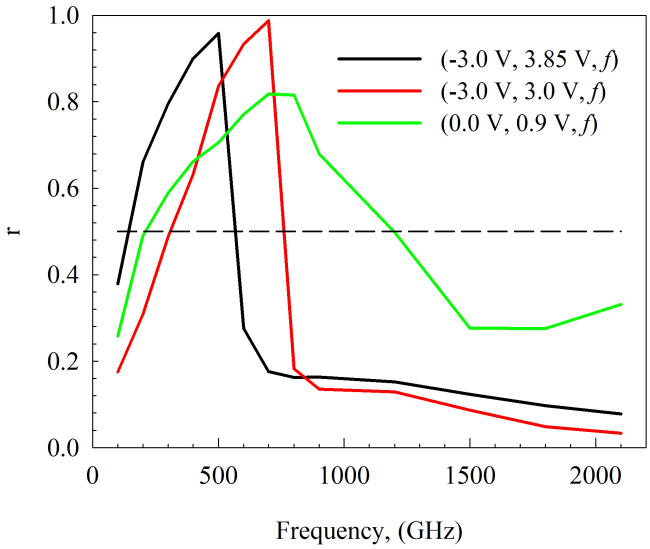

Figure B.12: Dependence of r on the bias point, frequency and amplitude of the applied signal for the reference HSBD simulated with the MC method. The dashed line corresponds to r= 0.5.

Fig. B.12 shows r for the reference HSBD under different applied signals simulated with the MC method ((-3.0 V, 3.85 V, f), (-3.0 V, 3.0 V, f) and (0.0 V, 0.9 V, f)). In this figure, $\tau_{m,e}$ has been calculated by MC simulations according to $\tau_{m,e} = m^*\mu_e/q = m^*v_e(x,t)/(E_e(x,t)q)$ where the electric field E_e and the electron velocity v_e have been evaluated in neutral regions of the epilayer. The conduction current has been evaluated as $J_e = qn_e(x,t)v_e(x,t)$ where $n_e(x,t)$ is the electron density.

Fig. B.12 shows that the ratio r increases with the frequency f of the applied signal[2] up to a frequency that depends on the applied waveform. For higher frequencies, $\tau_{m,e}$ decreases because of the increment of the L-intervalley scattering probability, what limits the current flowing in the device (saturation phenomenon [Kol92]) and, therefore, r decreases.

According to the current response obtained from the MC simulation of the reference HSBD under the signals (-3.0 V, 3.85 V, f), see Fig. B.1(a), (-3.0 V, 3.0 V, f) and (0.0 V, 0.9 V, f) -presented in Fig. B.13- the first kind of *NHOs* appears for $r > 0.5$. Therefore, it is necessary that the applied signal leads to values of $\tau_{m,e}dJ_e/dt$ of the order of J_e in the SBD to excite the *NHOs*.

B.3.2 Second kind of *NHOs*

From Section B.1, we know that a new kind of *NHOs* is generated in the reference SBD under applied signals (-3.0 V, 3.85 V, f) with f higher than 600 GHz. Fig. B.14 shows how the position

[2] $J \simeq -qN_e dw_{depl}/dt$ where $w_{depl} \sim (2\varepsilon_0\varepsilon_r(V_{bi} - V_{app})/(qN_e))^{0.5}$ and $r \sim 2\pi f\tau_{m,e}((V_{bi} - V_0)/(V_{bi} - V_0 - V_1))^{0.5}$

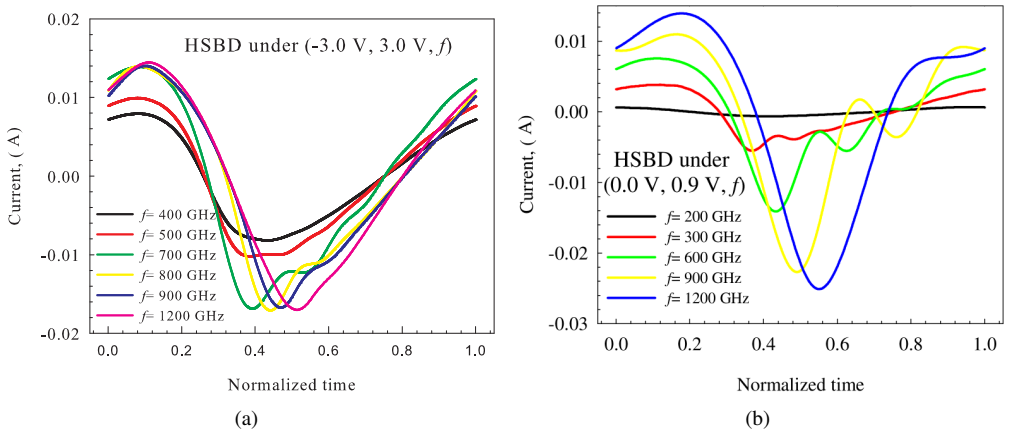

Figure B.13: Current response obtained from the MC simulation of the reference HSBD under (a) (-3.0 V, 3.0 V, f) and (b) (0.0 V, 0.9 V, f).

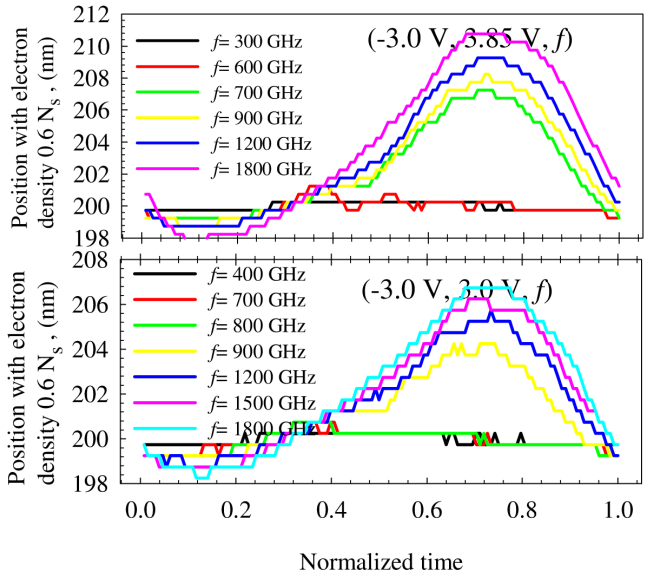

Figure B.14: Time evolution of the position with electron density 0.6 N_s from the MC simulation of the reference SBD under (-3.0 V, 3.85 V, f) and (-3.0 V, 3.0 V, f) for different frequencies f. The Schottky contact is at position 0 nm.

of the device with electron density 0.6 times the doping of the substrate N_s evolves under the signals (-3.0 V, 3.85 V, f) and (-3.0 V, 3.0 V, f) (note that according to Fig. B.2(b), the width of the depletion region does not reach the $n^+ - n$ transition under the applied signals). The second kind of *NHOs* appears when the $n^+ - n$ junction is modulated by the applied signal. Therefore, its origin is equivalent to the origin of the first kind of oscillations (Subsection B.3.1), i.e. the modulation of the nonlinear $n^+ - n$ junction [Abd92] by the inertial motion of the charge carriers in the substrate and the epilayer.

Fig. B.15 presents the electric field profiles at different normalized times for the reference SBD under (-3.0 V, 3.85 V, f) for f= 600 GHz and 700 GHz. The high electric field induced in the epilayer of the SBD, see Fig. B.15, leads to a high occupation of the upper valleys of the semiconductor (higher than 85 %) and to the enhancement of the $n^+ - n$ potential barrier.

Since the analytical models presented in section B.2 do not include an accurate model for the

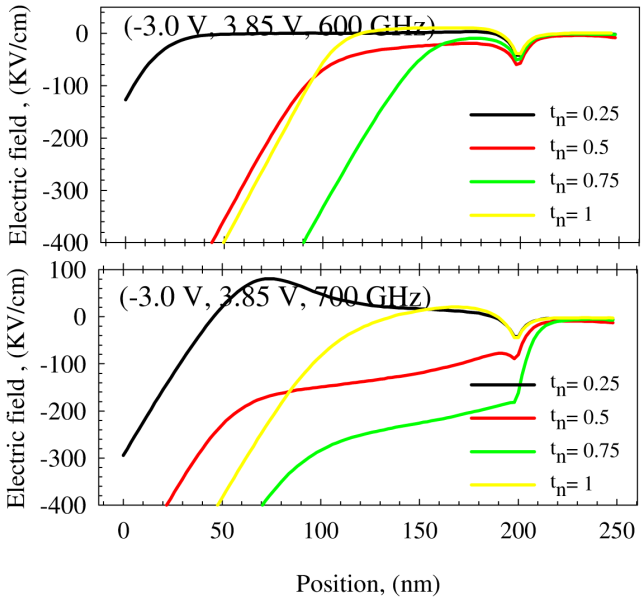

Figure B.15: Electric field profiles of the reference SBD under (-3.0 V, 3.85 V, f) with f= 600 GHz and 700 GHz, obtained from MC simulations at different normalized times t_n. Position 0 corresponds to the Schottky contact.

$n^+ - n$ transition, the MB and the LEC models do not predict the second kind of *NHOs*.

Appendix C

Additional studies about noise in Schottky diodes

C.1 Equations comparing the RC resonance for GaAs and GaN Schottky diodes

The following equations present the ratios of the central frequency, f_{RC}, the amplitude, $S_I(f_{RC})$, and the bandwidth at -3 dB, Δf_{RC}, for the RC resonance of GaN and GaAs Schottky diodes. They have been obtained from eqs. (4.33) and (4.35) particularized for homogenous diodes, [Shi05].

$$\rho_f = f_{RC,GaN}/f_{RC,GaAs} = \left[\frac{(m^{*2}\varepsilon_r)_{GaAs}}{(m^{*2}\varepsilon_r)_{GaN}}\frac{(V_{bi}-V)_{GaN}}{(V_{bi}-V)_{GaAs}}\right]^{1/4} \simeq 0.58\left[\frac{(V_{bi}-V)_{GaN}}{(V_{bi}-V)_{GaAs}}\right]^{1/4} \tag{C.1}$$

$$\rho_S = S_I(f_{RC,GaN})/S_I(f_{RC,GaAs}) = \frac{(\varepsilon_r m^* \mu)_{GaN}}{(\varepsilon_r m^* \mu)_{GaAs}}\rho_f^2\frac{1-(f_{pe}/f_{RC})^2_{GaN}}{1-(f_{pe}/f_{RC})^2_{GaAs}} \simeq 2.43\frac{\mu\,|_{GaN}}{\mu\,|_{GaAs}}\rho_f^2\frac{1-(f_{pe}/f_{RC})^2_{GaN}}{1-(f_{pe}/f_{RC})^2_{GaAs}} \tag{C.2}$$

$$\rho_\Delta = \Delta f_{RC,GaN}/\Delta f_{RC,GaAs} = \frac{1}{\rho_f}\frac{\left[\sqrt{f_{sc}^4+(4\pi f_{sc}f_{RC})^2}\right]_{GaN}}{\left[\sqrt{f_{sc}^4+(4\pi f_{sc}f_{RC})^2}\right]_{GaAs}} \tag{C.3}$$

where $\Delta f_{RC} = f_b - f_a = (f_b^2 - f_a^2)/(f_a + f_b) \simeq ((f_{sc}^4 + (4\pi f_{sc}f_{RC})^2)^{1/2})/(2f_{RC})$; f_a and f_b are frequencies such that $S_I(f_a) = S_I(f_b) = S_I(f_{RC})/2$ and $f_a < f_{RC} < f_b$, and μ is the low field electron mobility. This expression for Δf_{RC} is obtained particularizing $S_I(f)$ given by eq. (4.33) for homogeneous diodes and solving the equation for the frequencies f such that $S_I(f) = S_I(f_{RC})/2$ ($S_I(f_{RC}) = 4k_BT\,2\pi C\,(f_{pe}^2 - f_{RC}^2)/f_{sc} = 4k_BTqN_eA\mu\,(1-r_d)$), where f_{RC} is the frequency of the returning carrier eq. (4.35) particularized for homogeneous diodes. The ratios ρ_S and ρ_Δ are valid only for homogeneous diodes.

Table C.1 shows the material parameters we have used when dealing with the analytical model of [Shi05]. μ_e and μ_s of Table C.1 represent the low field electron mobilities obtained from MC simulation of bulk GaAs and GaN semiconductors at 300 K with doping concentrations equal to the doping concentrations of the epilayer and the substrate of the reference Schottky diode, respectively. The rest of parameters presented in this table can be found in [Fis88, Mad04].

Table C.1: Parameters for GaAs and GaN used in chapter 4 and this appendix.

	GaAs	GaN
ε_r	12.9	8.9
m^*	0.063	0.222
μ_e, $(m^2/(\mathrm{Vs}))$	0.5068[a]	0.0674[a]
μ_s, $(m^2/(\mathrm{Vs}))$	0.2701[b]	0.0338[b]

[a] From MC simulation of bulk semiconductor doped with $10^{17} cm^{-3}$ at 300 K.

[b] From MC simulation of bulk semiconductor doped with $2\,10^{18} cm^{-3}$ at 300 K.

C.2 Partition noise

Ref. [Shi03b] presents a mathematical framework for the analysis of the partition noise in bulk semiconductors associated with the random transitions of carriers between two or more physically distinct groups of electron states located in momentum space. For such a subdivision to take place, the characteristic time of carrier exchange between groups must be much longer than that of intra-group transitions. The fluctuations of the relative occupation of these groups in momentum space manifest themselves as a source of fluctuations with respect to the usual velocity fluctuations. To simplify the analysis of these fluctuations, two groups of carriers in the momentum space are assumed. The average velocity of the carriers and the average relative population of each group are denoted by $\overline{v_i}$ and $\overline{p_i}$ $(i = 1,2)$, respectively. Under dc conditions, the spectral density of the velocity fluctuations is given by, [Shi03b]:

$$S_{\delta v\delta v}(f) = S^{nopart}_{\delta v\delta v}(f) + S^{part}_{\delta v\delta v}(f) = S^{nopart}_{\delta v\delta v}(f) + \frac{4(\overline{v_1}-\overline{v_2})^2\overline{p_1 p_2}\tau_g}{1+(2\pi f)^2\tau_g^2} \tag{C.4}$$

where $S^{nopart}_{\delta v\delta v}(f)$ is the part of the spectral density which does not include partition noise, i.e., related to the fluctuations of the velocity in each group of carriers, and τ_g is the characteristic time of the intergroup exchange.

Under cyclostationary conditions of fundamental frequency f_{ex}, the correlation function of the fluctuations of the velocity is a function of two relevant times, namely, $\theta \in [0, 1/f_{ex}]$ and the correlation time τ. By taking the Fourier transform of the correlation function with respect to τ gives the spectral density $S_{\delta v\delta v}(\theta, f)$, which depends on θ, see section 4.1.1. Under these conditions, the statistical independence of the velocity fluctuations inside the groups δv_i for each one of the two groups of carriers and of the fluctuations in their populations δp_i will take place only when $f_{ex} >> 1/\tau_g$. Under the conditions $f_{ex} >> 1/\tau_g$, only the average velocity of the carriers in each group will follow the variations of the applied excitation. By assuming that $\overline{v_i}(t) = \overline{v_i}\cos(2\pi f_{ex} t + \phi_i)$, the spectral density of the carrier velocity fluctuations is given by, [Shi03b]:

$$S_{\delta v\delta v}(\theta, f) = S^{nopart}_{\delta v\delta v}(\theta, f) + \frac{1}{4}\left[S^{part}_{\delta v\delta v}(f - f_{ex}) + S^{part}_{\delta v\delta v}(f + f_{ex})\right] + \frac{1}{2}S^{part}_{\delta v\delta v}(f)cos(4\pi f_{ex}\,\theta) \tag{C.5}$$

where $S^{nopart}_{\delta v\delta v}(t, f)$ is the part of the spectral density which does not include partition noise, and $S^{part}_{\delta v\delta v}(f)$ is given by eq. (C.4). According to eq. (C.5), under cyclostationary conditions part of the partition noise is upconverted to the frequency f_{ex} (terms $S^{part}_{\delta v\delta v}(f - f_{ex}) + S^{part}_{\delta v\delta v}(f + f_{ex})$). There is also a contribution of the partition noise that depends on θ.

Fig. C.1 shows the spectral density of the current fluctuations $S_I(f)$ calculated as described in section 4.1.1 for the GaAs $n^+ - n$ reference Schottky diode in chapter 4 under sinusoidal excitation of frequencies 600 GHz and 900 GHz at different amplitudes; Fig. C.2 presents the average occupation

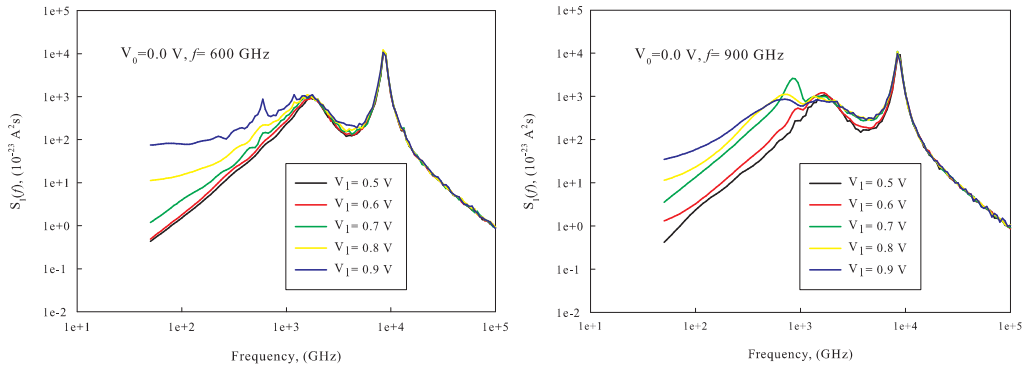

Figure C.1: Noise spectra of the GaAs $n^+ - n$ reference Schottky diode under excitations of different amplitude. Bias V_0= 0.0 V and f_{ex}= 600 and 900 GHz.

of the L valley under these conditions. When the amplitude of the excitation becomes sufficiently high for intervalley $\Gamma - L$ transfer, a peak at the excitation frequency appears in the spectral density, according to [Shi03b]. This peak initially rise with the amplitude of the excitation. When the ratio between the amplitude and the frequency of the excitation overpass its optimum value, the amplitude of the peak decreases and slightly shifts to higher frequencies. At 900 GHz this optimum ratio occurs for the amplitude 0.7 V and near 0.9 V at 600 GHz, Fig. C.1. A similar performance is described in [Shi03b] for intervalley transfer in bulk GaAs.

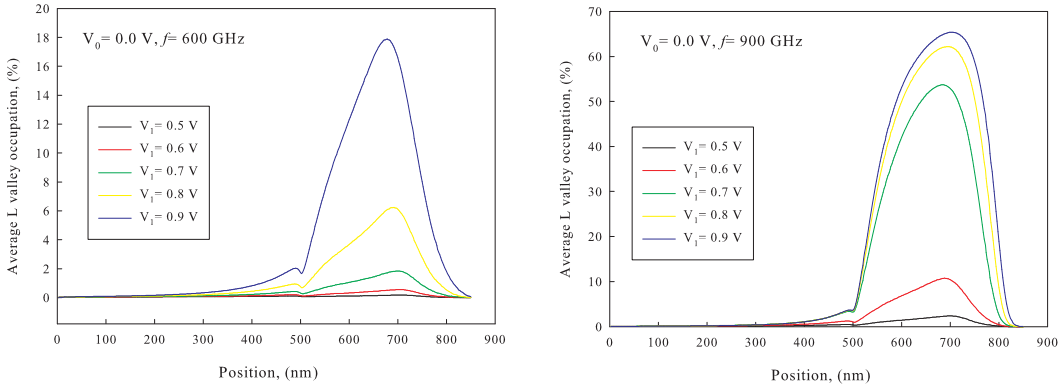

Figure C.2: Relative occupation of the L valley for the GaAs $n^+ - n$ reference Schottky diode in chapter 4 under excitation of frequencies 600 and 900 GHz , at bias 0.0 V and different amplitudes.

Appendix D

Additional data for the multipliers

This appendix presents an analysis of the physical processes limiting the performance of the diodes in the multipliers considered in chapter 5. Physics-based DD and MC models are used to evaluate the internal distributions of some magnitudes of the diode, e.g., the electron concentration, the electron velocity, the electric field or the occupation of the upper valleys as a function of time and position in the diode under periodic excitations. In the figures for the internal distributions as a function of the position in the diode, it has been assumed that the ohmic contact is located at position 0 nm, as shown in Fig. D.1.

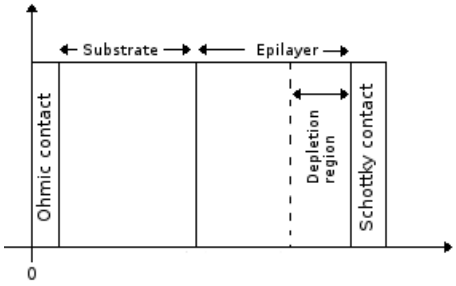

Figure D.1: Scheme of the Schottky diode, showing the position of the ohmic and Schottky contacts assumed in this appendix.

D.1 The 200 GHz doubler

Fig. D.2 (see Fig. 5.7(a)) presents the efficiency and different characteristics of the diodes for the 200 GHz doubler [Cha04] described in Table 5.1 at different input powers. The analysis of these figures indicate:

- Figs. D.2(d), (e) and (f) show that MC predicts lower electric fields in the undepleted region of the epilayer for the simulated input powers. Hence, velocity saturation effects are not limiting the performance of this multiplier. However, DD model predicts electric fields higher than MC in the undepleted epilayer for input powers $P_{d,in}$ higher than 10 dBm.
- According to MC, DD_0 and LEC models, at input powers higher than 15 dBm, the efficiency is limited due the initiation of the varistor operation mode: see the onset of the dc current in Fig. D.2(b) when voltage swing is close to flat band, Fig. D.2(c).

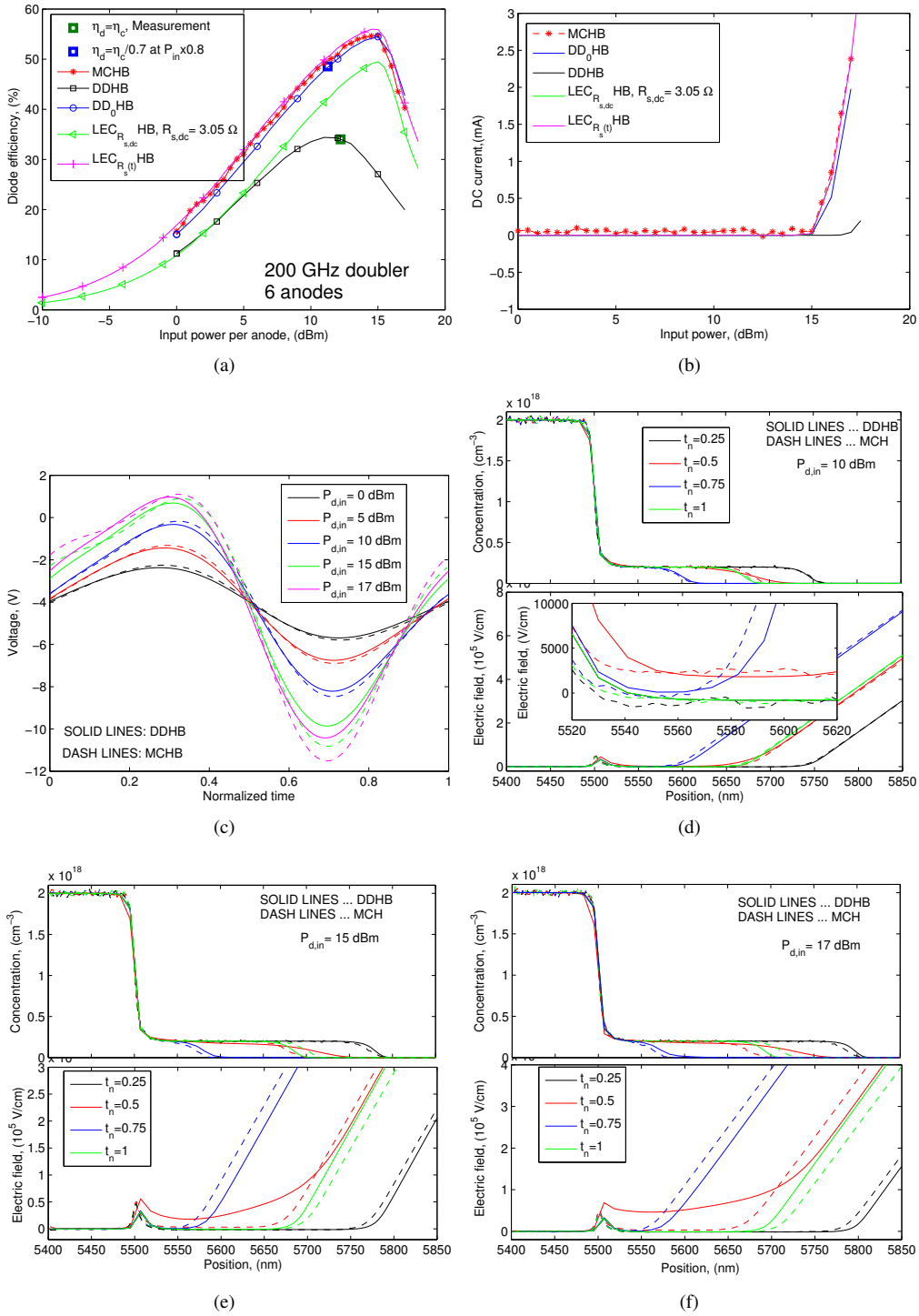

Figure D.2: (a) Diode efficiency of the 200 GHz doubler with epilayer doping 2x10^{17} cm^{-3} in [Cha04] (Table 5.1), (b) dc current of one diode of the doubler and (c) voltage waveforms at the terminals of the diode at different $P_{d,in}$ obtained with different diode models. (d), (e) and (f) show the electron concentration and the electric field as a function of the position (the ohmic contact is located at position 0 nm) at different normalized times (times normalized by one period of the applied signal) at input powers $P_{d,in}$= 10 dBm, 15 dBm and 17 dBm respectively, obtained with DD and MC models.

D.2 The 400 GHz doubler

Fig. D.3 presents the efficiency and different characteristics of the diodes in the 400 GHz doubler [Mai03] described in Table 5.1 at different input powers. The performance of the diodes in this doubler is similar to the diodes in the 200 GHz doubler [Mai03]:

- Figs. D.3(c) and D.3(d) show that the depletion region of the diodes reaches the substrate at normalized time higher than 0.4.
- There are not any velocity saturation effects. Fig. D.3(e), that presents the time evolution of the electric field in the epilayer (evaluated at 20 nm from the n^+-n transition) at different input powers, shows low electric fields in the undepleted epilayer (only undepleted at normalized times lower than 0.4, see Figs D.3(c) and D.3(d))
- At input powers higher than 12 dBm, the operation of the diodes is limited due the initiation of the varistor operation when voltage swing is close to flat band, Fig. D.3(b).

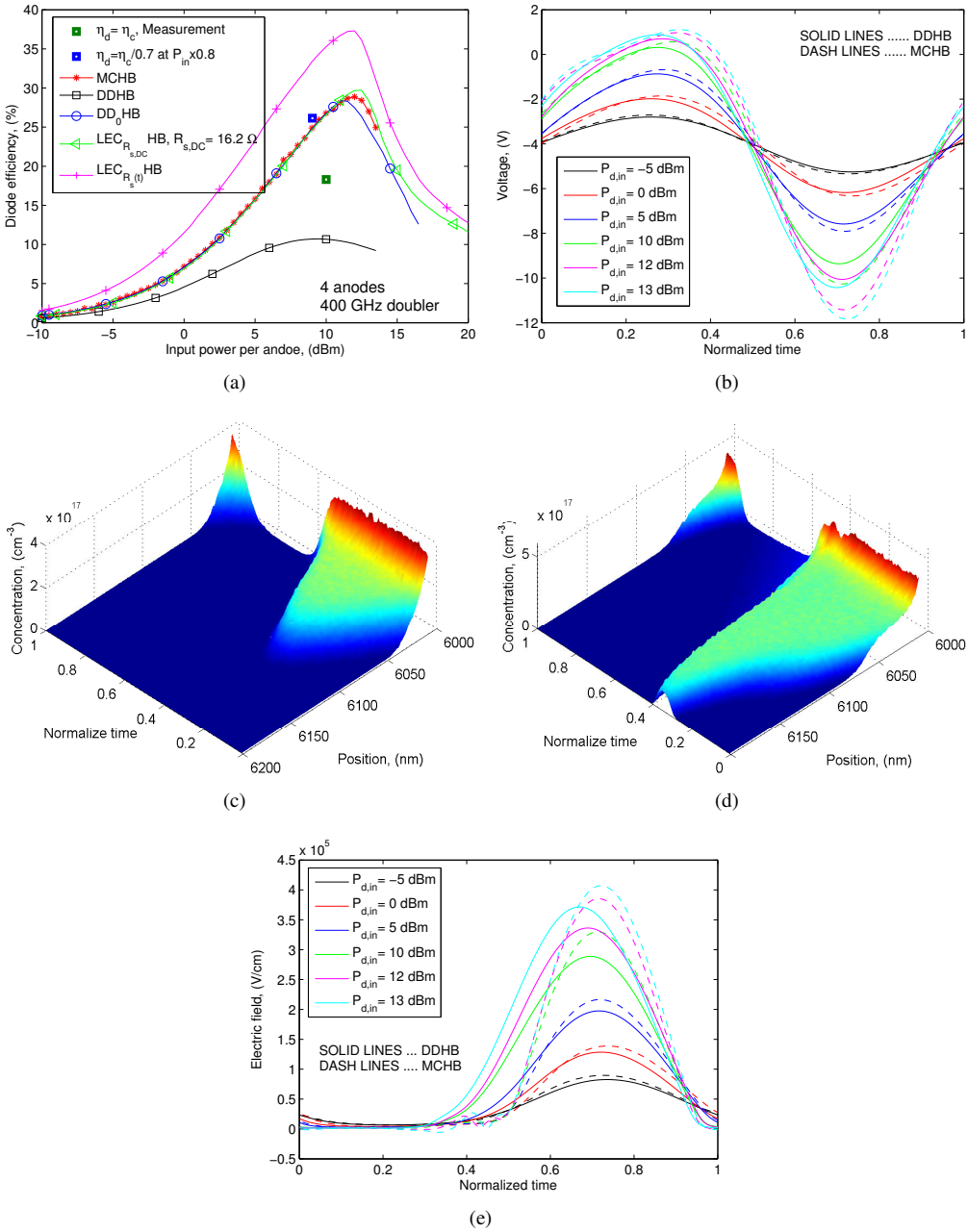

Figure D.3: (a) Diode efficiency of the 400 GHz doubler in [Mai03] (Table 5.1) and (b) voltage waveform at the terminals of the diode at different $P_{d,in}$ obtained with different diode models. (c) and (d) show the electron concentration in the epilayer of the diode at input power $P_{d,in}$= 5 dBm and 13 dBm respectively, from MCHB (Schottky contact at position 6200 nm). (e) shows the electric field as a function of the normalized time, evaluated in the epilayer at 20 nm from the n^+-n transition.

D.3 The 800 GHz doubler

Fig. D.4 presents the efficiency and different characteristics of the diodes in the 800 GHz doubler [Cha02] described in Table 5.1 at different input powers. The most relevant results in this figure are:

- At input powers higher than 5 dBm, the agreement among MCHB, DD_0HB and $LEC_{R_s(t)}$HB disappears. On the other hand, a good agreement is observed between MCHB and LEC_{R_sLC}HB for the whole range of input power. These results indicate that carrier inertia effects are important in the performance of the diodes at this frequency. A good agreement is observed between DD_0HB and $LEC_{R_s(t)}$HB, but they do not model carrier inertia, leading to higher efficiencies than MCHB and LEC_{R_sLC}HB.
- At P_{in}= 10 dBm, the occupation of the L valley in the undepleted epilayer is higher than 20 % (electric fields as high as 10 KV/cm and L valley occupation around 15 % are predicted by the MC model at P_{in}= 8.5 dBm), see Figs. D.4(c) and D.4(d). These results indicate that velocity saturation effects are beginning, but they are not limiting the performance of this multiplier. Besides, the good agreement between MCHB and LEC_{R_sLC}HB, which does not model velocity saturation effects (LEC models assume constant low field electron mobility), indicates that velocity saturation effects can be neglected for this doubler but carrier inertia has to be taken into account.
- Fig. D.4(b) and the good agreement with LEC_{R_sLC}HB show that the limitation of the efficiency is due to the initiation of the varistor operation conditions.
- DD predicts velocity saturation at input powers higher than 0 dBm, because DD evaluates locally the electron mobility.

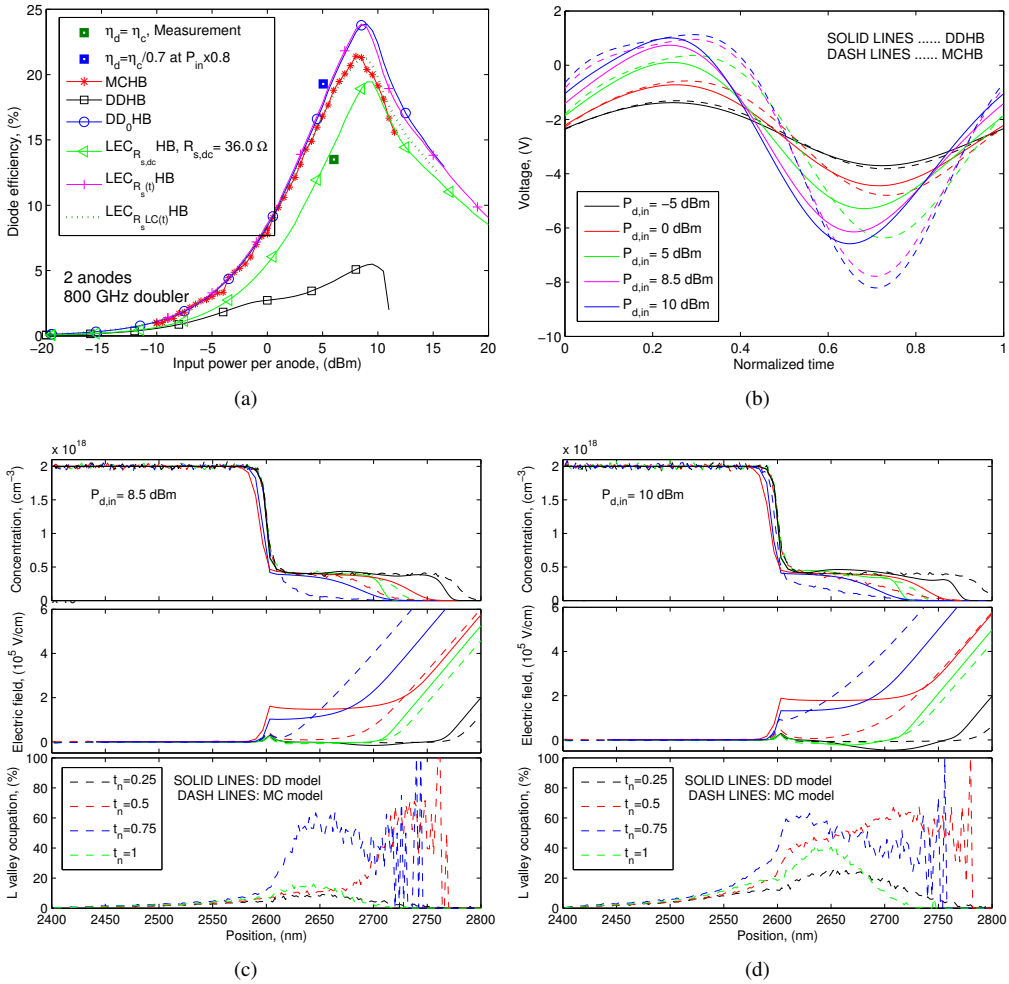

Figure D.4: (a) Diode efficiency of the 800 GHz doubler in [Cha02] (Table 5.1) with different models and (b) the voltage waveforms at the terminals of each diode as a function of the input power per anode. The electron concentration, the electric field and the occupation of the L-valley as a function of the position at different normalized times (times normalized by one period of the applied signal) at input powers (c) $P_{d,in}$= 5 dBm and (d) $P_{d,in}$= 8.5 dBm, obtained with DD and MC models.

D.4 The 1500 GHz doubler

Fig. D.5 presents the efficiency and different characteristics of the diodes in the 1500 GHz doubler [Cha04] described in Table 5.1 at different input powers. The most relevant results in these figures are:

- The performance of the diodes in this doubler are affected by carrier inertia, nonstationary effects and velocity saturation. Fig. D.5(b) shows that the velocity-field loops from MC simulations deviate from the steady-state curve as the input power increases due to these effects.
- At input powers higher than -2 dBm, the electrons in the epilayer gain enough energy from the electric field to be scattered to the upper valleys - at 0 dBm, the L-valley occupation is higher than 20 %- what results in the degradation of the efficiency due to velocity saturation effects.
- Simulations with the DD model show that velocity saturation begins to affect the performance of the diode at $P_{d,in}$= -7.5 dBm, see Fig. D.5(c), where DD predicts electric fields in the undepleted epilayer as high as 30 KV/cm at $P_{d,in}$= -5 dBm.

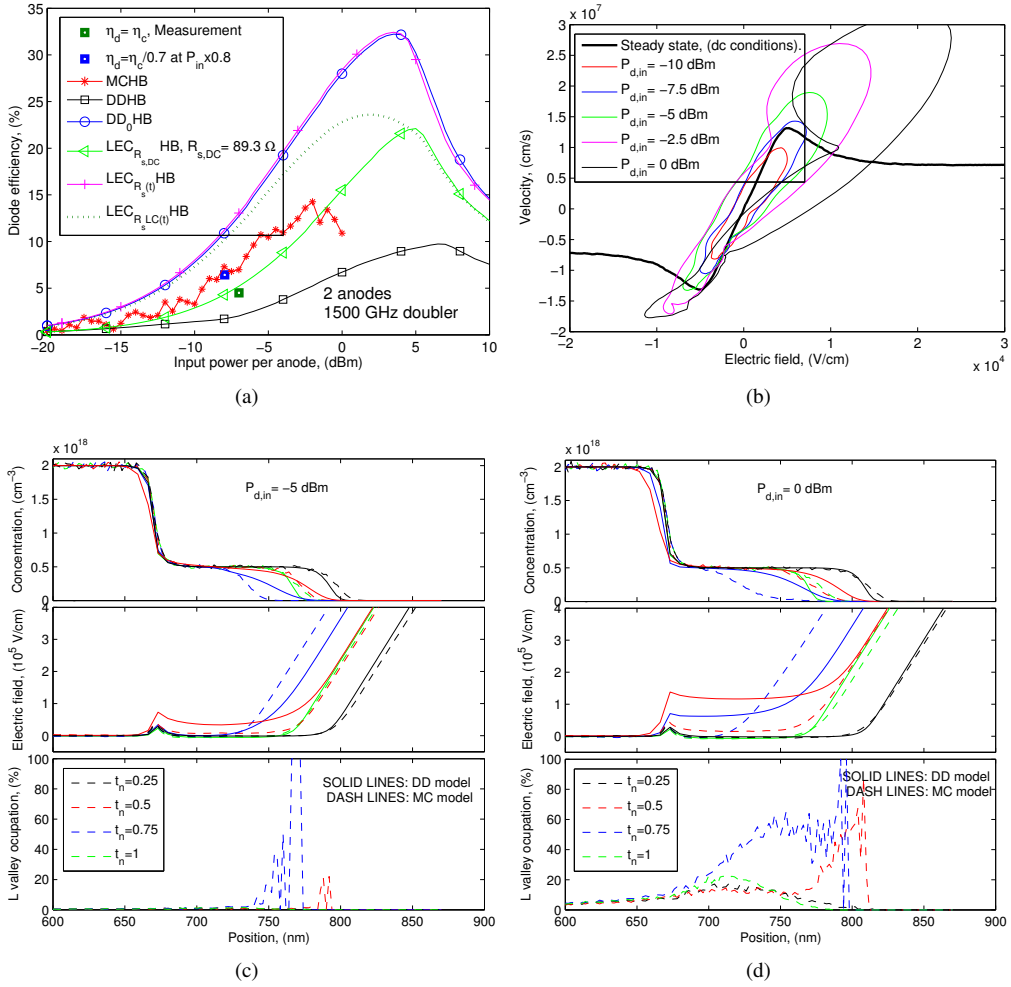

Figure D.5: (a) Diode efficiency of the 1500 GHz doubler in [Cha04] (Table 5.1) with different models, (b) velocity-field loops in the undepleted epilayer of the diode obtained with MC at different input powers. Electron concentration, electric field and occupation of the L-valley as a function of the position at different normalized times (times normalized by one period of the applied signal) at input powers (c) $P_{d,in}$= -5 dBm and (d) $P_{d,in}$= 0 dBm, obtained with DD and MC models.

D.5 The 300 GHz tripler

Fig. D.6 presents the efficiency and different characteristics of the diodes in the 300 GHz tripler [Mae08] described in Table 5.1 at different input powers. The most relevant results from the analysis of this figure are:

- Velocity saturation is not limiting the performance of this device, since low electric fields and close to zero L valley occupation are observed in Fig. D.6(c) and D.6(d). As a consequence, a good agreement is observed among MCHB, DD$_0$HB and LEC$_{R_s(t)}$HB.
- The efficiency decreases at input powers higher than 5 dBm because the onset of the varistor operation, observed in Fig. D.6 (b) by the onset of the dc current.

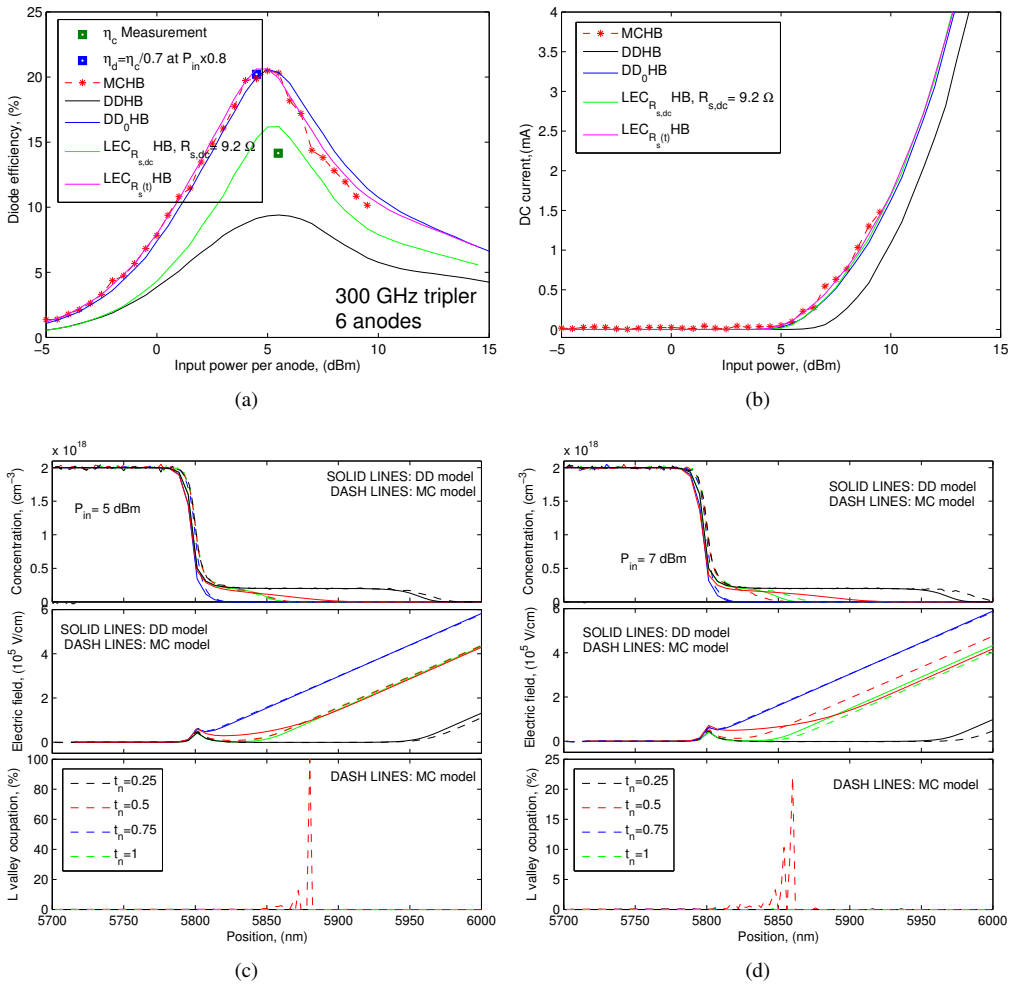

Figure D.6: (a) Diode efficiency and (b) dc current per anode of the 300 GHz tripler in [Mae08] (Table 5.1) with different models as a function of the input power per anode. Electron concentration, electric field and occupation of the L-valley as a function of the position at different normalized times (times normalized by one period of the applied signal) at input powers (c) $P_{d,in}$= 5 dBm and (d) $P_{d,in}$= 7 dBm, obtained with DD and MC models.

D.6 The 600 GHz tripler

Fig. D.7 presents the efficiency and different characteristics of the diodes in the 600 GHz tripler [Mae05b] described in Table 5.1 at different input powers. The most relevant results from the analysis of this figure are:

- A good agreement is observed among MCHB, DD_0HB, $LEC_{R_s(t)}HB$ and $LEC_{R_sLC(t)}HB$ up to 5 dBm. At higher input powers, this agreement disappears due to velocity saturation effects: According to Figs. D.7(b) and D.7(c), MCHB predicts high electric fields and high occupation of the L-valley in the undepleted regions of the epilayer at input powers higher than 5 dBm.
- At 7.5 dBm, the L-valley occupation from MC simulations is as high as 50 %, leading to a strong degradation of the efficiency.
- Fig. D.7(b) shows that the velocity-field loops from MC simulations are far from the static velocity-field curves, due to the nonstationary electron transport effects, section 3.1.5.

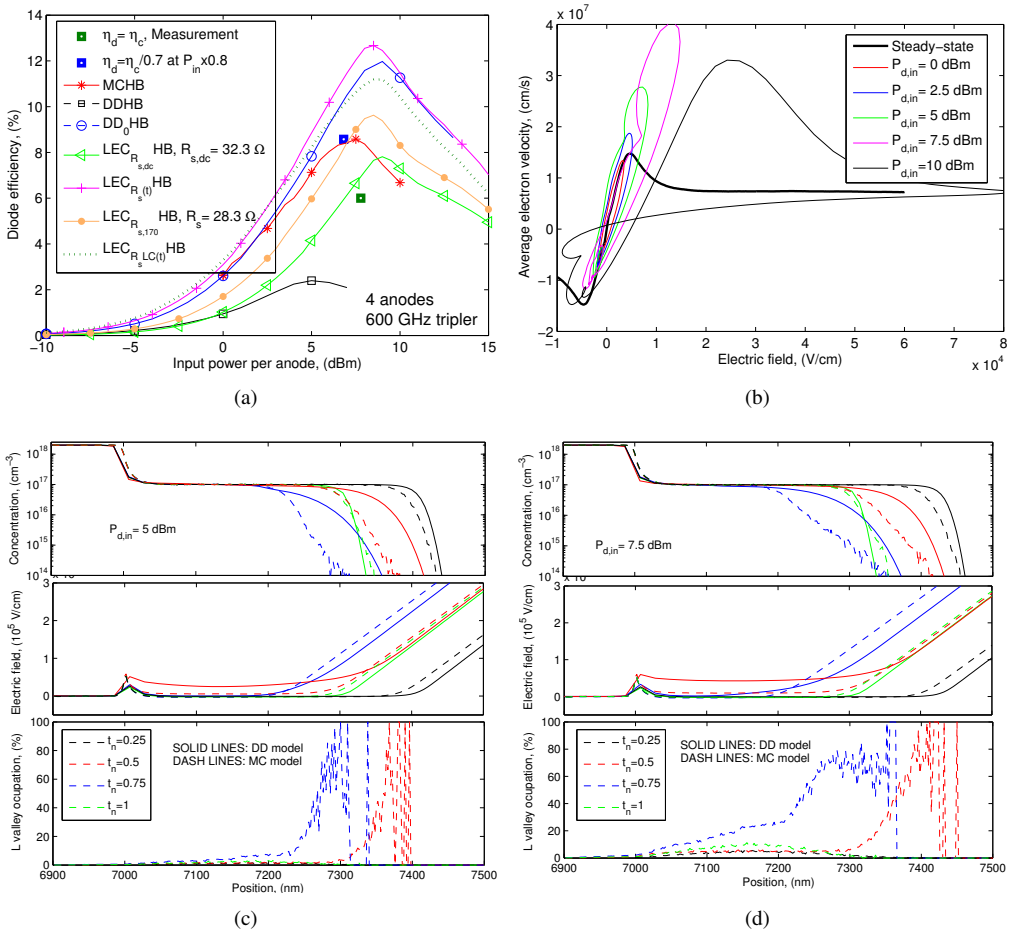

Figure D.7: (a) Diode efficiency of the 600 GHz tripler in [Mae05b] (Table 5.1) with different models, (b) velocity-field loops in the undepleted epilayer of the diode obtained with MC at different input powers. Electron concentration, electric field and occupation of the L-valley as a function of the position at different normalized times (times normalized by one period of the applied signal) at input powers (c) $P_{d,in}$= 5 dBm and (d) $P_{d,in}$= 7.5 dBm, obtained with DD and MC models.

D.7 The 900 GHz tripler

Fig. D.8 presents the efficiency and different characteristics of the diodes in the 900 GHz tripler [Mae10a] described in Table 5.1 at different input powers. The performance of this tripler is similar to the performance of the 300 GHz tripler previously described:

- Velocity saturation is not limiting the performance of the device, since low electric fields and close to zero L valley occupation are observed in Fig. D.8(c) and D.8(d). As a consequence, a good agreement is observed among MCHB, DD_0HB and $LEC_{R_s(t)}$HB.
- The efficiency decreases at input powers higher than 7 dBm because of the initiation of the varistor operation, observed in Fig. D.8 (b) by the onset of the dc current.

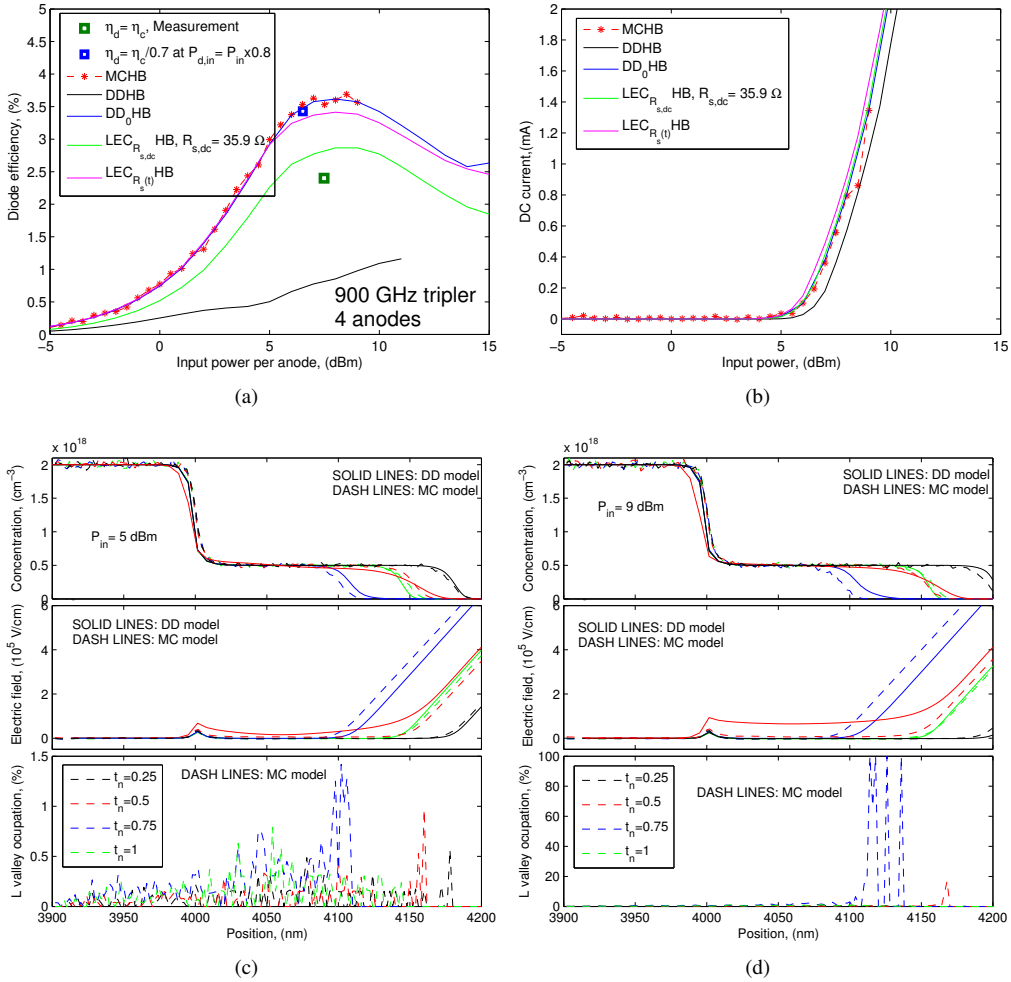

(a) (b) (c) (d)

Figure D.8: (a) Diode efficiency and (b) dc current per anode of the 900 GHz tripler in [Mae10a] (Table 5.1) with different models as a function of the input per anode. Electron concentration, electric field and occupation of the L-valley as a function of the position at different normalized times (times normalized by one period of the applied signal) at input powers (c) $P_{d,in}$= 5 dBm and (d) $P_{d,in}$= 9 dBm, obtained with DD and MC models.

D.8 The 2.7 THz tripler

Fig. D.9 presents the efficiency and different characteristics of the diodes in the 2.7 THz tripler [Mae12] described in Table 5.1 at different input powers. The most relevant results from the analysis of this figure are:

- The depletion region reaches the substrate at $P_{d,in}$= -5 dBm and higher input powers, see Fig. D.9(c).
- A good agreement is observed between DD_0HB and $LEC_{R_s(t)}HB$. The discrepancies between DD_0HB and $LEC_{R_sLC(t)}HB$ in Fig. D.9 indicate that carrier inertia is important at these frequencies. Also, the comparison of the velocity-field loops from MCHB and the steady-state curve in Fig. D.9(b) show the importance of nonstationary effects in the modelling of this tripler.
- Velocity saturation limits the performance of this tripler. As the input power increases, the electric field and the occupation of the upper valleys in the undepleted epilayer of the diode increase, what results in the degradation of the efficiency. When the L valley occupation reaches 50 % at $P_{d,in}$= 3 dBm, see Fig. D.9(d), an abrupt decrease in the efficiency is observed in Fig. D.9(a).
- Fig. D.9(a) shows the efficiency calculated with MCHB using Maxwell-Boltzamann and Fermi-Dirac statistics. It is observed that both statistics lead to similar efficiencies for the tripler.

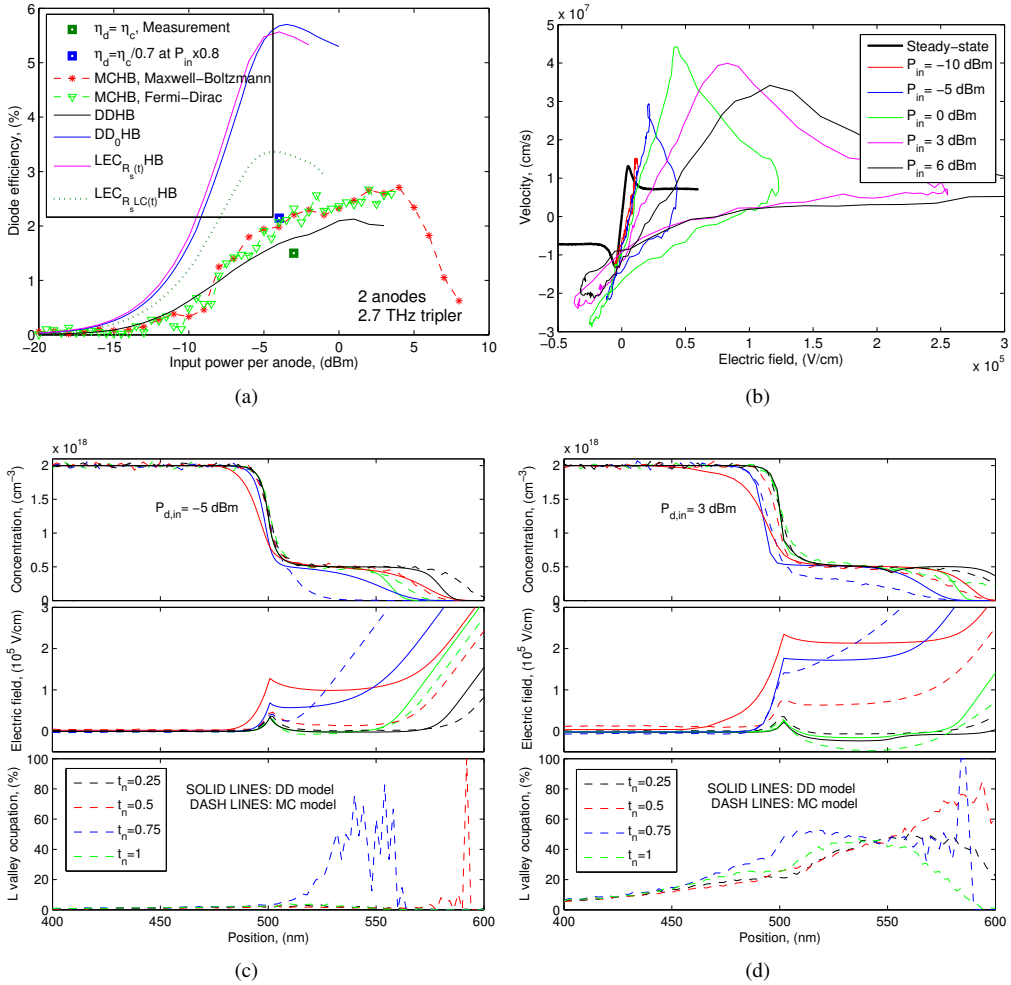

Figure D.9: (a) Diode efficiency of the 2.7 THz tripler in [Mae05b] (Table 5.1) with different models, (b) velocity-field loops in the undepleted epilayer of the diode obtained with MC at different input powers. Electron concentration, electric field and occupation of the L-valley as a function of the position at different normalized times (times normalized by one period of the applied signal) at input powers (c) $P_{d,in}$= -5 dBm and (d) $P_{d,in}$= 3 dBm, obtained with DD and MC models.

D.9 Analysis of the GaN based multipliers

This section present an analysis of the physical processes limiting the performance of the multipliers based on GaN semiconductor described in section 5.5. Table D.1 summarizes the characteristics of the diodes used in these multipliers, see Table 5.6. These characteristics have been obtained to maximize the efficiency at the available input power, using the DDHB tool. The accuracy of the DD model for the simulation of GaN multipliers has been shown in section 5.5.

Table D.1: Characteristics of the GaN frequency multipliers considered in the simulations.

Stage	f_{out}, (GHz)	$P_{in,tot}$, (mW)	V_{bias}, (V)	N_e, (cm^{-3})	L_e, (nm)	Area, (μm^2)	$C_{j,0}$,[1] (fF)	$R_{s,dc}$[1] (Ω)	V_{BD},[1] (V)
0.2 THz doubler, 2 anodes	200	400	-15	5x10^{16}	650	40	21.7	49.9	-133
0.4 THz doubler, 1 anode	400	70	-5	5x10^{16}	400	10	5.4	156.8	-94
0.3 THz tripler, 2 anodes	300	400	-10	5x10^{16}	550	57	30.9	32.2	-118

[1] Calculated with the DD model. For $R_{s,dc}$, similar values are obtained with MC.

D.9.1 Analysis of the GaN 200 GHz doubler

The characteristics of the diode considered in Fig. D.10 are the result of the optimization process presented in [Sil08]. Fig. D.10 shows the efficiency and different characteristics of the diodes for the GaN 200 GHz doubler described in Table 5.6. The most important conclusions from these figures are:

- Physics-based models show that the depletion region reaches the substrate at input powers $P_{d,in}$ higher than 5 dBm. It can be seen is Fig. D.10(c) and D.10(d) at $P_{d,in}$= 15 and 25 dBm, respectively.
- According to MC, the occupation of the upper valleys is practically zero for the power swept in Fig. D.10(a). At input power higher than 10 dBm, the agreement among MCHB and DD$_0$HB disappears. This is due to the increase of the polar optical phonon emission as the electrons gain energy from the electric field, what degrades the electron mobility. According to the analysis in section 3.2, this scattering mechanism occurs when the electric field is higher than $\sim$ 40 KV/cm (it depends on doping). Fig. D.10(c) shows that at 15 dBm, fields close to 40 KV/cm exist in the undepleted epilayer (t_n= 0.5, at positions between 5000 and 5150 nm).
- The efficiency decreases at input powers higher than 23 dBm because of the initiation of the varistor operation, observed in Fig. D.10 (b) by the onset of the dc current.

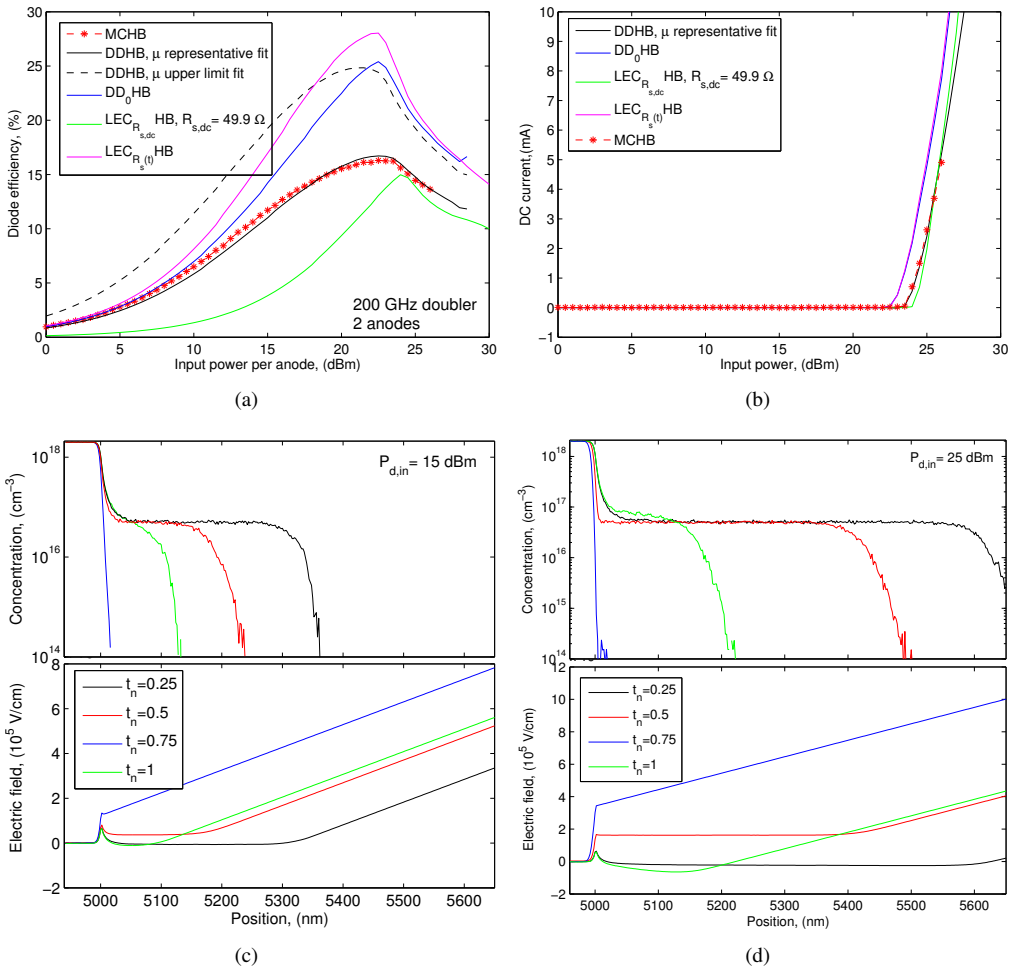

Figure D.10: (a) Diode efficiency and (b) dc current per anode of the GaN 200 GHz doubler described in Table 5.6 as a function of the input power per anode, obtained with different models. Electron concentration and electric field as a function of the position at different normalized times (times normalized by one period of the applied signal) at input powers (c) $P_{d,in}$= 15 dBm and (d) $P_{d,in}$= 25 dBm, obtained with MC model.

D.9.2 Analysis of the GaN 400 GHz doubler

Fig. D.11 shows the results of the optimization of the 400 doubler based on the GaN Schottky diode described in Table D.1. The load impedance in these simulations have been selected to maximize the efficiency at the input power of maximum efficiency. In Figs. D.11(a) and D.11(b), doping of $3x10^{16}$ cm^{-3} has been selected and an analysis of the efficiency with the epilayer length and bias point is presented. For each bias point simulated in these figures, there is an optimum epilayer length L_e. If L_e is too short, the width of the depletion region reaches the substrate and degrades the nonlinear capacitance, and, hence, the efficiency. If L_e is too large, there will be a region of the epilayer that remains undepleted, increasing the series resistance and decreasing the efficiency. When the bias point V_{bias} is more negative, the swing of the nonlinear capacitance increases, what increases the efficiency. These figures show that for V_{bias} lower than -5 V, the increase of the efficiency is negligible, since the nonlinear capacitance is nearly flat for very negative voltages. Fig. D.11(c) shows the maximum efficiency obtained for the GaN 400 GHz doubler for different epilayer doping (for each doping, the epilayer length and bias point have selected to maximize the efficiency, as was shown in Figs. D.11(a) and D.11(b)). It can be seen that the maximum efficiency is obtain for N_e= $5x10^{16}$ cm^{-3}. For lower epilayer doping, the velocity saturation is more important, what leads to higher series resistance, and the maximum efficiency obtained is lower. For higher doping, velocity

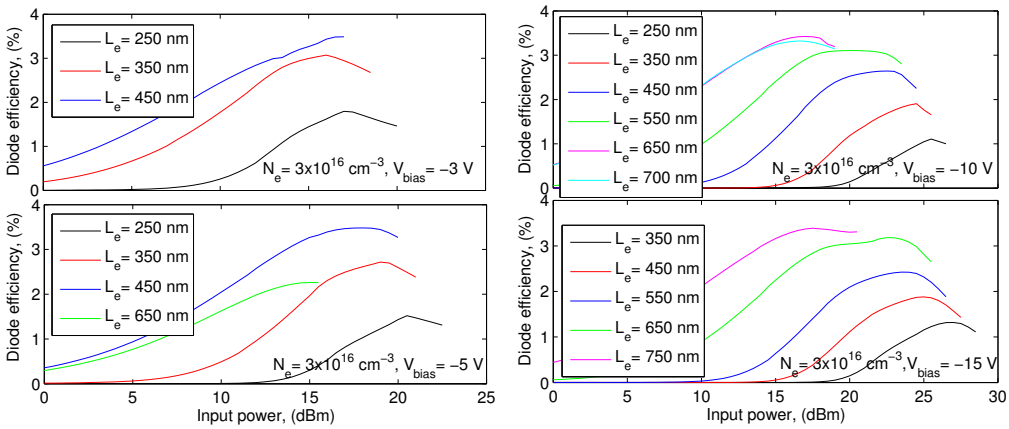

Figure D.11: Diode efficiency of the 400 GHz doubler based on the GaN Schottky diode described in Table D.1 for doping $3x10^{16}$ cm^{-3} and different epilayer lengths and bias points, subfigures (a) and (b). (c) Diode efficiency of the GaN 400 GHz doubler for different epilayer dopings. For each doping, the bias point and the epilayer length have been selected to maximize the efficiency. Results obtained with DDHB.

saturation effects are mitigated and the series resistance is lower, but the modulation of the nonlinear capacitance of the diode is lower.

Fig. D.12 presents the efficiency, the dc current, the electron concentration and the electric field of the 400 GHz doubler based on the optimum diode from the analysis on Fig. D.11, see Table D.1. Some results are obtained from the analysis of these figures:

- Physics-based models show that the depletion region reaches the substrate at input powers $P_{d,in}$ higher than 5 dBm. It can be seen in Fig. D.12(c) and D.12(d) at $P_{d,in}$= 15 and 20 dBm, respectively.
- According to MC, the L valley occupation is practically zero for the power swept in Fig. D.12. At input power higher than 10 dBm, the agreement among MCHB and DD_0HB disappears. This is due to the increase of the polar optical phonon emission as the electrons gain energy from the electric field, as was explained for the GaN 200 GHz doubler.
- The efficiency decreases at input powers higher than 18 dBm because of the initiation of the varistor operation, observed in Fig. D.12 (b) by the onset of the dc current.

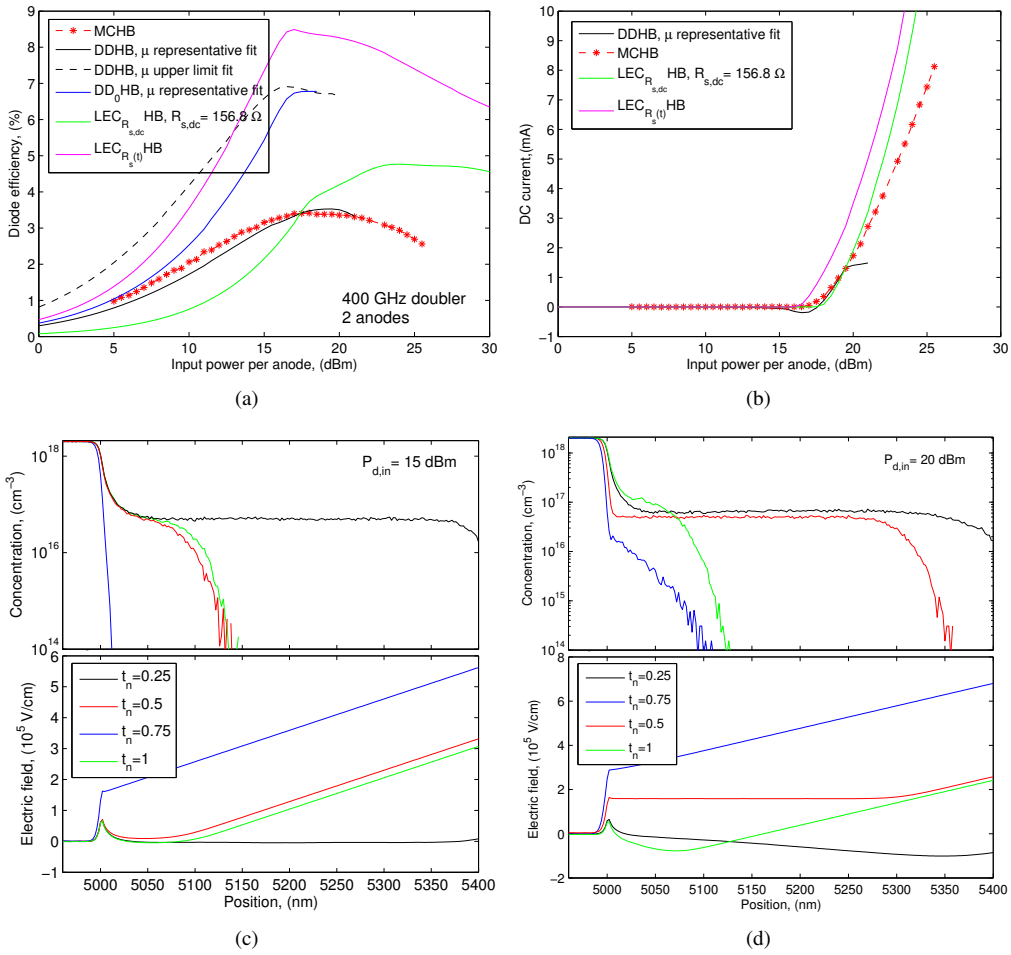

Figure D.12: (a) Diode efficiency and (b) dc current per anode of the GaN 400 GHz doubler described in Table D.1 as a function of the input power per anode, obtained with different models. Electron concentration and electric field as a function of the position at different normalized times (times normalized by one period of the applied signal) at input powers (c) $P_{d,in}$= 15 dBm and (d) $P_{d,in}$= 20 dBm, obtained with DD and MC models.

D.9.3 Analysis of the GaN 300 GHz tripler

The characteristics of the diodes in the GaN 300 GHz tripler in Table D.1 are the results of the optimization of the efficiency. Fig. D.13 shows the results from the optimization of the epilayer length, the epilayer doping and the bias point, as was done for the GaN 400 GHz doubler in the previous section.

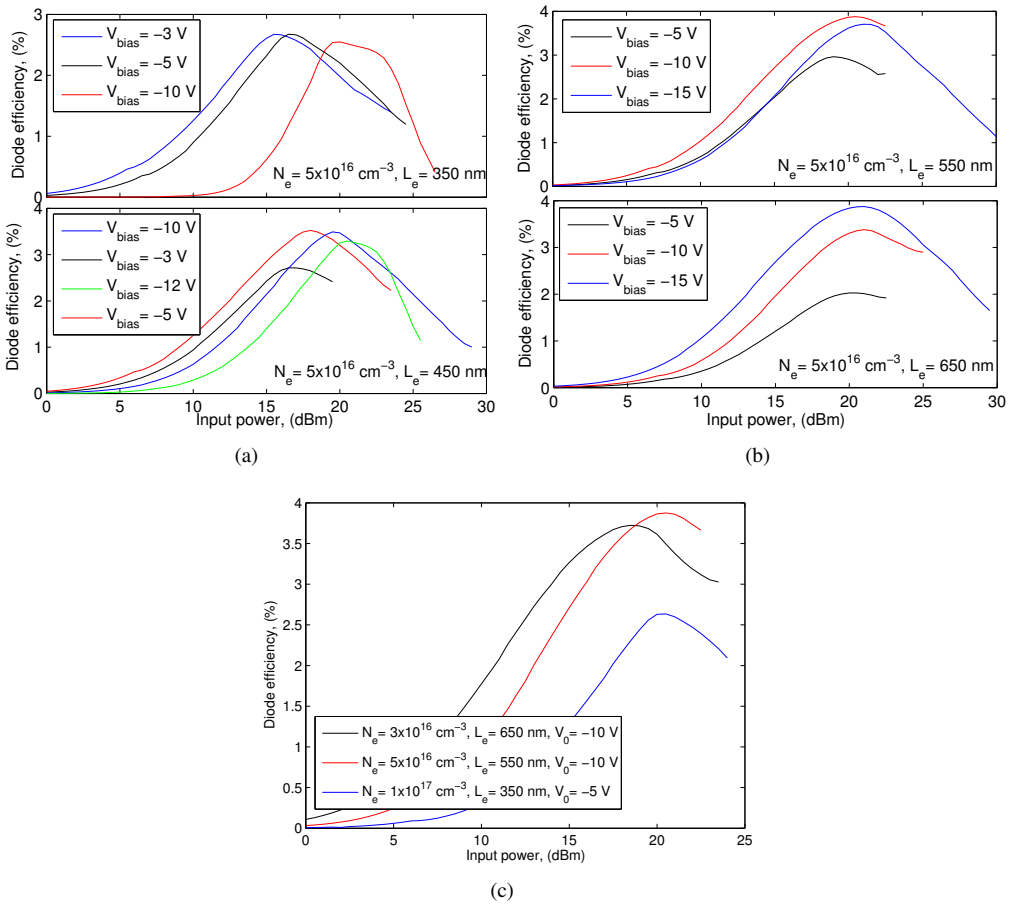

Figure D.13: Diode efficiency of the 300 GHz tripler based on the GaN Schottky diode described in Table D.1 for doping $5\text{x}10^{16}$ cm^{-3} and different epilayer lengths and bias points, subfigures (a) and (b). (c) Diode efficiency of the GaN 300 GHz tripler for different epilayer doping. For each doping, the bias point and the epilayer length have been selected to maximize the efficiency. Results obtained with DDHB.

Fig. D.14 presents the efficiency and different characteristics of the diodes for the optimum GaN 300 GHz tripler described in Table D.1. The most important conclusions from these figures are the following:

- Physics-based models show that the depletion region reaches the substrate at input powers $P_{d,in}$ higher than 5 dBm. It can be seen in Fig. D.14(c) and D.14(d) at $P_{d,in}$= 15 and 25 dBm, respectively.

- For the power range considered, there is not occupation of the upper valleys of the semiconductor. The agreement between MCHB and DD$_0$HB disappears at input power higher than 10 dBm, due to the degradation of the electron mobility associated to the increase of the polar optical phonon emission scattering, as described for the previous GaN doublers.

- The efficiency decreases at input powers higher than 23 dBm because of the initiation of the varistor operation, observed in Fig. D.14 (b) by the onset of the dc current.

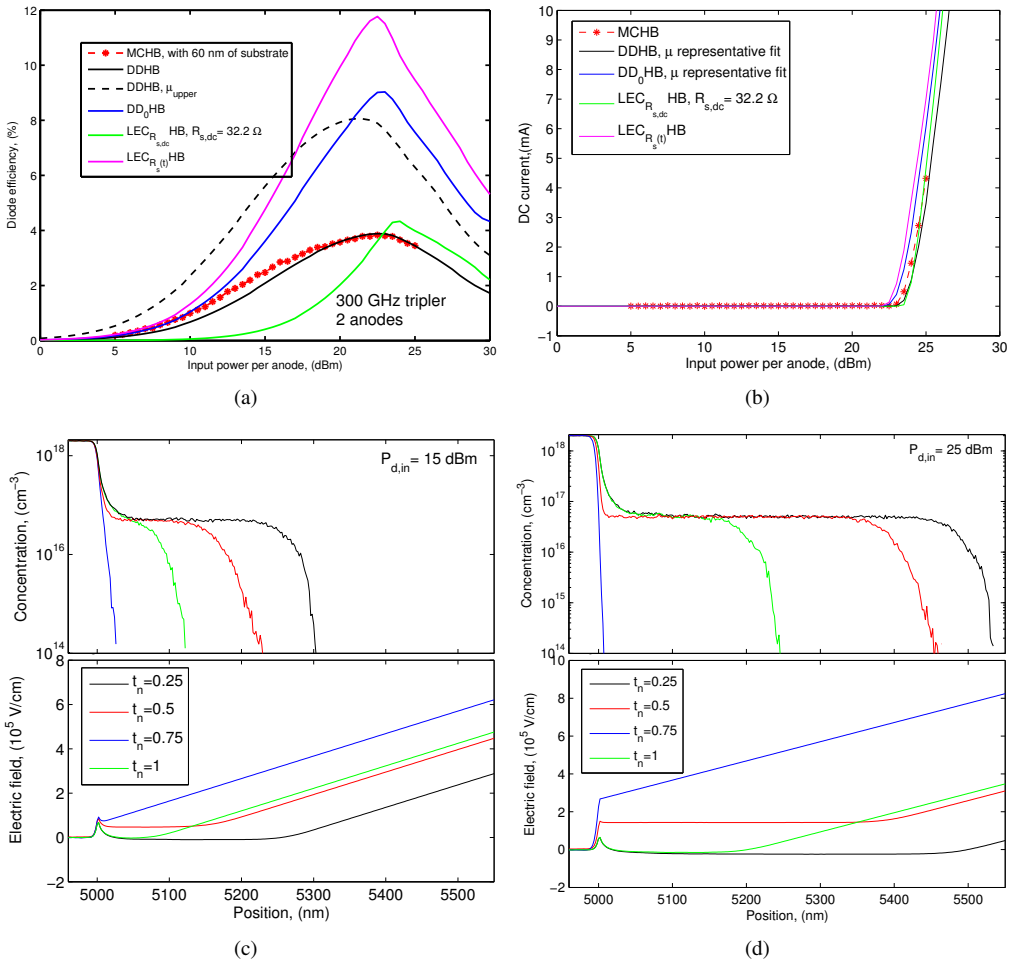

Figure D.14: (a) Diode efficiency and (b) dc current per anode of the GaN 300 GHz tripler described in Table D.1 as a function of the input power per anode, obtained with different models. Electron concentration and electric field as a function of the position at different normalized times (times normalized by one period of the applied signal) at input powers (c) $P_{d,in}$= 15 dBm and (d) $P_{d,in}$= 25 dBm, obtained with MC models.

Appendix E

Conversion matrix formalism

This appendix presents an overview of the conversion matrix formalism for the analysis of Schottky mixers, following the description presented in [Hel78a, Ker79a, Ker79b, Maa93, Maa88]. A procedure to include the parasitic capacitances of the diode in the formalism is presented. Also a technique to evaluate the conversion matrix using models like DD is indicated. On the other hand, the conversion matrix analysis is extended to take into account the noise correlation properties due to the time variation of the series resistance of the diode under the LO signal.

The conversion matrix technique has been used in this thesis to calculate the equivalent input noise temperature of Schottky mixers in chapter 6, using simple LEC models based on an equivalent circuit model of the Schottky contact in series with a constant series resistance ($\mathrm{LEC}_{R_{s,dc}}$) or a time varying resistance ($\mathrm{LEC}_{R_s(t)}$).

E.1 Small-signal analysis

The analysis of mixers with the conversion matrix or large-signal-small-signal approach assumes that the nonlinear device is pumped by a single large sinusoidal signal (LO) together with another signal which much smaller amplitude (RF). In this technique, the nonlinear device is analysed firstly under the large-signal excitation only, usually via de harmonic-balance method. Finally, the nonlinear elements in the equivalent circuit of the device are converted to small-signal, linear, time varying elements and the small-signal analysis is performed [Maa88].

In general, when a nonlinear element is pumped by two signals of different frequencies, current and voltages appear in the device at the mixing frequencies $mf_{LO}+nf_{RF}$ where m and n are integers. If the RF signal is at such a low level that it does not generate harmonics and the other is a large signal sinusoid of frequency f_{LO}, the mixing frequencies are $f = \pm f_{RF} + nf_{LO}$. These frequencies consist of two tones on either side of each large-signal harmonic frequency, separated by $f_{IF} = |f_{LO} - f_{RF}|$. A commonly used notation to represent these mixing frequencies is [Maa88]:

$$f_n = f_{IF} + nf_{LO} \tag{E.1}$$

The frequencies represented by eq. (E.1) are only half of the mixing frequencies: the negative components of the lower sidebands and the positive components of the upper sidebands. Frequencies f_n have all the information of the mixing frequencies, since negative -and positive- frequency components are complex conjugates pairs and only the knowledge of one is necessary. The small-signal

voltage and currents in the nonlinear device can be expressed in frequency domain as:

$$v'(t) = \sum_{k=-\infty}^{k=\infty} V_k \exp(j\omega_k t) \tag{E.2}$$

$$i'(t) = \sum_{k=-\infty}^{k=\infty} I_k \exp(j\omega_k t) \tag{E.3}$$

where $\omega_k = 2\pi f_k$ with f_k is given by eq. (E.1). The primes indicate that $v'(t)$ and $i'(t)$ are sums of positive- and negative-frequency phasor components in eq. (E.1), not the complete time waveforms.

Following the analysis presented in [Hel78a, Maa88], the relation between the small-signal voltage and current, in the frequency domain, for the Schottky junction represented by the simple equivalent circuit of Fig. 2.5 is:

$$\begin{bmatrix} I^*_{-N} \\ I^*_{-N+1} \\ I^*_{-N+2} \\ \dots \\ I^*_{-1} \\ I_0 \\ I_1 \\ \dots \\ I_N \end{bmatrix} = \left(\begin{bmatrix} G_0 & G_{-1} & G_{-2} & \dots & G_{-2N} \\ G_1 & G_0 & G_{-1} & \dots & G_{-2N+1} \\ G_2 & G_1 & G_0 & \dots & G_{-2N+2} \\ \dots & \dots & \dots & \dots & \dots \\ G_{N-1} & G_{N-2} & G_{N-3} & \dots & G_{-N-1} \\ G_N & G_{N-1} & G_{N-2} & \dots & G_{-N} \\ G_{N+1} & G_N & G_{N-1} & \dots & G_{-N+1} \\ \dots & \dots & \dots & \dots & \dots \\ G_{2N} & G_{2N-1} & G_{2N-2} & \dots & G_0 \end{bmatrix} + \right.$$

$$\left. \begin{bmatrix} j\omega_{-N} & 0 & 0 & \dots & \dots & 0 \\ 0 & j\omega_{-N+1} & 0 & \dots & \dots & 0 \\ 0 & 0 & j\omega_{-N+2} & \dots & \dots & 0 \\ \dots & \dots & \dots & \dots & \dots & \dots \\ \dots & \dots & \dots & \dots & \dots & \dots \\ 0 & 0 & \dots & j\omega_0 & \dots & 0 \\ \dots & \dots & \dots & \dots & \dots & \dots \\ 0 & 0 & \dots & \dots & 0 & j\omega_N \end{bmatrix} \begin{bmatrix} C_0 & C_{-1} & C_{-2} & \dots & C_{-2N} \\ C_1 & C_0 & C_{-1} & \dots & C_{-2N+1} \\ C_2 & C_1 & C_0 & \dots & C_{-2N+2} \\ \dots & \dots & \dots & \dots & \dots \\ C_{N-1} & C_{N-2} & C_{N-3} & \dots & C_{-N-1} \\ C_N & G_{N-1} & C_{N-2} & \dots & C_{-N} \\ C_{N+1} & C_N & C_{N-1} & \dots & C_{-N+1} \\ \dots & \dots & \dots & \dots & \dots \\ C_{2N} & C_{2N-1} & C_{2N-2} & \dots & C_0 \end{bmatrix} \right) \begin{bmatrix} V^*_{-N} \\ V^*_{-N+1} \\ V^*_{-N+2} \\ \dots \\ V^*_{-1} \\ V_0 \\ V_1 \\ \dots \\ V_N \end{bmatrix} \tag{E.4}$$

or in matrix form:

$$\mathbf{I} = \mathbf{Y_d} \mathbf{V} \tag{E.5}$$

where

$$\mathbf{Y_d} = \mathbf{G_j} + j\Omega \mathbf{C_j}. \tag{E.6}$$

In these matrix equations G_k and C_k are the coefficients of the Fourier series of the nonlinear conductance $g_j(t) = 1/R_j(t)$ (R_j represents the differential resistance of the junction) and the nonlinear capacitance $C_j(t)$ of the Schottky junction under the large signal excitation of frequency f_{LO} (obtained from harmonic-balance simulations). V_k and I_k in $\mathbf{V}$ and $\mathbf{I}$, respectively, are the sideband frequency components of $v'(t)$ and $i'(t)$ as expressed in eqs. (E.2) and (E.3), respectively. The vectors in eq. (E.4) have been truncated to a limit of $k = \pm N$ for $\mathbf{V}$ and $\mathbf{I}$ and $k = \pm 2N$ for G_k and C_k. It is assumed that these vectors are negligible beyond these limits. The impedance conversion matrix of the Schottky junction is $\mathbf{Z_d} = \mathbf{Y_d^{-1}}$. A conversion matrix for the Schottky diode including the constant series resistance of the diode R_s is:

$$\mathbf{Z_c} = R_s \mathbf{1} + (\mathbf{G_j} + j\Omega \mathbf{C_j})^{-1}, \tag{E.7}$$

where $\mathbf{1}$ is the identity matrix. If the series resistance of the diode is considered time varying, it has to be analysed as is done for the nonlinear resistance of the Schottky junction. In such a case, the matrix $\mathbf{R_s} = R_s \mathbf{1}$ in eq. (E.7) is not a diagonal matrix [Maa05]. The conversion matrix $\mathbf{Z_c}$ relates the small-signal current and voltage components at the frequencies given by eq. (E.1) at the diode terminals as:

$$\mathbf{V_d} = \mathbf{Z_c} \mathbf{I_d} \tag{E.8}$$

or

$$\mathbf{I_d} = \mathbf{Y_c} \mathbf{V_d} \tag{E.9}$$

where $\mathbf{Y_c} = (\mathbf{Z_c})^{-1}$. Eq. (E.8) or eq. (E.9) provide a system of equations that can be used to evaluate the conversion matrix of a diode using more complex diode models as DD or MC. If a set of current $\mathbf{I_d}$ and voltage $\mathbf{V_d}$ vectors are obtained from a proper number M of different simulations (a set of M independent multi-tone harmonic balance simulations of the mixer using as RF signal a small signal with frequencies f_n eq. (E.1)), the conversion matrix $\mathbf{Y_c}$ can be numerically evaluated. Since the conversion matrix is the same for the set of M pairs of current and voltage vectors, eq. (E.9) for the M vectors [Cid03] is:

$$[\mathbf{I_d^{(1)}}, \mathbf{I_d^{(2)}}, ..., \mathbf{I_d^{(M)}}] = \mathbf{Y_c}[\mathbf{V_d^{(1)}}, \mathbf{V_d^{(2)}}, ..., \mathbf{V_d^{(M)}}] \tag{E.10}$$

and the conversion matrix $\mathbf{Y_c}$ results:

$$\mathbf{Y_c} = [\mathbf{I_d^{(1)}}, \mathbf{I_d^{(2)}}, ..., \mathbf{I_d^{(M)}}].[\mathbf{V_d^{(1)}}, \mathbf{V_d^{(2)}}, ..., \mathbf{V_d^{(M)}}]^{-1} \tag{E.11}$$

where the superscript indicates one of the *M= 2(N+1)* multi-tone harmonic balance simulations. Since the matrix of voltages has to be invertible, the M simulations are carried out exciting the diode with the LO signal and an RF signal of the set of intermodulation frequencies given by eq. (E.1) [Cid03]. These simulations have to be carried out with a multi-tone harmonic balance to obtain the voltage and current at the different intermodulation frequencies. Besides, since the conversion matrix depends on the LO signal, all the simulations have to be performed with the same value of LO power.

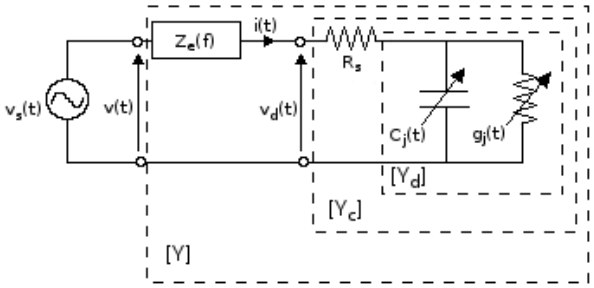

Figure E.1: Small-signal equivalent circuit of the mixer, representing the different definitions of admittance conversion matrix. $v_s(t)$ represent the RF excitation and $Z_e(f)$ is the circuit impedance at the frequency f.

An augmented matrix that includes also the embedding impedance of the mixer circuit is usually defined:

$$\mathbf{Z} = \mathbf{Z_c} + \mathbf{Z_e} \tag{E.12}$$

where $\mathbf{Z_e}$ is the conversion matrix of the time-invariant impedances of the circuit, which is a diagonal matrix having the elements $Z_e(f_n)$. The augmented admittance conversion matrix is $\mathbf{Y} = \mathbf{Z}^{-1}$. The augmented conversion matrix relates the vector of mixing current and voltage components at the source terminals[1], see Fig. E.1. The small-signal input and output impedance of the pumped diode are given by [Maa88]:

$$Z_{in}(f_{RF}) = \frac{1}{Y_{1,1}} - Z_e(f_{RF}) \tag{E.13}$$

$$Z_{out}(f_{IF}) = \frac{1}{Y_{0,0}} - Z_e(f_{IF}) \tag{E.14}$$

where the elements $Y_{p,q}$ are the elements of the matrix $\mathbf{Y}$ that relate the voltage and current small-signal components V_q and I_q of the vectors. The diode impedance at any other mixing frequency is

[1] Since the small-signal source is a sinusoidal voltage at frequency f_q the vector of voltages in the augmented matrix has only one nonzero component, V_q.

calculated similarly. The conversion loss from RF to IF (ratio of available RF power to the output power at the IF frequency) can be evaluated using the augmented conversion matrix:

$$L_c = \frac{P_{av,RF}}{P_{del,IF}} = \frac{1}{4|Y_{0,1}|^2 \mathrm{Re}\{Z_e(f_{IF})\}\mathrm{Re}\{Z_e(f_{RF})\}} \tag{E.15}$$

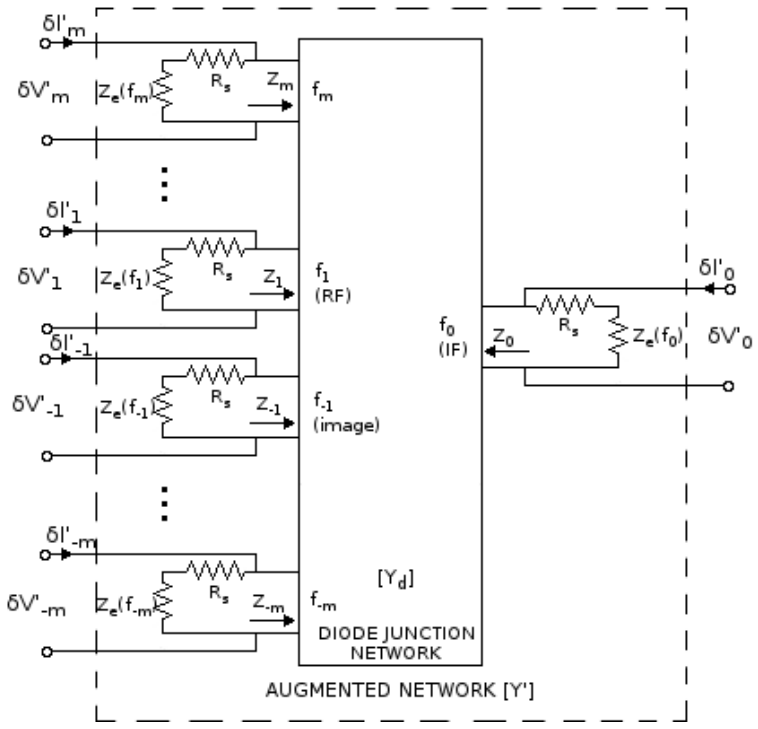

Figure E.2: Small signal representation of the mixer as a multifrequency linear multiport circuit. The voltage and current $\delta V'_m$ and $\delta I'_m$ at any port m are the small-signal components at frequency $f_{IF} + mf_{LO}$ of the augmented network; each port represents one sideband frequency. Reproduced from [Ker79a].

In [Ker79a] an equivalent approach is presented where the small-signal diode circuit is represented as a multifrequency linear multiport network as shown in Fig. E.2. The series resistance of the diode is treated as part of the embedding circuit, and the analysis is performed in terms of the augmented network enclosed by the dashed line in Fig. E.2. The small-signal currents at each frequency are expressed in terms of the small-signal voltages and the augmented conversion matrix $\mathbf{Y}'$:

$$\mathbf{I}' = \mathbf{Y}'\mathbf{V}' \tag{E.16}$$

where $\mathbf{I}'$ is the vector of signal sources replaced by equivalent current sources $\delta I'_m$, see Fig. E.2, and:

$$\mathbf{Y}' = \mathbf{Y_d} + \mathbf{diag}\left[\frac{1}{R_s + Z_e(f_n)}\right]. \tag{E.17}$$

The augmented impedance conversion matrix is $\mathbf{Z}' = (\mathbf{Y}')^{-\mathbf{1}}$:

$$\mathbf{V}' = \mathbf{Z}'\mathbf{I}' \tag{E.18}$$

The conversion matrix $\mathbf{Z}'$ can be evaluated numerically, using diode models more accurate than the equivalent circuit. Once $\mathbf{Z_c}$ has been evaluated numerically as described in eq. (E.10), e.g. with DDHB, the contribution of the undepleted epialyer and the substrate of the diode to the conversion matrix can be evaluated according to:

$$\mathbf{R_{s,num}} = \mathbf{Z_c} - (\mathbf{G_j} + j\Omega\mathbf{C_j})^{-1} \tag{E.19}$$

where the matrix $\mathbf{G_j}$ and $\mathbf{C_j}$ can be evaluated from the simulation results with the numerical model considered. This equation implies to assume a model for the current through the Schottky contact based on the conduction current (characterized by $\mathbf{G_j}$) and the nonlinear capacitance ($\mathbf{C_j}$). Once $\mathbf{R_{s,num}}$ is known, the matrix $\mathbf{Z'}$ can be formed using eq. (E.17) and (E.18).

To determine the port impedance at frequency f_m, Z_m, as defined in Fig. E.2, the corresponding circuit impedance $Z_e(f_m)$ is open-circuited and it follows that

$$Z_m = Z'_{mm,\infty} \tag{E.20}$$

where the subindex ∞ indicates that $Z_e(f_m)$ is open-circuited. The IF output impedance of the diode is evaluated as:

$$Z_{out}(f_{IF}) = Z_0 + R_s. \tag{E.21}$$

Similarly is done for any other mixing frequency. This impedance is equivalent to eq. E.14. The conversion loss can be also written using $\mathbf{Z'}$ [Ker79a]:

$$L_c = \frac{1}{4|\mathbf{Z'_{0,1}}|^2} \frac{|Z_e(f_0)+R_s|^2}{\mathrm{Re}[Z_e(f_0)]} \frac{|Z_e(f_1)+R_s|^2}{\mathrm{Re}[Z_e(f_1)]} \tag{E.22}$$

This equation for the conversion loss is equivalent to eq. (E.15).

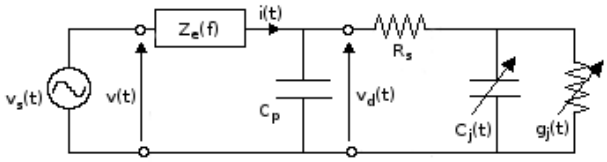

Figure E.3: Small-signal equivalent circuit of the mixer, representing the the parasitic capacitance C_p. $v_s(t)$ represent the RF excitation and $Z_e(f)$ is the circuit impedance at the frequency f.

A parasitic capacitance C_p in parallel with the Schottky diode is usually considered in Schottky mixers, see Fig. E.3. The impedance conversion matrix of this time invariant element is a diagonal matrix whose matrix elements are the impedance at the frequency corresponding to the location in the matrix $(1/(j2\pi f_n C_p))$. Its inclusion in the augmented matrix eq. (E.12) is straightforward, an impedance matrix in parallel with the diode matrix $\mathbf{Z_c}$, eq. (E.7). In the evaluation of the augmented matrix $\mathbf{Z'}$ given by eq. (E.18), the impedance due to the parasitic capacitance is in parallel with the circuit impedance and the equivalent impedance in series with the series resistance of the diode. To calculate the impedance of the pumped diode at frequency f_m -Z_m, eq. (E.20)- without including the contribution of the parasitic capacitance, the equivalent impedance of the circuit impedance in parallel with the parasitic impedance at the frequency f_m must be open-circuited.

E.2 Mixer noise

The dominant noise sources in Schottky diodes are shot and thermal noise, see chapter 4. Hot electron noise and intervalley transfer noise are important when high electric fields are generated in the undepleted regions of the diode.

Under dc applied voltages, the mean-square shot-noise current due to carriers crossing randomly the Schottky barrier is [Maa93]:

$$\overline{i_s^2} = 2qIB, \tag{E.23}$$

where q is the absolute value of the electron charge, B is the bandwidth and I is the junction current not including the noise itself. This spectral density is flat (alternatively "white") up to frequencies on the order of the reciprocal transit time[2] and drops steeply at higher frequencies.

[2]Time of flight for electrons which reach the Schottky contact [Tri86]

Thermal noise is originated by the fluctuations in the velocity of the electrons due to their random motion in the semiconductor (lossy resistor). The mean-square open-circuit noise voltage of a resistance R_s is [Maa93]:

$$\overline{v_t^2} = 4k_BTR_sB, \tag{E.24}$$

and the mean-square short-circuit current is:

$$\overline{i_t^2} = \frac{4k_BTB}{R_s}, \tag{E.25}$$

where T is the absolute temperature. See chapter 4 for a detailed analysis of noise sources in Schottky diodes. The equivalent circuit of the noisy diode, including shot and thermal noise sources, is shown in Fig. E.4(a), connected to the circuit impedance. In Fig. E.4(b) the voltage noise source has been converted to a current noise source via Norton's theorem, as is shown in Fig. E.4(c).

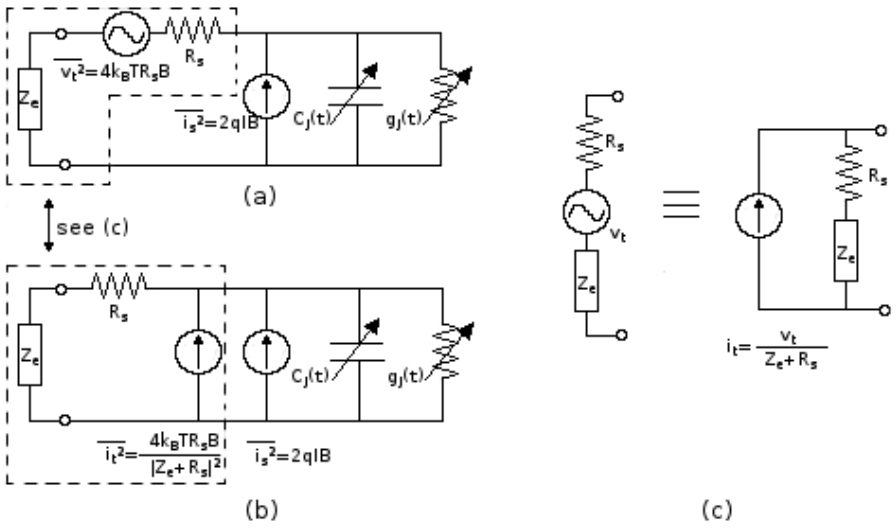

Figure E.4: Noise equivalent circuit of the diode. (a) Thermal noise in R_s treated as a voltage source; (b) thermal noise source converted to a current source via (c) the Norton's theorem

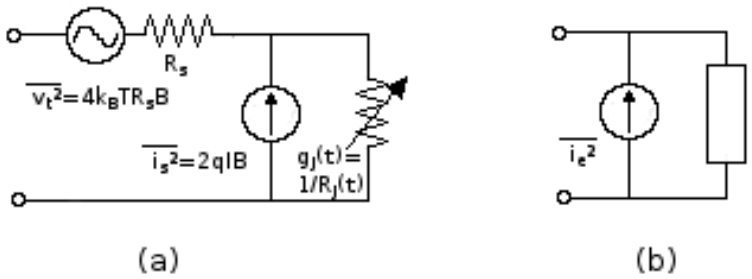

Figure E.5: (a) Noise equivalent circuit of the Schottky diode under dc conditions and (b) equivalent circuit obtained with the Norton's theorem

The equivalent circuit of the noisy diode can be used to demonstrate eq. (4.30) for the combined contribution to the low frequency region of the noise spectrum of shot and thermal noise sources under dc conditions:

$$\overline{i_e^2} = \frac{2qIR_j^2B}{(R_s+R_j)^2} + \frac{4k_BTR_sB}{(R_s+R_j)^2} \tag{E.26}$$

where R_j is the differential resistance of the Schottky junction. Under dc conditions, there is not current through the nonlinear capacitance and the equivalent circuit of the noisy diode can be simplified as shown in Fig. E.5. Using Norton's theorem, the circuit in Fig. E.5(a) can be replaced by an impedance in parallel with a current noise source, given by:

$$i_e = i_s + \frac{v_j}{R_j}, \text{ or} \tag{E.27}$$

$$i_e = \frac{v_t - v_j}{R_s} \tag{E.28}$$

where v_j is the small-signal noise voltage between the terminals of the Schottky junction. From these equations, v_j can be written:

$$v_j = \frac{v_t - R_s i_s}{1 + \frac{R_s}{R_j}}. \tag{E.29}$$

Using eq. (E.29) in eq. (E.27):

$$i_e = \frac{i_s R_j}{R_s + R_j} + \frac{v_t}{R_s + R_j}. \tag{E.30}$$

With eq. (E.30), the mean-square noise current of the Norton equivalent circuit is:

$$\overline{i_e^2} = \frac{\overline{i_s^2} R_j^2}{(R_s + R_j)^2} + \frac{\overline{v_t^2}}{(R_s + R_j)^2} + \frac{2\overline{i_s v_t} R_j}{(R_s + R_j)^2}. \tag{E.31}$$

Assuming that shot and thermal noise are uncorrelated $\overline{i_s v_t} = 0$ and replacing eqs. (E.23) and (E.24) in eq. (E.31), eq. (E.26) is obtained.

E.2.1 Shot noise

When the LO signal is applied, the current in the diode is time varying and shot noise eq. (E.23) is also a time varying function at the frequency of the LO signal. The noise components at each mixing frequency $f_n = f_{IF} + n f_{LO}$ are converted to the other mixing frequencies by the fundamental LO frequency and its harmonics. Hence, the components down-converted to the IF frequency are correlated [Hel78a, Maa93]. On the other hand, thermal noise remains constant under LO excitation since the series resistance is assumed constant in the simple LEC model.

The shot noise current in the diode junction at each mixing frequency can be expressed via a vector [Hel78a, Maa93]:

$$\delta \mathbf{I_S} = \begin{bmatrix} \delta I^*_{S,-N} \\ \delta I^*_{S,-N+1} \\ \delta I^*_{S,-N+2} \\ \cdots \\ \delta I^*_{S,-1} \\ \delta I_{S,0} \\ \delta I_{S,1} \\ \cdots \\ \delta I_{S,N} \end{bmatrix} \tag{E.32}$$

where $\delta I_{S,n}$ is the shot noise current component at the mixing frequency f_n. Using eq. (E.18), the IF output noise voltage due to shot noise is determined:

$$\delta V_{S,0} = \mathbf{Z'_0} \delta \mathbf{I_S} \tag{E.33}$$

where $\mathbf{Z'_0}$ is the row of the matrix $\mathbf{Z'}$ corresponding to the IF frequency (mixing frequency f_0 in eq. (E.1)). The ensemble average of $|\delta V_{S,0}|^2$ is:

$$< |\delta V_{S,0}|^2 > = \mathbf{Z'_0} < \delta \mathbf{I_S} \delta \mathbf{I_S^\dagger} > \mathbf{Z'_0}^\dagger \tag{E.34}$$

where $< ... >$ denotes ensemble average and † means complex conjugate transpose. The matrix $< \delta I_S \delta I_S^{\dagger} >$ is the shot noise correlation matrix. The (m,n) element of this matrix represents the correlation between the mixing frequencies f_m and f_n and is given by [Hel78a, Maa93]:

$$< \delta I_{S,m} \delta I_{S,n}^{*} >= 2qI_{m-n}B \tag{E.35}$$

where I_{m-n} is one of the Fourier coefficients of the local oscillator conduction current through the Schottky barrier and * denotes the complex conjugate.

E.2.2 Thermal noise

The thermal noise due to R_s can be treated analogously. If the series resistance R_s is assumed constant under the LO signal, the thermal noise components at different frequencies are not correlated and the thermal noise correlation matrix is simply a diagonal matrix [Hel78a, Maa93]. The IF output noise voltage due to thermal noise is:

$$\delta V_{T,0} = \mathbf{Z_0'} \delta \mathbf{I_T} \tag{E.36}$$

where $\delta \mathbf{I_T}$ is the noise current vector due to thermal noise, as was shown for shot noise via eq. (E.32). The ensemble average of $|\delta V_{T,0}|^2$ is:

$$< |\delta V_{T,0}|^2 >= \mathbf{Z_0'} < \delta \mathbf{I_T} \delta \mathbf{I_T^{\dagger}} > \mathbf{Z_0'}^{\dagger} \tag{E.37}$$

The terms of the diagonal thermal noise correlation matrix are give by [Ker79a, Maa93]:

$$< \delta I_{T,m} \delta I_{T,m}^{*} >= \begin{cases} \frac{4k_B T R_s B}{|Z_e(f_m)+R_s|^2}, & m \neq 0 \\ \frac{4k_B T R_s B}{|Z_0|^2}, & m = 0 \end{cases} \tag{E.38}$$

If it is assumed that the series resistance of the diode is modulated by the LO signal, the mean-square thermal-noise current in Fig. E.4 can be written as:

$$\overline{i^2(t)} = \frac{4k_B T R_s(t) B}{|Z_e(f_{IF}) + R_s(t)|^2} = \frac{|Z_e(f_{IF}) + R_{s,dc}|^2 R_s(t)}{R_{s,dc} |Z_e(f_{IF}) + R_s(t)|^2} \frac{4k_B T R_{s,dc} B}{|Z_e(f_{IF}) + R_{s,dc}|^2} = f_M^2(t) \frac{4k_B T R_{s,dc} B}{|Z_e(f_{IF}) + R_{s,dc}|^2} \tag{E.39}$$

where $f_M(t)$ is the modulation function and $R_{s,dc}$ is the constant series resistance of the diode, considered as a reference. According to [Maa05], the current noise correlation matrix of a modulated noise source is given by:

$$< \delta \mathbf{I_M} \delta \mathbf{I_M^{\dagger}} >= \mathbf{F_M} < \delta \mathbf{I_U} \delta \mathbf{I_U^{\dagger}} > \mathbf{F_M}^{\dagger} \tag{E.40}$$

where $< \delta \mathbf{I_U} \delta \mathbf{I_U^{\dagger}} >$ is the noise correlation matrix of the unmodulated noise source and $\mathbf{F_M}$ is the square-matrix of coefficients of the Fourier series F_k of the modulation function $f_M(t)$ (modulated by the LO exclusively):

$$F_M = \begin{bmatrix} F_0 & F_{-1} & F_{-2} & ... & F_{-2N} \\ F_1 & F_0 & F_{-1} & ... & F_{-2N+1} \\ F_2 & F_1 & F_0 & ... & F_{-2N+2} \\ ... & ... & ... & ... & ... \\ F_{N-1} & F_{N-2} & F_{N-3} & ... & F_{-N-1} \\ F_N & F_{N-1} & F_{N-2} & ... & F_{-N} \\ F_{N+1} & F_N & F_{N-1} & ... & F_{-N+1} \\ ... & ... & ... & ... & ... \\ F_{2N} & F_{2N-1} & F_{2N-2} & ... & F_0 \end{bmatrix} \tag{E.41}$$

Using eq. (E.40) and the expression for $f_M(t)$ determined by eq. (E.39), the effect of the modulation of thermal noise is included in the conversion matrix formalism.

E.2.3 Hot electron noise

Hot electrons are generated in the undepleted part of the epilayer if the electric field is high enough. In thermodynamic equilibrium, the electrons in the semiconductor have the same average temperature as the crystal lattice. When an electric field is applied (nonthermodynamic equilibrium), the electrons gain energy from the electric field and the electron energy distribution can no longer be described by a Maxwell-Boltzmann distribution function (thermodynamic equilibrium). Heating of the electron energy distribution causes the noise to exceed that predicted by eq. (4.17) for the pure thermal noise [Fab95].

Models for hot electron noise make use of the fact that the average electron in the epilayer must gain energy from the electric field at the same rate it loses energy to the lattice. Equating the two rates yields the electron distribution temperature as [Heg85, Cro87, Fab95]:

$$T_e = T + KI^2 \tag{E.42}$$

where I is the current through the epilayer and K is the noise constant given by:

$$K = \frac{2\tau_e}{3k_B q \mu_e N_e^2 A^2}, \tag{E.43}$$

τ_e is the average relaxation time of the electrons ($\sim$ 1 ps, [Heg85, Cro87, Tho04]), μ_e is the low field electron mobility, N_e is the epilayer doping concentration and A is the diode area. The excess noise temperature due to hot electron noise is the difference between T_e and the thermal noise temperature T (thermal noise previously described), i.e, $T_{hot} = KI^2$.

The noise source due to hot electrons must be transformed into an equivalent source in parallel with the diode junction, in such a way that its contribution to the voltage across the IF load remains unchanged, as was done for the thermal noise in Fig. E.4. Using analogous considerations as for shot and thermal noise sources, and following [Cro87], the elements of the current noise correlation matrix due to hot electron noise are given by [Cro87]:

$$< \delta I_{H,m} \delta I_{H,n}^* >= \frac{4k_B \Delta f}{R_s} \Theta_{m-n} \beta_m \beta_n^* \tag{E.44}$$

where Θ_{m-n} and β_p are:

$$\Theta_{m-n} = f_{LO} \int_{-1/2f_{LO}}^{1/2f_{LO}} KI^2 \exp[-j(m-n)2\pi f_{LO} t] dt, \tag{E.45}$$

$$\beta_p = \begin{cases} R_s/(R_s + Z_e(f_p)), & p \neq 0 \\ -R_s/Z_0, & p = 0 \end{cases} \tag{E.46}$$

The ensemble average of $|\delta V_{H,0}|^2$ is:

$$< |\delta V_{H,0}|^2 >= \mathbf{Z_0'} < \delta \mathbf{I_H} \delta \mathbf{I_H^\dagger} > \mathbf{Z_0'}^\dagger \tag{E.47}$$

If the series resistance is considered time varying, the modulated current noise correlation matrix has to be calculated as described for thermal noise.

The total mean-squared noise voltage at the IF frequency is the sum of eqs. (E.34), (E.37) and (E.47):

$$< |\delta V_{N,0}|^2 >= \mathbf{Z_0'}(< \delta \mathbf{I_S} \delta \mathbf{I_S^\dagger} > + < \delta \mathbf{I_T} \delta \mathbf{I_T^\dagger} > + < \delta \mathbf{I_H} \delta \mathbf{I_H^\dagger} >) \mathbf{Z_0'}^\dagger \tag{E.48}$$

When R_s is assumed constant, the noise power delivered to the output load at IF frequency is:

$$P_0 = \frac{<|\delta V_{N,0}|^2> \mathrm{Re}\{Z_e(f_0)\}}{|Z_e(f_0)+R_s|^2} \tag{E.49}$$

and the single side band noise temperature:

$$T_{SSB} = \frac{P_0 L_c}{K_B \Delta f}. \tag{E.50}$$

If the series resistance is assumed time varying, the evaluation of P_0 has to take into account that the series resistance in described by a non diagonal matrix $\mathbf{Z_{R_s}}$, as was previously explained. The matrix associated to the series resistance in series with the embedding impedance of the diode is denoted as:

$$\mathbf{Z_{re}} = \mathbf{Z_{R_s}} + \mathbf{Z_e}. \tag{E.51}$$

$\mathbf{Y_{re}} = \mathbf{Z_{re}}^{-1}$ denotes the associated admittance matrix. The noise current at IF frequency through the series combination of the embedding impedance and the time varying series resistance is given by:

$$\delta I'_{N,0} = \mathbf{Y_{re,0}} \delta \mathbf{V_N} \tag{E.52}$$

where $\mathbf{Y_{re,0}}$ is the row of the matrix $\mathbf{Y_{re}}$ corresponding to the IF frequency and $\delta \mathbf{V_N}$ is the noise voltage vector, whose component 0 is defined in eq. (E.48). The ensemble average of $<|\delta I'_{N,0}|^2>$ is:

$$<|\delta I'_{N,0}|^2> = \mathbf{Y_{re,0}} < \delta \mathbf{V_N} \delta \mathbf{V_N}^\dagger > \mathbf{Y_{re,0}}^\dagger. \tag{E.53}$$

Using that $\delta \mathbf{V_N} = \mathbf{Z'}(\delta \mathbf{I_S} + \delta \mathbf{I_T} + \delta \mathbf{I_H})$, eq. (E.53) can be written as:

$$<|\delta I'_{N,0}|^2> = \mathbf{Y_{re,0}} \mathbf{Z'} (< \delta \mathbf{I_S} \delta \mathbf{I_S}^\dagger > + < \delta \mathbf{I_T} \delta \mathbf{I_T}^\dagger > + < \delta \mathbf{I_H} \delta \mathbf{I_H}^\dagger >) \mathbf{Z'}^\dagger \mathbf{Y_{re,0}}^\dagger. \tag{E.54}$$

The noise power delivered to the output load at IF frequency is:

$$P_0 = <|\delta I'_{N,0}|^2> \mathrm{Re}\{Z_e(f_0)\} \tag{E.55}$$

and the noise temperature is evaluated by eq. (E.50).

When there is a parasitic capacitance in parallel with the Schottky diode, the circuit impedances that appear in the current noise correlation matrix must be replaced by the corresponding impedance of the circuit impedance in parallel with the parasitic impedance. Besides, the noise power P_0 given by eq. (E.49) has to be modified to evaluate the power dissipated in the real part of the circuit impedance at the IF frequency.

In the noise analysis of mixers presented in chapter 6, the equations for the noise temperature assuming a constant series resistance, eqs. (E.49) and (E.50), and a time varying resistance eq. (E.55) have been used for the $\mathrm{LEC}_{R_{s,dc}}$ and $\mathrm{LEC}_{R_s(t)}$ models, respectively. Besides, the effects of the parasitic capacitance in the noise temperature described in this section have been considered in the calculation of the noise temperature carried out in chapter 6, see Table 6.3.

E.3 Subharmonic mixers

For the simulation of noise in antiparallel diode pair subharmonic mixers, the conversion matrix developed in [Ker79a] has been used. Having determined the large-signal waveforms at the diodes, the small-signal properties of the two diodes mixer can be obtained by an extension of the theory developed in [Hel78a] for the single diode mixers. Fig. E.6 presents an scheme of the two pumped diodes connected via their mount to the external sources and loads at the various side-band frequencies. In [Ker79a], the two diodes and their mount are represented as three interconnected networks

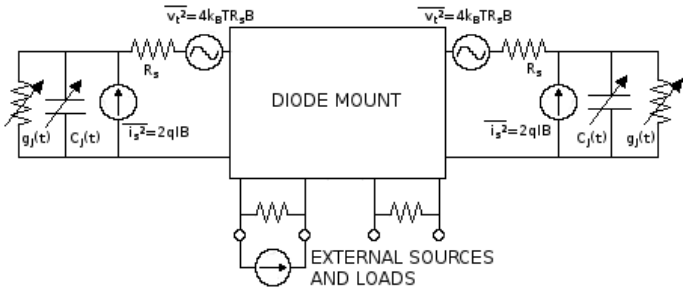

Figure E.6: Circuit of the two-diode mixer. Reproduced from [Ker79a].

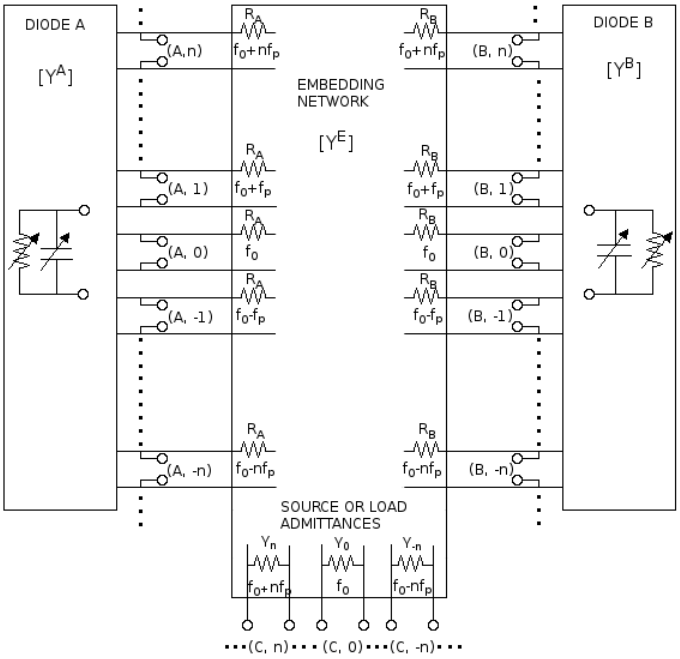

Figure E.7: Representation of the mixer as a multifrequency multiport network. The embedding network contains the series resistance of the diodes and all source and load admittances Y_k connected externally to the diode mount. Reproduced from [Ker79a].

(multifrequency multiport network representation) as shown in Fig. E.7. In this representation, the embedding network includes the diode mount, the series resistance and all source and load admittances connected externally to the mount. For the notation of the ports in this representation, it is used a letter (A, B or C) to denote each of three faces of the embedding network and a positive or negative integer to denote the sideband frequency. The admittance matrix of the embedding network

is denoted by $\mathbf{Y^E}$, and the numbering of row and columns in this matrix is:

	(A,N) ... $(A,0)$ ... $(A,-N)$	(B,N) ... $(B,0)$ ... $(B,-N)$	(C,N) ... $(C,0)$ ... $(C,-N)$
(A,N) ... $(A,0)$ ... $(A,-N)$			
(B,N) ... $(B,0)$ ... $(B,-N)$			
(C,N) ... $(C,0)$ ... $(C,-N)$			

(E.56)

Matrix $\mathbf{Y^E}$ can be partitioned in nine equal-sized submatrix. The parallel connection of the two pumped diodes, represented by matrixes $\mathbf{Y^A}$ and $\mathbf{Y^B}$, see Fig. E.7, with the embedding network results in an overall admittance matrix $\mathbf{Y^M}$:

$$\mathbf{Y^M} = \left[\begin{array}{c|c|c} \mathbf{Y^A + Y^E_{AA}} & \mathbf{Y^E_{AB}} & \mathbf{Y^E_{AC}} \\ \hline \mathbf{Y^E_{BA}} & \mathbf{Y^B + Y^E_{BB}} & \mathbf{Y^E_{BC}} \\ \hline \mathbf{Y^E_{CA}} & \mathbf{Y^E_{CB}} & \mathbf{Y^E_{CC}} \end{array}\right] \tag{E.57}$$

The IF output impedance of the mixer is given by [Ker79a]:

$$Z_{out} = \mathbf{Z}^{\mathbf{M},o/c}_{(C,0)(C,0)} \tag{E.58}$$

where $\mathbf{Z^{M}}^{o/c} = (\mathbf{Y^{M},}^{o/c})^{-1}$ and $\mathbf{Y^{M},}^{o/c}$ is the admittance matrix of the mixer setting to zero the IF load admittance. Following [Ker79a], the conversion loss from RF to IF is given by:

$$L_c = \frac{1}{4|\mathbf{Z^M}_{(C,0)(C,1)}|^2 \mathrm{Re}[Y_1]\mathrm{Re}[Y_0]} \tag{E.59}$$

where Y_0 and Y_1 are the IF load admittance and the RF source admittance, respectively.

The analysis of noise of the two pumped diode is similar to the results presented for the single-diode mixer. According to [Ker79a], it can be assumed that there is not correlation between the noise components of the two didoes. Using the superscripts A and B to distinguish between the two diodes connected to the faces A and B of the embedding network, it follows that the shot noise correlation matrix for the two diode mixer is (see eq. (E.35)):

$$\begin{aligned} < \delta I^A_{S,m} \delta I^{A*}_{S,n} > &= 2qI^A_{m-n}B \\ < \delta I^B_{S,m} \delta I^{B*}_{S,n} > &= 2qI^B_{m-n}B \\ < \delta I^A_{S,m} \delta I^{B*}_{S,n} > &= 0. \end{aligned} \tag{E.60}$$

To characterize the thermal noise performance of the two diodes mixer, the embedding network is regarded as composed of two parallel connected subnetworks, one at temperature T, and the other, containing only the external terminations, at absolute zero temperature, since thermal noise due to external terminations is not considered. If the admittance matrices of these subnetworks are respectively $\mathbf{Y^{E},}^{unterm}$ and $\mathbf{Y^{E},}^{term}$, then $\mathbf{Y^E}$ is written:

$$\mathbf{Y^E} = \mathbf{Y^{E},}^{unterm} + \mathbf{Y^{E},}^{term}. \tag{E.61}$$

It is possible to write the correlation matrix of the thermal noise for the two diode mixer as (since $\mathbf{Y}^{\mathbf{E},term}$ is at zero temperature contributes nothing) [Ker79a]:

$$< \delta I_{T(X,m)} \delta I_{T(Y,n)} >= 4k_B T \mathrm{Re}[\mathbf{Y}^{\mathbf{E},unterm}_{(X,m)(Y,n)}]B \tag{E.62}$$

where *(X,m)* and *(Y,n)* represent any of the ports defined in Fig. E.7 (X and Y can be any of three faces of the embedding network A, B or C, and the index m and n represent any of the mixing frequencies eq. (E.1)).

To determine the equivalent input noise temperature of the two-diode mixer we first determine the IF output noise power due to shot and thermal noise, using the correlation properties given by eqs. (E.60) and (E.62). The calculation of the IF output noise power and the equivalent input noise temperature is similar to the description carried out for the single-diode mixer, eqs. (E.48), (E.49) and (E.50), see [Ker79a].

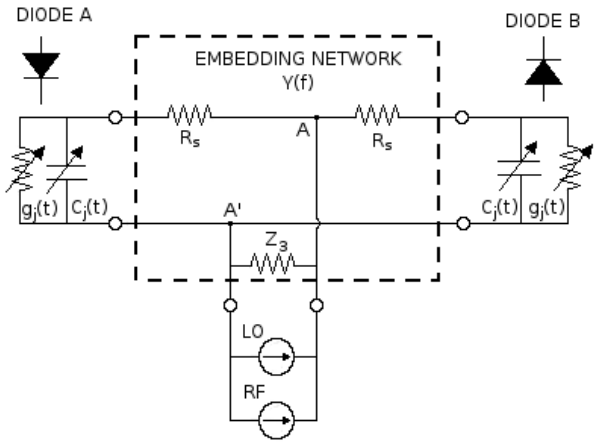

Figure E.8: Equivalent circuit of subharmonically pumped mixer.Z_3 represents the source or load impedance and depends on frequency. In practice, Z_3 would consist of a number of source or load impedances connected to AA' by filter circuits which separate the various sidebands and LO harmonics.

Fig. E.8 shows the circuit of the antiparallel diode pair subharmonically pumped mixer used in the simulations of chapter 6. At any frequency f, the admittance matrix of the embedding network of this circuit is [Ker79b]:

$$\mathbf{Y}(f) = \frac{1}{R_s} \begin{bmatrix} 1 & 0 & -1 \\ 0 & 1 & -1 \\ -1 & -1 & 2 + R_s/Z_3 \end{bmatrix} \tag{E.63}$$

The elements of the admittance matrix $\mathbf{Y}^{\mathbf{E}}$ of the multiport embedding network are determined using the elements of the matrix $\mathbf{Y}(f)$:

$$\begin{bmatrix} Y^E_{(A,n)(A,n)} = Y_{1,1}(f_n), & Y^E_{(A,m)(A,n)} = 0 \\ Y^E_{(A,n)(B,n)} = Y_{1,2}(f_n), & Y^E_{(A,m)(B,n)} = 0 \\ Y^E_{(A,n)(C,n)} = Y_{1,3}(f_n), & Y^E_{(A,m)(C,n)} = 0 \\ \cdot & \cdot \\ \cdot & \cdot \\ \cdot & \cdot \end{bmatrix} \tag{E.64}$$

where the dependence of the elements of $\mathbf{Y}(f)$ on the mixing frequency f_n is due to the dependence of Z_3 on f_n. The overall admittance matrix $\mathbf{Y}^{\mathbf{M}}$ is then formed by adding the admittance matrix of the two Schottky junctions as described by eq. (E.57).

Appendix F

Additional results for Schottky mixers

This appendix presents additional results about the physical processes limiting the performance of the diodes in the mixers analysed in chapter 6. The internal distributions of some magnitudes of the diodes analysed in this appendix like the electric field or the charge concentration, have been obtained only under the LO excitation. This procedure assumes that the behavior of the diode is determined by the LO power (the LO power is some orders of magnitude higher than the RF power considered in mixer simulations).

F.1 The 86-106 GHz fundamental mixer

Fig. F.1 presents the conversion losses of the 86-106 GHz fundamental mixer [Ali93a] at f_{IF}= 10 GHz and 2 GHz, Table 6.3, obtained with different diode models. The dc current, the LO voltage waveforms at the terminals of the diode, the electric field and charge concentration are also shown in the figure for different LO powers. The most important results from the analysis of the this figure are:

- Conversion loss from simulations with f_{IF}= 2 GHz are similar to the results with f_{IF}= 10 GHz, and about 1 dB lower than measurements, Figs. F.1(a) and (b). According to [Ali93b], the differences between measured and simulated results can be due to power losses by conversion to other frequencies where the terminating embedding impedances have real parts and discrepancies in the measured embedding impedances at the first and second harmonics between the microwave model of the receiver structure and the actual receiver at 90 GHz.
- The conversion loss decreases rapidly with the LO power until the region of constant conversion loss is reached. This region begins at P_{LO} higher than 1 mW, when flat band conditions are reached, see Figs. F.1(c) and F.1(d). Higher LO input power does not decrease the conversion loss.
- Fig. F.1(e) and F.1(f) show that velocity saturation is not affecting the performance of this mixer (low electric field in the undepleted epilayer).

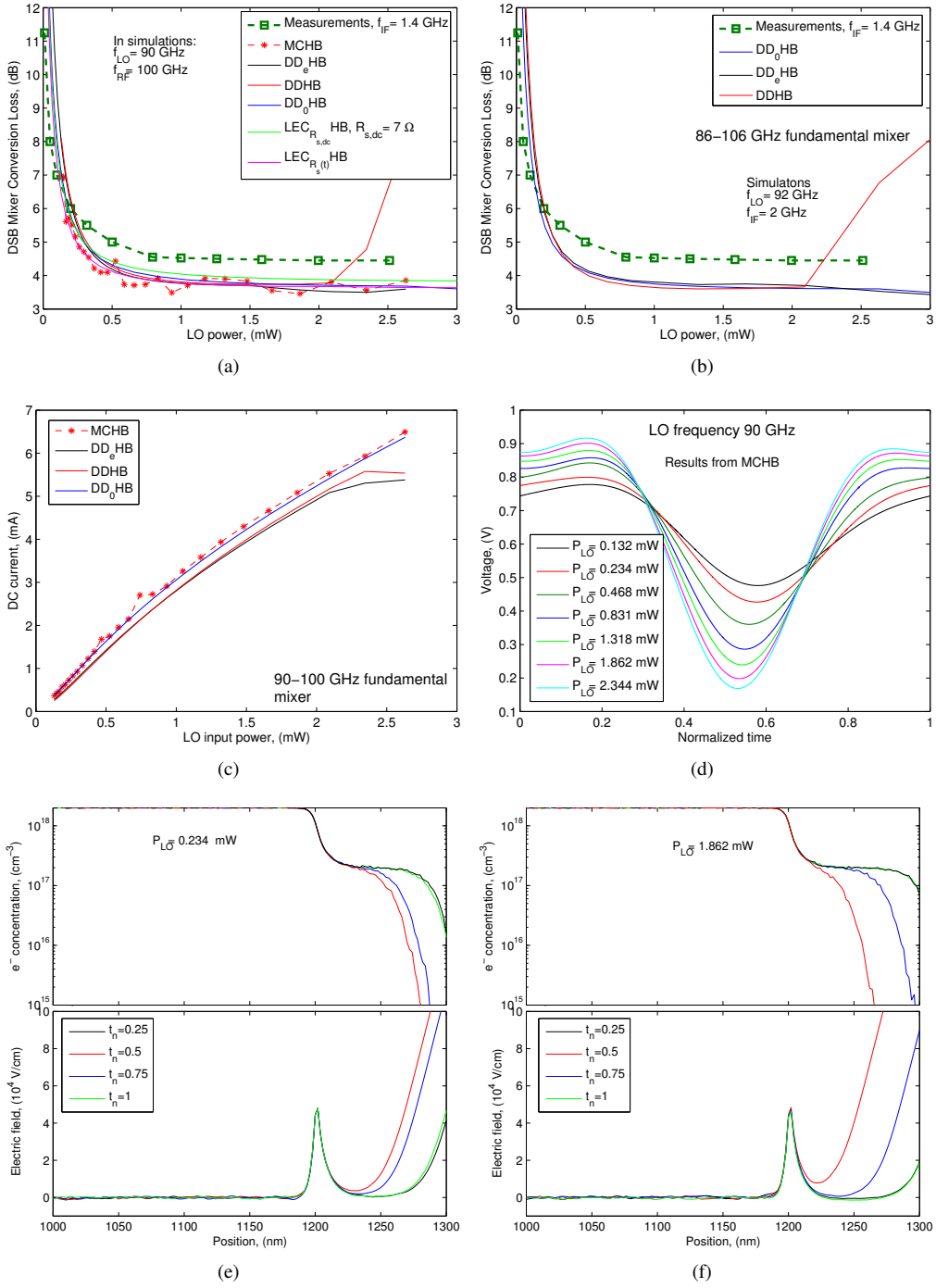

Figure F.1: Conversion losses at (a) f_{IF}= 10 GHz and (b) f_{IF}= 2 GHz of the 86-106 GHz fundamental single-ended mixer [Ali93a], Table 6.3, obtained with different models. Subfigures (c) and (d) present the dc current and the LO voltage waveforms as a function of the LO power. Subfigures (e) and (f) show the electron concentration and the electric field in the diodes at LO power P_{LO}= 0.23 mW and P_{LO}= 1.86 mW, respectively, obtained from MC simulations.

F.2 The 300-360 GHz sub-harmonic mixer

Fig. F.2 presents the conversion losses of the 300-360 GHz sub-harmonically pumped mixer [Tho04, Tho05], see Table 6.3, at (a) f_{IF} = 24 GHz and (b) f_{IF} = 2 GHz, and various parameters of the diodes as a function of the LO power. From the analysis of these figures, it can be concluded:

- When the intermediate frequency simulated is 2 GHz (measured results are at f_{IF} = 1.5 GHz), the agreement between measured and DDHB simulated results is slightly better.
- The minimum conversion losses are reached around 2.5 mW, when the diode exceed the flat-band condition for part of the LO cycle [Cro86], see Fig. F.2(d).
- At LO powers higher than 2.5 mW, the conversion losses from simulations are degraded due to the effect of the series resistance R_s on the conversion losses. This effect is more pronounced for high values of the LO drive: As the LO power increases, the average value of the junction resistance R_j decreases, and the conversion losses decrease. Then, as the average value of R_j approaches R_s, more power is dissipated in R_s and the conversion losses increase [Mes57], as observed in Fig. F.2(a) at P_{LO} higher than 2.5 mW.
- At high LO powers, see Fig. F.2(e), when the diode is beyond flat band, high electric fields are generated in the epilayer, which increase the average kinetic electron energy. Despite of the increase of the electron energy, it is not expected to provide an important increase of the hot electron noise since the temporal average electron energy is close to the equilibrium energy, see Fig. F.2(e).

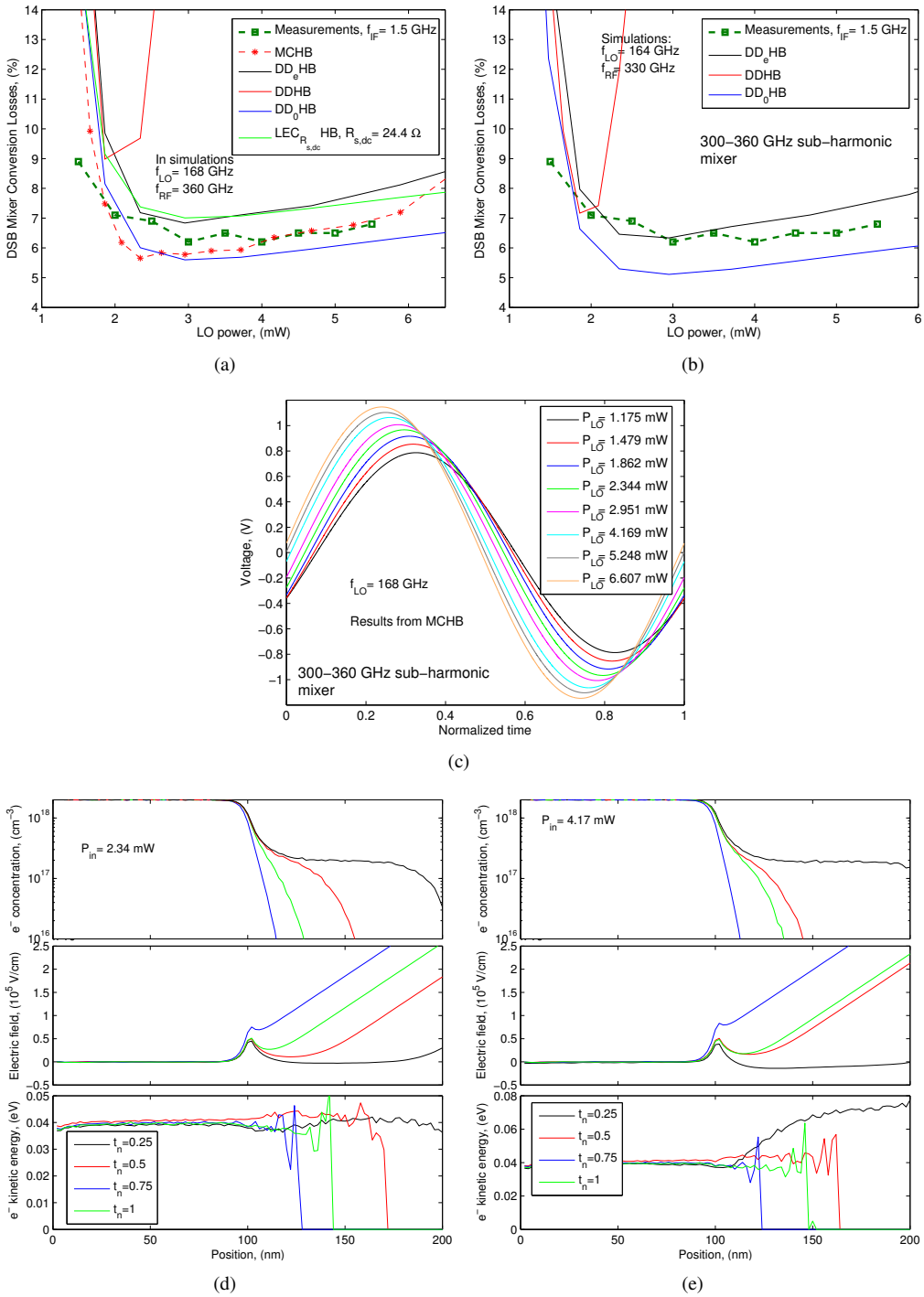

Figure F.2: Conversion losses at (a) f_{IF}= 24 GHz and (b) f_{IF}= 2 GHz of the 300-360 GHz sub-harmonic mixer [Tho04, Tho05], Table 6.3, obtained with different models. Subfigure (c) presents the LO voltage waveforms as a function of the input power and (d) and (e) the electron concentration, the electric field and the electron kinetic energy in the diodes at P_{LO}= 2.34 mW and P_{LO}= 4.17 mW, respectively, obtained from MC simulations.

F.3 The 585-690 GHz fundamental mixer

Fig. F.3 presents the conversion losses of the 585-690 GHz fundamental mixer [Hes97] at f_{IF}= 30 GHz and 2 GHz, Table 6.3, obtained with different diode models. The dc current, the voltage waveforms at the terminals of the diode, electron concentration, electric field and electron energy are also shown in the figure for different LO powers. The most important results from the analysis of the this figure are:

- According to Figs. F.3(a) and (b), similar conversion losses are obtained simulating f_{IF}= 30 GHz and 2 GHz.
- As expected, the minimum conversion losses in simulations occur when the diode is operating in the vicinity of flat-band conditions, $P_{LO} \sim$ 1.3 mW and it degrades at higher LO power as was explained for the 300-360 GHz SHP mixer.
- At P_{LO} higher than 1.3 mW, high fields appear in the undepleted region of the epilayer (diode working beyond flat-band), see Figs. F.3(e) and F.3(f). However, these fields are not high enough to transfer electrons to the upper valleys. The energy of the electrons increases due to the action of these electric fields, see Fig. F.3(f), although it is not expected to provided an important increase of the hot electron noise contribution, as was explained for the 300-360 SHP mixer.

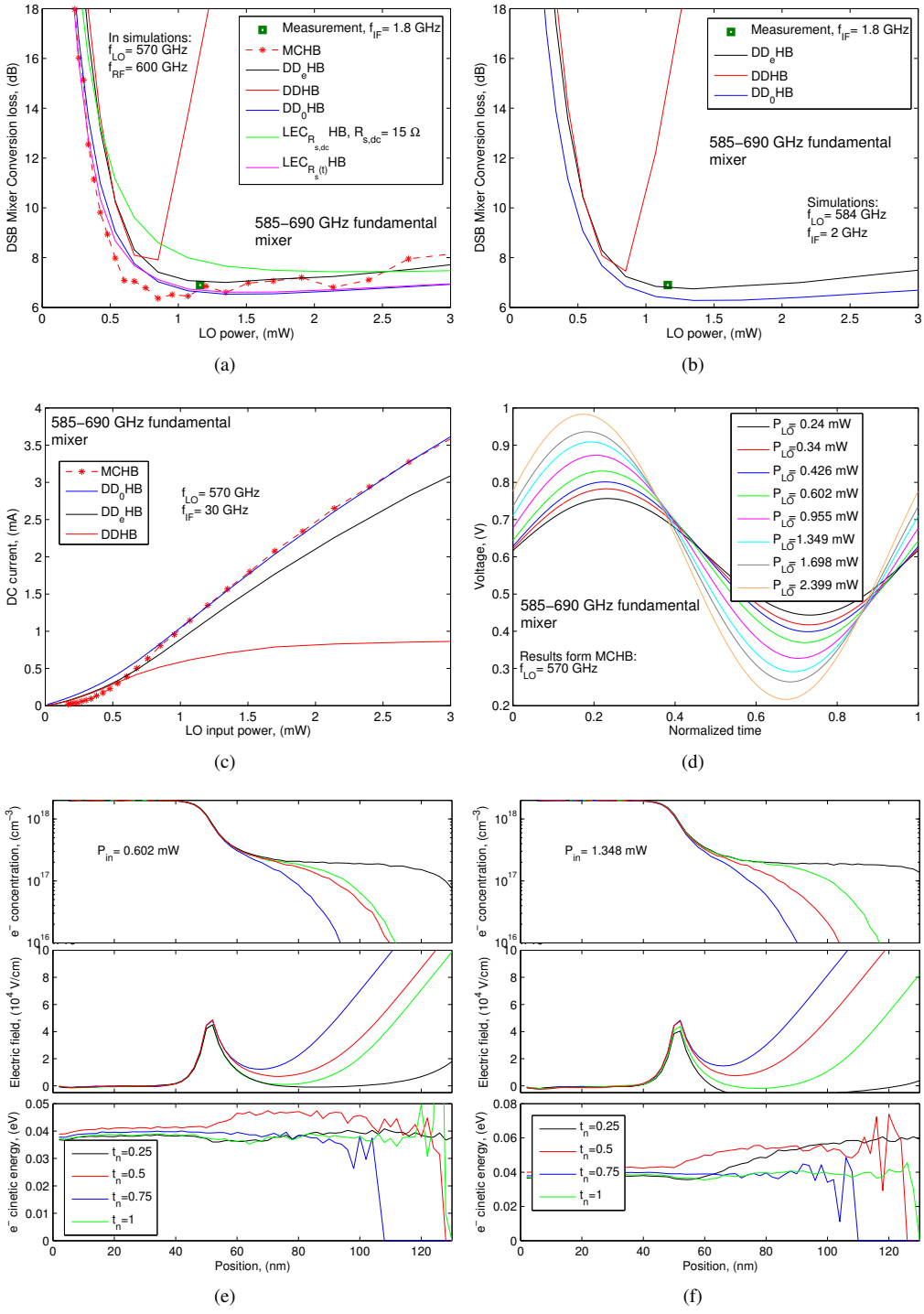

Figure F.3: Conversion losses at (a) f_{IF}= 30 GHz and (b) f_{IF}= 2 GHz of the 585-690 GHz fundamental mixer [Hes96, Hes97], Table 6.3, obtained with different models. Subfigures (c) and (d) present the dc current and the LO voltage waveforms as a function of the LO power. Subfigures (e) and (f) show the electron concentration, the electric field and the average electron kinetic energy in the diodes at P_{LO}= 0.6 mW and P_{LO}= 1.35 mW, respectively, obtained from MC simulations.

F.4 The 835-900 GHz fundamental balanced mixer

Fig. F.4 presents the conversion losses of the 835-900 GHz fundamental balanced mixer [Tho10c] at f_{IF}= 30 GHz and 2 GHz, Table 6.3, obtained with different diode models. The dc current, the voltage waveforms at the terminals of the diode pair, electric field and charge concentration are also shown in this figure for different LO powers. The most relevant results from the analysis of the this figure are similar to those of the previous mixers:

- Minimum conversion loss around 0.5 mW when the diodes operate in the vicinity of flat band conditions and degradation of the conversion losses at higher LO powers. The LO power in these figures represents the total input power for the two diodes.
- At P_{LO} higher than 0.5 mW, high electric fields are generated in the undepleted region of the epilayer, what increases the the average electron energy. The increase of the electron energy in the epilayer is not very high with respect to the equilibrium value.
- The results from MCHB in Fig. F.4(a) present fluctuations of $\pm$ 0.5 dB which are from numerical origin, related to dependence of the accuracy of the MC simulations with the number and particles simulated, see appendix A. These fluctuations can be avoided by increasing the number of simulated particles and the time of simulations, but with an higher computational cost.

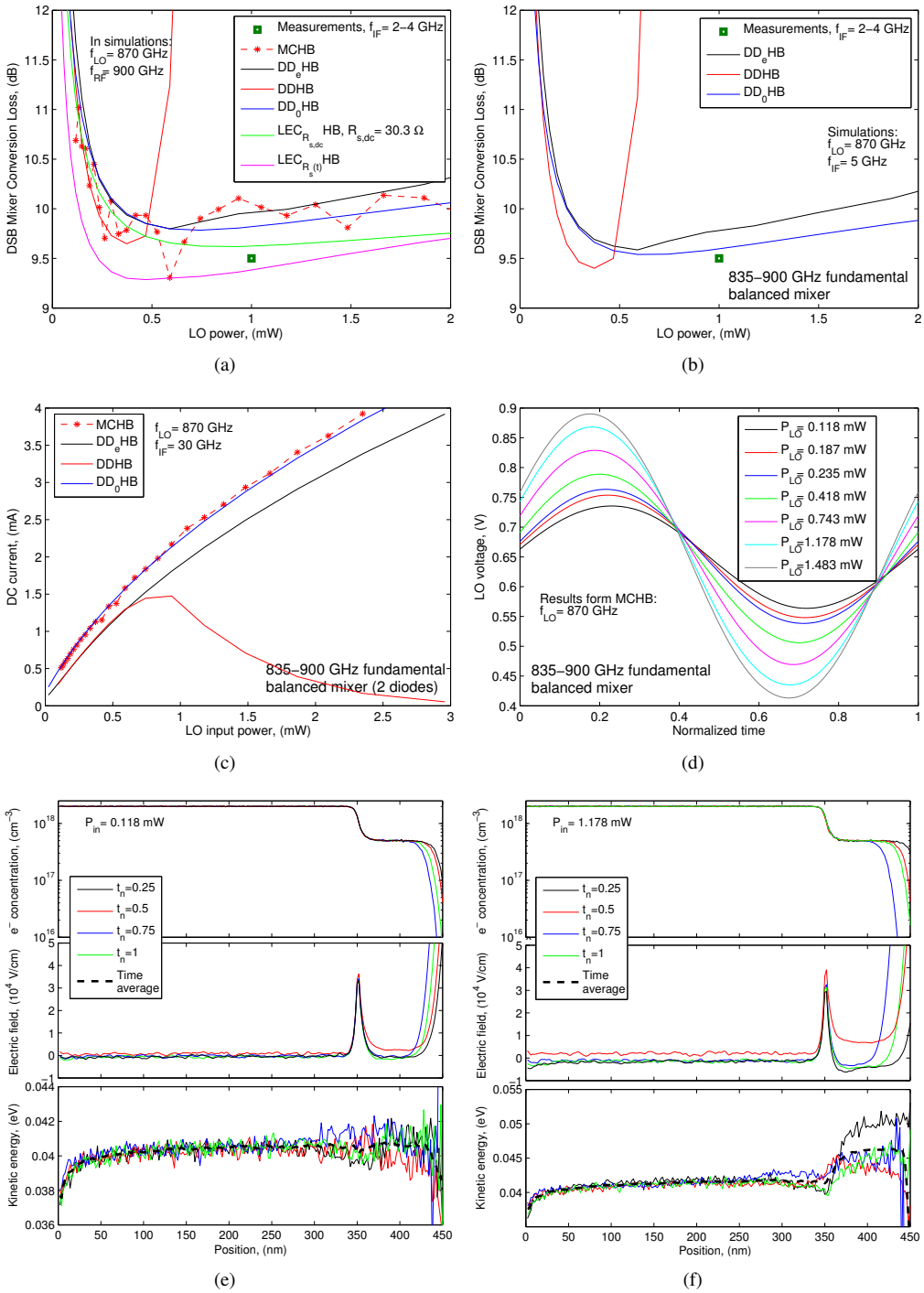

Figure F.4: Conversion losses at (a) f_{IF}= 30 GHz and (b) f_{IF}= 5 GHz of the 835-900 GHz fundamental balanced mixer [Tho10b, Tho10c], Table 6.3, obtained with different models. Subfigures (c) and (d) present the dc current and the LO voltage waveforms as a function of the LO power. Subfigures (e) and (f) show the electron concentration, the electric field and the average kinetic energy of the electrons in the diodes at P_{LO}= 0.118 mW and P_{LO}= 1.178 mW, respectively, obtained from MC simulations.

F.5 The 2.5 THz fundamental mixer

Fig. F.5 presents the conversion losses of the 2.5 THz fundamental mixer [Sie99] at f_{IF} = 25 GHz, Table 6.3, obtained with different diode models. The dc current, the voltage waveforms at the terminals of the diode, the electron concentration, the electric field and L valley occupation are also shown in the figure for different LO powers. The most relevant results from the analysis of the this figure are:

- The enhanced DD model (DD_e) [Sil09] is not updated to take into account the characteristics of the diode in the 2.5 THz fundamental mixer. Hence, there is not a good agreement between DD_eHB and MCHB in Fig. F.5(a).
- The minimum conversion loss occurs at LO power around 5 mW, when the diodes operate in the vicinity of flat band conditions. At this LO power, the L valley occupation in the undepleted epilayer reaches 20 %, see Fig. F.5(d).
- Velocity saturation limits the performance of this mixer. At LO powers higher than 5 mW, the L valley occupation increases abruptly up to 60 % what increases the series resistance of the diode and degrades the conversion losses, see Fig. F.5(e).
- The dc current in Fig. F.5(c) with MC decreases at LO power higher than 5 mW. At these powers, the upper valleys of the semiconductor are highly populated, Fig. F.5(e). Due to the lower electron mobility in the upper valleys, the modulation of the nonlinear junction resistance decreases, limiting the generation mixing products, and, hence, the dc component.
- The inclusion of the Fermi-Dirac statistics in the MC model has a low impact on the conversion losses of the mixer, see Fig. F.5(a).

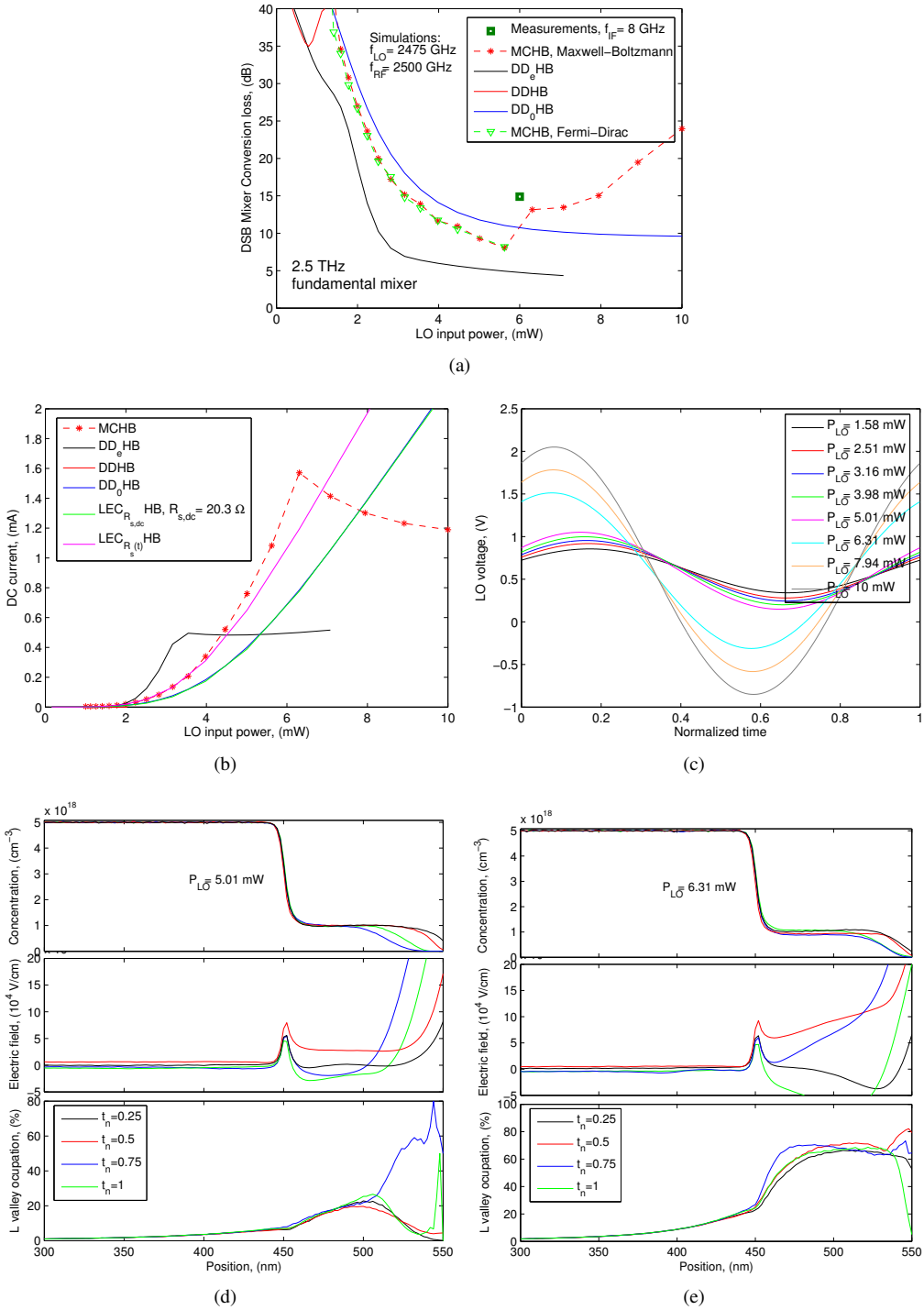

Figure F.5: Conversion losses at (a) f_{IF}= 25 GHz for the 2.5 THz fundamental mixer [Sie99], Table 6.3, obtained with different models. Subfigures (b) and (c) present the dc current and the LO voltage waveforms as a function of the LO power. Subfigures (d) and (e) show the electron concentration, the electric field and the L valley occupation for the diode at P_{LO}= 5 mW and P_{LO}= 6.3 mW, respectively, obtained from MC simulations.

F.6 The 4.75 THz fundamental balanced mixer

Fig. F.6 presents the conversion losses of the 4.75 THz fundamental mixer [Bet96] at f_{IF}= 25 GHz, Table 6.3, obtained with different diode models. The dc current, the voltage waveforms at the terminals of the diode, electric field and charge concentration are also shown in the figure for different LO powers. The most relevant results from the analysis of the this figure are:

- The enhanced DD model (DD_e) [Sil09] is not updated yet for the characteristics of the diode in the 5 THz fundamental mixer (epilayer doping 1x10^{18} cm^{-3} and length 30 nm). Hence, there is not a good agreement between DD_eHB and MCHB in Fig. F.6(a).
- The depletion region of the diode reaches the substrate even at 0.3 mW of input power, see Fig. F.6.
- The minimum conversion loss occurs at LO power around 1 mW, when the diode operates in the vicinity of flat band conditions. At these LO powers, the L valley occupation in the undepleted epilayer reaches 5 %, see Fig. F.6(d). At higher LO powers (the diode works beyond flat band), the series resistance of the diode increases, due the increase of the occupation of the L valley (20 % at P_{LO}= 1.26 mW, Figs. F.6(e)) and the conversion loss increases.
- The inclusion of the Fermi-Dirac statistics in the MC model has a low impact on the conversion loss of the mixer, see Fig. F.6(a).

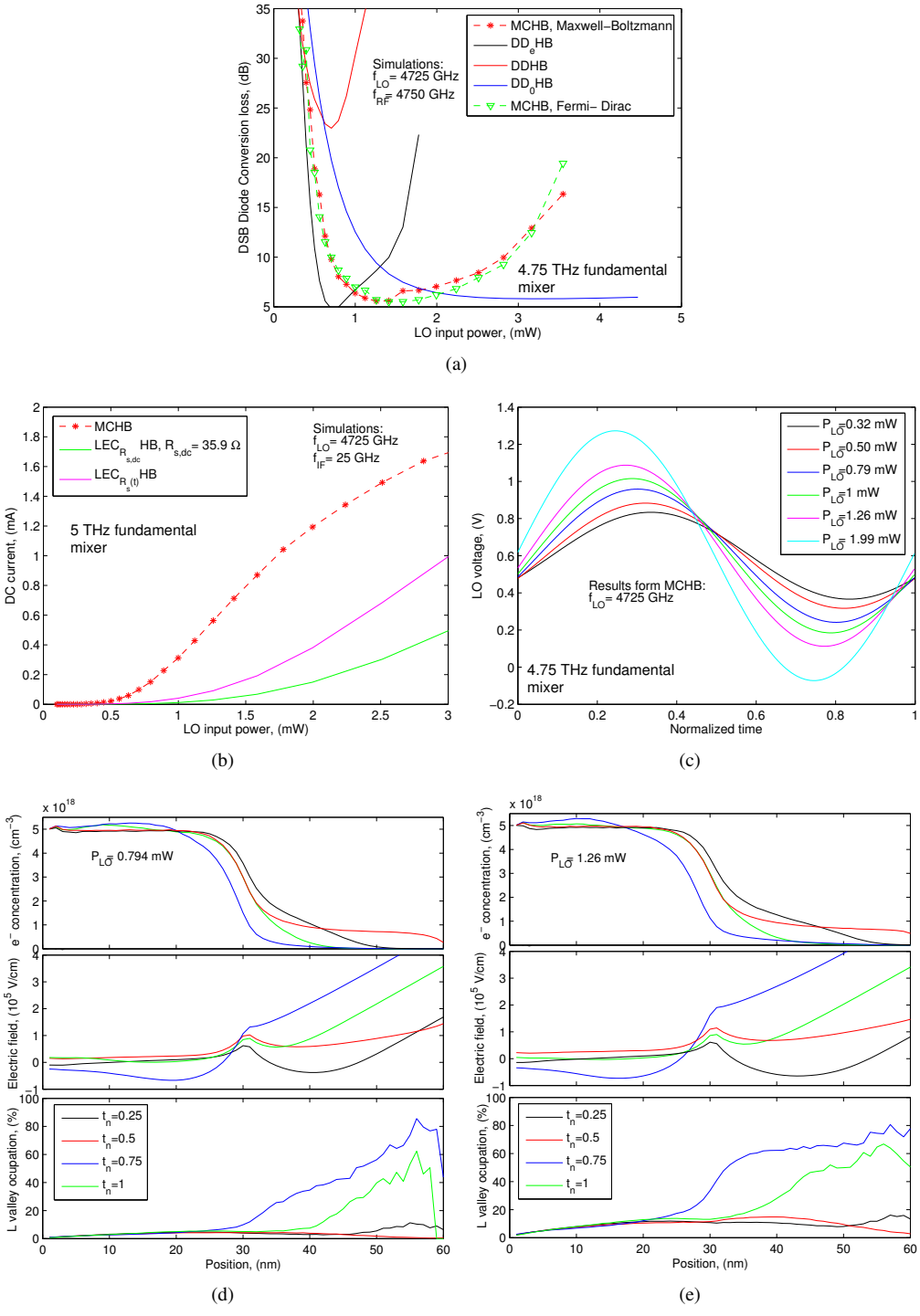

Figure F.6: (a) Conversion losses at f_{IF}= 25 GHz of the 4.75 THz fundamental balanced mixer [Bet96], Table 6.3, obtained with different models. Subfigures (b) and (c) present the dc current and the LO voltage waveforms as a function of the LO power. Subfigures (d) and (e) show the electron concentration, the electric field and the L valley occupation for the diode at P_{LO}= 0.794 mW and P_{LO}= 1.26 mW, respectively, obtained from MC simulations.

Appendix G

Analysis of cyclostationary noise in Schottky diodes

G.1 Theoretical background

Under periodic time varying conditions of fundamental frequency f_{in}, the stochastic processes representing fluctuations, both at circuit and microscopic levels are amplitude modulated by the time varying noiseless working point. This causes frequency conversion effects on the device external noise spectra [Bon01a, Bon01b, Bon03]. Therefore, noise processes are converted into cyclostationary processes. An important feature of cyclostationarity is the appearance of frequency correlation in the spectral representation of the noise processes. Under harmonic amplitude modulation of the stationary noise fluctuations, the spectral components at frequencies f_1 and f_2 are uncorrelated unless two harmonics $n_i f_{in}$ and $n_j f_{in}$ exist such that f_1-$n_i f_{in}$=f_2-$n_j f_{in}$=f, see Fig. G.1.

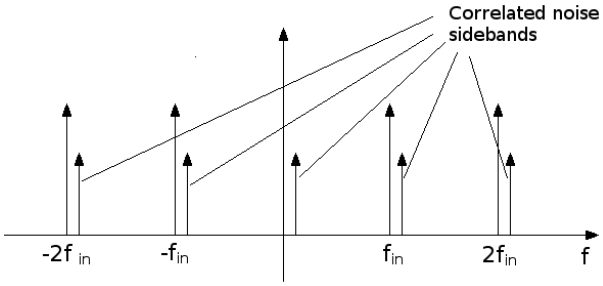

Figure G.1: Noise sidebands and their correlation.

Cyclostationary processes $x(t)$ (x can represent the current in the device, the voltage at the terminals, the velocity of the carriers, etc.) are characterized by mean $< x(t) >$ and correlation function $R_x(t_1,t_2)$ which are periodic in time with period T=$1/f_{in}$, see [Gar88, Bon01a, Bon02]:

$$< x(t) >=< x(t+T) > \tag{G.1}$$

$$R_x(t_1,t_2) =< x(t_1)x(t_2) >= R_x(t_1+T,t_2+T) \tag{G.2}$$

where $< . >$ denotes ensemble average. With a change of variables $t_1 = t+\tau/2$ and $t_2 = t-\tau/2$, the autocorrelation function eq. (G.2)is expressed as:

$$R_x(t,\tau) =< x(t+\tau/2)x(t-\tau/2) > \tag{G.3}$$

which is a function of two independent variables t and τ, and it is periodic in t with period T for each value of τ. Hence, $R_x(t,\tau)$ can be developed in Fourier series:

$$R_x(t,\tau) = \sum_{n=-\infty}^{n=\infty} R_x^{(n)}(\tau)\exp(j2\pi n f_{in} t). \tag{G.4}$$

For cyclostationay processes, the instantaneous or time varying spectral density is defined:

$$S_x(t,f) = \int_{-\infty}^{\infty} R_x(t,\tau)\exp(-j2\pi f\tau)d\tau. \tag{G.5}$$

The Fourier series representing this periodic function can be expressed as:

$$S_x(t,f) = \sum_{n=-\infty}^{n=\infty} S_x^{(n)}(f)\exp(j2\pi n f_{in} t). \tag{G.6}$$

It can be shown that:

$$S_x^{(n)}(f) = \int_{-\infty}^{\infty} R_x^{(n)}(\tau)\exp(-j2\pi f\tau)d\tau. \tag{G.7}$$

For $n = 0$ this expression reduces to the conventional power spectral density function, that is, the spectral density of time-averaged power. However, for $n \neq 0$, $S_x^{(n)}(f)$ represents the density of spectral correlation, that is, the density of correlation between spectral components at the frequencies $f + nf_{in}/2$ and $f - nf_{in}/2$. Therefore, the cyclostationary noise spectral representation is reduced to the so-called sideband correlation matrix (SCM), which depends on the frequency f and whose diagonal components are the power spectral density. The (k,l) element of the sideband correlation matrix can be expressed as [Bon01a, Bon02]:

$$(S_x(f))_{k,l} = S_x^{(k-l)}(f + \frac{k+l}{2} f_{in}). \tag{G.8}$$

G.2 Noise in Schottky diodes under periodic excitations

In this section, noise in Schottky diodes under periodic excitations (cyclostationary noise) is analysed. As a reference, the diode in the 585-690 GHz fundamental mixer described in Table 6.3 has been selected (A= 1.13 μm^2, R_s= 15Ω, $C_j(0)$= 1.8 fF, ϕ_b= 0.85 V, N_e= 2x10^{17} cm^{-3}, L_e= 80 nm).

Fig. G.2 shows the power noise spectral density $S_I^{(0)}(f)$ obtained from Monte Carlo simulations of the reference diode under bias point of 0.6 V and sinusoidal voltages of amplitude 0.2 V and different input frequencies f_{in}. As a reference, the noise spectra under dc conditions 0.6 V has been included in the figure. The characteristics of these noise spectra were described in chapter 4: A low frequency region determined by shot and thermal noise contributions, limited by the returning carrier peak and a second peak at higher frequencies related to plasma effects.

The performance of the low frequency region of the noise spectra in Fig. G.2 calculated with the MC model[1] is shown in Fig. G.3 as a function of the input frequency. Eq. (4.30) which describes the shot and thermal noise contributions of the noise spectra of Schottky diodes under dc conditions, has been converted to a time varying function $S_I(t,0)$ by assuming that the conduction current, the junction resistance and the series resistance of the diode are time varying under periodic signals:

$$S_I(t,0) = \frac{2qI(t)R_j(t)^2}{(R_s(t)+R_j(t))^2} + \frac{4K_BTR_s(t)}{(R_s(t)+R_j(t))^2}. \tag{G.9}$$

Eq. (G.9) has been evaluated using $\mathrm{LEC}_{R_s(t)}$ and $\mathrm{LEC}_{R_sLC(t)}$ models and the results for $S_I^{(0)}(f = 0\,\mathrm{GHz})$ have been included in Fig. G.3. Also the contribution $S_I^{(0)}$=2qI_0 where I_0 is the dc component

[1] $S_I^{(0)}(f)$ at low frequencies f with MC is evaluated at frequency f= 20 GHz.

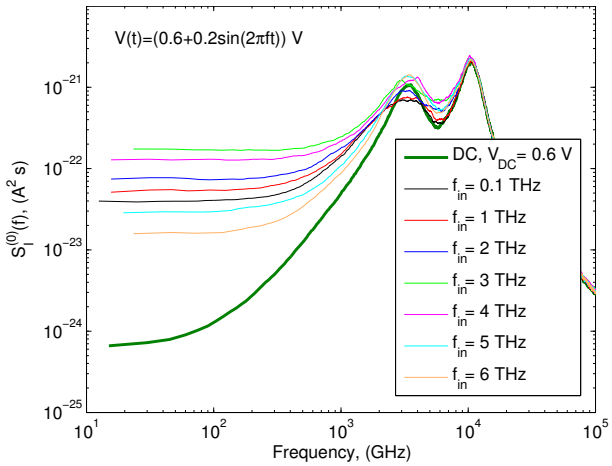

Figure G.2: Current noise spectral density $S_I^{(0)}(f)$ of the reference diode under bias point 0.6 V and sinusoidal voltages of amplitude 0.2 V and different input frequencies f_{in}, obtained with the MC model.

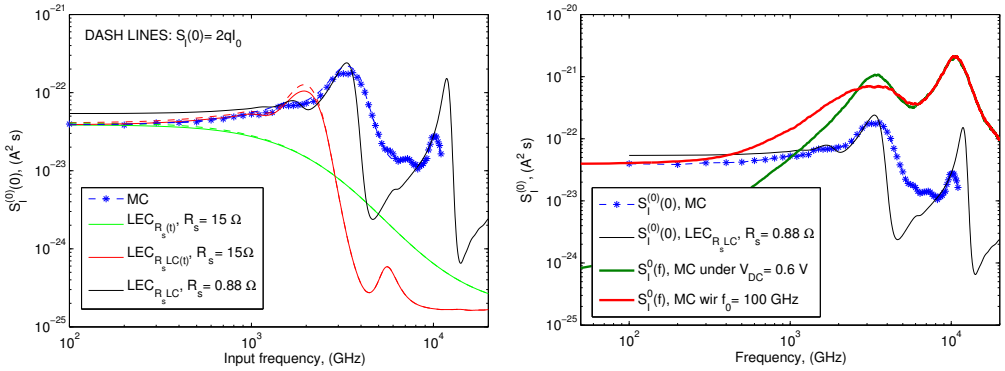

(a) (b)

Figure G.3: (a) Current noise spectral density $S_I^{(0)}(f \sim 0\,\text{GHz})$ at low frequencies under bias voltage 0.6 V and sinusoidal voltages of amplitude 0.2 V and different frequencies, obtained with MC and eq. (G.9) evaluated with different LEC models. In (b), $S_I^{(0)}(f \sim 0\,\text{GHz})$ is compared with the current noise spectra $S_I^{(0)}(f)$ presented in Fig. G.2 under V_{dc}= 0.6 V and under the sinusoidal voltage of input frequency 100 GHz.

of the conduction current evaluated with each model is shown in the figure. According to Fig. G.3(a), $S_I^{(0)}(f \sim 0\,\text{GHz})$ and $2qI_0$ evaluated with MC and $\text{LEC}_{R_sLC(t)}$ models increase as the the input frequency increases. Both quantities exhibit two resonances when the input frequency is comparable to the frequency of the returning carrier f_{RC} and the hybrid plasma f_{HP} peaks, respectively. This is observed in Fig. G.3(b), where $S_I^{(0)}(f \sim 0\,\text{GHz})$ as a function of the input frequency is compared with the current noise spectral density $S_I^0(f)$ under the sinusoidal voltages of frequency 100 GHz, see Fig. G.2. According to the discussion in the introduction, the noise at low frequencies f under periodic excitation of fundamental frequency f_{in} is the result of the up-conversion and down-conversion of noise components which frequencies $f_i = f + n_i f_{in}$, see Fig. G.1. When the input frequency f_{in} is close to f_{RC} or f_{HP}, the noise components located in the vicinity of the returning carrier or hybrid plasma peaks are down-converted to the low frequency f, what originates the peaks in $S_I^{(0)}(f \sim 0\,\text{GHz})$ observed in Fig. G.3, respectively. The results with eq. (G.9) evaluated with a $\text{LEC}_{R_sLC(t)}$ model predict the two peaks in $S_I^{(0)}(f \sim 0\,\text{GHz})$ when f_{in} is close to f_{RC} and f_{HP}, respectively. However, due to the simplicity of this model, it is not able to reproduce the results obtained with

MC. The values of the series resistance used in the $\mathrm{LEC}_{R_sLC(t)}$ model have been modified in order to get a better agreement with MC, see Fig. G.3. Simpler models based on $\mathrm{LEC}_{R_{s,dc}}$ or $\mathrm{LEC}_{R_s(t)}$ are not able to predict the increase of $S_I^{(0)}(f \sim 0\,\mathrm{GHz})$ when the input frequency increases, neither the two peaks predicted by MC simulations, Fig. G.3.

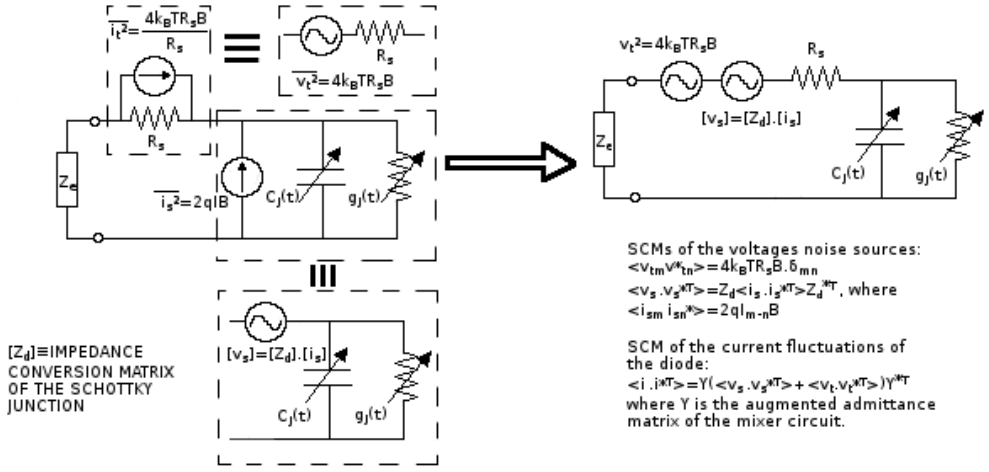

Figure G.4: Noise equivalent circuit of the Schottky diode and transformation between equivalent current and voltage noise sources. Notation used in appendix E.

The noise analysis under time varying conditions carried out with eq. (G.9) is equivalent to the noise analysis used in the CM formalism, see appendix E. In order to show such equivalence, the SCM obtained with eqs. (G.8) and (G.9) is compared with the analytical equations in the frequency domain for the SCM used in the CM formalism. A $\mathrm{LEC}_{R_{s,dc}}$ model has been used in the evaluation of both SCMs, since it is a common model used in the CM formalism. Some important assumptions made by eq. (G.9) have to be pointed out, in order to compare the SCMs obtained with the two techniques under the same conditions:

1. Eq. (G.9) neglects the effect of the junction capacitance in the noise spectrum. Hence, to carry out the comparison of the SCMs, a LEC model without junction capacitance has been used.

2. In the CM formalism, the thermal noise source of the series resistance of the diode is usually converted to an equivalent current noise source in parallel with the current shot noise source [Hel78a, Maa93], see Fig. E.4. Due to this transformation, the impedance of the circuit at the different intermodulation products appears in the SCM. However, the equivalent current noise source based on eq. (G.9) assumes that the circuit impedances are zero at all the intermodulation products. Hence, short circuit conditions have to be assumed in the evaluation of the equivalent thermal noise source in the CM formalism.

3. Eq. (G.9) gives the current noise spectrum of the diode, i.e. the SCM of the current fluctuations of the diode, while in the usual formulation of the CM [Hel78a, Maa93], the SCMs of each current noise source are firstly evaluated, and then they are used to calculate the SCM of the voltage fluctuations of the diode, see appendix E.2. Hence, to compare the SCMs obtained with both techniques, each noise source in the CM formalism has been converted to an equivalent voltage noise source, and then they have been used to calculate the SCM of the current fluctuations of the diode. Fig. G.4 presents an scheme of the transformation of the current noise sources in the diode to equivalent voltage noise sources[2].

[2]The calculation of the equivalent noise temperature of mixers using the voltage noise sources as indicated in Fig. G.4 gives the same noise temperature than using the most common configuration based on the equivalent current noise sources.

Eqs. (G.10) and (G.11) show the 3x3 SMCs obtained for the 585-690 GHz fundamental mixer described in Table 6.3 at f_{LO}= 584 GHz, f_{RF}= 586 GHz and P_{LO}= 1 mW calculated with eqs. (G.9) and (G.8) and the conversion matrix formalism using previous assumptions, respectively. A good agreement is observed between the two SCMs.

$$(S_I)_{k,l} = 2.075x10^{-22} \begin{bmatrix} 1 & 0.857+j0.142 & 0.517+j0.177 \\ 0.857-j0.142 & 1 & 0.857+j0.142 \\ 0.517-j0.177 & 0.857-j0.142 & 1 \end{bmatrix}, \text{with } \mathrm{S_I(t,0)}. \quad \text{(G.10)}$$

$$(S_I)_{k,l} = 2.096x10^{-22} \begin{bmatrix} 0.996 & 0.855+j0.142 & 0.514+j0.176 \\ 0.855-j0.142 & 1 & 0.855+j0.142 \\ 0.855-j0.142 & 0.855-j0.142 & 0.996 \end{bmatrix}, \text{with CM}. \quad \text{(G.11)}$$

The correlation matrix of the diode can be evaluated directly with the Monte Carlo model since $S_I(t,f)$ is obtained directly from the Monte Carlo simulations. Eqs. G.12 and G.13 compare the 3x3 SCM of the current fluctuations of the diode in the 585-690 GHz fundamental mixer described in Table 6.3 at f_{LO}= 570 GHz, f_{RF}= 600 GHz and P_{LO}= 1 mW, obtained with the MC model under the voltage waveforms from MCHB simulations and the CM formalism with $\mathrm{LEC}_{R_{s,dc}}$. In this comparison, the point 2) of the previous discussion has been applied in the evaluation of the SCM with the CM formalism. Note that with the MC model, the impact of the junction capacitance on the noise spectrum is taken into account inherently (point 1)). Although there are significant differences between the values of the elements of the two SCMs, both matrices present similar relations among the elements of the matrix.

$$(S_I)_{k,l} = 2.47x10^{-22} \begin{bmatrix} 1 & 0.13+j0.76 & -0.45+j0.40 \\ 0.13-j0.76 & 0.90 & 0.14+j0.78 \\ -0.45-j0.40 & 0.14-j0.78 & 0.99 \end{bmatrix}, \text{with MC}. \quad \text{(G.12)}$$

$$(S_I)_{k,l} = 1.86x10^{-22} \begin{bmatrix} 0.97 & 0.10+j0.67 & -0.41-j0.15 \\ 0.10-j0.67 & 0.80 & 0.10+j0.67 \\ -0.41-j0.15 & 0.10-j0.67 & 1 \end{bmatrix}, \text{with CM}. \quad \text{(G.13)}$$

Bibliography

[Abd92] H. S. Abdel-Aty-Zohdy, P. S. Gudem, and S. D. MacFarlane. "Device models and simulation of high-low doping transition regions and their effects on N-MOSFET circuits". In *Proc. 35th Midwest Symp. Circuits and Systems*, pp. 416–420, 1992.

[Ais84] A. Aishima and Y. Fukushima. "Numerical study of an n-gallium arsenide diode distributed oscillator". *J. Appl. Phys.*, Vol. 56, No. 4, pp. 1086–1092, 1984.

[Alai] "Alain Mastrini personal website". http://aramis.obspm.fr/ maestrini/Work/Home.html.

[Alb98] J. Albrecht, R. Wang, P. Ruden, M. Farahmand, and K. Brennan. "Electron transport characteristics of GaN for high temperature device modeling". *J. Appl. Phys.*, Vol. 83, No. 9, pp. 4777–4781, May 1998.

[Ald08] B. Alderman, H. Sanghera, B. Thomas, D. Matheson, A. Maestrini, H. Wang, J. Treuttel, J. Siles, S. Davies, and T. Narhi. "Integrated Schottky Structures for Applications Above 100 GHz". In *European Microwave Integrated Circuit Conference (EuMIC)*, pp. 202–205, Oct. 2008.

[Ald11] B. Alderman, M. Henry, H. Sanghera, H. Wang, S. Rea, B. Ellison, and P. de Maagt. "Schottky diode technology at Rutherford Appleton Laboratory". In *IEEE International Conference on Microwave Technology Computational Electromagnetics (ICMTCE)*, pp. 4–6, May 2011.

[Ali14] N. Alijabbari, M. Bauwens, and R. Weikle. "160 GHz Balanced Frequency Quadruplers Based on Quasi-Vertical Schottky Varactors Integrated on Micromachined Silicon". *IEEE Trans. Terahertz Sci. Tech.*, Vol. 4, No. 6, pp. 678–685, Nov. 2014.

[Ali93a] W. Y. Ali-Ahmad, W. Bishop, T. Crowe, and G. Rebeiz. "An 86-106 GHz quasi-integrated low noise Schottky receiver". *IEEE Trans. Microw. Theory Techn.*, Vol. 41, No. 4, pp. 558–564, 1993.

[Ali93b] W. Ali-Ahmad. *Millimeter and submillimeter-wave integrated horn antenna Schottky receivers*. Tesis Doctoral, University of Michigan, 1993.

[Ali93c] W. Ali-Ahmad, W. Bishop, T. Crowe, and G. Rebeiz. "A submillimeter-wave planar low noise Schottky receiver". In *IEEE MTT-S Int. Microw. Symp. Dig.*, pp. 527–530 vol.2, 1993.

[Ali94] W. Y. Ali-Ahmad and G. Rebeiz. "A 335 GHz quasi-optical Schottky receiver". *IEEE Microw. Guided Wave Lett.*, Vol. 4, No. 2, pp. 37–39, 1994.

[Ali98] F. Alimenti, P. Ciampolini, P. Mezzanotte, L. Roselli, R. Sorrentino, and G. Stopponi. "Towards the global modeling of high frequency electronic circuits by using the lumped-element extension of FDTD method". In *Signals, Systems, and Electronics, 1998. ISSSE 98. 1998 URSI International Symposium on*, pp. 216–218, Sep 1998.

[Ant90] P. Antognetti and G. Massobrio. *Semiconductor device modeling with Spice*. McGraw-Hill, Inc., New York, NY, USA, 1990.

[Anw01] A. Anwar, S. Wu, and R. T. Webster. "Temperature dependent transport properties in GaN, $Al_xGa_{1-x}N$, and $In_xGa_{1-x}N$ semiconductors". *IEEE Trans. Electron Devices*, Vol. 48, No. 3, pp. 567–572, Mar. 2001.

[App07] R. Appleby and H. Wallace. "Standoff Detection of Weapons and Contraband in the 100 GHz to 1 THz Region". *IEEE Trans. Antennas Propag.*, Vol. 55, No. 11, pp. 2944–2956, Nov. 2007.

[Bar02] J. Barker, R. Akis, D. Ferry, S. Goodnick, T. Thornton, D. Koleske, A. Wickenden, and R. Henry. "High-field transport studies of GaN". *Physica B: Condensed Matter*, Vol. 314, pp. 39 – 41, 2002.

[Bar05] J. M. Barker, D. K. Ferry, D. D. Koleske, and R. J. Shul. "Bulk GaN and AlGaN/GaN heterostructure drift velocity measurements and comparison to theoretical models". *J. Appl. Phys.*, Vol. 97, No. 6, 2005.

[Bet42] H. Bethe. *Theory of the Boundary Layer of Crystal Rectifiers*. *Report (Massachusetts Institute of Technology. Radiation Laboratory)*, Radiation Laboratory, Massachusetts Institute of Technology, 1942.

[Bet96] A. Betz and R. Boreiko. "A Practical Schottky Mixer for 5 THz (Part II)". In *Proc. 7th Int. Symp. Space Terahertz Tech.*, p. 503, Mar. 1996.

[Bha92] K. Bhaumik, B. Gelmont, R. Mattauch, and M. Shur. "Series impedance of GaAs planar Schottky diodes operated to 500 GHz". *IEEE Trans. Microw. Theory Techn.*, Vol. 40, No. 5, pp. 880–885, 1992.

[Bha95] U. V. Bhapkar. *Monte Carlo Simulation of Gallium Arsenide Schottky Diodes for Terahertz Frequencies*. Tesis Doctoral, Virginia Univ., 1995.

[Bha97] U. V. Bhapkar and M. S. Shur. "Monte Carlo calculation of velocity-field characteristics of wurtzite GaN". *J. Appl. Phys.*, Vol. 82, No. 4, pp. 1649–1655, 1997.

[Bis93] W. L. Bishop, T. W. Crowe, and R. J. Mattauch. "Planar GaAs Schottky Diode Fabrication: Progress and Challenges". In *Proc. 4th Int. Symp. Space Terahertz Tech.*, Abr. 1993.

[Blo70] K. Bløtekjaer. "Transport equations for electrons in two-valley semiconductors". *IEEE Trans. Electron Devices*, Vol. 17, pp. 38–47, Jan. 1970.

[Bof60] A. Boff, J. Moll, and R. Shen. "A new high-speed effect in solid-state diodes". In *ISSCC Dig. Tech. Papers*, pp. 50 – 51, Feb. 1960.

[Bon01a] F. Bonani and G. Ghione. *Noise in Semiconductor Devices: Modeling and Simulation*. *Advanced Microelectronics*, Springer, 2001.

[Bon01b] F. Bonani, S. Guerrieri, G. Ghione, and M. Pirola. "A TCAD approach to the physics-based modeling of frequency conversion and noise in semiconductor devices under large-signal forced operation". *IEEE Trans. Electron Devices*, Vol. 48, No. 5, pp. 966–977, May 2001.

[Bon02] F. Bonani, S. Guerrieri, and G. Ghione. "Noise source modeling for cyclostationary noise analysis in large-signal device operation". *IEEE Trans. Electron Devices*, Vol. 49, No. 9, pp. 1640–1647, Sep. 2002.

[Bon03] F. Bonani, S. Guerrieri, and G. Ghione. "Physics-based simulation techniques for small- and large-signal device noise analysis in RF applications". *IEEE Trans. Electron Devices*, Vol. 50, No. 3, pp. 633–644, Mar 2003.

[Bou12] F. Boussaha, J. Kawamura, J. Stern, A. Skalare, and V. White. "A Low Noise 2.7 THz Waveguide-Based Superconducting Mixer". *IEEE Trans. Terahertz Sci. Tech.*, Vol. 2, No. 3, pp. 284–289, May 2012.

[Bro03] E. R. Brown. "THz generation by photomixing in ultrafast semiconductors". *Int. J. Hi. Spe. Ele. Syst.*, Vol. 13, pp. 497–545, 2003.

[Bro50] H. Brooks and C. Herring. "Scattering by ionized impurities in semiconductors". *Phys. Rev.*, Vol. 83, pp. 879–885, 1950.

[Bru01] J. Bruston, A. Maestrini, D. Pukala, S. Martin, B. Nakamura, and I. Mehdi. "A 1.2 THz Planar Tripler Using GaAs Membrane Based Chips". In *Proc. 12th Int. Symp. Space Terahertz Tech.*, p. 310, San Diego, California, Dic. 2001.

[Bru84] R. Brunetti and C. Jacoboni. "Analysis of the stationary and transient autocorrelation function in semiconductors". *Phys. Rev. B*, Vol. 29, No. 10, pp. 5739–5748, May 1984.

[Bry12] T. Bryllert, A. Malko, J. Vukusic, and J. Stake. "A 175 GHz HBV Frequency Quintupler With 60 mW Output Power". *IEEE Microw. Compon. Lett.*, Vol. 22, No. 2, pp. 76–78, Feb. 2012.

[Bur65] C. Burckhardt. "Analysis of Varactor Frequency Multipliers for Arbitrary Capacitance Variation and Drive Level". *Bell Syst. Tech. J.*, Vol. 44, No. 4, pp. 675–692, Apr. 1965.

[Cha02] G. Chattopadhyay, E. Schlecht, J. Gill, S. Martin, A. Maestrini, D. Pukala, F. Maiwald, and I. Mehdi. "A broadband 800 GHz Schottky balanced doubler". *IEEE Microw. Wireless Compon. Lett.*, Vol. 12, pp. 117–118, Apr. 2002.

[Cha03] G. Chattopadhyay, E. Schlecht, F. Maiwald, R. J. Dengler, J. C. Pearson, and I. Mehdi. "Frequency multiplier response to spurious signals and its effect on local oscillator systems in millimeter and submillimeter wavelengths". In *Millimeter and Submillimeter Detectors for Astronomy*, pp. 480–488, Feb. 2003.

[Cha04] G. Chattopadhyay, E. Schlecht, J. S. Ward, J. J. Gill, H. H. S. Javadi, F. Maiwald, and I. Mehdi. "An All-Solid-State Broad-Band Frequency Multiplier Chain at 1500 GHz". *IEEE Trans. Microw. Theory Techn.*, Vol. 52, pp. 1538–1547, May. 2004.

[Cha07] G. Chattopadhyay. "Sensor Technology at Submillimeter Wavelengths for Space Applications". In *Proc. 2nd International Conference on Sensor Technology*, Palmerston North, New Zealand, Nov. 2007.

[Cha08] G. Chattopadhyay. "Submillimeter-Wave Coherent and Incoherent Sensors for Space Applications". In *Sensors*, pp. 387–414, Springer Berlin Heidelberg, 2008.

[Cha11a] G. Chattopadhyay. "Technology, Capabilities, and Performance of Low Power Terahertz Sources". *IEEE Trans. THz Sci. Technol.*, Vol. 1, No. 1, pp. 33–53, Sep. 2011.

[Cha11b] G. Chattopadhyay, E. Schlecht, C. Lee, J. Gill, R. Lin, S. Sin, I. Mehdi, W. Deal, K. K. Loi, P. Nam, and B. Rodriguez. "670 GHz Schottky Diode Based Subharmonic Mixer with CPW Circuits and 70 GHz IF". In *Proc. 22rd Int. Symp. Space Terahertz Tech.*, Tucson, AZ, Apr. 2011.

[Cha64] K. S. Champlin, D. B. Armstrong, and P. D. Gunderson. "Charge carrier inertia in semiconductors". *Proc. IEEE*, Vol. 52, pp. 677–685, Jun. 1964.

[Cha78] K. Champlin and G. Eisenstein. "Cutoff Frequency of Submillimeter Schottky-Barrier Diodes". *IEEE Trans. Microw. Theory Techn.*, Vol. 26, pp. 31–34, Jan. 1978.

[Che88] M. Cheng and E. E. Kunhardt. "Electron energy distributions, transport parameters and rate coefficients in GaAs". *J. Appl. Phys.*, Vol. 63, 1988.

[Che92] D. Chen, E. Kan, U. Ravaioli, C.-W. Shu, and R. Dutton. "An improved energy transport model including nonparabolicity and non-Maxwellian distribution effects". *IEEE Electron Device Lett.*, Vol. 13, No. 1, pp. 26–28, Jan 1992.

[Cia96] P. Ciampolini, P. Mezzanotte, L. Roselli, and R. Sorrentino. "Accurate and efficient circuit simulation with lumped-element FDTD technique". *IEEE Trans. Microw. Theory Techn.*, Vol. 44, No. 12, pp. 2207–2215, Dec 1996.

[Cid03] A. Cidronali, G. Loglio, J. Jargon, K. Remley, D. DeGroot, D. Schreurs, K. Gupta, and G. Manes. "RF and IF mixer optimum matching impedances extracted by large-signal vectorial measurements". In *European Gallium Arsenide and Other Compound Semiconductors Application Symposium (GAAS)*, Munich, Germany, Oct. 2003.

[Coh75] M. Cohn, J. E. Degenford, and B. Newman. "Harmonic Mixing with an Antiparallel Diode Pair". *IEEE Trans. Microw. Theory Techn.*, Vol. 23, No. 8, pp. 667–673, 1975.

[Coj04a] O. Cojocari, B. Mottet, M. Rodriguez-Girones, S. Biber, L. Marchand, L.-P. Schmidt, and H. L. Hartnagel. "A new structural approach for uniform sub-micrometer anode metallization of planar THz Schottky components". *Semicond. Sci. Technol.*, Vol. 19, No. 3, p. 537, 2004.

[Coj04b] O. Cojocari, V. Popa, V. V. Ursaki, I. M. Tiginyanu, K. Mutamba, M. Saglam, and H. L. Hartnagel. "Micrometer-size GaN Schottky-diodes for mm-wave frequency multipliers". In *Proc. Joint 29th Int. Infrared Millimeter-Waves Conf. /12th Int. Terahertz Elect. Conf.*, pp. 317–318, 2004.

[Con50] E. Conweel and V. F. Weisskopft. "Theory of impurity scattering in semiconductors". *Phys. Rev*, Vol. 77, pp. 388–393, 1950.

[Cro05] T. W. Crowe, W. L. Bishop, D. W. Porterfield, J. L. Hesler, and I. Weikle, R. M. "Opening the terahertz window with integrated diode circuits". *IEEE J. Solid-State Circuits*, Vol. 40, pp. 2104–2110, Oct. 2005.

[Cro10] T. W. Crowe, J. L. Hesler, C. Pouzou, W. L. Bishop, and G. S. Schoenthal. "Development and Characterization of a 1.9 THz LO Source". In *Proc. 21th Int. Symp. Space Terahertz Tech.*, p. 472, Oxford, UK, Mar. 2010.

[Cro11] T. Crowe, J. Hesler, S. Retzloff, C. Pouzou, and G. Schoenthal. "Solid-State LO Sources for Greater than 2 THz". In *Proc. 22nd Int. Symp. Space Terahertz Tech.*, Tucson, Arizona, Apr. 2011.

[Cro66] C. Crowell and S. Sze. "Current transport in metal-semiconductor barriers". *Solid-State Electron.*, Vol. 9, No. 11Ű12, pp. 1035 – 1048, 1966.

[Cro86] T. Crowe and R. Mattauch. "Conversion Loss in GaAs Schottky-Barrier Mixer Diodes". *IEEE Trans. Microw. Theory Techn.*, Vol. 34, No. 7, pp. 753–760, Jul. 1986.

[Cro87] T. Crowe and R. Mattauch. "Analysis and Optimization of Millimeter-And Submillimeter-Wavelength Mixer Diodes". *IEEE Trans. Microw. Theory Techn.*, Vol. 35, No. 2, pp. 159–168, 1987.

[Cro89] T. W. Crowe. "GaAs Schottky barrier mixer diodes for the frequency range 1-10 THz". *Int. J. Infrared Millimeter Waves*, Vol. 10, No. 7, pp. 765–777, Jul. 1989.

[Cro92] T. Crowe, R. Mattauch, H. Roser, W. Bishop, W. Peatman, and X. Liu. "GaAs Schottky diodes for THz mixing applications". *Proc. IEEE*, Vol. 80, pp. 1827–1841, Nov. 1992.

[Cro93] T. Crowe, W. Peatman, R. Zimmermann, and R. Zimmermann. "Consideration of velocity saturation in the design of GaAs varactor diodes". *IEEE Microw. Guided Wave Lett.*, Vol. 3, pp. 161–163, Jun. 1993.

[Dic67] L. Dickens. "Spreading Resistance as a Function of Frequency". *IEEE Trans. Microw. Theory Techn.*, Vol. 15, No. 2, pp. 101–109, 1967.

[Doy09] D. Doyle, G. Pilbratt, and J. Tauber. "The Herschel and Planck Space Telescopes". *Proc. IEEE*, Vol. 97, No. 8, pp. 1403–1411, Aug. 2009.

[Dra13] V. Drakinskiy, P. Sobis, H. Zhao, T. Bryllert, and J. Stake. "Terahertz GaAs Schottky diode mixer and multiplier MIC's based on e-beam technology". In *Int. Conf. on Indium Phosphide and Related Mater. (IPRM)*, pp. 1–2, 2013.

[Eas95] J. East. "Monte Carlo simulation of Schottky barrier mixers and varactors". In *Proc. 6th Int. Symp. Space Terahertz Tech.*, Pasadena, California, Mar. 1995.

[Eri01] N. R. Erickson, G. Narayanan, R. M. Grosslein, S. Martin, P. Smith, I. Mehdi, M. Coulomb, and G. Demartinez. "Monolithic THz Frequency Multipliers". In *Proc. 12th Int. Symp. Space Terahertz Tech.*, p. 297, San Diego, California, Feb. 2001.

[Eri02] N. Erickson, G. Narayanan, R. Grosslein, A. G. Chattopadhyay, A. Maestrini, E. Schlecht, I. Mehdi, and S. Martin. "1500 GHz Tunable Source Using Cascaded Planar Frequency Doublers". In *Proc. 13th Int. Symp. Space Terahertz Tech.*, p. 177, Cambridge, Massachusetts, Mar. 2002.

[Eri08] N. R. Erickson. "A Schottky-Diode Balanced Mixer for 1.5 THz". In *Proc. 19th Int. Symp. Space Terahertz Tech.*, 2008.

[Eri10] N. R. Erickson and T. M. Goyette. "TeraHertz Schottky-Diode Balanced Mixers". In *Proc. 21st Int. Symp. Space Terahertz Tech.*, 2010.

[Eri98] N. R. Erickson. "Diode frequency multipliers for THz local oscillator applications". In *Proc. SPIE*, pp. 75–84, Kona, Hawaii, Jul. 1998.

[Fab85] M. Faber, J. Archer, and R. Mattauch. "A High Efficiency Frequency Doubler for 100 GHz". In *IEEE MTT-S Int. Microw. Symp. Dig.*, pp. 363–365, 1985.

[Fab95] M. Faber, J. Chramiec, and M. Adamski. *Microwave and millimeter-wave diode frequency multipliers*. Artech House, 1995.

[Far01] M. Farahmand, C. Garetto, E. Bellotti, K. F. Brennan, M. Goano, E. Ghillino, G. Ghione, J. Albrecht, and P. P. Ruden. "Monte Carlo simulation of electron transport in the III-nitride wurtzite phase materials system: binaries and ternaries". *IEEE Trans. Electron Devices*, Vol. 48, No. 3, pp. 535–542, 2001.

[Fis88] M. V. Fischetti and S. E. Laux. "Monte Carlo analysis of electron transport in small semiconductor devices including band-structure and space-charge effects". *Phys. Rev. B*, Vol. 38, No. 14, pp. 9721–9745, Nov. 1988.

[Fou99] B. E. Foutz, S. K. OLeary, M. Shur, and L. F. Eastman. "Transient electron transport in wurtzite GaN, InN, and AlN". *J. Appl. Phys.*, Vol. 85, No. 11, pp. 7727–7734, 1999.

[Fue98] J. G. de la Fuente. *Modelado físico de dispositivos basados en heteroestructuras para aplicaciones de radiofrecuencia*. Tesis Doctoral, Escuela Técnica Superior de Ingenieros de Telecomunicación (Universidad Politécnica de Madrid), 1998.

[Gao07] J. Gao, M. Hajenius, Z. Q. Yang, J. J. A. Baselmans, P. Khosropanah, R. Barends, and T. Klapwijk. "Terahertz Superconducting Hot Electron Bolometer Heterodyne Receivers". *IEEE Trans. Appl. Supercond.*, Vol. 17, No. 2, pp. 252–258, Jun. 2007.

[Gar88] W. Gardner. "Signal interception: a unifying theoretical framework for feature detection". *IEEE Trans. Commun.*, Vol. 36, No. 8, pp. 897–906, Aug. 1988.

[Gar91] D. Garfield, R. Mattauch, and S. Weinreb. "RF performance of a novel planar millimeter-wave diode incorporating an etched surface channel". *IEEE Trans. Microw. Theory Techn.*, Vol. 39, No. 1, pp. 1–5, 1991.

[Gat91] I. R. Gatland. "Theory of a nonharmonic oscillator". *Am. J. Phys.*, Vol. 59, No. 2, pp. 155–158, 1991.

[Gau95] G. Gauthier, W. Ali-Ahmad, T. Budka, D. Filipovic, and G. Rebeiz. "A uniplanar 90-GHz Schottky-diode millimeter-wave receiver". *IEEE Trans. Microw. Theory Techn.*, Vol. 43, No. 7, pp. 1669–1672, 1995.

[Gea93] S. Gearhart, J. Hesler, W. Bishop, T. Crowe, and G. Rebeiz. "A wide-band 760-GHz planar integrated Schottky receiver". *IEEE Microw. Guided Wave Lett.*, Vol. 3, No. 7, pp. 205–207, 1993.

[Gea94] S. Gearhart and G. Rebeiz. "A monolithic 250 GHz Schottky-diode receiver". *IEEE Trans. Microw. Theory Techn.*, Vol. 42, No. 12, pp. 2504–2511, 1994.

[Gel98] B. Gelmont, D. Woolard, J. Hesler, and T. Crowe. "A degenerately-doped GaAs Schottky diode model applicable for terahertz frequency regime operation". *IEEE Trans. Electron Devices*, Vol. 45, pp. 2521–2527, Dec. 1998.

[Gis89] J. Gismero. *Análisis y diseño de osciladores de microondas mediante la técnica de balance armónico*. Tesis Doctoral, Escuela Técnica Superior de Ingenieros de Telecomunicación (Universidad Politécnica de Madrid), 1989.

[Goa00a] M. Goano, E. Bellotti, E. Ghillino, C. Garetto, G. Ghione, and K. F. Brennan. "Band structure nonlocal pseudopotential calculation of the III-nitride wurtzite phase materials system. Part II. Ternary alloys $Al_xGa_{1-x}N$, $In_xGa_{1-x}N$, and $In_xAl_{1-x}N$". *J. Appl. Phys.*, Vol. 88, No. 11, pp. 6476–6482, 2000.

[Goa00b] M. Goano, E. Bellotti, E. Ghillino, G. Ghione, and K. F. Brennan. "Band structure nonlocal pseudopotential calculation of the III-nitride wurtzite phase materials system. Part I. Binary compounds GaN, AlN, and InN". *J. Appl. Phys.*, Vol. 88, No. 11, pp. 6467–6475, 2000.

[Gon91] T. González, J. E. Velázquez, P. M. Gutiérrez, and D. Pardo. "Five-valley model for the study of electron transport properties at very high electric fields in GaAs". *Semicond. Sci. Technol.*, Vol. 6, No. 9, Sep. 1991.

[Gon93a] T. González and D. Pardo. "Ensemble Monte Carlo with Poisson solver for the study of current fluctuations in homogeneous GaAs structures". *J. Appl. Phys.*, Vol. 73, No. 11, pp. 7453–7464, 1993.

[Gon93b] T. Gonzalez, D. Pardo, L. Varani, and L. Reggiani. "The microscopic interpretation of electron noise in Schottky-barrier diodes". In *Proc. 23rd European Solid State Device Research Conf. ESSDERC '93*, pp. 115–118, 1993.

[Gon93c] T. Gonzalez, D. Pardo, L. Varani, and L. Reggiani. "Monte Carlo analysis of noise spectra in Schottky-barrier diodes". *Appl. Phys. Lett.*, Vol. 63, No. 22, pp. 3040–3042, 1993.

[Gon96] T. González and D. Pardo. "Physical models of ohmic contact for Monte Carlo device simulation". *Solid-State Electron.*, Vol. 39, No. 4, pp. 555 – 562, 1996.

[Gon97] T. González, D. Pardo, L. Reggiani, and L. Varani. "Microscopic analysis of electron noise in GaAs Schottky barrier diodes". *J. Appl. Phys.*, Vol. 82, No. 5, pp. 2349–2358, 1997.

[Gra00] J. Grajal, V. Krozer, E. Gonzalez, F. Maldonado, and J. Gismero. "Modeling and design aspects of millimeter-wave and submillimeter-wave Schottky diode varactor frequency multipliers". *IEEE Trans. Microw. Theory Techn.*, Vol. 48, pp. 700–711, Apr. 2000.

[Gra10] T. de Graauw *et al.* "The Herschel-Heterodyne Instrument for the Far-Infrared (HIFI)". *Astron. Astrophys.*, Vol. 518, Jul. 2010.

[Gro84] R. Grondin, P. Blakey, and J. East. "Effects of transient carrier transport in millimeter-wave GaAs diodes". *IEEE Trans. Electron Devices*, Vol. 31, pp. 21–28, Jan. 1984.

[Gru93a] V. Gruzinskis, E. Starikov, and P. Shiktorov. "Conservation equations for hot carriers - I. Transport models". *Solid-State Electron.*, Vol. 36, No. 7, pp. 1055 – 1066, 1993.

[Gru93b] V. Gruzinskis, E. Starikov, and P. Shiktorov. "Conservation equations for hot carriers - II. Dynamic features". *Solid-State Electron.*, Vol. 36, No. 7, pp. 1067 – 1075, 1993.

[Gru93c] V. Gruzinskis, E. Starikov, P. Shiktorov, L. Reggiani, M. Saraniti, and L. Varani. "Hydrodynamic analysis of DC and AC hot-carrier transport in semiconductors". *Semicond. Sci. Technol.*, Vol. 8, No. 7, p. 1283, 1993.

[Gru94a] A. Grub, V. Krozer, A. Simon, and H. L. Hartnagel. "Design Optimization of Schottky Barrier Diodes at THz Frequencies". In *Proc. 5th Int. Symp. Space Terahertz Tech.*, Ann Arbor, Michigan, May 1994.

[Gru94b] V. Gruzinskis, E. Starikov, and P. Shiktorov. "Monte Carlo simulation of hot carrier noise in short n + nn + diodes". *Physica Scripta*, Vol. 1994, No. T54, p. 146, 1994.

[Gru94c] V. Gruzinskis, E. Starikov, P. Shiktorov, L. Reggiani, and L. Varani. "Hydrodynamic approach to noise spectra in unipolar semiconductor structures". *Appl. Phys. Lett.*, Vol. 64, No. 13, pp. 1662–1664, Mar. 1994.

[Han75] P. H. Handel. "1/f noise- An infrared phenomenon". *Phys. Rev. Lett.*, Vol. 34, 1975.

[Heg85] G. Hegazi, A. Jelenski, and K. Yngvesson. "Limitations of Microwave and Millimeter-Wave Mixers Due to Excess Noise". *IEEE Trans. Microw. Theory Techn.*, Vol. 33, No. 12, pp. 1404–1409, 1985.

[Hel07] E. H. Hellen and M. J. Lanctot. "Nonlinear damping of the LC circuit using antiparallel diodes". *Am. J. Phys.*, Vol. 75, No. 4, pp. 326–330, 2007.

[Hel78a] D. Held and A. Kerr. "Conversion Loss and Noise of Microwave and Millimeterwave Mixers: Part 1–Theory". *IEEE Trans. Microw. Theory Techn.*, Vol. 26, pp. 49–55, Feb. 1978.

[Hel78b] D. Held and A. Kerr. "Conversion Loss and Noise of Microwave and Millimeterwave Mixers: Part 2–Experiment". *IEEE Trans. Microw. Theory Techn.*, Vol. 26, No. 2, pp. 55–61, Feb. 1978.

[Hen10] M. Henry, B. Alderman, B. Moyna, S. Rea, H. Sanghera, and D. Matheson. "High performance component development at RAL for the ISMAR Instrument". In *Proc. 21st Int. Symp. Space Terahertz Tech.*, p. 302, Oxford, UK, Mar. 2010.

[Hes96] J. L. Hesler. *Planar Schottky Diodes In Submillimeter-Wavelength Waveguide Receivers*. Tesis Doctoral, Universtiy of Virginia, Jan. 1996.

[Hes97] J. Hesler, W. Hall, T. Crowe, R. Weikle, B. S. Deaver, R. Bradley, and S.-K. Pan. "Fixed-tuned submillimeter wavelength waveguide mixers using planar Schottky-barrier diodes". *IEEE Trans. Microw. Theory Techn.*, Vol. 45, No. 5, pp. 653–658, 1997.

[Hes98] J. L. Hesler and B. L. Gelmont. "A Discussion of Power Coupling Bandwidth Limitations of Planar Schottky Diodes at Submillimeter Wavelengths". In *Proc. 9th Int. Symp. Space Terahertz Tech.*, p. 173, Pasadena, California, Mar. 1998.

[Hes99] J. Hesler, K. Hui, S. He, and T. W. Crowe. "A Fixed-Tuned 400 GHz Subharmonic Mixer Using Planar Schottky Diodes". In *Proc. 10th Int. Symp. Space Terahertz Tech.*, Charlottesville, Virginia, Mar. 1999.

[Hje90] H. Hjelmgren. "Numerical modeling of hot electrons in n-GaAs Schottky-barrier diodes". *IEEE Trans. Electron Devices*, Vol. 37, No. 5, pp. 1228–1234, May 1990.

[Hje91] H. Hjelmgren, E. Kollberg, and L. Lundgren. "Numerical simulations of the capacitance of forward-biased Schottky-diodes". *Solid-State Electron.*, Vol. 34, No. 6, pp. 587 – 590, 1991.

[Hje94] H. Hjelmgren and T. W. Tang. "Thermionic emission in a hydrodynamic model for heterojunction structures". *Solid-State Electron.*, Vol. 37, No. 9, pp. 1649–1657, 1994.

[Hoc88] R. W. Hockney and J. W. Eastwood. *Computer simulation using particles*. IOP, 1988.

[Hoo76] F. Hooge. "1/f noise". *Physica B+C*, Vol. 83, No. 1, pp. 14 – 23, 1976.

[Hui00] K. Hui, J. Hesler, D. Kurtz, W. Bishop, and T. Crowe. "A micromachined 585 GHz Schottky mixer". *IEEE Microw. Guided Wave Lett.*, Vol. 10, No. 9, pp. 374–376, 2000.

[Jac06] B. Jackson, G. de Lange, T. Zijlstra, M. Kroug, J. Kooi, J. Stern, and T. Klapwijk. "Low-noise 0.8-0.96- and 0.96-1.12-THz superconductor-insulator-superconductor mixers for the Herschel Space Observatory". *IEEE Trans. Microw. Theory Techn.*, Vol. 54, No. 2, pp. 547–558, Feb. 2006.

[Jac83] C. Jacoboni and L. Reggiani. "The Monte Carlo method for the solution of charge transport in semiconductor with applications to covalent materials". *Rev. Mod. Phys.*, Vol. 55, p. 645, 1983.

[Jac89a] C. Jacoboni and P. Lugli. *The Monte Carlo Method for Semiconductor Device Simulation*. Springer-Verlag, New York, 1989.

[Jac89b] C. Jacoboni and P. Lugli. *The Monte Carlo method for semiconductor device simulation*. Springer- Verlag, 1989.

[Jel84] A. Jelenski, M. V. Schneider, A. Y. Cho, E. R. Kollberg, and H. Zirath. "Noise Measurements and Noise Mechanisms in Microwave Mixer Diodes". In *IEEE MTT-S Int. Microwave Symp. Digest*, 1984.

[Jin10] C. Jin, D. Pavlidis, and L. Considine. "A novel GaN-based high frequency varactor diode". In *European Microwave Integrated Circuits Conference (EuMIC)*, pp. 118–121, 2010.

[Jin13] C. Jin, M. Zaknoune, D. Ducatteau, and D. Pavlidis. "E-beam Fabricated GaN Schottky diode: High-frequency and non-linear properties". In *IEEE MTT-S Int. Microwave Symp. Digest*, pp. 1–4, June 2013.

[Jon95] J. R. Jones, S. H. Jones, and G. B. Tait. "Self Consistent Physics-Based Numerical Device and Harmonic Balance Circuit Analysis of Heterostructure Barrier and Schottky Barrier Varactors Including Thermal Effects". In *Proc. 6th Int. Symp. Space Terahertz Tech.*, Pasadena, California, Mar. 1995.

[Jos95] R. P. Joshi and D. K. Ferry. "Calculations of the temperature and field dependent electronic mobility in β-SiC". *Solid-State Electron.*, Vol. 38, No. 11, pp. 1911–1916, Nov. 1995.

[Jun08] C. Jung, H. Wang, A. Maestrini, and Y. Jin. "Fabrication of GaAs Schottky Nano-diodes with T-Anodes for Submillimeter Wave Mixers". In *Proc. 19th Int. Symp. Space Terahertz Tech.*, Groningen, The Netherlands, Apr. 2008.

[Kal13] G. Kalita, R. Hirano, M. E. Ayhan, and M. Tanemura. "Fabrication of a Schottky junction diode with direct growth graphene on silicon by a solid phase reaction". *J. Phys. D: Appl. Phys.*, Vol. 46, No. 45, p. 455103, 2013.

[Kar07] A. Karpov, D. Miller, J. A. Stern, B. Bumble, H. G. LeDuc, and J. Zmuidzinas. "Development of 1 THz SIS mixer for SOFIA". In *Proc. 18th Int. Symp. Space Terahertz Tech.*, 2007.

[Kar09] A. Karpov, D. Miller, J. Stern, B. Bumble, H. LeDuc, and J. Zmuidzinas. "Development of Low Noise THz SIS Mixer Using an Array of Nb/Al-AlN/NbTiN Junctions". *IEEE Trans. Appl. Supercond.*, Vol. 19, No. 3, pp. 305–308, Jun. 2009.

[Kee83] N. J. Keen and H. Zirath. "Hot-electron noise generation in gallium-arsenide Schottky-barrier diodes". *Electron. Lett.*, Vol. 19, pp. 853–854, 1983.

[Kel79] W. Kelly and G. Wrixon. "Conversion Losses in Schottky-Barrier Diode Mixers in the Submillimeter Region". *IEEE Trans. Microw. Theory Techn.*, Vol. 27, pp. 665–672, Jul. 1979.

[Ker75] A. Kerr. "A Technique for Determining the Local Oscillator Waveforms in a Microwave Mixer (Short Papers)". *IEEE Trans. Microw. Theory Techn.*, Vol. 23, pp. 828–831, Oct. 1975.

[Ker79a] A. Kerr. "Noise and Loss in Balanced and Subharmonically Pumped Mixers: Part I–Theory". *IEEE Trans. Microw. Theory Techn.*, Vol. 27, No. 12, pp. 938–943, Dec. 1979.

[Ker79b] A. Kerr. "Noise and Loss in Balanced and Subharmonically Pumped Mixers: Part II–Application". *IEEE Trans. Microw. Theory Techn.*, Vol. 27, No. 12, pp. 944–950, Dec. 1979.

[Kho08] P. Khosropanah, W. Zhang, J. N. Hovenier, J. R. Gao, T. M. Klapwijk, M. I. Amanti, G. Scalari, and J. Faist. "3.4 THz heterodyne receiver using a hot electron bolometer and a distributed feedback quantum cascade laser". *J. Appl. Phys.*, Vol. 104, No. 11, 2008.

[Kin07] M. Kintis, X. Lan, F. Fong, D. Sawdai, K. Loi, K. Kono, and A. Gutierrez. "An MMIC Pulse Generator Using Dual Nonlinear Transmission Lines". *IEEE Microw. Wirel. Compon. Lett.*, Vol. 17, No. 6, pp. 454 –456, Jun. 2007.

[Kol92] E. Kolberg, T. Tolmunen, M. Frerking, and J. East. "Current saturation in submillimeter-wave varactors". *IEEE Trans. Microw. Theory Techn*, Vol. 40, pp. 831–838, May 1992.

[Kom00] S. Komiyama, O. Astafiev, V. Antonov, T. Kutsuwa, and H. Hirai. "A single-photon detector in the far-infrared range". *Nature*, Vol. 403, No. 6768, pp. 405–407, Ene. 2000.

[Koo14] J. Kooi, R. Chamberlin, R. Monje, A. Kovacs, F. Rice, H. Yoshida, B. Force, K. Cooper, D. Miller, M. Gould, D. Lis, B. Bumble, R. LeDuc, J. Stern, and T. Phillips. "Performance of the Caltech Submillimeter Observatory Dual-Color 180-720 GHz Balanced SIS Receivers". *IEEE Trans. Terahertz Sci. Tech.*, Vol. 4, No. 2, pp. 149–164, Mar. 2014.

[Kro97] V. Krozer. "Material parameters of InGaAs". Technical report, TU Chemnitz,, 1997. internal report (available at request).

[Kum05] J. Kumagal. "Space mountain [submillimeter radio telescopes]". *IEEE Spectr.*, Vol. 42, No. 12, pp. 12–14, Dec. 2005.

[Kun88] K. Kundert, G. Sorkin, and A. Sangiovanni-Vincentelli. "Applying harmonic balance to almost-periodic circuits". *IEEE Trans. Microw. Theory Techn.*, Vol. 36, No. 2, pp. 366–378, Feb. 1988.

[Lab06] P. P. Labs. "A new breed of comb generators featuring low phase noise and low input power". *Microw. J.*, Vol. 49, No. 5, pp. 278–280, 2006.

[Lee07] A. W. M. Lee, Q. Qin, S. Kumar, B. S. Williams, Q. Hu, and J. L. Reno. "High-power and high-temperature THz quantum-cascade lasers based on lens-coupled metal-metal waveguides". *Opt. Lett.*, Vol. 32, No. 19, pp. 2840–2842, Oct. 2007.

[Lee94] T.-H. Lee, C.-Y. Chi, J. East, G. Rebeiz, and G. Haddad. "A novel biased anti-parallel Schottky diode structure for subharmonic mixing". *IEEE Microw. Guided Wave Lett.*, Vol. 4, No. 10, pp. 341–343, 1994.

[Lee99] C. Lee, B. Gelmont, D. Woolard, and C. Fazi. "A Modified Harmonic-Balance Analysis of Schottky Diode Multipliers Based Upon a Hydrodynamic Transport Model". In *Proc. 10th Int. Symp. Space Terahertz Tech.*, p. 312, Charlottesville, Virginia, Mar. 1999.

[Leu07] G. Leuzzi and V. Stornelli. "Global Modeling Analysis of HEMTs by the Spectral Balance Technique". *IEEE Trans. Microw. Theory Techn.*, Vol. 55, No. 6, pp. 1405–1412, Jun. 2007.

[Lev01] M. Levinshtein, S. Rumyantsev, and M. Shur. *Properties of Advanced Semiconductor Materials: GaN, AIN, InN, BN, SiC, SiGe. A Wiley-Interscience publication*, Wiley, 2001.

[Lin10] M. Lin, Y. Zhang, and Z. Zhang. "Design and characterization of SRD-based comb generator". In *CPEM*, pp. 728 –729, Jun. 2010.

[Lin14] J.-H. Lin, J.-J. Zeng, and Y.-J. Lin. "Electronic transport for graphene/n-type Si Schottky diodes with and without H_2O_2 treatment". *Thin Solid Films*, Vol. 550, No. 0, pp. 582 – 586, 2014.

[Lin98] C.-I. Lin, A. Simon, M. Rodriguez-Girones, H. Hartnagel, P. Zimmermann, R. Zimmermann, and R. Henneberger. "Planar Schottky diodes for submillimeter wave applications". In *Proc. IEEE 6th International Conference on Terahertz Electronics*, pp. 135–138, Sep. 1998.

[Lip97] R. Lipsey, S. Jones, J. Jones, T. Crowe, L. Horvath, U. Bhapkar, and R. Mattauch. "Monte Carlo harmonic-balance and drift-diffusion harmonic-balance analyses of 100-600 GHz Schottky barrier varactor frequency multipliers". *IEEE Trans. Electron Devices*, Vol. 44, pp. 1843–1850, Nov. 1997.

[Lip98] R. Lipsey and S. Jones. "Accurate design equations for 50-600 GHz GaAs Schottky diode varactor frequency doublers". *IEEE Trans. Electron Devices*, Vol. 45, pp. 1876–1882, Sep. 1998.

[Lun00] M. Lundstrom. *Fundamentals of Carrier Transport*. Cambridge University Press, Cambridge, U.K., 2nd Ed., 2000.

[Maa05] S. Maas. *Noise in linear and nonlinear circuits*. *Artech House microwave library*, Artech House, 2005.

[Maa88] S. Maas. *Nonlinear microwave circuits*. *The Artech House microwave library*, Artech House, Incorporated, 1988.

[Maa93] S. Maas. *Microwave mixers*. Artech House, Boston, MA, 2nd Ed., 1993.

[Mad04] O. Madelung. *Semiconductors: Data Handbook*. Springer, Berlin, 2004.

[Mae01] A. Maestrini, J. Bruston, D. Pukala, S. Martin, and I. Mehdi. "Performance of a 1.2 THz frequency tripler using a GaAs frameless membrane monolithic circuit". In *IEEE MTT-S Int. Microw. Symp. Dig.*, pp. 1657–1660, Phoenix, AZ, May 2001.

[Mae03] A. Maestrini, J. Ward, J. Gill, G. Chattopadhyay, F. Maiwald, K. Ellis, H. Javadi, and I. Mehdi. "A planar-diode frequency tripler at 1.9 THz". In *IEEE MTT-S Int. Microw. Symp. Dig.*, pp. 747–750, Philadelphia, PA, Jun. 2003.

[Mae04] A. Maestrini, J. Ward, J. Gill, H. Javadi, E. Schlecht, G. Chattopadhyay, F. Maiwald, N. Erickson, and I. Mehdi. "A 1.7-1.9 THz local oscillator source". *IEEE Microw. Wireless Compon. Lett.*, Vol. 14, pp. 253–255, Jun. 2004.

[Mae05a] A. Maestrini, C. Tripon-Canseliet, J. S. Ward, H. Javadi, J. Gill, G. Chattopadhyay, E. Schlecht, and I. Mehdi. "Multi-anode frequency triplers at sub-millimeter wavelengths". In *Proc. 16th Int. Symp. Space Terahertz Tech.*, Pasadena, CA, May 2005.

[Mae05b] A. Maestrini, J. Ward, J. Gill, H. Javadi, E. Schlecht, C. Tripon-Canseliet, G. Chattopadhyay, and I. Mehdi. "A 540-640-GHz high-efficiency four-anode frequency tripler". *IEEE Trans. Microw. Theory Techn.*, Vol. 53, pp. 2835–2843, Sep. 2005.

[Mae05c] A. Maestrini, J. Ward, H. Javadi, C. Tripon-Canseliet, J. Gill, G. Chattopadhyay, E. Schlecht, and I. Mehdi. "Local oscillator chain for 1.55 to 1.75 THz with 100-μW peak power". *IEEE Microw. Wireless Compon. Lett.*, Vol. 15, pp. 871–873, Dec. 2005.

[Mae06] A. Maestrini, C. Tripon-Canseliet, J. S. Ward, J. J. Gill, and I. Mehdi. "A High Efficiency Multiple-Anode 260-340 GHz Frequency Tripler". In *Proc. 17th Int. Symp. Space Terahertz Tech.*, Paris, France, May 2006.

[Mae08] A. Maestrini, J. Ward, C. Tripon-Canseliet, J. Gill, C. Lee, H. Javadi, G. Chattopadhyay, and I. Mehdi. "In-Phase Power-Combined Frequency Tripler at 300 GHz". *IEEE Microw. Wireless Compon. Lett.*, Vol. 18, pp. 218–220, Mar. 2008.

[Mae10a] A. Maestrini, J. Ward, J. Gill, C. Lee, B. Thomas, R. Lin, G. Chattopadhyay, and I. Mehdi. "A Frequency-Multiplied Source With More Than 1 mW of Power Across the 840-900 GHz Band". *IEEE Trans. Microw. Theory Techn.*, Vol. 58, pp. 1925–1932, Jul. 2010.

[Mae10b] A. Maestrini, B. Thomas, H. Wang, C. Jung, J. Treuttel, Y. Jin, G. Chattopadhyay, I. Mehdi, and G. Beaudin. "Schottky diode-based terahertz frequency multipliers and mixers". *C. R. Phys.*, Vol. 11, No. 7-8, pp. 480–495, 2010.

[Mae11] A. Maestrini, I. Mehdi, R. Lin, J. V. Siles, C. Lee, J. Gill, G. Chattopadhyay, E. Schlecht, B. Thomas, and J. Ward. "A 2.5-2.7 THz Room Temperature Electronic Source". In *Proc. 22nd Int. Symp. Space Terahertz Tech.*, Tucson, Arizona, Apr. 2011.

[Mae12] A. Maestrini, I. Mehdi, J. Siles, J. Ward, R. Lin, B. Thomas, C. Lee, J. Gill, G. Chattopadhyay, E. Schlecht, J. Pearson, and P. Siegel. "Design and Characterization of a Room Temperature All-Solid-State Electronic Source Tunable From 2.48 to 2.75 THz". *IEEE Trans. THz Sci. Technol.*, Vol. 2, pp. 177–185, Mar. 2012.

[Mai01a] F. Maiwald, S. Martin, J. Bruston, A. Maestrini, T. Crawford, and P. H. Siegel. "Design and Performance of A 2.7 THz Waveguide Tripler". In *Proc. 12th Int. Symp. Space Terahertz Tech.*, p. 320, San Diego, California, Feb. 2001.

[Mai01b] F. Maiwald, S. Martin, J. Bruston, A. Maestrini, T. Crawford, and P. Siegel. "2.7 THz waveguide tripler using monolithic membrane diodes". In *IEEE MTT-S Int. Microw. Symp. Dig.,*, pp. 1637–1640, Phoenix, AZ, May 2001.

[Mai02] F. Maiwald, E. Schlecht, G. Chattopadhyay, A. Maestrini, and J. Gill. "Planar GaAs Schottky diode frequency multiplier chains up to 3 THz". Technical report, Institute of Microwave Engineering, Darmstadt, Germany, May 2002.

[Mai03] F. Maiwald, E. Schlecht, A. Maestrini, G. Chattopadhyay, J. C. Pearson, D. Pukala, and I. Mehdi. "THz frequency multiplier chains based on planar Schottky diodes". In *Proc. SPIE*, pp. 447–458, Feb. 2003.

[Mal12] A. Malko, T. Bryllert, J. Vukusic, and J. Stake. "High efficiency and broad-band operation of monolithically integrated W-Band HBV frequency tripler". In *Int. Conf. on Indium Phosphide and Related Mater. (IPRM)*, pp. 92–94, Aug. 2012.

[Mal13] A. Malko, T. Bryllert, J. Vukusic, and J. Stake. "Silicon Integrated InGaAs/InAlAs/AlAs HBV Frequency Tripler". *IEEE Electron Device Lett.*, Vol. 34, No. 7, pp. 843–845, Jul. 2013.

[Man56] J. Manley and H. Rowe. "Some General Properties of Nonlinear Elements-Part I. General Energy Relations". *Proc. IRE*, Vol. 44, No. 7, pp. 904 –913, Jul. 1956.

[Man91] N. S. Mansour, K. Diff, and K. F. Brennan. "Ensemble Monte Carlo study of electron transport in degenerate bulk GaAs". *J. Appl. Phys.*, Vol. 70, No. 11, pp. 6854–6859, Dec. 1991.

[Mar00] S. Marazita, W. Bishop, J. Hesler, K. Hui, W. Bowen, and T. Crowe. "Integrated GaAs Schottky mixers by spin-on-dielectric wafer bonding". *IEEE Trans. Electron Devices*, Vol. 47, No. 6, pp. 1152–1157, 2000.

[Mar01] S. Martin, B. Nakamura, A. Fung, P. Smith, J. Bruston, A. Maestrini, F. Maiwald, P. Siegel, E. Schlecht, and I. Mehdi. "Fabrication of 200 to 2700 GHz multiplier devices using GaAs and metal membranes". In *IEEE MTT-S Int. Microw. Symp. Dig.*, pp. 1641–1644 vol.3, May 2001.

[Mat00] J. Mateos, T. González, D. Pardo, V. Hoel, H. Happy, and A. Cappy. "Improved Monte Carlo algorithm for the simulation of δ-doped AlInAs/GaInAs HEMTs". *IEEE Trans. Electron Devices*, Vol. 47, No. 1, pp. 250–253, Jan 2000.

[Mat07] J. Mateos, S. Pérez, I. Íniguez-de-la Torre, D. Pardo, and T. González. "Monte Carlo simulation of AlGaN/GaN heterostructures". In *Spanish Conference on Electron Devices*, pp. 84–87, 2007.

[Mat77] R. J. Mattauch and F. S. Fei. "Local-oscillator-induced noise in GaAs Schottky mixer diodes". *Electron. Lett.*, Vol. 13, pp. 22–23, 1977.

[Maz87] C. Maziar and M. Lundstrom. "Monte Carlo simulation of GaAs Schottky barrier behaviour". *Electron. Lett.*, Vol. 23, No. 2, pp. 61–62, Jan. 1987.

[McA87] C. C. McAndrew, E. L. Heasell, and K. Singhal. "A comprehensive transport model for semiconductor device simulation". *Semicond. Sci. Technol.*, Vol. 2, No. 10, p. 643, 1987.

[Meh98] I. Mehdi, P. Siegel, D. A. Humphrey, T.-H. Lee, R. Dengler, J. E. Oswald, A. Pease, R. Lin, H. Eisele, R. Zimmermann, and N. Erickson. "An all solid-state 640 GHz subharmonic mixer". In *IEEE MTT-S Int. Microw. Symp. Dig.*, pp. 403–406, 1998.

[Mes57] G. Messenger and C. T. McCoy. "Theory and Operation of Crystal Diodes as Mixers". *Proc. IRE*, Vol. 45, No. 9, pp. 1269–1283, Sep. 1957.

[Mol62] J. Moll, S. Krakauer, and R. Shen. "P-N Junction Charge-Storage Diodes". *Proc. IRE*, Vol. 50, No. 1, pp. 43 –53, Jan. 1962.

[New91] T. Newman and K. Ng. "A submillimeter-wave planar diode mixer-design and evaluation". In *IEEE MTT-S Int. Microw. Symp. Dig.*, pp. 1293–1296, 1991.

[New99] T. Newman and N. Erickson. "A planar varactor array multiplier chain to 300 GHz". In *IEEE MTT-S Int. Microw. Symp. Dig.*, pp. 135–138, Anaheim, CA, Jun. 1999.

[Ng98] H. M. Ng, D. Doppalapudi, T. D. Moustakas, N. G. Weimann, and L. F. Eastman. "The role of dislocation scattering in n-type GaN films". *Appl. Phys. Lett.*, Vol. 73, No. 6, pp. 821–823, 1998.

[Nou94] J.-P. Nougier. "Fluctuations and noise of hot carriers in semiconductor materials and devices". *IEEE Trans. Electron Devices*, Vol. 41, No. 11, pp. 2034–2049, 1994.

[Oh11] S. Oh and D. Wentzloff. "A step recovery diode based UWB transmitter for low-cost impulse generation". In *ICUWB*, pp. 63 –67, Sep. 2011.

[Pag58] C. H. Page. "Harmonic Generation with Ideal Rectifiers". *Proc. IRE*, Vol. 46, No. 10, pp. 1738–1740, Oct. 1958.

[Pap91] A. Papoulis. *Probability, Random Variables, and Stochastic Processes*. McGraw-Hill, 1991.

[Pas07] E. Pascual, R. Rengel, and M. Martin. "Monte Carlo analysis of tunneling and thermionic transport in a reverse biased Schottky diode". In *Spanish Conference on Electron Devices*, pp. 108–111, Jan. 2007.

[Pea11] J. C. Pearson, B. J. Drouin, A. Maestrini, M. I., J. Ward, R. H. Lin, S. Yu, J. J. Gill, B. Thomas, C. Lee, G. Chattopadhyay, E. Schlecht, F. W. Maiwald, P. F. Goldsmith, and P. Siegel. "Demonstration of a room temperature 2.48–2.75 THz coherent spectroscopy source". *Rev. Sci. Instrum.*, Vol. 82, No. 9, p. 093105, Sep. 2011.

[Pen62] P. Penfield and R. Rafuse. *Varactor applications*. MIT Press, Cambridge, MA, 1962.

[Per00] S. Pérez, T. González, S. L. Delage, and J. Obregon. "Microscopic analysis of generation-recombination noise in semiconductors under dc and time-varying electric fields". *J. Appl. Phys.*, Vol. 88, No. 2, pp. 800–807, 2000.

[Per04a] S. Pérez, T. González, P. Shiktorov, E. Starikov, V. Gruzhinskis, L. Reggiani, L. Varani, and J. C. Vaissiere. "Noise in Schottky-barrier diodes: from static to large-signal operation". *Proc. SPIE*, Vol. 5470, 2004.

[Per04b] D. Persano, M. Zarcone, G. Ferrante, P. Shiktorov, E. Starikov, V. Gruzinskis, S. Pérez, T. González, L. Reggiani, L. Varani, and J. C. Vaissiere. "Monte Carlo simulation of high-order harmonic generation in bulk semiconductors and submicron structures". *Physica Status Solidi (c)*, Vol. 1, No. 6, pp. 1367–1376, 2004.

[Per05] S. Pérez and T. González. "Current noise spectra of Schottky barrier diodes with electron traps in the active layer". *J. Appl. Phys.*, Vol. 97, No. 7, p. 073708, 2005.

[Per08] J. V. S. Pérez. *Design and Optimization of Frequency Multipliers and Mixers at Millimeter and Submillimeter-Wave Bands*. Tesis Doctoral, Technical University of Madrid, Madrid, Spain, 2008.

[Per13] C. Pérez-Moreno, J. Grajal, and D. Pardo. "Electro-thermal modelling for millimeter-wave circuit design". In *Proc. 38th Int. Conf. Infrared, Millimeter and Terahertz Waves*, pp. 1–2, Sep. 2013.

[Pey13] E. Peytavit, P. Latzel, F. Pavanello, G. Ducournau, and J.-F. Lampin. "CW Source Based on Photomixing With Output Power Reaching 1.8 mW at 250 GHz". *IEEE Electron Device Lett.*, Vol. 34, No. 10, pp. 1277–1279, Oct. 2013.

[Poo69] H. Poon and H. Gummel. "Modeling of emitter capacitance". *Proc. IEEE*, Vol. 57, No. 12, pp. 2181–2182, Dec. 1969.

[Por07] D. Porterfield. "High-Efficiency Terahertz Frequency Triplers". In *IEEE MTT-S Int. Microw. Symp. Dig.*, pp. 337–340, 2007.

[Rad07] V. Radisic, X. Mei, W. Deal, W. Yoshida, P. H. Liu, J. Uyeda, M. Barsky, L. Samoska, A. Fung, T. Gaier, and R. Lai. "Demonstration of Sub-Millimeter Wave Fundamental Oscillators Using 35-nm InP HEMT Technology". *IEEE Microw. Compon. Lett.*, Vol. 17, No. 3, pp. 223–225, Mar. 2007.

[Rai92] A. Raisanen. "Frequency multipliers for millimeter and submillimeter wavelengths". *Proc. IEEE*, Vol. 80, pp. 1842–1852, Nov. 1992.

[Red06] A. Redo-Sanchez, N. Karpowicz, J. Xu, and X.-C. Zhang. "Damage and defect inspection with terahertz waves". In *Proc. 4th International Workshop on Ultrasonic and Advanced Methods for Nondestructive Testing and Material Characterization*, 2006.

[Ree12] T. B. Reed, M. J. W. Rodwell, Z. Griffith, P. Rowell, M. Field, and M. Urteaga. "A 58.4 mW solid-state power amplifier at 220 GHz using InP HBTs". In *IEEE MTT-S Int. Microw. Symp. Dig.*, pp. 1–3, Jun. 2012.

[Ree68] H. D. Rees. "Calculation of steady state distribution function by exploiting stability". *Phys. Lett.*, Vol. 26A, 1968.

[Reg87] L. Reggiani, P. Lugli, and V. Mitin. "Monte Carlo algorithm for generation-recombination noise in semiconductors". *Appl. Phys. Lett.*, Vol. 51, No. 12, pp. 925–927, 1987.

[Reg90] L. Reggiani, T. Kuhn, L. Varani, D. Gasquet, J. C. Vaissiere, and J. P. Nougier. "A Monte Carlo simulator including generation recombination processes". In *20th European Solid State Device Research Conference, 1990. ESSDERC '90.*, pp. 489–492, Sep. 1990.

[Reg92] L. Reggiani, K. T., and L. Varani. "Noise and correlation functions of hot carriers in semiconductors". *Appl. Phys. A.*, Vol. 54, 1992.

[Ren08] C. Renaud, L. Ponnampalam, F. Pozzi, E. Rouvalis, D. Moodie, M. Robertson, and A. Seeds. "Photonically enabled communication systems beyond 1000 GHz". In *International topical meeting on microwave photonics, 2008, jointly held with the 2008 asia-pacific microwave photonics conference. mwp/apmp 2008.*, pp. 55–58, Sep. 2008.

[Rho88] E. H. Rhoderick and R. H. Williams. *Metal-semiconductor contacts*. Clarendon Press, Oxford, U.K., 2nd Ed., 1988.

[Ric07] P. Richards. "Cosmic Microwave Background experiments - past, present and future". In *Proc. Joint 32nd Int. Infrared Millimeter-Waves Conf. /15th Int. Terahertz Elect. Conf.*, pp. 12–15, Sep. 2007.

[Ruc70] J. G. Ruch and W. Fawcett. "Temperature Dependence of the Transport Properties of Gallium Arsenide Determined by a Monte Carlo Method". *J. Appl. Phys.*, Vol. 41, No. 9, pp. 3843–3849, 1970.

[Sal70] A. A. M. M. Saleh. *Theory of resistive mixers*. Tesis Doctoral, Massachusetts Institute of Technology, 1970.

[Sam08] L. Samoska, W. Deal, G. Chattopadhyay, D. Pukala, A. Fung, T. Gaier, M. Soria, V. Radisic, X. Mei, and R. Lai. "A Submillimeter-Wave HEMT Amplifier Module With Integrated Waveguide Transitions Operating Above 300 GHz". *IEEE Trans. Microw. Theory Techn.*, Vol. 56, No. 6, pp. 1380–1388, Jun. 2008.

[Sam11] L. Samoska. "An Overview of Solid-State Integrated Circuit Amplifiers in the Submillimeter-Wave and THz Regime". *IEEE Trans. THz Sci. Technol.*, Vol. 1, No. 1, pp. 9–24, Sep. 2011.

[San01] J. E. Sánchez, G. Bosman, and M. E. Law. "Device simulation of generation-recombination noise under periodic large-signal conditions". In *Proc. IEDM Technical Digest Electron Devices Meeting Int*, 2001.

[San89] P. Sandborn, A. Rao, and P. Blakey. "An assessment of approximate nonstationary charge transport models used for GaAs device modeling". *IEEE Trans. Electron Devices*, Vol. 36, pp. 1244–1253, Jul. 1989.

[San94] T. G. Sánchez. *Análisis del ruido electrónico en materiales y dispositivos semiconductores ununipolar mediante el método de Monte Carlo*. Tesis Doctoral, Universidad de Salamanca, Salamanca, 1994.

[Sch01a] E. Schlecht, G. Chattopadhyay, A. Maestrini, D. Pukala, J. Gill, S. Martin, F. Maiwald, and I. Mehdi. "A High-Power Wideband Cryogenic 200 GHz Schottky Substrateless Multiplier: Modeling, Design and Results". In *Proc. 9th. Int. Conf. Terahertz Electronics*, Charlottesvile, VA, 2001.

[Sch01b] E. Schlecht, F. Maiwald, G. Chattopadhyay, S. Martin, and I. Mehdi. "Design Considerations for Heavily-doped Cryogenic Schottky Diode Varactor Multipliers". In *Proc. 12th Int. Symp. Space Terahertz Tech.*, San Diego, CA, Feb. 2001.

[Sch02] E. T. Schlecht, G. Chattopadhyay, A. Maestrini, D. Pukala, J. Gill, and I. Mehdi. "Harmonic balance optimization of terahertz Schottky diode multipliers using an advanced device mode". In *Proc. 13th Int. Symp. Space Terahertz Tech.*, Cambridge, Massachusetts, Mar. 2002.

[Sch03] E. Schlecht, J. Gill, P. Siegel, J. Oswald, and I. Mehdi. "Novel Designs for Submillimeter Subharmonic and Fundamental Schottky Mixers". In C. Walker and J. Payne, Eds., *Proc. 14th Int. Symp. Space Terahertz Tech.*, p. 118, Abr. 2003.

[Sch05] F. Schwierz. "An electron mobility model for wurtzite GaN". *Solid-State Electronics*, Vol. 49, No. 6, pp. 889 – 895, 2005.

[Sch07a] E. Schlecht, J. Gill, R. Dengler, R. Lin, R. Tsang, and I. Mehdi. "First Wideband 520-590 GHz Balanced Fundamental Schottky Mixer". In *Proc. 18st Int. Symp. Space Terahertz Tech.*, California, USA, Mar. 2007.

[Sch07b] E. Schlecht, J. Gill, R. Dengler, R. Lin, R. Tsang, and I. Mehdi. "A Unique 520-590 GHz Biased Subharmonically-Pumped Schottky Mixer". *IEEE Microw. Wireless Compon. Lett.*, Vol. 17, No. 12, pp. 879–881, 2007.

[Sch10] E. Schlecht, J. Gill, R. Lin, R. Dengler, and I. Mehdi. "A 520-590 GHz Crossbar Balanced Fundamental Schottky Mixer". *IEEE Microw. Wireless Compon. Lett.*, Vol. 20, No. 7, pp. 387–389, 2010.

[Sch38] W. Schottky. "Halbleitertheorie der Sperrschicht". *Naturwissenschaften*, Vol. 26, No. 52, pp. 843–843, 1938.

[Sch95] W. L. Schroeder and I. Wolff. "Monte-Carlo study of high-frequency, large-signal transport parameters for physics based device simulation". *IEEE Trans. Electron Devices*, Vol. 42, pp. 819–827, May. 1995.

[Sch98] E. Schöll. *Theory of Transport Properties of Semiconductor Nanostructures*. Springer, 1998.

[Sec13] C. Seco, V. López, G. Arauz, A. Redo, J. Palacios, and J. Tejada. "Goya's artwork imaging with Terahertz waves". *ArXiv e-prints*, May. 2013.

[Sel84] S. Selberherr. *Analysis and Simulation of Semiconductor Devices*. Springer-Verlag, New York, 1984.

[Sem00] A. Semenov, H.-W. Hübers, J. Schubert, G. Gol'tsman, A. Elantiev, B. Voronov, and E. Gershenzon. "Frequency Dependent Noise Temperature of the Lattice Cooled Hot-Electron Terahertz Mixer". In *Proc. 11th Int. Symp. Space Terahertz Tech.*, pp. 39–48, Ann Arbor, MI,, May. 2000.

[Seo11] M. Seo, M. Urteaga, J. Hacker, A. Young, Z. Griffith, V. Jain, R. Pierson, P. Rowell, A. Skalare, A. Peralta, R. Lin, D. Pukala, and M. Rodwell. "InP HBT IC Technology for Terahertz Frequencies: Fundamental Oscillators Up to 0.57 THz". *IEEE J. Solid-State Circuits*, Vol. 46, No. 10, pp. 2203–2214, Oct. 2011.

[Shi00] P. Shiktorov, E. Starikov, V. Gruzinskis, T. González, J. Mateos, D. Pardo, L. Reggiani, L. Varani, and J. Vaissiere. "Langevin forces and generalized transfer fields for noise modeling in deep submicron devices". *IEEE Trans. Electron Devices*, Vol. 47, No. 10, pp. 1992–1998, Oct. 2000.

[Shi02] P. Shiktorov, E. Starikov, V. Gruzinskis, L. Reggiani, L. Varani, and J. C. VaissiÃĺre. "Monte Carlo calculation of electronic noise under high-order harmonic generation". *Appl. Phys. Lett.*, Vol. 80, No. 25, pp. 4759–4761, 2002.

[Shi03a] P. Shiktorov, E. Starikov, V. Gruzinskis, S. Pérez, T. González, L. Reggiani, L. Varani, and J. C. Vaissière. "Monte Carlo simulation of threshold bandwidth for high-order harmonic extraction". *IEEE Trans. Electron Devices*, Vol. 50, No. 5, pp. 1171–1178, 2003.

[Shi03b] P. Shiktorov, E. Starikov, V. Gruzinskis, S. Pérez, T. González, L. Reggiani, L. Varani, and J. C. Vaissiere. "Upconverson of partition noise in semiconductors operating under periodic large-signal conditions". *Phys. Rev. B*, Vol. 67, 2003.

[Shi04] P. Shiktorov, E. Starikov, V. Gruzinskis, S. Perez, T. Gonzalez, L. Reggiani, L. Varani, and J. Vaissiere. "Monte Carlo simulation of Schottky diodes operating under terahertz cyclostationary conditions". *IEEE Electron Device Lett.*, Vol. 25, pp. 1–3, Jan. 2004.

[Shi05] P. Shiktorov, E. Starikov, V. Gruzinskis, L. Reggiani, L. Varani, and J. C. Vaissiere. "Analytical model of high-frequency noise spectrum in Schottky-barrier diodes". *IEEE Electron Device Lett.*, Vol. 26, No. 1, pp. 2–4, 2005.

[Shi06] P. Shiktorov, E. Starikov, V. Gruzinskis, S. Pérez, T. González, L. Reggiani, L. Varani, and J. C. Vaissière. "Theoretical investigation of Schottky-barrier diode noise performance in external resonant circuits". *Semicond. Sci. Technol.*, Vol. 21, No. 4, p. 550, 2006.

[Shi07] S. Shitov, O. Koryukin, Y. Uzawa, T. Noguchi, A. Uvarov, M. Bukovski, and I. Cohn. "Design of Balanced Mixers for ALMA Band-10". *IEEE Trans. Appl. Supercond.*, Vol. 17, No. 2, pp. 347–350, Jun. 2007.

[Shi12] S. Shiba, Y. Irimajiri, T. Yamakura, H. Maezawa, N. Sekine, I. Hosako, and S. Yamamoto. "3.1-THz Heterodyne Receiver Using an NbTiN Hot-Electron Bolometer Mixer and a Quantum Cascade Laser". *IEEE Trans. THz Sci. Technol.*, Vol. 2, No. 1, pp. 22–28, Jan. 2012.

[Shi99] P. Shiktorov, E. Starikov, V. Gruzinskis, T. Gonzalez, J. Mateos, D. Pardo, L. Reggiani, L. Varani, J. Vaissiere, and J.-P. Nougier. "Spatiotemporal correlation of conduction current fluctuations within a hydrodynamic-Langevin scheme". *Appl. Phys. Lett.*, Vol. 74, No. 5, pp. 723–725, Feb. 1999.

[Sie02] P. H. Siegel. "Terahertz technology". *IEEE Trans. Microw. Theory Techn.*, Vol. 50, pp. 910–928, Mar. 2002.

[Sie04] P. Siegel. "Terahertz technology in biology and medicine". *IEEE Trans. Microw. Theory Techn.*, Vol. 52, No. 10, pp. 2438–2447, Oct. 2004.

[Sie07] P. Siegel. "THz Instruments for Space". *IEEE Trans. Antennas Propag.*, Vol. 55, pp. 2957–2965, Nov. 2007.

[Sie84] P. Siegel and A. Kerr. "The Measured and Computed Performance of a 140–220 GHz Schottky Diode Mixer". *IEEE Trans. Microw. Theory Techn.*, Vol. 32, No. 12, pp. 1579–1590, 1984.

[Sie93] P. Siegel, R. Dengler, I. Mehdi, J. Oswald, W. Bishop, T. Crowe, and R. Mattauch. "Measurements on a 215-GHz subharmonically pumped waveguide mixer using planar back-to-back air-bridge Schottky diodes". *IEEE Trans. Microw. Theory Techn.*, Vol. 41, No. 11, pp. 1913–1921, 1993.

[Sie98] P. Siegel, I. Mehdi, R. Dengler, T.-H. Lee, D. A. Humphrey, A. Pease, R. Zimmermann, and P. Zimmermann. "A 640 GHz planar-diode fundamental mixer/receiver". In *IEEE MTT-S Int. Microw. Symp. Dig.*, pp. 407–410, 1998.

[Sie99] P. H. Siegel, R. P. Smith, M. C. Graidis, and S. C. Martin. "2.5 THz GaAs monolithic membrane-diode mixer". *IEEE Trans. Microw. Theory Techn.*, Vol. 47, pp. 596–604, May. 1999.

[Sil08] J. V. Siles and J. Grajal. "Capabilities of GaN Schottky Multipliers for LO Power Generation at Millimeter-Wave Bands". In *Proc. 9th Int. Symp. Space Terahertz Tech.*, p. 504, Abr. 2008.

[Sil09] J. Siles, J. Grajal, and A. Di Carlo. "Design of Submillimeter Schottky Mixers Under Flat-Band Conditions Using an Improved Drift-Diffusion Model". *IEEE Microw. Compon. Lett.*, Vol. 19, No. 3, pp. 167–169, 2009.

[Sil10] J. V. Siles and J. Grajal. "Physics-Based Design and Optimization of Schottky Diode Frequency Multipliers for Terahertz Applications". *IEEE Trans. Microw. Theory Techn.*, Vol. 58, pp. 1933–1942, Jul. 2010.

[Sim93] A. Simon, A. Grub, V. Krozer, K. Beilenhoff, and H. Hartnagel. "Planar THz Schottky diode based on quasi vertial diode structure". In *Proc. 4th Int. Symp. Space Terahertz Tech.*, 1993.

[Sob11] P. Sobis. *Advanced Schottky Diode Receiver Front-ends for Terahertz Applications*. Tesis Doctoral, Chalmers University of Technology, 2011.

[Spa68] A. Y. Spasov. "Forced oscillations in an oscillating circuit utilising nonlinear capacitance". *Electron. Lett.*, Vol. 4, No. 17, pp. 365–366, 1968.

[Sta05] E. Starikov, P. Shiktorov, V. Gruinskis, L. Varani, J. C. Vaissière, C. Palermo, and L. Reggiani. "Monte Carlo calculations of static and dynamic electron transport in nitrides". *J. Appl. Phys.*, Vol. 98, No. 8, 2005.

[Sta06] J. Stake, T. Bryllert, T. A. Emadi, M. Sadeghi, and J. Vukusic. "High efficiency HBV multipliers". *Proc. 1st European Microwave Integrated Circuits Conference*, pp. 39–42, 2006.

[Sta98] E. Starikov, P. Shiktorov, V. Gruzinskis, L. Varani, J. Vaissiere, J.-P. Nougier, T. Gonzalez, J. Mateos, D. Pardo, and L. Reggiani. "Transfer impedance calculations of electronic noise in two-terminal semiconductor structures". *J. Appl. Phys.*, Vol. 83, No. 4, pp. 2052–2066, Feb. 1998.

[Ste94] M. A. Stettler and M. Lundstrom. "A detailed investigation of heterojunction transport using a rigorous solution to the Boltzmann equation". *IEEE Trans. Electron Devices*, Vol. 41, No. 4, pp. 592–600, Apr 1994.

[Str62] R. Stratton. "Diffusion of Hot and Cold Electrons in Semiconductor Barriers". *Phys. Rev.*, Vol. 126, pp. 2002–2014, Jun 1962.

[Sua06] A. Suárez and R. Melville. "Simulation-assisted design and analysis of varactor-based frequency multipliers and dividers". *IEEE Trans. Microw. Theory Techn.*, Vol. 54, No. 3, pp. 1166–1179, Mar. 2006.

[Sze07] S. M. Sze. *Physics of semiconductor devices*. John Wiley and Sons, third edition Ed., 2007.

[Tan12] A. Y. Tang, E. Schlecht, R. Lin, G. Chattopadhyay, C. Lee, J. Gill, I. Mehdi, and J. Stake. "Electro-Thermal Model for Multi-Anode Schottky Diode Multipliers". *IEEE Trans. THz Sci. Technol.*, Vol. 2, No. 3, pp. 290–298, 2012.

[Tay11] Z. Taylor, R. Singh, D. Bennett, P. Tewari, C. Kealey, N. Bajwa, M. Culjat, A. Stojadinovic, H. Lee, J. Hubschman, E. Brown, and W. Grundfest. "THz Medical Imaging: in vivo Hydration Sensing". *IEEE Trans. THz Sci. Technol.*, Vol. 1, No. 1, pp. 201–219, Sep. 2011.

[Tho04] B. Thomas. *Etude et réalisation d'une tête de réception hétérodyne en ondes submillimétriques pour l'étude des atmosphères et surfaces de planètes*. Tesis Doctoral, Laboratoire d'Etude du Rayonnement et de la Matière en Astrophysique, Observatoire de Paris, Dec. 2004.

[Tho05] B. Thomas, A. Maestrini, and G. Beaudin. "A low-noise fixed-tuned 300-360 GHz subharmonic mixer using planar Schottky diodes". *IEEE Microw. Wireless Compon. Lett.*, Vol. 15, No. 12, pp. 865–867, 2005.

[Tho08a] B. Thomas, B. Alderman, D. Matheson, and P. de Maagt. "A Combined 380 GHz Mixer/Doubler Circuit Based on Planar Schottky Diodes". *IEEE Microw. Wireless Compon. Lett.*, Vol. 18, No. 5, pp. 353–355, 2008.

[Tho08b] B. Thomas, A. Maestrini, D. Matheson, I. Mehdi, and P. de Maagt. "Design of an 874 GHz biasable sub-harmonic mixer based on MMIC membrane planar Schottky diodes". In *Proc. 33rd Int. Conf. Infrared, Millimeter, and Terahertz Waves*, pp. 1 –2, Sep. 2008.

[Tho09] B. Thomas, S. Rea, B. Moyna, B. Alderman, and D. Matheson. "A 320-360 GHz Subharmonically Pumped Image Rejection Mixer Using Planar Schottky Diodes". *IEEE Microw. Wireless Compon. Lett.*, Vol. 19, No. 2, pp. 101–103, 2009.

[Tho10a] B. Thomas, J. Gill, A. Maestrini, C. Lee, R. Lin, S. Sin, A. Peralta, and I. Mehdi. "An integrated 520-600 GHz sub-harmonic mixer and tripler combination based on GaAs MMIC membrane planar Schottky diodes". In *Proc. 35th Int. Conf. Infrared, Millimeter and Terahertz Waves*, pp. 1–2, Rome, Italy, 2010.

[Tho10b] B. Thomas, A. Maestrini, J. Gill, C. Lee, R. Lin, I. Mehdi, and P. de Maagt. "An 874 GHz fundamental balanced mixer based on MMIC membrane planar Schottky diodes". In *Proc. 21st Int. Symp. Space Terahertz Tech.*, Oxford, UK, Mar. 2010.

[Tho10c] B. Thomas, A. Maestrini, J. Gill, C. Lee, R. Lin, I. Mehdi, and P. de Maagt. "A Broadband 835-900 GHz Fundamental Balanced Mixer Based on Monolithic GaAs Membrane Schottky Diodes". *IEEE Trans. Microw. Theory Techn.*, Vol. 58, No. 7, pp. 1917–1924, 2010.

[Tho11] B. Thomas, J. Siles, J. Gill, C. Lee, K. Cooper, A. Maestrini, S. Gulkis, and I. Mehdi. "560 GHz, 664 GHz and 1.2 THz Schottky Based MMIC Sub-Harmonic Mixers for Planetary Atmospheric Remote Sensing and FMCW radar". In *Proc. 22rd Int. Symp. Space Terahertz Tech.*, pp. 139–142, Tucson, AZ, Apr. 2011.

[Tho12] B. Thomas, J. Siles, E. Schlecht, A. Maestrini, G. Chattopadhyay, C. Lee, C. Jung, I. Mehdi, and S. Gulkis. "First results of a 1.2 THz MMIC sub-harmonic mixer based GaAs Schottky diodes for planetary atmospheric remote sensing". In *Proc. 23rd Int. Symp. Space Terahertz Tech.*, Tokio, Japan, Apr. 2012.

[Tom93] K. Tomizawa. *Numerical Simulation of Submicron Semiconductor Devices*. Artech House, 1993.

[Ton07] M. Tonouchi. "Cutting-edge terahertz technology". *Nat. Photonics*, Vol. 1, pp. 97–105, 2007.

[Tre09] J. Treuttel, B. Thomas, A. Maestrini, H. Wang, B. Alderman, J. Siles, S. Davis, and T. Narhi. "A 380 GHz sub-harmonic mixer using MMIC foundry based Schottky diodes transferred onto quartz substrate". In *Proc. 20th Int. Symp. Space Terahertz Tech.*, Charlottesville, Virginia, Apr. 2009.

[Tri86] M. Trippe, G. Bosman, and A. van der Ziel. "Transit-Time Effects in the Noise of Schottky-Barrier Diodes". *IEEE Trans. Microw. Theory Techn.*, Vol. 34, No. 11, pp. 1183–1192, 1986.

[Unit] "United Monolithic Semiconductor". http://www.ums-gaas.com/.

[Var94] L. Varani, L. Reggiani, T. Kuhn, T. González, and D. Pardo. "Microscopic simulation of electronic noise in semiconductor materials and devices". *IEEE Trans. Electron Devices*, Vol. 41, No. 11, pp. 1916–1925, 1994.

[Virg] "Virginia Diodes Inc". http://www.virginiadiodes.com.

[Vli71] K. M. van Vliet. "Markov approach to density fluctuations due to transport and scattering. II applications". *J. Math. Phys.*, Vol. 12, No. 9, pp. 1998–2012, 1971.

[Vli75] K. M. van Vliet, A. Friedmann, R. J. J. Zijlstra, A. Gisolf, and A. van der Ziel. "Noise in single injection diodes. II. Applications". *J. Appl. Phys.*, Vol. 46, No. 4, pp. 1814–1823, 1975.

[Vli91] C. M. V. Vliet. "A survey of results and future prospects on quantum 1ÆŠf noise and 1ÆŠf noise in general". *Solid-State Electronics*, Vol. 34, No. 1, pp. 1 – 21, 1991.

[Vuk12] J. Vukusic, T. Bryllert, Ø. Olsen, J. Hanning, and J. Stake. "Monolithic HBV-Based 282-GHz Tripler With 31-mW Output Power". *IEEE Electron Device Lett.*, Vol. 33, No. 6, pp. 800–802, Jun. 2012.

[Wad09] A. Wade, G. Fedorov, D. Smirnov, S. Kumar, B. S. Williams, Q. Hu, and J. L. Reno. "Magnetic-field-assisted terahertz quantum cascade laser operating up to 225 K". *Nat. Photonics*, Vol. 3, 2009.

[Wan08] H. Wang, A. Maestrini, B. Thomas, B. Alderman, and G. Beaudin. "Development of a Two-Pixel Integrated Heterodyne Schottky Diode Receiver at 183 GHz". In *Proc. 19th Int. Symp. Space Terahertz Tech.*, Groningen, The Netherlands, Apr. 2008.

[Wan96] L. Wang, M. Nathan, T. H. Lim, M. Khan, and Q. Chen. "High barrier height GaN Schottky diodes: Pt/GaN and Pd/GaN". *Appl. Phys. Lett.*, Vol. 68, No. 9, pp. 1267–1269, Feb. 1996.

[War03] J. Ward, F. Maiwald, G. Chattopadhyay, E. Schlecht, A. Maestrini, J. Gill, and I. Mehdi. "1400-1900 GHz Local Oscillators for the Herschel Space Observatory". In *Proc. 14th Int. Symp. Space Terahertz Tech.*, p. 94, Tucson, Arizona, Abr. 2003.

[War04] J. Ward, E. Schlecht, G. Chattopadhyay, A. Maestrini, J. Gill, F. Maiwald, H. Javadi, and I. Mehdi. "Capability of THz sources based on Schottky diode frequency multiplier chains". In *IEEE MTT-S Int. Microw. Symp. Dig.*, pp. 1587–1590, Jun. 2004.

[Wei98] N. Weimann, L. F. Eastman, D. Doppalapudi, H. M. Ng, and T. Moustakas. "Scattering of electrons at threading dislocations in GaN". *J. Appl. Phys.*, Vol. 83, No. 7, pp. 3656–3659, Apr. 1998.

[Wil06] B. Williams, S. Kumar, Q. Hu, and J. Reno. "High-power terahertz quantum-cascade lasers". *Electron. Lett.*, Vol. 42, No. 2, pp. 89–91, Jan. 2006.

[Woo09] A. Wootten and A. Thompson. "The Atacama Large Millimeter/Submillimeter Array". *Proc. IEEE*, Vol. 97, No. 8, pp. 1463–1471, Aug. 2009.

[Xia07] Q. Xiao, J. L. Hesler, T. W. Crowe, B. S. Deaver, and R. M. Weikle. "A 270-GHz Tuner-Less Heterostructure Barrier Varactor Frequency Tripler". *IEEE Microw. Compon. Lett.*, Vol. 17, No. 4, pp. 241–243, 2007.

[Yan06] Z. Yan, Y. Ying, H. Zhang, and H. Yu. "Research progress of terahertz wave technology in food inspection". In *Proc. SPIE*, Oct. 2006.

[Zha12] H. Zhao, V. Drakinskiy, P. Sobis, J. Hanning, T. Bryllert, A.-Y. Tang, and J. Stake. "Development of a 557 GHz GaAs monolithic membrane-diode mixer". In *23rd Int. Conf. on Indium Phosphide and Related Mater. (IPRM)*, pp. 102–105, 2012.

[Zhu10] A. Zhu, F. Sheng, and A. Zhang. "An implementation of step recovery diode-based UWB pulse generator". In *ICUWB*, pp. 1 –4, Sep. 2010.

[Zie70] A. Van der Ziel. *Noise; sources, characterization, measurement*. Prentice-Hall, 1970.

[Zie88] A. van der Ziel. "Unified presentation of 1/f noise in electron devices: fundamental 1/f noise sources". *Proc. IEEE*, Vol. 76, No. 3, pp. 233–258, Mar. 1988.

[Zir86] H. Zirath. "High-frequency noise and current-voltage characteristics of mm-wave platinum n-n+ GaAs Schottky barrier diodes.". *J. Appl. Phys.*, Vol. 60, No. 4, p. 1399, 1986.

[Zmu07] J. Zmuidzinas. "Technology for Submillimeter Astronomy". In *IEEE MTT-S Int. Microw. Symp. Dig.*, pp. 1861–1864, Jun. 2007.